BSPE25120-109-12

# 얼음의 미세구조 특성연구를 통한 저온 정화기술 및 환경/에너지 신소재 개발

# Investigation of ice microstructure properties for developing low-temperature purification and environment/energy materials

KOPRI
극지연구소

2026. 2. 28.

한 국 해 양 과 학 기 술 원
부 설 극 지 연 구 소

# 제 출 문

극지연구소장 귀하

본 보고서를 “얼음의 미세구조 특성연구를 통한 저온 정화기술 및 환경/에너지 신소재 개발” 과제의 최종보고서로 제출합니다.

2026. 2. 28.


연 구 책 임 자 : 김 기 태

참 여 연 구 원 : 이 준 혁, 김 한 우, 김 대 영, 이 두 형, 박 기 태, 김 보 미, 도 학 원, 이 성 구, 조 성 미, 박 지 수, 이 민 경, 이 정 은, 김 성 한, 남 성 진, 손 영 주, 강 정 호, 남 승 일, 김 옥 선, 정 현 영, 김 봄 이, Nguyen Quoc Anh, 안 용 윤, 소 정 하, 남 예 원, 김 현 철, 김 희 중, 서 민 주, 김 보 근

위탁연구기관명(책임자): 경 북 대 학 교(최 철 호), 경 북 대 학 교(박 현 웅), 한국에너지공과대학교(최 원 용), 포 항 공 과 대 학 교(박 문 정), 한 림 대 학 교(김 정 원)


KOPRI 극지연구소

# 보고서 초록

<table>
<tr><td>과제관리번호</td><td>PE25120</td><td>연구기간</td><td>2020.1.1.-2025.12.31.</td><td>단계 구분</td><td>-</td></tr>
<tr><td rowspan="2"><u>연구사업명</u></td><td>중 사 업 명</td><td colspan="4">기관목적사업(2020년 이후)</td></tr>
<tr><td>세부사업명</td><td colspan="4">기관고유사업</td></tr>
<tr><td rowspan="2">연구과제명</td><td>중 과 제 명</td><td colspan="4"></td></tr>
<tr><td>세부(단위)과제명</td><td colspan="4">얼음의 미세구조 특성연구를 통한 저온 정화기술 및 환경/에너지 신소재 개발</td></tr>
<tr><td>연구책임자</td><td>김기태</td><td>해당단계<br>참여연구원수</td><td>총 : 35 명<br>내부 : 24 명<br>외부 : 11 명</td><td>해당단계<br>연구비</td><td>정부: 2,668,700천원<br>기업: 천원<br>계: 2,668,700천원</td></tr>
<tr><td>연구기관명 및<br>소속부서명</td><td colspan="2">한국해양과학기술원 부설 극지연구소 (빙하지권연구본부)</td><td colspan="2">참여기업명</td><td></td></tr>
<tr><td>국제공동연구</td><td colspan="5">상대국명 : 일본, 체코, 미국, 스페인, 이탈리아, 스웨덴<br>상대국연구기관명 : 저온과학연구소, Masaryk대, Univ. South Florida, CSIC, CNR, 칼택, UC 어바인, 윌리엄 앤드 메리 대학교 버지니아 해양과학연구소, 예테보리대</td></tr>
<tr><td>위 탁 연 구</td><td colspan="5">연구기관명 : 경북대, 한국에너지공대, 포항공대, 한림대<br>연구책임자 : 최철호, 박현웅, 최원용, 박문정, 김정원</td></tr>
<tr><td colspan="4">요약(연구결과를 중심으로 개조식 500자이내)</td><td>보고서<br>면수</td><td>545</td></tr>
<tr><td colspan="6">· 얼음 미세구조 특성 및 제어기작 연구<br>- 물리·화학적 요인에 따른 얼음 미세구조 변화 연구<br>- 재결정화를 통한 동결농축현상 조절 및 얼음 미세구조 내 물리화학적 특성 연구<br><br>· 얼음 내 생지화학 현상 특성 연구<br>- 얼음 내 변환된 오염물질의 독성 및 환경영향 연구<br>- 얼음에서 일어나는 독특한 지구화학반응과 극지방 자연현상의 상관성 연구<br>- 얼음 내 생물의 생체분자 특성 연구 및 저온 생존전략 연구<br><br>· 저온 정화기술 및 환경/에너지 신소재 개발<br>- 동결정화기술 실용화를 위한 파일럿 스케일 테스트<br>- 얼음특성기반의 환경/에너지 신소재 특성평가 및 시제품 제작</td></tr>
<tr><td rowspan="2">색 인 어<br>(각 5개 이상)</td><td>한 글</td><td colspan="4">얼음, 미세구조, 화학반응, 할로겐, 화학적 풍화, 동결정화</td></tr>
<tr><td>영 어</td><td colspan="4">ice, microstructure, chemical reaction, halogen, chemical weathering, freezing purification</td></tr>
</table>

KOPRI 극지연구소

# 요 약 문

## Ⅰ. 제 목

얼음의 미세구조 특성연구를 통한 저온 정화기술 및 환경/에너지 신소재 개발

## Ⅱ. 연구개발의 목적 및 필요성

얼음은 지구 담수의 대부분을 차지하며 지표 환경, 물질 순환, 기후 조절 과정에서 중요한 역할을 수행한다. 얼음이 형성되는 과정에서는 표면, 결정립계, 준액체층 등 다양한 미세구조가 생성되며, 이로 인해 얼음 내에서 일어나는 화학반응은 수용액 상 반응과는 본질적으로 다른 특성을 보인다. 특히 동결 과정에서 용질이 결정립계 및 준액체층으로 농축되는 동결농축효과로 인해, 저온 환경에서도 화학 반응이 빠르게 진행되는 특이한 현상이 나타난다. 그러나 이러한 얼음 미세구조 내의 특이한 반응 환경에 관한 연구는 실험적 접근의 한계로 인해 매우 제한적으로 이루어져 왔다. 또한 얼음 미세구조 내에는 박테리아 및 미생물과 같은 생명체가 서식하며, 이들의 대사 활동은 얼음의 물성 변화와 지구 화학물질 순환에 영향을 미칠 수 있음에도 불구하고 이에 관한 체계적인 연구는 부족한 실정이다.

본 연구과제는 얼음 미세구조의 형성 및 제어 메커니즘을 규명함으로써, 얼음 내에서 일어나는 환경화학반응과 생지화학 현상을 이해하고, 저온 정화기술 및 환경·에너지 분야에 적용 가능한 신소재를 개발하는 것을 최종 목표로 하였다. 1단계에서 확보한 기초 연구 성과를 바탕으로, 2023~2025년에 수행한 2단계 연구에서는 얼음 미세구조 제어 기술의 고도화와 동결 기반 정화·소재 기술의 실증 가능성 확보에 중점을 두어 진행하였다.

## Ⅲ. 연구개발의 내용 및 범위

· 얼음 미세구조 특성 및 제어기작 연구
· 얼음 내 생지화학 현상 특성연구
· 저온 정화기술 및 환경/에너지 신소재 개발

## Ⅳ. 연구개발결과

**· 얼음 미세구조 특성 및 제어기작 연구**

- 물리·화학적 요인에 따른 얼음 미세구조 변화 연구
- 재결정화를 통한 동결농축현상 조절 및 얼음 미세구조 내 물리화학적 특성 연구

· **얼음 내 생지화학 현상 특성연구**

- 얼음 내 변환된 오염물질의 독성 및 환경영향 연구
- 얼음에서 일어나는 독특한 지구화학반응과 극지방 자연현상의 상관성 연구
- 얼음 내 생물의 생체분자 특성 연구 및 저온 생존전략 연구

· **저온 정화기술 및 환경/에너지 신소재 개발**

- 동결정화기술 실용화를 위한 파일럿 스케일 테스트
- 얼음 특성 기반의 환경/에너지 신소재 특성 평가 및 시제품 제작

## Ⅴ. 연구개발결과의 활용계획

연구를 통하여 얼음 미세구조의 특성 및 제어 방법, 화학반응에 대한 체계적인 이해를 확보하였으며, 이를 기반으로 동결농축을 이용한 저온 정화기술과 환경·에너지 신소재 개발의 실증 가능성을 제시하였다. 본 과제에서 구축한 연구 인프라와 실험 플랫폼은 향후 심화 연구 및 대형 융합 연구의 기반으로 활용될 수 있을 것이다.

또한 연구 성과는 얼음 미세구조와 화학반응에 대한 교육·연구 자료로 활용되어 얼음과학이라는 미개척 연구 분야를 선도하고, 극지 환경 및 기후변화 이해에 기여할 수 있을 것이다. 나아가 동결 기반 정화 및 소재 기술은 친환경 수처리, 저에너지 공정, 고부가가치 소재 개발 등 실용화 연구로 확장하여 산업적·사회적 활용이 가능할 것으로 기대된다.

KOPRI 극지연구소

# S U M M A R Y

## (영 문 요 약 문)

## I. Title

Investigation of ice microstructure properties for developing low-temperature purification and environment/energy materials

## II. Purpose and Necessity of R&D

Ice constitutes the majority of the Earth's freshwater resources and plays a crucial role in surface environments, material cycling, and climate regulation. During ice formation, various microstructural features—such as surfaces, grain boundaries, and quasi-liquid layers—are generated, resulting in chemical reactions within ice that are fundamentally different from those occurring in aqueous solutions. In particular, the freeze-concentration effect, in which solutes are enriched at grain boundaries and quasi-liquid layers during freezing, leads to unusually rapid chemical reactions even under low-temperature conditions.

Despite these unique reactive environments, studies on chemical reactions within ice microstructures and their environmental implications have remained extremely limited due to experimental challenges and the inherent complexity of ice systems. Moreover, ice microstructures host living organisms such as bacteria and microorganisms, whose metabolic activities can influence the physical properties of ice and global biogeochemical cycles; however, systematic investigations into these processes are still insufficient.

The ultimate goal of this research project is to elucidate the formation and control mechanisms of ice microstructures and to advance the understanding of environmental chemical and biogeochemical processes occurring within ice, thereby enabling the development of low-temperature purification technologies and novel materials applicable to environmental and energy fields. In particular, the second stage of the project (2023 - 2025) focused on advancing ice microstructure control technologies and demonstrating the feasibility of freeze-based purification and materials technologies, building upon the fundamental research outcomes achieved in the first stage.

## III. Contents and Extent of R&D

· Investigation of ice microstructure characteristics and control mechanisms

· Characterization of biogeochemical phenomena occurring within ice

· Development of low-temperature purification technologies and environmental/energy materials

## IV. R&D Results

· **Investigation of Ice Microstructure Characteristics and Control Mechanisms**

- Studies on changes in ice microstructures under varying physical and chemical conditions
- Control of freeze-concentration phenomena through recrystallization and investigation of physicochemical properties within ice microstructures

· **Characterization of Biogeochemical Phenomena within Ice**

- Evaluation of toxicity and environmental impacts of transformed contaminants within ice
- Studies on the correlation between unique geochemical reactions in ice and natural polar environmental phenomena
- Investigation of biomolecular characteristics of organisms inhabiting ice and their low-temperature survival strategies

· **Development of Low-Temperature Purification Technologies and Environmental/Energy Materials**

- Pilot-scale testing for the practical implementation of freeze crystallization technologies
- Characterization and prototyping of environmental and energy materials based on ice-specific properties

## V. Application Plans of R&D Results

Through the second of the project, a systematic understanding of ice microstructure control and ice-related chemical reactions has been established. Based on these achievements, the feasibility of low-temperature purification technologies utilizing freeze concentration, as well as the development of environmental and energy materials, has been demonstrated. The research infrastructure and experimental platforms established in this project can serve as a foundation for future advanced and large-scale interdisciplinary research.

Furthermore, the outcomes of this research can be utilized as educational and research resources on ice microstructures and chemical reactions, contributing to the advancement of ice science as an emerging research field and enhancing the understanding of polar environments and climate change. Ultimately, freeze-based purification and materials technologies are expected to be extended toward practical applications, including environmentally friendly water treatment, low-energy processes, and the development of high-value-added materials, thereby enabling broad industrial and societal utilization.

KOPRI
극지연구소

# C O N T E N T S

## (영 문 목 차)


Chapter 1. Introduction ····· 10
Section 1. Background and Necessity of R&D ····· 10
Section 2. Purpose and Scope of R&D ····· 11

Chapter 2. Current R&D Status in Korea and Other Nations ····· 13
Section 1. Study of Ice Microstructural Characterization ····· 13
Section 2. Understanding the Environmental Chemical Reactions in Ice Microstructures ····· 16
Section 3. Fundamental studies of Application Technologies Based on Low-temperature Ice Properties ····· 20
Section 4. Ice Chemistry Research Groups ····· 20

Chapter 3. R&D Implementation Contents and Results ····· 36

Section 1. Antarctic ozone hole modifies iodine geochemistry on the Antarctic Plateau ····· 36
Section 2. Freezing-Induced Simultaneous Reduction of Chromate and Production of Molecular Iodine: Mechanism, Kinetics, and Practical Implications ····· 56
Section 3. Freezing-accelerated removal of chromate by biochar synthesized from waste rice husk ····· 78
Section 4. Entangled Iodine and Hydrogen Peroxide Formation in Ice ····· 103

Section 1. Antarctic Ozone Hole Modifies Iodine Geochemistry on the Antarctic Plateau ····· 36
Section 2. Freezing-Induced Simultaneous Reduction of Chromate and Production of Molecular Iodine: Mechanism, Kinetics, and Practical Implications ····· 56
Section 3. Freezing-Accelerated Removal of Chromate by Biochar Synthesized from Waste Rice Husk ····· 78
Section 4. Entangled Iodine and Hydrogen Peroxide Formation in Ice ····· 103
Section 5. Chemical Weathering of Granite in Ice and Its Implication for Weathering in Polar Regions ····· 113
Section 6. Frozen Hydrogen Peroxide and Nitrite Solution: The Acceleration of Benzoic Acid Oxidation via the Decreased pH in Ice ····· 132
Section 7. Ten-Minute Synthesis of Highly Conductive Polymer Nanosheets on Ice Surfaces: Role of Ice Crystallinity ····· 159
Section 8. Activation of Peroxymonosulfate by Bicarbonate and Acceleration of the Reaction by Freezing ····· 176


KOPRI 극지연구소

Section 9. Proton Transport and Related Chemical Processes of Ice ····· 200
Section 10. Freezing-Enhanced Oxidation of Iodide by Hydrogen Peroxide in the Presence of Antifreeze Proteins from the Arctic Yeast Leucosporidium Sp. AY30 ····· 229
Section 11. Importance of Rigidity of Ice-Binding Protein (FfIBP) for Hyperthermal Hysteresis Activity and Microbial Survival ····· 250
Section 12. Ice-Templated Synthesis of Tungsten Oxide Nanosheets and Their Application in Arsenite Oxidation ····· 281
Section 13. Frozen Clay Minerals as a Potential Source of Bioavailable Iron and Magnetite ····· 311
Section 14. Detoxification of Arsenite by Iodide in Frozen Solution ····· 338
Section 15. Catalytic Behavior of Nitrous Acid for Acetaminophen Transformation during the Freezing Process ····· 362
Section 16. Production of Molecular Iodine via a Redox Reaction between Iodate and Organic Compounds in Ice ····· 387
Section 17. A Novel Simultaneous Abatement of Bromate and Diphenyl Phosphate Using the Freezing Process ····· 407
Section 18. Cryoprotective Polyol-Induced Ice Microstructure Development and Enhanced Chromium(VI) Reduction in Polycrystalline Structures ····· 431
Section 19. Freezing-Enhanced Degradation of Azo Dyes in the Chloride-Peroxymonosulfate System ····· 454
Section 20. Crystallization Mechanisms of Porous and Compact Amorphous Solid Water Films · 480
Section 21. Bromide Oxidation by Bromate in a Frozen Solution and Reactive Bromine Species Production ····· 499

Chapter 4. Degree of R&D Goal Achievement and Degree of Contribution to Outside Research Institute ····· 526
Section 1. Achievement of R&D Goals ····· 526
Section 2. External Contribution ····· 535

Chapter 5. Application Plans of R&D Results ····· 536

Chapter 6. Overseas Science and Technology Information Collected in the R&D Process ····· 538
Section 1. Institute of Low Temperature Science, Hokkaido University ····· 538
Section 2. Consiglio Nazionale delle Ricerche - Istituto di Scienze Polari ····· 541

KOPRI 극지연구소

# 목 차


제 1 장. 서론 ····· 10
제 1 절. 연구개발의 배경 및 필요성 ····· 10
제 2 절. 연구개발의 목적 및 범위 ····· 11

제 2 장. 국내외 기술개발 현황 ····· 13
제 1 절. 얼음 미세구조 특성 연구 ····· 13
제 2 절. 얼음 미세구조에서 일어나는 환경화학반응 이해 ····· 16
제 3 절. 저온응용기술 기초 연구 ····· 20
제 4 절. 얼음화학 연구 그룹 ····· 20

제 3 장. 연구개발수행 내용 및 결과 ····· 36
제 1 절. 남극 오존홀에 의한 남극고원의 요오드 지구화학거동 변동연구 ····· 36
제 2 절. 동결을 이용한 독성크롬 제거 및 유용 요오드 회수 연구 ····· 56
제 3 절. 바이오촤와 동결을 이용한 크롬 중금속 제거에 관한 연구 ····· 78
제 4 절. 얼음내 요오드에 의한 과산화수소 생성기작 연구 ····· 103
제 5 절. 얼음에서 일어나는 화강암의 화학적 풍화작용과 극지방 풍화작용에 대한 영향 ····· 113
제 6 절. 동결된 과산화수소와 아질산염 용액: 얼음 내 pH 감소에 따른 벤조산 산화 가속화 ····· 132
제 7 절. 얼음 표면특성을 이용한 고전도성 고분자 나노시트의 10분 합성법 연구: 얼음 결정성의 역할 ····· 159
제 8 절. 중탄산염에 의한 과산화일황산염의 활성화와 동결에 의한 반응속도의 가속화 연구 ····· 176
제 9 절. 얼음내 양성자 이동 및 관련된 화학적 과정 ····· 200
제 10 절. 북극 효모 유래 Leucosporidium sp. AY30 동결 방지 단백질 (LeIBP) 존재 하에서 동결시 나타나는 과산화수소에 의한 요오드 이온 산화 반응 촉진 연구 ····· 229
제 11 절. 고활성 및 미생물 생존을 위한 결빙방지 단백질(FfIBP)의 강성의 중요성 ····· 250
제 12 절. 얼음템플릿을 이용한 산화텅스텐 나노시트합성 및 비소 산화에의 응용 ····· 281
제 13 절. 생물이용가능 철과 자철석의 잠재적 공급원으로서의 점토광물 동결 연구 ····· 311
제 14 절. 동결 중 요오드에 의한 비소의 독성제거 ····· 338
제 15 절. 동결 중 아질산의 촉매거동에 의한 아세트아미노펜 화학 변환 ····· 362
제 16 절. 얼음 내 아이오데이트와 유기 분자체 사이의 환원 반응을 통한 요오드 분자의 생성 ····· 387
제 17 절. 브롬산과 유기인산을 동시처리하는 새로운 동결수처리기술 ····· 407
제 18 절. 동결방지 폴리올에 의한 얼음 미세구조 조절과 다결정 얼음에서의 6가 크롬 환원 반응 연구 ····· 431
제 19 절. 염화물-과황산염 시스템에서 아조염료의 동결 분해 ····· 454
제 20 절. 다공성 및 비다공성 비결정성 얼음 박막의 결정화 기작 연구 ····· 480

제 21 절. 동결 중 브롬산에의한 브롬 산화와 이로 인한 활성브롬종 발생 ····· 499

제 4 장. 연구개발목표 달성도 및 대외기여도 ····· 526
제 1 절. 연구개발목표 달성도 ····· 526
제 2 절. 대외 기여도 ····· 535

제 5 장. 연구개발결과의 활용계획 ····· 536

제 6 장. 연구개발과정에서 수집한 해외과학기술정보 ····· 538
제 1 절. 일본 홋카이도 대학교 저온과학연구소 ····· 538
제 2 절. 이탈리아 CNR-ISP ····· 541

KOPRI
극지연구소

# 제 1 장

# 서 론

김기태

한국해양과학기술원 부설 극지연구소

## 제 1 절. 연구개발의 배경 및 필요성

얼음은 물이 고체 상태로 응고된 단순한 물질로 인식되기 쉽지만, 물과는 다른 특성이 많이 있으며, 또한 지구환경과 자연현상 전반에 걸쳐 매우 중요한 역할을 수행한다. 극지방의 빙하와 해빙은 지구 담수의 대부분을 저장하고 있으며, 지표면의 상당 부분을 덮음으로써 태양 복사 에너지의 흡수와 반사를 조절하고 지구 열평형 유지에 기여한다. 또한 대기 중에서도 수증기의 응결과 동결을 통해 얼음 입자가 형성되며, 이 과정에서 다양한 물리·화학적 상호작용이 일어나 구름 형성, 강수, 대기 화학 반응 등 여러 자연현상을 유발한다. 특히 남극 성층권 구름 내 얼음 입자 표면에서 촉진되는 할로겐 화학 반응이 오존층 파괴의 주요 원인으로 작용한다는 사실은 얼음 표면 화학의 중요성을 대표적으로 보여주는 사례이다.

이처럼 지구환경에서 역할뿐 아니라, 얼음은 인간의 일상생활과 산업 활동에도 직·간접적인 영향을 미친다. 얼음의 낮은 마찰 특성은 이동과 스포츠 활동에 활용되기도 하지만, 도로 인프라 등에서는 결빙으로 인한 안전 문제를 초래하기도 한다. 또한 동결은 식품, 의약품, 생체 시료 보존에 널리 활용되고 있으나, 동결과정에서 형성되는 얼음 미세결정은 조직 손상이나 품질 저하의 원인이 되기도 한다. 이러한 상반된 특성은 얼음의 물리·화학적 성질을 정밀하게 이해하고 제어할 필요성을 시사한다.

최근에는 얼음에서 일어나는 화학 반응이 기존의 인식과 달리 매우 독특한 특성을 보인다는 사실이 주목받고 있다. 일반적으로 온도가 낮아질수록 화학 반응 속도가 감소한다는 아레니우스 이론에 따라 얼음 환경에서는 화학 반응이 거의 일어나지 않는 것으로 여겨져 왔다. 그러나 동결 과정에서 특정 반응들이 오히려 빠르게 진행되거나, 수용액 상에서는 관찰되지 않는 반응 경로가 나타난다는 연구 결과들이 지속적으로 보고되고 있다. 이러한 현상은 얼음이 단일한 고체상이 아니라, 표면, 결정립계, 준액체층 등 다양한 미세구조를 포함하고 있으며, 이들 영역에서 용질이 농축되거나 특이한 반응 환경이 형성되어 발생한다.

그럼에도 불구하고, 얼음 미세구조 내에서 일어나는 화학 반응과 물질 거동에 대한 연구는 실험적 접근의 어려움과 분석 기술의 한계로 인해 상대적으로 미진한 상태에 머물러 왔다. 기존 연구는 주로 빙하 흐름, 해빙 면적 변화, 알베도 변화 등 거시적 현상에 집중됐으며, 분자

및 미세구조 수준에서의 얼음 화학에 대한 체계적인 이해는 충분히 축적되지 못하였다. 그러나 얼음의 미세구조와 그 내부 반응을 분자 수준에서 이해하는 것은 극지 환경 변화 해석은 물론, 미래 기후 변화 예측의 정확도를 높이는 데에도 필수적인 요소로 인식되고 있다.

특히 얼음 미세구조 내에는 박테리아와 미생물 등 생명체가 서식하며, 이들의 대사 활동은 얼음의 물성 변화와 함께 탄소, 질소, 할로겐, 금속 물질 등의 지구 화학물질 순환에 영향을 미칠 수 있음이 밝혀지고 있다. 이러한 생지화학적 현상은 기존의 극지 환경 모델에서 충분히 고려되지 못한 요소로, 얼음 미세구조를 기반으로 한 체계적인 연구를 통해 극지 및 전 지구적 화학 물질 순환에 대한 이해를 보완할 필요가 있다.

더 나아가, 동결 과정에서 나타나는 동결농축효과와 특이한 화학 반응성을 응용하면, 저온 환경에서도 소량의 에너지와 시약으로 오염물질을 효과적으로 제거할 수 있는 새로운 정화 기술 개발이 가능하다. 이는 기존 고에너지 기반 수처리 공정을 대체하거나 보완할 수 있는 친환경·저에너지 정화 기술로서의 잠재력을 지닌다. 또한 얼음 표면과 준액체층은 반응 주형 또는 촉매로 작용할 수 있어, 이를 활용한 고성능 환경·에너지 신소재 및 3차원 나노구조체 합성으로의 확장 가능성도 크다.

본 연구는 이러한 배경을 바탕으로, 얼음 미세구조의 형성 및 제어 메커니즘을 더욱 정밀하게 규명하고, 얼음 내 화학·생지화학 반응을 실제 환경 및 공정에 적용할 수 있는 수준으로 확장하는 데 중점을 두었다. 이를 통해 얼음 기반 저온 정화기술과 환경·에너지 신소재 개발의 실증 가능성을 제시하고, 국내에서는 아직 연구 기반이 미약한 얼음 화학 및 미세구조 연구 분야를 선도함과 동시에 국제 연구 네트워크를 강화하여 우리나라 극지 연구의 학문적·기술적 위상을 제고하고자 하였다.

KOPRI 극지연구소

## 제 2 절. 연구개발의 목적 및 범위

“얼음의 미세구조 특성연구를 통한 저온 정화기술 및 환경·에너지 신소재 개발” 과제는 2020년부터 2025년까지 총 6년간 수행되는 중장기 연구로, 2020~2022년의 1단계와 2023~2025년의 2단계로 구성되어 있다. 본 과제의 최종 목표는 얼음의 물리적·화학적·생물학적 특성을 기초과학적으로 규명하고, 이를 바탕으로 극지 환경에서 얼음이 수행하는 역할을 이해함과 동시에 얼음 특성 기반의 저온 정화기술 및 환경·에너지 신소재를 개발하는 데 있다.

1단계 연구에서는 얼음 미세구조에 대한 기초 연구를 중심으로, 저온 환경에서 일어나는 화학 반응을 환경화학적 관점에서 이해하고, 얼음 화학 연구를 수행하기 위한 실험적·분석적 기반을 구축하는 데 중점을 두었다. 이를 위해 얼음 표면 및 준액체층과 같은 핵심 미세구조의 물리·화학적 특성을 규명하고, 동결농축효과에 의해 유도되는 특이한 화학 반응의 존재와 메커니즘을 확인하였다. 또한 극지 환경을 모사한 실험과 현장 시료 분석을 통해 얼음 내 할로겐, 금속, 유기오염물질의 거동을 조사하고, 얼음 내 생명체의 활동이 화학 물질 순환에 미치는 영향을 탐색하였다. 이와 함께 얼음의 특이한 반응 환경을 활용한 전도성 고분자 및 나노소재 합

성 가능성을 제시하고, 국내외 연구 네트워크를 구축하여 얼음 화학 연구의 학문적 기반을 확립하였다.

2단계 연구(2023~2025년)에서는 1단계에서 축적한 실험 인프라와 연구 성과를 바탕으로, 연구 범위를 물리·화학·생물 영역으로 확장하고, 얼음 미세구조의 제어 가능성을 중심으로 응용 연구를 본격화하였다. 특히 얼음 미세구조 형성 및 변화 메커니즘을 정밀하게 제어함으로써, 동결농축효과와 저온 화학 반응을 조절, 활용하는 것을 핵심 목표로 설정하였다.

이를 통해 동결 기반 오염물질 분리·정화 기술의 실증 가능성을 검증하고, 얼음 특성을 주형으로 활용한 환경·에너지 신소재 및 3차원 나노구조체 개발을 수행하였다. 또한 얼음 내 생지화학 반응과 미생물 활동을 연계하여, 극지 환경에서의 물질 순환과 자연 현상에 대한 이해를 심화하고, 실험실 규모 연구를 실제 환경 및 공정 적용으로 확장할 수 있는 기반을 마련하였다.

본 과제는 극지연구소를 중심으로 국내외 대학·연구기관·산업체와의 협력 연구 체계를 구축하여 수행되었으며, 공동연구를 통해 다양한 분야의 전문성을 융합하였다. 본 과제에서 구축된 저온 실험 장비와 분석 플랫폼은 얼음 화학뿐만 아니라 환경·재료·에너지 분야의 후속 연구에도 활용될 수 있는 공용 연구 자산으로 기능하고 있다.

이처럼 본 연구는 1단계에서 확립한 얼음 화학의 기초적 이해를 토대로, 2단계에서 얼음 미세구조 제어와 응용 기술 개발로 연구의 무게중심을 이동함으로써, 얼음 기반 저온 정화기술 및 환경·에너지 신소재 개발이라는 최종 목표를 달성하고자 하였다.

KOPRI
극지연구소

# 제 2 장

# 국내외 기술개발 현황

## 제 1 절. 얼음 미세구조 특성 연구

### 1. 얼음 표면 및 준액체층의 물리·화학적 특성 연구 동향

- 얼음에서 아질산염의 산화 반응 속도가 동결농축효과에 의해 물에서보다 10만 배 빨라짐이 보고됨. 이는 동결 과정에서 용해되어 있던 화학 물질들이 성장하는 얼음 결정에서 배제되어 (그림 1) 얼음 결정 사이 준액체층에 농축, 동결농축효과에 의해 반응 속도가 증가하기 때문임 (Takenaka *et al.* 1992).
- 지구상에 존재하는 얼음은 자연 현상에 큰 영향을 줌. 지구의 약 10%를 덮고 있는 얼음은 태양빛을 흡수, 반사하거나 융해, 응고 과정에서 지구의 열평형에 중요한 역할을 함 (Petrenko *et al.* 1999). 특히 구름, 눈과 같이 입자의 크기가 작아 표면적이 넓은 형태의 얼음은 얼음 표면의 성질에 더하여 화학 물질을 흡착, 저장, 방출하거나 화학반응이 일어나는 매질 역할을 함 (그림 2). 이러한 과정에서 얼음 입자 표면에 여러 물질이 저장된 후 이동, 방출되어 자연 현상에 영향을 줄 수 있음 (Bartels-Rausch *et al.* 2012).
- 얼음 표면이 촉매로 작용하는 광화학 반응은 오존층 파괴에 주된 역할을 하는 것으로 알려짐. 남극 성층권 구름 내 얼음입자에서 태양광에 의해 염소 라디칼이 형성되고 이 라디칼이 계절성 오존층 파괴 촉매로 작용함 (Solomon *et al.* 1986; Molina *et al.* 1987).
- 미국 오클라호마 대학교 Paul Devlin 교수 연구진은 얼음 나노입자를 형성하여 투과 적외선 분광기로 관측하는 방법을 개발하여, 오랫동안 얼음의 화학적 성질을 연구해 왔음. 초기의 대표적 연구로는 얼음 내 물 분자를 동위원소로 표지하여 관찰하는 방법으로 얼음 내 양성자의 이동이 양성자 도약과 분자 재배향 두 가지 메커니즘이 모두 작용하는 것을 분리하여 관찰하였음 (Wooldridge *et al.* 1988). 이후 얼음 내 양성자 결함 연구에 집중하여, 얼음 표면에 황화수소와 같은 화학 물질을 흡착하여 내부에 결함을 유발하며 양성자 교환을 촉진할 수 있음을 보였으며 (Devlin *et al.* 2007), 얼음 표면에 암모니아 또는 이산화황이 흡착하였을 때의 구조 또는 반응을 연구하였음 (Jagoda-Cwiklik *et al.* 2008). 또한 얼음 내 수소이온과 수산화이온의 분포 특성으로 인한 얼음 내부와 표면의 결함 밀도 차이가 대기 중 전기장을 유발하여 번개의 원인이 될 수도 있음을 제안하였음 (Devlin, 2011).
- 영국 리버풀 대학교 Andrew Hodgson 교수 그룹과 미국 캘리포니아 대학교 Miquel Salmeron 교수 그룹은 금속, 염, 산화물 등의 다양한 종류의 표면에 물 분자가 흡착하여 얼음이 될 때의 구조를 비롯한 특성을 연구하고 있음. 이들의 연구를 통해 표면의 물질 및

평면에 따라 물 분자의 흡착 특성이 변하는 복잡한 양상을 가지며, 얼음이 잘 형성되는 표면과 그렇지 않은 표면이 있음을 확인함 (Hodgson *et al.* 2009).

- 얼음의 온도가 녹는점보다 낮을 때도 얼음 표면 근처의 분자 배열이 얼음보다는 물에 가까워져 준액체층이 형성되는 현상을 표면 사전용해라고 함. 이러한 표면 준액체층의 형성은 19세기에 패러데이가 제안하였으나, 지금까지도 밝혀지지 않은 부분이 많음. 표면 준액체층의 깊이를 측정하기 위하여 분광 분석, 현미경 및 탐침 연구, 이론 모델링 등 다양한 연구 방법이 사용되었으나, 방법별로 측정된 준액체층 두께에는 차이가 있고, 준액체층이 생성되는 온도에도 논란이 있음 (그림 4).
- 일본 도쿄공업대학 Tetsuo Okada 교수 연구진은 동결된 NaCl 수용액을 X-선 형광 분석법을 이용하여 다양한 이온의 농도 분포 이미지를 획득하여 이들의 준액체층 동결농축 특성을 연구하였음 (그림 5). 또한 3차원 이온 농도 분포로부터 준액체층의 구조를 제안하였음 (Tokumasu *et al.* 2016).
- 일본 홋카이도 저온연구소의 Gen Sazaki 교수 연구진은 단일 얼음 결정이 아닌 자연계의 얼음과 유사한 다결정계 얼음의 시간에 따른 미세구조의 동역학적 특성에 대하여 보고한 바 있음 (Chen *et al.* 2020). 이후 후속 연구로서 다결정계 얼음의 성장에 따라 얼음 결정 표면에서 나타나는 일시적인 불안정성을 단분자 수준에서 열역학적으로 해석하여 보고한 바 있음 (Murata *et al.* 2022).
- 미국 펜실베이니아 대학 David Goldsby 교수 연구진은 얼음의 변형행동에 따른 흐름법칙 정립을 목표로 20년 이상 얼음 고압저온 변형실험을 실시해 왔음 (그림 6). 최근 불순물을 함유한 얼음 변형실험을 실시하여 새로운 흐름법칙을 정립하였지만, 실험결과를 지구 내 극지 등에 적용하지 못하고 화성의 얼음층(South Polar Layered Deposits, SPLD) 형성을 설명함 (Qi *et al.* 2018).
- 중국과학원 Jianjun Wang 교수 연구진은 얼음 내 내입된 할로겐 원소의 농도와 종류에 따라 얼음 결정의 크기 성장이 서로 다르게 일어난다는 사실을 보고한 바 있음 (그림 7). 불순물로서 첨가된 할로겐 원소의 종류와 농도에 따라 얼음 결정 크기를 조절하여 이를 서로 다른 크기를 가지는 다공성 미세구조 탬플릿으로 활용할 수 있음을 보고함 (He *et al.* 2017).
- 선행 연구들에서 얼음 미세구조에 관한 연구가 어느 정도 진행되었음을 알 수 있으나, 규명되지 않은 부분이 여전히 있음. 얼음의 화학 반응은 얼음 결정 내부보다는 표면 또는 얼음 내부 결정 사이에 존재하는 준액체층에서 주로 일어나므로, 온도, 생성 조건, 불순물 등에 의한 표면 및 준액체층의 특성 변화를 규명하는 것은 얼음에서 일어나는 화학 반응을 이해, 예측하는 데 있어서 필수적임.

## 2. 극지유래 결빙방지단백질의 얼음결합도메인의 구조 분석 및 변형라이브러리제작

- 결빙방지단백질은 얼음결합단백질(ice-binding protein, IBP)의 한 종류로, 얼음의 하나 혹

은 그 이상의 면에 결합하는 단백질임. 얼음결정은 여러 면을 갖고 있으며, 결빙방지단백질이 그중 하나의 면에 결합하게 되면 얼음결정의 성장은 지연되고, 이 과정 동안 또 다른 결빙방지단백질이 얼음의 다른 면에 결합하도록 함으로써 얼음의 성장을 억제하며 얼음결정은 순수한 수분상태에서 넓고 평평한 디스크 형태로 형성되지만, 결빙방지단백질이 존재하면 얼음결정은 육각형 또는 피라미드 형태 등 다양하게 형성함으로써 얼음의 미세구조를 조절함.

- 부동단백질(Antifreeze protein, AFP)은 IBP의 한 종류로 남극어류에서 처음 보고되었으며, 이후 곤충의 혈액에서도 발견되었음. AFP는 얼음에 결합하여 첫 번째 형성된 얼음핵의 성장을 억제하고, 어는점을 녹는점 아래로 낮추는 기능(thermal hysteresis, TH)을 함으로써 2차적인 얼음핵(ice nuclei)이 형성되는 과정을 억제하여 최종적으로 얼음결정이 형성되기 시작하는 온도점을 낮추는 역할을 하는 것으로 보고됨. 이러한 TH활성은 영하의 온도조건에 서식하는 어류 및 곤충의 체액(body fluid)이 어는 것을 막기 위해 필요하며, 어류의 경우 약 0~-2 ℃조건에 서식하지만 육상 곤충의 경우 더 낮은 온도 (약 -20 ℃)에서 견뎌야 하므로 어는점을 2~13 ℃까지 낮출 수 있음이 보고됨 (Capicciotti *et al.* 2012).
- 결빙회피기작을 갖는 어류나 곤충과 달리, 결빙저항성을 갖는 생물에서 IBP는 낮은 TH활성을 보이지만, 결빙저항성을 갖는 생물(특히 식물)은 동결된 상태에서 일어나는 반복적인 얼음결정의 재결합과정을 통해 세포가 손상되는 얼음재결정화(ice-recrystallization) 과정에 대한 저항성을 가짐. 얼음결정이 세포 밖에 존재하더라도 얼음결정이 반복적인 재결정화 과정을 겪게 되면 세포에 물리적 손상을 주게 되며, 이 과정을 통해 식물세포는 건조와 병원균 감염의 조건에 노출됨. 결빙방지단백질은 IRI 활성을 갖는 단백질을 지칭하며, 세포 내·외부에 존재하는 얼음결정이 반복적으로 재결정화되는 과정을 억제하고 이미 형성된 얼음핵의 크기를 작게 유지함으로써 세포의 손상을 줄이는 역할을 함 (Bar Dolev *et al.* 2016, 그림 8).
- 결빙방지단백질을 동결보존 및 냉동식품(cryopreservation and frozen food)에 응용하려는 시도가 있음. 높은 TH활성을 갖는 AFP가 세포 동결보존의 첨가제로 연구됐으나 AFP의 농도, 추가적인 동결보존제의 첨가 여부, 세포의 종류 및 냉동-해동 방법 등에 따라 세포를 보호하기도 하고 혹은 세포를 더욱 손상하기도 하는 매우 대조적인 연구 결과를 보여주었음. 어류의 AFP는 높은 TH활성을 가지나 냉동 및 해동 과정 중에 바늘 모양(spicular shape)의 얼음결정을 형성함으로써 세포보호에 부정적 영향을 미치는 것으로 보고되어 있어, 새로운 결빙방지단백질의 탐색이 요구됨.
- 냉동식품 산업의 생산 및 운반 과정 동안에 온도 변화로 인해 냉동과 해동이 반복되어 얼음 결정이 커지면서 아이스크림, 냉동 생선 및 고기류의 질감과 식감을 떨어뜨리며 영양소를 파괴하기도 함. 최근 토마토, 딸기, 베리류 등의 조직이 연한 과일을 냉동식품으로 제작하는 과정 중에 얼음결정이 커지는 것을 방지하기 위해 식품산업 분야에서 결빙방지단백질에 주목하고 있음.
- 결빙방지단백질은 다양한 생물군에서 발견되었지만 주로 TH활성이 높은 것으로 알려져 있으며, IRI활성이 높은 단백질의 활용연구는 미비함. 본 연구팀의 선행연구를 통해 발견한

높은 IRI활성을 갖는 결빙방지단백질은 현재까지 연구된 바 없는 단백질 구조로 되어 있으며, 그 효과 또한 높아 냉동 세포의 보존제, 식품산업 분야 및 작물의 형질 개선 등에도 적용할 수 있는 신소재로 판단됨.

## 제 2 절. 얼음 미세구조에서 일어나는 환경화학반응 이해

### 1. 동결 활성화를 이용한 유/무기 오염물질 독성변화 기작 연구 동향

- 한림대학교와 극지연구소에서는 일반적인 수환경에서 존재하고 인간 산업활동에 의해 생성된 유기오염물질(푸르푸릴 알코올, 시메티딘, 트립토판, 페놀, 4-클로로페놀, 비스페놀 A)을 얼음상에서 과요오드산염($IO_4^-$)으로 산화하여 빠르게 분해하는 연구를 진행함. 일반적으로 과요오드산염($IO_4^-$)은 다당류, 알긴산염, 아미노산염, 페놀화합물 등 다양한 유기성분들의 산화에 이용되어왔음. 그러나 수처리용 화학산화제로서의 과요오드산염은 산화 반응에 비효율적인 물질로 알려져 있음. 이러한 과요오드산염의 활성을 높이기 위하여 전통적인 방법으로는 자외선이나 초음파를 이용하는 등 많은 에너지를 투입하여 $IO_3$·나 ·OH과 같은 활성산소종(reactive oxygen species)을 생성하였음. 그러나 동결을 이용하는 방법은 극지방 환경이나 저위도 지방에서 계절변화에 따른 기온의 강하만으로 유기오염물질 분해를 이끌어낼 수 있다는 장점이 있음. 과요오드산염($IO_4^-$)과 유기오염물질 사이의 반응은 액상에서는 거의 일어나지 않았으나, 동결된 상태에서는 반응이 효과적으로 이루어짐 (Choi *et al.* 2018). 대표적으로 푸르푸릴 알코올(furfuryl alcohol, FFA)의 분해효율이 가장 뛰어났으며, 트립토판, 시메티딘, 페놀, 비스페놀 A, 4-클로로페놀 순으로 분해효율이 높음을 실험을 통해 확인함 (그림 9). 추가적으로 과요오드산염($IO_4^-$) 100 μM으로 푸르푸릴 알코올을 반복적으로 분해할 수 있음을 확인하였음. 이는 실제 수처리 공정에서 필수적인 공정의 경제성과 지속성, 그리고 반복성을 입증한 결과로 수처리 공정에서 동결을 이용한 유기오염물질 분해의 효율성과 효용성을 입증함.
- 광업과 중공업은 상당한 양의 중금속 폐수를 생산하며, 이의 방류는 환경과 수자원 모두를 오염시킴. 전 세계적으로 전기도금, 전자, 금속세정 및 섬유산업에서 배출되는 많은 폐수에서 니켈이온($Ni^{2+}$)이 최대 허용한계치를 초과하여 검출되는 일이 일반적임. 이러한 폐수는 동식물에게 해롭고 더 나아가 인간에게도 매우 치명적임. 니켈은 병리학적으로 인간에게 매우 유해하며, 인간의 폐와 신장의 손상, 위장 장애, 폐섬유증, 신부종, 피부염과 같은 심각한 질환을 일으킬 수 있음. 따라서 폐수에서 중금속 저감 처리를 할 필요가 있음. 이러한 경로로 자연호소수에 유입된 $Ni^{2+}$의 거동을 황화니켈($NiSO_4$)을 이용하여 분석하였음. 실험 결과, 호소는 동결 시 표면부터 동결이 일어나게 되고 황화니켈의 농도가 비교적 저농도 조건일 때에는 얼음에 의한 분리효율이 동결 시 얼음의 동결비에 큰 영향을 받지 않았음. 그 원인은 농도가 낮을 때는 니켈의 확산속도가 얼음의 동결속도를 초과하기 때문임. 반면 고농도일 때에는 얼음에 의한 분리 효율이 얼음의 동결비에 큰 영향을 받았는데, 그 이유는 얼음의 동결속도가 니켈의 확산속도를 초과하기 때문임 (Hasan *et al.* 2016). 오

염물질을 함유한 호소수의 표면이 냉각된 대기에 의해서 동결이 일어나게 되면 최상층의 물은 빠른 속도로 동결이 이루어지게 되고 이는 결국 물속에 포함된 오염물질의 확산 속도를 초과하게 됨. 이러한 이유로 얼음의 동결속도가 오염물질의 확산속도를 초과하게 되면 상대적으로 많은 양의 오염물질이 얼음결정 사이, 즉 준액체층에 갇히는 현상이 일어남. 반면 표면 얼음의 하부쪽은 동결 속도가 점차 저하되면서 오염물질의 확산속도가 얼음의 동결속도를 초과하여 얼음에 의한 오염물질의 분리도가 높아짐. 보통 광산이나 니켈 가공 산업에서 배출되는 유출물은 호소에 의해 희석되어 $Ni^{2+}$의 농도는 매우 낮음 (그림 10). 따라서 자연동화(자연결빙)는 기온이 영하로 떨어지는 지역에서 지속할 수 있는 정화 기술이 될 가능성이 있음.

- 싱가포르 난양공대에서는 인간이 일상생활에서 사용하는 개인관리용품 및 의약품(Pharmaceuticals and personal care products, PPCP)에 의해 자연수계로 유입되는 물질들이 기온 강하로 인한 결빙 때문에 기존 수계에 흔히 존재하는 아질산염(nitrite, $NO_2^-$)과 반응하여 분해되는 반응에 관하여 연구하였음. 개인관리용품의 주요 성분은 설폰아마이드(sulfonamide)로, 상당량이 하수나 동물의 거름과 같은 고체 폐기물의 처리를 통해 환경으로 방출됨. 아질산염은 암모늄 산화 또는 질산염 감소과정에 관여하는 중요한 매개로 일반적으로 수계에 1 ppm에서 수천 ppm의 농도로 널리 분포하고 있음. 이 연구에서는 개인관리용품의 대표 물질로 설파메톡사졸(sulfamethoxazole, SMX)을 사용하였음. 영하 20 ℃에서 $NO_2^-$ 50 mg/L 와 SMX 10 mg/L이 포함된 용액을 pH 7.5 조건에서 동결하였을 경우 $NO_2^-$가 $NO_3^-$로 환원되고 설파메톡사졸은 모두 분해, 전환되었음 (Sun *et al.* 2017, 그림 11). 이와 같은 결과는 동결로 얼음결정이 생성되며 일어나는 동결농축효과로 설명할 수 있음. 또한 상온에서 무시할 수 있는 아질산염에 의한 설폰아마이드 분해가 동결 과정에서 상당히 가속될 수 있음을 입증하였음. 활성산소인 질산염과 수산화반응과는 별개로 동결 중에 산화종인 활성산소가 아질산염에서 생성되어 설파메톡사졸의 변형에 중요한 역할을 했을 가능성이 있다는 것을 실험을 통해 밝힘. 이 결과는 추운 환경에서의 자연적인 동결에 의한 자정작용에 대한 새로운 가능성을 제공함. 또한 환경 액체 샘플을 보존하고 대상 화합물들 사이의 물리적/화학적 상호작용을 피하기 위해 동결 방법을 재고하는 연구자들에게 새로운 가능성을 시사함.
- 인간 활동에 의해 토양 및 수서환경 내 노출된 오염물질의 정화를 위하여 동결-해동 주기(Freezing-thawing cycle)를 가지는 나라들에서는 계절적 특징을 활용하여 동결 과정 중 일어나는 오염물질의 구조 및 성상 변화를 통한 친환경 자정작용 연구를 시도하고 있음. 동결-해동 과정 중 다양한 유/무기 오염 물질(비스페놀 A, 페놀, 크롬, 비소 등)의 독성이 줄어드는 방향으로 변화가 일어난다는 보고가 있었음에도 실제 생물에게 미치는 영향에 관한 연구는 미미한 수준임 (Kim *et al.* 2015; Ju *et al.* 2017; Bower *et al.* 2014). 또한 동결방식의 자정작용 연구는 토양 및 지하수에 한하여 연구가 진행되고 있어 수서 환경 및 수생 생물을 연구한 결과는 전무함. 이에 동결 방식에 의한 수서 환경 내 오염물질의 변화를 측정하고 실제 수서 생물 내에서의 독성 변화를 측정함으로써 친환경 수처리 기술의 가능성을 타진하고자 함.

## 2. 저온환경에서 유해중금속 이온의 용출 현상 규명

- 중금속의 하나인 크롬은 0가, +2가, +3가, +6가의 다양한 형태를 가질 수 있음. 수계에서 크롬은 대부분 3가($Cr^{3+}$)와 6가($Cr^{6+}$) 형태로 존재하며, 6가 크롬은 3가 크롬에 비하여 독성이 강하며 발암물질인 것으로 알려져 있음 (Richard *et al.* 1991). 수은은 수계에서 0가 또는 +2가 형태로 존재하며, +2가 수은이 메틸화 과정을 거쳐 메틸수은(MeHg)으로 변환되면 체내에 축적되기 쉬운 형태가 되어 생물축적(bioaccumulation) 현상이 일어날 수 있음 (Fitzgerald *et al.* 2007).
- 최근 얼음에서 크롬 또는 비소와 같은 중금속의 산화수가 변화되는 반응을 이용하여 중금속의 독성을 감소시키는 오염물질 저감반응으로서의 얼음화학이 연구되고 있음 (Kim *et al.* 2011; Kim *et al.* 2015). 그러나 반대로 얼음에서 일어나는 산화환원반응에 의하여 중금속의 산화수가 변화됨에 따라 중금속의 독성이 증가할 수 있으나 이러한 관점에서의 연구는 이루어지고 있지 않음. 따라서 3가 크롬의 6가 크롬으로의 변환 과정 및 2가 수은의 메틸화 과정을 저온 환경에서 연구하고자 함.

## 3. 얼음 내 유/무기물의 활성화로 인한 산화종 생성기작 연구

- 극지방의 얼음 또는 상층 대기에서 발생하는 산화종은 극지 대기에서 일어나는 산화-환원 작용에서 중요한 위치를 차지하고 있음. 기존의 산화종 연구는 태양광 조사로 인한 분자 내 전자 여기로 인하여 형성되는 광화학 과정에 초점을 맞추고 있었음. 최근 십여 년간 빛이 없을 때도 발생하는 산화종의 생성 기작 연구가 진행됐으며, 얼음 내 할로겐 물질의 산성화가 산화종 생성에 기여한다는 가설이 꾸준히 제기되어 왔으나 할로겐 산화물을 중간체로 한 산화종 생성 기작 연구는 제한적임 (O'Dowd *et al.* 2002, 그림 12).
- 극지방의 할로겐 물질은 오존층 파괴에 직접 관여하는 물질로서 다년간 연구됐음. 얼음에 내입 된 할로겐 물질은 전자 이동 및 산화-환원에 기여하여 활성 할로겐 물질을 형성하며, 활성 할로겐 물질은 산화종 형성의 중간체 역할을 함. 얼음 표면 및 내부 준액체층은 양성자와 수산화 라디칼, 물 분자 등이 고농도로 농축된 환경임. 얼음 내의 농축 조건 하에서의 전자 이동으로 인한 산화-환원 반응은 수용액 상태보다 더 높은 빈도로 일어나게 되며 이를 통하여 활성 할로겐 물질 중간체와 산화종 생성이 증대될 수 있음.
- 스페인 Universidad Nacional de Educación a Distancia(UNED)의 Óscar Gálvez는 동결 과정에서 발생하는 활성 요오드가 극지방 대기의 산화종 총량에 미치는 영향을 분석하기 위해, 동결 요오드산염 용액의 광분해 과정에서 활성 요오드종의 방출을 확인. 이 과정을 모델에 적용하여 대기 중 요오드 산화물 농도가 기존 모델 대비 최대 1.0 pptv 높은 수준으로 나타남을 확인하여 극지 대기의 활성 할로겐 방출 기작을 새롭게 제시함 (Fernandez *et al.* 2019).
- 미국 미시간 대학의 Kerri A. Pratt 교수는 북극 대기에 존재하는 요오드 분자 및 활성 요오드, 그리고 해빙의 요오드 이온을 측정함으로써 얼음에 의하여 요오드의 활성이 증대됨을 입증함. 이 연구는 눈 위 10 cm의 대기를 측정하여 눈 위에서 요오드 분자가 다량 측

정되며, 따라서 동결로 인하여 증대되는 광화학 반응이 북극 대기의 전체 요오드 농도에 크게 관여하는 중요한 기작임을 확인. 또한 해빙수에서의 요오드 이온 농도가 해수의 요오드 농도보다 천 배 이상 높은 것을 확인. 이는 눈에서의 동결 과정이 요오드 활성에 중요한 기작임을 시사함 (Raso *et al.* 2017, 그림 13).

- 미국 빌라노바 대학의 Amanda M. Grannas 교수는 자연계의 용존 유기물(dissolved natural organic matter, DOM)을 포함한 수용액의 동결 과정에서 활성산소종인 단일항 산소(singlet oxygen, $^1O_2$) 생성이 증대됨을 보고함. 단일항 산소는 광화학 반응으로 형성되나 자연계에서는 그 형성 비율이 낮음. 연구진은 DOM을 포함한 얼음의 광화학 반응이 용액상에서의 반응보다 천 배 이상 증대됨을 확인. 동결 온도에 따라 단일항 산소의 생성량이 달라졌음. 이 연구는 자연계의 눈이나 얼음이 활성산소종의 주요한 공급원이 될 수 있음을 제시 (Fede *et al.* 2015, 그림 14).

## 4. 동결에 의한 철의 생지화학적 용출기작 연구

- 최근 얼음에서 일어나는 화학반응에 의하여 산화철로부터 생물이 이용할 수 있는 형태의 철이 용출되는 것으로 연구되고 있으며, 이러한 반응은 액상에 비하여 얼음상에서 빠른 속도로 일어나는 것으로 연구됨 (Jeong *et al.* 2012; Jeong *et al.* 2015).
- 철 동위원소는 해양에 존재하는 철과 관련하여 농도만으로 알 수 없는 해양 철의 기원을 추정하는 철의 생지화학적 순환 이해에 이용되고 있음 (Conway *et al.* 2014; Abadie *et al.* 2017, 그림 15). 고환경 연구에서는 과거 자연환경을 추정하는 과정에서 생물에 의한 철 동위원소 분별과정이 제시되었으며 (Johnson *et al.* 2008), 실험실 실험을 통해 기존의 인식과 달리 산에 의한 용출 반응, 산화철의 구조 특성 등에 따라 비생물적 반응에 의해서도 철 동위원소의 분별과정이 일어날 수 있음이 제시됨 (Anbar *et al.* 2000; Bullen *et al.* 2001). 산화철의 용출과 관련하여 자연에서 일어나는 생지화학적 반응을 이해하기 위하여 동결에 의한 철 동위원소의 분별과정을 연구할 필요가 있음.
- 미국 및 러시아 등지의 얼음동굴에서 반복적인 동결과 해동에 의해 형성된 탄산염 광물이 보고된 바 있음. 이러한 탄산염 광물은 동결 시 용질이 준액체층으로 농축되어 형성되는 것으로 연구되었으며, 용질의 종류에 따라 동결 시 얼음에 남아있거나 준액체층으로 이동하려는 정도가 다르기 때문에 얼음동굴에서 동결 반응에 의해 형성된 탄산염 광물은 특징적인 화학적 조성을 보이는 경향이 있음 (Žak *et al.* 2018). 따라서 얼음동굴 내에서 발견되는 탄산염 광물 연구는 해당 지역의 과거 기후를 이해하는 데 도움이 될 수 있음 (Munroe *et al.* 2021, 그림 16).
- 극지방의 해수가 낮은 기온에 의해 동결될 때, 해수 내 높은 농도로 존재하는 황산염 및 탄산염과 나트륨, 칼슘 이온 등이 준액체층에 농축되어 석고(gypsum, $CaSO_4{\cdot}2H_2O$), 탄산염 광물(ikaite, $CaCO_3{\cdot}6H_2O$), 미라빌석(mirabilite, $Na_2SO_4{\cdot}10H_2O$) 등이 형성될 수 있음이 연구된 바 있음(Geilfus *et al.* 2013; Butler and Kennedy, 2015, 그림 17). 해수의 동결되는 온도에 따라 형성되는 광물의 종류가 달라지는 것으로 연구됨. FREZCHEM 모델링을 통하여 해수가 얼 때 해수의 용질 성분, 농도, 온도 등의 조건이 달라짐에 따라 어떤 광물이

형성될 것인지 계산하여 동결 해수 광물 형성 반응을 이해하고자 하는 연구가 수행됨 (Marion *et al.* 2010).

## 제 3 절. 저온응용기술 기초 연구

- 얼음표면에서 헥세인의 졸-겔 반응 및 수화 반응을 유도하여 두께 0.5~1 nm의 이산화티타늄 나노 디스크를 개발함(Kim *et al.* 2013). 얼음화학특성(준액체층 등) 및 동결주물방법(freeze-casting method)을 활용한다면 다양한 활용도와 높은 성능을 지닌 환경·에너지 소재를 합성할 수 있으리라 여겨짐 (그림 18).
- 동결주물방법(freeze-casting method)을 이용하여 3차원 구조의 다공성 나노 복합체 개발이 가능함. 얼음을 주형으로 사용하여 다공성 3차원 그래핀-귀금속 나노복합단일체를 합성하는 데 성공하였으며, 이 소재는 전자파 차폐 성능이 뛰어나며, 메탄올을 전기산화하는 성능이 높음을 보임 (Sahoo *et al.* 2015, 그림 19). 다른 연구에서는 얼음을 주형으로 사용해 $SnO_2$ 나노입자가 3차원 그래핀 내에 포함된 구조를 제작하였음. 이 소재는 다공성이므로 넓은 표면적을 가지고 있으며, 전기 및 이온 전도성이 높아 나트륨 저장 성능 및 방전 성능이 뛰어남 (Pei *et al.* 2015).
- 다양한 제어 조건 하에 얼음 표면과 아닐린 사이의 수소결합에 의한 대면적의 고결정성 2차원 전도성 고분자(폴리아닐린) 합성 가능성을 규명하였으며, 이렇게 합성된 폴리아닐린은 기존 합성된 폴리아닐린보다 40배 높은 전기전도성을 지님 (Choi *et al.* 2015, 그림 20). 이러한 얼음화학 특성을 응용하여 다양한 고분자 합성이 가능할 것으로 여겨지며, 이를 위해서는 in-situ grazing X-ray 실험을 통한 전도성 고분자 배향 규명, 얼음 표면의 준액체층의 성질과 전도성 고분자 배향 간의 상관관계를 더욱 깊이 있게 규명해야 할 필요성이 있음.

## 제 4 절. 얼음화학 연구 그룹

### 1. 체코 마사릭 대학교

- 체코 마사릭 대학교는 Department of Chemistry and Research Centre for Toxic Compounds in the Environment (RECETOX) 부서의 Dominik Heger 그룹을 중심으로 자연상 얼음 및 얼음 내 불순물에 관한 연구와 자연에서 일어나는 동결 및 동결 건조 과정에 대한 기초 연구 및 각종 유기 분자체와 얼음의 상호작용을 통한 화학적 변화에 관한 연구를 수행해오고 있음. 이 그룹은 얼음화학 연구에 있어 영국 남극조사소(British Antarctic Survey), 오스트리아 인스브루크 대학, 대한민국 극지연구소 등과 국제 협력 연구 또한 진행 중임.
- 유기화합물의 얼음 표면 또는 얼음 결정 사이의 준액체층으로의 이동 및 분자 거동에 관

한 연구를 수행함. 얼음상에 존재하는 유기 분자체의 흡수, 방출, 미세구조 변화, 반응성 변화 등의 물리화학적 특성을 연구함. 또한 동결로 인하여 얼음과 용액 사이 계면에서 발생하는 전위성과 양성자의 변화, 화합물-얼음 사이의 상호작용을 분광학적 기법으로 연구함.

- 얼음 표면에 나프탈렌 기체가 흡착되었을 때, 저온(77 K)의 비결정형 얼음 위에서는 흡착된 나프탈렌 분자가 비결정형으로 존재하며, 고온(253 K)의 결정형 얼음 위에서는 나프탈렌 분자 또한 결정형으로 존재함을 형광 분석 방법과 시차 주사 열량 분석법을 통해 입증함 (Ondrušková *et al.* 2018, 그림 21). 기존의 얼음 표면 분자 거동 연구는 무기 분자체에 대해서는 많이 연구되었으나, 방향족 고리형 분자체의 극저온 얼음 표면상 거동 연구는 처음으로 보고됨. 이 연구는 얼음 온도에 따라 유기 분자체의 얼음 표면 흡착 후 거동이 달라짐을 보였다는 점에서 향후 분자 거동 모델링 및 자연에서의 화학 반응 연구에 있어 중요한 의미가 있음.
- 동결은 준액체층 내부에 농축된 물질의 화학적 변화와 산성도 변화를 동시에 일으킴. 약염기성(pH 8.0)의 인산염 완충 용액을 동결 및 건조하여 각 상태에서의 산성도를 측정함. 동결 과정에서 산성도의 변화가 두드러지게 나타났으며 동결 건조 후에도 원래 산성도까지 회복되지 않음. 이 결과를 통하여 동결 및 동결 건조 과정에서 나타나는 산성도 변화는 동결과 건조 과정에서 모두 유의미하게 작용함을 입증함. 이 결과는 동결 건조 공정을 사용하는 제약, 생화학 물질 합성 등에서 응용될 수 있음 (Vetráková *et al.* 2017, 그림 22).

KOPRI 극지연구소

## 2. 스위스 Paul Scherrer Institut

- 스위스 Paul Scherrer Institut(PSI) 내 Laboratory of Environmental Chemistry(LUC)의 표면화학 그룹은 대류권에서 일어나는 활성 기체 및 에어로졸 입자의 화학적 반응을 통제된 실험실 조건에서 연구하고 있음. 대기에서 화학적 반응을 거친 에어로졸 입자와 가스는 이동하여 눈과 함께 고산빙하에 쌓이게 됨. LUC의 분석화학그룹은 빙하코어를 분석하여 과거의 대기오염 수준, 환경 상태, 기후 변화를 재구성함. 해당 그룹은 대기 중 물질이 화학적 반응을 거치고 이동하여 눈과 얼음에서 불순물로 존재하기까지의 과정을 연구하는 MiSo(Microscale Distribution of Impurities in SnOw and Glacier Ice) 프로젝트 이후, 얼음의 계면 화학을 연구하는 “Interfacial Chemistry of Ice: Photolysis and Acid-Base Equilibria in the QLL and Brine project”를 시작함.
- 얼음 계면의 산-염기 화학 연구: 동결 또는 액상 상태에서 대기와 물의 계면에서 일어나는 질산 및 아질산의 해리와 광화학 반응은 질소산화물의 양을 조절하여 대기의 산화력을 변화시키는 역할을 하므로 많은 과학적 관심을 받아옴. 산의 해리에는 산이 수소결합을 형성하는 능력이 중요한 것으로 알려져 있으며, 이러한 산의 해리는 대기에서 일어나는 비균질적인 반응에 중요한 역할을 함. 물의 계면이 물 전체(bulk)에 비하여 특이한 화학적 특성을 보인다는 것이 잘 알려져 있음에도 불구하고 계면에서의 산-염기 화학은 잘 연구되지 않음. 특히 강산인 질산과 염산은 농축된 수용액 표면과 얼음 표면에서 해리되지 않고 분

자 형태로 안정화되는 것이 관찰되었는데, 이러한 표면에서의 특이한 현상은 표면에서 수소 분자를 형성하는 능력을 잃는 것과 관계된 것으로 판단되고 있음. 따라서 해당 프로젝트에서는 -40 ℃부터 0 ℃의 온도 범위에서 액상 상태와는 구별되는 계면 화학의 이해를 도모하고자 함.

- 얼음 형성 입자의 화학적 매핑(mapping) 연구: 얼음 형성을 관찰하기 위하여 X-ray 현미경과 분광분석법을 이용하는 장비를 개발하여 35 nm의 공간 분해능으로 얼음 핵입자의 물리·화학적 특성을 연구함. X-ray 현미경을 이용하여 빙핵을 직접적으로 관찰하는 첫 번째 시도로, X-ray 투과도를 유지하며 습도 및 온도를 조절하여 빙핵 형성을 관찰하는 것이 관건임. 대기 중 먼지 입자와 관련된 얼음 형성을 관찰하기 위하여 철을 포함한 광물을 이용함. 떨어뜨려준 물방울이 관찰되는 시점과 얼음이 처음으로 관찰되어 성장하는 시점의 온도와 습도를 측정함. 연구에 이용된 부분 동결 기술은 낮은 온도에서 에어로졸 입자의 반응과 관계된 화학적 변화 관찰에 이용할 수 있음.
- 얼음 표면에서 물리흡착 및 용매화된 염화수소의 공존 현상 연구: 계면에서 일어나는 강산의 이온화는 환경 과학, 빙권 과학, 촉매 연구 및 재료 과학에서 중요한 의미가 있음. 해당 연구그룹에서는 X선 광전자 분광계(XPS)를 이용하여 253 K에서 염화수소가 분자 및 해리된 상태 모두 표면에 적게 흡착되는 것을 직접적으로 관찰함. XPS를 이용한 깊이 프로파일에서 이러한 결과가 얼음의 가장 바깥쪽 표면에 염화수소 분자가 물리적으로 흡착되는 것과 계면 영역의 깊은 곳에서 용매화가 발생할 때 일어나는 염화수소의 해리 때문인 것을 확인함. Complementary X-ray 흡광법을 이용하여 계면 영역에서 염소이온의 존재가 수소결합에 중요한 역할을 하는 것을 확인함. 이러한 연구는 대기-얼음 간의 계면에서의 비균질성과 계면에서 일어나는 과정에 대한 산-염기 개념의 이용에 대한 해답을 제시할 수 있음.

# 참고문헌


Abadie, C.; Lacan, F.; Radic, A.; Pradoux, C.; Poitrasson, F., 2017, Iron Isotopes Reveal Distinct Dissolved Iron Sources and Pathways in The Intermediate Versus Deep Southern Ocean. *Proc. Natl. Acad. Sci. U.S.A.* 114, 858-863.

Anbar, A.; Roe, J.; Barling, J.; Nealson, K. 2000, Nonbiological Fractionation of Iron Isotopes. *Science* 288, 126-128.

Bar Dolev, M.; Braslavsky, I.; Davies, P. L., 2016, Ice-Binding Proteins and Their Function. *Annu. Rev. Biochem* 85, 515-542.

Bartels-Rausch, T.; Bergeron, V.; Cartwright, J. H. E.; Escribano, R.; Finney, J. L.; Grothe, H.; Gutiérrez, P. J.; Haapala, J.; Kuhs, W. F.; Pettersson, J. B. C.; Price, S. D.; Sainz-Díaz, C. I.; Stokes, D. J.; Strazzulla, G.; Thomson, E. S.; Trinks, H.; Uras-Aytemiz, N., 2012, Ice Structures, Patterns, and Processes: A View across the Icefields. *Rev. Mod. Phys.* 84, 885-944.

Bower, J. P.; Anastasio, C., 2014, Degradation of Organic Pollutants in/on Snow and Ice by Singlet Molecular Oxygen ($^1O^*_2$) and an Organic Triplet Excited State. *Environ. Sci.: Processes Impacts* 16, 748-756.

Bullen, T. D.; White, A. F.; Childs, C. W.; Vivit, D. V.; Schulz, M. S., 2001, Demonstration of Significant Abiotic Iron Isotope Fractionation in Nature. *Geology* 29, 699-702.

Butler, B. M.; Kennedy, H. J., 2015, An Investigation Of Mineral Dynamics in Frozen Seawater Brines by Direct Measurement with Synchrotron X?Ray Powder Diffraction. *J. Geophys. Res. Oceans* 120, 5686-5697.

Capicciotti, C. J.; Leclére, M.; Perras, F. A.; Bryce, D. L.; Paulin, H.; Harden, J.; Liu, Y.; Ben, R. N., 2012, Potent Inhibition of Ice Recrystallization by Low Molecular Weight Carbohydrate-Based Surfactants and Hydrogelators. *Chem. Sci.* 3, 1408-1416.

Chen, J.; Maki, T.; Nagashima, K.; Murata, K.-i.; Sazaki, G., 2020, Quasi-Liquid Layers in Grooves of Grain Boundaries and on Grain Surfaces of Polycrystalline Ice Thin Films. *Cryst. Growth Des.* 20, 7188-7196.

Choi, I. Y.; Lee, J.; Ahn, H.; Lee, J.; Choi, H. C.; Park, M. J., 2015, High-Conductivity Two-Dimensional Polyaniline Nanosheets Developed on Ice Surfaces. *Angew. Chem. Int. Ed.* 54, 10497-10501.

Choi, Y.; Yoon, H.-I.; Lee, C.; Vetrakova, L.; Heger, D.; Kim, K.; Kim, J., 2018, Activation of Periodate by Freezing for the Degradation of Aqueous Organic Pollutants. *Environ. Sci. Technol.* 52, 5378-5385.

Conway, T. M.; John, S. G., 2014, Quantification of Dissolved Iron Sources to the North Atlantic Ocean. *Nature* 511, 212-215.


KOPRI 극지연구소

Devlin, J. P., 2011, Relating the Current Science of Ion-Defect Behavior in Ice to a Plausible Mechanism for Directional Charge Transfer During Ice Particle Collisions. *Phys. Chem. Chem. Phys.* 13, 19707-19713.

Devlin, J. P.; Buch, V., 2007, Evidence for the Surface Origin of Point Defects in Ice: Control of Interior Proton Activity by Adsorbates. *J. Chem. Phys.* 127, 091101.

Fede, A.; Grannas, A. M., 2015, Photochemical Production of Singlet Oxygen from Dissolved Organic Matter in Ice. *Environ. Sci. Technol.* 49, 12808-12815.

Fernandez, R. P.; Carmona-Balea, A.; Cuevas, C. A.; Barrera, J. A.; Kinnison, D. E.; Lamarque, J.-F.; Blaszczak-Boxe, C.; Kim, K.; Choi, W.; Hay, T.; Blechschmidt, A.-M.; Schönhardt, A.; Burrows, J. P.; Saiz-Lopez, A., 2019, Modeling the Sources and Chemistry of Polar Tropospheric Halogens (Cl, Br, and I) Using the Cam-Chem Global Chemistry-Climate Model. *J. Adv. Model. Earth Syst.* 11, 2259-2289.

Fitzgerald, W. F.; Lamborg, C. H.; 2007, Hammerschmidt, C. R., Marine Biogeochemical Cycling of Mercury. *Chem. Rev.* 107, 641-62.

Geilfus, N. X.; Galley, R.; Cooper, M.; Halden, N.; Hare, A.; Wang, F.; Søgaard, D.; Rysgaard, S., 2013, Gypsum Crystals Observed in Experimental And Natural Sea Ice. *Geophys. Res. Lett.* 40, 6362-6367.

Hasan, M.; Louhi-Kultanen, M., 2016, Water Purification of Aqueous Nickel Sulfate Solutions by Air Cooled Natural Freezing. *Chem. Eng. J.* 294, 176-184.

He, Z.; Liu, K.; Wang, J., 2018, Bioinspired Materials for Controlling Ice Nucleation, Growth, and Recrystallization. *Acc. Chem. Res.* 51, 1082-1091.

Hodgson, A.; Haq, S., 2009, Water Adsorption and the Wetting of Metal Surfaces. *Surf. Sci. Rep.* 64, 381-451.

Jagoda-Cwiklik, B.; Devlin, J.; Buch, V., 2008, Spectroscopic and Computational Evidence for $SO_2$ Ionization on 128 K Ice Surface. *Phys. Chem. Chem. Phys.* 10, 4678-4684.

Jeong, D.; Kim, K.; Choi, W., 2012, Accelerated Dissolution of Iron Oxides in Ice. *Atmos. Chem. Phys.* 12, 11125-11133.

Jeong, D.; Kim, K.; Min, D. W.; Choi, W., 2015, Freezing-Enhanced Dissolution of Iron Oxides: Effects of Inorganic Acid Anions. *Environ. Sci. Technol.* 49, 12816-12822.

Johnson, C. M.; Beard, B. L.; Roden, E. E., 2008, The Iron Isotope Fingerprints of Redox and Biogeochemical Cycling in Modern and Ancient Earth. *Annu. Rev. Earth Planet. Sci.* 2008, 36, 457-493.

Ju, J.; Kim, J.; Vetráková, Ľ.; Seo, J.; Heger, D.; Lee, C.; Yoon, H. I.; Kim, K.; Kim, J., 2017, Accelerated Redox Reaction between Chromate and Phenolic Pollutants During Freezing. *J. Hazard. Mater.* 329, 330-338.

Kim, G.; Jo, C.; Kim, W.; Chun, J.; Yoon, S.; Lee, J.; Choi, W., 2013, $TiO_2$ Nanodisks

Designed for Li-Ion Batteries: A Novel Strategy for Obtaining an Ultrathin and High Surface Area Anode Material at the Ice Interface. *Energy Environ. Sci.* 6, 2932-2938.

Kim, K.; Choi, W., 2011, Enhanced Redox Conversion of Chromate and Arsenite in Ice. *Environ. Sci. Technol.* 45, 2202-2208.

Kim, K.; Kim, J.; Bokare, A. D.; Choi, W.; Yoon, H. I.; Kim, J., 2015, Enhanced Removal of Hexavalent Chromium in the Presence of $H_2O_2$ in Frozen Aqueous Solutions. *Environ. Sci. Technol.* 49, 10937-10944.

Marion, G. M.; Mironenko, M. V.; Roberts, M. W., 2010, Geosciences, Frezchem: A Geochemical Model for Cold Aqueous Solutions. *Comput. Geosci.* 36, 10-15.

Molina, M. J.; Tso, T. L.; Molina, L. T.; Wang, F. C. Y. 1987, Antarctic Stratospheric Chemistry of Chlorine Nitrate, Hydrogen Chloride, and Ice: Release of Active Chlorine. *Science* 238, 1253-1257.

Munroe, J.; Kimble, K.; Spötl, C.; Marks, G. S.; Mcgee, D.; Herron, D., 2021, Cryogenic Cave Carbonate and Implications for Thawing Permafrost at Winter Wonderland Cave, Utah, Usa. *Sci. Rep.* 11, 6430.

Murata, K.-i.; Sato, M.; Uwaha, M.; Saito, F.; Nagashima, K.; Sazaki, G., 2022, Step-Bunching Instability of Growing Interfaces between Ice and Supercooled Water. *Proc. Natl. Acad. Sci. U.S.A.* 119, e2115955119.

O'Dowd, C. D.; Jimenez, J. L.; Bahreini, R.; Flagan, R. C.; Seinfeld, J. H.; Hämeri, K.; Pirjola, L.; Kulmala, M.; Jennings, S. G.; Hoffmann, T., 2002, Marine Aerosol Formation from Biogenic Iodine Emissions. *Nature* 417, 632-636.

Ondrušková, G.; Krausko, J.; Stern, J. N.; Hauptmann, A.; Loerting, T.; Heger, D., 2018, Distinct Speciation of Naphthalene Vapor Deposited on Ice Surfaces at 253 or 77 K: Formation of Submicrometer-Sized Crystals or an Amorphous Layer. *J. Phys. Chem. C* 122, 11945-11953.

Pei, L.; Jin, Q.; Zhu, Z.; Zhao, Q.; Liang, J.; Chen, J., 2015, Ice-Templated Preparation and Sodium Storage of Ultrasmall $SnO_2$ Nanoparticles Embedded in Three-Dimensional Graphene. *Nano Res.* 8, 184-192.

Petrenko, V. F.; Whitworth, R. W. 1999, Physics of Ice; Oxford University Press.

Qi, C.; Stern, L. A.; Pathare, A.; Durham, W. B.; Goldsby, D. L., 2018, Inhibition of Grain Boundary Sliding in Fine-Grained Ice by Intergranular Particles: Implications for Planetary Ice Masses. *Geophys. Res. Lett.* 45, 12,757-12,765.

Raso, A. R. W.; Custard, K. D.; May, N. W.; Tanner, D.; Newburn, M. K.; Walker, L.; Moore, R. J.; Huey, L. G.; Alexander, L.; Shepson, P. B.; Pratt, K. A., 2017, Active Molecular Iodine Photochemistry in the Arctic. *Proc. Natl. Acad. Sci. U.S.A.* 114, 10053-10058.

Richard, F. C.; Bourg, A. C. M., 1991, Aqueous Geochemistry of Chromium: A Review. *Water Res.* 25, 807-816.

Sahoo, P. K.; Aepuru, R.; Panda, H. S.; Bahadur, D., 2015, Ice-Templated Synthesis of Multifunctional Three Dimensional Graphene/Noble Metal Nanocomposites and Their Mechanical, Electrical, Catalytic and Electromagnetic Shielding Properties. *Sci. Rep.* 5, 17726.

Slater, B.; Michaelides, A., 2019, Surface Premelting of Water Ice. *Nat. Rev. Chem.* 3, 172-188.

Solomon, S.; Garcia, R. R.; Rowland, F. S.; Wuebbles, D. J. 1986, On the depletion of Antarctic ozone. *Nature* 321, 755-758.

Sun, F.; Xiao, Y.; Wu, D.; Zhu, W.; Zhou, Y., 2017, Nitrite-Driven Abiotic Transformation of Sulfonamide Micropollutants During Freezing Process. *Chem. Eng. J.* 327, 1128-1134.

Takenaka, N.; Ueda, A.; Daimon, T.; Bandow, H.; Dohmaru, T.; Maeda, Y. 1996, Acceleration Mechanism of Chemical Reaction by Freezing: The Reaction of Nitrous Acid with Dissolved Oxygen, *J. Phys. Chem.* 100, 13874-13884.

Takenaka, N.; Ueda, A.; Maeda, Y. 1992, Acceleration of the Rate of Nitrite Oxidation by Freezing in Aqueous Solution. *Nature* 358, 736.

Tokumasu, K.; Harada, M.; Okada, T., 2016, X-Ray Fluorescence Imaging of Frozen Aqueous Nacl Solutions. *Langmuir* 32, 527-533.

Vetráková, Ľ.; Vykoukal, V.; Heger, D., 2017, Comparing the Acidities of Aqueous, Frozen, and Freeze-Dried Phosphate Buffers: Is There a "pH Memory" Effect? *Int. J. Pharm.* 530, 316-325.

Wooldridge, P. J.; Devlin, J. P., 1988, Proton Trapping and Defect Energetics in Ice from FT-IR Monitoring of Photoinduced Isotopic Exchange of Isolated $D_2O$. *J. Chem. Phys.* 88, 3086-3091.

Žák, K.; Onac, B. P.; Kadebskaya, O. I.; Filippi, M.; Dublyansky, Y.; Luetscher, M., 2018, Cryogenic Mineral Formation in Caves. *in* Ice Caves, Elsevier: pp. 123-162.

# 그림

Nature 1992

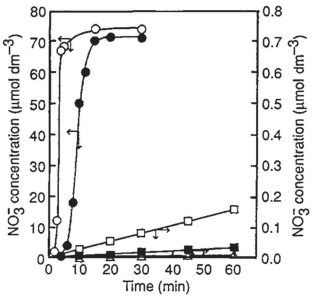



FIG. 1 Time profile of the reaction of $HNO_2$ with dissolved oxygen at pH 4.0. ○, Freezing process with coolant at −45 °C; ●, freezing process with coolant at −21 °C; □, in solution at 60 °C; ■, in solution at 25 °C; △, in solution at 4 °C. Different scales are used for results on freezing and in solution. The initial concentration of N(III) was $1.0\times10^{-4}$ mol dm$^{-3}$, and that of dissolved oxygen was $4.4\times10^{-4}$ for the freezing process and $2.5\times10^{-4}$ mol dm$^{-3}$ for the solution.

J. Phys. Chem. 1996

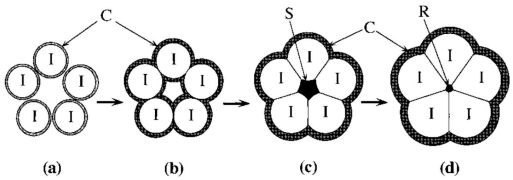



**Figure 11.** Illustrative elucidation of acceleration mechanism by freezing. Only five single ice crystals are depicted for simplicity. I, single crystal of ice; C, concentrated phase; S, solution confined in the solution surrounded by walls of ice grains; R, concentrated solution in which the reaction is accelerated. See text for descriptions of a−d.

**그림 1.** (좌) 얼음 표면에서 빨라지는 화학 반응, (우) 동결농축효과 (Takenaka *et al.* 1992 and Takenaka *et al.* 1996)

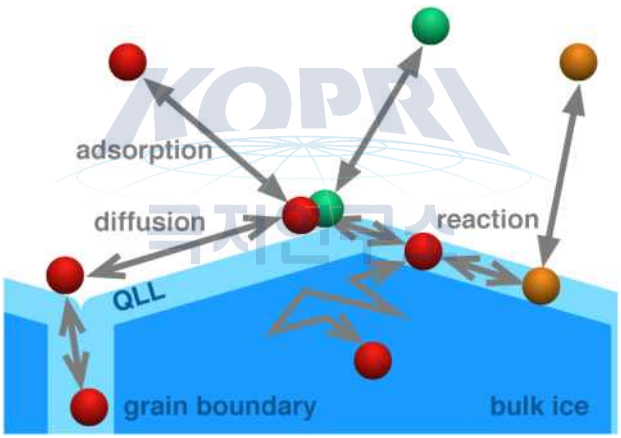



**그림 2.** 얼음 표면에서의 화학 물질의 거동 (Bartels-Rausch *et al.* 2012)

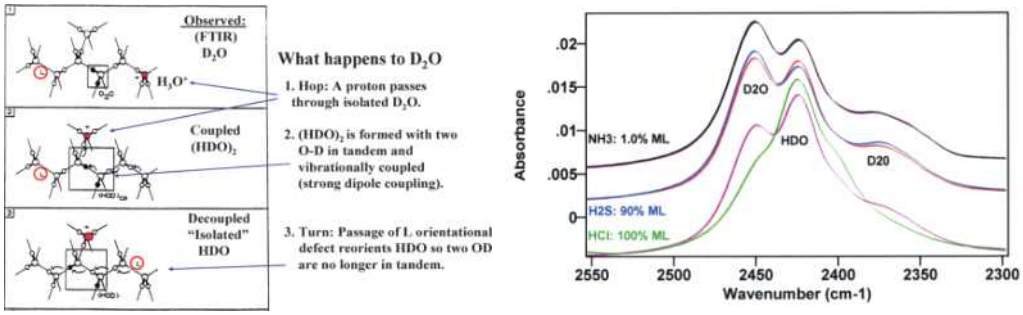



**그림 3.** (좌) 얼음 내 양성자 결함의 이동 모식도, (우) 표면 흡착에 따른 얼음 스펙트럼 변화 (Devlin, J. P. 2011)

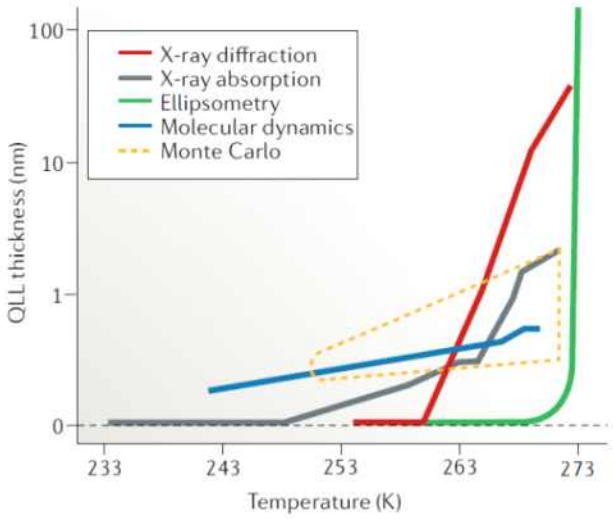



**그림 4.** 다양한 실험 방법에서 측정된 준액체층 두께 (Slater *et al.* 2019)

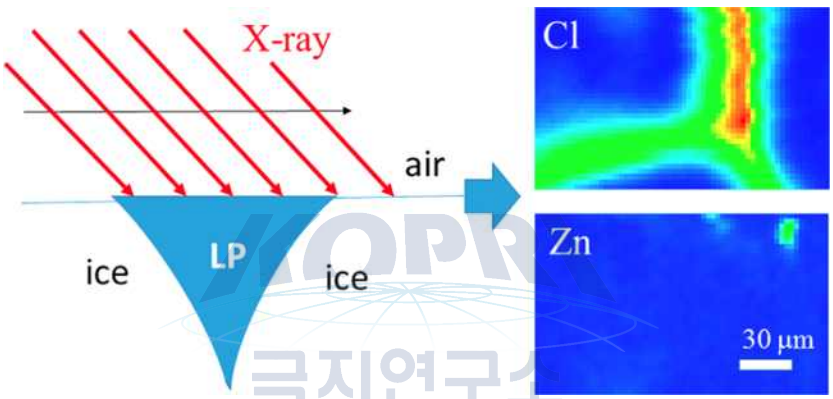



**그림 5.** 동결농축효과로 인한 용질의 얼음 내 분포 (Tokumasu *et al.* 2016)

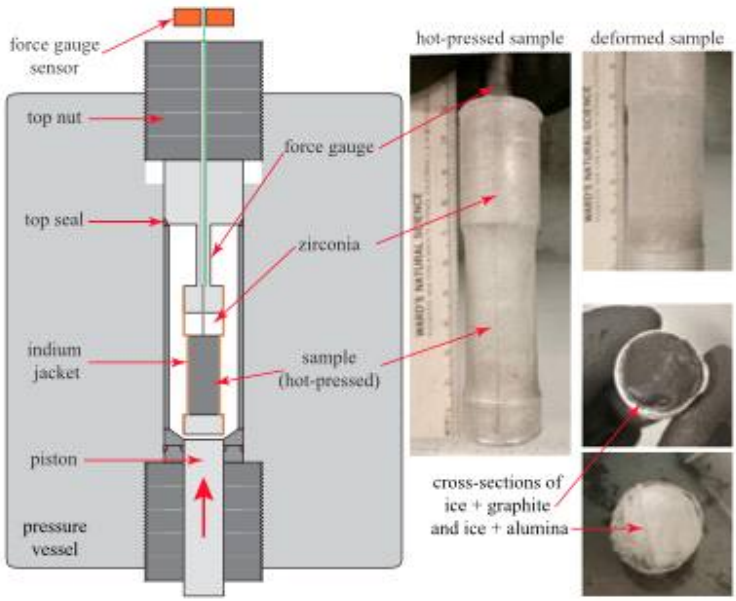



**그림 6.** 얼음 내 불순물(흑연, 알루미나)을 함유한 고압저온 변형실험의 장비 및 샘플 (Qi *et al.* 2018)

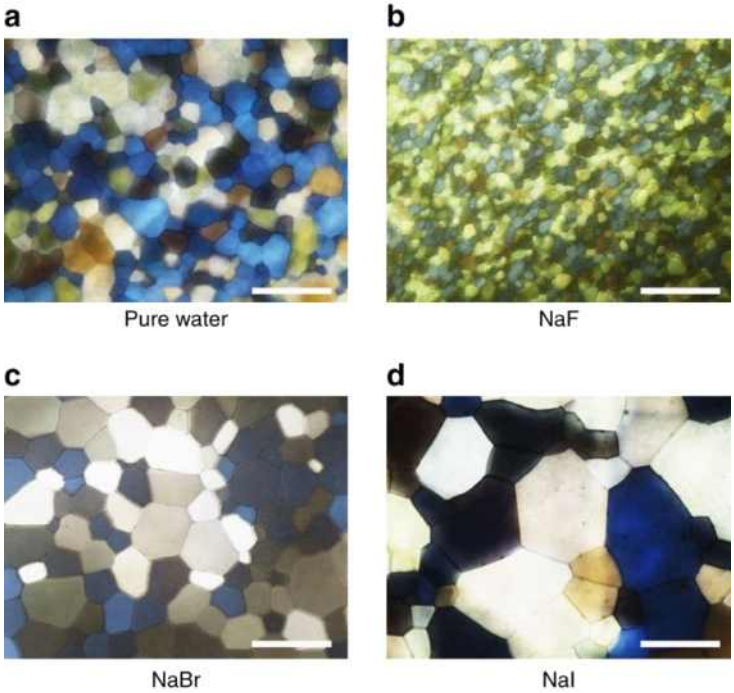



**그림 7.** 얼음 내 할로겐 이온 불순물의 종류에 따른 얼음 결정 크기 변화 이미지 (He *et al.* 2017)

KOPRI
극지연구소

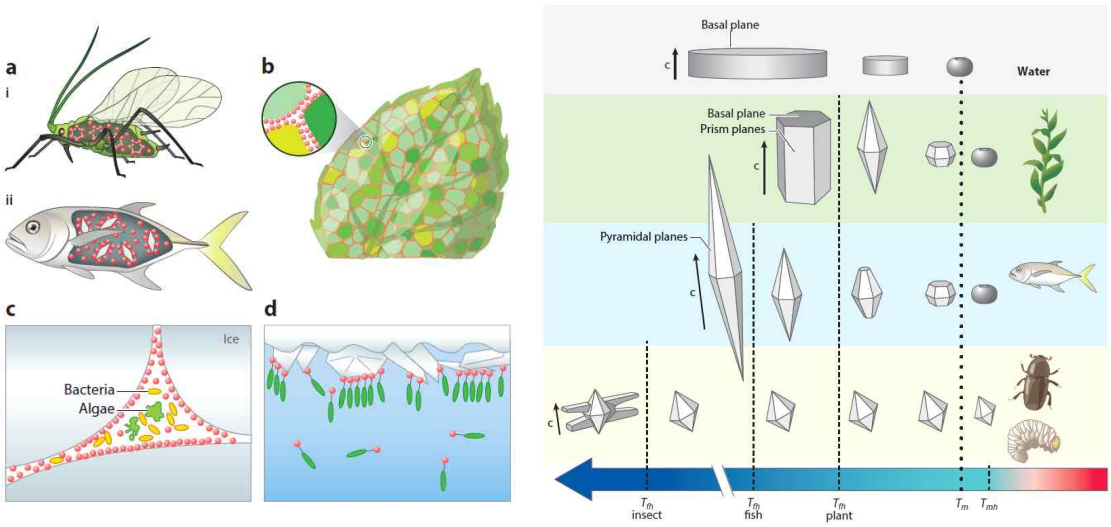



**그림 8.** IBP 단백질의 종류 및 그에 따른 얼음결정모양과 TH 활성 (Bar Dolev *et al.* 2016)

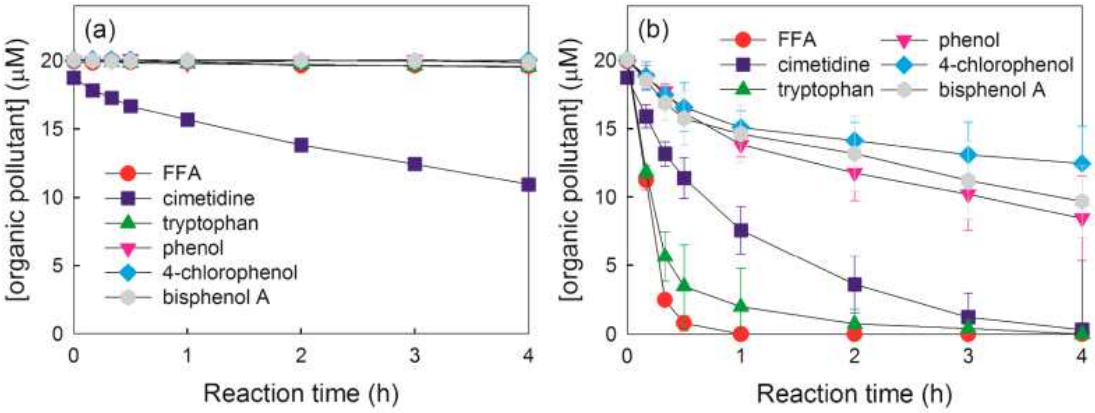



**그림 9.** 과요오드산염($IO_4^-$)과 여러 유기오염물질의 (a) 액상과 (b) 동결시의 시간에 따른 분해도 그래프(Choi *et al.* 2018)

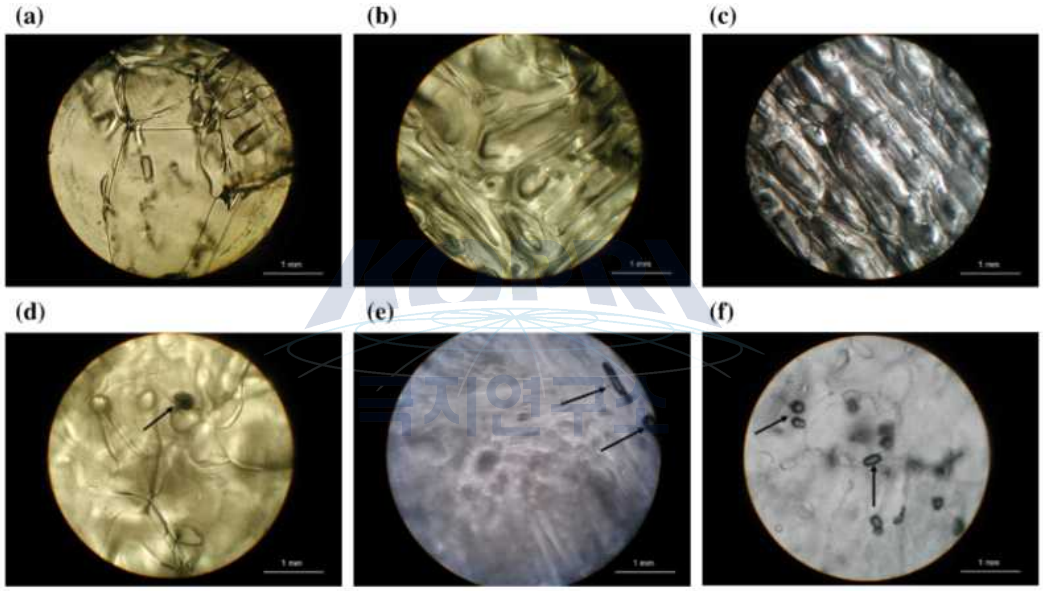



**그림 10.** 동결속도에 따른 황산니켈의 갇힘 현상(Hasan *et al.* 2016)

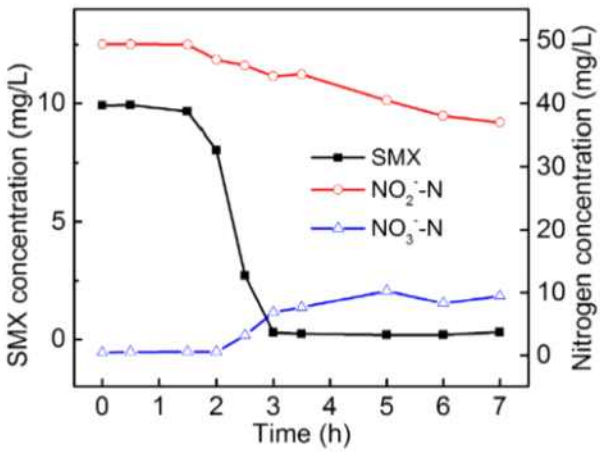



**그림 11.** -20 ℃, pH 7.5에서 시간에 따른 설파메톡사졸(SMX), 아질산염($NO_2^-$), 질산염($NO_3^-$)의 농도 변화. (Sun *et al.* 2017)

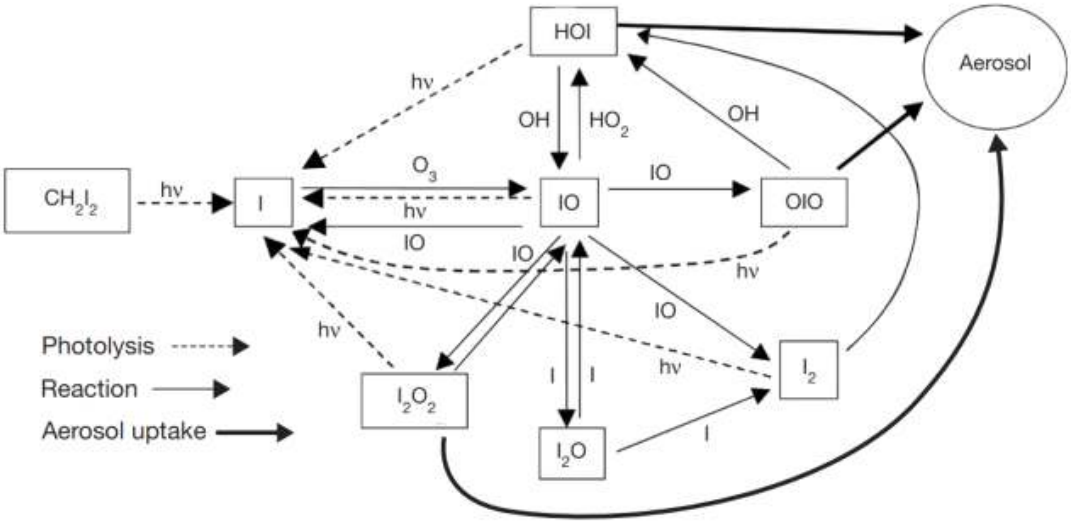



**그림 12.** 극지방 대기에서 나타나는 활성 요오드와 산화종의 화학적 반응 경로(O'Dowd *et al.* 2002)

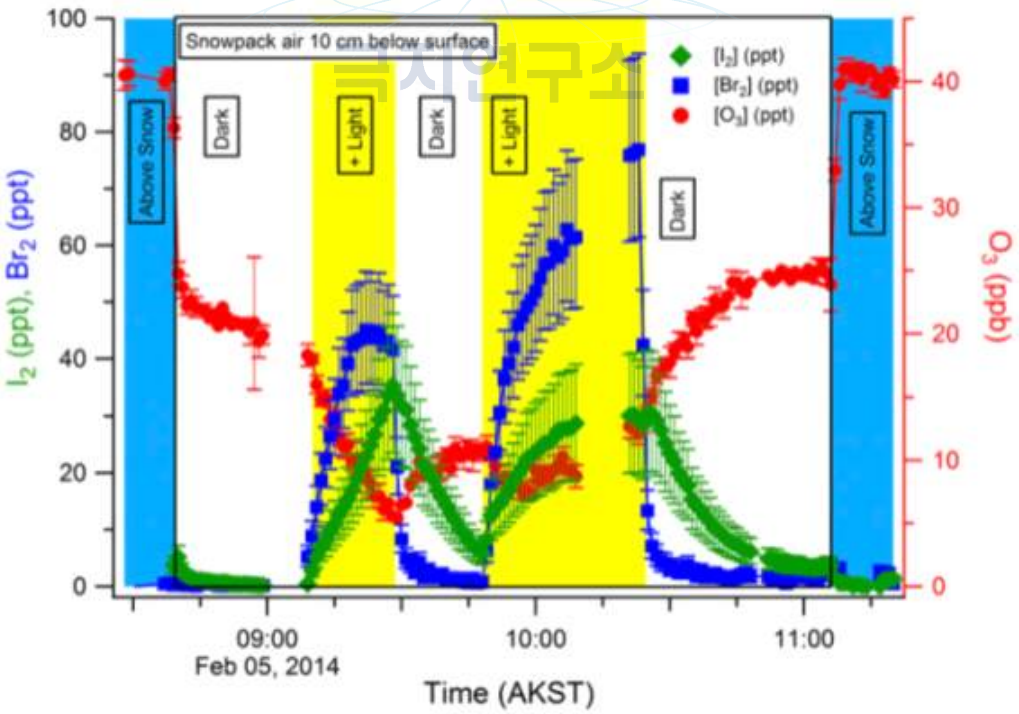



**그림 13.** 북극 지표의 눈 위 10 cm 대기에서 나타나는 할로겐 분자의 시간에 따른 농도

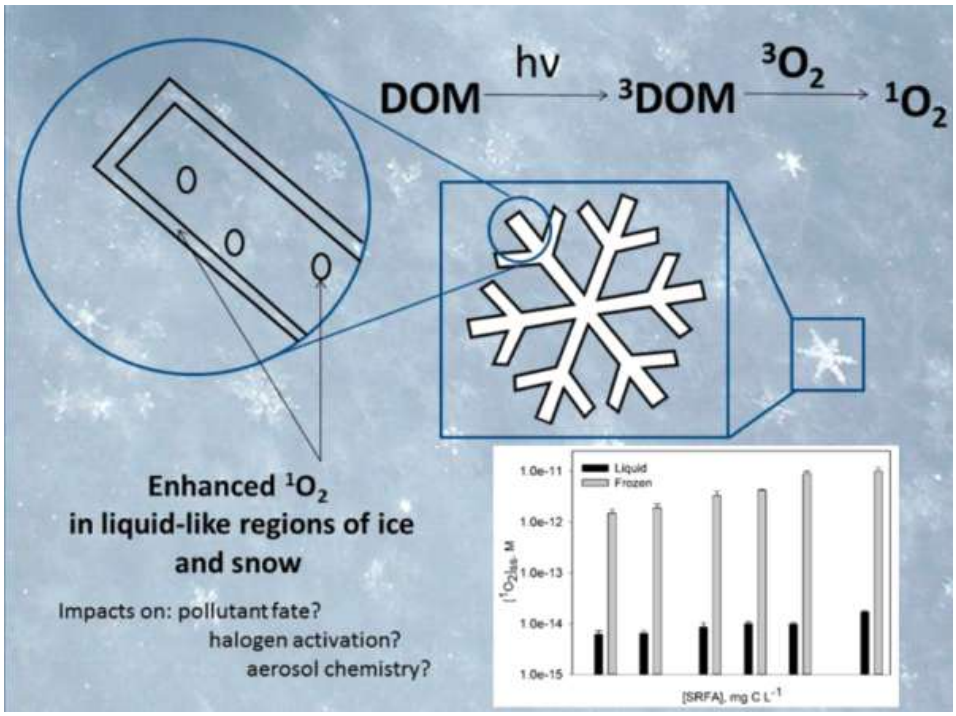



**그림 14.** 용존 유기물이 포함된 얼음 상에서 나타나는 단일항 산소의 형성 모식도 (Fede *et al.* 2015)

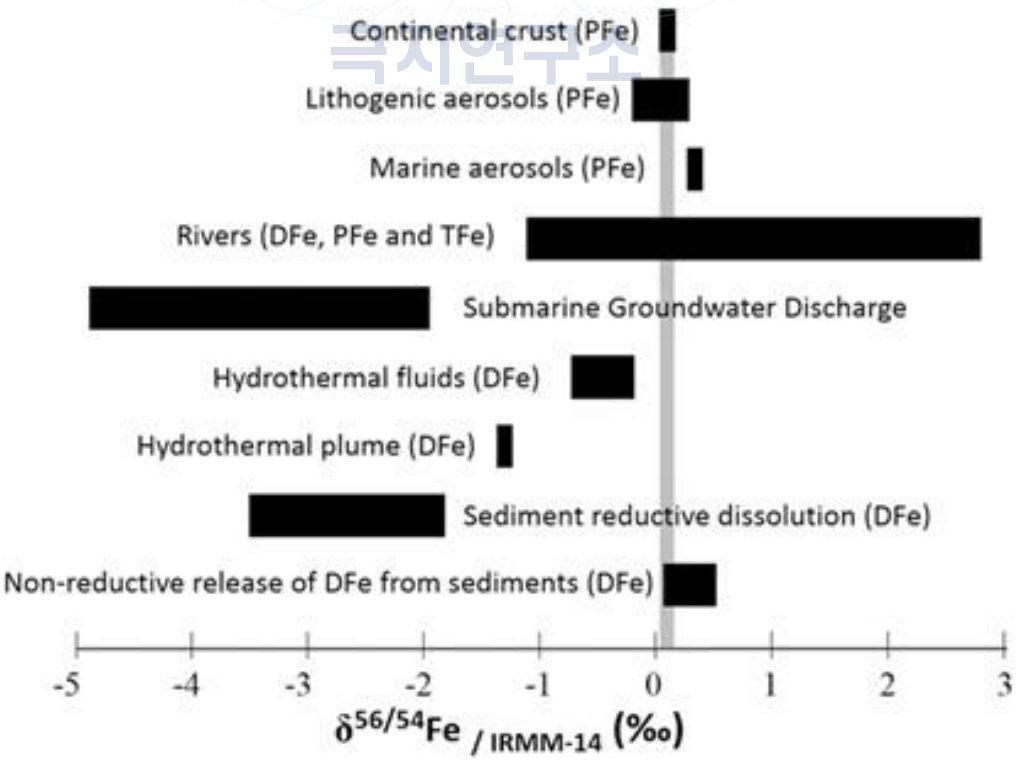



**그림 15.** 기원에 따른 해양 철 동위원소의 값 (Abadie *et al.* 2017)

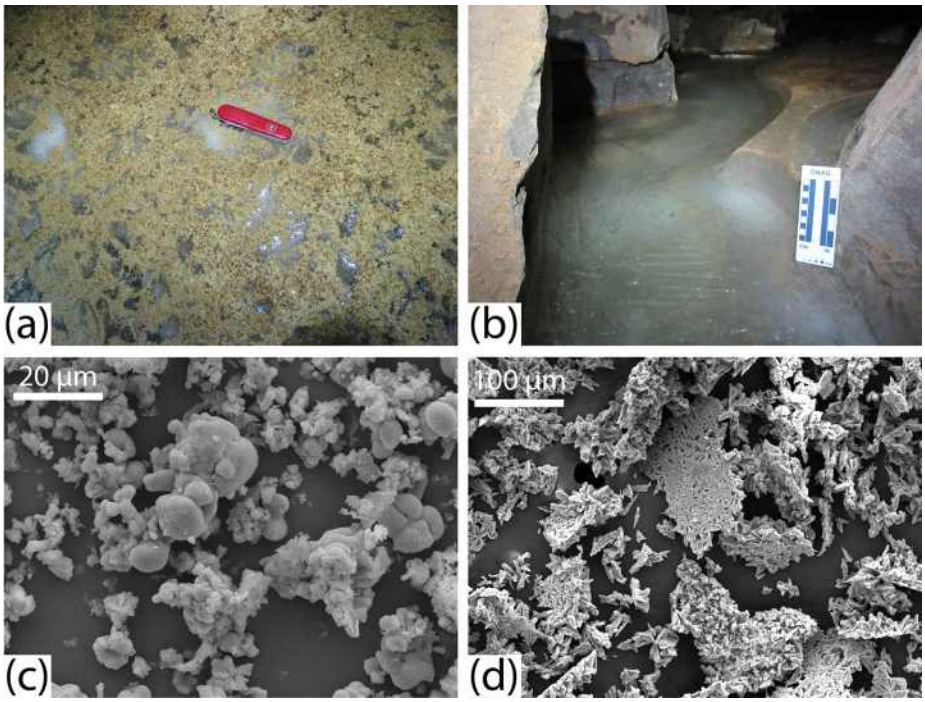



**그림 16.** 얼음동굴에서 발견된 탄산염 광물의 사진 및 SEM 분석 이미지 (Munroe *et al.* 2021)

KOPRI 극지연구소

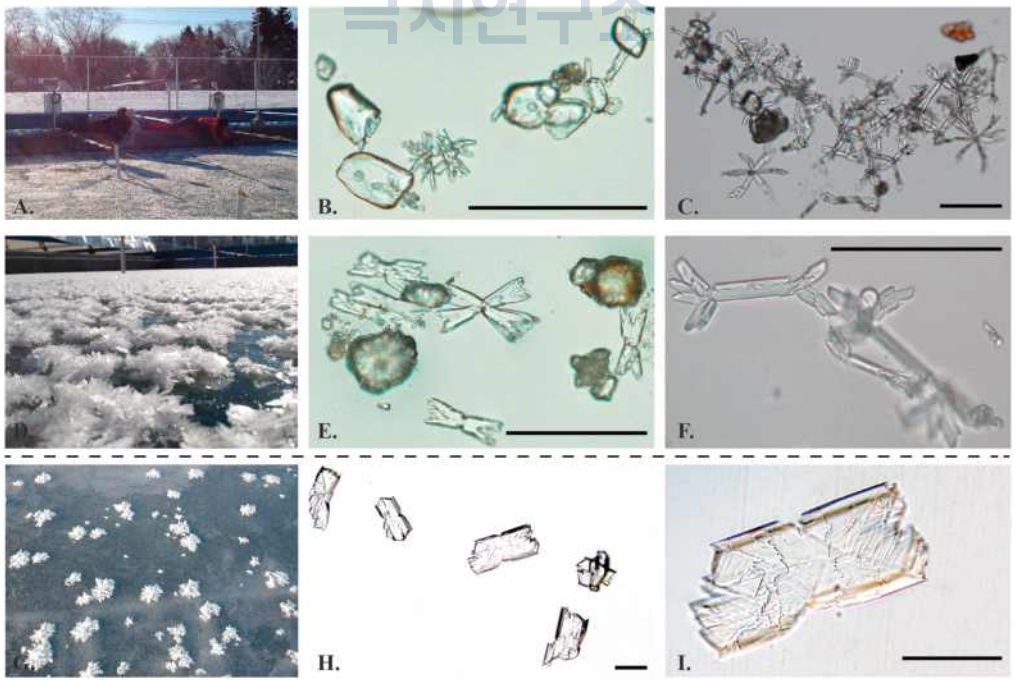



**그림 17.** 해수 동결 실험으로 형성된 ikaite 및 gypsum 광물 사진(Geilfus *et al.* 2013)

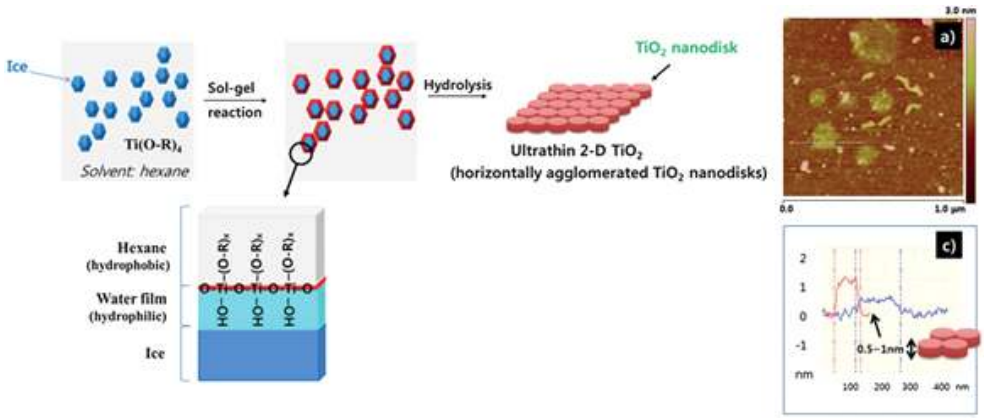



**그림 18.** 얼음 표면에서 이산화티타늄 나노 디스크 합성 (Kim *et al.* 2013)

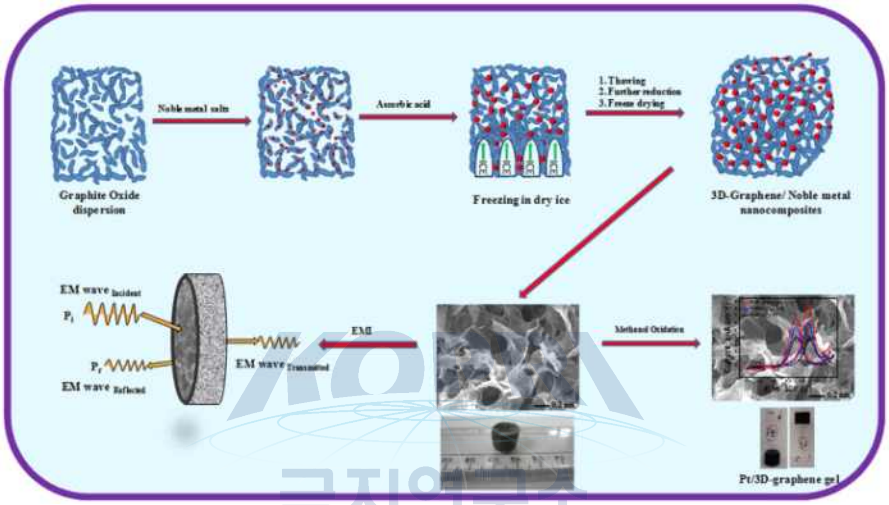



**그림 19.** 3차원 그래핀-귀금속 나노복합단일체 합성 과정 (Sahoo *et al.* 2015)

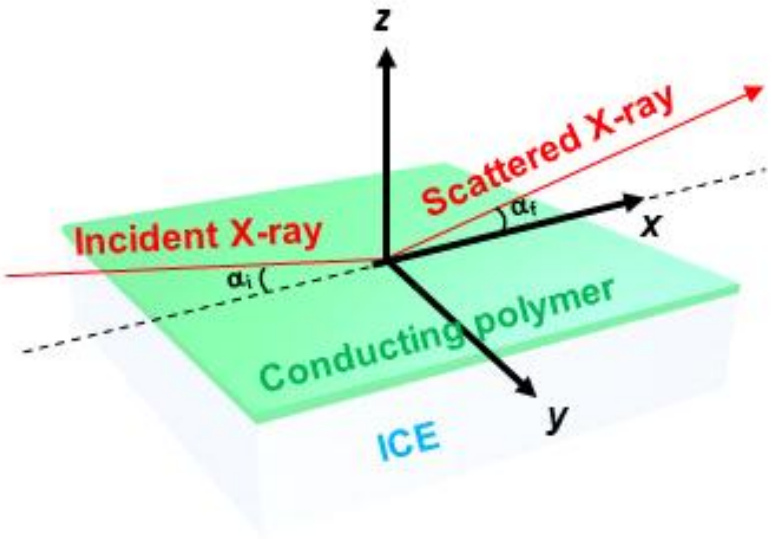



**그림 20.** 얼음 표면에서 합성된 2차원 전도성 고분자의 in-situ grazing X-ray 실험(Choi *et al.* 2015).

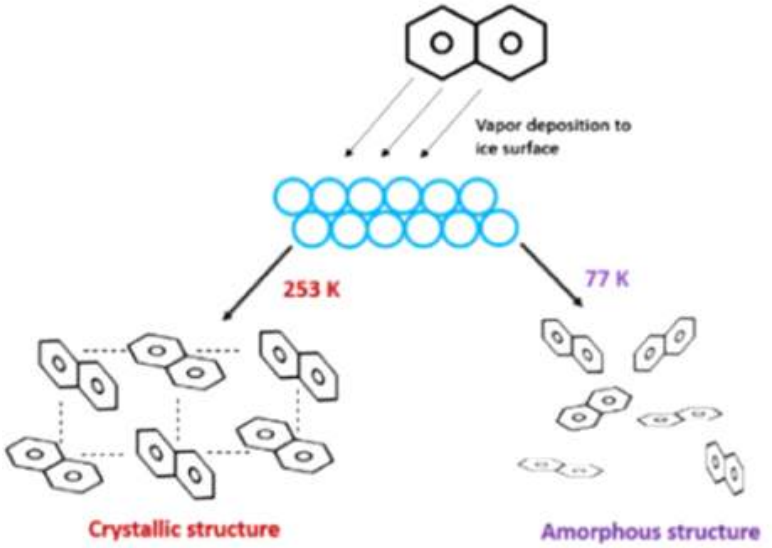



**그림 21.** 얼음 표면에 흡착된 나프탈렌 기체의 얼음 표면 온도에 따른 거동(Ondrušková *et al.* 2018)

KOPRI
극지연구소

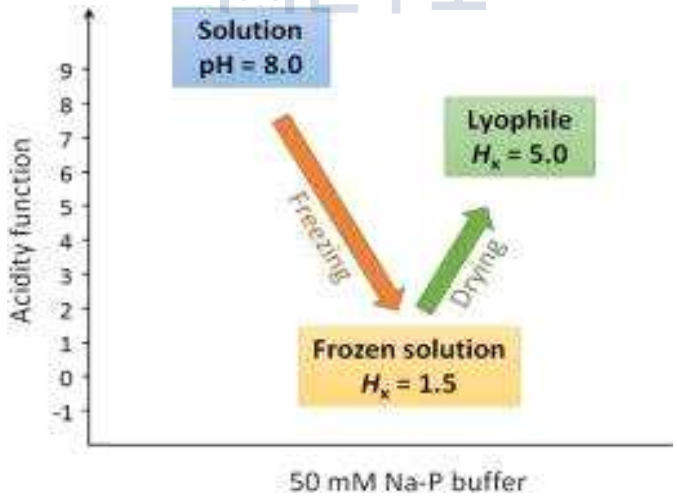



**그림 22.** 동결 및 동결 건조에 따른 인산염 완충 용액의 산성도 변화 모식도(Vetráková *et al.* 2017)

# 제 3 장

# 연구개발수행 내용 및 결과

## 제 1 절. Antarctic ozone hole modifies iodine geochemistry on the Antarctic Plateau①

Andrea Spolaor[1,2,*], Francois Burgay[2,3], Rafael P. Fernandez[4], Clara Turetta1,2, Carlos A. Cuevas[5], Kitae Kim[6], Douglas E. Kinnison[7], Jean-Francois Lamarque[7], Fabrizio de Blasi[1,2], Elena Barbaro[1,2], Juan Pablo Corella[5,8], Paul Vallelonga[9,10], Massimo Frezzotti[11], Carlo Barbante[1,2] & Alfonso Saiz-Lopez[5,*]

[1]Institute of Polar Sciences, CNR-ISP

[2]Department of Environmental Sciences, Informatics and Statistics, University Ca'Foscari of Venice

[3]Paul Scherrer Institute, Laboratory of Environmental Chemistry

[4]Institute for Interdisciplinary Science, National Research Council (ICB-CONICET), FCEN-UNCuyo

[5]Department of Atmospheric Chemistry and Climate, Institute of Physical Chemistry Rocasolano, CSIC

[6]Korea Polar Research Institute

[7]National Center for Atmospheric Research

[8]CIEMAT, Environmental Department

[9]Physics of Ice, Climate and Earth, Niels Bohr Institute, University of Copenhagen,

[10]UWA Oceans Institute, University of Western Australi

[11]Department of Science, University of Roma Tre

KOPRI 극지연구소

① 본 연구는 유럽연합 집행위원회(ERA-PLANET)의 일환인 iCUPE(Integrative and Comprehensive Understanding on Polar Environments) 프로젝트(보조금 협약 번호 689443)를 통해 유럽연합의 Horizon 2020 연구 및 혁신 프로그램의 지원을 받았으며, 또한 이탈리아 남극 연구 국가 프로그램(Programma Nazionale per la Ricerca in Antartide, PNRA, 과제 번호 PNRA16_00295)의 지원을 받았다. 본 연구는 또한 유럽연합 Horizon 2020 연구 및 혁신 프로그램 하에서 유럽연구위원회 집행기관(European Research Council Executive Agency)의 지원(프로젝트 'ERC-2016-COG 726349 CLIMAHAL')을 받았다. NCAR는 미국 국립과학재단(National Science Foundation)의 보조금(Grant Number 1852977)에 의해 지원된다. R.P.F.는 CONICET-UNCuyo(SIIP-06/M111) 및 ANPCyT(PICT 2015-0714)로부터의 재정적 지원에 감사를 표한다. 본 연구는 또한 본 과제(PE20030)와 로마 트레 대학교 과학부에 대한 지원금(MIUR-Italy Dipartimenti di Eccellenza)의 지원을 받아 수행되었으며, 결과는 *Nat. Commun.* 2021, 12, 5836에 출간되었다.

## Abstract

Polar stratospheric ozone has decreased since the 1970s due to anthropogenic emissions of chlorofluorocarbons and halons, resulting in the formation of an ozone hole over Antarctica. The effects of the ozone hole and the associated increase in incoming UV radiation on terrestrial and marine ecosystems are well established; however, the impact on geochemical cycles of ice photoactive elements, such as iodine, remains mostly unexplored. Here, we present the first iodine record from the inner Antarctic Plateau (Dome C) that covers approximately the last 212 years (1800–2012 CE). Our results show that the iodine concentration in ice remained constant during the pre-ozone hole period (1800–1974 CE) but has declined twofold since the onset of the ozone hole era (~1975 CE), closely tracking the total ozone evolution over Antarctica. Based on ice core observations, laboratory measurements and chemistry–climate model simulations, we propose that the iodine decrease since ~1975 is caused by enhanced iodine re-emission from snowpack due to the ozone hole–driven increase in UV radiation reaching the Antarctic Plateau. These findings suggest the potential for ice core iodine records from the inner Antarctic Plateau to be as an archive for past stratospheric ozone trends.

The stratospheric ozone layer, which extends from the tropopause (≈17 km in the tropics and ≈11 km in the polar regions) to the upper stratosphere (≈35 km), completely absorbs the 220 - 290 nm component of the solar electromagnetic spectrum[1] and constitutes a natural shielding that reduces the amount of biologically harmful radiation reaching the Earth's surface within the 290 - 320 nm band[2]. In the mid-1970s, it was hypothesized that the massive emission of chlorofluorocarbons (CFCs) and halons, commonly used as propellants, solvents and refrigerants, could lead to a decrease in stratospheric ozone concentrations[3,4]. These compounds, when exposed to UV radiation, release halogen radicals in the stratosphere that lead to ozone destruction through catalytic cycles[5,6]. The effectiveness of CFCs and halons in depleting stratospheric ozone is maximized at the poles, where the Antarctic ozone hole was identified in the mid-1980s[7]. The effects of enhanced solar UV radiation, resulting from stratospheric ozone loss, on human health[8] and terrestrial[5,9] and marine[10] ecosystems have been well established. However, a limited number of investigations[11,12,13] have been performed to evaluate the impact of ozone hole formation and evolution on the geochemical cycle of photoactive species deposited on polar snow and ice.

In this work, we report the first iodine record from an ice core collected at Dome C (inner East Antarctic Plateau), covering the period of 1800 - 2012. Among the three available Antarctic iodine records[14,15], this is the only one that covers both the pre-ozone

hole and the ozone hole periods and enables us to evaluate the influence of increasing incoming solar UV radiation on the snowpack-atmosphere iodine exchange equilibrium during the ozone hole period (1975 - 2012). Combining field observations, laboratory measurements and chemistry-climate model simulations, we find that the iodine concentration in ice remained relatively stable during the pre-ozone hole period (1800 - 1974) but has gradually declined by a factor of 2 since the onset of the Antarctic ozone hole in the mid-1970s. We suggest that the enhanced incoming solar UV radiation reaching the Antarctic snowpack due to the formation of the Antarctic ozone hole has significantly amplified the ice-to-atmosphere iodine mass transfer, altering the natural geochemical cycle and mobilization of this essential element on the Antarctic Plateau.

## Results and discussion

### The Dome C iodine records

In 1996, a French-Italian team established the first summer camp at Dome C, the inner Antarctic Plateau, and a new all-year facility, Concordia Station (3233 m a.s.l.; 75°05'59"S, 123°19'56"E, ~1200 km from the Southern Ocean), became winter-over operational during the 2005 season. A 13.72 m shallow ice core was drilled close to Concordia during 2012. This record covers ~212 years, from 1800 to 2012. The ice core chronology of the shallow core, which has an estimated ice age uncertainty of up to 5 years, is based on the annual snow accumulation and on the observed $nssSO_4^{2-}$ spikes from the most important past volcanic events[16,17] (see Supplementary Material S1, hereafter SM). Due to the very dry conditions, low precipitation (25 - 30 mm water equivalent per year, mm w.e. $yr^{-1}$) and very thin atmospheric boundary layer (surface pressure of ~650 hPa), Dome C is an ideal site to study snow photochemical processes and snow-atmosphere exchange of reactive elements[18,19,20].

The shallow ice core was sampled at 5 (±1) cm resolution, and for each sample, total iodine (I) and sodium (Na) were measured using an inductively coupled plasma sector field mass spectrometer (ICP-SFMS, see the "Methods" section). Both iodine and sodium are mainly emitted by seawater and sea ice within coastal regions and are transported inland[21,22]. As sodium does not experience photochemical degradation during transport or after deposition, it is widely used as a conservative tracer[23]. To support the 13.72 m-deep shallow core, a 1.3 m-deep snow pit (Sp2013) and a 4 m-deep snow pit (Sp2017) were dug in December 2013 and December 2017, respectively (see S2 in the SM for further details).

The average iodine concentration for the entire ice core record was 0.056±0.037 (1σ) ng $g^{-1}$. To detect a possible tipping point discontinuity within the iodine record, we used the Change-Point Analysis test (CPAt[24], see S3 in the SM). The results suggest that the

iodine concentration record shifted in 1975 (p-value=0.001) with a confidence interval of 90%. Based on the CPAt test, we identified two main periods for the iodine record, one from 1800 to 1974 and the other from 1975 to 2012. The average iodine concentration for the period of 1800 - 1974 remains constant at 0.060±0.039 ng $g^{-1}$, decreasing by almost half to an average concentration of 0.032±0.015 ng $g^{-1}$ for the period of 1975 - 2011 (Fig. 1).

## UV radiation reaching the Antarctic Plateau

To evaluate the hypothesis that the increased UV radiation reaching the Antarctic Plateau due to ozone hole formation has altered iodine concentrations within the ice core, we computed the total ozone column (TOC) and ozone hole evolution during the 1950 - 2010 period using the CAM-Chem chemistry-climate model[25,26] (see "Methods"). Remarkably, the modelled TOC trend above Dome C (TOCDC) matches the iodine record both before and after the observed tipping point discontinuity (Fig. 1c), which coincides with the initial stages of ozone hole formation in ~19755. Furthermore, the modelled mean actinic flux at 300 nm ($AF^{300}$, Fig. 1a) within the closest model grid point to Dome C (74.84° S; 122.5°E; grid resolution 1.9° × 2.5°, see "Methods") completely mirrors the iodine record and total ozone trend (Fig. 1c), highlighting the large radiative changes affecting the inner Antarctic surface due to ozone hole formation.

We computed the mean modelled $TOC^{DC}$ and $AF^{300}$ during the sunlit period of each year (i.e., from 1 September to 28 February) before and after the iodine tipping point and considered these values to be representative of the pre-ozone hole (1950 - 1974) and ozone hole (1975 - 2011) periods. Within these periods, the modelled $TOC^{DC}$ decreased from 334 ± 16 DU (1950 - 1974) to 266 ± 41 DU (1975 - 2017). Consequently, this stratospheric ozone reduction drove an increase in $AF^{300}$ at Dome C from 1.05 × $10^{11}$ to 4.36 × $10^{11}$ quanta $cm^{-2}$ $s^{-1}$ $nm^{-1}$. Note that the mean ozone reduction and the actinic flux enhancement reaching the inner Antarctic surface strongly depend on the specific wavelength, location and period (i.e., early spring or mid-summer) considered. A sensitivity analysis of the spatiotemporal variability in these quantities is provided in section S6 in the SM.

During the ozone hole period, the correlation between [I] and sunlit $TOC^{DC}$ has a positive and significant Pearson coefficient, whereas no significant correlation was found for the pre-ozone hole period (pre-1975: r =−0.1, p-value = 0.65; post-1975: r = 0.398, p-value = 0.015; see S3.3 in the SM). Similarly, [I] and UV forcing, expressed as AF300, were uncorrelated before 1975, while they were anti-correlated afterwards, indicating a direct effect induced by the stronger UV radiation reaching the Antarctic Plateau (pre-1975: r = −0.018, p-value = 0.93; post-1975: r = −0.401, p-value = 0.015; S3.4 in the SM). These significant correlations suggest a direct linkage between stratospheric ozone

and UV radiation reaching the inner Antarctic Plateau surface, which in turn would alter the postdepositional processes controlling the preservation of iodine within the snowpack, as described below.

**Role of ozone hole in the iodine geochemical cycle**

To evaluate the physicochemical processes behind the observed negative correlation between UV surface radiation and ice core iodine, we turn to condensed phase iodine photochemistry. Within liquid aerosols and ice crystals, inorganic iodine is mostly in ionic form as iodide ($I^-(aq)$) and iodate ($IO_3^-(aq)$)[27]. Although iodate is supposed to be more stable than iodide, several studies highlighted that the actual $I^-(aq)/IO_3^-(aq)$ ratio depends on the sampling location, with $I^-(aq)$ being the most abundant species in polar environments[28]. Indeed, investigations performed on the Talos Dome Antarctic ice core (www.taldice.org 72°49'S, 159°11'E, 2315 m a.s.l., accumulation of 80 mm w.e. $yr^{-1}$) highlighted that $I^-(aq)$ is more stable than $IO_3^-(aq)$[15]. Both iodine species showed strong photoactivity in snow matrices since they are enriched during the polar night and depleted during summer[29,30,31]. Under laboratory and simulated Antarctic radiation conditions, it was observed that iodate UV absorption and its subsequent photoreduction ($IO_3^-(aq) + h\nu \rightarrow IO(g) + O_2^-(aq)$) were enhanced in the 275 - 400 nm range, with a maximum peak at 295 nm[32]. Similar conclusions were also reported for the photooxidation of iodide into $I_2(g)$ in real snow samples spiked with known amounts of iodide and exposed to Antarctic sunlight ($O_2(aq) + 4H^+(aq) + 6I^-(aq) \rightarrow 2H_2O + 2\ I_3^-(aq)$; $I_3^-(aq) \leftrightarrow I_2(g) + I^-(aq)$)[33]. Within this photooxidation mechanism that leads to the release of $I_2(g)$ to the atmosphere, a charge-transfer complex with oxygen ($I^- \cdot O_2(aq)$) is formed. This complex has a local absorption maximum between 280 and 330 nm, i.e., encompassing the same spectral range where the largest changes in incoming UV radiation were observed between the pre- and post-ozone hole periods (Fig. 2a).

Given that iodide abundance in polar ice is higher than iodate, we conducted a timeline simulation of iodine photoactivation within ice and snowpack (J-iodine, Fig. 2b) by computing the wavelength integral of the measured iodide absorption spectra multiplied by the modelled AF reaching the inner Antarctic surface during the 1950 - 2010 period (see "Methods"). We find that the normalized J-iodine trend shows consistent agreement with the iodine decrease observed for the Dome C ice record. This finding suggests the occurrence of UV-driven re-emission and mobilization of snow-trapped iodide to the gas phase, following the photooxidation of iodine in ice and subsequent release of $I_2(g)$ to the atmosphere[34]. Indeed, J-iodine remained relatively constant during the pre-1975 period, then increased ~1.5-fold for the mean ozone hole era and ~2.0-fold for the 2006 - 2012 period. This change is indicative of a continuous change in the efficiency of re-emission processes

of ice-trapped iodine that altered the steady state equilibrium, assuming that the iodine deposition velocity remains unaltered (see next section). Due to the pronounced changes in AF intensity reaching the inner Antarctic surface above and below 300 nm during different seasons, the post-1975 J-iodine enhancement computed here is very sensitive to the upper bandwidth limit and to the month used to perform the wavelength integration. Indeed, a sensitivity analysis indicates that up to fourfold more efficient iodide photodissociation efficiency is obtained when the narrower 280 - 307 nm AF band is considered, while an equivalent ~5-fold J-iodine enhancement is reached if only the October mean evolution is used (see Supplementary Figs. 5 and 6). Therefore, regardless of the exact wavelength interval and seasonal period considered, our combined experimental and modelling results indicate that the increase in UV solar radiation observed since the onset of the ozone hole has promoted the release of active iodine from the snowpack to the atmosphere. This validation corroborates our hypothesis that stronger UV radiation led to the enhanced re-emission of iodine deposited on polar ice, thereby explaining the overall decrease in iodine concentration at Dome C during the 1975 - 2012 period.

### Possible competitive processes (CPs)

To explain the observed shift in the iodine trend at Dome C, we explored different alternative hypotheses that involve possible competitive processes (CPs), such as (a) changes in site snow accumulation, (b) dependence on snow pack physical characteristics, (c) snow pack postdepositional processes and spatial variability, (d) changes in the transport mechanism from the coast to the site, and (e) changes in the strength of coastal source emissions. In the SM (S7), we also discuss the possible effects of sample storage on iodine loss from firn samples. All these alternative hypotheses were refuted, as they failed to provide a consistent explanation that connects theory with observations, as discussed below. Additional iodine ice core records exist in both the Arctic and Antarctic and are discussed in the SM (S4 and Supplementary Fig. 1); however, these records do not provide additional information for explaining the Dome C iodine trend.

### CP(a) - Change in snow accumulation

The inner Antarctic Plateau is characterized by low accumulation rates and cold temperatures that can affect snow metamorphism. Due to the very low annual snow deposition[35], it is possible to estimate snow accumulation at Dome C only at pluriannual scale using snow/firn core analysis. However, the average snow accumulation rate computed during different studies is very similar: for the period of 1955 - 1998, the rate was 26 ± 1.3 mm w.e. $yr^{-1}$; for the period of 1816 - 1998, it was 25 ± 1.3 mm w.e. $yr^{-1}$ [36]; and for the 2006 - 2013 period[35], the rate was 27 mm w.e. $yr^{-1}$. This result leads

to the conclusion that the snow accumulation rate at this location has not changed significantly over the last 200 years and that in the worst scenario, it might have affected the iodine signal by no more than 10%. Note that the spatial variability in accumulation might lead to interannual variability but will not affect the recorded trend (Supplementary Fig. 4, lower panel and Supplementary Table 2). For this reason, we assume a constant snow accumulation rate over the entire period covered by the ice core record, and we discard the possibility that snow accumulation changes can explain the large observed reduction in iodine concentration since 1975.

We also investigated the possible role of the precipitation seasonality at Dome C. Combining a Lagrangian trajectory model output and the European Re-Analysis ERA40 data (from 1980 to 2011), it is reported that ~35 - 40% of the annual precipitation at Dome C occurred during the summer season (December to February) with the remaining 60 - 65% being homogenously distributed among the remaining months[37]. We found that the seasonality of snow precipitation is negligible due to the wind redistribution of snow accumulation at the surface[38]. UV can penetrate the snowpack for the first 20 - 30 cm, which corresponds to 2 - 3 years of burial snow due to the low snow accumulation rate at Dome C[38]. Independently of the seasonal precipitation pattern, all the iodine present in the annual snow layers would experience a similar photochemical activation, thereby greatly minimizing the hypothetical role of a seasonal precipitation pattern change. However, the potential impact of systematic changes in precipitation seasonality over several years remains an uncertainty for the interpretation of future iodine ice core records and might contribute to the observed spatial variability.

### CP(b) - Role of snow pack physical characteristics

The snow density can affect the chemical signal both by modifying the extent of light penetration and by changing the gas permeability within the snow pack. The average snow density at Dome C increases with depth, making the snow layers progressively less permeable to gas movement until the close-off depth is reached (≈80 m depth). The gaseous species can move within the snow/ice grains until reaching this depth, but their escape into the atmosphere is potentially facilitated by the higher porosity of the surface layers (i.e., with a lower density). However, the decline in iodine concentration was observed only in the topmost 3.5 m (1.2 m w.e.) of the snow pack (Fig. 1c), and the direct comparison with the Sp2017 iodine and density profiles does not endorse this hypothesis (see Supplementary Fig. 3). Indeed, the Sp2017 density profile presents a typical shallow density increase in the topmost 3.5 m (from 0.32 to 0.38 kg $L^{-1}$), which cannot justify the observed iodine behaviour.

Another process that can affect the stabilization of iodine species in snow is grain size.

The grain size increases with depth[40], reducing the specific surface where gas-phase iodine can be bound and/or absorbed. If a relationship between the grain size and iodine concentration existed, we might expect an enhancement of iodine concentration in the topmost part of the record, but we observe the opposite. Snow grain size was measured in Sp2017, and similar to snow density, it cannot explain the iodine trend (Supplementary Fig. 3).

Finally, snow metamorphism is mainly driven by the temperature gradient prevailing in the first metres of snow between the polar summers and winters and occurs on timescales on the order of weeks or months. Continuous snow temperature measurements are routinely performed at Dome C down to 10 m depth[41]. The largest difference in temperature during the year is measured in the uppermost 2 m, particularly at the surface where the ΔT can reach 44 °C. Note that the largest measured temperature gradient at 2.5 m depth is 8 °C (Supplementary Table 3), which slows snow metamorphosis and possible related processes. In our shallow core, the iodine shift is detected at a depth of 3.5 m. Moreover, when considering iodine postdepositional processes within the snow pack, we need to consider that iodine photochemical activation is fast and can cause a loss of up to 90% of the deposited iodine within a day[31,42]. The radiative transfer within the snowpack will be further discussed in the next paragraph, but it suggests that the snow metamorphism, the physical characteristics of the snowpack and its sintering process play a negligible role in describing the observed iodine trend.

**CP(c) - Inner snow pack postdepositional processes and UV light penetration**

We also investigated the effects of UV penetration into snowpack. UV light can penetrate the snowpack for the first 20 - 30 cm[39], corresponding to 2 - 3 years of burial due to the low snow accumulation rate at Dome C. UV light penetration would have caused the re-emission of iodide as gaseous I2 into the atmosphere for ~2 - 3 years. However, if this case were true for iodine, we would expect a similar iodine concentration along the entire core or, alternatively, iodine accumulation would occur in the surface layers due to the migration of gaseous iodine from the deeper sections of the core. Evidence that UV penetration in snowpack does not play a significant role also comes from the availability of additional iodine records (i.e., Sp2013 and Sp2017) that showed similar trends and concentrations over the last 40 years (Supplementary Table 2 and Supplementary Fig. 4). Furthermore, our iodine analyses from the Law Dome (LD) ice core, which has an average annual snow accumulation of ≈740 mm w.e. yr−1 (i.e., ~30 times Dome C), showed well-preserved iodine peaks corresponding to the winter periods (polar night)[14,29]. If light penetration determined re-emission from the snowpack, we would expect

a smoother signal in the record compared with the observed sharp peaks. On these grounds, we argue that the iodine trend is influenced by the enhancement of UV radiation and the increase in photoreactivity on the surface snow instead of depending on postdepositional processes occurring within the compacted deep ice. This finding is also supported by the different trend of iodine, which decreases from the surface to 3.5 m (1975 CE), in comparison with other photochemical species analysed in Sp2017 (Supplementary Fig. 4).

**CP(d) - Changes in the transport mechanism from the coast to the site**

To understand whether changes in the transport mechanisms from the coast to Dome C played a role in explaining the iodine behaviour, we evaluated how sodium concentration has changed over the last two centuries. Overall, the sodium average concentration for the entire record was 41 ± 19 (1σ) ng g−1; however, a slight increase was recorded from 1975 to 2012 (50 ± 23 ng g−1) compared with the period spanning 1800 to 1975 (39 ± 14 ng $g^{-1}$). Note that the ice core record had some gaps from 1989 to 1997 that were filled with Na concentration data retrieved from Sp2013 and Sp2017 (see S3.5 in the SM), producing a merged sodium (NaM) and iodide (IM) record for direct comparison.

Comparing the NaM and IM profiles, we observe that they have opposite trends during the last few decades (Fig. 3). The increase in sodium concentration recorded since the mid-1970s suggests enhanced transport from the coast to Dome C. This finding is consistent with model simulations and observations that report a poleward shift in the mid-latitude jet stream[43,44] and with the enhanced cyclonic activity driven by the phase change in the Interdecadal Pacific Oscillation (IPO) as well as strengthening of westerlies due to global warming[45]. However, the enhanced poleward transport is not mirrored by the iodine record, which, conversely, has decreased since 1975. The decoupling between NaM and IM is corroborated by the Pearson correlation coefficients calculated for the periods of 1800 - 1974 and 1975 - 2017 (see S3.5 in the SM). A significant statistical correlation existed between iodine and sodium during the pre-ozone hole period (1800 - 1974; r = 0.44; p-value < 0.0001) but not for the ozone hole period (r = −0.1; p-value = 0.54). Thus, the statistical tests support that between 1800 and 1974, iodine and sodium were transported and deposited following similar mechanisms. Once deposited on the snowpack, iodine experienced postdepositional processes whose efficiency remained relatively constant throughout the entire pre-ozone hole period investigated in this study (Figs. 1 and 3). The decoupling observed since 1975 is inconsistent with an iodine decrease driven by changes in atmospheric transport. All of these previous studies provide additional evidence that the different behaviours of Na and I from 1975 to 2017 at Dome C were associated with processes that interfered with iodine deposition and preservation in the snowpack rather

than with changes in the snow accumulation rate, coastal source strength or transport efficiency. In fact, enhanced tropospheric transport from the coast to the Antarctic inland[45] would have caused an increase in both Na and I concentrations.

### CP(e) – Possible changes in the strength of coastal source emissions

Finally, we explored the possible changes in the strength of iodine emissions from coastal areas. However, this hypothesis is not supported by models or observations. Note that the most relevant iodine source on a global scale is the ocean, providing ~2.3 Tg(I) yr $^{1}$ of organic (mostly $CH_3I$) and inorganic (I2 and HOI) iodine[46,47]. Global iodine emissions show strong latitudinal variability, with stronger emissions in the tropical and mid-latitude oceans and significantly decreasing emissions towards the poles[48]. In polar regions, iodine sources are mainly connected to first-year sea ice[49,50], with both macro- and microalgae living under sea ice51 and abiotic activation of iodine on sea ice and snow surfaces[22,52] playing a role. Both the biological and abiotic iodine emissions in the polar regions depend on the thickness and extent of seasonal sea ice, being more prominent for thinner sea ice and large extensions of first-year sea ice. A trend of increasing Antarctic seasonal sea ice extent has been observed for the last decades up to 2014, followed by a decline from 2015 to 2017[53]. Thus, it would be expected that in any case, coastal sea ice emissions of iodine increased during the studied period, contrary to what we observed in the ice core record.

This study suggests that the human-induced stratospheric ozone hole has altered the natural geochemical cycle of iodine. Combining field measurements (ice core, snow pit, surface snow observations) with laboratory (iodine absorption spectra, UV-driven photooxidative mechanisms) and modelling (ozone hole evolution and associated actinic flux changes) results, we conclude that the enhanced incident UV radiation due to the ozone hole has caused a continuous decline in iodine concentration in ice in inner Antarctica since ~1975. This recent phenomenon has modified the previously steady iodine equilibrium between snowpack and the atmosphere in the interior of Antarctica by increasing re-emissions from snowpack. The resulting increase in ice-to-atmosphere iodine mass transfer has relevant implications for polar tropospheric chemistry and for the Earth's radiative budget since iodine catalytic cycles play a crucial role in the destruction of tropospheric ozone[26,27,54,55] and can also act as cloud condensation nuclei (CCN)[56,57,58]. Furthermore, surface re-emission of iodine from central Antarctica and subsequent redistribution by atmospheric transport could potentially be a source of the widespread distribution of iodine observed by satellite measurements over the entire Antarctic continent59. Finally, given the direct link observed between ice core iodine at Dome C and stratospheric ozone hole evolution, we suggest that the ice core iodine present on the Antarctic Plateau may potentially serve as an archive for past stratospheric ozone changes

at centennial to millennial time scales.

## Methods

### Shallow core processing and analysis

The shallow core was cut and sampled at 5 ± 1 cm resolution using a ceramic knife and rinsed with ultrapure water (UPW) after each use. Only the central part of the core was used for the analysis, and the outer 2 cm was removed by scraping with a ceramic knife. The core samples were processed at the Institute of Polar Sciences of the National Research Council (ISP-CNR) in a class 1000 inorganic clean room under a class 100 laminar-flow bench. Iodine and sodium analyses in the snow pit and ice core samples were conducted on melted and non-acidified samples. Total sodium (Na) and iodine (I) concentrations were determined by ICP-SFMS following Spolaor et al.[60]. Each analytical run started and ended with a UPW cleaning session of 3 min to ensure a stable background level throughout the analysis. The external standards that were used to calibrate the analytes were prepared by diluting a 1000 ppm stock IC (ion chromatography) standard solution (TraceCERT® purity grade, Sigma-Aldrich, MO, USA). The standard concentrations ranged between 1 and 200 ng g−1 for sodium and 0.005 and 0.200 ng g−1 for iodine. The relative standard deviation (RSD %) was low for all analytes, ranging from 3 to 4% for sodium and 2 to 5% for iodine. The instrumental limit of detection (LoD), calculated as three times the standard deviation of the blank (n = 10), was 1 ng g−1 for Na and 0.003 ng g−1 for I. We evaluated the stability of iodine by repeating the analysis of a selected sample multiple times. We did not observe any significant iodine loss during the analytical run (≈12 h).

### CAM-Chem chemistry-climate model setup: Halogen chemistry and radiative transfer

The stratospheric ozone hole evolution, as well as the radiative transfer of ultraviolet (UV) actinic flux reaching the Antarctic surface, was computed using the global 3-D chemistry-climate model CAM-Chem (Community Atmospheric Model with chemistry, version 4)[61], which is the atmospheric component within the CESM framework (Community Earth System Model)[62]. The model setup follows the CCMI-REFC1 recommendation for 1950 - 2010 simulations (i.e., we forced the model with prescribed sea surface temperatures and sea ice distributions)[63] but incorporates an explicit treatment of very-short lived (VSL) chlorine, bromine and iodine sources and chemistry[46,47,64,65,66]. The model configuration used here is identical to the one used previously to compare CAM-Chem results with Arctic iodine ice records[26], although here, we extracted monthly output with the wavelength-dependent actinic flux at all atmospheric layers and the surface. Additional

details of the CAM-Chem configuration and validation are provided in S5 of the SM.

CAM-Chem shows a good ability to reproduce the size and depth of ozone hole evolution within chemistry-climate simulations[25] and presents excellent agreement with satellite ozone observations during the modelled period (Supplementary Fig. 2). The total ozone column polar cap ($TOC^{SP}$) used for the model validation was computed as the cosine-weighted mean within the 63°S - 90°S latitudinal band during October. The model mean output during the austral sunlit period (i.e., from 1 September to 28 February of next year) was computed to perform the correlations with the ice core record. The complete sunlit period (spring + summer) was selected because even when the largest changes in TOC and $AF^{300}$ associated with the ozone hole are observed during spring, the overall intensity of UV radiation reaching the Antarctic surface maximizes during the summer because of the higher solar zenith angle (SZA). The 300 nm wavelength bin used for the actinic flux computation at the model surface ($AF^{300}$) has an ~3.5 nm width and is centred at 300.5 nm. AF300 values were extracted at the grid point closest to Dome C on the Antarctic Plateau (74.84° S; 122.5°E; grid resolution 1.9° × 2.5°; model mean altitude of 3300 m a.s.l.; see S5 in the SM).

The iodide photolysis rate constant within the snowpack (J-iodine) was determined offline following Eq. (1)

$$I-iodine(yr) = \int \sigma^{Abs}(\lambda) \times AF^{surf}(\lambda, yr) \times \Phi(\lambda) d\lambda$$

where $\sigma^{Abs}(\lambda)$ is the absorption spectrum of iodide as a function of wavelength ($\lambda$) measured in iodine-containing frozen solutions[33]; $AF^{surf}(\lambda, yr)$ is the wavelength-dependent surface CAM-Chem actinic flux reaching Dome C for each year (yr); and $\Phi(\lambda)$ is the quantum yield for the initial UV absorption step leading to the formation of triiodide in the frozen solution, assumed to be unity ($\Phi(\lambda) = 1$). The wavelength integration used to compute annual J-iodine was performed for the 280 - 313 nm bandwidth; below 280 nm, the transmittance of the Pyrex filter used for measuring $\sigma^{Abs}(\lambda)$ was considerably reduced, while above 313 nm, the iodide absorbance of iodide and the $I^- - O_2(aq)$ complex rapidly dropped to zero[33]. The resolutions of the CAM-Chem wavelength bins used to compute J-iodine are provided in the SM. Due to the rapid increase in $AF^{surf}$ intensity within the 290 - 330 nm range, as well as on the seasonal changes in the net solar radiation reaching the polar regions between spring, summer and fall, the absolute J-iodine computation is very sensitive to the upper bandwidth limit used for wavelength integration and to the monthly period of time considered for each year. A sensitivity analysis is provided in section S6 of the SM (Supplementary Figs. 5 and 6).

## REFERENCES


1. Orphal, J. et al. Absorption cross-sections of ozone in the ultraviolet and visible spectral regions: Status report 2015. *J. Mol. Spectrosc.* **327**, 105 - 121 (2016).
2. Williamson, C. E. et al. Solar ultraviolet radiation in a changing climate. *Nat. Clim. Change* **4,** 434 - 441 (2014).
3. Molina, M. J. & Rowland, F. S. Stratospheric sink for chloro fluoromethanes: hlorine atom-catalysed destruction of ozone. *Nature* **249,** 810 - 812 (1974).
4. McElroy, M. B., Salawitch, R. J., Wofsy, S. C. & Logan, J. A. Reductions of ntarctic ozone due to synergistic interactions of chlorine and bromine. *Nature* **321,** 759 - 762 (1986).
5. Solomon, S. Stratospheric ozone depletion: a review of concepts and history. *Rev. Geophys* **37,** 275 - 316 (1999).
6. Newman, P. A. et al. What would have happened to the ozone layer if chloro fluorocarbons (CFCs) had not been regulated? *Atmos. Chem. Phys.* **9,** 2113 - 2128 (2009).
7. Farman, J. C., Gardiner, B. G. & Shanklin, J. D. Large losses of total ozone in Antarctica reveal seasonal $ClO_x/NO_x$ interaction. *Nature* **315,** 207 - 210 (1985).
8. Slaper, H., Velders, G. J. M., Daniel, J. S., de Gruijl, F. R. & van der Leun, J. C. Estimates of ozone depletion and skin cancer incidence to examine the Vienna Convention achievements. *Nature* **384,** 256 - 258 (1996).
9. Ballaré, C. L., Mazza, C. A., Austin, A. T. & Pierik, R. Canopy Light and Plant Health. *Plant Physiol.* **160,** 145 (2012).
10. Llabrés, M. et al. Impact of elevated UVB radiation on marine biota: a meta-analysis. *Glob. Ecol. Biogeogr.* **22,** 131 - 144 (2013).
11. McCabe, J. R., Thiemens, M. H. & Savarino, J. A record of ozone variability in South Pole Antarctic snow: Role of nitrate oxygen isotopes. *J. Geophys. Res. Atmospheres* https://doi.org/10.1029/2006JD007822 (2007).
12. Jones, A. E. & Wolff, E. W. An analysis of the oxidation potential of the South Pole boundary layer and the influence of stratospheric ozone depletion. *J. Geophys. Res.* Atmospheres https://doi.org/10.1029/2003JD003379 (2003).
13. Lamarque, J.-F., McConnell, J. R., Shindell, D. T., Orlando, J. J. & Tyndall, G. S. Understanding the drivers for the 20th century change of hydrogen peroxide in Antarctic ice-cores. *Geophys. Res. Lett.* https://doi.org/10.1029/2010GL045992 (2011).
14. Vallelonga, P. et al. Sea-ice-related halogen enrichment at Law Dome, coastal East Antarctica. *Clim. Past.* **13,** 171 - 184 (2017).
15. Spolaor, A. et al. Halogen species record Antarctic sea ice extent over glacial-interglacial periods. *Atmos. Chem. Phys.* **13,** 6623 - 6635 (2013).


KOPRI 극지연구소

16. Parrenin, F. et al. The EDC3 chronology for the EPICA Dome C ice core. *Clim. Past.* **3,** 485 – 497 (2007).
17. Gautier, E., Savarino, J., Erbland, J., Lanciki, A. & Possenti, P. Variability of sulfate signal in ice core records based on five replicate cores. *Clim. Past.* **12,** 103 – 113 (2016).
18. Song, S. et al. Understanding mercury oxidation and air – snow exchange on the East Antarctic Plateau: a modeling study. *Atmos. Chem. Phys.* **18,** 15825 – 15840 (2018).
19. Savarino, J. et al. Oxygen isotope mass balance of atmospheric nitrate at Dome C, East Antarctica, during the OPALE campaign. *Atmos. Chem. Phys.* **16,** 2659 – 2673 (2016).
20. Blunier, T., Floch, G. L., Jacobi, H.-W. & Quansah, E. Isotopic view on nitrate loss in Antarctic surface snow. *Geophys. Res. Lett.* https://doi.org/10.1029/2005GL023011 (2005).
21. Legrand, M. et al. Year-round records of bulk and size-segregated aerosol composition in central Antarctica (Concordia site) – Part 1: Fractionation of sea-salt particles. *Atmos. Chem. Phys.* **17,** 14039 – 14054 (2017).
22. Fernandez, R. P. et al. Modeling the Sources and Chemistry of Polar Tropospheric Halogens (Cl, Br, and I) Using the CAM-Chem Global Chemistry-Climate Model. *J. Adv. Modeling Earth Syst.* **11,** 2259 – 2289 (2019).
23. Ayers, G. P., Gillett, R. W., Cainey, J. M. & Dick, A. L. Chloride and bromide loss from sea-salt particles in southern ocean air. *J. Atmos. Chem.* **33,** 299 – 319 (1999).
24. Taylor, W. A. Change-point analysis: a powerful new tool for detecting changes. Baxter Healthcare Corporation, Round Lake, IL 60073, Taylor Enterprise. (2000).
25. Fernandez, R. P., Kinnison, D. E., Lamarque, J. F., Tilmes, S. & Saiz-Lopez, A. Impact of biogenic very short-lived bromine on the Antarctic ozone hole during the 21st century. *Atmos. Chem. Phys.* **17,** 1673 – 1688 (2017).
26. Cuevas, C. A. et al. Rapid increase in atmospheric iodine levels in the North Atlantic since the mid-20th century. *Nat. Commun.* **9,** 1452 (2018).
27. Saiz-Lopez, A. et al. Atmospheric chemistry of iodine. *Chem. Rev.* **112,** 1773 – 1804 (2012).
28. Gilfedder, B. S., Lai, S. C., Petri, M., Biester, H. & Hoffmann, T. Iodine speciation in rain, snow and aerosols. *Atmos. Chem. Phys.* **8,** 6069 – 6084 (2008).
29. Spolaor, A. et al. Seasonality of halogen deposition in polar snow and ice. *Atmos. Chem. Phys.* **14,** 9613 – 9622 (2014).
30. Frieb, U., Deutschmann, T., Gilfedder, B. S., Weller, R. & Platt, U. Iodine monoxide in the Antarctic snowpack. *Atmos. Chem. Phys.* **10,** 2439 – 2456 (2010).
31. Spolaor, A. et al. Diurnal cycle of iodine, bromine, and mercury concentrations in

Svalbard surface snow. *Atmos. Chem. Phys.* **19,** 13325 – 13339 (2019).

32. Gálvez, Ó., Baeza-Romero, M. T., Sanz, M. & Saiz-Lopez, A. Photolysis of frozen iodate salts as a source of active iodine in the polar environment. *Atmos. Chem. Phys.* **16,** 12703 – 12713 (2016).
33. Kim, K. et al. Production of molecular iodine and tri-iodide in the frozen solution of iodide: implication for polar atmosphere. *Environ. Sci. Technol.* **50,** 1280 – 1287 (2016).
34. Kim, K., Choi, W., Hoffmann, M. R., Yoon, H.-I. & Park, B.-K. Photoreductive dissolution of iron oxides trapped in ice and its environmental implications. *Environ. Sci. Technol.* **44,** 4142 – 4148 (2010).
35. Genthon, C., Six, D., Scarchilli, C., Ciardini, V. & Frezzotti, M. Meteorological and snow accumulation gradients across Dome C, East Antarctic plateau. *Int. J. Climatol.* **36,** 455 – 466 (2016).
36. Frezzotti, M. et al. Spatial and temporal variability of snow accumulation in East Antarctica from traverse data. *J. Glaciol.* **51,** 113 – 124 (2005).
37. Scarchilli, C., Frezzotti, M. & Ruti, P. Snow precipitation at four ice core sites in East Antarctica: provenance, seasonality and blocking factors. *Clim. Dyn.* **37,** 2107 – 2125 (2011).
38. Picard, G., Arnaud, L., Caneill, R., Lefebvre, E. & Lamare, M. Observation of the process of snow accumulation on the Antarctic Plateau by time lapse laser scanning. *Cryosphere* **13,** 1983 – 1999 (2019).
39. France, J. L. et al. Snow optical properties at Dome C (Concordia), Antarctica; implications for snow emissions and snow chemistry of reactive nitrogen. *Atmos. Chem. Phys.* **11,** 9787 – 9801 (2011).
40. Champollion, N. et al. Marked decrease in the near-surface snow density retrieved by AMSR-E satellite at Dome C, Antarctica, between 2002 and 2011. *Cryosphere* **13,** 1215 – 1232 (2019).
41. Macelloni, G. et al. Ground-based L-band emission measurements at dome-C Antarctica: the DOMEX-2 experiment. *IEEE Trans. Geosci. Remote Sens.* **51,** 4718 – 4730 (2013).
42. Spolaor, A. et al. Feedback mechanisms between snow and atmospheric mercury: results and observations from field campaigns on the Antarctic plateau. *Chemosphere* **197,** 306 – 317 (2018).
43. Polvani, L. M., Waugh, D. W., Correa, G. J. P. & Son, S.-W. Stratospheric ozone depletion: the main driver of twentieth-century atmospheric circulation changes in the Southern Hemisphere. *J. Clim.* **24,** 795 – 812 (2010).
44. Banerjee, A., Fyfe, J. C., Polvani, L. M., Waugh, D. & Chang, K.-L. A pause in Southern Hemisphere circulation trends due to the Montreal Protocol. *Nature* **579,** 544

KOPRI 극지연구소

- 548 (2020).

45. Stammerjohn, S. E. & Scambos, T. A. Warming reaches the South Pole. Nat. Clim. Change ,https://doi.org/10.1038/s41558-020-0827-8 (2020). 46. Saiz-Lopez, A. et al. Iodine chemistry in the troposphere and its effect on ozone. *Atmos. Chem. Phys.* **14,** 13119 - 13143 (2014).
47. Prados-Roman, C. et al. A negative feedback between anthropogenic ozone pollution and enhanced ocean emissions of iodine. *Atmos. Chem. Phys.* **15,** 2215 - 2224 (2015).
48. Carpenter, L. J. Iodine in the marine boundary layer. *Chem. Rev.* **103,** 4953 - 4962 (2003).
49. Atkinson, H. M. et al. Iodine emissions from the sea ice of the Weddell Sea. *Atmos. Chem. Phys.* **12,** 11229 - 11244 (2012).
50. Abbatt, J. P. D. et al. Halogen activation via interactions with environmental ice and snow in the polar lower troposphere and other regions. *Atmos. Chem. Phys.* **12,** 6237 - 6271 (2012).
51. Saiz-Lopez, A., Blaszczak-Boxe, C. S. & Carpenter, L. J. A mechanism for biologically induced iodine emissions from sea ice. *Atmos. Chem. Phys.* **15,** 9731 - 9746 (2015).
52. Raso, A. R. W. et al. Active molecular iodine photochemistry in the Arctic. *Proc. Natl Acad. Sci. USA* **114,** 10053 (2017).
53. Parkinson, C. L. A 40-y record reveals gradual Antarctic sea ice increases followed by decreases at rates far exceeding the rates seen in the Arctic. *Proc. Natl Acad. Sci. USA* **116,** 14414 (2019).
54. Saiz-Lopez, A. et al. Boundary layer halogens in coastal Antarctica. *Science* **317,** 348 - 351 (2007).
55. Schonhardt, A. et al. Observations of iodine monoxide columns from satellite. *Atmos. Chem. Phys.* **8,** 637 - 653 (2008).
56. O 'Dowd, C. D. et al. Marine aerosol formation from biogenic iodine emissions. *Nature* **417,** 632 - 636 (2002).
57. Sipilä, M. et al. Molecular-scale evidence of aerosol particle formation via sequential addition of $HIO_3$. *Nature* **537,** 532 (2016).
58. Baccarini, A. et al. Frequent new particle formation over the high Arctic pack ice by enhanced iodine emissions. *Nat. Commun.* **11,** 4924 (2020).
59. Schonhardt, A. et al. Simultaneous satellite observations of IO and BrO over Antarctica. *Atmos. Chem. Phys.* **12,** 6565 - 6580 (2012).
60. Spolaor, A. et al. Canadian Arctic sea ice reconstructed from bromine in the Greenland NEEM ice core. *Sci. Rep.* **6,** 33925 (2016).
61. Lamarque, J. F. et al. CAM-chem: description and evaluation of interactive atmospheric chemistry in the Community Earth System Model. *Geosci. Model Dev.* **5,**

KOPRI 극지연구소

369 - 411 (2012).
62. Tilmes, S. et al. Representation of the Community Earth System Model (CESM1) CAM4-chem within the Chemistry-Climate Model Initiative(CCMI). *Geosci. Model Dev.* **9,** 1853 - 1890 (2016).
63. Eyring, V. et al. Overview of IGAC/SPARC Chemistry - Climate Model Initiative (CCMI) Community Simulations in Support of Upcoming Ozone and Climate Assessments. 48 - 66 (2013).
64. Ordóñez, C. et al. Bromine and iodine chemistry in a global chemistry-climate model: description and evaluation of very short-lived oceanic sources. *Atmos. Chem. Phys.* **12,** 1423 - 1447 (2012).
65. Fernandez, R. P., Salawitch, R. J., Kinnison, D. E., Lamarque, J. F. & Saiz-Lopez, A. Bromine partitioning in the tropical tropopause layer:implications for stratospheric injection. *Atmos. Chem. Phys.* **14,** 13391 - 13410(2014).
66. Saiz-Lopez, A. et al. Injection of iodine to the stratosphere. *Geophys Res Lett.* **42,** 6852 - 6859 (2015).

KOPRI
극지연구소

## FIGURES

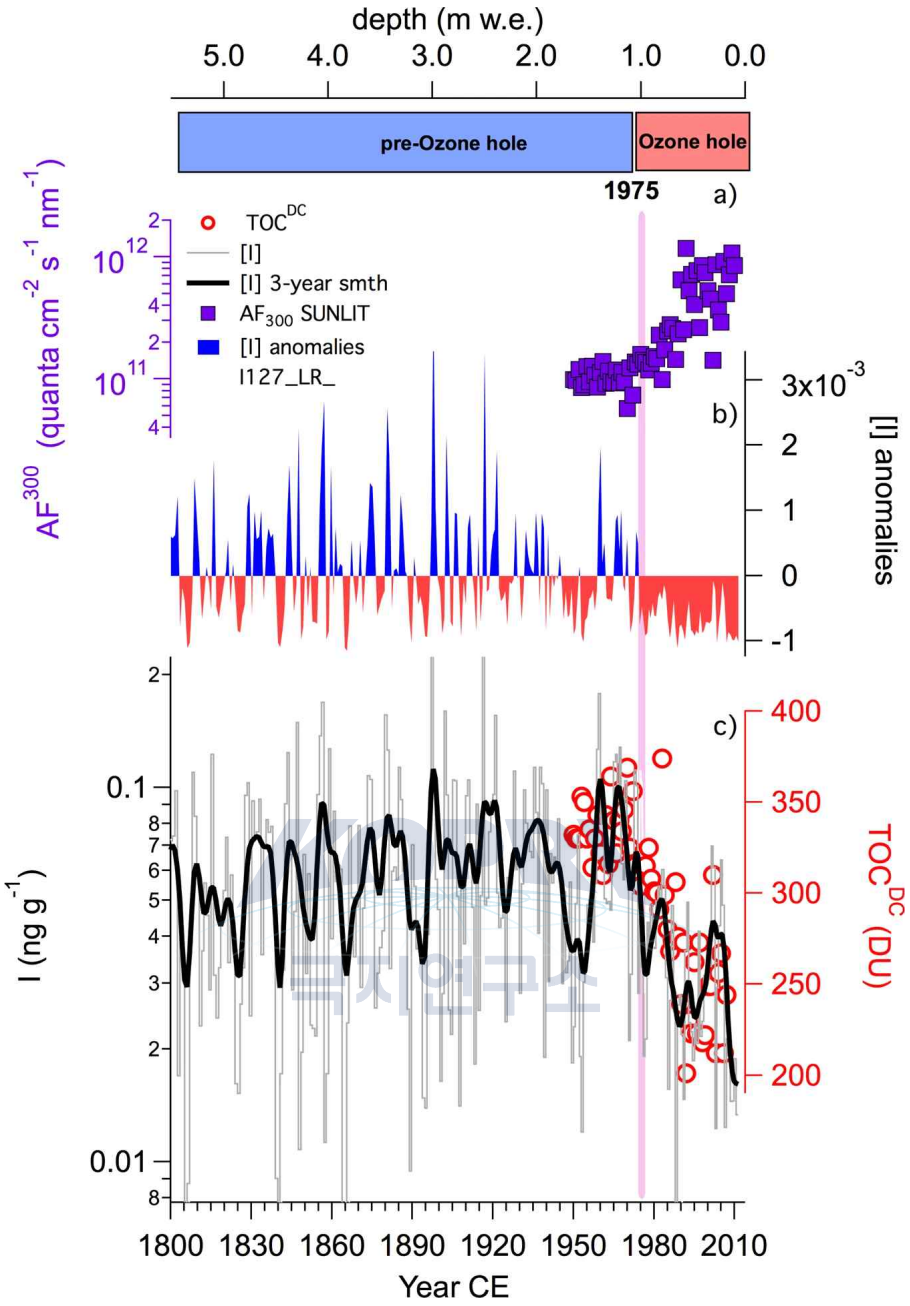



**Fig. 1 Evolution of iodine concentration and stratospheric ozone over Dome C.** Iodine concentration (grey line, raw data; bold black line, 10 year smoothing) and [I] anomalies, expressed as ng $g^{-1}$ (blue, positive; red, negative; solid lines with respect to the mean iodine concentration for the period of 1800 - 2012), were compared with the mean total ozone column above Dome C during the sunlit (1 September to 28 February) period of each year (red dots, $TOC^{DC}$ in Dobson units). The top panel shows the modelled mean sunlit Actinic Flux at 300 nm (purple square, $AF^{300}$, quanta $cm^{-2}$ $s^{-1}$ $nm^{-1}$) at the Antarctic surface within the closest model grid point to Dome C. The decrease in iodine concentration coincides with the decrease in $TOC^{DC}$ and mirrors the increase in modelled $AF^{300}$. The pink vertical bar shows the tipping point determined for [I] (1975 CE), which is considered to be the starting date for the ozone hole period.

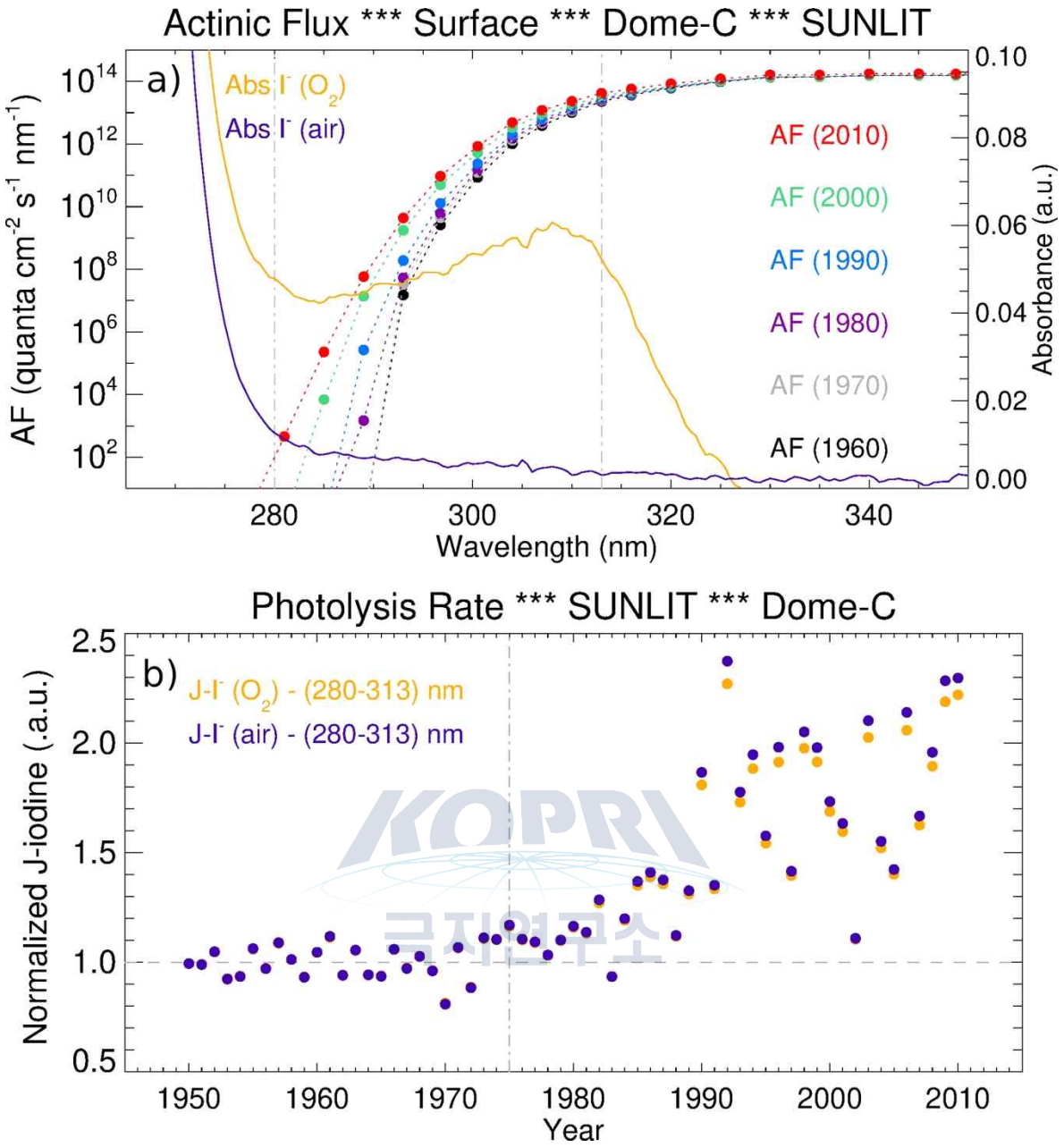



**Fig. 2 Iodine photochemical enhancement during the ozone hole period.** Modelled actinic flux (AF) and iodine photoactivation efficiency (J-iodine) at the snow surface in Dome C. a Wavelength-dependent AF reaching the model surface every decade since the 1960s (colour dots, left Y-axis). The right Y-axis shows the absorbance spectra of a frozen iodide solution in equilibrium with oxygen ($I^-(O_2)$) and air ($I^-$(air)) environments. b The normalized J-iodine of snow-trapped iodine between 1950 and 2010 relative to the mean J-iodine for the pre-1975 period (dashed-grey horizontal line in (b)). J-iodine wavelength integration was performed within the 280 - 313 nm band (see dashed-grey vertical lines in (a)) and continuously increased after 1975 due to the ozone holedriven enhancement in UV radiation during the sunlit period of each year (i.e., from 1 September to 28 February)

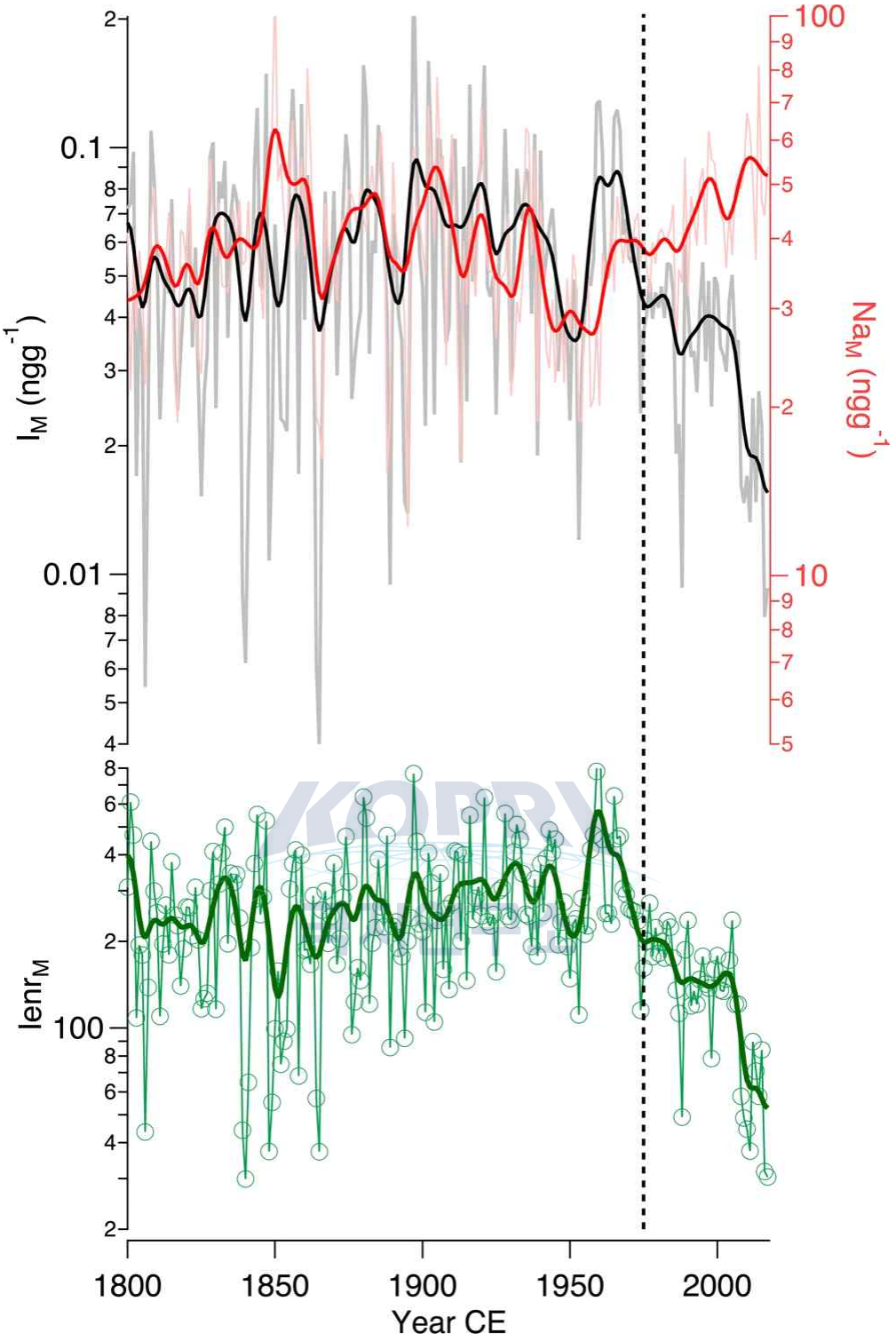



**Fig. 3 Iodine and sodium merged record from Dome C.** The upper panel shows the merged 1-year smooth records (see S3.5 in the SM for details) using snow pits and ice core data (iodine merged in black－$I_M$- and sodium merged in red－$Na_M$). Light grey and red lines show the raw data, and red and bold curves show the 5-year smoothing. The lower panel shows the iodine enrichment ($I^{enr}$ = I/(Na*0.00000568, where 0.00000568 is the I/Na mass ratio in seawater), where the solid green line shows the 5-year smoothing. The dashed vertical line indicates the tipping point discontinuity at 1975 CE.

# 제 2 절. Freezing-Induced Simultaneous Reduction of Chromate and Production of Molecular Iodine: Mechanism, Kinetics, and Practical Implications②

Kitae Kim[1,2], Hyun Young Chung[1,2], Bomi Kim[1,2], Gracie Wong[3], Anh Quoc Khuong Nguyen[4], Saewung Kim[3], and Jungwon Kim[3,5]

[a]Korea Polar Research Institute (KOPRI)
[b]Department of Polar Sciences, University of Science and Technology (UST)
[c]Department of Earth System Science, University of California,
[d]Department of Chemistry, Hallym University
[e]Department of Environmental Sciences and Biotechnology, Hallym University

## Abstract

A new method for the concurrent treatment of Cr(VI)-contaminated wastewater and production of the useful $I_2$ chemical was developed. The method is based on the redox reaction between Cr(VI) and $I^-$ that occurs when an aqueous wastewater solution containing Cr(VI) and $I^-$ is frozen, producing $I_2$ and allowing for the effective removal of Cr. The redox reaction occurs primarily due to the accumulation of Cr(VI), $I^-$, and protons in the ice grain boundaries formed during freezing (i.e., the freeze concentration effect). This effect was verified by confocal Raman spectroscopy and the experiments varying $I^-$ concentration and pH. The reduction of Cr(VI) (20 μM) was near complete after freezing at $I^-$ concentrations ≥ 100 μM, pH ≤ 3.0, and temperatures ≤ −10 °C. The freezing method (liquid cooling vs air cooling) had little effect on the final Cr(VI) reduction efficiency, but had a significant effect on the Cr(VI) reduction rate. The freezing method was also tested with Cr(VI)-contaminated electroplating wastewater samples and simultaneous Cr(VI) reduction and $I_2$ production proceeded rapidly in a frozen solution but was not observed in an aqueous solution. Additionally, other substances in electroplating wastewater did not reduce the rate and final efficiency of Cr(VI) reduction and $I_2$ production. Therefore, the freezing/Cr(VI)/$I^-$ system can be considered a feasible approach to water-energy nexus technology for simultaneous $I_2$ production and Cr(VI)-contaminated wastewater treatment.

② 본 연구는 극지연구소 본 과제(PE21120), PM20030 과제, 과학기술정보통신부 한국연구재단 과제 (NRF-2019R1C1C1004640) 지원으로 수행되었으며, *Environ. Sci. Technol.* 2020, 54(24) 16204-16211에 출간되었다.

## 1. Introduction

Chromium (Cr) is a heavy metal that is widely used in industrial processes such as wood preservation, leather tanning, chrome plating, metallurgy, and pigment manufacturing.[1] These processes produce large amounts of Cr-containing wastewater that need to be treated. Cr can be found in different forms with oxidation states ranging from −2 to +6. Among various Cr species, hexavalent chromium (Cr(VI)) and trivalent chromium (Cr(III)) are dominant in water. Compared to Cr(VI), Cr(III) is far less toxic and easier to physically remove;[2] therefore, the reduction of Cr(VI) to Cr(III) is necessary to physically remove Cr in wastewater by precipitation, ion exchange, adsorption, and coagulation.[3-5] In this regard, a variety of chemical and photochemical methods including zero-valent iron ($Fe^0$),[6] ferrous ion ($Fe^{2+}$),[7] hydrogen peroxide ($H_2O_2$),[8] copper-doped titanium dioxide (Cu-$TiO_2$) with UV-A light,[9] and polyaniline-modified tin dioxide (PANI/$SnO_2$) with visible light[10] have been employed to convert Cr(VI) to Cr(III).

Generally, chemical reactions in aqueous media (i.e., at temperatures above the freezing point) are faster than those in ice media (i.e., at temperatures below the freezing point). However, several examples demonstrating enhanced chemical reactions in ice media have been reported in the literature. Freezing has significantly enhanced the humification of phenolic compounds by nitrite ($NO_2^-$).[11] The $NO_2^-$-mediated conversion of iodate ($IO_3^-$) into molecular iodine ($I_2$), which was negligible in aqueous solutions, has been clearly observed in frozen solutions.[12] In addition, the freezing process significantly accelerated the degradation of organic pollutants by peroxymonosulfate ($HSO_5^-$),[13] periodate ($IO_4^-$),[14] and $NO_2^-$[15]. These behaviors are contrary to Arrhenius law which shows that reaction rates decrease with decreasing the temperature. These contrasting behaviors proceed primarily due to the freeze concentration effect. Frozen solutions contain small pockets of liquid between ice crystals, which are often referred to as ice grain boundaries. Solutes primarily exist in the ice grain boundaries within a frozen solution.[16, 17] This phenomenon increases the concentrations of solutes and the collision frequency between solutes, thereby enhancing chemical reactions.[18] Under acidic conditions, protons also accumulate in the ice grain boundaries in frozen solutions.[19] The resulting decrease in pH provides optimal conditions for proton-coupled chemical reactions.

The reduction rate of Cr(VI) to Cr(III) increases with increasing concentrations of Cr(VI) and reductants. Additionally, the reduction of Cr(VI) is favored in acidic conditions because protons are required in the Cr(VI) reduction process ($HCr^{VI}O_4^- + 7H^+ + 3e^- \rightarrow$ Cr(III) + $4H_2O$).[20] In this regard, the freezing process, which can increase solute concentration and decrease pH, was recently applied to the reduction of Cr(VI). $H_2O_2$,[20] $NO_2^-$,[21] and 4-chlorophenol[22] were used as reductants in the freezing-induced Cr(VI) reduction processes. All reductants previously reported showed enhanced reduction efficiency of

Cr(VI) in a frozen solution when compared with its counterpart in an aqueous solution. However, the oxidized forms of the reductants in the previously reported studies (i.e., $H_2O$, $NO_3^-$, and hydroquinone/benzoquinone) are toxic or invaluable, limiting their practical applications in Cr(VI) reduction.

Although freezing-induced Cr(VI) reduction systems have previously been reported, developing an economical and eco-friendly freezing system for Cr(VI) reduction remains a challenging issue. In this study, we developed a new freezing-induced Cr(VI) reduction system using iodide ($I^-$) as a reductant. This system not only reduces Cr(VI) to Cr(III), but also generates $I_2$, which is frequently used as a catalyst or reagent in various organic synthetic processes and as an antimicrobial substance in pharmaceutical production.[23, 24] The dual-function of the freezing/Cr(VI)/$I^-$ system (i.e., the simultaneous reduction of Cr(VI) and production of $I_2$) provides a favorable system for wastewater treatment and resource recovery. The reduction efficiencies of Cr(VI) in frozen solutions are measured under various experimental conditions and compared with those in aqueous solutions. In addition, the reaction mechanism between Cr(VI) and $I^-$ in frozen solution is discussed. Finally, the practical viability of the freezing/Cr(VI)/$I^-$ system is verified using Cr(VI)-contaminated wastewater samples taken from an electroplating factory.

KOPRI 극지연구소

## 2. Experimental Section

### 2.1 Chemicals

Chemicals used in this work include the following: sodium dichromate dihydrate ($Na_2Cr_2O_7 \times 2H_2O$, Cr(VI), Aldrich, ≥99.5%), potassium iodide (KI, Samchun chemical, ≥ 99.5%), acetone ($C_3H_6O$, Junsei, ≥98.0%), sulfuric acid ($H_2SO_4$, Aldrich, ≥96.0%), 1,5-diphenylcarbazide ($C_{13}H_{14}N_4O$, DPC, Aldrich, ≥98.8%), perchloric acid ($HClO_4$, Aldrich, 1M), sodium hydroxide (NaOH, Samchun chemical, 1M). Ultrapure deionized water (≥18.2 MΩ×cm) produced by a water purification system (Barnstead Milli-Q Direct 16) was used to prepare experimental solutions. Cr(VI)-contaminated wastewater produced from a local electroplating factory in Republic of Korea ([Cr(VI)] ≈ 600 mM and pH ≈ 0.4) was used without pretreatment.

### 2.2 Experimental Procedure

Aliquots of chemical stock solutions ([Cr(VI)] = 2 mM and [$I^-$] = 1 mM) were added to deionized water in a beaker to yield desired initial concentrations for the experimental solutions (usually [Cr(VI)] = 20 $\mu$M and [$I^-$] = 100 $\mu$M)). The initial pH of the solution was adjusted using a $HClO_4$ or NaOH solution (usually pH = 3.0). Ten mL of the Cr(VI) and $I^-$ solution was transferred to a 15 mL plastic conical tube (Falcon) and sealed with a

plastic cap. The plastic conical tubes containing aqueous solution of Cr(VI) and $I^-$ were placed in a laboratory-made conical tube holder installed inside the temperature-controlled ethanol bath. The temperature of ethanol was adjusted to the desired temperature (usually −20 °C or 25 °C) before putting the plastic conical tubes into the temperature-controlled ethanol bath. The start of the reaction time is considered to be when the plastic conical tubes are placed into the temperature-controlled ethanol bath. The plastic conical tubes were withdrawn from the temperature-controlled ethanol bath at regular time intervals and put into a lukewarm water bath at 35 °C for 1 min. The frozen samples completely thawed within 1 min. The aqueous (or melted) samples were analyzed immediately afterwards. All experiments were performed at least twice to confirm data reproducibility.

### 2.3 Chemical Analyses

The concentration of Cr(VI) was measured using the spectrophotometric method with 1,5-diphenylcarbazide (DPC) reagent.[25] To make the DPC reagent, DPC powder (0.05 g) was added to a mixture of acetone (25 mL) and sulfuric acid (250 μL). The DPC reagent (250 μL) was added to the aqueous sample diluted 6-fold (3 mL) and mixed vigorously for 1 min. The absorbance of the aqueous sample colored by DPC reagent was measured at 540 nm using a UV−visible spectrophotometer (Shimadzu UV-2600) after 1 h in the dark. The Cr(VI) concentration in the solution was retrieved using the absorbance value at 540 nm and the calibration curve of sodium dichromate dihydrate.

Quantitative analysis of $I^-$ was performed using an ion chromatograph (Dionex ICS-1100) equipped with a Dionex AERS 500 suppressor, a Dionex IonPac AS19 column, and a conductivity detector. The eluent was made by the potassium hydroxide (KOH) eluent generator cartridge (Dionex EGC III). The flow rate and concentration gradient of the eluent (KOH) were 1.0 mL/min and 10−45 mM, respectively. The concentration of $I^-$ was determined based on the calibration curve of potassium iodide. The production of $I_2$ and $I_3^-$ was monitored by measuring the absorbances of the aqueous sample at 460 nm and 353 nm, respectively. The absorbances were converted to the concentrations of $I_2$ and $I_3^-$ using the Beer-Lambert law with the molar absorption coefficients (ε) for $I_2$ and $I_3^-$ (ε = 746 $M^{-1}$ $cm^{-1}$ at 460 nm and 26,400 $M^{-1}$ $cm^{-1}$ at 353 nm, respectively[26]).

Confocal Raman spectroscopy was used to monitor the spatial distributions and disappearances of Cr(VI) in the frozen solutions without melting. One droplet of the aqueous solution ([Cr(VI)] = 1 mM, $[I^-]$ = 1 mM, and pH = 3.0) was dropped on a temperature-controlled microscope stage (Linkam Scientific THMS600). The temperature was decreased from 0 to −20 °C at a rate of −1.5 °C/min by liquid nitrogen. The images of the distribution of Cr(VI) concentration in the frozen solution were obtained by measuring the Raman intensity at 852 $cm^{-1}$ using a confocal Raman spectroscope

(Renishaw inVia Qontor) with monochromatic laser (532 nm) irradiation.

## 3. Results and Discussion

### 3.1 Reduction of Cr(VI) by $I^-$ in aqueous and frozen solutions

The reduction of Cr(VI) by $I^-$ in frozen solutions at −20 °C was measured and compared with that in aqueous solutions at 25 °C under the conditions of [Cr(VI)] = 20 μM, [$I^-$] = 100 μM, and pH = 3.0 (Figure 1a). The concentration of Cr(VI) rapidly decreased after freezing and was almost zero (less than 0.5 μM) after 20 min in the frozen solution. However, the reduction of Cr(VI) was negligible in the aqueous solution. In the absence of $I^-$ in a frozen solution, Cr(VI) was reduced by only a small amount (less than 2.0 μM after 2 h of reaction) through the proton-mediated pathway ($4HCr^{VI}O_4^- + 16H^+ \rightarrow 4Cr(III) + 3O_2 + 10H_2O$)[27]. The control experiments in the absence of freezing or $I^-$ indicate that $I^-$ and freezing synergistically accelerate the reduction of Cr(VI). Therefore, Cr(VI) reduction is significantly enhanced in the presence of $I^-$ after freezing because $I^-$ can act as a reductant for Cr(VI) in frozen solutions.

To verify the role of $I^-$ as a reductant, the products generated from the oxidation of $I^-$ by Cr(VI) (i.e., $I_2$ and $I_3^-$) were spectrophotometrically investigated (Figure 1b). In an aqueous solution containing Cr(VI) and $I^-$, the UV-visible absorption spectra did not change, whereas two new peaks were observed when the aqueous solution was frozen for 2 h. The absorption band at 288 nm after freezing indicates the production of $I_3^-$ in the frozen solution. The presence of the peak at 460 nm is primarily attributed to the formation of $I_2$.[26] The production of the oxidized forms of $I^-$ (i.e., $I_2$ and $I_3^-$) after freezing clearly indicates that $I^-$ can act as a reductant for Cr(VI) in a frozen solution. It should be noted that the peak at 353 nm observed in the frozen solution after 2 h is primarily responsible for the generation of $I_3^-$, which exhibits the maximum absorption wavelengths at both 288 and 353 nm,[26] rather than the existence of Cr(VI).

Figure 1c shows time profiles of $I^-$, $I_2$, and $I_3^-$ concentrations in the aqueous and frozen solutions containing Cr(VI) and $I^-$. Consistent with the limited reduction of Cr(VI) observed in an aqueous solution, the concentration of $I^-$ did not change and the production of $I_2$ and $I_3^-$ was negligible in the aqueous solution. On the other hand, the concentration of $I^-$ decreased while concentrations of $I_2$ and $I_3^-$ increased with reaction time in the frozen solution. The iodine mass balance (($[I^-] + 2 \times [I_2] + 3 \times [I_3^-]$)/(initial $[I^-]$) × 100 (%)) in the frozen solution was almost 100% throughout the reaction period, confirming that the conversions of $I^-$ to $I_2$ (Reaction (1)) and $I_3^-$ (Reaction (2)) are the primary oxidation pathways and production of other oxidized forms of $I^-$ is negligible. Between $I_2$ and $I_3^-$, the production of $I_2$ was much higher than that of $I_3^-$. This result indicates that

the direct conversion of $I^-$ to $I_2$ (Reaction (1)) is favored in a frozen solution and/or $I_3^-$, which is produced from the oxidation of $I^-$ through Reaction (2), rapidly dissociates into $I^-$ and $I_2$ in frozen solutions (Reaction (3)).

$$2HCr^{VI}O_4^- + 6I^- + 14H^+ \rightarrow 2Cr(III) + 3I_2 + 8H_2O \quad (1)$$

$$2HCr^{VI}O_4^- + 9I^- + 14H^+ \rightarrow 2Cr(III) + 3I_3^- + 8H_2O \quad (2)$$

$$I_3^- \rightarrow I^- + I_2 \quad (3)$$

### 3.2 In situ monitoring of $I^-$-mediated reduction of Cr(VI) in the ice grain boundaries

Because protons are involved in the $I^-$-mediated reduction of Cr(VI) (Reactions (1) and (2)), the pH of solution (i.e., the concentration of protons) significantly affects the kinetics of Cr(VI) reduction. When the acidic solution is frozen, protons are expelled from the ice crystals and situated in the ice grain boundaries. Protons continue to accumulate in the ice grain boundaries as ice crystals grow during the freezing process.[19] The extremely acidic environment induced by the freeze concentration effect can facilitate $I^-$-mediated reduction of Cr(VI) by providing sufficient protons for Reactions (1) and (2). In addition, the accumulation of both Cr(VI) and $I^-$ in the ice grain boundaries during freezing is likely to have a synergistic effect on the $I^-$-mediated reduction of Cr(VI) by increasing the chance of collisions between Cr(VI) and $I^-$ for their redox transformation (see Thermodynamic interpretation of redox reaction between Cr(VI) and $I^-$ in the Supporting Information (SI)).

The distribution of Cr(VI) concentration in the frozen solution was monitored in situ (without melting) using confocal Raman spectroscopy. When the aqueous solution of Cr(VI) was frozen, the ice crystals and ice grain boundaries were clearly distinct (Figure 2a). It has been reported that in an aqueous solution, the specific Raman peak of Cr(VI), which is identified by the Cr−O stretching mode, is observed in the range of 800−1000 $cm^{-1}$ and its wavenumber position depends on the Cr(VI) concentration and pH.[28, 29] Two points representing the ice crystal (black circle) and ice grain boundary (red circle) were selected (Figure 2a), and the Raman spectra at each of the points were recorded (Figure 2b). The characteristic Raman Cr(VI) peak at 852 $cm^{-1}$ was clearly detected in the ice grain boundary region while no Raman peaks were observed in the ice crystal region. Furthermore, the distribution of Cr(VI) concentration in the frozen solution was investigated by measuring the Raman intensity at 852 $cm^{-1}$ for the area within the white square (Figure 2c). The relative Raman intensities (i.e., the relative concentrations) of Cr(VI) are displayed on a rainbow scale, where red represents the highest and black represents the lowest concentrations. The ice grain boundary regions are marked with red, orange, yellow, and green, while the ice crystal regions are blue, indigo, violet, and black. This Cr(VI) concentration distribution image of the frozen Cr(VI) solution implies that Cr(VI)

significantly accumulates in ice grain boundaries by exclusion from ice crystals after freezing.

To provide convincing evidence for Cr(VI) reduction by $I^-$ in the ice grain boundaries during freezing, the change in Cr(VI) concentration in the ice grain boundary region was monitored in situ by measuring the Raman spectra of Cr(VI) as a function of reaction time (Figure 3). The Raman intensity at 852 $cm^{-1}$, which is proportional to the Cr(VI) concentration, gradually decreased with reaction time (Figure 3 inset). The change from red to green in the ice grain boundary region over time in the Cr(VI) concentration distribution images shown in Figure 4 also demonstrates the decreasing concentration of Cr(VI) in the ice grain boundary region with increasing reaction time. Based on the results in Figures 3 and 4, it can be concluded that the redox reaction between Cr(VI) and $I^-$ occurs within the ice grain boundaries and not the ice crystals.

### 3.3 Verification of freeze concentration effect

To verify our hypotheses that the freeze concentration effect accelerates $I^-$-mediated reduction of Cr(VI) by decreasing pH and increasing $I^-$ concentration locally, the effects of pH decrease, $I^-$ concentration increase, and their synergistic effect on Cr(VI) reduction were investigated in an aqueous solution (Figure 5). When the only concentration of $I^-$ was increased by 100-fold (i.e., to $[I^-]$ = 10 mM) from the reference conditions (i.e., $[I^-]$ = 100 μM and pH = 3.0), the reduction of Cr(VI) by $I^-$ was not observed. Simply decreasing pH from 3.0 to 1.3 enhanced Cr(VI) reduction, however the effect was minor. With both the pH decrease and $I^-$ concentration increase, Cr(VI) reduction was significantly enhanced. When the concentrations of $I^-$ and protons were increased by 100-fold and 50-fold respectively, the Cr(VI) reduction efficiency in the aqueous solution was comparable to that in the frozen solution. These results confirm that the enhanced $I^-$-mediated reduction of Cr(VI) in frozen solution is ascribed to the accumulation of both solutes and protons in the ice grain boundary during freezing, not solely the concentration effect of either solutes or protons.

### 3.4 Cr(VI) reduction efficiencies in frozen solutions under various conditions

We investigated the effect of $I^-$ concentration, pH, temperature, and freezing method on the reduction efficiency of Cr(VI) by $I^-$ ((initial [Cr(VI)] - [Cr(VI)] after 2 h of reaction)/(initial [Cr(VI)]) × 100 (%)) in a frozen solution (Figure 6). In an aqueous solution at 25 °C, Cr(VI) reduction was essentially not observed with $I^-$ concentrations of up to 100 μM. On the other hand, the reduction efficiency of Cr(VI) increased with increasing $[I^-]$ at −20 °C (Figure 6a), which is attributed to $I^-$ acting as the primary reductant for Cr(VI) in the frozen solutions. The experimental molar ratios of added $[I^-]$ to

reduced [Cr(VI)] were 2.0−5.2 (2.0, 2.3, 3.3, and 5.2 at [$I^-$] = 5, 10, 50, and 100 μM, respectively), which are similar to the theoretical molar ratios according to Reactions (1) and (2) (3.0−4.5). The slight difference between experimental and theoretical molar ratios can be attributed to the proton-mediated reduction of Cr(VI) in a frozen solution (at low [$I^-$]) and the residual (unreacted) $I^-$ after 2 h of reaction (at high [$I^-$]).

The reduction efficiencies of Cr(VI) in a frozen solution were also measured in the pH range 2.0−6.0 and compared to those in an aqueous solution (Figure 6b). The reduction of Cr(VI) by $I^-$ in an aqueous solution was negligible in the pH range 3.0−6.0. At pH = 2.0, the Cr(VI) reduction efficiency was less than 12%. In a frozen solution, reduction of Cr(VI) by $I^-$ was observed at all pH values tested. Cr(VI) reduction efficiency increased with decreasing pH and was nearly 100% at pH = 3.0. The inverse relationship between Cr(VI) reduction efficiency and pH is attributed to the need for protons in the $I^-$-mediated Cr(VI) reduction process in frozen solutions. Most Cr(VI)-contaminated waters such as electroplating wastewater and leachates containing Cr(VI) are very acidic (pH < 2.0),[30, 31] making the freezing/Cr(VI)/$I^-$ system applicable for Cr(VI) reduction without acidification.

Figure 6c shows the temperature-dependent reduction efficiency of Cr(VI) with a reaction time of 2 h. A temperature-controlled ethanol bath was used to reduce the temperature of the plastic conical tubes containing Cr(VI) and $I^-$ down to −80 °C. On the other hand, the plastic conical tubes containing Cr(VI) and $I^-$ were introduced into liquid nitrogen to freeze down to −196 °C. At temperatures between −10 and −196 °C, the effect of the freezing temperature on Cr(VI) reduction efficiency was minor. Cr(VI) reduction was nearly 100% in frozen solutions at all temperatures tested. This indicates that Cr(VI) reduction by $I^-$ proceeds efficiently once the aqueous solution is frozen.

We also compared the Cr(VI) reduction efficiencies using two freezing systems: an ethanol bath (coolant: ethanol) and refrigerator (coolant: air). The Cr(VI) reduction efficiencies of the two systems after a reaction time of 2 h were almost the same (Figure 6d). However, the time at which the reduction process began was different between two freezing systems. The reduction of Cr(VI) in the ethanol bath started shortly (i.e., within 10 min) after putting the plastic conical tubes containing Cr(VI) and $I^-$ into the ethanol bath. In the refrigerator, Cr(VI) reduction occurred at least 10 min after the start time. The reduction of Cr(VI) was almost complete within 20 min in the ethanol bath, while it took over 30 min to complete in the refrigerator (Figure 6d inset). This result demonstrates that the freezing method, or more precisely the type of coolant, plays an important role in determining the start time and rate of Cr(VI) reduction by influencing the growth rate of ice crystals (i.e., the degree of the freeze concentration effect over reaction time).

### 3.5 Practical viability of the freezing/Cr(VI)/$I^-$ system for the simultaneous Cr(VI)

**reduction and $I_2$ production**

Iodine is one of the rarest nonmetals in the lithosphere with estimated global reserves of about 15 million tons. The annual global production of iodine for industrial use is about 30,000 tons and is mainly produced in Chile and Japan.[32, 33] Among the various iodine species, $I_2$ in particular has found a wide range of practical applications. $I_2$ has been frequently employed as a catalyst for organic syntheses through the Diels-Alder reaction, aldol reaction, Michael addition, and esterification.[34-36] It can be used as a chemical reagent to induce iodination and oxidation reactions.[37-39] In addition, various pharmaceuticals such as iodine tincture, Lugol's solution, and Povidone-iodine contain $I_2$ as an antimicrobial substance.[40] Industrial production of $I_2$ has primarily been carried out by two methods: the oxidation of $I^-$ by molecular chlorine ($Cl_2$) and the reduction of $IO_3^-$ by sulfur dioxide ($SO_2$).[41] However, the corrosive property and low selectivity of $Cl_2$ and $SO_2$ limit the feasibility of these methods for $I_2$ production.[42, 43] Moreover, the $Cl_2$ and $SO_2$-mediated $I_2$ production systems can generate toxic compounds.[44]

If the production of useful $I_2$ accompanied by the removal of toxic Cr(VI) is achievable, this dual-function system provides an economical and eco-friendly solution in water-energy nexus technology for simultaneous reduction of Cr(VI) and production of $I_2$.[45, 46] To verify the viability of the freezing/Cr(VI)/$I^-$ system for simultaneous Cr(VI) reduction and $I_2$ production, we performed the experiments using Cr(VI)-containing electroplating wastewater from a factory in Republic of Korea (Figure 7). The chemical composition of the electroplating wastewater is listed in Table S1 in the SI. When the diluted electroplating wastewater ([Cr(VI)] = 20 μM) was used as a source of Cr(VI), simultaneous Cr(VI) reduction (Figure 7a) and $I_2$ production (Figure 7b) was observed in frozen solutions, but not in aqueous solutions. Most importantly, both the Cr(VI) reduction and $I_2$ production efficiencies of the electroplating wastewater were similar to those of the artificial Cr(VI) solutions. This suggests that other substances in electroplating wastewater do not inhibit the redox reaction between Cr(VI) and $I^-$ in the frozen state. $I^-$-contaminated brines ([$I^-$] = a few mM)[47] and discharged effluents from brine treatment plants ([$I^-$] = hundreds of μM)[48] can be a source of $I^-$. Wastewaters produced from liquid crystal display (LCD) manufacturing plants contain high concentrations of both Cr(VI) and $I^-$ (dozens of mM).[42, 49] The freezing/Cr(VI)/$I^-$ system would be most economical when wastewater originally containing both Cr(VI) and $I^-$ like LCD wastewater is used.

Previously developed systems can either successfully reduce Cr(VI) or produce $I_2$, but not both. We have shown that wastewater containing Cr(VI) can produce the $I_2$ chemical while being treated. This dual-function system has the potential to be more economical and eco-friendly than any single-function system. The freezing/Cr(VI)/$I^-$ system has worked efficiently with Cr(VI)-containing electroplating wastewater produced from a factory and

produced similar results to the artificial solutions tested. In addition, $I^-$ is almost selectively converted to $I_2$ by Cr(VI) in frozen solutions and the generation of other volatile iodine-containing compounds is negligible, enabling the freezing/Cr(VI)/$I^-$ system to produce pure $I_2$ without a post separation process. $I_2$ molecules produced in frozen solutions are spontaneously emitted into the atmosphere after melting, allowing for the recovery of $I_2$ from treated wastewater. The captured air containing $I_2$ can be used directly when low concentrations of $I_2$ are required. Nanomaterials and hydrogels capable of adsorbing $I_2$ reversibly can be used to obtain high concentrations of $I_2$.[50-52] Therefore, the freezing/Cr(VI)/$I^-$ system can be proposed to be a new water-energy nexus technology for simultaneous reduction of Cr(VI) and production of $I_2$.

KOPRI
극지연구소

# REFERENCES


1. Barnhart, J. Occurrences, uses, and properties of chromium. *Regul. Toxicol. Pharmacol.* **1997**, *26*, S3-S7.
2. Cunha, G. C.; Peixoto, J. A.; Souza, D. R.; Romão, L. P. C.; Macedo, Z. S. Recycling of chromium wastes from the tanning industry to produce ceramic nanopigments. *Green Chem.* **2016**, *18*, 5342-5356.
3. Barrera-Díaz, C. E.; Lugo-Lugo, V.; Bilyeu, B. A review of chemical, electrochemical and biological methods for aqueous Cr(VI) reduction. *J. Hazard. Mater.* **2012**, *223-224*, 1-12.
4. Pakade, V. E.; Tavengwa, N. T.; Madikizela, L. M. Recent advances in hexavalent chromium removal from aqueous solutions by adsorptive methods. *RSC Adv.* **2019**, *9*, 26142-26164.
5. Zhang, Q.; Song, Y.; Amor, K.; Huang, W. E.; Porcelli, D.; Thompson, I. Monitoring Cr toxicity and remediation processes - combining a whole-cell bioreporter and Cr isotope techniques. *Water Res.* **2019**, *153*, 295-303.
6. Kang, S.; Wang, G.; Zhao, H.; Cai, W. Highly efficient removal of hexavalent chromium in aqueous solutions via chemical reduction of plate-like micro/nanostructured zero valent iron. *RSC Adv.* **2017**, *7*, 55905-55911.
7. Qin, G.; Mcguire, M. J.; Blute, N. K.; Seidel, C.; Fong, L. Hexavalent chromium removal by reduction with ferrous sulfate, coagulation, and filtration: a pilot-scale study. *Environ. Sci. Technol.* **2005**, *39*, 6321-6327.
8. Griend, D. A. V.; Golden, J. S.; Arrington, C. A. Kinetics and mechanism of chromate reduction with hydrogen peroxide in base. *Inorg. Chem.* **2002**, *41*, 7042-7048.
9. Yin, R.; Ling, L.; Xiang, Y.; Yang, Y.; Bokare, A. D.; Shang, C. Enhanced photocatalytic reduction of chromium (VI) by Cu-doped $TiO_2$ under UV-A irradiation. *Sep. Purif. Technol.* **2018**, *190*, 53-59.
10. Li, J.; Peng, T.; Zhang, Y.; Zhou, C.; Zhu, A. Polyaniline modified $SnO_2$ nanoparticles for efficient photocatalytic reduction of aqueous Cr(VI) under visible light. *Sep. Purif. Technol.* **2018**, *201*, 120-129.
11. Min, D. W.; Kim, K.; Lui, K. H.; Kim, B.; Kim, S.; Cho, J.; Choi, W. Abiotic formation of humic-like substances through freezing-accelerated reaction of phenolic compounds and nitrite. *Environ. Sci. Technol.* **2019**, *53*, 7410-7418.
12. Kim, K.; Ju, J.; Kim, B.; Chung, H. Y.; Vetráková, Ľ.; Heger, D.; Saiz-Lopez, A.; Choi, W.; Kim, J. Nitrite-induced activation of iodate into molecular iodine in frozen solution. *Environ. Sci. Technol.* **2019**, *53*, 4892-4900.


KOPRI 극지연구소

13. Le, N. T. H.; Ju, J.; Kim, B.; Kim, M. S.; Lee, C.; Kim, S.; Choi, W.; Kim, K.; Kim, J. Freezing-enhanced non-radical oxidation of organic pollutants by peroxymonosulfate. *Chem. Eng. J.* **2020**, *388*, 124226.

14. Choi, Y.; Yoon, H.-I.; Lee, C.; Vetráková, Ľ.; Heger, D.; Kim, K.; Kim, J. Activation of periodate by freezing for the degradation of aqueous organic pollutants. *Environ. Sci. Technol.* **2018**, *52*, 5378-5385.

15. Sun, F.; Xiao, Y.; Wu, D.; Zhu, W.; Zhou, Y. Nitrite-driven abiotic transformation of sulfonamide micropollutants during freezing process. *Chem. Eng. J.* **2017**, *327*, 1128-1134.

16. Bartels-Rausch, T.; Jacobi, H.-W.; Kahan, T. F.; Thomas, J. L.; Thomson, E. S.; Abbatt, J. P. D.; Ammann, M.; Blackford, J. R.; Bluhm, H.; Boxe, C.; Domine, F.; Frey, M. M.; Gladich, I.; Guzmán, M. I.; Heger, D.; Huthwelker, Th.; Klán, P.; Kuhs, W. F.; Kuo, M. H.; Maus, S.; Moussa, S. G.; McNeill, V. F.; Newberg, J. T.; Pettersson, J. B. C.; Roeselová, M.; Sodeau, J. R. A review of air-ice chemical and physical interactions (AICI): liquids, quasi-liquids, and solids in snow. *Atmos. Chem. Phys.* **2014**, *14*, 1587-1633.

17. O'Concubhair, R.; Sodeau, J. R. The effect of freezing on reactions with environmental impact. *Acc. Chem. Res.* **2013**, *46*, 2716-2724.

18. Heger, D.; Jirkovský, J.; Klán, P. Aggregation of methylene blue in frozen aqueous solutions studied by absorption spectroscopy. *J. Phys. Chem. A* **2005**, *109*, 6702-6709.

19. Heger, D.; Klánová, J.; Klán, P. Enhanced protonation of cresol red in acidic aqueous solutions caused by freezing. *J. Phys. Chem. B* **2006**, *110*, 1277-1287.

20. Kim, K.; Kim, J.; Bokare, A. D.; Choi, W.; Yoon, H.-I.; Kim, J. Enhanced removal of hexavalent chromium in the presence of $H_2O_2$ in frozen aqueous solutions. *Environ. Sci. Technol.* **2015**, *49*, 10937-10944.

21. Kim, K.; Chung, H. Y.; Ju, J.; Kim, J. Freezing-enhanced reduction of chromate by nitrite. *Sci. Total Environ.* **2017**, *590-591*, 107-113.

22. Ju, J.; Kim, J.; Vetráková, Ľ.; Seo, J.; Heger, D.; Lee, C.; Yoon, H.-I.; Kim, K.; Kim, J. Accelerated redox reaction between chromate and phenolic pollutants during freezing. *J. Hazard. Mater.* **2017**, *329*, 330-338.

23. Parvatkar, P. T.; Manetsch, R.; Banik, B. K. Metal-free cross-dehydrogenative coupling (CDC): molecular iodine as a versatile catalyst/reagent for CDC reactions. *Chem. - Asian J.* **2019**, *14*, 6-30.

24. Uchiyama, S.; Dahesh, S.; Nizet, V.; Kessler, J. Enhanced topical delivery of non-complexed molecular iodine for methicillin-resistant Staphylococcus aureus

decolonization. *Int. J. Pharm.* **2019**, *554*, 81-86.

25. Eaton, A. D., Clesceri, L. S., Greenberg, A. E., Franson, M. A. H., Eds. Standard Methods for the Examination of Water and Wastewater, 19th, ed.; American Public Health Association: Washington, DC, **1995**.
26. Awtrey, A. D.; Connick, R. E. The absorption spectra of $I_2$, $I_3^-$, $I^-$, $IO_3^-$, $S_4O_6^=$ and $S_2O_3^=$. Heat of the reaction $I_3^- = I_2 + I^-$. *J. Am. Chem. Soc.* **1951**, *73*, 1842-1843.
27. Kim, K.; Choi, W. Enhanced redox conversion of chromate and arsenite in ice. *Environ. Sci. Technol.* **2011**, *45*, 2202-2208.
28. Ravindranath, S. P.; Henne, K. L.; Thompson, D. K.; Irudayaraj, J. Raman chemical imaging of chromate reduction sites in a single bacterium using intracellularly grown gold nanoislands. *ACS Nano* **2011**, *5*, 4729-4736.
29. Heyns, J. B. B.; Cruywagen, J. J.; Carron, K. T. Raman spectroscopic investigation of chromium(VI) equilibria—Another look. *J. Raman Spectrosc.* **1999**, *30*, 335-338.
30. Chen, S.-S.; Cheng, C.-Y.; Li, C.-W.; Chai, P.-H.; Chang, Y.-M. Reduction of chromate from electroplating wastewater from pH 1 to 2 using fluidized zero valent iron process. *J. Hazard. Mater.* **2007**, *142*, 362-367.
31. Wang, F.; Yang, W.; Zheng, F.; Sun, Y. Removal of Cr (VI) from simulated and leachate wastewaters by bentonite-supported zero-valent iron nanoparticles. *Int. J. Environ. Res. Public Health* **2018**, *15*, 2162.
32. Yoshimura, A.; Zhdankin, V. V. Advances in synthetic applications of hypervalent iodine compounds. *Chem. Rev.* **2016**, *116*, 3328-3435.
33. Muramatsu, Y.; Wedepohl, K. H. The distribution of iodine in the earth's crust. *Chem. Geol.* **1998**, *147*, 201-216.
34. von der Heiden, D.; Bozkus, S.; Klussmann, M.; Breugst, M. Reaction mechanism of iodine-catalyzed Michael additions. *J. Org. Chem.* **2017**, *82*, 4037-4043.
35. Chuang, T.-H.; Chang, W.-Y.; Li, C.-F.; Wen, Y.-C.; Tsai, C.-C. Substituent effects on the iodine-catalyzed thermal cyclization of 3,4-diphenylbuta-1,3-dienyl isocyanates: mechanistic studies. *J. Org. Chem.* **2011**, *76*, 9678-9686.
36. Breugst, M.; von der Heiden, D. Mechanisms in iodine catalysis. *Chem. - Eur. J.* **2018**, *24*, 9187-9199.
37. Küpper, F. C.; Feiters, M. C.; Olofsson, B.; Kaiho, T.; Yanagida, S.; Zimmermann, M. B.; Carpenter, L. J.; Luther III, G. W.; Lu, Z.; Jonsson, M.; Kloo, L. Commemorating two centuries of iodine research: an interdisciplinary overview of current research. *Angew. Chem., Int. Ed.* **2011**, *50*, 11598-11620.
38. Wei, W.; Shao, Y.; Hu, H.; Zhang, F.; Zhang, C.; Xu, Y.; Wan, X. Coupling of methyl

KOPRI 극지연구소

ketones and primary or secondary amines leading to α-ketoamides. *J. Org. Chem.* **2012**, *77*, 7157-7165.

39. Li, X.; Wang, X.; Wang, Z.; Yan, X.; Xu, X. TBHP-induced iodocyclization with I2: atom economic synthesis of iodinated isoxazolines in water under mild conditions. *ACS Sustainable Chem. Eng.* **2019**, *7*, 1875-1878.
40. He, S.; Wang, B.; Chen, H.; Tang, C.; Feng, Y. Preparation and antimicrobial properties of gemini surfactant-supported triiodide complex system. *ACS Appl. Mater. Interfaces* **2012**, *4*, 2116-2123.
41. Kaiho, T., Ed. Iodine Chemistry and Applications; John Wiley & Sons, Inc.: Hoboken, **2015**.
42. Kim, H. I.; Wijenayake, J. J.; Mohapatra, D.; Rout, P. C. A process to recover high purity iodine in wastewater from liquid crystal display (LCD) manufacturing industry. *Hydrometallurgy* **2018**, *181*, 91-96.
43. Vlasov, G. A.; Bushina, N. D.; Buravtseva, G. I.; Mukhametshina, L. V. Improvement of the iodine and bromine production processes. Russ. *J. Appl. Chem.* **2001**, *74*, 1093-1097.
44. Wenten, I. G.; Julian, H.; Panjaitan, N. T. Ozonation through ceramic membrane contactor for iodide oxidation during iodine recovery from brine water. *Desalination* **2012**, *306*, 29-34.
45. Schnoor, J. L. Water-energy nexus. *Environ. Sci. Technol.* **2011**, *45*, 5065.
46. Kim, J.; Monllor-Satoca, D.; Choi, W. Simultaneous production of hydrogen with the degradation of organic pollutants using $TiO_2$ photocatalyst modified with dual surface components. *Energy Environ. Sci.* **2012**, *5*, 7647-7656.
47. Collins, A. G. Chemistry of some Anadarko Basin brines containing high concentrations of iodide. *Chem. Geol.* **1969**, *4*, 169-187.
48. Harkness, J. S.; Dwyer, G. S.; Warner, N. R.; Parker, K. M.; Mitch, W. A.; Vengosh, A. Iodide, bromide, and ammonium in hydraulic fracturing and oil and gas wastewaters: environmental implications. *Environ. Sci. Technol.* **2015**, *49*, 1955-1963.
49. Veriansyah, B.; Kim, J.-D.; Lee, Y.-W. Simultaneous recovery of chromium and destruction of organics from LCD manufacturing process wastewater by supercritical water oxidation. *J. Cleaner Prod.* **2007**, *15*, 972-978.
50. Sun, H.; Mu, P.; Xie, H.; Zhu, Z.; Liang, W.; Zhou, Z.; Li, A. Efficient capture and reversible storage of radioactive iodine by porous graphene with high uptake. *ChemistrySelect* **2018**, *3*, 10147-10152.
51. Valizadeh, B.; Nguyen, T. N.; Smit, B.; Stylianou, K. C. Porous metal-organic

KOPRI 극지연구소

framework@polymer beads for iodine capture and recovery using a gas-sparged column. *Adv. Funct. Mater.* **2018**, *28*, 1801596.

52. Gambhir, D.; Venkateswarulu, M.; Verma, T.; Koner, R. R. High adsorption capacity of an sp2/sp3-N-rich polymeric network: from molecular iodine capture to catalysis. *ACS Appl. Polym. Mater.* **2020**, *2*, 152-158.

KOPRI
극지연구소

## FIGURES

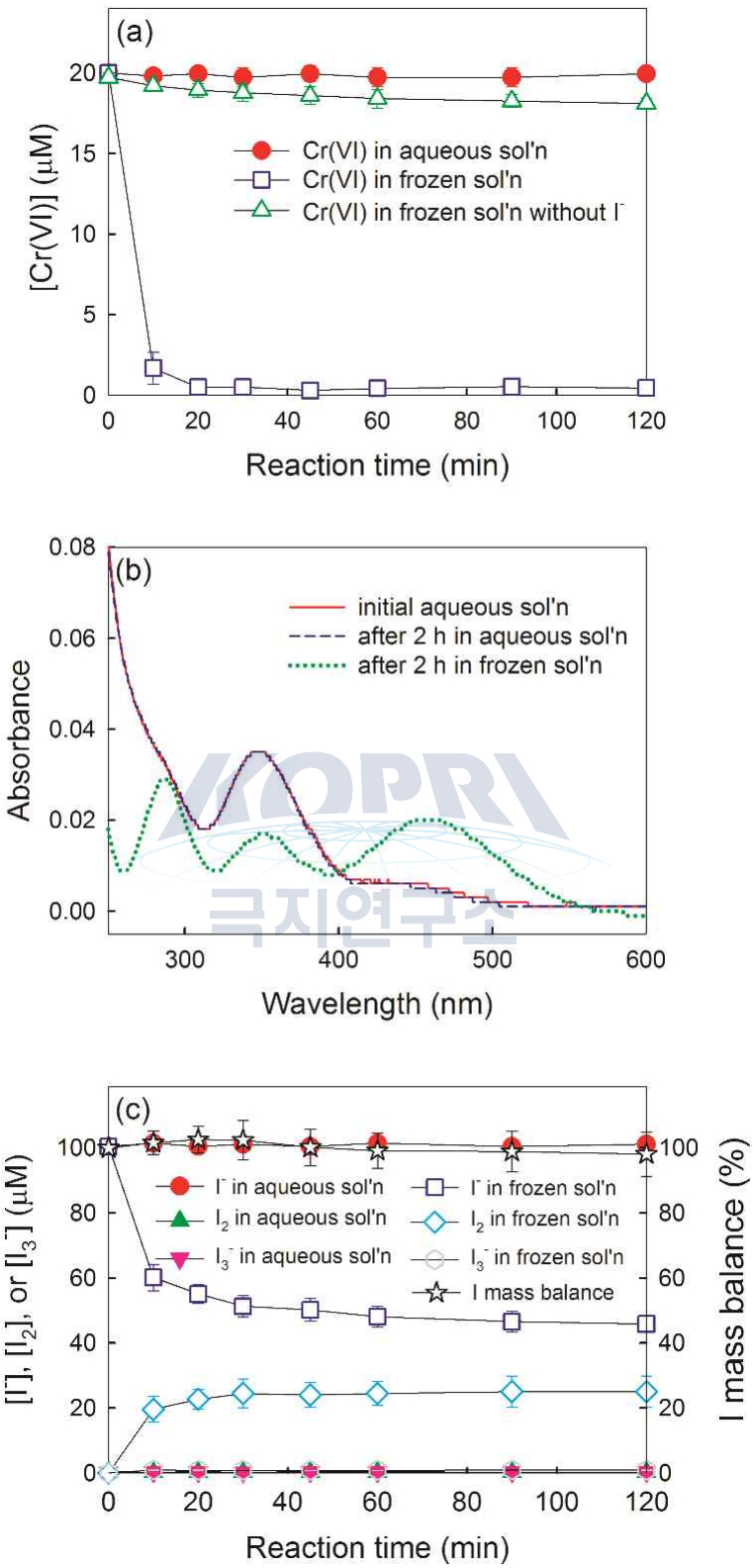



Fig. 1. (a) Time profiles of Cr(VI) concentration, (b) absorbance changes, and (c) time profiles of $I^-$, $I_2$, and $I_3^-$ concentrations in aqueous and frozen solutions containing Cr(VI) and $I^-$. Experimental conditions: [Cr(VI)] = 20 $\mu$M, [$I^-$] = 100 $\mu$M, pH = 3.0, and reaction temperature = 25 °C for aqueous phase reaction or - 20 °C for frozen phase reaction.

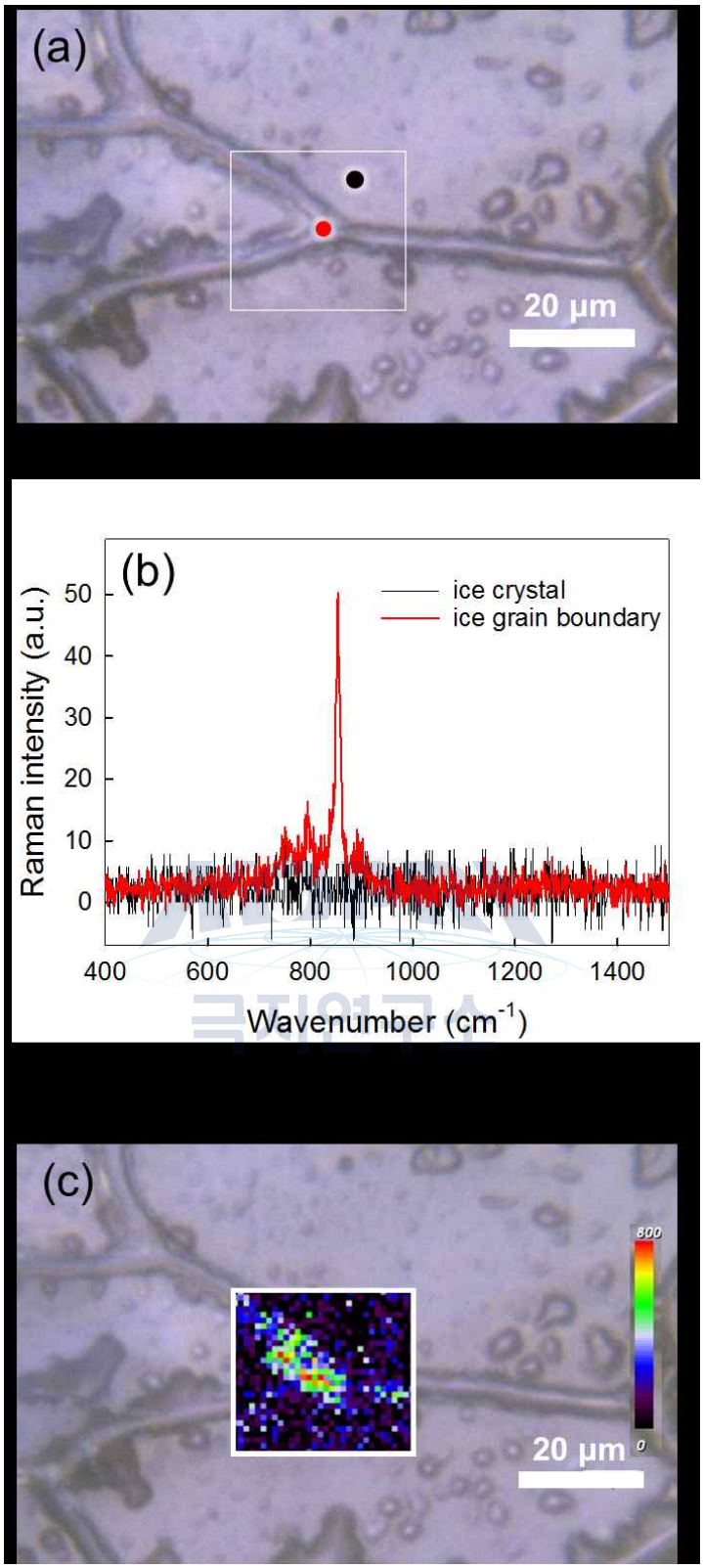



Fig. 2. (a) Optical image of a frozen Cr(VI) solution, (b) Raman spectra measured at the ice grain boundary (red circle) and ice crystal (black circle) in (a), and (c) Cr(VI) concentration distribution image of frozen Cr(VI) solution. Experimental conditions: [Cr(VI)] = 1 mM, pH = 3.0, and freezing temperature = 0 → −20 °C at a rate of −1.5 °C/min.

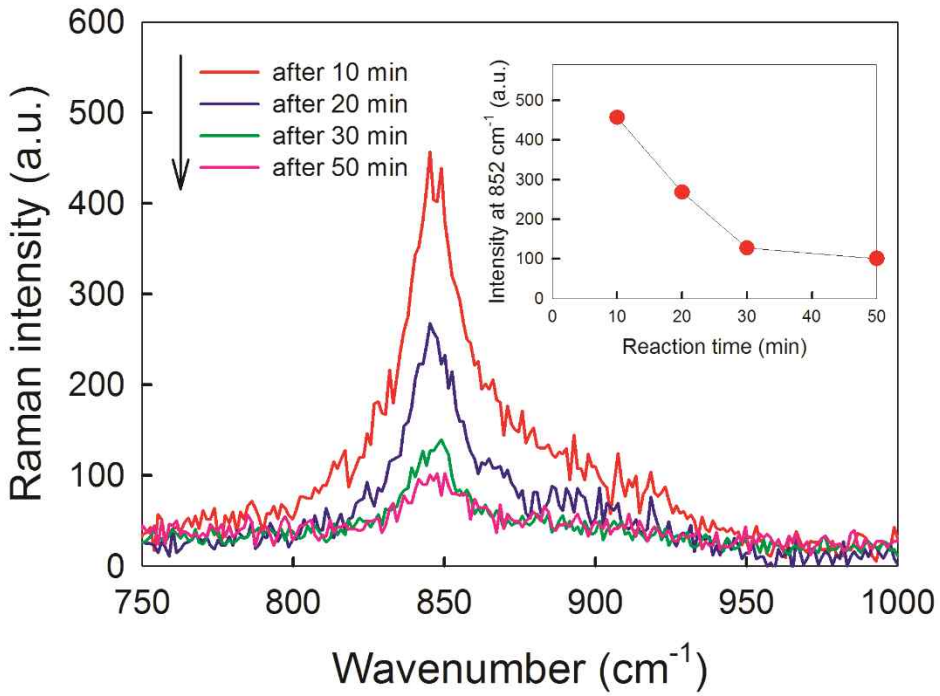



Fig. 3. Raman spectra measured in the ice grain boundary region of a frozen solution containing Cr(VI) and $I^-$. Experimental conditions: [Cr(VI)] = 1 mM, [$I^-$] = 1 mM, pH = 3.0, and freezing temperature = 0 → −20 °C at a rate of −1.5 °C/min. Reaction time is defined as the time after the temperature of the microscope stage has reached −20 °C.

KOPRI 극지연구소

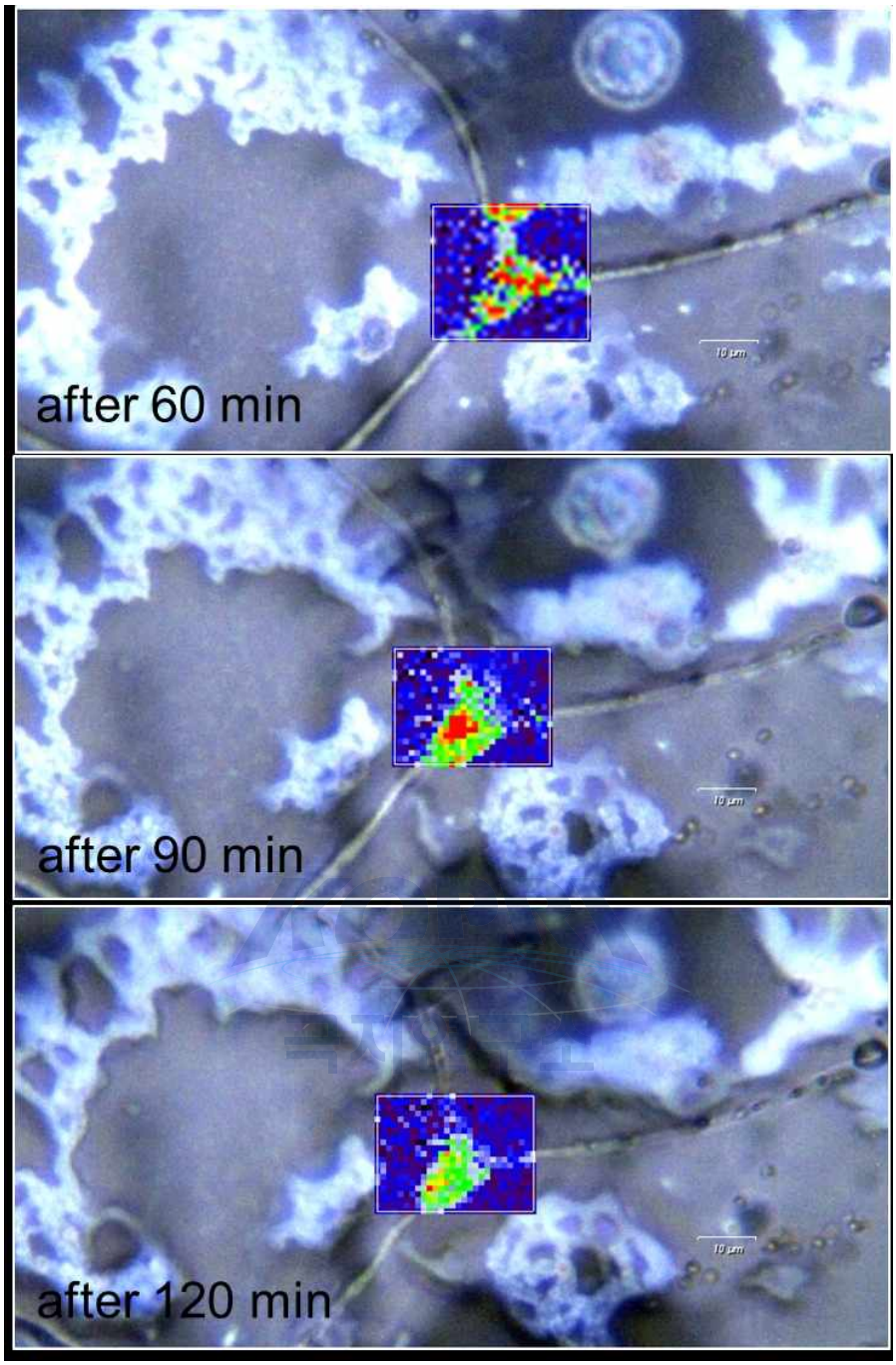



Fig. 4. Cr(VI) concentration distribution images of a frozen solution containing Cr(VI) and $I^-$. Experimental conditions: [Cr(VI)] = 1 mM, [$I^-$] = 1 mM, pH = 3.0, and freezing temperature = 0 → −20 °C at a rate of −1.5 °C/min. Reaction time is defined as the time after the temperature of the microscope stage has reached −20 °C.

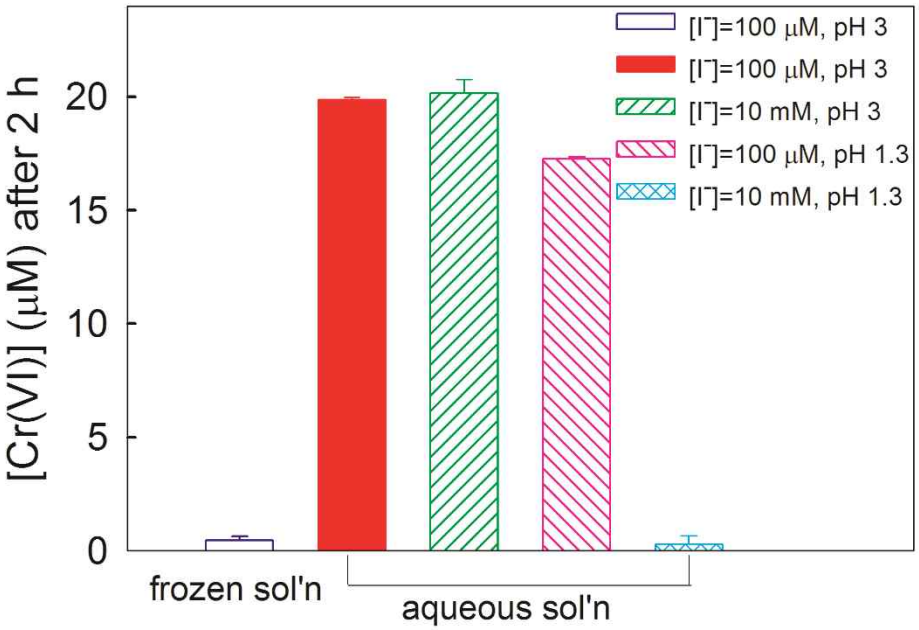



Fig. 5. Effect of $I^-$ concentration increase and/or pH decrease on Cr(VI) reduction. Experimental conditions: [Cr(VI)] = 20 $\mu$M, [$I^-$] = 100 $\mu$M or 10 mM, pH = 3.0 or 1.3, reaction time = 2 h, and reaction temperature = 25 °C for aqueous phase reaction or −20 °C for frozen phase reaction.

KOPRI
극지연구소

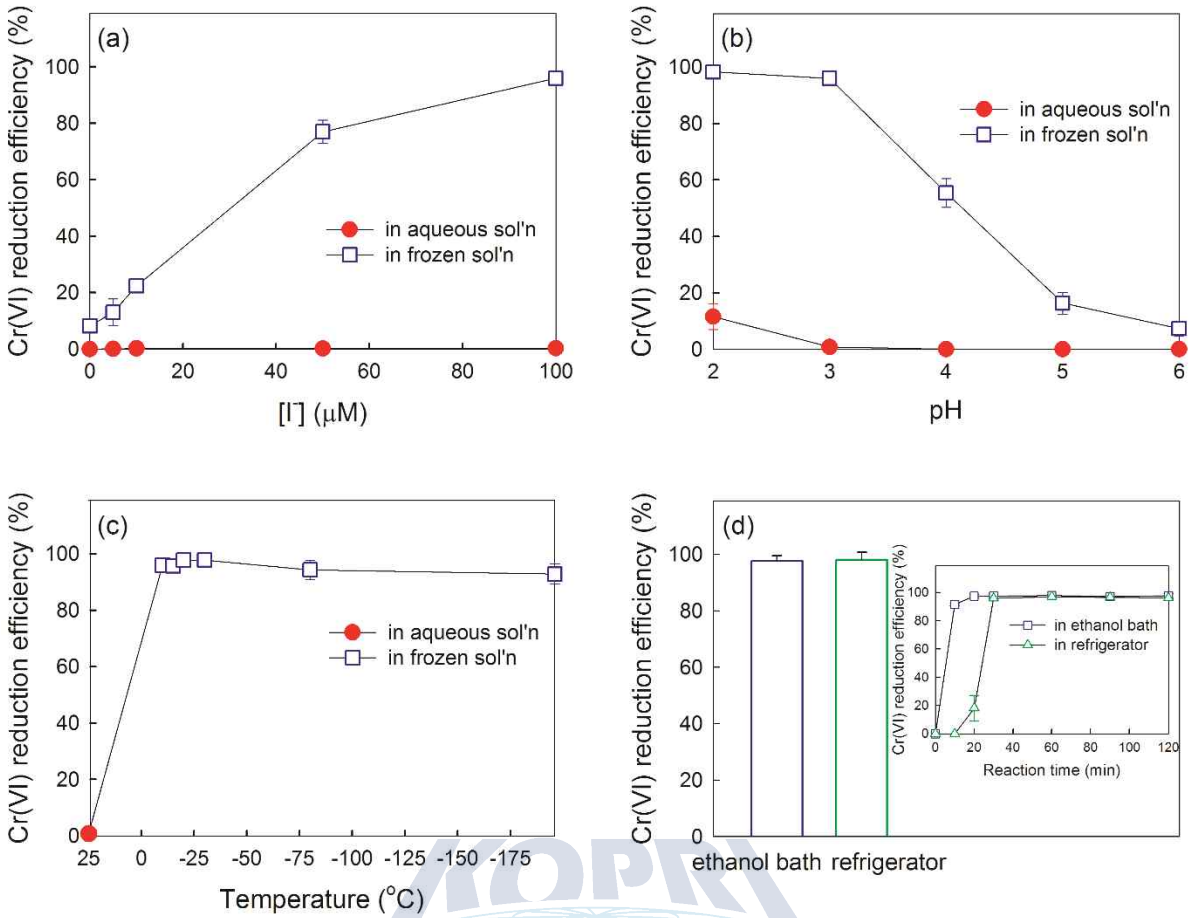



Fig. 6. Effect of (a) $I^-$ concentration, (b) pH, (c) temperature, and (d) freezing method on the Cr(VI) reduction efficiency. Experimental conditions: [Cr(VI)] = 20 $\mu$M, [$I^-$] = 0−100 $\mu$M, pH = 2.0−6.0, reaction temperature = 25 ~ −196 °C, and reaction time = 2 h.

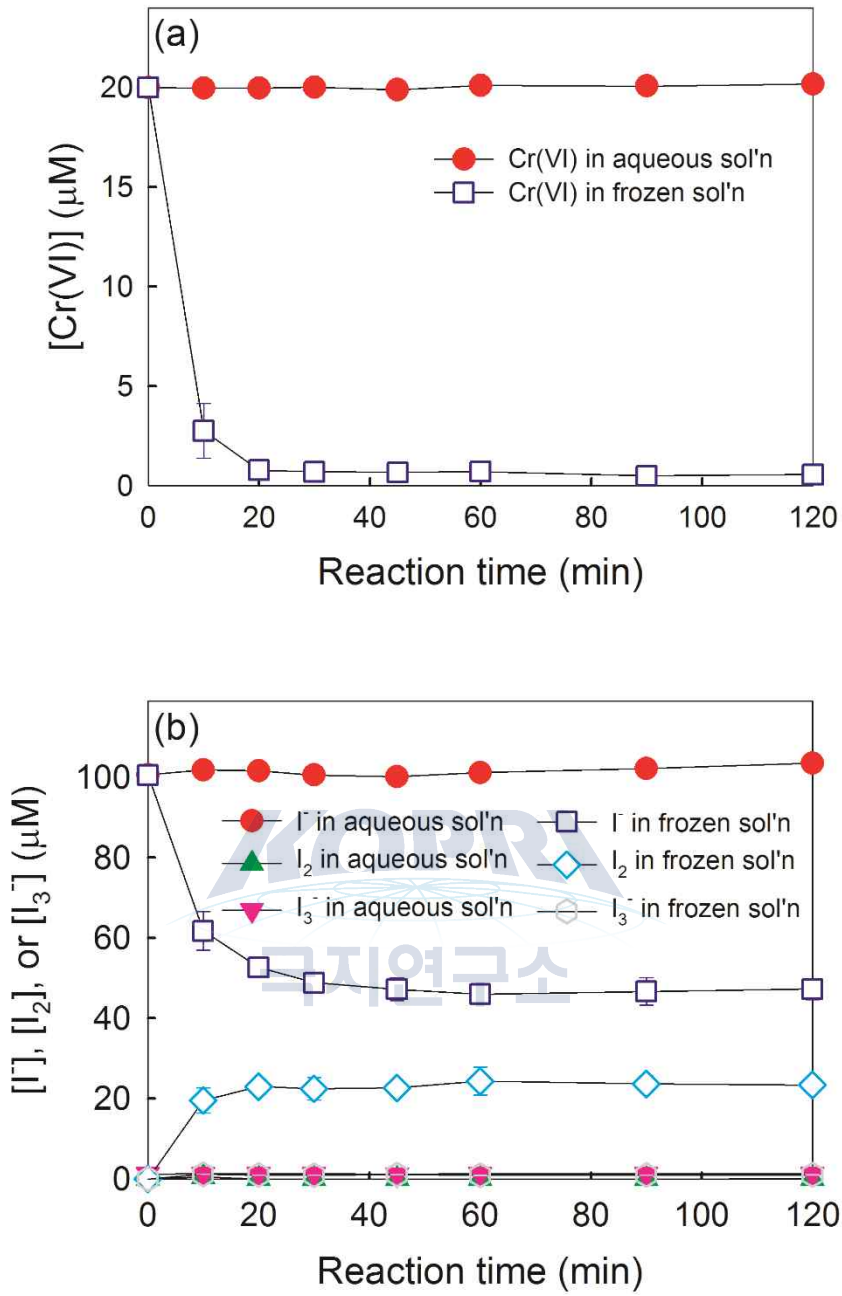



Fig. 7. Simultaneous (a) reduction of Cr(VI) and (b) production of $I_2$ in the Cr(VI)-contaminated electroplating wastewater after $I^-$ addition and freezing. Experimental conditions: [Cr(VI)] = 20 $\mu$M in the diluted electroplating wastewater, [$I^-$] = 100 $\mu$M, pH = 3.0, and reaction temperature = 25 °C for aqueous phase reaction or - 20 °C for frozen phase reaction.

# 제 3 절. Freezing-accelerated removal of chromate by biochar synthesized from waste rice husk③

Tae Uk Han[1], Jungwon Kim[2], Kitae Kim[1,3*]

[1]Korea Polar Research Institute (KOPRI), Incheon 21990, Republic of Korea

[2]Department of Environmental Sciences and Biotechnology, Hallym University, Chuncheon, Gangwon-do 24252, Republic of Korea

[3]Department of Polar Sciences, University of Science and Technology (UST), Incheon 21990, Republic of Korea

## Abstract

The application of biochar has been considered a promising method for remediating contaminated water, as biochar exhibits a redox activity for environmentally relevant redox reactions. Although the mechanisms of various redox reactions by biochar in water have been widelyinvestigated, investigations of reaction in ice have not beenattempted. In this study, the freezing-accelerated removal of chromate (Cr(VI)) by biochar synthesized from waste rice husks (RH-BC) was investigated in water (25 °C) and ice (-20 °C). The reduction of Cr(VI) with RH-BC was insignificant in water, whereas an enhanced reduction efficiency of Cr(VI) was observed in ice due to the freeze concentration phenomenon. The enhanced redox reaction between Cr(VI) and dissolved organic matter (DOM) is primarily responsible for the accelerated Cr(VI) reduction in ice, wherein DOM is a primary component of RH-BC. Experiments on various conditions of pH and RH-BC concentrations reveal that Cr(VI) is heavily reduced at low pH values and an aggregation of RH-BC in ice can inhibit the reduction efficiency of Cr(VI) due to a decrease in active sites. The removal of Cr(VI) by RH-BCwas successfully achieved with real Cr(VI)-contaminated wastewater in ice; this elucidated the environmental relevance of freezing-assisted Cr(VI) removal in cold regions.

## 1. Introduction

Biochar (BC) is a carbon-rich and porous solid product produced by thermal decomposition (pyrolysis) under $O_2$-limited conditions [1]. Owing to its unique properties, such as large amounts of functional groups and high contents of organic carbon and ash [2, 3], BC has received significant attention as a cost-effective material for environmental

③ 본 연구는 본 연구과제(PE20030)의 지원을 받아 수행되었다. 연구 결과는 *Sep. Purif. Technol.* 2020, 250, 117233에 출판되었다.

applications; these include carbon sequestration, greenhouse gas reduction, improvement of soil fertility, and immobilization and remediation of contaminated water and soil [4]. As a field that extensively utilizes BC, research on the usage of BC as a sorbent and/or reductant has been extensively performed for the removal of environmental pollutants such as dyes [5, 6], phenols [7], pesticides [8],and heavy metal ions [9] in water and soil.

According to the literature, BC has specifically shown a strong affinity for heavy metals because of its properties such as its porous structure and the existence of several functional groups on its surface [3, 10, 11]. Among heavy metal ions, chromium is a common element in Earth's crust, which is widely used in various industries such as metallurgy, dye and pigment, corrosion inhibition, leather tanning, and electroplating [12]. Trivalent chromium (i.e., Cr(III)) and hexavalent chromium (i.e., Cr(VI), chromate) are the most stable oxidation states of chromium. In addition, Cr(VI) is approximately 500-1,000 times more hazardous than Cr(III) in terms of its carcinogenic and mutagenic effects on biological systems [13]. Thus, Cr(VI) is widely restricted based on the European Restriction of Hazardous Substances (RoHS) Directive and the removal and/or reduction of Cr(VI) by BC has been extensively explored [14-18]. Dong et al. [15] proposed a two-step removal mechanism of Cr(VI) under acidic media by using sugar beet tailing (SBT)-BC, wherein Cr(VI) was preferentially reduced to Cr(III) via electrostatic attraction between negatively charged Cr(VI) (i.e., $HCrO^{4-}$) and positively charged BC; this was followed by the complexation of Cr(III) with functional groups on SBT-BC. Li et al. [3] reviewed several articles to provide insights for the adsorption mechanisms of metal ions by BC; they also proposed the following Cr(VI) sorption mechanisms according to the literature: (1) electrostatic attraction and reduction of Cr(VI) and (2) complexation of Cr(III) on BC surface. Moreover, they reported that the reduction pathways of Cr(VI) in an aqueous solution could be divided into direct (i.e., reduction by solubilized BC components) and indirect (i.e., reduction on a biochar surface) pathways.

Although BC is considered as a promising material for Cr(VI) reduction and adsorption from water, its actual performance is significantly lower than those of conventional sorbents [19]. To solve technical issues, numerous studies designed to enhance the performance of BC have been extensively performed via chemical modifications and physical modifications [20-23]. Typical chemical modification methods include methanol and amino modifications and acid/base treatments to enhance the adsorption capacity by modifying the surface functional groups of BC [21]. Impregnating BC with metal oxide is another chemical modification method. The nanosized metal oxideparticles on the BC surface can act as active sorption sites, which results in an improvement of the sorption ability for heavy metal ions [19, 24]. Meanwhile, physical modification methods such as steam activation and gas purging use oxidizing agents (CO2, steam, and air) without any

chemicals to enlarge the surface area, pore volume, and structure of microporous BC [25].Although these modification techniques increase the efficiency of the BC as a sorbent, reductant, and soil conditioner, additional costs for the modification process are required. Further, incorrect modification can cause the abilities of BC to diminish, such as the reduction inporosity and the decrease in surface area.

The freezing process is a possible method for enhancing BC performance. It is commonly accepted that chemical reactions slow down as temperature drops and ice crystal is inert as reaction media. However, some reactions such as redox conversions and the dissolution of solid particles can be accelerated by freezing [12, 13, 26-28]. This is because solutes, protons, and/or solid particles dramatically accumulate in ice grain boundaries, which are the liquid compartments between ice crystals by exclusion from solid ice crystals during freezing; this is termed as the freeze concentration effect. Numerous studies have continuously investigated enhanced redox conversions in the ice phase between Cr(VI) and some species such as arsenite (As(III)) [12], dissolved organic matter (DOM) [29], hydrogen peroxide ($H_2O_2$) [30], phenolic compounds [13], and nitrite ($NO_2^-$) [31]. However, a drawback in the reduction of Cr(VI) is that the concentration of total chromium remains in the system.

Therefore, the freezing-induced reduction and adsorption of Cr(VI) by BC was attempted to achieve the enhanced Cr(VI) removal efficiency in the ice phase. In this study, we used the BC synthesized from waste rice husks(RH-BC), and investigated the reduction and adsorption efficiency of Cr(VI) by RH-BC in the ice phase (i.e., at -20 ℃) in comparison with its counterpart in the water phase (i.e., at 25 ℃). The redox conversion of Cr(VI)/RH-BC was accelerated in ice; however, it was negligible in water. To elucidate the freezing-enhanced reduction of Cr(VI) by RH-BC in ice, the redox conversion kinetics of Cr(VI) with dissolved organic matter (DOM) derived from raw RH-BC as well as washed RH-BC in both ice and water were also explored as a function of various experimental conditions. By understanding the combination results, this research will be able to provide fundamental data for the actual commercialization of the RH-BC/freezing system.

## 2. Materials and methods

### 2.1. Material and chemicals

The waste rice husks (RH), which was collected from a rice millcompany in the Republic of Korea, was cryo-milled and dried at 105 ℃. To minimize theheat and mass transfer inhibition effect, particle sizes below 500 mm were collected and used for each experiment. The real Cr(VI)-containing wastewater was obtained from a local electroplating plant in the Republic of Korea. All chemicals and reagents were used without further

purification in this study including as follows: sodium dichromate dihydrate ($Na_2Cr_2O_7 \cdot 2H_2O$, Cr(VI), Sigma-Aldrich, ≥ 99.5 %), 1,5-diphenylcarbazide ($C_6H_5NHNHCONHNHC_6H_5$, DPC, Sigma-Aldrich, ≥ 99.95 %), sulfuric acid ($H_2SO_4$, Kanto, ≥ 96.0 %), acetone ($CH_3COCH_3$, Kanto, ≥ 99.5%), cresol red ($C_{21}H_{18}O_5S$, Sigma-Aldrich, ≥ 95.0%).

### 2.2. Thermogravimetric and product analysis

The thermogravimetric (TG) analyzer (Pyris Diamond, PerkinElmer Co.) was used to establish the thermal properties of RH and determine the reaction temperature for the RH-BC production. For TG analysis, the sample (5 mg) was heated from ambient temperature to 700 °C at a heating rate of 20 °C/min under nitrogen flow (100 mL/min). Multi-shot gas chromatography/mass spectrometry (GC/MS) (7890A/5975C inert, Agilent Technologies) analysis via pyrolyzer (Py; EGA/Py-3030D, Frontier Laboratories Ltd.) was also carried out to determine the detailed information on the evolved chemicals in each thermal zone [32]. The detailed Py-GC/MS operational conditions are given in the supplementary information section (Table S1).

### 2.3. Sample preparation and characterization

To produce RH-BC, 20 g of dried RH was heated non-isothermally from ambient temperature to 300 °C at a heating rate of 10 °C/min, under a nitrogen flow rate of 500 mL/min using fixed-bed reactor. RH-BC was cryo-milled with liquid nitrogen using a milling machine and sieved to make its particle size below 63 mm, which is hereafter referred to as raw RH-BC. Washed RH-BC and DOM separated from raw RH-BC were also prepared to deeply investigate Cr(VI) conversion pathways. For DOM preparation, 10 g of raw RH-BC was placed into the reaction vessel with 1 L of the ultrapure deionized (DI) water (18.3 M • cm, Human-Power I+ water purification system, Human Co.)for 24 h, and then filtered by a membrane (0.22 mm, Durapore membrane filters, Millipore Co.). The residual raw RH-BC was washed four additional times using the same method for DOM preparation to sufficiently remove DOM; this process is hereafter referred to as washed RH-BC. All of the samples were dried at 105 °C for at least 24 h beforeeach experiment.

Proximate, ultimate analysis, and higher heating value (HHV) measurements were conducted to investigate the physico-chemical properties of RH and RH-BC according to established procedures reported elsewhere [32]. The physico-chemical properties of RH and RH-BC are summarized in Table S2 (Supplementary Information). To determine the qualitative characterization of DOM, a fluorescent excitation-emission matrix (EEM) measurement was performed using a fluorescence spectrophotometer (FLS-1000, Edinburgh Instruments Ltd.); this process used excitation wavelengths from 240 to 450nm with scanning emission spectra from 250 to 580 nm at 5 nm intervals. The DOM concentrations

were measured by a total organic carbon (TOC) analyzer equipped with a nondispersive infrared sensor (NDIR) (TOC-VCSH, Shimadzu Co.). For the analysis of RH-BC functional groups, the Fourier transform infrared spectroscopy (FTIR) spectrum was also analyzed via a FTIR instrument (NICOLET iN10 MX, Thermo Fisher, Co.) using the attenuated total reflection (ATR) mode.

### 2.4. Experimental procedure

The reduction of Cr(VI) by raw RH-BC, washed RH-BC, and DOM applied in this study were classified depending on the adding substance types. In case of experiments for the reduction of Cr(VI) by raw and washed RH-BC, 10 mL of solution containing the desired amount of RH-BC (1 g/L ~ 10 g/L) and concentration of Cr(VI) (usually, 20 mM) was prepared in a conical tube (15 mL). The pH value of solution containing RH-BC was adjusted to the desired experimental values (3.0 - 5.0) using a $HClO_4$ (1 M) and NaOH (1 M). For the redox conversion of Cr(VI) by DOM, 10 mL of Cr(VI) containing solution with the same concentration of DOM as raw RH-BC was prepared with the conditions of $[Cr(VI)]_i$ = 20 mM, $[DOM]_i$ = 6.553 mg C/L, and $[pH]_i$ = 3.0 - 5.0. The prepared conical tubes were located at the same time (t = 0)in a rack in a cryogenic ethanol bath, which were pre-adjusted at 25 ℃ (for the reaction in water) and -20 ℃ (for the reaction in ice). At each fixed time interval, the samples collected from each ethanol bath were thawed in lukewarm water (40 ℃). Then, the solution containing raw and washed RH-BC was filtered using a 0.45 mm syringe filter to remove RH-BC particles. The filtered solution (i.e., the solution separated from Cr(VI)/RH-BC) and DOM containing solution (i.e., Cr(VI)/DOM) were immediately analyzed to determine the residual concentrations of Cr(VI) and total chromium. To measure the concentrations of Cr(VI) and total chromium in the solution, we used the 1, 5-diphenylcarbazide (DPC) method and inductively coupled plasma-optical emission spectroscopy (ICP-OES; iCAP 6300 Duo, Thermo Fisher Co.), respectively, according to established procedures reported elsewhere [30]. All data were obtained from the average values of three replicates to confirm data reproducibility.

### 2.5. pH measurement of frozen solution

To estimate the pH of the frozen solution, a UV-visible spectrometer equipped with an integrating sphere (Cary 5000, Agilent Technologies) was used, and the pH value of the frozen solution was calculated according to the procedure reported by Ju et al. [13]. Cresol red (CR) was used as a pH indicator because CR exists in three different forms depending on the pH, and each form has a different maximum absorption wavelength ($\lambda_{max}$ = 518 nm for diprotonated CR, $\lambda_{max}$ = 434 nm for monoprotonated CR, and ëmax = 573 nm for deprotonated CR). To determine the relative concentrations of two CR forms (i.e.,

[monoprotonated CR]/[diprotonated CR] or [deprotonated CR]/[monoprotonated CR]) in the frozen solution, the *lsqnonneg* function of Matlab was used as follows:

$$\sum_{\lambda=400nm}^{\lambda=650nm}(A \cdot a + B \cdot b - X)^2 = \text{ minimum value} \quad (1)$$

where X is the absorbance of the frozen solution, A and B donate the absorbance of pure deprotonated and monoprotonated CR (or the absorbance value of pure monoprotonated and deprotonated CR), respectively, and a and b (non-negative parameters) are the relative concentrations of diprotonated and monoprotonated CR (or the relative concentrations of monoprotonated and deprotonated CR) in the frozen solution, respectively. The pure ice was used as a reference. The pH of the frozen solution was estimated by eq. (2), where $pK_{a1}$ = 1.10 and $pK_{a2}$ = 8.15 [13].

$$pH = pKa_1 + \log\frac{monoprotonated\ CR}{deprotonated\ CR} \quad \text{or} \quad pKa_2 + \frac{deprotonated\ CR}{monoprotonated\ CR} \quad (2)$$

## 3. Results and discussion

### 3.1. Characterization of RH and RH-BC

Fig. 1a shows the TG and derivative TG (DTG) curves for RH at a heating rate of 20 °C/min. Lignocellulosic biomass, which consists of hemicellulose, cellulose, and lignin, decomposes typically at the temperature zone between 200 °C and 400 °C. The DTG curve in Fig. 1a shows that RH decomposition involves complex reaction patterns (i.e., shoulder, main, and tailing peaks) owing to the unique thermal stability of each component (hemicellulose: ~200 - 400 °C, cellulose: ~300 - 400 °C, and lignin: ~200 - 600 °C) [33]. The detailed pyrolysis behavior of RH with respect to its major components (hemicellulose, cellulose, and lignin) is explained in the supplementary information.

In terms of BC production, pyrolysis temperature is one of the key factors used to control the quantities of functional groups on BC surfaces [3]. At higher temperatures, the amounts of O-containing functional groups (carboxyl, alcohol and hydroxyl groups) are reduced with the production of large amounts of volatile oxygenated compounds because of the acceleration of dehydration reactions of biomass components at higher temperatures [34]. These O-containing functional groups may not only participate in the adsorption of chromium (i.e., mainly Cr(III)), but they also can act as an electron-donor (ED) for Cr(VI) reduction [3]. Multi-shot GC/MS analysis results (Fig. 1b) confirmed that large amounts of functional groups on the BC surface could be removed together with producing a large quantity of volatile O-containing compounds (acids, anhydro-sugars, phenols and so on) when applying higher temperatures. Therefore, it is suitable that BC was produced at a lower temperature (300 °C) because BC having higher amounts of functional groups increases the reduction and/or adsorption of chromium [35].

Fig. 1c shows the FTIR spectrum of raw RH-BC, and the four functional groups characterize the raw RH-BC [15, 36]. The broad band of 3100 - 3700 $cm^{-1}$ was mainly assigned to the -OH stretching vibration. The peaks between 1400 to 1710 $cm^{-1}$ could correspond to C-O stretching (carbonyl -C=O and carboxyl -COOH; 1706 $cm^{-1}$) and C=C stretching of the benzene ring skeleton from aromatics (1410 - 1680 $cm^{-1}$). The final peak observed between 950 - 1200 $cm^{-1}$ represented -C-O vibrations of phenols. Among the functional groups, carboxyl and hydroxyl groups reportedly play important roles in metal sorption [3]. Specifically, in the case of Cr(VI) reduction and adsorption, these functional groups can be involved in reducing Cr(VI) to Cr(III), and in subsequentCr(III) complexation on raw RH-BC [15].

### 3.2. Cr(VI) reduction by RH-BC in aqueous solution and ice

The reduction of Cr(VI) by RH-BC in ice (-20 ℃) and water (25 ℃) were investigated, and the results were compared. Fig. 2a which shows the time profiles of Cr(VI) concentrations in water and ice, revealed that the reduction of Cr(VI) was negligible in the water phase. However, in the ice phase, it was significant in the ice phaseand it proceeded even in the absence of raw RH-BC owing to the enhanced proton-mediated reduction process (i.e., $4HCr(VI)O_4^- + 16H^+ \rightarrow 4Cr^{3+} + 3O^{2+}\ 10H_2O$; $E^0 = 0.15\ V_{NHE}$) in the liquid grain boundary during the freezing process [30, 31]. However, the degree of reduction in the absence of raw RH-BC in the ice phase was much lower than that observed in the presence of raw RH-BC (i.e., after a 6 h reaction, 19.64 mM of Cr(VI) was reduced in the presence of raw RH-BC vs. the reduction of 4.86 mM of Cr(VI) in the absence of raw RH-BC). This finding indicatesthat the raw RH-BC mediated reduction process is the main reduction pathway for Cr(VI) reduction in ice.

The enhanced RH-BC-mediated Cr(VI) reduction observed in ice possibly resulted from the DOM that eluted from raw RH-BC and/or from RH-BC itself. To further understand the RH-BC-mediated Cr(VI) reduction pathway, experiments on Cr(VI) reduction by washed RH-BC and DOM separated from raw RH-BC were also performed in the water and ice phases (Fig. 2b). The DOM concentration was adjusted to be the same as the DOM concentration associated with 1 g/L of raw RH-BC. The reduction kinetics of Cr(VI) by DOM during freezing were dramatically accelerated compared with those in the water phase. However, the reduction efficiency of Cr(VI) by washed RH-BC in the ice phase quite decreased compared with those of raw RH-BC. This result implies that the enhanced Cr(VI) reduction by raw RH-BC in the ice phase was most likely due to the redox reaction between Cr(VI) and DOM.

Fig. 3 shows the EEM spectrum for the qualitative characterization of DOM. The region

can be assigned as humic acid-like matter (poly-phenolic compounds consisted of quinone, phenol, catechol, sugar moieties and so on) [37, 38]. This means that DOM is an effective ED for Cr(VI) reduction because polydentate ligands can more easily form a precursor (chromate ester intermediate) for the reduction of Cr(VI) [12, 39]. After 6 h of reaction in the presence of DOM, the residual concentrations of DOM were 6.051 mg C/L and 4.723 mg C/L in water and ice, respectively. Similarly, larger amounts of DOM were oxidized and removed in the ice phase during the experiments with raw and washed RH-BC. The initial concentrations of DOM were 6.553 mg C/L for raw RH-BC and 4.415 mg C/L for washed RH-BC, respectively. The residual concentrations of DOM ([DOM]f) after the 6 h reaction were 5.844 (raw RH-BC) and 4.273 mg C/L(washed RH-BC) in water, whereas the concentrations in ice were $[DOM]_f$ = 4.568 (raw RH-BC) and 2.471 mg C/L (washed RH-BC). Therefore, the enhanced redox reaction between Cr(VI) and DOM in the ice phase was the main pathway of the accelerated Cr(VI) transformation by raw RH-BC (i.e., the simultaneous reduction of Cr(VI) and oxidation of DOM).

Notably, the reduction efficiency of Cr(VI) by raw RH-BC was higher than that by DOM in both water and ice. The consumption amount of DOM in the Cr(VI)/raw RH-BC system was also higher than that in Cr(VI)/DOM system. This means that the redox reaction of Cr(VI)/DOM increased in both water and ice when DOM co-existed with RH-BC. O-containing functional groups in BC act as an ED and BC acts as electron shuttle for Cr(VI) reduction under co-exist system of BC and other ED compounds, and it results in the enhanced Cr(VI) transformation [18]. Therefore, the synergistic effect on Cr(VI) reduction by raw RH-BC might occur because BC can act as an electron shuttle to electron transfersbetween DOM and Cr(VI) with the role as an ED.

### 3.3. Reduction of Cr(VI) in water and ice under various conditions

#### 3.3.1. The effect of pHi on Cr(VI) reduction in water and ice

Fig. 4a and 4b show the effect of pHion Cr(VI) reduction by DOM in water and ice. The rate of Cr(VI) reduction by DOM in ice (Fig. 4a) was higher than that in water (Fig. 4b). Fig. 4c - 4f, which show the pH-dependent reduction of Cr(VI) by RH-BC revealed that the difference in the rates of Cr(VI) reduction by RH-BC in water (Fig. 4c and 4e) and ice (Fig. 4d and 4f) was negligible. Additionally, there was an increase in the Cr(VI) reduction efficiencies of DOM and RH-BC in water as $pH_i$ decreased, indicating that the $pH_i$ of the system has a significant effect on Cr(VI) removal efficiency, which was enhanced to a greater extent by lower $pH_i$ values. This behavior is expected given that the reduction of Cr(VI) to Cr(III) requires protons ($HCrO_4^- + 7H^+ + 3^{e-} \rightarrow Cr^{3+} + 4H_2O$). The enhanced reduction of Cr(VI) during freezing could be attributed to the lowering of the pH values of the grain boundary via the freeze concentration phenomenon [13, 30]. The

concentration of protons under acidic condition increases by 2 - 4 orders of magnitude in ice compared with water [40, 41].

To verify the pH decrease during freeze process, the solution containing these solutes was prepared under the conditions of $[Cr(VI)]_i$ = 20 mM, $[DOM]_i$ = 6.553 mg C/L and $[pH]_i$ = 3.0. The pH of the frozen solution was estimated by measuring the UV-vis absorption spectra of CR as a pH indicator [13]. As shown in Fig. 5, the maximum absorption of CR in water at pH = 3.0 was observed at 434 nm (monoprotonated form of CR), whereas that in ice changed from 434 nm to 518 nm (deprotonated form of CR). Therefore, this result confirms that the pH of the frozen solution was lowered by freezing, and the calculated pH of the frozen solution was approximately 0.55.

Even though the Cr(VI) reduction rates in ice were higher than those in water, in the ice phase, the conversion efficiency of Cr(VI) by DOM observed at $pH_i$ = 2.0 was lower than that observed at $pH_i$ = 3.0, possibly owing to Cr(VI) speciation as a function of pH. During the freezing process, there was a decrease in the pH value of the reaction system (Fig. 5); thus, the concentration of the solid form of Cr(VI) (i.e., $Cr(VI)O_3$, equilibrium solid-state of $H_2Cr(VI)O_4$) increased at the grain boundary, bringing about a hindering effect on Cr(VI) reduction owing to the diffusion limitation between Cr(VI) and DOM [13]. Meanwhile, it is worth noting that in ice at pHi values in the range of 2.0 - 3.0, the rates of Cr(VI) reduction by raw RH-BC were higher than those brought about by DOM, suggesting that the synergistic effect on Cr(VI) reduction by raw RH-BC in ice can be realized by accumulating RH-BC particles together with Cr(VI) and DOM at the grain boundary. As a result, a larger reduction of Cr(VI) in ice by RH-BC can be achieved due to the freeze concentration effect under the acidic solution (pHi < 3.0). In addition, the real Cr(VI)-containing wastewater is usually acidic, which means that the reduction of Cr(VI) in ice is suitable [42].

### 3.3.2. The effect of RH-BC dosage on Cr(VI) reduction in water and ice

Fig. 6 shows the residual concentration of Cr(VI) in water and ice with respect to the RH-BC dosage after the 6 h reaction. In the water phase, the final concentration of Cr(VI) slightly decreased as the concentration of washed RH-BC increased (17.93 - 16.14 mM, Fig. 6a); however, the degree of Cr(VI) reduction was negligible even at 10 times of the washed RH-BC dosage (Fig. 6a). Enhanced reduction efficiencies of Cr(VI) by washed RH-BC in ice were observed due to the freeze concentration effect, and the maximum efficiency of Cr(VI) reduction was achieved in the ice phase at 3 g/L of washed RH-BC. In the Cr(VI) reduction by raw RH-BC (Fig. 6b), the reduction efficiencies of Cr(VI) in water were also lower than those in ice,and residual concentrations of Cr(VI) in water reached the equilibrium (ca. 12 mM) above 2 g/L of the raw RH-BC dosage.

Although the residual concentrations of Cr(VI) were very similar (0.40 – 1.01 mM), the lowest concentration of Cr(VI) was observed at 3 g/L of raw RH-BC. Notably, this behavior was only observed in the ice phase. This can be explained by the inhibitory effects for Cr(VI) reduction caused by BC particle aggregation, which are clearly visible at higher BC concentrations [43, 44]. Solid particles are highly aggregated in ice grain boundaries by freezing [26]. The RH-BC particle aggregation in ice reduces available active sites (i.e., O-containing functional groups on BC surface) and ability as electron shuttle for Cr(VI) reduction [45, 46]. In addition, the aggregation can be enhanced by DOM [47]. DOM tends to sorb to the BC surface, and the aggregation of BC particles is accelerated at a high concentration of DOM [47]. As expected, the initial DOM concentration increased (raw RH-BC: 6.553 ~ 41.565 mg C/L, washed RH-BC 4.415 ~ 9.162 mg C/L) with the RH-BC dosage (Table 1). However, the concentration of DOM did not follow proportionally as the RH-BC concentration increased. For example, measured $[DOM]_i$ values at 10 g/L of washed and raw RH-BC were 9.162 mg C/L and 41.565 mg C/L, respectively; these values were lower than the theoretical DOM values of washed RH-BC (44.15 mg C/L) and raw RH-BC (65.53 mg C/L). The results imply that a significant amount of DOM was attached on the RH-BC's surfaces, which resulted in the enhancement of RH-BC aggregation. In addition, the consumption amount of DOM (Δ[DOM]) in ice was also higher than that in water. Δ[DOM] values in the range of 4 – 10 g/L of RH-BC in the ice phase were higher than Δ[DOM] values at 3 g/L of RH-BC; however, the reduction efficiencies of Cr(VI) in ice were maximized at 3 g/L of RH-BC. This means that DOM will likely sorb on the RH-BC surface to form the RH-BC/DOM complex rather than participate in the redox reaction with Cr(VI) when the RH-BC aggregation begins acceleration. Therefore, the decreased reduction efficiency of Cr(VI) by RH-BC in ice at above 3 g/L of RH-BC was likely due to the hindering effects caused by RH-BC aggregation [44-47].

The effect of RH-BC dosage on the adsorptive removal of chromium was also investigated in water and ice (Fig. 7). Although the reduction efficiency of Cr(VI) in the ice phase was maximized at 3 g/L of RH-BC, the adsorption capacity in ice positively correlated with the RH-BC dosage. This can be explained by an increase of the total amount of adsorption sites [43], and an increased adsorption capacity by forming RH-BC/DOM complexes at a high concentration of RH-BC [48]. DOM attached on a BC surface can increase the adsorption capacity due to connection role of DOM between chromium and BC [46, 48]. Therefore, the aggregation of RH-BC as the RH-BC concentration increases does not affect the adsorption capacity of chromium on RH-BC; rather,the adsorption efficiency increases due to the increase of total adsorption sitesand increased connecting ability of DOM between chromium and RH-BC.

### 3.4. Freeze concentration effect on the Cr(VI) reduction by RH-BC

The enhanced reduction of Cr(VI) by raw RH-BC in ice should be due to the freeze concentration effect. To verify the freeze concentration effect, the reduction of Cr(VI) in water at a high concentration of raw RH-BC (10 g/L) and/or low pH (2.0) was investigated to compare the results at the reference conditions ([raw RH-BC] = 1 g/L and pH = 3.0 in water and ice). As shown in Fig. 8, the reduction of Cr(VI) by raw RH-BC positively correlated with the RH-BC and proton concentration in the water phase. Although the reduction efficiencies of Cr(VI) in water positively correlated with the RH-BC dosage and proton concentration, the reduction efficiencies of Cr(VI) were lower than that of the reference condition for ice when both the concentrations of raw RH-BC and protons increased by 10 times. This result implies that protons and/or RH-BC might be concentrated in ice grain boundaries more than 10 times (Fig. 5).

### 3.5. Reduction of Cr(VI) in real Cr(VI)-contaminated wastewater by RH-BC

Small residual concentrations of Cr(VI) and DOM in the solution after 6 h reaction are considered to be optimal from the perspective of reducing harm to humans and the environment because Cr(VI) is more harmful than Cr(III), and DOM also could be considered as an organic pollutant. According to the legislation of the Korea Ministry of Environment, only effluents with a TOC level below 15 mg C/L will be discharged from a wastewater treatment facility at region I (clean area) after 2020. In general, the TOC levels of rivers and lakes range from 2 to 10 mg C/L [49]. Therefore, we selected the reaction conditions with the highest Cr(VI) reduction and DOM concentration below 10 mg C/L after 6 h reaction in the ice phase, and applied these conditions to the real Cr(VI)-contaminated wastewater (electroplating wastewater) containing Cr(VI) and various metals (Table S3). Fig. 9 shows the residual concentration of Cr(VI) in artificial Cr(VI) wastewater and real Cr(VI)-contaminated wastewater after the 6 h reaction in water and ice. The reduction of Cr(VI) in Cr(VI)-contaminated wastewater by raw RH-BC was also negligible in water, whereas it was dramatically enhanced in ice. These results implythat enhanced reductions of real Cr(VI)-containing wastewater byraw RH-BC may be feasible via the freezing process.

## 4. Conclusion

We investigated the enhanced reduction of Cr(VI) by BC in ice in comparison with its counterpart in water. To this end, the BCs synthesized by waste rice husks (RH-BC) were used because these husks are one of the most abundant types of biomass worldwide. The reduction efficiency of Cr(VI) by RH-BC in ice was dramatically enhanced, whereas it was extremely slow in water. This reveals that DOM was main reductant for Cr(VI) reduction

and RH-BC acted as an electron shuttle. During freezing, Cr(VI), DOM, and protons accumulated in the grain boundary due to the freeze concentration effect, which accelerated the redox reaction between Cr(VI) and DOM. The application of RH-BC inthe reduction and removal of Cr(VI) seems to be beneficial because the reductive transformation of Cr(VI) by ions or soluble chemicals via redox reactions cannot reduce the total amounts of chromium. In addition, the reduction of Cr(VI) in real Cr(VI)-contaminated wastewater by RH-BC was also dramatically accelerated in ice and was comparable to that in the artificial Cr(VI) wastewater. Therefore, the freezing process combined with RH-BC application is an effective and practical treatment method for the reduction and removal of Cr(VI)-containing wastewater. In addition, the proposed freezing-assisted Cr(VI) removal by RH-BC might be feasible in real cold environments such as permafrost, polar regions, and mid-latitudes during the winter season.

KOPRI
극지연구소

# REFERENCES


1. C. Jeon, K.L. Solis, H.-R. An, Y. Hong, A.D. Igalavithana, Y.S. Ok, Sustainable removal of Hg(II) by sulfur-modified pine-needle biochar, J. Hazard. Mater. 338 (2020) 122048.
2. M. Vithanage, I. Herath, S. Joseph, J. Bundschuh, N. Bolan, Y.S. Ok, M.B. Kirkham, J. Rinklebe, Interaction of arsenic with biochar in soil and water: A critical review, Carbon 113 (2017) 219-230.
3. H. Li, X. Dong, E.B. da Silva, L.M. de Oliveira, Y. Chen, L.Q. Ma, Mechanisms of metal sorption by biochars: Biochar characteristics and modifications, Chemosphere 178 (2017) 466-478.
4. A.U. Rajapaksha, Y.S. Ok,A. El-Naggar, H. Kim, F. Song, S. Kang, Y.F. Tsang, Dissolved organic matter characterization of biochars produced from different feedstock materials, J. Environ. Manage. 233 (2019) 393-399.
5. Y. Qiu, Z. Zheng, Z. Zhou, D. Sheng, Effectiveness and mechanisms of dye adsorption on a straw-based biochar, Bioresour. Technol. 100 (2009) 5348-5351.
6. D.D. Sewu, P. Boakye, S.H. Woo, Highly efficient adsorption of cationic dye by biochar produced with Korean cabbage waste, Bioresour. Technol. 224 (2017) 206-213.
7. M.B. Ahmed, J.L. Zhou, H.H. Ngo, M.A.H. Johir, K. Sornalingam, Sorptiveremoval of phenolic endocrine disruptors by functionalized biochar: Competitive interaction mechanism, removal efficacy and application in wastewater, Chem. Eng. J. 335 (2018) 801-811.
8. A. Mandal, N. Singh, T.J. Purakayastha, Characterization of pesticide sorption behaviour of slow pyrolysis biochars as low cost adsorbent for atrazine and imidacloprid removal, Sci. Total Environ. 577 (2017) 376-385.
9. J.H. Park, S.-J. Lee, M.-E. Lee, J.W. Chung, Comparison of heavy metal immobilization in contaminatedsoils amended with peat moss and peat moss-derived biochar, Environ. Sci.: Processes Impacts 18 (2016) 514-520.
10. X. Tan, Y. Liu, G. Zeng, X. Wang, X. Hu, Y. Gu, Z. Yang, Application of biochar for the removal of pollutants from aqueous solutions, Chemosphere 125 (2015) 70-85.
11. X. Xiao, B. Chen, Z. Chen, L. Zhu, J.L. Schnoor, Insight into multiple and multilevel structures of biochars and their potential environmental applications: A critical review, Environ. Sci. Technol. 52 (2018) 5027-5047.
12. K. Kim, W. Choi, Enhanced redox conversion of chromate and arsenite in ice, Environ. Sci. Tehcnol. 45 (2011) 2202-2208.
13. J. Ju, J. Kim, L. Vetráková, J. Seo, D. Heger, C. Lee, H.-I. Yoon, K. Kim, J. Kim,


KOPRI 극지연구소

Accelerated redox reaction between chromate and phenolic pollutants during freezing, J. Hazard. Mater. 329 (2017) 330-338.

14. D. Mohan, S. Rajput, V.K. Singh, P.H. Steele, C.U. Pittman Jr., Modeling and evaluation of chromium remediation from water using low cost bio-char, a green adsorbent, J. Hazard. Mater. 188 (2011) 319-333.
15. X. Dong, L.Q. Ma, Y. Li, Characteristics and mechanisms of hexavalent chromium removal by biochar from sugar beet tailing, J. Hazard. Mater. 190 (2011) 909-915.
16. Y.-S. Shen, S.-L. Wang, Y.-M. Tzou, Y.-Y. Yan, W.-H. Kuan, Removal of hexavalent Cr by coconut coir and derived chars - The effect of surface functionality, Bioresour. Technol. 104 (2012) 165-172.
17. N. Zhao, Z. Yin, F. Liu, M. Zhang, Y. Lv, Z. Hao, G. Pan, J. Zhang, Environmentally persistent free radicals mediated removal of Cr(VI) from highly saline water by corn straw biochars, Bioresour. Technol. 260 (2018) 294-301.
18. X. Xu, H. Huang, Y. Zhang, Z. Xu, X. Cao, Biochar as both electron donor and electron shuttle for the reduction transformation of Cr(VI)during its sorption, Environ. Pollut. 244 (2019) 423-430.
19. L. Wang, Y. Wang, F. Ma, V. Tankpa, S. Bai, X. Guo, X. Wang, Mechanisms and reutilization of modified biochar used for removal of heavy metals from wastewater: A review, Sci. Total Environ. 668 (2019) 1298-1309.
20. Y. Han, X. Cao, X. Ouyang, S.P. Sohi, J. Chen, Adsorption kinetics of magnetic biochar derived from peanut hull on removal of Cr (VI) from aqueous solution: Effects of production conditions and particle size, Chemosphere 145 (2016) 336-341.
21. A.U. Rajapaksha, S.S. Chen, D.C.W. Tsang, M. Zhang, M. Vithanage, S. Mandal, B. Gao, N.S. Bolan, Y.S. Ok, Engineered/designer biochar for contaminant removal/immobilization from soil and water: Potential and implication of biochar modification, Chemosphere 148 (2016) 276-291.
22. H. Dong, J. Deng, Y. Xie, C. Zhang, Z. Jiang, Y. Cheng, K. Hou, G. Zeng, Stabilization of nanoscale zero-valent iron (nZVI) with modified biochar for Cr(VI) removal from aqueous solution, J. Hazard. Mater. 332 (2017) 79-86.
23. Y. Zhu, H. Li, G. Zhang, F. Meng, L. Li, S. Wu, Removal of hexavalent chromium from aqueous solution by different surface-modified biochars: Acid washing, nanoscale zero-valent iron and ferric iron loading, Bioresour. Tehcnol. 261 (2018) 142-150.
24. X. Hu, Z. Ding, A.R. Zimmerman, S. Wang, B. Gao, Batch and column sorption of arsenic onto iron-impregnated biochar synthesized through hydrolysis, Water Res. 68 (2015) 206-216.

KOPRI 극지연구소

25. J. Wang, S. Wang, Preparation, modification and environmental application of biochar: A review, J. Clean. Prod. 227 (2019) 1002-1022.

26. K. Kim, W. Choi, M.R. Hoffmann, H.-I. Yoon, B.-K. Park, Photoreductive dissolution of iron oxides trapped in ice and its environmental implications, Environ. Sci. Technol. 44 (2010) 4142-4148.

27. S.P.M. Menacherry, K. Kim, W. Lee, C.H. Choi, W. Choi, Ligand-specific dissolution of iron oxides in frozen solutions, Environ. Sci. Technol. 52 (2018) 13766-13773.

28. K. Kim, J. Ju, B. Kim, H.Y. Chung, L. Vetráková, D. Heger, A. Saiz-Lopez, W. Choi, J. Kim, Nitrite-induced activation of iodate into molecular iodine in frozen solution, Environ. Sci. Technol. 53 (2019) 4892-4900.

29. X. Dong, X, L.Q. Ma, J. Gress, W. Harris, Y. Li, Enhanced Cr(VI) reduction and As(III) oxidation in ice phase: Important role of dissolved organic matter from biochar, J. Hazard. Mater. 267 (2014) 62-70.

30. K. Kim, J. Kim. A.D. Bokare, W. Choi, H.-I. Yoon, J. Kim, Enhanced removal of hexavalent chromium in the presence of H2O2 in frozen aqueous solutions, Environ. Sci. Technol. 49 (2015) 10937-10944.

31. K. Kim, H.Y. Chung, J. Ju, J. Kim, Freezing-enhanced reduction of chromate by nitrite, Sci. Total Environ. 590-591 (2017) 107-113.

32. T.U. Han, Y.-M. Kim, M.Z. Siddiqui, T. Lee, A. Watanabe, N. Teramae, S. Kim, Y.-K. Park, Non-isothermal pyrolysis properties of Laminaria japonica, J. Anal. Appl. Pyrolysis 130 (2018) 277-284.

33. Y.-M. Kim, S. Kim, T.U. Han, Y.-K. Park, C. Watanabe, Pyrolysis reaction characteristics of Korean pine (Pinus koraiensis) nut shell, J. Anal. Appl. Pyrolysis 110 (2014) 435-441.

34. Q. Abbas, G. Liu, B. Yousaf, M.U. Ali, H. Ullah, M.A.M. Munir, R. Liu, Contrasting effects of operating conditions and biomass particle size on bulk characteristics and surface chemistry of rice husk derived-biochars, J. Anal. Appl. Pyrolysis 134 (2018) 281-292.

35. L. Zhou, Y. Liu, S. Liu, Y. Yin, G. Zeng, X. Tan, X. Hu, X. Hu, L. Jiang, Y. Ding, S. Liu, X. Huang, Investigation of the adsorption-reduction mechanisms of hexavalent chromium by ramie biochars of different pyrolytic temperatures, Bioresour. Tehcnol. 218 (2016) 351-359.

36. K.H. Kim, J.-Y. Kim, T.-S. Cho, J.W. Choi, Influence of pyrolysis temperature on physicochemical properties of biochar obtained from the fast pyrolysis of pitch pine (Pinus rigida), Bioresour. Technol. 118 (2012) 158-162.

37. W. Chen, P. Westerhoff, J.A. Leenheer, K. Kooksh, Fluorescence excitation-emission matrix regional integration to quantify spectra for dissolved organic matter, Environ. Sci. Technol. 37 (2003) 5701-5710.

38. J. Wei, C. Tu, G. Yuan, D. Bi, H. Wang, L. Zhang, B.K.G. Theng, Pyrolysis temperature-dependent changes in the characteristics of biochar-borne dissolved organic matter and its copper binding properties, Bull. Environ. Contam. Toxicol. 103 (2019) 169-174.

39. Y.B. Atalay, R.F. Carbonaro, D.M. Di Toro, Distribution of proton dissociation constants for model humic and fulvic acid molecules, Environ. Sci. Technol. 43 (2009) 3626-3631.

40. D. Heger, J. Jirkovský, P. Klán, Aggregation of methylene blue in frozen aqueous solutions studied by absorption spectroscopy, J. Phys. Chem. A 109 (2005) 6702-6709.

41. D. Heger, J. Jirkovský, P. Klán, Enhanced protonation of cresol red in acidic aqueous solutions caused by freezing, J. Phys. Chem. B 110 (2006) 1277-1287

42. G. Moussavi, B. Barikbin, Biosorption of chromium(VI) from industrial wastewater onto pistachio hull waste biomass, Chem. Eng. J. 162 (2010) 893-900.

43. X. Chen, G. Chen, L. Chen, Y. Chen, J. Lehmann, M.B. McBride, A.G. Hay, Adsorption of copper and zinc by biochars produced from pyrolysis of hardwood and corn straw in aqueous solution, Bioresour. Technol. 102 (2011) 8877-8884.

44. J. Xu, Y. Yin, Z. Tan, B. Wang, X. Guo, X. Li, J. Liu, Enhanced removal of Cr(VI) by biochar with Fe as electron shuttles, J. Environ. Sci. 78 (2019) 109-117.

45. A. Shakya, T. Agarwal, Removal of Cr(VI) from water using pineapple peel derived biochars: Adsorption potential and re-usability assessment, J. Mole. Liq. 293 (2019) 111497.

46. Z. Yang, T. Sun, E. Subdiaga, M. Obst, S.B. Haderlein, M. Maisch, R. Kretzschmar, L.T. Angenent, A. Kappler, Aggregation-dependent electron transfer via redox-active biochar particles stimulate microbial ferrihydrite reduction, Sci. Total Environ. 703 (2020) 135515.

47. W. Yang, J. Shang, P. Sharma, B. Li, K. Liu, M. Flury, Colloidal stability and aggregation kinetics of biochar colloids: Effects of pyrolysis temperature, cation type, and humic acid concentrations, Sci. Total Environ. 658 (2019) 1306-1315.

48. J. Shang, M. Zong, Y. Yu, X. Kong, Q. Du, Q. Liao, Removal of chromium (VI) from water using nanoscale zerovalent iron particles supported on herb-residue biochar, J. Environ. Manage. 197 (2017) 331-337.

49. E.M. Thurman, Organic Geochemistry of Natural Waters. Springer Science & Business

KOPRI 극지연구소

Media (2012).

KOPRI
극지연구소

# TABLE

Table 1. The reduced concentration of DOM (△[DOM][a]) in water and ice after 6 h reaction.

| | Washed RH-BC | | | | | | Raw RH-BC | | | | | |
|---|---|---|---|---|---|---|---|---|---|---|---|---|
| Biochar (g/L) | 1 | 2 | 3 | 4 | 5 | 10 | 1 | 2 | 3 | 4 | 5 | 10 |
| $[DOM]_i$ | 4.415 ± 0.106 | 4.713 ± 0.064 | 5.339 ± 0.035 | 6.024 ± 0.042 | 6.832 ± 0.094 | 9.162 ± 0.065 | 6.553 ± 0.062 | 10.641 ± 0.304 | 14.060 ± 0.072 | 18.383 ± 0.013 | 22.432 ± 0.408 | 41.565 ± 0.085 |
| Water Δ[DOM][a] | 0.142 ± 0.021 | 0.34 ± 0.220 | 0.815 ± 0.015 | 0.940 ± 0.030 | 1.792 ± 0.210 | 1.886 ± 0.016 | 0.709 ± 0.060 | 1.163 ± 0.215 | 1.523 ± 0.040 | 2.185 ± 0.009 | 2.356 ± 0.134 | 6.730 ± 0.765 |
| Ice Δ[DOM] [a] | 1.944 ± 0.101 | 2.196 ± 0.045 | 2.609 ± 0.066 | 3.073 ± 0.027 | 3.261 ± 0.015 | 3.353 ± 0.045 | 1.985 ± 0.030 | 4.354 ± 0.245 | 5.149 ± 0.039 | 7.947 ± 0.467 | 8.265 ± 0.045 | 25.255 ± 0.003 |

[a]mg C/L: $[DOM]_I$ - $[DOM]_f$, where $[DOM]_f$ is final concentration of [DOM] in solution after 6 h reaction.

KOPRI 극지연구소

# FIGURES

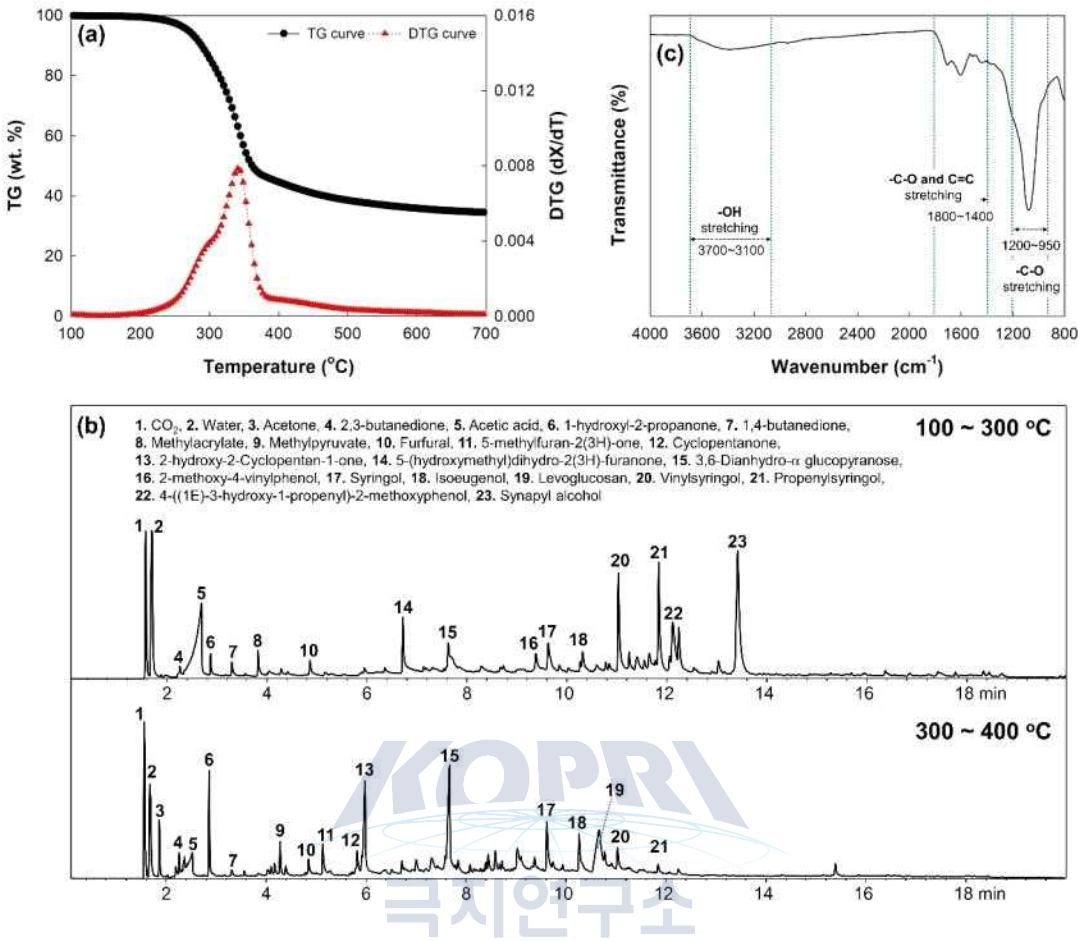



Fig. 1. Characterization of RH and RH-BC: (a) TG and DTG curves of RH, (b) Pyrograms obtained from multi-shot GC/MS analysis of RH, and (c) FTIR spectrum of RH-BC.

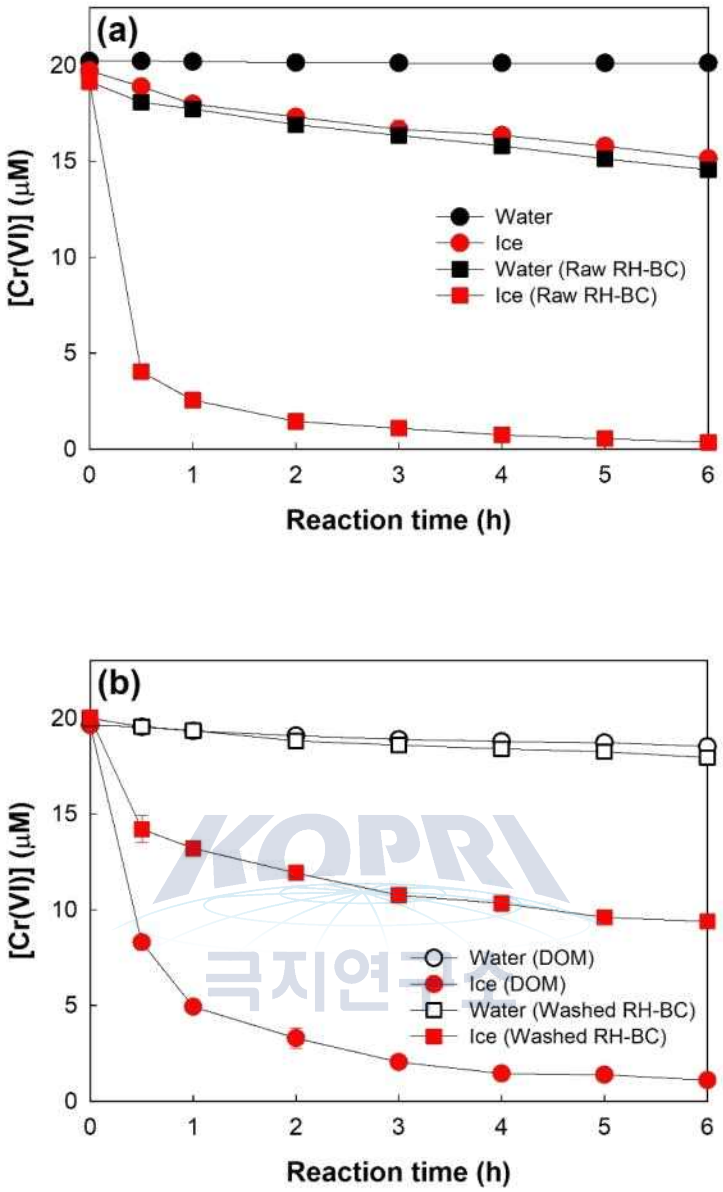



Fig. 2. Time profiles of Cr(VI) concentration with (a) raw RH-BC and (b) DOM and washed RH-BC in water and ice. Experimental conditions were as follow: (a) $[Cr(VI)]_i$ = 20 mM, [raw RH-BC] = 1 g/L, and $[pH]_i$ = 3.0; (b-1) experiment on Cr(VI) reduction by DOM: $[Cr(VI)]_i$ = 20 mM, [DOM]i= 6.553 mg C/L, and $[pH]_i$ = 3.0; (b-2) experiment on Cr(VI) reduction by washed RH-BC: $[Cr(VI)]_i$ = 20 mM, [washed RH-BC] = 1 g/L, and $[pH]_i$ = 3.0.

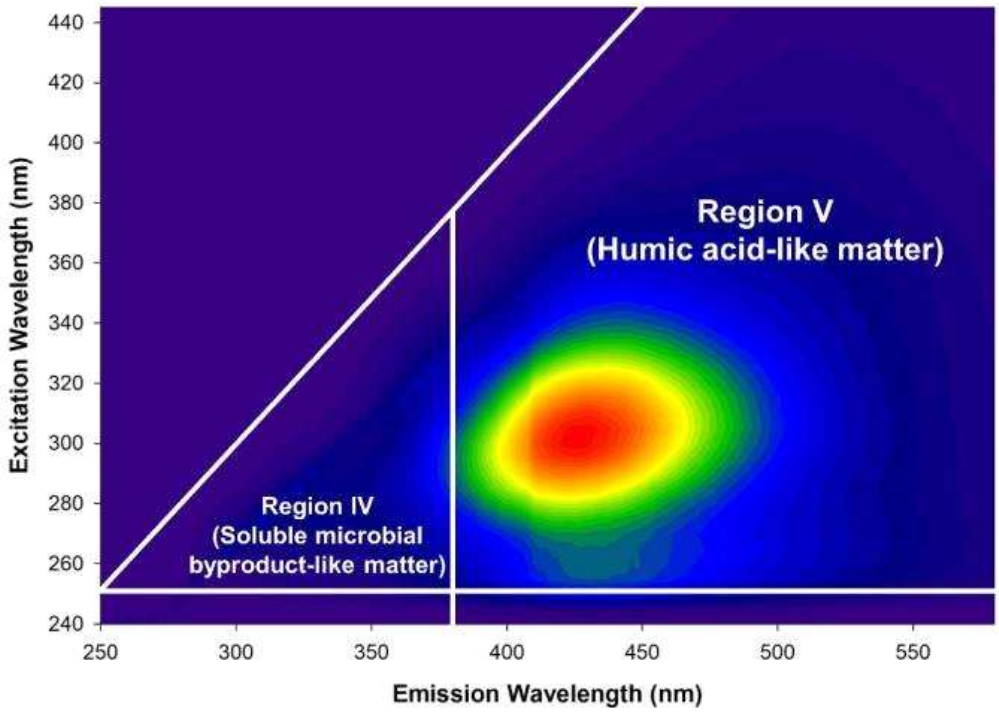



Fig. 3. Excitation-emission matrix (EEM) fluorescence spectroscopy of DOM.

KOPRI
극지연구소

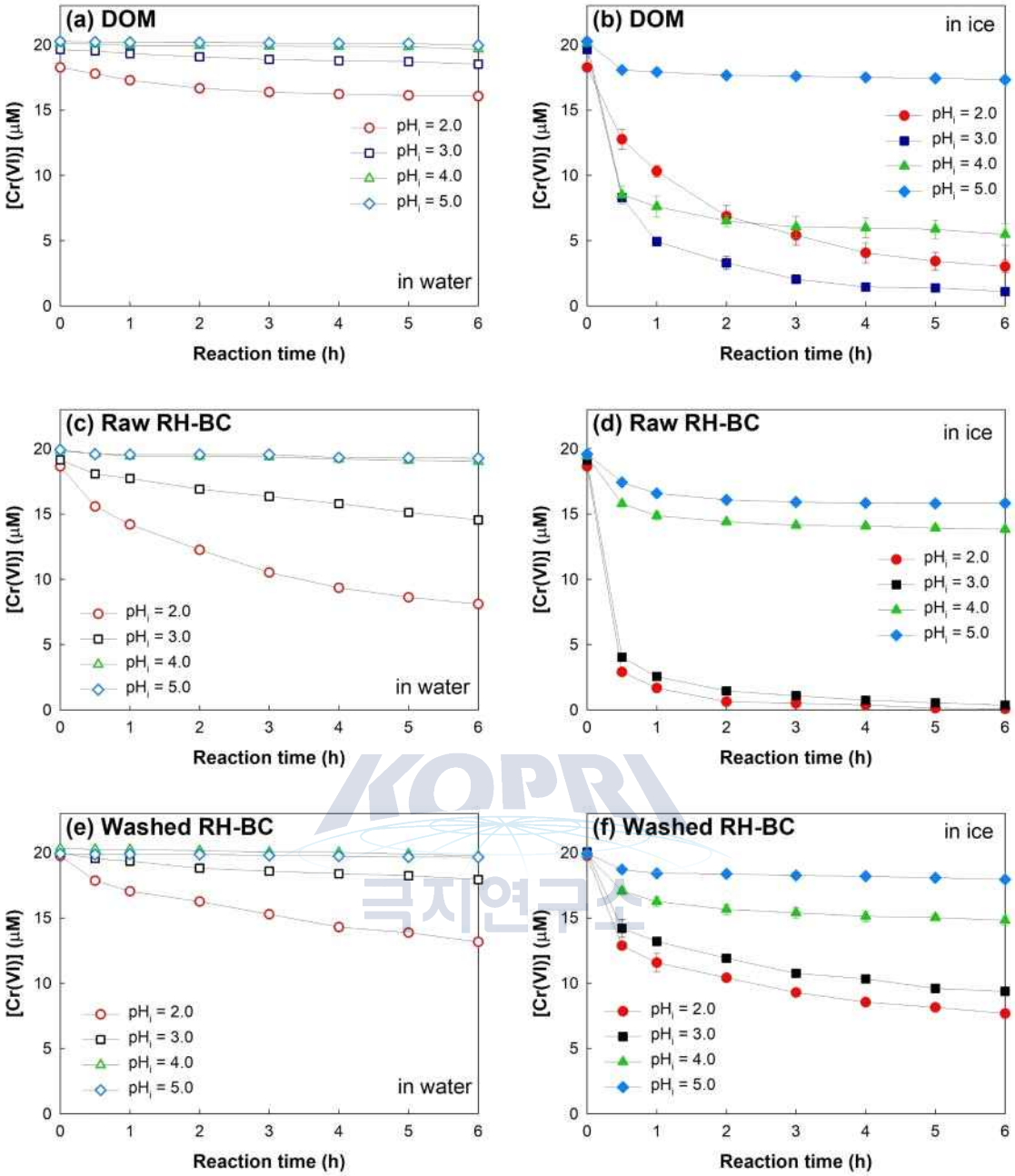



Fig. 4. Effect of pHion the redox conversion of Cr(VI) by DOM (for a and b), raw RH-BC (for c and d) and washed RH-BC (for e and f) in water and ice. Experimental condition were as follow: $[Cr(VI)]_i$ = 20 mM; (a and b), $[DOM]_i$ = 6.553 mg C/L and $[pH]_i$ = 2.0 ~ 5.0; (c and d) [raw RH-BC] = 1 g/L, and $[pH]_i$ = 2.0 ~ 5.0; (e and f) [washed RH-BC] = 1 g/L, and $[pH]_i$ = 2.0 ~ 5.0.

KOPRI 극지연구소

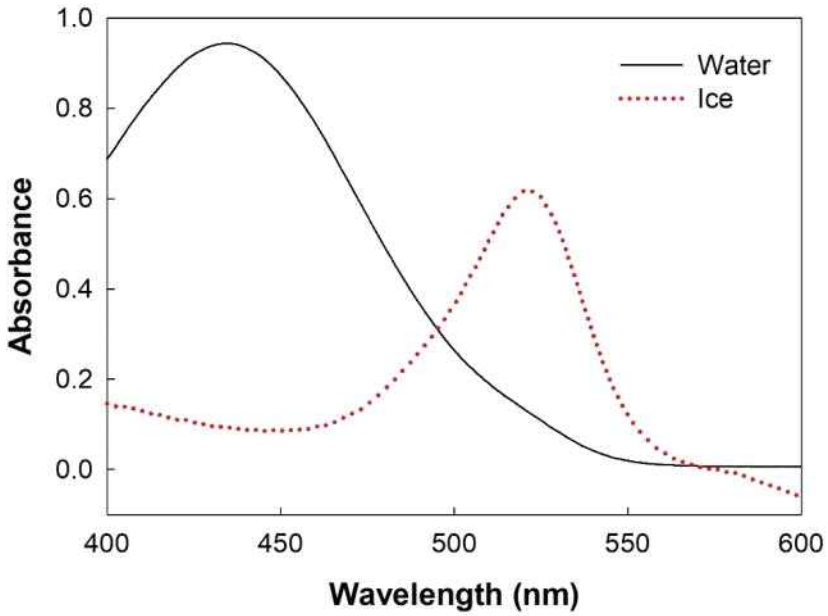



Fig. 5. UV-vis absorption spectra of CR before and after freezing. Experimental conditions were as follow: $[Cr(VI)]_i$ = 20 mM, [DOM]i = 6.553 mg C/L, and $[pH]_i$ = 3.0.

KOPRI
극지연구소

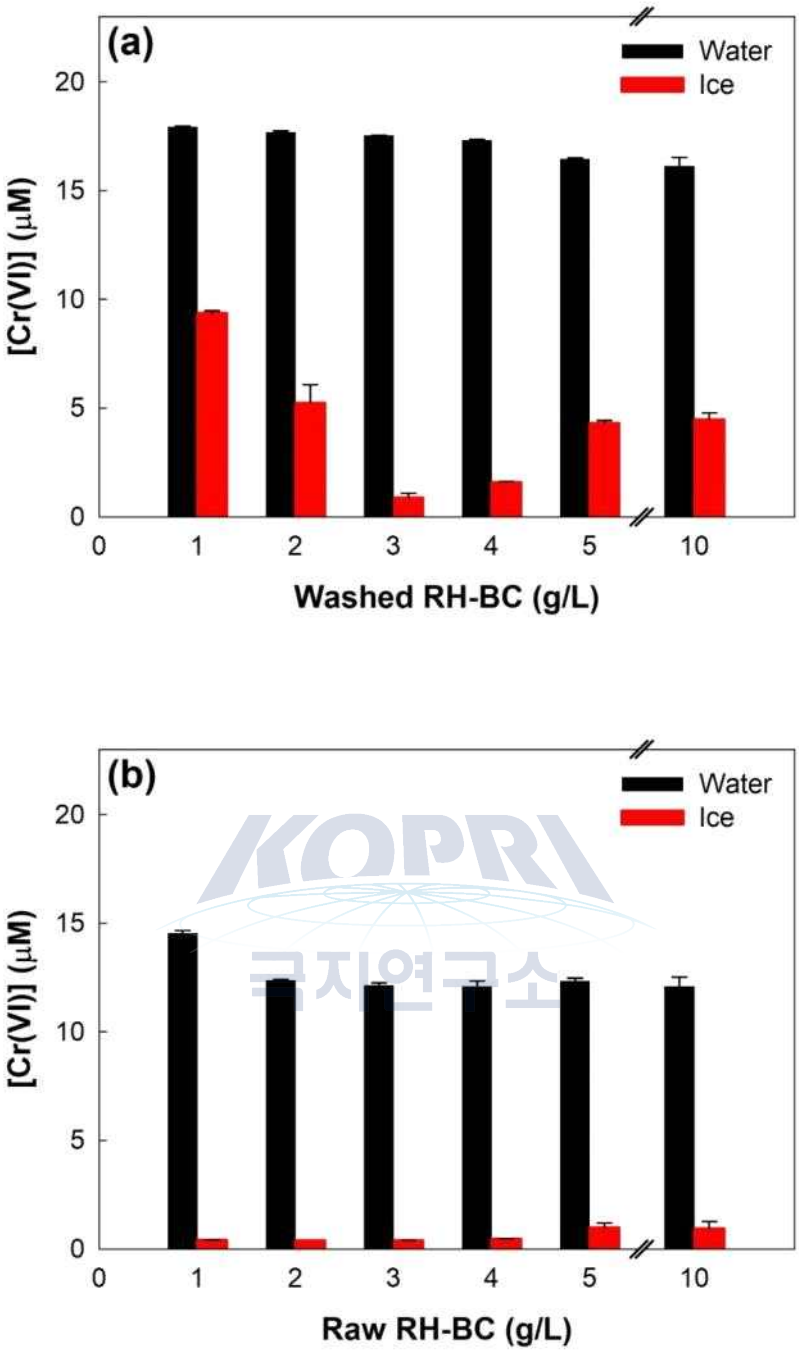
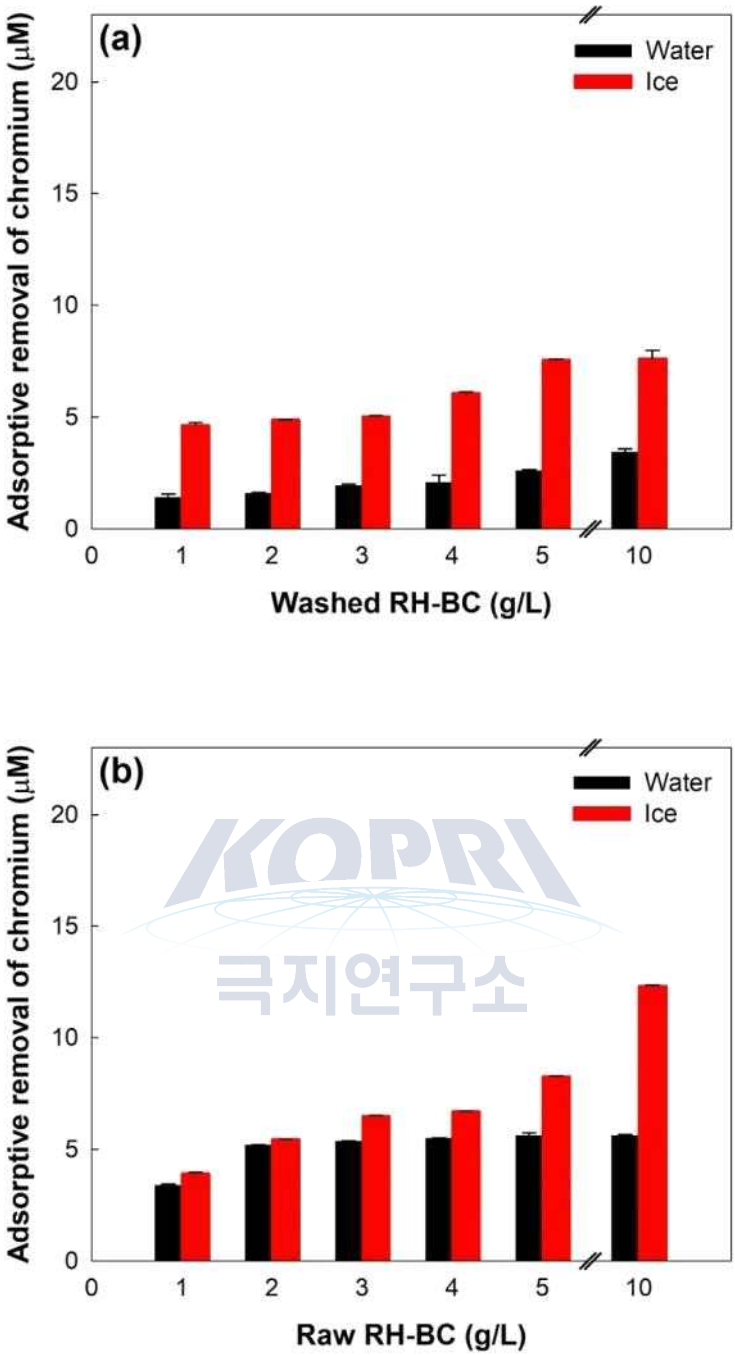



Fig. 6. Effect of RH-BC dosage on Cr(VI) reduction by (a) washed RH-BC and (b) raw RH-BC in water and ice. Experimental condition were as follow: reaction time = 6 h, $[Cr(VI)]_i$ = 20 mM, [RH-BC] = 1 ~ 10 g/L, and $[pH]_i$ = 3.0.




KOPRI
극지연구소

Fig. 7. Effect of RH-BC dosage on adsorptive removal of chromium (mM) by (a) washed RH-BC and (b) raw RH-BC in water and ice. Experimental condition were as follow: reaction time = 6 h, $[Cr(VI)]_i$ = 20 mM, [RH-BC] = 1 ~ 10 g/L, and $[pH]_i$ = 3.0.

# 제 4 절. Entangled Iodine and Hydrogen Peroxide Formation in Ice④

Yong Su Baek[1], Kitae Kim[2,3], Alfonso Saiz-Lopez[4], Dae Wi Min[2], Bomi Kim[2,3], Wonyong Choi[5] and Cheol Ho Choi[1]

[1]Department of Chemistry and Green-Nano Materials Research Center, College of Natural Sciences, Kyungpook National University

[2]Korea Polar Research Institute (KOPRI)

[3]Department of Polar Sciences, University of Science and Technology (UST)

[4]Department of Atmospheric Chemistry and Climate, Institute of Physical Chemistry Rocasolano, CSIC

[5]Division of Environmental Science and Engineering, Pohang University of Science and Technology (POSTECH)

## Abstract

Ice-core records show that anthropogenic pollution has increased the global atmospheric concentrations of hydrogen peroxide and iodine since the mid-20th century. Here, for the first time, we demonstrate a highly efficient mechanism that synergistically produces them in icy water conditions. This reaction is aided by a key intermediate $IO_2H$, formed by an $I^-$ ion with a dissolved $O_2$ in acidic icy water, which produces both I as well as $O_2H$ radicals. I recombines with $I^-$ to produce $I_2^-$ at a diffusion-limited rate, followed by formation of $I_3^-$ through disproportionation, while $O_2H$ yields $H_2O_2$ with $I^-$ and proton dissolved in icy water.

It is known that the Arctic surface serves as a source of atmospheric trace gases and particles and provides an environment for multiphase reactions.[1] However, global warming is changing the Arctic surface much more quickly than any other surface on Earth through the rapid shrinkage of sea ice.[2] Consequently, there is an urgent need to predict its future climate impacts. The photochemical snowpack production of $Cl_2$, BrCl and $I_2$ shows the Arctic surface contribution to the molecular halogens of the near-surface Arctic troposphere,[3,4] which is also closely related to the springtime 'bromine explosion'.[5] On the

④ 이 연구는 본 과제(KOPRI, PE19200)의 지원을 받았다. Alfonso Saiz-Lopez는 유럽 연합의 Horizon 2020 연구 및 혁신 프로그램(프로젝트 ERC-2016- COG 726349 CLIMAHAL)에 따라 유럽 연구위원회 집행 기관의 재정 지원을 받았다. 연구 결과는 *Phys. Chem. Chem. Phys.*, 2020, 22, 16532-16535에 출간되었다.

other hand, ice core records show remarkable increases in the concentrations of iodine and $H_2O_2$ from anthropogenic pollution over the last ~200 years.[6-8] These increases have been especially steep in the past few decades. Both near-surface measurements and the deep ice core analysis indicate active chemical processes in ice especially in recent years. However, the corresponding condensed phase halogen photochemical mechanisms and its relations with $H_2O_2$ is still not clearly understood.

Here, we perform state-of-the-art theoretical method to reveal a novel and entangled condensed-phase mechanism, where two completely different $H_2O_2$ and iodine species are generated simultaneously in acidic icy water. This is the first mechanism proposed for the direct formation of $H_2O_2$ in ice cores or icy conditions in polar regions. Despite the low temperature environment, this new mechanism demonstrates an active and rich ice chemistry that has significant implications for the ice-to-atmosphere reactive trace gas emissions and their associated effects on the oxidative capacity of the polar atmosphere, and for the interpretation of the variability of iodine and $H_2O_2$ in ice core records. The rapid change of the Arctic surface due to global warming will dramatically impact this condensed phase mechanism, subsequently affecting polar atmospheric chemistry.

Present high-level quantum mechanical calculations were performed using the GAMESS program.[9] The Stevens-Krauss (SBKJC) VDZ effective core potential basis set was adopted for iodine.[10] The standard cc-pVTZ basis was adopted for O and H atoms. This mixed basis set was denoted MIXED and used for all calculations. The B3LYP functionals were utilized for all density functional theory (DFT) and time-dependent DFT (TD-DFT)[11] calculations. Due to the significantly multi-referenced nature of the $I^-\cdot O_2$ complex, the complete active space self-consistent field method (CASSCF)[12] was adopted to optimize its geometry. Single-point energy calculations were then performed according to the second-order multi-reference perturbation theory (MCQDPT2).[13] The same single-point calculations were performed at these geometries using DFT theory for comparison. Both DFT and CASSCF were utilized for the $IO_2H$ structures. The excited states were calculated using the TD-DFT and MCQDPT2 methods. The geometries of $IO_2H$ at the $S_2$ and S3 minima and the conical intersections (CI) of $S_3/S_2$ and $S_4/S_3$ were optimized using TD-DFT. The minimum energy paths (MEPs) between the important points were obtained by the nudged elastic band (NEB) method.[14]

High-level quantum mechanical calculations indicated that the binding strength of the $I^-\cdot O_2$ complex, which was suggested as the initial primary intermediate in the formation of triiodide ($I_3^-$),[15] was extremely weak (Fig. 1a,b and Table SI 1a, ESI† ), if they form a complex. Furthermore, the experimentally observed absorption band[16] from 280 to 330 nm, did not correspond to our theoretical excitation energies (Table SI 2, ESI† ). An alternative $I_3^-$ formation mechanism was thus necessary to explain the overall reaction[17] in equation

(1).

$$O_2\ (aq) + 4H^+ + 6I^- \rightarrow 2H_2O + 2I_3^- \quad (1)$$

The oxidative formation of $I_3^-$ is extremely slow in aqueous solutions, but is significantly faster in frozen water. $I_3^-$ generation also increases significantly under solar irradiation ($\lambda > 300$ nm) and at low pH. This peculiarity has been attributed to the concentration of iodide and dissolved $O_2$ upon freezing, as they are mostly trapped within the ice crystal grain boundaries.[15]

We concluded that the protonated $IO_2H$ species formed instead of $I^-\cdot O_2$ (Fig. 1c,d). The excitation of $IO_2H$ to the $S_4$ (308 nm) and $S_3$ (328 nm) states in Table SI 3 (ESI† ) correlated well with the experimentally observed absorption band from 280 to 330 nm. The formation of this new species was highly favourable, since the protonation of $I^-\cdot O_2$ by hydronium was highly exothermic. The enthalpies of reaction for this protonation were −170.7 and −127.7 kcal/mol in the singlet and triplet states, respectively (Table SI 1b, ESI † ). On the other hand, the protonation of $I^-\cdot O_2$ by water was endothermic (Table SI 1c, ESI† ). These results could naturally explain the strong dependence of $[I_3^-]$ on pH.[15] No charge transfer was indicated in the $I^-\cdot O_2$ complex, but complete or overcharge transfer occurred in $IO_2H$. The charge transfer is critical in the subsequent formation of radicals. This demonstrated the dramatic impact of protonation, which made the dissociation of $IO_2H$ to I and hydroperoxyl ($O_2H$) radicals plausible. $O_2H$ is known to be the main source of hydrogen peroxide,[18] an important oxidant, in both the atmosphere and in biomedical environments.[19,20] With respect to radical dissociation, the binding energies of $IO_2H$ in the singlet and triplet states (Fig. 1c,d) were 18.4 and 5.7 kcal/mol, respectively. The weakly bound triplet state corresponded to an elongated I−O bond length of 2.83 Å, which indicated the I and $O_2H$ radicals nearly dissociated without irradiation. This provided a specific mechanism for the experimentally observed formation of $I_3^-$ in the absence of light.[1]

In contrast, the dissociation of $IO_2H$ in the singlet state required extra energy due to its stronger binding energy ~18.4 kcal/mol. As discussed above, its singlet $S_3$ and $S_4$ states corresponded well to the experimentally measured absorption from 280 to 330 nm (Table SI 3, ESI† ). According to the oscillator strengths, initial absorption would excite $IO_2H$ from its ground state ($S_0$) to the $S_4$ and/or $S_3$ states. To understand the singlet photochemical processes after absorption, the important points on the excited potential energy surfaces were located using TD-DFT calculations. This yielded the $S_{2min}$, $S_{3min}$, $CI_{S4/S3}$ and $CI_{S3/S2}$ structures in Fig. 1e - h. $S_{2min}$ and $S_{3min}$ represented the minima of the $S_2$ and $S_3$ excited states, respectively. $CI_{S4/S3}$ and $CI_{S3/S2}$ were the conical intersections (CIs) between the $S_4/S_3$ and $S_3/S_2$ states, respectively. A CI can be a good pathway for the nonadiabatic transition between electronic states.[21] The following monatomic energy decrease process

from the initial Franck-Condon (FC) region was observed without any intervening reaction barrier: $FC_{S4} \rightarrow CI_{S4/S3} \rightarrow S_{3min} \rightarrow CI_{S3/S2} \rightarrow S_{2min}$. This provided an efficient photochemical pathway for $IO_2H$ dissociation. Complete charge transfer of $I^-$ occurred in the process, resulting in a nearly broken 2.98 Å I−O bond at $S_{2min}$. The fate of the transition from the $S_3$ excited state was similar to that of $S_4$, and the transition from the $S_2$ state to $S_{2min}$ was direct. Regardless of the excited state, the photo-excitation of singlet $IO_2H$ consistently and efficiently produced an iodine radical. This explained the strong solar irradiation effect ($\lambda >$ 300 nm) on iodine radical production in ice observed in the laboratory and in the field.

The striking and unexpected implication of these results was the formation of $O_2H$ radical via the dissociation of $IO_2H$ in both dark and illuminated conditions. With an additional iodide ion and a proton, the hydroperoxyl radical can undergo a series of reactions to produce hydrogen peroxide.[17]

$$O_2H + I^- \rightarrow IO_2H^- + H^+ \rightarrow I\cdots O_2H_2 \rightarrow I + H_2O_2 \quad (2)$$

According to our quantum mechanical calculations, the formation of $IO_2H^-$ and $I\cdots O_2H_2$ was highly exothermic (Fig. SI 1a,b, ESI† ). The enthalpies of $IO_2H^-$ and $I\cdots O_2H_2$ formation were −18.1 and −141.0 kcal/mol, respectively (Table SI 1f,g, ESI† ). $I\cdots O_2H_2$ readily dissociated into an I radical and H2O2 (Table SI 1h, ESI† ). The direct formation of hydrogen peroxide in ice cores or icy conditions in polar regions has never before been suggested. This new $H_2O_2$ formation process was much more exothermic than that of $I_3^-$ (Fig. SI 2, ESI† ). The conversion of $I_3^-$ to $I_2$ in aqueous conditions has an equilibrium constant of ~700 ($I_2 + I^- \rightleftharpoons I_3^-$).[22] The final $[H_2O_2]/[I_3^-]$ ratio was thus expected to be quite large. A schematic representation of the overall reaction is shown in Fig. 2. The initial weak $I^-\cdot O_2$ complex forms $IO_2H$ by protonation in its triplet state, which undergoes near dissociation in the triplet state or forms stable $IO_2H$ in the singlet state. We propose that the $IO_2H$ in the triplet state results in the production of I and hydroperoxyl ($O_2H$) radicals in darkness, while $IO_2H$ in the singlet produces them when it is irradiated with light. The I radicals generated in our mechanism can also be utilized for the formation of $I_2-$. On the other hand, $O_2H$ radicals can easily react with excess $I^-$ and protons to form $H_2O_2$.

The proposed mechanism in Fig. 2 differs markedly from the $I^-\cdot O_2$ complex mechanism.[23] Although the mechanism of Gardner et al. explains the role of dissolved $O_2$ in $I_3^-$ formation, it fails to address the strong influence of pH and photochemical effects during $I_3^-$ production.

We then examined iodine concentrations in an ice core from the east coast of Greenland (71º 30' N, 26º 72' W)[8] (Fig. 3a) and hydrogen peroxide concentrations in ice cores from central Greenland (72º 34' N, 37º 38' W) and south Greenland (65º 11' N, 43º 49' W)[6] (Fig. 3b) to identify correlations between the two species. The I and $H_2O_2$ concentrations in the

ice cores remained nearly flat from 1750 to 1940, and a local minimum was observed around 1960. Iodine concentrations have risen three-fold since then, reaching an average value of 0.38 ng $g^{-1}$ in the years from 2001 to 2011. Although no data for $H_2O_2$ from the past decade was available, $H_2O_2$ concentrations increased markedly through the 1970s and 1980s until 1986 in the ice cores from central and south Greenland. There were positive correlations between the concentrations of iodine and $H_2O_2$ in both the central Greenland ice core ($\rho$ = 0.164, s = 0.028) and the south Greenland ice core ($\rho$ = 0.218, s = 0.003) (Table SI 4, ESI† ).

Since the concentration data of iodine and $H_2O_2$ from the same ice core can not be obtained, the corresponding data of ice cores from the geographically similar area were utilized instead. Nonetheless, the correlations between concentrations of iodine and $H_2O_2$ were not negligible when compared to the correlation between the $H_2O_2$ concentrations in the Greenland ice cores ($\rho$ = 0.371, s = 0.000). The statistical analysis thus indicated a correlation between the iodine and $H_2O_2$ concentrations with 95 - 99% confidence levels. The statistical analysis of the ice cores was consistent with our theoretical models, which suggested an entangled interaction between iodine and $H_2O_2$ in ice. Future increases in iodine concentrations are likely (Cuevas et al., 2018) and may lead to an increase in $H_2O_2$ concentrations in polar regions. The concentrations of these two species in the ice cores were also compared to tropospheric ozone concentrations from 1950 to 1986 (Fig. 3c). The iodine and $H_2O_2$ concentrations also had nonnegligible correlations with the global increase in ozone concentrations (Table SI 4, ESI† )

Our study has produced a new and detailed condensed-phase chemical mechanism that shows a strong interaction between $H_2O_2$ and iodine in ice. The key $IO_2H$ intermediate forms through protonation, which highlights the importance of pH. $IO_2H$ subsequently undergoes a series of photochemical reactions that produce both $H_2O_2$ and iodine. Iodine has been shown to dramatically reduce polar tropospheric ozone depletion during the spring. Our results also suggest an accumulation of $H_2O_2$ at the same time, which has not been identified in polar atmospheric chemistry simulations. Nonetheless, both $H_2O_2$ and iodine significantly impact the Earth's oxidative capacity, particularly in polar regions. Their condensed-phase chemistry thus requires further investigation, especially since the Arctic surface is undergoing rapid transformation.

KOPRI 극지연구소

## NOTES AND REFERENCES


1. K. A. Pratt, *Trends Chem.,* **2019**, *1*, 545 - 548.
2. Uma S. Bhatt, Donald A. Walker, John E. Walsh, Eddy C. Carmack, Karen E. Frey, Walter N. Meier, Sue E. Moore, Frans-Jan W. Parmentier, Eric Post, Vladimir E. Romanovsky, William R. Simpson, *Annu. Rev. Env. Resour.,* **2014**, *39*, 57 - 89.
3. A. R. W. Raso, K. D. Custard, N. W. May, D. Tanner, M. K. Newburn, L. Walker, R. J. Moore, L. G. Huey, L. Alexander, P. B. Shepson and K. A. Pratt, *Proc. Natl. Acad. Sci. U.S.A.,* **2017**, *114*, 10053 - 10058.
4. K. D. Custard, A. Raso, P. B. Shepson and R. M. Staebler, Production and Release of Molecular Bromine and Chlorine from the Arctic Coastal Snowpack, *ACS Earth and Space Chem., 1*, 142 - 151, **2017**.
5. L. A. Barrie, J. W. Bottenheim, R. C. Schnell, P. J. Crutzen and R. A. Rasmussen, *Nature,* **1988**, *334*, 138 - 141.
6. A. Sigg and A. Neftel, *Nature,* **1991**, *351*, 557 - 559.
7. J.-F. Lamarque, J. R. McConnell, D. T. Shindell, J. J. Orlando and G. S. Tyndall, *Geophys. Res. Lett.,* **2011**, *38*, n/a - n/a.
8. C. A. Cuevas, N. Maffezzoli, J. P. Corella, A. Spolaor, P. Vallelonga, H. A. Kjær, M. Simonsen, M. Winstrup, B. Vinther, C. Horvat, R. P. Fernandez, D. Kinnison, J.-F. Lamarque, C. Barbante and A. Saiz-Lopez, *Nat. Commun.,* **2018**, *9*, 1 - 6.
9. M. W. Schmidt, K. K. Baldridge, J. A. Boatz, S. T. Elbert, M. S. Gordon, J. H. Jensen, S. Koseki, N. Matsunaga, K. A. Nguyen, S. J. Su, T. L. Windus, M. Dupuis and J. A. Montgomery, *J. Comput. Chem.,* **1993**, *14*, 1347-1363.
10. T. R. Cundari and W. J. Stevens, *J. Chem. Phys.,* **1993**, *98*, 5555-5565.
11. E. Runge and E. K. U. Gross, *Phys. Rev. Lett.,* **1984**, *52*, 997 - 1000.
12. M. W. Schmidt and M. S. Gordon, *Annu. Rev. Phys. Chem.,* **1998**, *49*, 233-266.
13. H. Nakano, *J. Chem. Phys,* **1993**, *99*, 7983-7992.
14. J. Kästner, J. M. Carr, T. W. Keal, W. Thiel, A. Wander and P. Sherwood, *J. Phys. Chem. A,* **2009**, *113*, 11856-11865.
15. K. Kim, A. Yabushita, M. Okumura, A. Saiz-Lopez, C. A. Cuevas, C. S. Blaszczak-Boxe, D. W. Min, H.-I. Yoon and W. Choi, Environ. *Sci. Technol.,* **2016**, *50*, 1280 - 1287.
16. H. Levanon and G. Navon, *J. Phys. Chem.,* **1969**, *73*, 1861 - 1868.
17. D. O'Sullivan and J. R. Sodeau, *J. Phys. Chem. A,* **2010**, *114*, 12208 - 12215.
18. D. Vione, V. Maurino, C. Minero and E. Pelizzetti, *Ann. Chim.,* **2003**, *93*, 477 - 488.


KOPRI 극지연구소

19. D. E. Heard and M. J. Pilling, *Chem. Rev.,* **2003**, *103*, 5163 - 5198.

20. R. Luc and C. Vergely, *Int J Biomed Sci,* **2008**, *4*, 255 - 259.

21. F. Bernardi, M. Olivucci and M. A. Robb, *Chem. Soc. Rev.,* **1996**, *25*, 321 - 328.

22. J. Yeo and W. Choi, *Environ. Sci. Technol.,* **2009**, *43*, 3784 - 3788.

23. J. M. Gardner, M. Abrahamsson, B. H. Farnum and G. J. Meyer, J. Am. *Chem. Soc.,* **2009**, *131*, 16206 - 16214.

KOPRI
극지연구소

## FIGURES

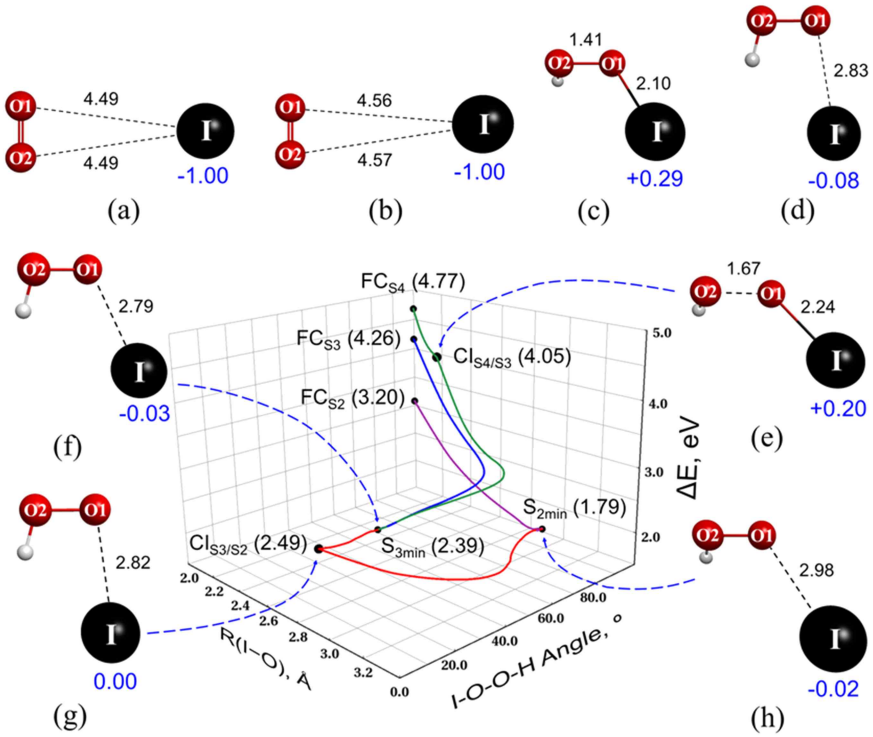



Fig. 1 The optimized structures of $I^{-}\cdot O_2$ complexes in the (a) singlet and (b) triplet states calculated using CASSCF(12,7)/MIXED-level theory. The bond lengths (black) are in Å, while the Mulliken atomic charges (blue) are in atomic units. The (a) is +24.1 kcal/mol higher than (b) according to MCQDPT2/MIXED theory. The binding energies between $O_2$ and $I^{-}$ are +0.3 kcal/mol (a) and −0.3 kcal/mol (b). The optimized structures of $IO_2H$ in the (c) singlet and (d) triplet states according to B3LYP/MIXED-level theory. According to this theory, (c) is −12.7 kcal/mol lower than (d). The corresponding binding energies between I and $O_2H$ radicals are −18.4 kcal/mol (c) and −5.7 kcal/mol (d). The important points in the singlet $S_4$, $S_3$ and $S_2$ states of (e) $CI_{S4/S3}$, (f) $S_{3min}$, (g) $CI_{S3/S2}$ and (h) $S_{2min}$ were located with TDDFT/B3LYP/MIXED. The energies relative to the ground state ($S_0$, eV) are shown in parentheses. The conical intersections are shown in (e) and (g), while (f) and (h) are minima. With respect to the I−O bond length and I−O−O−H torsion, the minimum energy paths (MEPs) from the Franck-Condon points $FC_{S4}$, $FC_{S3}$ and $FC_{S2}$ to other points were obtained by the nudged elastic band (NEB) method.

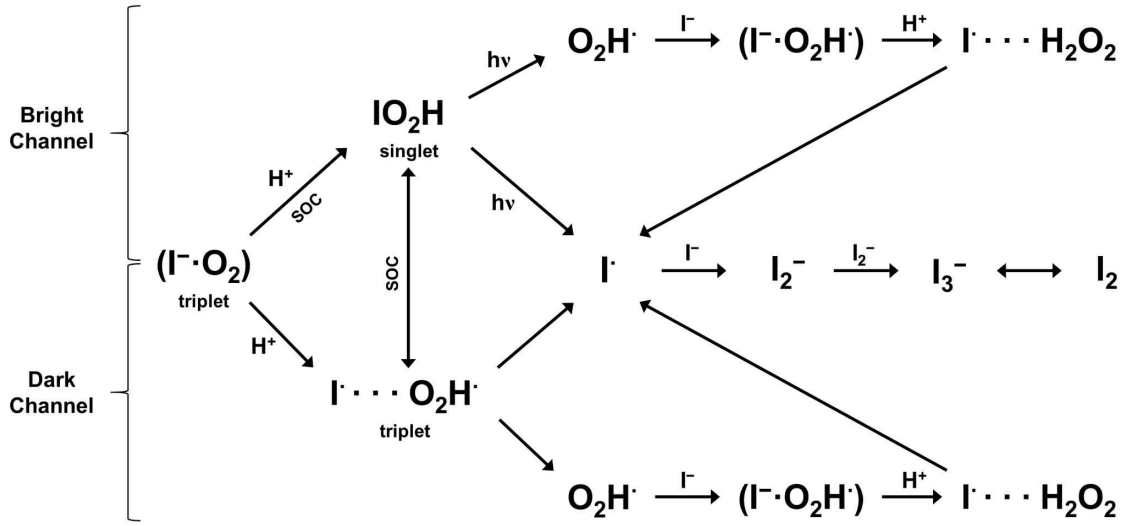
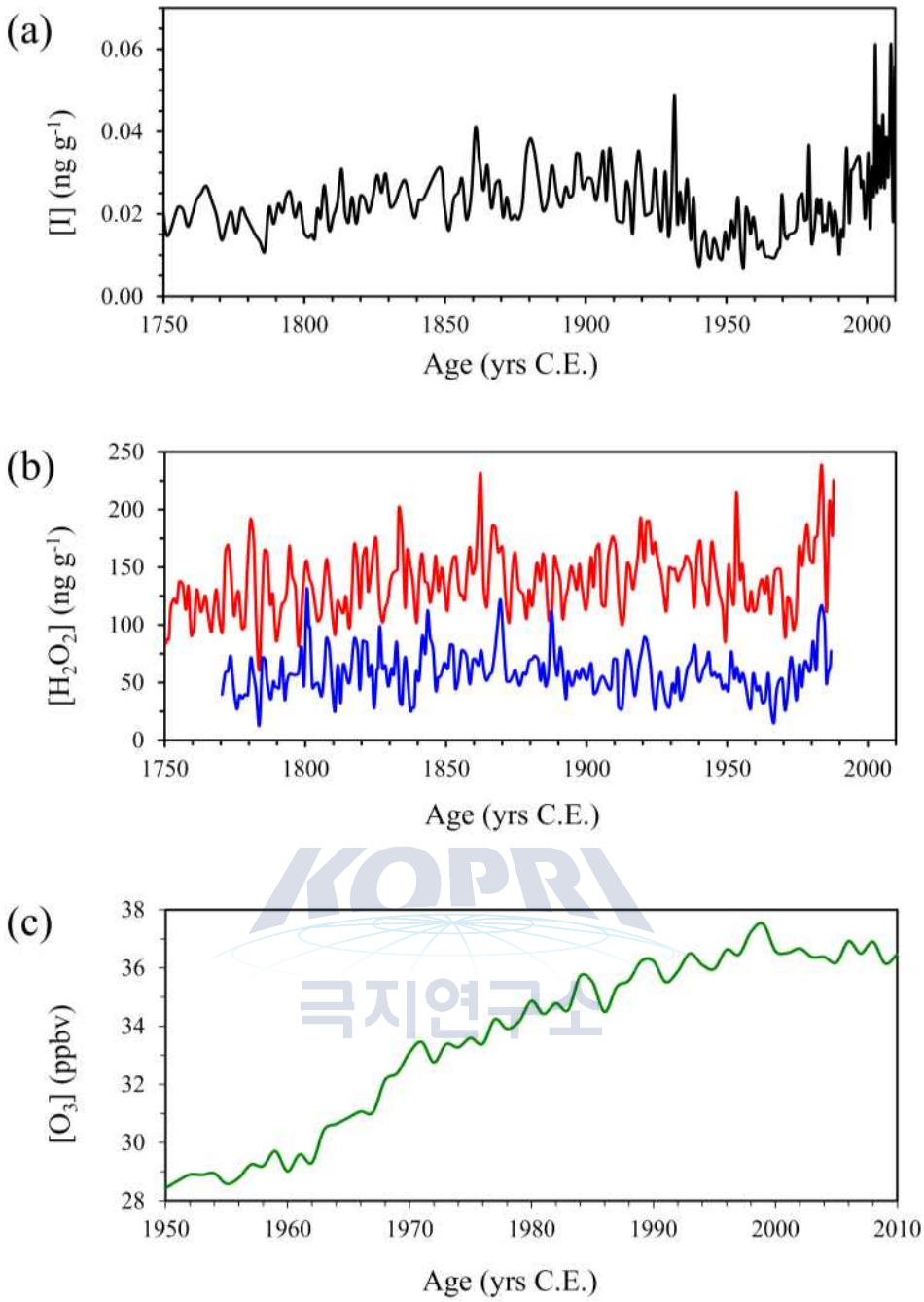



Fig. 2 A schematic diagram of the reactions in the overall iodine and $H_2O_2$ formation mechanisms. The process assumes sufficient concentrations of $I^-$ and $O_2$ in ice. $H^+$ and hn indicate acidic conditions and photo-irradiation, respectively. Intersystem crossing through spin-orbit coupling (SOC) results in the formation of $IO_2H$ in the singlet state. $IO_2H$ in the triplet state produces an $O_2H\cdot$ radical (Fig. 1d), while $O_2H\cdot$ radical generation by the more stable singlet $IO_2H$ requires photo-excitation. $O_2H\cdot$ radical forms the $I^-\cdot O_2H\bullet$ complex with iodide. Protonation in frozen water yields $I\cdots O_2H_2$, which eventually produces the $I\cdot$ radical and $H_2O_2$.

KOPRI 극지연구소




KOPRI
극지연구소

Fig. 3 (a) Annual mean iodine concentrations in an ice core from the east coast of Greenland (71º 30' N, 26º 72' W).[8] (b) $H_2O_2$ concentrations in ice cores from central Greenland (72º 34' N, 37º 38' W, red) and south Greenland (65º 11' N, 43º 49' W, blue),[6] (c) Ozone over the North Atlantic region (20º N - 70º N, 75º W - 0º).[8]

# 제 5 절. Chemical Weathering of Granite in Ice and Its Implication for Weathering in Polar Regions⑤

Hyun Young Chung,[1,2] Jaewoo Jung,[1] Du Hyeong Lee,[1] Sunghan Kim,[1] Min Kyung Lee,[1] Jae Il Lee,[1] Kyu-Cheul Yoo,[1] Yong Il Lee[1] and Kitae Kim[1,2]

[1]Korea Polar Research Institute

[2]University of Science and Technology

## Abstract

Recently, it has been reported that some chemical reactions are enhanced in below-freezing conditions. Despite the high denudation typical of polar regions, chemical weathering that occurs under ice has not been investigated. In this study, we investigated the dissolution of granite in ice. The mixture of granite and deionized water (DW) or solution adjusted to pH 2 or 3 was split into two groups: the test group was frozen at −20 °C, while the control was maintained at room temperature. After 29 days of batch experiments, the filtrate was analyzed to measure the concentrations of cations and silica. The filtered powder was analyzed to investigate the mineral compositions and crystallinities of the granite before and after the experiments. Despite the low temperature, a significant quantity of cations ($Na^+$, $K^+$, $Mg^{2+}$, $Ca^{2+}$) were dissolved out, even from the ice samples. During X-ray diffraction (XRD) analysis, the decreased crystallinities of granite in ice samples were identified regardless of the pH condition. To verify the observed freeze concentration effect, the concentration of granite in the ice grain boundaries was observed using optical microscopy with a cold chamber. The low concentration of silica in the ice samples could explain the silica anomaly in polar regions. This study also provides a new perspective for the dissolution mechanism in polar regions.

## 1. Introduction

Chemical weathering has been studied for its ability to sequester atmospheric carbon dioxide. Silicate weathering has a net effect of sequestration of atmospheric carbon dioxide relative to geologic time, whereas carbonate weathering has no net effect.[1] Chemical weathering occurs when minerals or rocks react with acidic or oxidizing substances.[2] It is known that chemical weathering is mainly dependent on climate (e.g., temperature and precipitation), parent material, and biota.[3-5] Meanwhile, mechanical weathering means

⑤ 본 연구는 본 과제(PE20030)의 지원을 받았으며, *Minerals* 2020, 10, 185에 출간되었다.

fragmentation of minerals or rocks or loss of materials and occurs without a chemical reaction.[2] Mechanical weathering is affected by elevation, relief, and runoff from the watershed.[4]

Polar regions have low annual precipitation, extremely cold temperatures, and no higher-order plants.[6,7] Thus, the extent of chemical weathering in polar regions is generally thought to be negligible. Nevertheless, some studies have found that chemical weathering in polar regions is comparable to temperate regions.[8,9] These studies concluded that the unexpected high chemical denudation in polar regions is the result of accelerated mechanical weathering along continuously exposed outcropping at a high flow rate.[10] Some studies also reported a high flux of cations (e.g., $K^+$ and $Ca^{2+}$) and relatively low silica flux in polar regions.[8] In previous studies, many factors such as rapid runoff, salt weathering, and micro-organisms have been suggested to promote chemical weathering in polar regions.[10 - 12] Moreover, some studies emphasized the importance of moisture availability to chemical weathering in these regions.[13,14] However, chemical weathering of rocks and minerals in a frozen state has not been studied extensively.[7,9] In this study, we investigated the chemical weathering of granite in ice under water-available conditions.

It has been reported that some chemical reactions can be accelerated in ice.[15,16] For example, nitrite oxidizes to nitrate ~1000 times faster in ice than in aqueous solution. [17] It is also reported that the dissolution of iron oxide to form soluble iron is significantly accelerated in ice, whereas such a reaction is negligible in aqueous solution.[16,18] These previous studies suggested that the enhanced dissolution of bioavailable iron is the result of a proton assisted reaction at the ice grain boundaries and the freeze concentration effect. When a solution is solidified, the solutes are rejected from the bulk ice and concentrated in the interfacial water layer along the ice grain boundary.[17] In the Antarctic Peninsula, the dominant parent materials are volcanic and granitic.[19] In this study, the effect of freezing on the dissolution of granite was investigated to reveal the dissolution mechanism of silicate minerals in polar regions.

## 2. Materials and Methods

### 2.1. Materials

A bulk granite sample (1 kg) was purchased from Ward's Science (#470026, granite (gray)). This granite was mainly composed of $SiO_2$ and $Al_2O_3$ as oxides (Table 1), and quartz, plagioclase, and mica were the dominant mineral compositions. DW used in this experiment was prepared with the Barnstead water purification system and checked before use as to whether it had 18.2 MΩcm TC of resistivity. Ammonium molybdate tetrahydrate [$(NH_4)6M_{o7}O_{24}.4H_2O$, Aldrich], hydrochloric acid (HCl, Aldrich, Incheon, Korea), oxalic acid

($HO_2CCO_2H$, Aldrich, Incheon, Korea), 4-methylaminophenol sulfate ($C_7H_9NO \cdot 1/2H_2SO_4$, Aldrich), sodium sulfite ($Na_2SO_3$, Aldrich), sulfuric acid [$H_2SO_4$, Aldrich], and sodium metasilicate nonahydrate ($Na_2O_3Si \cdot 9H_2O$, Aldrich) were used to analyze the silica ($SiO_2$) concentration of the filtrate. Concentrated hydrochloric acid was used to make an acidic solution in batch experiments. The reagents used in this study were higher than ACS grade.

### 2.2. Pretreatment and Batch Experiments

A bulk rock sample was sliced into small chips with a diamond blade and washed with distilled water. The pieces were then air-dried and ground to a powder using a ring mill (Figure 1). Concentrated HCl was diluted to make the desired pH solution. A sterile petri dish with a 60 mm diameter was used as the reactor. After pouring 10 mL of HCl solution or DW into 0.1 g of granite powder, the petri dish was sealed with parafilm. Each sample was made in triplicates for reproducibility. Aqueous samples were kept at room temperature and in darkness. Ice samples were frozen at −20 °C in an air-controlled freezer for 29 days. Aqueous and ice samples for the first day of the experiment (reaction time = 0 days) were filtered immediately after the HCl solution was poured into the granite powder. The total time for this procedure was sub-thirty minutes. The ice samples were thawed with lukewarm water at 30 - 40 °C. Then, the aqueous and thawed ice samples were filtered using a 0.2 μm pore size filter. After filtering the time = 0 days samples, the measured pH values were 9.74 for DW, 3.94 for pH 3 solution, and 2.01 for pH 2 solution.

### 2.3. Chemical and Optical Analyses

The chemical composition of the sample material was analyzed using a micro X-ray fluorescence analyzer (μ-XRF, M4 Tornado, Bruker, Karlsruhe, Germany). The X-ray (Mo) source was operated at 50 kV and 600 μA and interacted with the sample for 1 s/scanning point. The distribution and amounts (wt.%) of K, Na, Ca, Mg, Al, Fe, Ti, Mn, and Si were measured at 20 points and, subsequently, averaged over these observation points. The error ranges for the m-XRF quantifications (wt.%) were approximately < 0.1% for K, Na, Ca, Mg, Al, Fe, Ti, and Mn, and 0.4% for Si. The pH meter (Thermo Scientific, Orion 3 star) was used to measure the pH of solutions. An ion chromatography system (Dionex ICS-1100, CERS 500 4 mm, CS12A) was used to analyze the cation concentration in the filtrate. The instrumental detection limits were: $Na^+$ 0.03 $mg \cdot L^{-1}$, $K^+$ 0.01 $mg \cdot L^{-1}$, $Mg^{2+}$ 0.05 $mg \cdot L^{-1}$, and $Ca^{2+}$ 0.12 $mg \cdot L^{-1}$. Methanesulfonic acid ($CH_3SO_3H$, Aldrich) was used in cation concentration analysis as an eluent. The eluent flow rate was 1.00 mL $min^{-1}$, and the suppressor was set to 59 mA. $SiO_2$ concentrations were analyzed colorimetrically with

a UV-Vis spectrophotometer (Shimadzu, UV-2600) at 810 nm.[20] When treating the cation concentration data, time = 0-day values were subtracted from each cation concentrations to set the start point as 0 mg $L^{-1}$. After filtering, the remaining solid material was air-dried. XRD analyses were performed using a Rigaku MiniFlex(II) automated diffractometer using Cu-Kα radiation. Random mount samples were prepared and measured at a scan speed of 1.5°/min and 0.02° step over the range of 2-theta angles (2° - 80°). Then Search-Match software was used to identify mineral assemblages.[21] Microscopic image was observed (Leika microsystem, Lens HC PLAN 10  20 BR, L 50/0.50) to investigate the ice grain boundary and freeze concentration effect. When observing the ice grain boundary optically, the solution was frozen on the linkam stage to  - 20 °C with the rate of  - 2 °C $min^{-1}$.

## 3. Results

### 3.1. Filtrate Analysis

The main oxide compositions of granite are silicon dioxide ($SiO_2$) and aluminum oxide ($Al_2O_3$); however, base cations (e.g., $K^+$, $Na^+$, $Ca^{2+}$, $Mg^{2+}$) also exist as a small fraction as oxides form (Table 1). After 29 days of the batch experiment, 0.27 mg $L^{-1}$ of Na+, 1.21 mg $L^{-1}$ of $K^+$, 0.18 mg $L^{-1}$ of $Mg^{2+}$, and 2.65 mg $L^{-1}$ of $Ca^{2+}$ were dissolved with DW in the aqueous phase (Figure 2). In the ice samples with DW, the dissolution of cations from granite powder was negligible. After 29 days of being saturated in the pH 3 solution, $Na^+$, $K^+$, $Mg^{2+}$, and $Ca^{2+}$ concentrations of filtrate increased as follows: 0.68 mg $L^{-1}$ of $Na^+$, 3.44 mg $L^{-1}$ of $K^+$, 1.17 mg·$L^{-1}$ of $Mg^{2+}$, and 5.59 mg $L^{-1}$ of $Ca^{2+}$. The dissolved cation concentrations in the ice conditions were lower than those in aqueous solution; however, the cation concentrations in ice samples with pH 3 solution were 140%, 216%, 544%, and 172% higher than each cation concentration in the aqueous solution with DW. The dissolution of granite powder for the frozen samples was notable with the pH 3 solution, in contrast to the negligible case with DW in ice. When a pH 2 solution was added to granite powder, the dissolution continued after seven days as opposed to after seven days with the pH 3 solution (Figure 3). After seven days, cation concentrations with pH 2 solution and granite powder in ice sample filtrate exceeded that of filtrate with DW in aqueous solution. After 29 days, 1.19 mg $L^{-1}$ of Na+, 9.63 mg $L^{-1}$ of K+, 7.50 mg $L^{-1}$ of $Mg^{2+}$, and 13.45 mg $L^{-1}$ of $Ca^{2+}$ were dissolved in aqueous solution. Filtrate of the ice samples yielded 0.46 mg $L^{-1}$ of $Na^+$, 4.22 mg $L^{-1}$ of K+, 3.34 mg $L^{-1}$ of $Mg^{2+}$, and 9.43 mg $L^{-1}$ of $Ca^{2+}$ (Table 2).

### 3.2. XRD Analysis and Amorphous Silica Formation

The results of the XRD analysis are represented in Figure 4. No other peaks from secondary phase minerals were observed in both aqueous and ice samples. Aqueous

experiment samples showed similar trends and intensities of XRD patterns as the granite powder before the experiment. However, general peak intensities were reduced in ice experiment samples compared to aqueous samples and initial granite for mica, plagioclase, and quartz. In the analysis of $SiO_2$ concentrations in the filtrate, the concentration in the aqueous solution experiment increased with time (Figure 5). However, $SiO_2$ concentrations in the ice experiment decreased from the initial concentration to zero, while other cation concentrations increased. In this case, the initial concentration was not subtracted from each filtrate concentration for $SiO_2$ concentrations.

### 3.3. Optical Images of Ice Grain Boundaries

When the HCl solution of pH 3 was frozen, an ice grain boundary formed. We were able to identify it using a microscope (Figure 6a). It is known that solutes are rejected from bulk ice and concentrated in the water layer along the ice grain boundary.[17] The interfacial water layer at the ice grain boundaries in our samples was found to contain high concentrations of solute. It has been reported that when an acid solution becomes frozen, the pH at the ice grain boundary decreases several orders than the solution pH because of the concentrated hydrogen ions.[22] After the mixture of pH 3 solution and granite powder was frozen, the granite powder became concentrated at the ice grain boundaries (Figure 6b). Granite powder was rejected during bulk ice formation, and the powder grains were trapped at the ice grain boundaries. Therefore, the dissolution of granite powder can occur at the ice grain boundaries as a result of concentrated hydrogen ions.

## 4. Discussion

### 4.1. The Mechanism behind the Dissolution of Granite in Ice

The cation concentrations in aqueous experiments were obviously higher than ice experiments, however, the dissolution of cations in ice was also considerable. The cation concentrations of filtrate with pH 2 solution were much higher than those of the pH 3 and DW experiments, both in aqueous and ice phases. Our results were consistent with previous research that reported high dissolution of silicate minerals at similarly low pH.[5] In previous studies, the chemical weathering in ice has not been considered. In studies of polar regions, the chemical weathering has been studied in summertime during an aqueous phase of meltwater.[7,9] However, the dissolution of granite also unexpectedly occurred to a certain degree in ice in this study.

It should be noted that the identification of the exact timing of reaction in frozen samples (during the freezing process, frozen state, or melting process) is still a controversial issue although the freezing and thawing time is significantly shorter than that

of the frozen state. The best way to know the timing of reaction is to analyze the ions during the frozen state. Unfortunately, the in-situ measurement is not technically available at the present time. In spite of the uncertainty, we thought that most of the dissolution process of granite in ice takes place during the frozen state and not the freezing or melting processes because of the comparably very short time to freeze and melt (about 30 min) samples. Furthermore, the amount of dissolved ions from granite during the thawing process could be very small based on the reaction rate in aqueous samples as shown in Figure 3. The duration of the frozen state until the first sample time (7 days, 168 h) is 336 times longer than melting time (about 30 min) and the amount of dissolved ions might be negligible. Furthermore, the enhanced dissolution of ions from granite between 7 and 14 days (Figure 3) also confirms that the significant dissolution of ions from granite takes place during the frozen state and not during thawing process. Nevertheless, the similar amount of dissolved ions from granite during 7 - 14 days at pH 3 is not sufficient to dispel the quick dissolution during the melting process. In order to generalize the comparable dissolution of granite in the ice phase, more experiments including a short time scale and various pH ranges should be carried out in the near future.

It was optically identified that the granite powder was trapped in the ice grain boundary. In the process of ice formation, the solutes, protons, and small particles are rejected from the bulk ice and concentrate in the ice grain boundary region, which is called the “freeze concentration effect”. It is also known that the pH of ice grain boundaries is lower by several orders than that of the solution before freezing.[17] In the surface-reaction model suggested by Furrer and Stumm, the dissolution rate is proportional to the concentration of surface species (protonates sites in this case) and the adsorption of $H^+$ to the surface, which occurred in interfacial regions between hydrous oxides and aqueous solution.[5,23] The proton-promoted rate of dissolution can be described as:

$$R_H = k_H[\equiv SOH_2^+]^n \quad (1)$$

where $k_H$ is the rate constant, $[\equiv SOH_2^+]$ is the concentration of hydrogen ions adsorbed to the surface, and n is the reaction order. n represents the number of protonation steps required for cation release from the surface and is equal to the oxidation number of the central cation in the oxide (e.g., n = 4 for $SiO_2$). Moreover, the dissolution rate of silicate minerals increases exponentially with a higher concentration of hydrogen ions at a pH below the acid transition point.[5] The acid transition point of silicate minerals is typically at pH 4 - 5. This can be described as:

$$R_H = k_H[H^+]^n \quad (2)$$

where $k_H$ is a rate constant and n is an exponent that varies with mineral composition. In

the ice grain boundary region, a lower pH than that of the original solution (pH 2 and 3) increased the rate of granite dissolution exponentially under the acid transition point (this reaction was restricted to the ice grain boundaries). Furthermore, the adsorption of hydrogen ions to the surface of the granite powder increased according to the freeze concentration effect in the ice grain boundary region.

### 4.2. Silica Polymerization in Ice and Its Implication for Polar Regions

In previous studies about chemical weathering conducted in polar regions, the cation concentrations of the meltwater in polar regions have been comparable to temperate regions, but the silica concentrations have been relatively low.[24] These studies concluded that the reason for the high cation concentrations is the high runoff and rapid flow rate of the meltwater in summertime. During this time, high runoff and rapid flow rate exposes rock to weathering agents (water and $CO_2$) continuously.[8,10] Previous studies emphasized the rapid dissolution of carbonate minerals, rather than focusing on silicate minerals. Our study has, therefore, expanded previous research by showing an increase in silica concentration (accompanied by other dissolved cations) during aqueous conditions, and a decreased silica concentration under ice conditions, even at low pH, and without carbonate minerals present in the source rock (Figure 5).

Some studies have reported that polymerized silica could be formed in ice, then the silica concentration could be reduced when a solution is stored in a frozen state, and when the solution has low salinity.[25,26] In the colorimetric method for silica concentration, molybdate acts as the color reagent. Molybdate only forms complexes with reactive silica, which is mono-type.[20] Therefore, the polymerized silica formed in ice could not make a complex with molybdate in this study. This explains the reduced silica concentrations present after the ice experiment. During XRD analysis, the intensities of granite powder for quartz, plagioclase, and mica are decreased as a result of the dissolution in the ice experiment (Figure 4). One more possible interpretation for the XRD results is the reaggregated silica in ice, which is dissolved once. Amorphous forms of solid can cause decreased and broadened peaks in XRD analyses.[27,28] In the ice experiments, the dissolved silica from the dissolution of granite could be polymerized to an amorphous form and aggregated at the surface of the granite powder.

Quartz is the slowest material of the silicate minerals to be dissolved with acid. [29] As such, our aqueous experiment contained only a small fraction of cations, which were dissolved rapidly in the acid solutions (Figures 2 and 3) and there was no considerable difference between the quartz intensities of granite powder before and after aqueous experiments (Figure 4). However, the intensities of the peaks for quartz decreased in XRD analysis in ice samples. This suggests a polymerization of dissolved quartz into an

amorphous solid. These reactions in ice could also be possible in polar regions. Therefore, the results of previous studies that reported the unexpected high concentration of cations and relatively low silica concentration in polar regions could be explained by the reactions in the ice observed in this study. Moreover, it was reported that a significant amount of silica is supplied from the ice sheet to seawater in an amorphous form in Greenland.[30] Comparable chemical weathering and formation of amorphous silica in ice in this study could be the plausible explanation for the field data collected in Greenland. Furthermore, the amorphous silica which is formed in ice could be the unrecognized form of silica in polar regions.

## 5. Conclusion

In this study, we conducted granite dissolution experiments in ice and investigated the mechanism of the dissolution, which, to the best of our knowledge, has not been considered in previous studies. Although the dissolution of granite was negligible in ice with DW, it was significant in ice with pH 2 and 3 solutions. Optical images show that the dissolution in ice is due to the freeze concentration effect of hydrogen ions at the ice grain boundaries (Figure 7). During XRD analysis, the intensities of the mineral peaks (quartz, plagioclase, and mica) decreased in the ice samples whereas no intensity decrease was identified in the aqueous phase samples. The results of XRD and silica concentration analyses suggested the probability of existence of amorphous silica in polar regions, which could be formed from the chemical reactions occurring in the ice. Previous studies investigating weathering in polar regions were focused on the weathering in the aqueous phase or the mechanical weathering with ice. This study provides the new insight that chemical weathering could occur as a result of the chemical reactions related to the freeze concentration effect in ice grain boundaries.

KOPRI 극지연구소

## REFERENCES


1. Berner, R.A. Weathering, plants, and the long-term carbon cycle. *Geochim. et Cosmochim. Acta* **1992**, *56*, 3225 - 3231.
2. Schlesinger, W.H.; Bernhardt, E.S. *Biogeochemistry: An Analysis of Global Change*; Academic Press: New York, NY, USA, **2013**.
3. White, A.F.; Blum, A.E. Effects of climate on chemical_ weathering in watersheds. *Geochim. et Cosmochim. Acta* **1995**, *59*, 1729 - 1747.
4. Gaillardet, J.; Dupre, B.; Louvat, P.; Allègre, C. Global silicate weathering and CO2 consumption rates deduced from the chemistry of large rivers. *Chem. Geol.* **1999**, *159*, 3 - 30.
5. Drever, J.; Stillings, L. The role of organic acids in mineral weathering. *Colloids Surfaces A: Physicochem. Eng. Asp.* **1997**, *120*, 167 - 181.
6. Bockheim, J.G. Properties and Classification of Cold Desert Soils from Antarctica. *Soil Sci. Soc. Am. J.* **1997**, *61*, 224 - 231.
7. Gooseff, M.N.; McKnight, D.; Lyons, W.B.; Blum, A.E. Weathering reactions and hyporheic exchange controls on stream water chemistry in a glacial meltwater stream in the McMurdo Dry Valleys. *Water Resour. Res.* **2002**, *38*, doi:10.1029/2001WR000834.
8. Anderson, S.; Drever, J.I.; Humphrey, N.F. Chemical weathering in glacial environments. *Geology* **1997**, *25*, 399.
9. Nezat, C.A.; Lyons, W.B.; Welch, K. Chemical weathering in streams of a polar desert (Taylor Valley, Antarctica). *GSA Bull.* **2001**, *113*, 1401 - 1408.
10. Huh, Y. Chemical weathering and climate – a global experiment: A review. *Geosci. J.* **2003**, *7*, 277 - 288.
11. Bisson, K.; Welch, K.; Welch, S.; Sheets, J.M.; Lyons, W.B.; Levy, J.; Fountain, A.G. Patterns and Processes of Salt Efflorescences in the McMurdo region, Antarctica. *Arctic, Antarct. Alp. Res.* **2015**, *47*, 407 - 425.
12. Maurice, P.A.; McKnight, D.; Leff, L.; Fulghum, J.E.; Gooseff, M.N. Direct observations of aluminosilicate weathering in the hyporheic zone of an Antarctic Dry Valley stream. *Geochim. et Cosmochim. Acta* **2002**, *66*, 1335 - 1347.
13. Hall, K.; Thorn, C.E.; Matsuoka, N.; Prick, A. Weathering in cold regions: Some thoughts and perspectives. Prog. *Phys. Geogr. Earth Environ.* **2002**, *26*, 577 - 603.
14. Hall, K. Evidence for freeze - thaw events and their implications for rock weathering in northern Canada: II. The temperature at which water freezes in rock. *Earth Surf. Process. Landforms* **2007**, *32*, 249 - 259.


KOPRI 극지연구소

15. Kim, K.; Yoon, H.-I.; Choi, W. Enhanced Dissolution of Manganese Oxide in Ice Compared to Aqueous Phase under Illuminated and Dark Conditions. *Environ. Sci. Technol.* **2012**, *46*, 13160 - 13166.

16. Kim, K.; Choi, W.; Hoffmann, M.R.; Yoon, H.-I.; Park, B.-K. Photoreductive Dissolution of Iron Oxides Trapped in Ice and Its Environmental Implications. *Environ. Sci. Technol.* **2010**, *44*, 4142 - 4148.

17. Takenaka, N.; Ueda, A.; Daimon, T.; Bandow, H.; Dohmaru, T.; Maeda, Y. Acceleration Mechanism of Chemical Reaction by Freezing: The Reaction of Nitrous Acid with Dissolved Oxygen. *J. Phys. Chem.* **1996**, *100*, 13874 - 13884.

18. Kim, K.; Menacherry, S.P.M.; Kim, J.; Chung, H.Y.; Jeong, D.; Saiz-Lopez, A.; Choi, W. Simultaneous and Synergic Production of Bioavailable Iron and Reactive Iodine Species in Ice. *Environ. Sci. Technol.* **2019**, *53*, 7355 - 7362.

19. Bockheim, J.G. *The Soils of Antarctica*; Springer: New York, NY, USA, **2015**.

20. Coradin, T.; Eglin, D.; Livage, J. The silicomolybdic acid spectrophotometric method and its application to silicate/biopolymer interaction studies. *J. Spectrosc.* **2004**, *18*, 567 - 576.

21. Jung, J.; Yoo, K.-C.; Lee, K.-H.; Park, Y.K.; Lee, J.I.; Kim, J. Clay Mineralogical Characteristics of Sediments Deposited during the Late Quaternary in the Larsen Ice Shelf B Embayment, Antarctica. *Minerals* **2019**, *9*, 153.

22. Heger, D.; Klanova, J.; Klán, P. Enhanced Protonation of Cresol Red in Acidic Aqueous Solutions Caused by Freezing. *J. Phys. Chem. B* **2006**, *110*, 1277 - 1287.

23. Furrer, G.; Stumm, W. The coordination chemistry of weathering: I. Dissolution kinetics of δ-$Al_2O_3$ and BeO. *Geochim. et Cosmochim. Acta* **1986**, *50*, 1847 - 1860.

24. Anderson, S. Biogeochemistry of Glacial Landscape Systems. *Annu. Rev. Earth Planet. Sci.* **2007**, *35*, 375 - 399.

25. Burton, J.D.; Leatherland, T.M.; Liss, P.S. THE REACTIVITY OF DISSOLVED SILICON IN SOME NATURAL WATERS. *Limnol. Oceanogr.* **1970**, *15*, 473 - 476.

26. Macdonald, R.; McLaughlin, F. The effect of storage by freezing on dissolved inorganic phosphate, nitrate and reactive silicate for samples from coastal and estuarine waters. *Water Res.* **1982**, *16*, 95 - 104.

27. Bates, S.; Zografi, G.; Engers, D.; Morris, K.; Crowley, K.; Newman, A.W. Analysis of Amorphous and Nanocrystalline Solids from Their X-Ray Diffraction Patterns. *Pharm. Res.* **2006**, *23*, 2333 - 2349.

28. Biswas, R.K.; Khan, P.; Mukherjee, S.; Mukhopadhyay, A.K.; Ghosh, J.; Muraleedharan, K. Study of short range structure of amorphous Silica from PDF using Ag radiation

KOPRI 극지연구소

in laboratory XRD system, RAMAN and NEXAFS. *J. Non-Crystalline Solids* **2018**, *488*, 1 - 9.

29. Hartmann, J.; West, A.J.; Renforth, P.; Köhler, P.; De La Rocha, C.L.; Dürr, H.; Scheffran, J.; Wolf-Gladrow, D.A. Enhanced chemical weathering as a geoengineering strategy to reduce atmospheric carbon dioxide, supply nutrients, and mitigate ocean acidification. *Rev. Geophys.* **2013**, *51*, 113 - 149.
30. Hawkings, J.; Wadham, J.L.; Benning, L.G.; Hendry, K.R.; Tranter, M.; Tedstone, A.J.; Nienow, P.; Raiswell, R. Ice sheets as a missing source of silica to the polar oceans. *Nat. Commun.* **2017**, *8*, 14198.

KOPRI
극지연구소

## TABLES AND FIGURES

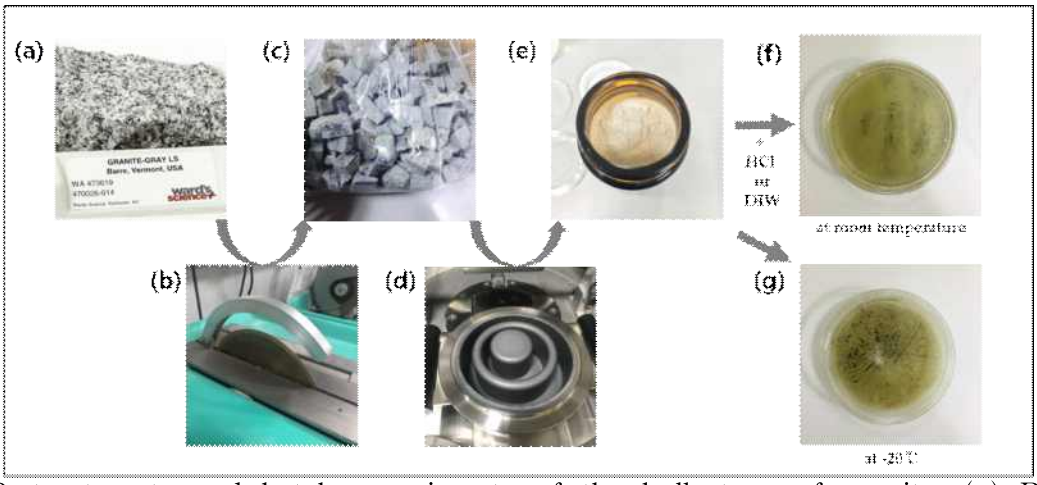



Fig. 1. Pretreatments and batch experiments of the bulk type of granite. (a) Bulk rock sample, (b) diamond blade, (c) small rock chips sliced with (b), (d) ring mill, (e) granite powder milled with (d), (f) aqueous sample at room temperature, and (g) ice sample at 20 °C.

KOPRI
극지연구소

Table 1. Chemical composition of granite powder used in this study analyzed by X-ray fluorescence spectroscopy.

| Oxide Composition | $SiO_2$ | $Al_2O_3$ | $K_2O$ | $Na_2O$ | $Fe_2O_3$ | CaO | MgO | $TiO_2$ | MnO |
|---|---|---|---|---|---|---|---|---|---|
| Weight Percentage (%) | 72.50 | 13.59 | 7.56 | 1.83 | 1.65 | 1.04 | 0.58 | 0.37 | 0.10 |

Table 2. Averaged dissolved cation concentrations after 29-day batch experiment analyzed by ion chromatography.

| | DW (aq) | DW (ice) | pH 3 (aq) | pH 3 (ice) | pH 2 (aq) | pH 2 (ice) |
|---|---|---|---|---|---|---|
| $[Na^+]$ | 0.27 | n.a. | 0.68 | 0.39 | 1.19 | 0.46 |
| $[K^+]$ | 1.21 | 0.01 | 3.44 | 2.61 | 9.63 | 4.22 |
| $[Mg^{2+}]$ | 0.18 | n.a. | 1.17 | 0.98 | 7.50 | 3.34 |
| $[Ca^{2+}]$ | 2.65 | 0.09 | 5.59 | 4.56 | 13.45 | 9.43 |

(unit: mg $L^{-1}$)

KOPRI 극지연구소

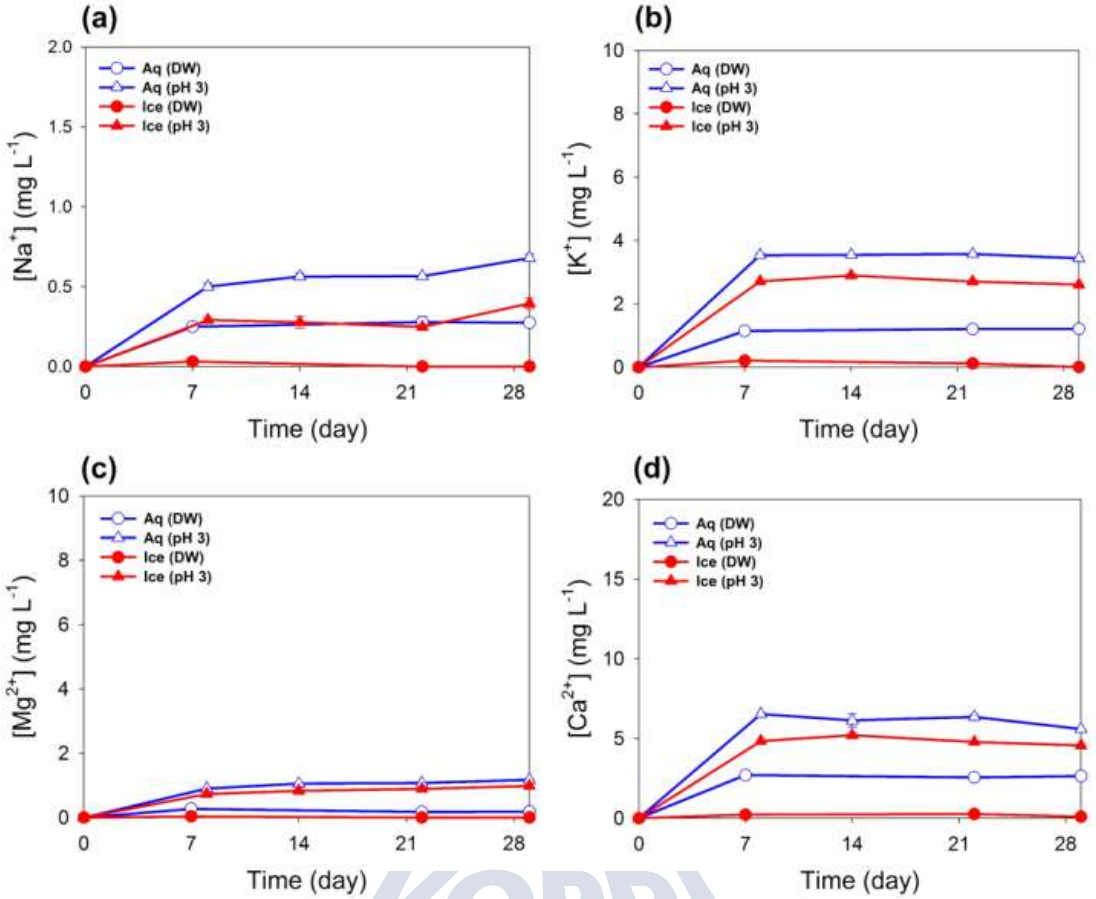



Fig. 2. Chemical composition changes of filtrate after a batch experiment with a pH 3 solution and DW. (a) [$Na^+$], (b) [$K^+$], (c) [$Mg^{2+}$], and (d) [$Ca^{2+}$].

KOPRI 극지연구소

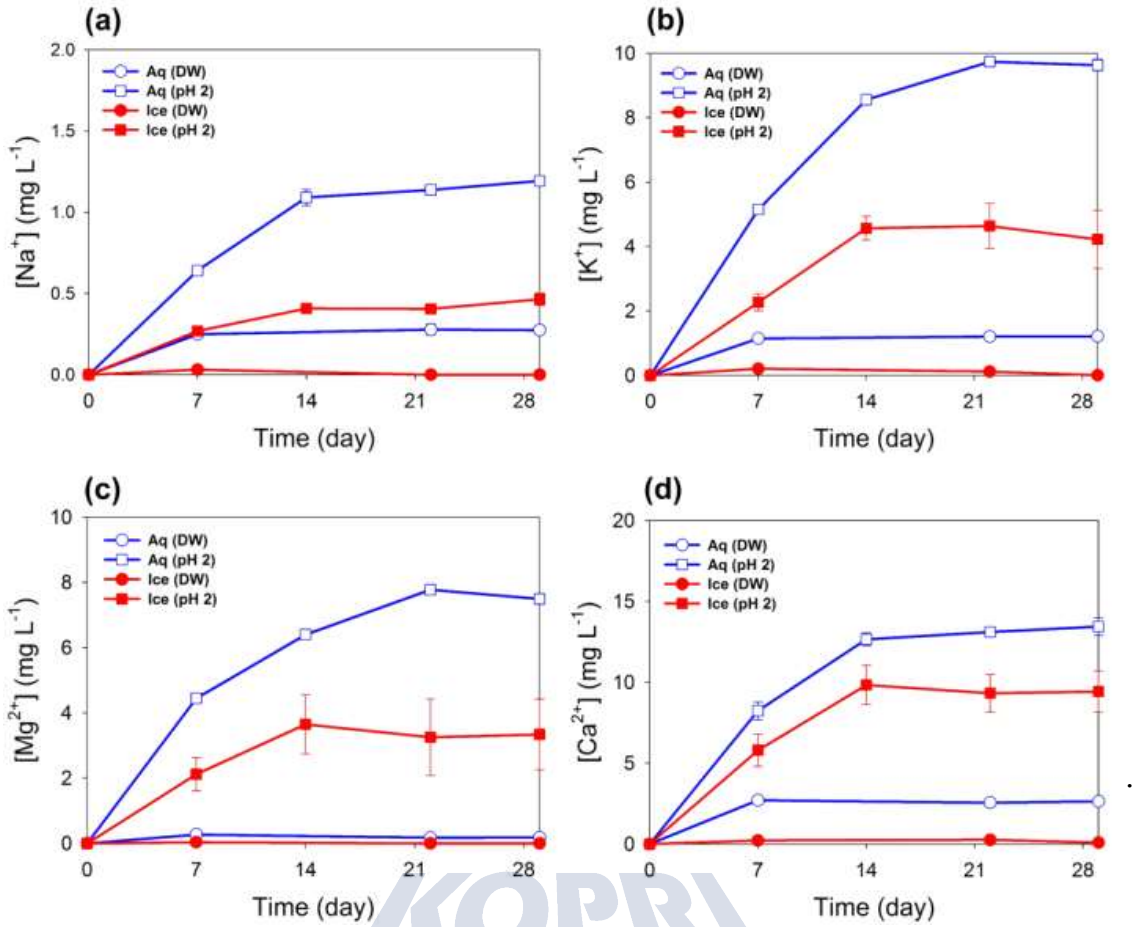



Fig. 3. Chemical composition changes of filtrate after batch experiment with pH 2 solution and DW. (a) [$Na^+$], (b) [$K^+$], (c) [$Mg^{2+}$], and (d) [$Ca^{2+}$].

KOPRI 극지연구소

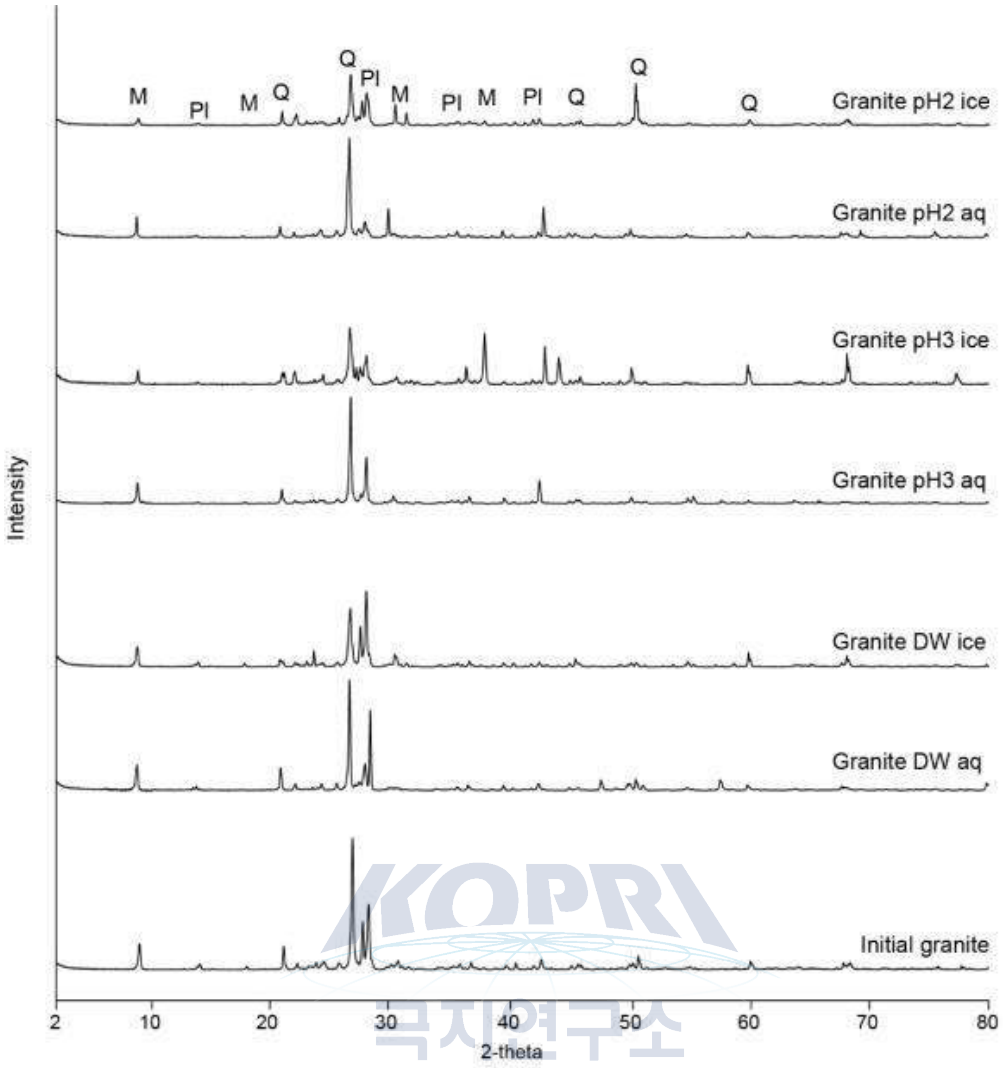



Fig. 4. XRD patterns for a fresh granite sample and filtered solid material after the 29-day batch experiment under different conditions; quartz (Q), plagioclase (Pl), and mica (M).

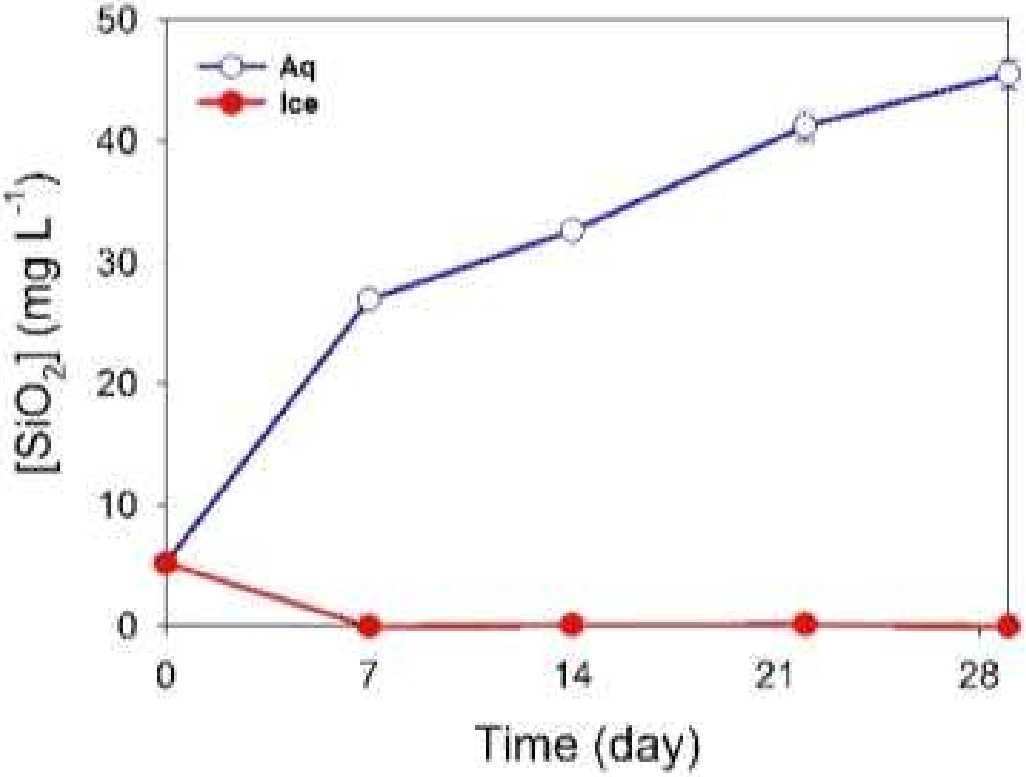



Fig. 5. $SiO_2$ concentration analysis of filtrate after a batch experiment with a pH 2 solution.

KOPRI
극지연구소

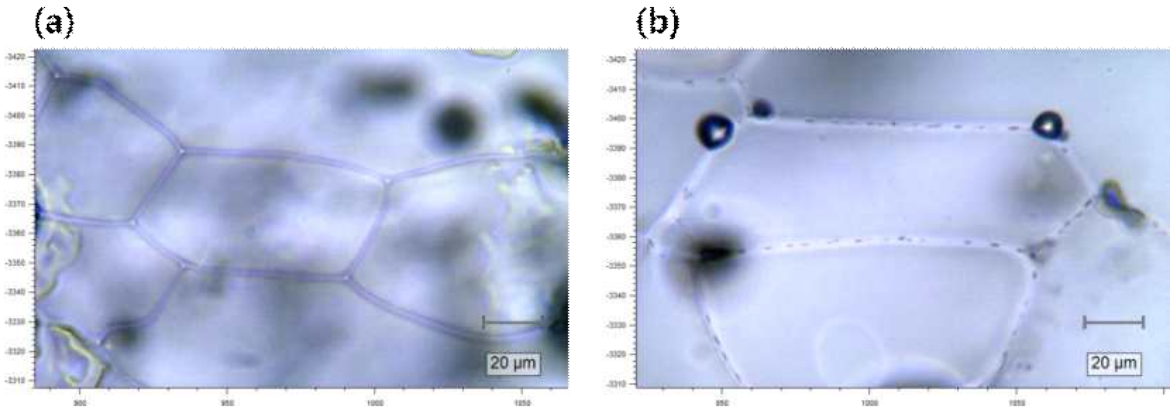



Fig. 6. Representative optical images of (a) pH 3 solution and (b) the mixture of pH 3 solution and granite powder frozen to －20 °C on the linkam stage with －2 °C $min^{-1}$ of freezing.

KOPRI
극지연구소

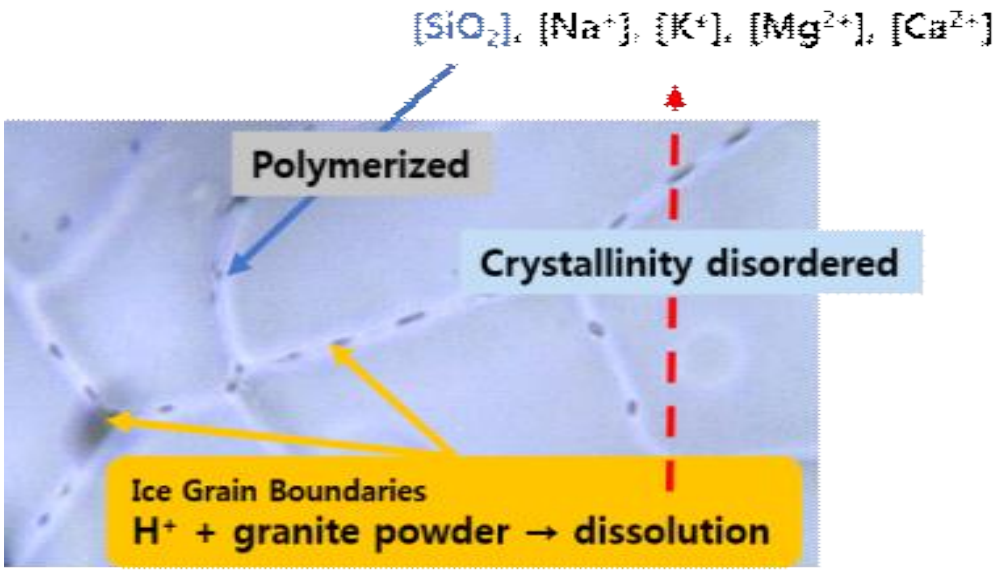



Fig. 7. Scheme of dissolution of granite in ice.

KOPRI
극지연구소

# 제 6 절. Frozen hydrogen peroxide and nitrite solution: the acceleration of benzoic acid oxidation via the decreased pH in ice⑥

Yong-Yoon Ahn[1], Jungwon Kim[2], and Kitae Kim[1,3]

[1]Korea Polar Research Institute (KOPRI)

[2]Department of Environmental Sciences and Biotechnology, Hallym University

[3]Department of Polar Science, University of Science of Technology (UST)

## Abstract

We investigated the benzoic acid oxidation via the reaction of hydrogen peroxide ($H_2O_2$) and nitrite ($NO_2^-$). The oxidation of benzoic acid by reactive nitrous acid (HONO) was negligible, and the reactivity of the $H_2O_2/NO_2^-$ system decreased with a decrease in temperature under aqueous conditions. However, freezing markedly accelerated the chemical reaction. Based on Raman microscope measurements, concentrated species were confirmed in certain regions of the ice. We proposed that the change in nitrite speciation (accordingly, a decrease in the pH below the pKa), derived from the freezing concentration effect, was the reason for the accelerated reactions. The oxidation characteristics of the system were monitored under varying conditions, such as the initial pH, dosage ratio, benzoic acid concentration, and reaction with various benzene derivatives. The UHPLC/ESI/MS measurement showed that peroxynitrous acid (HOONO)-mediated oxidation generated the hydroxylated and nitrated by-products. Additionally, decarboxylated products were detected, indicating direct electron transfer from the organic compounds to HOONO. As freezing is a global phenomenon, and $H_2O_2$ and $NO_2^-$ are ubiquitous in the environment, the transformation of aromatic compounds with $H_2O_2/NO_2^-$ in cold environments must be considered in environmental chemistry.

## 1. Introduction

The environmental chemistry of aromatic substances is of great importance because they influence Earth's carbon cycle.[1-6] Among the variety of species associated with hydrocarbon transformation, nitrite has been intensively highlighted owing to its importance in photochemistry as a source of nitric oxide and hydroxyl radicals, as well as its inherent

⑥ 이 연구는 본 과제(PE21120)와 해양수산부가 후원하는 "극지 유래 생물자원을 활용한 항생제 후보물질 개발 (15250103, KOPRI Grant PM21030)"과제의 지원을 받았으며, *Environ. Sci. Technol.* 2022, 56(4), 2323-2333 에 출간되었다.

reactivity when protonated to form nitrous acid.[4-11] Generally, most studies on nitrite chemistry have focused on aqueous and gaseous phase reactions. However, its unique behavior during freezing has also been identified and analyzed.[12-14] This unique behavior is the significant acceleration of the reaction during freezing compared with the liquid phase when the pH is approximately 4.[15, 16]

This freezing-induced acceleration is mostly caused by the freeze concentration effect, which refers to the accumulation of dissolved species in the liquid-like layer of ice (or the ice grain boundary).[15] However, Takenaka et al.[13] inferred that the reaction involving nitrite during freezing cannot be interpreted solely based on the freeze concentration effect; the speciation of nitrite to nitrous acid must be considered. Although the substances concentrated at the ice grain boundaries, the nitrite reactivity during freezing was inert at circumneutral and alkaline pH conditions.[15, 16] Additionally, many studies have reproduced the phenomenon of a 2~4-fold decrease in the pH in the liquid-like region of ice when the pH before freezing was slightly acidic; these studies have proposed that proton accumulation and cation-anion separation at the ice grain boundary and ice-bulk were mainly responsible for this phenomenon.[17-23] Accordingly, in this acidic environment in ice, nitrite can transform to reactive nitrous acid (HONO; pKa = 3.4) and the nitrous acidium ion ($H_2ONO^+$; pKa = 1.7),[24] despite a circumneutral pH before freezing. These substances can react with aromatic compounds, such as guaiacol6, methylcatechol[5], acetaminophen[25], and phenol[3, 26] to generate nitrated aromatic compounds, which have important role in environmental chemistry.

In addition to the reaction of nitrous acid, enhanced phenol nitration has been reported, which was caused via the introduction of hydrogen peroxide into a nitrite solution.[3] Previous studies have shown that nitrite does not react with hydrogen peroxide at an appreciable rate, but nitrous acid reacts rapidly with hydrogen peroxide and transforms into peroxynitrous acid (HOONO), which is responsible for the accelerated nitrophenol generation. Although the reaction mechanism of HOONO is not yet fully understood, its reactivity has been ascribed to (i) one- or two-electron transfer oxidation, (ii) the generation of $NO_2^+$ ion from the heterolytic cleavage of the peroxo O-O bond, or (iii) the formation of a $[\bullet NO_2 + \bullet OH]_{cage}$ caged radical pair or its individual free radicals through the homolytic cleavage of the peroxo O-O bond.[27-34] Hence, HOONO behaves not only as a nitration reagent, but also as a hydroxylation reagent.[35] Numerous studies have discussed the reactions with HOONO with respect to the generation of •OH based on the apparent observation of hydroxylated by-products;[28, 34, 36, 37] other studies have also proposed that •OH cannot be generated from the homolysis of HOONO.[30, 38, 39] Owing to its complex chemistry, these controversies have not been resolved until now. However, regardless of the detailed reaction mechanism, HOONO can be regarded as a sufficiently strong oxidant,

which reacts non-selectively with various organic compounds in the environment, as well as •OH.

In this study, we propose a novel chemical reaction mechanism, i.e., the accelerated oxidation of aromatic substances in the frozen hydrogen peroxide and nitrite solution. We tested the oxidation of benzoic acid (BA) as a representative aromatic compound, because its structure is ubiquitous in various organic compounds in the environment[1] and drugs,[40] and it resists the oxidative attack of HONO, as shown in our experiment. This negligible reactivity is important because many studies on aromatic nitration have discussed nitration-prone compounds, such as phenol, to analyze the role of nitrous acid;[3, 5, 6, 27, 28] However, we also need to consider nitration-resistant compounds under certain conditions. Furthermore, low temperatures inhibit aromatic nitration,[4] such that freezing-accelerated BA transformation can provide new HOONO-mediated pathways in environmental chemistry. Accordingly, we compared the transformation efficiency of BA in aqueous and frozen system. We attempted to reveal the reason for accelerated BA oxidation in the frozen system, which is related to the acid dissociation constant of nitrite and the acidity in the ice. We confirmed the freeze concentration in the ice. We then tested the influence of the stoichiometric ratio between the reactants. The substrate dependent reactivity of the system was also investigated. The reaction by-products were detected to understand the characteristics of oxidation. The system was also investigated in imitated natural conditions, i.e., water environments (stream or rain) and freezing conditions (ethanol bath or air-cooling). Water freezing commonly occurs in the upper atmosphere, polar regions, and middle latitude in winter. Hydrogen peroxide and nitrite are present in water droplets, haze, rain, and surface water, among others, which can be frozen. Based on these circumstances, our study demonstrates the important role of freezing in the transformation of organic compounds in the environment.

## 2. Experimental Section

### 2.1 Chemicals

The chemical reagents used in this study are listed in the Supporting Information (TEXT S1). All chemicals were of reagent grade and were used as received without any further purification. The entire chemical solutions used in this study were prepared with ultrapure deionized water (18.2 MΩ•cm), which was produced by a Milli-Q Water Purification System (Millipore). The natural waters (i.e., rain and stream) were obtained as follows: We gathered rainwater at the rooftop of the KOPRI building from September 28 to 29, 2021. We collected stream water from Seongbuk stream, Korea, on October 6, 2021. All collected natural waters were filtered using a 0.2 μm PTFE filter and stored in a

refrigerator.

### 2.2 Experimental procedure

The test solution was prepared in a 100 mL glass beaker. The 100 mM of $H_2O_2$, $NaNO_2$, and 10 mM of BA stock solutions were appropriately added to the beaker to obtain the desired concentration. Then, $HClO_4$ solutions were added to obtain the initial pH value. Next, 10 mL of this solution was poured into a 15 mL polypropylene conical tube sealed with a cap. The conical tube containing the test solution was placed in an ethanol-cooling bath, which was precooled to the desired temperature (−20, −10, 5, 15, 25, and 35℃). The number of conical tubes was selected according to the time-sampling points. These preparation procedures were conducted as fast as possible (approximately 30 s was required), and we assigned the moment at which the conical tubes were immersed in the cooling bath as the starting point (i.e., t = 0). The frozen conical tube was withdrawn from the cooling bath at a particular time and then placed in a lukewarm water bath at 30℃ to thaw the ice for chemical analysis. Note that the influence of the thawing in 30℃ within 10 min is negligible as presented in Figure 1 (see 35℃ in Figure 1). After thawing, the samples were analyzed immediately. At least two runs of each experiment were performed to confirm the data reproducibility. When we needed to freeze the solution using the air-cooling system, the conical tubes were placed in a custom-made Low Temperature Chamber which operated at −20℃ with marginal temperature variation from the programmed value.

KOPRI 극지연구소

### 2.3 Analytical methods

High-Pressure-Liquid-Chromatography (HPLC) (Agilent, 1260 Infinity II) was employed to analyze the organic compounds in this study. The organic compounds are identified by examinations of the retention time (Poroshell 120 EC-C18 column (4.6 mm × 150 mm) was used) and the absorbance (using a variable wavelength detector (G7114 1260VWD)). In the analysis, 0.1% (v/v) phosphoric acid and acetonitrile were used as eluents, and the composition ratio between them varied according to the target organic compound.

The nitrite and nitrate concentrations were measured using an ion chromatograph (Dionex ICS-1100) with a suppressor (Dionex AERS 500), column (Dionex IonPac AS23), and conductivity detector. Sodium carbonate and bicarbonate solution (0.477 g and 0.067 g in 1 L, respectively) were used for elution.

The $H_2O_2$ concentration was measured via the modified iodometry method, as described in Klassen et al..[41] Specifically, 0.05 mL of sample was mixed with 2.85 mL of 10 mM KI (in 10 mM $NaHCO_3$) and 0.1 mL of 10 mM ammonium molybdate (total volume of 3 mL); this solution was incubated in the atmosphere for 1 h. The absorbance at a wavelength of

352 nm was monitored to calibrate $H_2O_2$ concentration. We confirmed that other oxidants, such as HONO, did not interfere with the signal, and was well-reproduced at various $H_2O_2$ concentration standards. UV-vis spectroscopy was used to monitor the $H_2O_2$ concentration with a UV-2600i (Shimadzu).

A confocal Raman microscope (Renishaw, InVia Qontor) was employed to obtain information on the reagent distribution in the ice without melting. A temperature-controlled microscope stage (Linkam scientific, THMS600) was used to freeze the sample with a cooling speed of −2℃/min and a terminal temperature of −20℃. The 532 nm laser was exposed for 1 s with data accumulation 10 times, and the laser power on the spot was less than 1.5 mW.

The oxidation by-products were analyzed using a UHPLC (Thermo Fisher Scientific, Vanquish) combined with a quadrupole-orbitrap mass spectrometer (Thermo Fisher Scientific, Q Exactive Focus). The separation was performed on a Hypersil GOLDTM aQ column with a mobile phase composed of 0.1% (v/v) formic acid (dissolved in LC-MS grade water) and neat acetonitrile (LC-MS grade) at a flow rate of 0.3 mL/min. Mass detection was carried out in negative electrospray ionization (ESI) mode, and the operating parameters were set as follows: a detection range of 50 to 550 m/z, with a resolution of 70,000, spray voltage of 4.00 kV, capillary temperature of 320℃, sheath gas flow rate of 40 a.u., auxiliary gas flow rate of 10 a.u., auxiliary gas heater temperature of 300℃, S lens RF level of 50.0, maximum injection time of 200 ms, and an automatic gain control (AGC) target of $1\times10^6$. The obtained total ion current (TIC) signals were analyzed using the Compound Discoverer 3.2$^{TM}$ (Thermo Fisher Scientific) software with Chemspider and mzCloud database to identify and confirm the detected by-products. Total organic carbon (TOC) was measured using a TOC Analyzer (TOC-LCPH, Shimadzu).

## 3. Results and Discussion

### 3.1 Freezing-induced enhancement of reaction between hydrogen peroxide and nitrite

Figure 1a shows the degradation of BA in the $H_2O_2/NO_2^-$ system at a pH of 4. In the aqueous cases (i.e., the temperature was > 0℃), the decrease in BA did not exceed 20% of its initial concentration during the reaction. However, when the solution was frozen (i.e., the temperature was −20 and −10℃), approximately half of the initial BA decomposed. The degradation of BA during freezing was not observed when $H_2O_2$ or $NO_2^-$ was absent from the solution (Figure 1a; pink triangle and blue circle). Similarly, the concentrations of $H_2O_2$ and $NO_2^-$ changed rapidly when the solution was frozen, whereas they gradually decreased when the solution was not frozen (Figure 1b). It is noteworthy that the initiation

of freezing in −10℃ required approximately 30 min, and the concentration change within that period was very little, but the remarkable change of concentration occurred after that period. Also, we emphasize that the concentration changes in the aqueous conditions were reduced with a decrease in the temperature. However, when the solution was frozen, the reaction between the reagents increased, and most of the $NO_2^-$ was converted to $NO_3^-$ (Figure S1). We note that although the only presence of $NO_2^-$ also showed a change in its concentration due to freezing, the rate was significantly lower than that in the case of its coexistence with $H_2O_2$ (Figure S1). Based on these observations, we concluded that $H_2O_2$ and $NO_2^-$ are essential for initiating BA degradation, and the reactions between them increased as a result of freezing. We also point out that approximately 20% of the total nitrite concentration occurred in a protonated form at a pH of 4, i.e., nitrous acid (Figure S2).[24] As a reactive nitrogen species, HONO can transform various aromatic compounds, including phenol, catechol, acetaminophen, aniline, and benzene.[2, 25, 26, 42] Additionally, Sun et al.[43] reported that freezing can accelerate sulfamethoxazole transformation by nitrite at circumneutral pH values. However, we found no BA decomposition by $NO_2^-$ at a pH of 2 −5 (note that, at a maximum, 80% of the $NO_2^-$ existed as HONO; Figure S2) in both the aqueous and frozen systems (Figure S3a). We expect that the negligible reactivity of HONO toward BA derives from the function of the electron-withdrawing carboxyl group, which resists the electrophilic substitution of HONO (or $NO^+$) on the aromatic ring of BA.[44] Thus, we inferred that the BA decomposition originated from the action of other reactive species, derived from the reaction between $H_2O_2$ and nitrite species (i.e., HONO and $NO_2^-$). According to previous studies, the reaction between H2O2 and $NO_2^-$ generates reactive peroxynitrous acid (HOONO) as follows:[3, 45, 46]

$$H_2O_2 + HONO \rightarrow HOONO + H_2O \quad (1)$$

$$HOONO \leftrightarrow OONO^- + H^+ \ (pK_a = 6.8) \quad (2)$$

$$HOONO \rightarrow NO_3^- + H^+ \quad \text{(isomerization)} \quad (3)$$

$$HOONO \rightarrow NO_2^+ + OH^- \ \text{(heterolytic cleavage)} \quad (4)$$

$$HOONO \leftrightarrow [\bullet NO_2 + \bullet OH]_{cage} \quad (5)$$

The $pK_a$ of $ONOO^-$ is 6.8; thus, it occurs as a protonated species in an acidic condition.[27] In the previous research, the activation energy of forming $NO_2^+$ and $HNO_3$ from the reaction of $H_2O_2$ and $HNO_2$ at pH 4.5 were calculated as 94±8 and 75±35 kJ/mol, respectively.[4] We noted that, under aqueous conditions at a pH of 4, we obtained the activation energy of $NO_2^-$ transformation of 38.56±3.27 kJ/mol from the plot of the Arrhenius relationship (Figure S4).

The decomposition of BA is sensitive to the pH. Figure 2a illustrates the pH dependence

of BA degradation in the $H_2O_2/NO_2^-$ system. We found that approximately 65% of the BA decomposed at a pH of 3, even under aqueous conditions, but freezing accelerated this reaction (note that the absence of $NO_2^-$ resulted in no degradation of BA; Figure S3b). Overall, the BA degradation efficiency decreased with an increase in the pH. Furthermore, there are no changes were observed at a pH of 5, regardless of freezing. As the $pK_a$ of nitrite is 3.4 ($HNO_2 \leftrightarrow NO_2^-$)[3, 10, 24], it is plausible that oxidant generation, which is responsible for BA degradation, is highly related to nitrite speciation. As demonstrated in previous studies, the $NO_2^-$ disappearance rate by $H_2O_2$ is significantly related to the pH and $pK_a$ values of the reactants.[3] This reaction eventually produces HOONO, but HOONO is rapidly decomposed and isomerized to a relatively stable form: nitrate ($NO_3^-$).[27] Accordingly, we found a positive relationship between the decomposition of BA and the conversion of $NO_2^-$ to $NO_3^-$ by $H_2O_2$ (see the aqueous cases in Figure 2). In addition, the molar ratio of the reaction between $H_2O_2$ and $NO_2^-$ is likely 1:1 because we observed that approximately 0.45 mM of $NO_3^-$ was generated from the reaction of 1 mM of $H_2O_2$ and 0.5 mM of $NO_2^-$ (an approximately 90% conversion from $NO_2^-$), with a remainder of approximately 0.5 mM of $H_2O_2$ (Figure 2b). Note that the effect of $NO_3^-$ on the system was negligible because the transformation of BA by 0.5 mM of $NO_3^-$ with and without $H_2O_2$ at a pH of 3 was ineffective, although nitric acid is a strong nitration reagent (the $pK_a$ of $HNO_3$ is $< -1$, such that it had likely fully dissociated and had no oxidative effect under our experimental condition; Figure S5). Furthermore, the oxidation of BA is likely caused by short-live substances because we found that only less than 5 μM of BA decomposition when BA was added later into the $H_2O_2/NO_2^-$ solution, which proceeded during the reaction between them (Figure S6). Thus, considering HOONO as the main oxidant is reasonable.

As shown in Figure 2, the reactivity of the system increased as pH decreased. Hence, the accelerated BA decomposition in ice can be interpreted as a freezing-induced decrease in the pH. It is remarkable that a slight generation of $NO_3^-$ was found at pH 5 in the frozen condition while no conversion to $NO_3^-$ was detected under aqueous conditions (Figure 2b). Owing to the freeze concentration effect, the liquid-like layer in the ice grain boundary can become more acidic via the freezing of an acidic solution.[15] According to studies on dichromate reduction in ice, freezing-induced changes in the pH change influence the reactivity of Cr species (roughly, pH 4 to 1) because the Cr(VI) species can be affected by the proton concentration and, consequently, its thermodynamic relationship in the system.[47-49] Similarly, during freezing, the speciation of $NO_2^-$ changes to more reactive HONO and its reactivity with $H_2O_2$ increased. To verify the pH drop phenomenon during freezing, it was visualized using cresol red (CR), which was employed as a pH indicator in the ice sample (Figure 3a). The color change in CR occurs if the pH of the system

changes from 4 to near 1.1 due to the $pK_a$ of CR.[15] As shown in the inset of Figure 3a, the light yellow color of the sample changed to light pink when the sample was completely frozen. In addition, the peak position of absorbance of the sample was found at 434 and 520 nm for the original and frozen samples, respectively, which are consistent with the reported values of the monoprotonated and diprotonated form of CR.[50] According to the Henderson-Hasselbalch equation, we assumed that the pH of the ice was < 1.435 (see Supporting Information TEXT S2 for a detailed description). However, we need to mention that the current level of understanding in thermodynamics in ice, such as an equilibrium constant at a liquid-like region, is very limited, but these issues are beyond the scope of the present study.[51, 52]

Figure 3b shows the freeze concentration effect at the ice grain boundary. The color in the center box represents the Raman signal intensity at this position (note that red and violet-black indicate a high and low intensity, respectively). The Raman peaks for $H_2O_2$, $NO_2^-$, and BA were well agreed with the literature.[53-55] As demonstrated, high signals occurred at the interfacial and vertex positions of the ice grains. This result indicates that the dissolved reagents apparently accumulated in a specific area (i.e., the ice grain boundary or micro pocket) in the ice. When we mixed all of the reagents comprising the $H_2O_2/NO_2^-$ system, we only found a weak peak at 877 $cm^{-1}$ (O-O stretching of $H_2O_2$) and a strong peak at 1050 $cm^{-1}$ ($NO_3$ in-phase symmetric stretching) in the scanned area due to the production of $NO_3^-$ from the reaction. As we examined the system within 30 min, this result reveals that the reaction occurred rapidly in the concentrated region. In addition, if some portion of HONO and $H_2O_2$ were incorporated in ice crystals by their distribution characteristics in water, its effects were not significant on BA degradation. This was determined using the Raman microscope; we found that most of the species concentrated in the grain boundary region.

### 3.2 Characteristic of BA oxidation via in-situ generated peroxynitrous acid in ice

Figure 4a and 4b show the influence that the initial $H_2O_2$:$NO_2^-$ ratio has on the BA decomposition in the aqueous and frozen systems. The initial $H_2O_2$ concentration was varied from 0.1 to 5 mM, and the initial $NO_2^-$ concentration was varied from 0.1 to 1 mM. The overall enhancement of BA decomposition was observed in the frozen samples compared with the aqueous cases. However, the same or higher amount of $NO2^-$, with respect to the amount of $H_2O_2$, inhibited the BA decomposition. Notably, the 1:1 $H_2O_2$:$NO_2^-$ ratio did not significantly inhibit BA degradation at pH 3 in the aqueous system, while the 1:2 $H_2O_2$:$NO_2^-$ ratio apparently inhibited BA degradation (Figure 4c). In fact, the initial BA concentration in our experiment was 0.02 mM; therefore, 1 mM of $NO_2^-$ was 50-fold higher than the BA concentration. Additionally, 0.1 mM of $H_2O_2$ and $NO_2^-$ (1:1 dosage

ratio), which only represents a five-fold higher $NO_2^-$ concentration with respect to the BA concentration, in the frozen system led to the decomposition of approximately 20% of BA (Figure 4b). These results suggest that $NO_2^-$ competes with BA owing to the oxidative attack of HOONO. However, if this speculation is true, a high initial concentration of BA can be more effectively decomposed than a low initial concentration of BA. Figure 4d demonstrates the influence of the initial BA concentration in the frozen $H_2O_2/NO_2^-$ system. The BA decomposition efficiency ($100 \times (1 - [BA]/[BA]_0)$; filled bar) decreased with an increase in the initial BA concentration; therefore, we questioned the possibility of the scavenging effect of $NO_2^-$. In contrast, when we compare the amount of decomposed BA with the BA dose, a positive relationship between them was established (empty bar). The 20 μM of BA decomposed at an initial BA concentration of 100 μM, while only 10 μM of BA was decomposed at an initial BA dosage of 20 μM. Based on this, we believe that the decline in the BA decomposition efficiency at high BA concentrations can be ascribed to the enhanced generation of by-products that compete with BA; the scavenging effect of $NO_2^-$ is an alternative scenario. Furthermore, the specific situation at the ice grain boundary should be considered to elucidate the inhibition via $NO_2^-$ in the frozen system because freeze concentration occurred. When we observed the disappearance of HONO with reactant concentrations of 10 mM and 1 mM in the aqueous solution at a pH of 3, the fast reaction occurred in the concentrated case, i.e., the reaction was almost completed within 10 min at 10 mM, whereas the reaction lasted for 60 min at 1 mM (Figure S7). Thus, we suggest that concentrated $NO_2^-$ reacts with HOONO and rapidly transforms to $NO_3^-$, thereby regenerating $NO_2^-$:

$$NO_2^- + HOONO \rightarrow NO_3^- + HONO \quad (6)$$

$$HONO \leftrightarrow NO_2^- + H^+ \ (pK_a = 3.4) \quad (7)$$

Consequently, although $NO_2^-$ was consumed by HOONO, a stoichiometric ratio of 1:1 between $H_2O_2$ and $NO_2^-$ can be established owing to the resupply of $NO_2^-$ (HONO reacts with $H_2O_2$) in this manner.

The reactivity of HOONO was estimated by testing the degradation of various benzene substituents in the frozen $H_2O_2/NO_2^-$ system (Figure 5). Overall, the $H_2O_2/NO_2^-$ cases showed observable reactivity, except in the terephthalic acid case, indicating the non-selective oxidative nature of HOONO. We suggest that the solubility of terephthalic acid (< 15 mg/L) resulted in a low degradation efficiency in the ice because we observed 50% of terephthalic acid degradation in the aqueous $H_2O_2/NO_2^-$ system at pH 3 (Figure S8). Although we showed the non-selective reactivity of HOONO, its efficiency differed from that of benzene derivatives. Note that one of the reaction modes of HOONO may

involve electrophilic substitution, and the electrophilic addition to the aromatic ring of the electrophile is negatively related to the Hammett constant. Accordingly, the degradation efficiencies of the substances in the frozen $H_2O_2/NO_2^-$ system decreased with an increase in the electrophilic substituent constant σ+ (Figure 5 upper row[56, 57]). This trend was also observed in the HONO system (i.e., the presence of only $NO_2^-$), but the HONO system was not appreciably reactive in other cases (Figure 5 middle and bottom rows). While, the degradation of substances in the frozen $H_2O_2/NO_2^-$ system was also related to the Hammett constant σ− and σp.[56-58] Although a decrease in chlorobenzene was observed, we speculate that this is occurred because of volatilization during freezing because chlorobenzene was also removed in the only-$H_2O_2$ case. However, the concentration of chlorobenzene was significantly lower in the case with $H_2O_2/NO_2^-$, showing the evident oxidation by HOONO.

### 3.3 Identification of reaction by-products

The reaction of HOONO involve direct oxidation, nitration, and hydroxylation.[27-35] Accordingly, we can observe hydroxylated by-products, as well as nitrated compounds and decarboxylated substrates. We first explored the by-products of BA degradation. We then degraded some selected BA derivatives that were used as the starting compounds, namely, 4-nitrobenzoic acid (nitrated compound) and 2- and 4-hydroxybenzoic acid (hydroxylated compound), to compare the results with BA degradation and examine the reaction pathway. Hereafter, we refer to “the starting compounds” (it is separated system; not by-products in the BA system!) as their abbreviations, i.e., the BZA ($H_2O_2$/benzoic acid/$NO_2^-$ system; red), the 2-HBA ($H_2O_2$/2-hydroxybenzoic acid /$NO_2-$ system; blue), the 4-HBA ($H_2O_2$/4-hydroxybenzoic acid /$NO_2^-$ system; green), and the 4-NBA ($H_2O_2$/4-nitrobenzoic acid /$NO_2^-$ system; yellow). Note that the signal in the BZA was amplified compared with the other starting compound system because the concentration of the other starting compounds was much higher (20 μM) than the BA oxidation products (~nM). Figure 6 shows the detected products in the starting compounds. Most importantly, we confirmed that the by-product signals apparently derived from the examined reaction (note that we can exclude the signal not derived from the oxidation of HOONO, such as $HClO_4$, by comparison with the background signals).

Interestingly, in the BZA, the aqueous (gray line at the top row) system showed an intense 2-hydroxybenzoic acid signal ([M−H]− m/z 137.0235), which was comparable with that in the frozen system (red line), even though the degradation of BA was not significant. Additionally, the peaks of 3- and 4-hydroxybenzoic acid were identifiable in the aqueous system, but their intensities were lower than those in the frozen system. At this moment, we noted that the relative intensities of those three hydroxybenzoic acid isomers

are not directly related to the concentration ratio: the ionization tendency affects the intensity (the estimated concentration of salicylic acid and 4-hydroxybenzoic acid in the frozen system was approximately 0.384 and 0.372 μM, respectively). Note that the aqueous system of pH 3 showed significant BA degradation (Figure 2), implying weakened reactivity in the $H_2O_2/NO_2^-$ system at a high pH. Otherwise, we found no other intense signal under aqueous conditions comparable to the frozen system (Figure S9). Furthermore, nitrobenzoic acids generation were negligible in the aqueous solution (Figure 6; gray in the top-right), such that the nitration reactivity of HOONO was likely weaker than the hydroxylation reactivity in aqueous condition (pH 4). It is noteworthy that the electrophilic aromatic substitution on the which has deactivating group prefer to attack the meta-position of the aromatic ring. Accordingly, we found that dominant 3-nitrobenzoic acid with respect to 4-nitrobenzoic acid. Furthermore, we found that BA degradation does not yield para-positioned dinitrobenzoic acid because there is no common peak position between the BZA and the 4-NBA (m/z 210.9994, middle row). Thus, the peak on red line at 8.9 min of m/z 210.9994 likely represented 3,5-dinitrobenzoic acid.

The production of dihydroxybenzoic acid (m/z 153.0185) was also differentiated in the starting compounds. While the BZA yielded three peaks, the 4-HBA yielded only one peak at a retention time of 5.5 min, and the 2-HBA yielded two peaks at 6.4 and 7.1 min. Therefore, the compound at 5.5 min did not contain an ortho-positioned hydroxyl group, and the remaining compounds did not have a para-positioned one. A reasonable explanation for this is that the meta-hydroxylation of hydroxybenzoic acid mainly occurred. To compare the characteristics of the •OH-involved reaction, we employed the Fenton system and compared it with the $H_2O_2/NO_2^-$ system (Figure S10). We found that the Fenton system also showed no common peak for dihydroxybenzoic acid at either the 2-HBA and the 4-HBA (Figure S10a). However, the 2-HBA showed 3 peaks at the Fenton system, while the $H_2O_2/NO_2^-$ system showed only 2 peaks at the 2-HBA (both the frozen and acidic aqueous cases; Figure S10b). Hence, we assume that the -OH addition to the ortho-position is not negligible when •OH attacks 2-hydroxybenzoic acid, while HOONO showed no responsible signal according to this. Therefore, we speculate that the oxidation mechanism between HOONO and •OH is slightly different. Besides, based on the mono-hydroxylation of BA, the both systems showed the apparent generation of 2-, 3-, and 4-hydroxybenzoic acid, and the signal ratios among the isomers were little different (note that we matched the BA decomposition at 50% of its initial concentration; Figure S10c). Again, we emphasize that the intensity ratio does not directly indicate the concentration ratio; rather, it was reported that the meta-hydroxybenzoic acid yield by •OH was highest among the isomers.59 In fact, although HOONO is not a radical oxidant, the $H_2O_2/NO_2^-$ system was ineffective with the addition of the radical scavenging reagent

methanol (Figure S11). We believe that the further studies clarify the characteristic differences between HOONO and •OH.

The features of trihydroxybenzoic acid (m/z 169.0136) were difficult to explain because there were many spread peaks, and the peak intensity was low. We believe that the peaks with retention time > 5 min were produced at the electrospray stage because they overlapped with their mother compounds, such as mono- and dihydroxybenzoic acid.[60] Similarly, the detected benzenediol peaks (m/z 109.0284), which have retention times > 5 min, might be produced from the transformation of the mother compounds by corona discharge.[61] However, those hydrophilic compounds were assuredly generated because the evident signals were found at early retention times (< 5 min; note that we confirmed that the catechol peak was positioned at 5 min).

Hydroxynitrobenzoic acid (m/z 182.0090) can be generated through two pathways: hydroxylation-first nitration-after, or vice versa. However, we propose that the former is more prone to occur than later because hydroxylated compounds are more easily decomposed than nitrated compounds, as illustrated in Figure 5. We found three peaks at 7.5, 8.4, and 8.6 min at the BZA with m/z 182.0090. The earliest peak was also appeared at the 2-HBA, and because no peak produced at this retention time in the 4-NBA, this is likely 2-hydroxy-3-nitrobenzoic acid. The middle one (8.4 min) is appeared at the 2-HBA and the 4-HBA both, so we suggest that the retention time of 2-hydroxy-5-nitrobenzoic acid is near to the retention time of 4-hydroxy-3-nitrobenzoic acid. From the comparison with the 4-NBA, we suggest that the 8.6 min is 3-hydroxy-4-nitrobenzoic acid. After, because the hydroxylation increases polarity of aromatic compounds, which result in the pulled retention times of m/z 198.0040 from the retention times of m/z 182.0090 in the C-18 column, so we can confirm that the dihydroxynitrobenzoic acid (m/z 198.0040) is without doubt generated.

We also suggest that the decarboxylation can occur during the oxidation. We found the clear signal of nitrophenol (m/z 138.0184), and hydroxynitrophenol (m/z 154.0137). The nitrophenol (bottom, third from left), at a position 8.7 min, was 4-nitrophenol because we confirmed its retention time via the comparison with a standard sample. The 4-HBA showed one peak with respect to this, such that decarboxylation occurred earlier than nitration. The 2-HBA showed no peaks of nitrophenol, such that ortho-positioned hydroxyl group likely provided decarboxylation resistant characteristics. The 8.9 min of m/z 138.0184 should be derived from the decarboxylation of 3-hydroxy-4-nitrobenzoic acid because there was no associated signal at the 2-HBA and the 4-HBA. Also, hydroxynitrophenol (m/z 154.0137) was likely mainly generated from the decarboxylation of dihydroxynitrobenzoic acid because the peaks were not well matched with the trend in m/z 138.0184 and m/z 109.0284 peaks. Hence, discussing the hydroxylation of nitrophenol and the nitration of

KOPRI 극지연구소

benzenediol based on this result is difficult. If the decarboxylation occurred at the very early stage of oxidation, we could identify it, but our UHPLC/ESI/MS technique was not suitable to detect benzene and phenol (we think that the APPI ionization source is more suitable for detecting the non-polar benzene molecule than ESI).

### 3.4 Freezing-induced BA degradation by $H_2O_2/NO_2^-$ system at natural imitated environment

As mentioned in Figure 4 and 5, the interaction between BA and HOONO can be affected by other species, such as by-products and nitrite. Generally, natural water contains many ingredients. As a result, BA degradation by the $H_2O_2/NO_2^-$ system could be retarded in natural environments. Additionally, ice production in an ethanol bath is more efficient than in a refrigerator (air-cooling) because the heat transfer rates between the two media are different. Thus, to assess the impact of the real condition, we observed the BA degradation efficiency of the $H_2O_2/NO_2^-$ system in an imitated natural environment using the air-cooling system and stream and rain waters (Figure 7). The constituents in different water conditions are listed in Table S1 (note that we added 1 mM of $H_2O_2$ and 0.5 mM of $NO_2^-$ in all waters and adjusted the initial pH of 4). Overall, the freezing method did not influence the BA degradation significantly. The difference between deionized water and rain was marginal, though the higher TOC with respect to the deionized water was measured in rainwater. Although the BA degradation in the stream water showed a retarded performance, the effect of freezing was also apparent in the stream. We believe that this retardation in the stream was derived from a higher concentration of species compared with the other two cases (Table S1).

### 3.5 Environmental implication

The $NO_2^-$ concentration varies depending on the situation: it is reported that ~few nM of nitrite presents at snow surface and droplet,[11, 62] but it can increase up to several ~hundred μM in fogwater,[62, 63] and significantly concentrated in the groundwater and municipal water due to industrial and agricultural activity.[64] Although $H_2O_2$ is not as stable as $NO_2^-$, $H_2O_2$ is also ubiquitous in aquatic environments: it can be produced by natural chemical reactions and biological processes.[65, 66] The presence of $H_2O_2$ has been identified in various environments, including polar regions.[67-69] Freezing occurs globally on Earth. While freezing generally freezes the progression of chemical reactions, it can accelerate the reaction under specific situations because the water transforms its phase into ice and generates highly concentrated microreactors inside (freeze concentration effect). The chemistry of nitrite is associated with this unique reaction, such that it can provide a highly oxidative environment for BA oxidation when it reacts with $H_2O_2$ under slightly acidic conditions.

According to this, although the role of freezing has not been significantly considered for the transformation of aromatic compounds as carbon budget yet, it needed to be accounted for in environment chemistry. After, proxynitrie can also be generated from the reaction of $N_3^-/O_3$ and $^{\bullet}NO/O_2^{\bullet -}$; thus, we further study the effect of freezing on these systems.

HOONO is generally considered to be a strong nitration reagent. However, it is also a strong hydroxylation reagent. There are many arguments regarding the derivation of hydroxylation, such as the generation of $^{\bullet}OH$. Although we found a different reaction pathway between the $H_2O_2/NO_2^-$ and the Fenton system, further studies are required to reveal the characteristics of HOONO.

KOPRI
극지연구소

## REFERENCES


1. Zhang, X.; Zhang, C.; Sun, X.; Yang, J.; Zhu, C. Mechanism and kinetic study of the reaction of benzoic acid with OH, NO3 and SO4− radicals in the atmosphere. *RSC Advances* **2019**, *9*, 18971-18977.
2. Min, D. W.; Kim, K.; Lui, K. H.; Kim, B.; Kim, S.; Cho, J.; Choi, W. Abiotic Formation of Humic-Like Substances through Freezing-Accelerated Reaction of Phenolic Compounds and Nitrite. *Environmental Science & Technology* **2019**, *53*, 7410-7418.
3. Vione, D.; Maurino, V.; Minero, C.; Borghesi, D.; Lucchiari, M.; Pelizzetti, E. New Processes in the Environmental Chemistry of Nitrite. 2. The Role of Hydrogen Peroxide. *Environmental Science & Technology* **2003**, *37*, 4635-4641.
4. Kroflič, A.; Huš, M.; Grilc, M.; Grgić, I. Underappreciated and Complex Role of Nitrous Acid in Aromatic Nitration under Mild Environmental Conditions: The Case of Activated Methoxyphenols. *Environmental Science & Technology* **2018**, *52*, 13756-13765.
5. Vidović, K.; Lašič Jurković, D.; Šala, M.; Kroflič, A.; Grgić, I. Nighttime Aqueous-Phase Formation of Nitrocatechols in the Atmospheric Condensed Phase. *Environmental Science & Technology* **2018**, *52*, 9722-9730.
6. Kroflič, A.; Grilc, M.; Grgić, I. Unraveling Pathways of Guaiacol Nitration in Atmospheric Waters: Nitrite, A Source of Reactive Nitronium Ion in the Atmosphere. *Environmental Science & Technology* **2015**, *49*, 9150-9158.
7. Park, J. Y.; Lee, Y. N. Solubility and decomposition kinetics of nitrous acid in aqueous solution. *The Journal of Physical Chemistry* **1988**, *92*, 6294-6302.
8. Kim, D.-h.; Lee, J.; Ryu, J.; Kim, K.; Choi, W. Arsenite Oxidation Initiated by the UV Photolysis of Nitrite and Nitrate. *Environmental Science & Technology* **2014**, *48*, 4030-4037.
9. Zepp, R. G.; Hoigne, J.; Bader, H. Nitrate-induced photooxidation of trace organic chemicals in water. *Environmental Science & Technology* **1987**, *21*, 443-450.
10. Riordan, E.; Minogue, N.; Healy, D.; O'Driscol, P.; Sodeau, J. R. Spectroscopic and Optimization Modeling Study of Nitrous Acid in Aqueous Solution. *The Journal of Physical Chemistry A* **2005**, *109*, 779-786.
11. Jacobi, H.-W.; Kleffmann, J.; Villena, G.; Wiesen, P.; King, M.; France, J.; Anastasio, C.; Staebler, R. Role of Nitrite in the Photochemical Formation of Radicals in the Snow. *Environmental Science & Technology* **2014**, *48*, 165-172.
12. Takenaka, N.; Ueda, A.; Maeda, Y. Acceleration of the rate of nitrite oxidation by


KOPRI 극지연구소

freezing in aqueous solution. *Nature* **1992**, *358*, 736-738.

13. Takenaka, N.; Ueda, A.; Daimon, T.; Bandow, H.; Dohmaru, T.; Maeda, Y. Acceleration Mechanism of Chemical Reaction by Freezing: The Reaction of Nitrous Acid with Dissolved Oxygen. *The Journal of Physical Chemistry* **1996**, *100*, 13874-13884.
14. Liu, X.; Huang, X.; Wu, Y.; Xu, Q.; Du, M.; Wang, D.; Yang, Q.; Liu, Y.; Ni, B.-J.; Yang, G.; Yang, F.; Wang, Q. Activation of nitrite by freezing process for anaerobic digestion enhancement of waste activated sludge: Performance and mechanisms. *Chemical Engineering Journal* **2020**, *387*, 124147.
15. Kim, K.; Ju, J.; Kim, B.; Chung, H. Y.; Vetráková, L. u.; Heger, D.; Saiz-Lopez, A.; Choi, W.; Kim, J. Nitrite-Induced Activation of Iodate into Molecular Iodine in Frozen Solution. *Environmental Science & Technology* **2019**, *53*, 4892-4900.
16. Kim, K.; Chung, H. Y.; Ju, J.; Kim, J. Freezing-enhanced reduction of chromate by nitrite. *Science of The Total Environment* **2017**, *590-591*, 107-113.
17. Kim, K.; Kim, J.; Bokare, A. D.; Choi, W.; Yoon, H.-I.; Kim, J. Enhanced Removal of Hexavalent Chromium in the Presence of $H_2O_2$ in Frozen Aqueous Solutions. *Environmental Science & Technology* **2015**, *49*, 10937-10944.
18. Robinson, C.; Boxe, C. S.; Guzmán, M. I.; Colussi, A. J.; Hoffmann, M. R. Acidity of Frozen Electrolyte Solutions. *The Journal of Physical Chemistry B* **2006**, *110*, 7613-7616.
19. Le, N. T. H.; Ju, J.; Kim, B.; Kim, M. S.; Lee, C.; Kim, S.; Choi, W.; Kim, K.; Kim, J. Freezing-enhanced non-radical oxidation of organic pollutants by peroxymonosulfate. *Chemical Engineering Journal* **2020**, *388*, 124226.
20. Choi, Y.; Yoon, H.-I.; Lee, C.; Vetráková, L. u.; Heger, D.; Kim, K.; Kim, J. Activation of Periodate by Freezing for the Degradation of Aqueous Organic Pollutants. *Environmental Science & Technology* **2018**, *52*, 5378-5385.
21. Krausková, Ľ.; Procházková, J.; Klašková, M.; Filipová, L.; Chaloupková, R.; Malý, S.; Damborský, J.; Heger, D. Suppression of protein inactivation during freezing by minimizing pH changes using ionic cryoprotectants. *International Journal of Pharmaceutics* **2016**, *509*, 41-49.
22. Bronshtein, V.; Chernov, A. Freezing potentials arising on solidification of dilute aqueous solutions of electrolytes. *Journal of Crystal Growth* **1991**, *112*, 129-145.
23. Imrichová, K.; Veselý, L.; Gasser, T. M.; Loerting, T.; Neděla, V.; Heger, D. Vitrification and increase of basicity in between ice Ih crystals in rapidly frozen dilute NaCl aqueous solutions. **2019**, *151*, 014503.

KOPRI 극지연구소

24. Anastasio, C.; Chu, L. Photochemistry of Nitrous Acid (HONO) and Nitrous Acidium Ion (H2ONO+) in Aqueous Solution and Ice. *Environmental Science & Technology* **2009**, *43*, 1108-1114.

25. Helaleh, M. I. H.; Korenaga, T. Fluorometric determination of nitrite with acetaminophen. *Microchemical Journal* **2000**, *64*, 241-246.

26. Vione, D.; Maurino, V.; Minero, C.; Pelizzetti, E. New Processes in the Environmental Chemistry of Nitrite: Nitration of Phenol upon Nitrite Photoinduced Oxidation. *Environmental Science & Technology* **2002**, *36*, 669-676.

27. Beckman, J. S.; Koppenol, W. H. Nitric oxide, superoxide, and peroxynitrite: the good, the bad, and ugly. *The American journal of physiology* **1996**, *271*, C1424-37.

28. Nonoyama, N.; Chiba, K.; Hisatome, K.; Suzuki, H.; Shintani, F. Nitration and hydroxylation of substituted phenols by peroxynitrite. Kinetic feature and an alternative mechanistic view. *Tetrahedron Letters* **1999**, *40,* 6933-6937.

29. Coddington, J. W.; Hurst, J. K.; Lymar, S. V. Hydroxyl Radical Formation during Peroxynitrous Acid Decomposition. *Journal of the American Chemical Society* **1999**, *121*, 2438-2443.

30. Pou, S.; Nguyen, S. Y.; Gladwell, T.; Rosen, G. M. Does peroxynitrite generate hydroxyl radical? *Biochimica et biophysica acta* **1995**, *1244*, 62-8.

31. Uppu, R. M.; Squadrito, G. L.; Pryor, W. A. Acceleration of peroxynitrite oxidations by carbon dioxide. *Archives of biochemistry and biophysics* **1996,** *327*, 335-43.

32. Lobachev, V.; Rudakov, E. Kinetics and Mechanism of the Oxidation of Alkanes and Alkenes with Peroxynitrous Acid in Aqueous Solution-Gas Phase Systems. *Kinetics and Catalysis - KINET CATAL-ENGL TR* **2005,** *46,* 344-353.

33. Vásquez-Vivar, J.; Santos, A. M.; Junqueira, V. B.; Augusto, O. Peroxynitrite-mediated formation of free radicals in human plasma: EPR detection of ascorbyl, albumin-thiyl and uric acid-derived free radicals. *Biochem J* **1996,** *314 ( Pt 3)*, 869-876.

34. Goldstein, S.; Merényi, G. Methods in Enzymology. *Academic Press* **2008**, Chapter 4 The Chemistry of Peroxynitrite: Implications for Biological Activity.

35. Halfpenny, E.; Robinson, P. L. 168. Pernitrous acid. The reaction between hydrogen peroxide and nitrous acid, and the properties of an intermediate product. *Journal of the Chemical Society (Resumed)* **1952,** 928-938.

36. Hogg, N.; Darley-Usmar, V. M.; Wilson, M. T.; Moncada, S. Production of hydroxyl radicals from the simultaneous generation of superoxide and nitric oxide. *Biochem J* **1992**, *281 ( Pt 2)*, 419-424.

37. Kaur, H.; Whiteman, M.; Halliwell, B. Peroxynitrite-Dependent Aromatic Hydroxylation

and Nitration of Salicylate and Phenylalanine. Is Hydroxyl Radical Involved? *Free Radical Research* **1997**, *26*, 71-82.

38. Kissner, R.; Nauser, T.; Kurz, C.; Koppenol, W. H. Peroxynitrous acid--where is the hydroxyl radical? *IUBMB life* **2003**, *55*, 567-72.
39. Koppenol, W. H.; Moreno, J. J.; Pryor, W. A.; Ischiropoulos, H.; Beckman, J. S. Peroxynitrite, a cloaked oxidant formed by nitric oxide and superoxide. *Chemical Research in Toxicology* **1992**, *5*, 834-842.
40. Kazakov, P.; Gorelenko, S.; Derevyagina, I.; Lukashov, O.; Mirzabekova, N. Oxidation of Substituted Toluenes by Nitric Acid. *Pharmaceutical Chemistry Journal* **2020**, *54*, 46-48.
41. Klassen, N. V.; Marchington, D.; McGowan, H. C. E. H2O2 Determination by the I3- Method and by KMnO4 Titration. *Analytical Chemistry* **1994**, *66*, 2921-2925.
42. Ohya, T.; Kanno, S. Formation of cyanide ion or cyanogen chloride through the cleavage of aromatic rings by nitrous acid or chlorine. XI: On the reaction of purine bases with hypochlorous acid in the presence of ammonium ion. *Chemosphere* **1989**, *19*, 1835-1842.
43. Sun, F.; Xiao, Y.; Wu, D.; Zhu, W.; Zhou, Y. Nitrite-driven abiotic transformation of sulfonamide micropollutants during freezing process. *Chemical Engineering Journal* **2017**, *327*, 1128-1134.
44. Deborde, M.; von Gunten, U. Reactions of chlorine with inorganic and organic compounds during water treatment—Kinetics and mechanisms: A critical review. *Water Research* **2008**, *42*, 13-51.
45. Trifonow, I. Eigenschaften und Struktur der Persalpetersäure. *Z. Anorg. Allg. Chem.* **1922**, *124*, 123-135.
46. Koppenol; H., W. Peroxynitrite Detection in Biological Media: Challenges and Advances. *The Royal Society of Chemistry* **2016**, Chapter 1 Peroxynitrite: The Basics.
47. Ju, J.; Kim, J.; Vetráková, Ľ.; Seo, J.; Heger, D.; Lee, C.; Yoon, H.-I.; Kim, K.; Kim, J. Accelerated redox reaction between chromate and phenolic pollutants during freezing. *Journal of Hazardous Materials* **2017**, *329*, 330-338.
48. Han, T. U.; Kim, J.; Kim, K. Freezing-accelerated removal of chromate by biochar synthesized from waste rice husk. *Separation and Purification Technology* **2020**, *250*, 117233.
49. Nguyen, Q. A.; Kim, B.; Chung, H. Y.; Kim, J.; Kim, K. Enhanced reduction of hexavalent chromium by hydrogen sulfide in frozen solution. *Separation and Purification Technology* **2020**, *251*, 117377.

KOPRI 극지연구소

50. Heger, D.; Klánová, J.; Klán, P. Enhanced Protonation of Cresol Red in Acidic Aqueous Solutions Caused by Freezing. *The Journal of Physical Chemistry B* **2006**, *110*, 1277-1287.

51. Lee, D. H.; Kang, H. Proton Transport and Related Chemical Processes of Ice. *The Journal of Physical Chemistry B* **2021**, *125*, 8270-8281.

52. Takenaka, N.; Bandow, H. Chemical Kinetics of Reactions in the Unfrozen Solution of Ice. *The Journal of Physical Chemistry A* **2007**, *111*, 8780-8786.

53. Vacque, V.; Sombret, B.; Huvenne, J. P.; Legrand, P.; Suc, S. Characterisation of the O-O peroxide bond by vibrational spectroscopy. Spectrochimica Acta Part A: *Molecular and Biomolecular Spectroscopy* **1997**, *53*, 55-66.

54. Irish, D. E.; Thorpe, R. V. Raman Spectral Studies of Cadmium - Nitrite Interactions in Aqueous Solutions and Crystals. **1975**, *53*, 1414-1423.

55. Gao, J.; Hu, Y.; Li, S.; Zhang, Y.; Chen, X. Adsorption of benzoic acid, phthalic acid on gold substrates studied by surface-enhanced Raman scattering spectroscopy and density functional theory calculations. *Spectrochimica Acta Part A: Molecular and Biomolecular Spectroscopy* **2013,** *104*, 41-47.

56. Lee, Y.; Yoon, J.; von Gunten, U. Kinetics of the Oxidation of Phenols and Phenolic Endocrine Disruptors during Water Treatment with Ferrate (Fe(VI)). *Environmental Science & Technology* **2005**, *39*, 8978-8984.

57. Leffler, J. E.; Grunwald, E. Rates and Equilibria of Organic Reactions. *John Wiley & Sons* **1963** (Dover reprint), Chapter 7 Extrathermodynamic Free Energy Relationships.

58. Palusiak, M.; Domagała, M.; Dominikowska, J.; Bickelhaupt, F. M. The substituent effect on benzene dications. *Physical Chemistry Chemical Physics* **2014**, *16*, 4752-4763.

59. Klein, G. W.; Bhatia, K.; Madhavan, V.; Schuler, R. H. Reaction of hydroxyl radicals with benzoic acid. Isomer distribution in the radical intermediates. *The Journal of Physical Chemistry* **1975**, *79*, 1767-1774.

60. Hassan, I.; Pavlov, J.; Errabelli, R.; Attygalle, A. B. Oxidative Ionization Under Certain Negative-Ion Mass Spectrometric Conditions. *Journal of the American Society for Mass Spectrometry* **2017**, *28*, 270-277.

61. Pei, J.; Hsu, C.-C.; Wang, Y.; Yu, K. Corona discharge-induced reduction of quinones in negative electrospray ionization mass spectrometry. *RSC Advances* **2017**, *7*, 43540-43545.

62. Acker, K.; Beysens, D.; Möller, D. Nitrite in dew, fog, cloud and rain water: An indicator for heterogeneous processes on surfaces. *Atmospheric Research* **2008**, *87,* 200-212.

KOPRI 극지연구소

63. Miller, D. R.; Byrd, J. E.; Perona, M. J. The source of Pb, Cu, and Zn in fogwater. *Water, Air, and Soil Pollution* **1987**, *32*, 329-340.

64. Philips, S.; Laanbroek, H. J.; Verstraete, W. Origin, causes and effects of increased nitrite concentrations in aquatic environments. *Reviews in Environmental Science and Biotechnology* **2002**, *1*, 115-141.

65. Clark, C. D.; De Bruyn, W. J.; Jakubowski, S. D.; Grant, S. B. Hydrogen peroxide production in marine bathing waters: Implications for fecal indicator bacteria mortality. *Marine pollution bulletin* **2008**, *56*, 397-401.

66. Möller, D. Atmospheric hydrogen peroxide: Evidence for aqueous-phase formation from a historic perspective and a one-year measurement campaign. *Atmospheric Environment* **2009**, *43*, 5923-5936.

67. Sakugawa, H.; Kaplan, I. R.; Tsai, W.; Cohen, Y. Atmospheric hydrogen peroxide. *Environmental Science & Technology* **1990**, *24*, 1452-1462.

68. Neftel, A.; Jacob, P.; Klockow, D. Measurements of hydrogen peroxide in polar ice samples. *Nature* **1984**, *311*, 43-45.

69. Kamiyama, K.; Motoyama, H.; Fujii, Y.; Watanabe, O. Distribution of hydrogen peroxide in surface snow over antarctic ice sheet. *Atmospheric Environment* **1996**, *30*, 967-972.

KOPRI
극지연구소

FIGURES

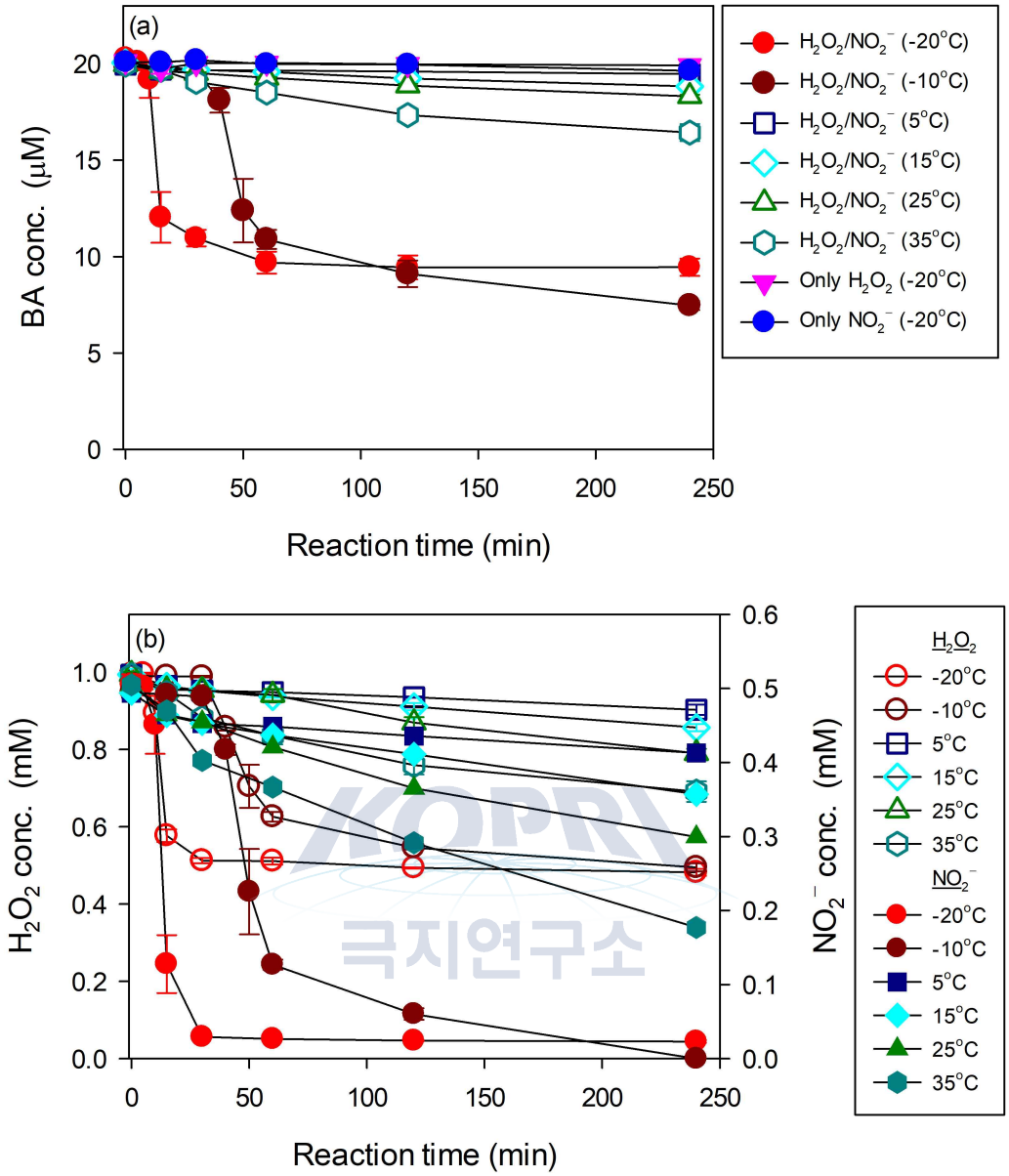



Fig. 1. Time profiles of substrate concentrations in the $H_2O_2/NO_2^-$ system. (a) the concentration of BA. (b) the concentration of $H_2O_2$ and $NO_2^-$. Experimental conditions: $[BA]_0$ = 20 μM; $[H_2O_2]_0$ = 1 mM; $[NO_2^-]_0$ = 0.5 mM; pHi = 4.0 (adjusted by $HClO_4$).

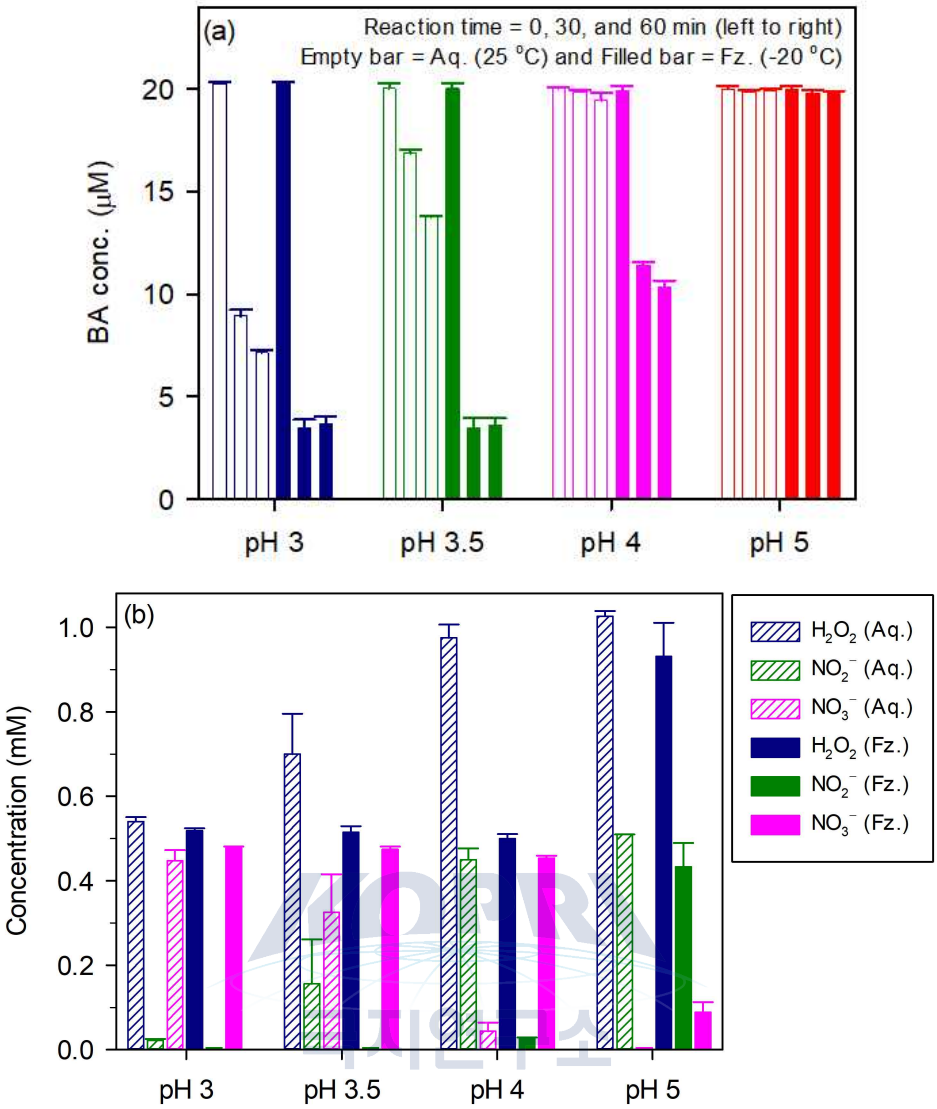



Fig. 2. Effect of pH on the $H_2O_2/NO_2^-$ system. (a) the concentration of BA. (b) the concentration of $H_2O_2$, $NO_2^-$, and $NO_3^-$. Experimental conditions: $[BA]_0$ = 20 μM; $[H_2O_2]_0$ = 1 mM; $[NO_2^-]_0$ = 0.5 mM; Temperature: the frozen system (Fz.) = −20℃; the aqueous system (Aq.) = 25℃; Reaction time = 1 h.

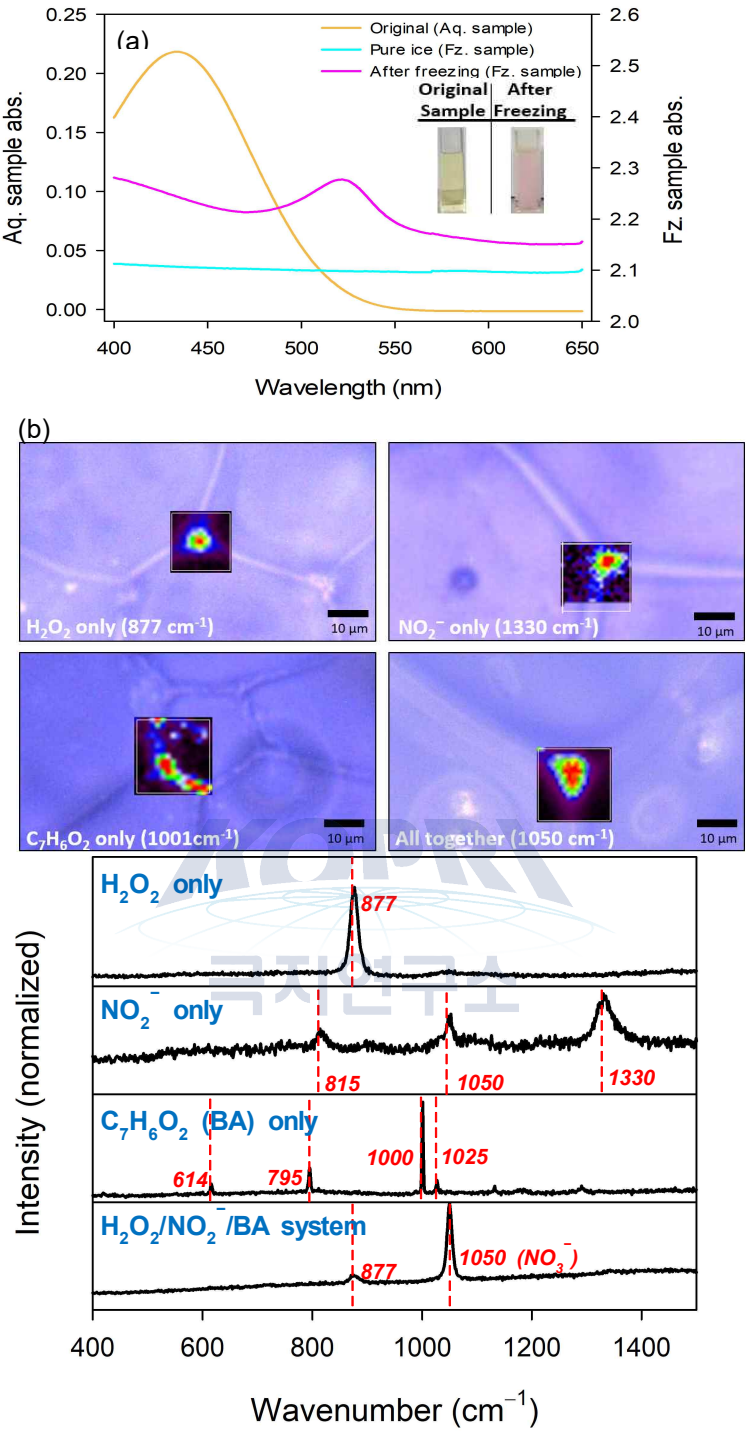



Fig. 3. (a) The UV-visible absorption spectra of CR. Insert = the color of cresol red. Experimental conditions: $[CR]_0$ = 10 μM; $[H_2O_2]_0$ = 1 mM; $[NO_2^-]_0$ = 0.5 mM; pHi = 4.0 (adjusted by $HClO_4$); Temperature: the frozen system (Fz.) = −20 ℃; the aqueous system (Aq.) = 25 ℃. (b) The microscope image of ice grain boundary and the distributions of reagents which are represented by the Raman peak intensity. Note that the peaks were normalized because of the relatively high intensity of $NO_3^-$ (1050 $cm^{-1}$) than the others. Experimental conditions: $[H_2O_2]_0$ = 40 mM; $[NO_2^-]_0$ = 20 mM; $[BA]_0$ = 1 mM; $[HCl]_0$ = 5 mM.

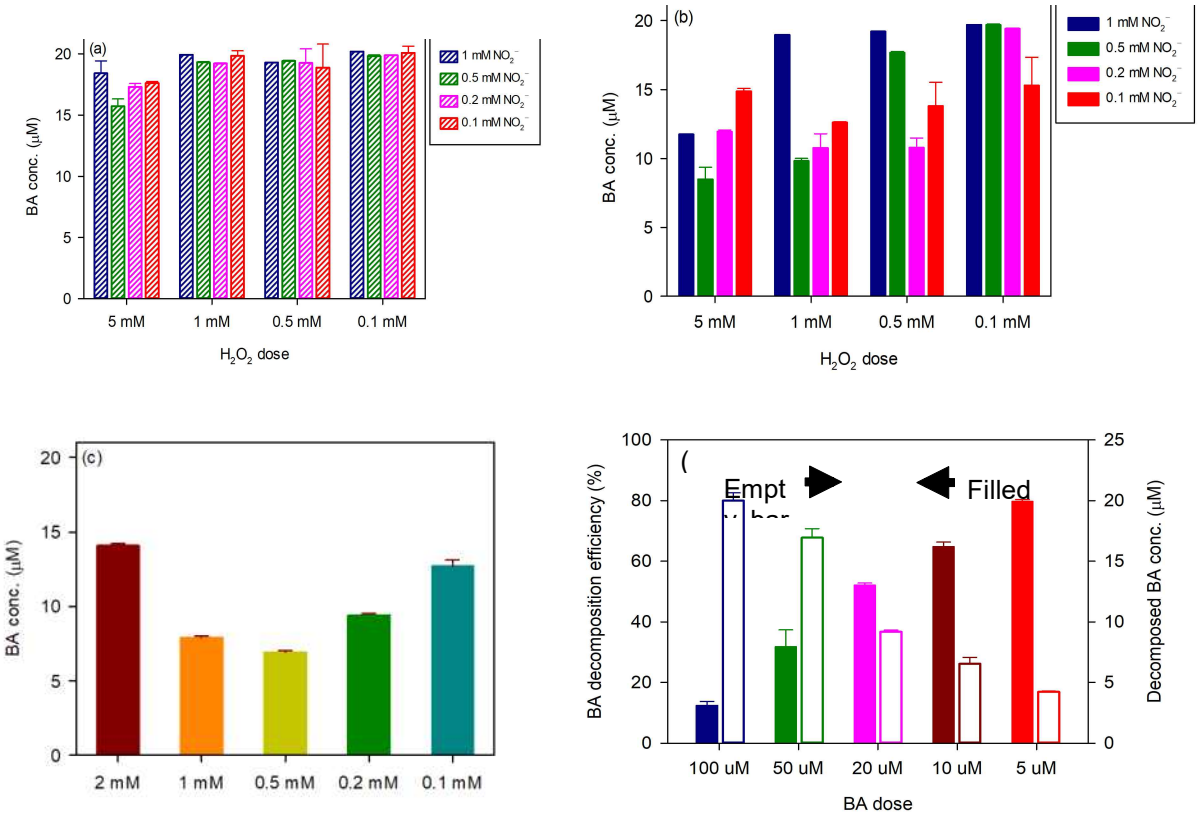



Fig. 4. The influence of the initial $H_2O_2$:$NO_2^-$ ratio on the BA decomposition in (a) the aqueous, and (b) the frozen $H_2O_2$:$NO_2^-$ — system. Experimental conditions: [BA]0 = 20 μM; $pH_i$ = 4.0 (adjusted by $HClO_4$); Reaction time = 1 h; Temperature: the frozen system (Fz.) = −20 ℃; the aqueous system (Aq.) = 25 ℃. (c) The acidic aqueous system of pH 3. Experimental conditions: $[BA]_0$ = 20 μM; $[H_2O_2]_0$ = 1 mM; $pH_i$ = 3.0 (adjusted by $HClO_4$); Reaction time = 1 h. (d) The influence of the initial BA concentration on the BA decomposition in the frozen $H_2O_2$:$NO_2^-$ — system. Experimental conditions: $[H_2O_2]_0$ = 1 mM; $[NO_2^-]_0$ = 0.5 mM; $pH_i$ = 4.0 (adjusted by $HClO_4$); Reaction time = 1 h.

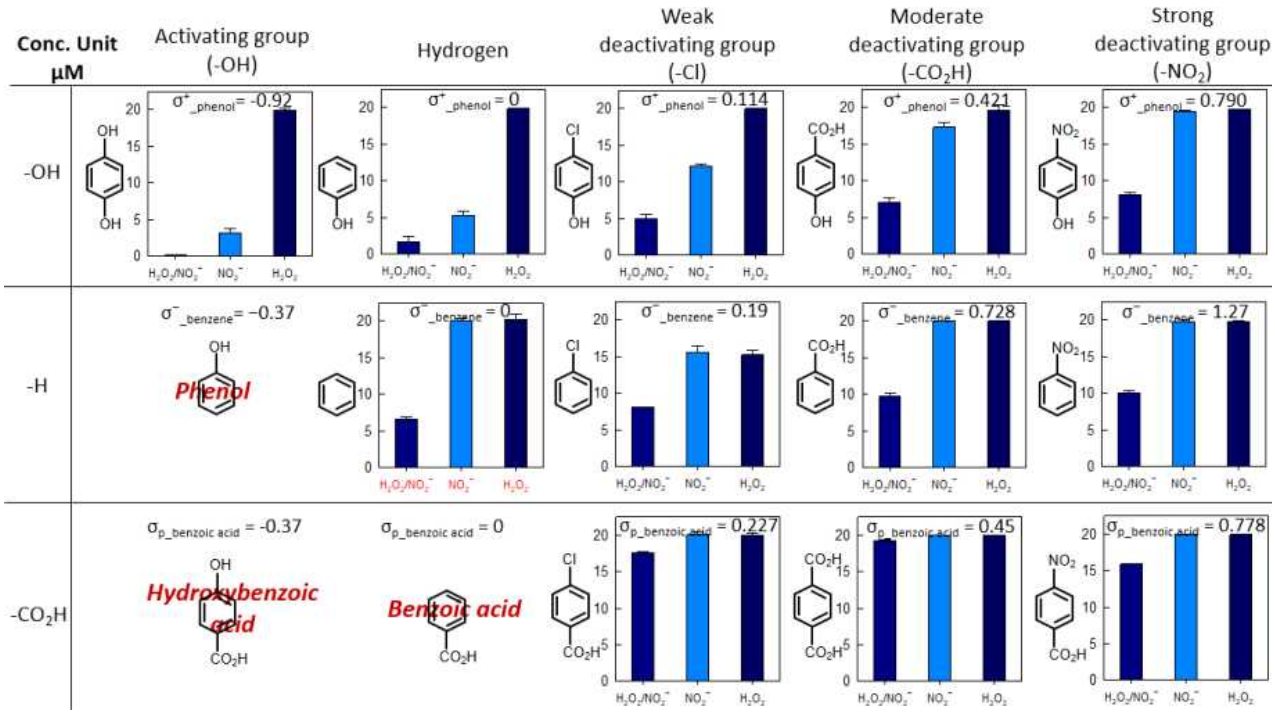



Fig. 5. Oxidative degradation of various benzene derivatives in the frozen $H_2O_2$:$NO_2^-$ system. Experimental conditions: $[Organics]_0$ = 20 μM; $[H_2O]_0$ = 1 mM; $[NO_2^-]0$ = 0.5 mM; pHi = 4.0; Reaction time = 1 h. The Hammett constants were obtained from the ref. 56-58.

KOPRI 극지연구소

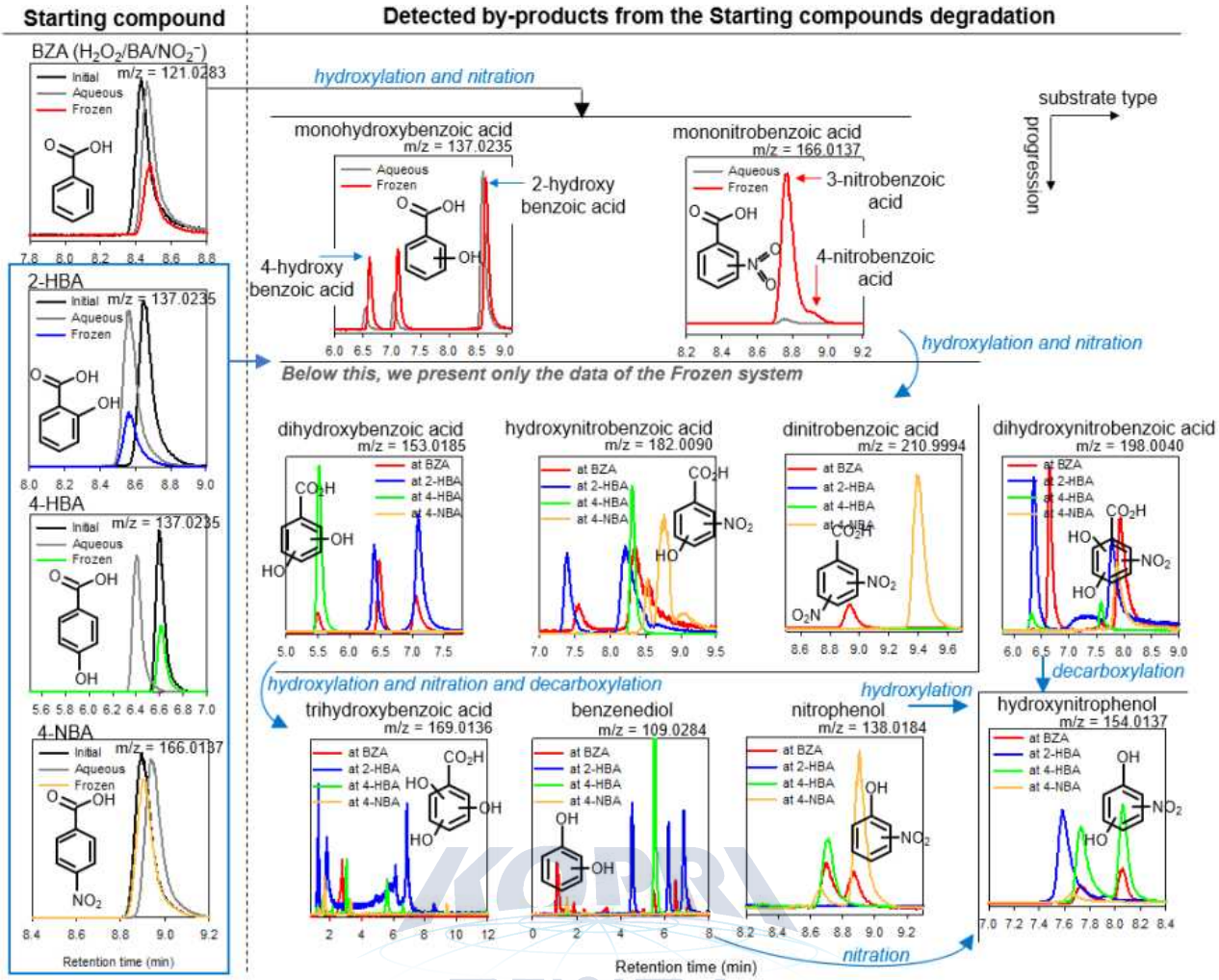



Fig. 6. The detected degradation by-products from LC-MS. Experimental conditions: [Organics]0 = 20 μM; $[H_2O_2]_0$ = 1 mM; $[NO_2^-]_0$ = 0.5 mM; pHi = 4.0 (adjusted by $HClO_4$); Temperature: the frozen system = −20 ℃; the aqueous system = 25 ℃; Reaction time = 1 h.

KOPRI 극지연구소

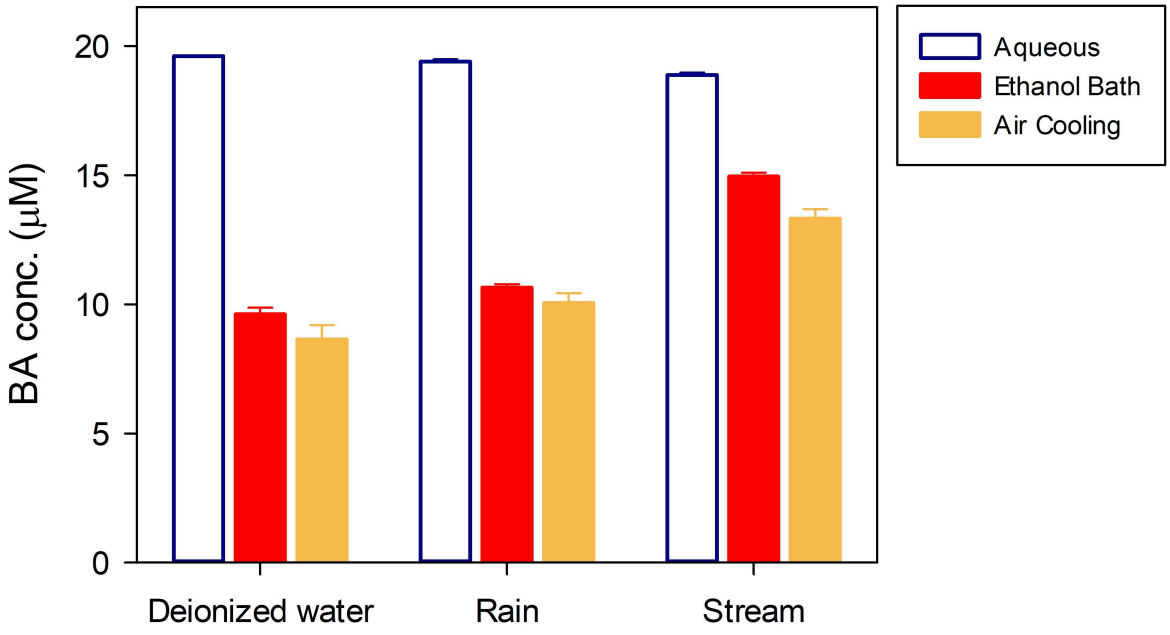



Fig. 7. The BA degradation by the $H_2O_2/NO_2^-$ system at natural imitated environments. Experimental conditions: $[BA]_0$ = 20 μM; $[NO_2^-]_0$ = 0.5 mM; $[H_2O_2]_0$ = 1 mM; Temperature: the frozen system (Fz.) = −20℃; the aqueous system (Aq.) = 25℃; Reaction time = 2 h; pH = 4 (adjusted by $HClO_4$).

KOPRI 극지연구소

# 제 7 절. Ten-Minute Synthesis of Highly Conductive Polymer Nanosheets on Ice Surfaces: Role of Ice Crystallinity⑦

Kyoungwook Kim[1], Bomi Kim[2], Kitae Kim[2], and Moon Jeong Park[1]

[1]Department of Chemistry, Division of Advanced Materials Science, Pohang University of Science and Technology (POSTECH)

[2]Korea Polar Research Institute (KOPRI)

## Abstract

Conducting polymers have been studied widely over the past decades for use as organic electrode materials owing to their high electrical conductivity and low-cost synthesis. Among the various synthesis methods reported, the recently established ice-assisted approach for developing conducting polymer nanosheets is regarded an advanced technology that allows for easy fabrication in an ecofriendly manner. However, the role of the crystallinity of the underlying ice surface in determining the physicochemical properties of the conducting polymers remains unclear. Here, the electronic properties and packing structure of polyaniline (PANI) nanosheets formed on ice surfaces are studied by controlling the ice crystallinity. Intriguingly, the crystallinity of the PANI nanosheets resembles that of the ice surfaces, in that the anisotropic growth of the PANI crystals with a face-on orientation occurs preferentially on high-crystalline ice surfaces. In addition, it is found that the development of highly crystalline PANI nanosheets results in efficient charge transport, owing to polaron delocalization in PANI with extended chain conformations and the improvement in the degree of backbone ordering because of the pre-organized aniline moieties on the ice surface.

## 1. Introduction

The ice-assisted synthesis of various functional materials has seen remarkable developments in the past few decades.[1-9] Owing to its advantages of a being simple technique (all that is involved is freezing and thawing), ice-related chemistry has been used successfully in various applications.[6,8,9-13] Representative examples of this include the design of ordered porous materials through the directional freezing technique,[3,14-16] with the aim of developing bioinspired materials with excellent mechanical properties[4,5,17,18] as well

⑦ 이 연구는 본 과제(PE21120)와 대한민국 과학기술정보통신부가 한국연구재단을 통하여 지원하는 과제(No. NRF-2017R1A2B3004763, No. 2018M3D1A1058624)의 지원을 받았으며, *Macromol. Rapid Commun.*, 2021, 42, 2100565에 출간되었음.

as high-performance electrodes with large surface areas for batteries and supercapacitors.[19-22]

Considering that ice inherently contains many impurities, ingenious approaches have been proposed for removing organic/inorganic contaminants from (ocean) water by freezing while controlling solute rejection and/or redistribution.[23-26] These research efforts have shown that freezing induces changes in the pH of salty water as cations and anions are rejected with different kinetics upon freezing, resulting in a charge imbalance, which is mitigated by the diffusion of protons and hydroxide ions.[27,28] This allows for unexpected chemical reactions to occur under cold conditions. For example, the oxidative decomposition of gallic acid occurs in acidic aqueous solutions upon freezing.[29] Based on the freeze concentration effect, cases of accelerated chemical reactions/biological processes at the interfaces of ice crystals have also been reported.[2,30,31] This implies that ice interfaces can serve as a unique chemical environment in which unprecedented chemical reactions can occur.

In this context, quasi-liquid layers (QLLs) formed on ice surfaces have long attracted research interest.[32-34] Progressing from being able to explain how one can skate on ice based on the discovery of QLLs centuries ago,[32] it has now been shown that while QLLs exhibit most of the physiochemical characterstics between solid ice and liquid water, some of their other important properties, such as their refractive index, are similar to those of liquid water.[33] Theoretical studies based on molecular dynamics simulations have further revealed that the diffusion coefficient of water molecules is higher in QLLs than that in bulk water. This is attributable to the lower connectivity of the hydrogen-bonding networks at the air - QLL interface.[34] The reported thickness of QLLs on ice surfaces varies from several angstroms to tens of nanometers as determined by several experimental and theoretical studies.[35-39] However, the exact range is still a subject of debate. Their thickness was found to be primarily dependent on the temperature. However, QLLs can even exist at temperatures as low as -70 ℃.[36,40] A recent study of ice surfaces using laser confocal microscopy coupled with differential interference contrast microscopy revealed that the formation of QLLs is affected by the crystalline nature of the ice used.[41] While it is fair to say that many phenomena that occur on the ice surface are yet unknown, QLLs, which form spontaneously at different temperatures, have high potential as a reaction space for facilitating chemical reactions.

Recent works by Park et al. on the formation of two-dimensional sheet-like conducting polymers on ice surfaces within a short reaction time (less than 5 min) are of significant importance in this regard. Nanosheets with high crystallinity and improved electrical conductivity (~ 30 S $cm^{-1}$) were established for ice-templated polyaniline (PANI)[42,43] and poly(3,4-ethylenedioxythiophene): poly(styrenesulfonate).[44] This was in stark contrast to the results of previous studies, which reported the formation of one-dimensional nanofiber

structures with low crystallinity and conductivity (less than 1 S $cm^{-1}$).[45] However, the underlying mechanism responsible for the effects of the crystallinity of the ice surface on the packing structure and electrical properties of the ice-templated conducting polymer nanosheets remains unknown. Here, we report the synthesis of PANI nanosheets on ice surfaces by controlling the crystallinity of the ice. Defect-free PANI nanosheets were obtained regardless of the crystallinity of the ice template. However, their electrical properties, packing structure, and crystal orientation could be significantly modulated by varying the crystallinity. Highly conducting PANI nanosheets were formed on highly crystalline ice surfaces, owing to polaron delocalization in PANI with extended chain conformations and the improved backbone ordering because of the ice-induced π-π stacking interactions.

## 2. Results and Discussion

Figure 1 shows the process for synthesizing PANI nanosheets on ice surfaces. First, a 0.25 M aniline solution in 1 M HCl was cast onto the ice surface at -5 °C. This was followed by the addition of a 0.25 M ammonium persulfate solution in 1 M HCl. After 5 min of the chemical oxidative polymerization of PANI on the ice surface at a constant temperature of -5 °C, it was observed that the colorless ice surface gradually turned blue, indicating the formation of pernigraniline salt. When the reaction was allowed to last for 10 min, the blue surface layer turned green, and PANI in the emeraldine salt state was formed.

The modulation of the crystallinity of the ice template used was the key strategy for controlling the electronic properties of the formed PANI nanosheets. For this, polyethylene glycol (PEG, Mn = 4,600 g $mol^{-1}$) was introduced as an oncotic agent during the freezing of the ice at -20 ℃.[46] Although the amount of PEG added was varied systematically to control the crystallinity of the ice, for brevity, we will discuss only the representative data obtained for an ice sample containing 2.5 wt% PEG (hereafter referred to as PEG-ice), which allowed for the defect-free synthesis of PANI nanosheets. Differential scanning calorimetry showed that the heat of melting and crystallization temperature of PEG-ice were lower than those of pure ice, resulting in a decrease in the degree of crystallinity from 92.4% (pure ice) to 76.0% (PEG-ice) (Figure S1). This was indicative of the cryoprotective effect of the added PEG.[46] Despite these differences in the ice crystallinities, the polymerization kinetics of PANI were not significantly affected. Thus, all the PANI nanosheets discussed in this study were obtained through a reaction performed at -5 ℃ for 10 min.

The optical micrographs in Figure 2a and 2b show the crystal grains formed on the pure

ice and PEG-ice surfaces; it can be seen that the average grain size is approximately 10 - 20 mm. The PEG mapping of PEG-ice was performed using low-temperature Raman spectroscopy based on the $CH_2$ scissoring vibrations of PEG at 1475 $cm^{-1}$; the exposure time was 0.1 s, and a 532-nm laser was used for the measurements. It was evident that PEG was highly localized in the liquid-like region at the grain boundaries of the ice crystals. As can be seen from Figure 2c, despite the difference in their crystallinities, both the pure ice and PEG-ice templates prepared at -20 °C have smooth surfaces that are free of cracks. Bright-field transmission electron microscopy (TEM) images of the PANI nanosheets formed on pure ice and PEG-ice are shown in Figure 2d and 2e, respectively. It can be seen that, qualitatively, the sheets have the same morphology and are free of nanofiber structures. We would like to mention that we deliberately show the parts with marked defects; otherwise, it would be difficult to distinguish the presence of thin sheets over a large area.

Next, we investigated the electrical properties of the ice-templated PANI nanosheets. The synthesized PANI nanosheets were transferred from the ice surfaces onto $Si/SiO_2$ wafers with gold electrodes (10 μm width and 10 μm gap) via the floating-off method, and their current - voltage profiles were evaluated. Figure 3a shows representative linear sweep voltammograms of the PANI nanosheets, measured in the voltage range of -1.0 to 1.0 V at room temperature. The thickness of each PANI film was measured using the height profile mode of a scanning probe microscope (SPM). The average thickness was 70 ± 4 nm, regardless of the type of ice template used. The representative height profile of a PANI nanosheet formed on pure ice is shown in the inset. The current values were normalized based on the thickness and area of the PANI nanosheets. As can be seen from the figure, the pure-ice-templated PANI nanosheet showed a high current flow of 19.6 A $cm^{-1}$ at 1.0 V, which was three times higher than that (6.7 A cm-1) of its PEG-ice-templated counterpart.

The electrical conductivity of each PANI nanosheet was calculated using the following equation:

$$\sigma = \frac{L \cdot I}{V \cdot A} \quad (1)$$

where L is the distance between the gold electrodes (10 μm), I is the current value, V is the applied voltage, and A is the cross-sectional area of the sample placed between the gap of the gold electrodes. The conductivities of the PANI sheets formed on pure ice and PEG-ice were highly dissimilar at 19.6 and 6.7 S cm-1, respectively, indicating that the electrical conductivity of ice-templated PANI decreases with a decrease in the crystallinity

of the ice template used. Nevertheless, considering that the commonly reported electrical conductivity of HCl-doped PANI is less than 1 S $cm^{-1}$,[45] it is likely that electron transfer occurs in ice-templated PANI nanosheets. It should also be noted that when PANI was synthesized by the chemical oxidative polymerization of an aniline solution containing PEG, typical nanofiber structures were formed, and the electrical conductivity was as low as 0.9 S $cm^{-1}$ (Figure S2). This confirms that the effect of the added PEG on the synthesis and electrical properties of PANI is not significant because the π-π stacking interactions of PANI are stronger than the interchain hydrogen bonding interactions of PEG and PANI.

To elucidate the mechanism responsible for the ice-crystallinity dependence of the electrical conductivity of PANI, the UV-visible spectra of the PANI nanosheets were measured. As shown in Figure 3b, the absorption peaks at 360, 432, and 877 nm seen in the case of PANI on pure ice correspond to π-$\pi^*$ transitions, polaron-$\pi^*$ transitions, and π-polaron transitions, respectively, indicating that the synthesized PANI nanosheets were in the emeraldine salt state.[47] While PANI on PEG-ice also showed analogous peaks related to π-$\pi^*$ transitions and polaron-π* transitions at 360 nm and 432 nm, respectively, the peak related to π-polaron transitions was significantly blue-shifted to 820 nm. This indicates that the polaron band of PANI on PEG-ice is narrow; this conclusion is in keeping with the conductivity results. Thus, the electronic structure of PANI nanosheets can be tuned through a simple but powerful ice-templated method based on the control of the crystallinity of the ice template.

Next, we examined the chemical structures of the ice-templated PANI nanosheets. As shown in Figure 4a, the PANI nanosheets showed similar FT-IR spectra, regardless of the type of ice template used. In addition, there was no noticeable difference in the doping levels of the PANI nanosheets, with all the peaks showing a similar peak ratio (approximately 1) for the peak related to quinoid at 1564 $cm^{-1}$ and that related to benzenoid at 1482 $cm^{-1}$. This indicated that both types of PANI nanosheets were in the emeraldine salt state.[48] A peak related to the C-N stretching vibrations in the quinoid-benzenoid-quinoid unit was seen at 1385 $cm^{-1}$ along with peaks related to secondary amines at 1296 and 1240 $cm^{-1}$ and a peak related to the C-H bending vibrations at 1122 $cm^{-1}$. Moreover, the intensities of the peaks of the two samples were similar. Hence, the higher conductivity of PANI on pure ice, which was three times that of PANI on PEG-ice, does not have a chemical origin. It was also confirmed that an undetectable amount of PEG remained in the PANI formed on PEG-ice.

The mechanism underlying the variations in the conductivity of PANI with the crystallinity of the ice template used was explored using low-temperature in-situ Raman spectroscopy. Figure 4b shows representative Raman spectra of the PANI nanosheets formed on pure ice and PEG-ice as measured after a 10-min reaction at -5 ℃ (without

KOPRI 극지연구소

tranferring steps onto other substrates). The characteristic peaks of PANI are assigned in the figure. Overall, the Raman intensities of the PANI nanosheets formed on PEG-ice were low. This was presumably owing to the low crystallinity of PANI on PEG-ice (see X-ray diffraction patterns in Figure S3), given that the Raman spectrum of a material is largely determined by its degree of ordering. This hypothesis was confirmed through Raman measurements performed on PANI films of similar thicknesses prepared by the conventional chemical oxidative polymerization of an aniline solution (Figure S4). The spectra were poorly resolved to the extent that it was difficult to assign the characteristic peaks.

Intriguingly, the Raman spectra of the PANI nanosheets formed on the different ice templates exhibited markedly different characteristic peaks. The two peaks at 1373 and 1630 $cm^{-1}$ correspond to the delocalized polarons in PANI.[49,50] These peaks were considerably weaker in the case of PANI on PEG-ice: $I_{1373}$ /$I_{1174}$ of 0.69 (pure ice), $I_{1364}$ /$I_{1166}$ of 0.24 (PEG-ice), $I_{1630}$ /$I_{1174}$ of 1.30 (pure ice), and $I_{1630}$ /$I_{1166}$ of 0.53 (PEG-ice). Nevertheless, given the fact that the Raman peaks of the delocalized polarons have rarely been observed in the case of PANI nanosheets synthesized through conventional methods (Figure S4), it can be assumed that polaron delocalization in the ice-templated PANI nanosheets has a determining effect on their conductivity, highlighting the unique advantages of ice surfaces as chemical reactors.

The appearance of these two peaks related to delocalized polarons can be attributed to the fact that the extended chain conformations improve the degree of ordering of the PANI backbones. It has been reported previously that PANI/graphene composites show polaron delocalization, which is attributable to graphene-induced π-π stacking interactions.[51,52] Moreover, in the case of solvent-treated camphorsulfonic-acid-doped PANI, the molecular packing of the PANI units is transformed from a random one to an ordered one.[50] Thus, ice templates play a crucial role in modulating the packing structure of the PANI units, resulting in a more planar structure with reduced backbone distortion. In addition, this effect becomes more pronounced when highly crystalline ice is used. We believe that the adsorption of aniline monomers onto the ice surface via hydrogen-bonding interactions at the beginning of the reaction is important for ensuring the packing of the preorganized monomers prior to polymerization.

To prove this, we performed in-situ grazing-incidence X-ray scattering (GIXS) experiments to elucidate the ordering of aniline on ice surfaces. For this, a thin ice substrate was prepared using Peltier modules to allow for both the reflection and transmission of the X-ray beam at the ice surfaces. Figure S5 shows a representative GIXS pattern, which was measured 5 min after casting the aniline monomer onto the ice surfaces at -5 °C. Intriguingly, a broad arc was observed at a q value of 17.5 $nm^{-1}$ in the out-of-plane direction; this corresponded to the π-π stacking of the aniline monomers

before the addition of ammonium persulfate. Thus, it can be inferred that the preorganization of the aniline moieties in QLLs occurs before polymerization, as stated above, and that the face-on orientation forms preferentially under the reaction conditions investigated in this study.

We further investigated the crystal orientations and packing structures of the ice-templated PANI nanosheets after their synthesis. For this, the PANI films were transferred onto Si wafers from the ice surfaces after a reaction time of 10 min via the float-off method. The GIXS patterns of the PANI nanosheets formed on pure ice and PEG-ice are shown in Figure 5a and 5b, respectively. For comparison, the results for solution-cast PANI formed on a Si wafer are also shown in Figure 5c; the solution was prepared by the conventional chemical oxidative polymerization of aniline. Scattering peaks were observed at q values of 6.3, 10.2, 14.4, and 17.6 $nm^{-1}$ in the case of all three samples; these corresponded to the (200), (201), (002), and (020) reflections of the PANI crystals.[42] Interestingly, a high-intensity arc pattern in the out-of-plane direction was again observed in the spectrum of the ice-templated PANI nanosheets. This dincated π-π stacked PANI molecules with a distance of 3.5 Å from an ice-surface-to-air to have face-on orientation. In addition, the strong in-plane peak related to the (200) plane with a spacing of 9.9 Å seen in the case of the ice-templated PANI nanosheets was indicative of laterally stacked lamellar crystals. The anisotropic orientation of the PANI crystals was in sharp contrast to the isotropic orientation of the conventional PANI structure.

To elucidate the role of the crystallinity of the ice substrate used on the crystalline structure of the formed PANI nanosheets, the 1D scattering intensity profiles of the three samples are shown in Figure 5d - e. The (020) π - π stacking peak was only visible in the out-of-plane direction in the case of the PANI nanosheets formed on pure ice (Figure 5d). On the other hand, although anisotropy was still observed, the PANI nanosheets formed on PEG-ice showed a π-π stacking peak in both the in-plane and out-of-plane directions (Figure 5e), as indicated by shading. Moreover, the scattering intensities of the (201) and (002) peaks were relatively stronger in the in-plane profile of the PANI nanosheets formed on pure ice compared with those of the PEG-ice-templated PANI nanosheets. Hence, one can conclude that the anisotropic growth of PANI crystals occurs predominantly on highly crystalline ice surfaces with a face-on orientation. With respect to the isotropic GIXS pattern of the conventional PANI films, the peak intensities in both the in-plane and out-of-plane profiles were similar, as shown in Figure 5f. This meant that the PANI nanosheets were randomly oriented and suggested that the use of an ice template is the key to synthesizing anisotropically arranged PANI crystals, as their orientation and packing structure are affected by the crystallinity of the underlying ice surface.

The proportion of the crystals with a face-on orientation was assessed for each PANI

sample by analyzing the azimuthal pole figure of the (020) π - π stacking peak (Figure S6).[53] The ratios of the proportion of crystals with the face-on orientation to that of the crystals with the edge-on orientation were calculated to be 3.7 and 3.0 for the PANI nanosheets formed on pure ice and PEG-ice, respectively; in contrast, the ratio was close to unity for conventional PANI.

It should be noted that the ice-templated synthesis of two-dimensional sheet-like conducting polymers was first reported by our group in 2015.[42] In our previous study, we had set the reaction temperature to 0 °C. However, we had observed significant surface melting of PEG-ice at this temperature. Therefore, the reaction temperature was lowered to -5 °C in the present study. However, this meant that more time was required to ensure that the aniline monomer uniformly covered the ice surfaces before the oxidizing agent was drop-cast on them (this was important for the formation of defect-free PANI nanosheets). We found that this caused a radical change in the π - π stacking direction, as we observed a dominant edge-on orientation in the case of the PANI nanosheets formed on ice surfaces at 0 ℃.

## 3. Conclusion

We studied the electrical properties, morphologies, and packing structures of PANI nanosheets formed on different types of ice surfaces with a focus on the effect of the crystallinity of the ice template used. By introducing 2.5-wt% PEG during the freezing of the ice at -20 °C, its crystallinity was lowered by 16%. This ice was then used as a template, and the results obtained were compared with those obtained with pure ice. The PANI nanosheets synthesized on both pure ice and PEG-ice exhibited a thickness of ~70 nm and had qualitatively similar morphologies, which were free of nanofiber structures. Furthermore, both types of nanosheets had a dominant face-on orientation and consisted of PANI crystals that showed anisotropic growth. In addition, the sheets showed high electrical conductivity, which was at least six times higher than the values commonly reported in the literature. Intriguingly, the electronic structure and crystal orientation appeared to be modulated by the crystallinity of the ice template used. The PANI nanosheets formed on pure ice showed a high conductivity of 19.6 S $cm^{-1}$ while the PEG-ice-templated nanosheets showed a value that was three times lower (6.7 S $cm^{-1}$). This enhancement can be attributed to the widening of the polaron band as well as the strong delocalized polarons in the PANI nanosheets formed on the highly crystalline ice surface, which is unprecedented. This results in an extended chain conformation and improvements in the backbone ordering of the PANI crystals because of the strong π-π stacking interactions, leading to a more planar structure. It was determined that the simple

preorganization of the aniline monomers on the ice template surface before polymerization is the key to the development of this packing structure. Thus, the proposed method should allow for the easy tuning of the electrical properties of conducting polymer films through a simple but powerful ice-assisted approach.

KOPRI
극지연구소

## REFERENCES


1. F. Yokoyama, I. Masada, K. Shimamura, T. Ikawa, K. Monobe, *Colloid Polym. Sci.* **1986**, *264*, 595.
2. N. Takenaka, A. Ueda,Y. Maeda, *Nature* **1992**, *358*, 736.
3. H. Zhang, I. Hussain, M. Brust, M. F. Butler, S. P. Rannard, A. I. Cooper, *Nature* **2005**, *4*, 787.
4. S. Deville, E. Saiz, R. K. Nalla, A. P. Tomsia, *Science* **2006**, *311*, 515.
5. E. Munch, M. E. Launey, D. H. Alsem, E. Saiz, A. P. Tomsia, R. O. Ritchie, *Science* **2008**, *322*, 1516.
6. G. Kim, C. Jo , W. Kim , J. Chun , S. Yoon , J. Lee, W. Choi, *Energy Environ. Sci.*, **2013**, *6*, 2932.
7. Q. Zhang, S. Huang, J. Deng, D. T. Gangadharan, F. Yang, Z. Xu, G. Giorgi, M. Palummo, M. Chaker, D. Ma, *Adv. Funct. Mater.* **2019**, *29*, 1902486.
8. I. M. Minisy, P. Bober, *Macromol. Rapid Commun.* **2020**, *41*, 2000364.
9. R. Du, J.-O. Joswig, R. Hübner, L. Zhou, W. Wei, Y. Hu, A. Eychmüller, *Angew. Chem. Int. Ed.* **2020**, *59*, 8293.
10. Q. Shi, Z. An, C.-K. Tsung, H. Liang, N. Zheng, C. J. Hawker, G. D. Stucky, *Adv. Mater.* **2007**, *19*, 4539.
11. A. Borisova, M. De Bruyn, V. L. Budarin, P. S. Shuttleworth, J. R. Dodson, M. L. Segatto, J. H. Clark, *Macromol. Rapid Commun.* **2015**, *36*, 774.
12. D. Chen, X. Xia, T. W. Wong, H. Bai, M. Behl, Q. Zhao, A. Lendlein, T. Xie, *Macromol. Rapid Commun.* **2017**, *38*, 1600746.
13. S. Jiang, N. Helfricht, G. Papastavrou, A. Greiner, S. Agarwai, *Macromol. Rapid Commun.* **2018**, *39*, 1700838.
14. J.-W. Kim, K. Tazumi, R. Okaji, M. Ohshima, *Chem. Mater.* **2009**, *21*, 3476.
15. S. An, H. J. Kim, S. Chi, J. Lee, *Macromol. Rapid Commun.* **2018**, *39*, 1800106.
16. L. Liu, L. Bai, A. Tripathi, J. Yu, Z. Wang, M. Borghei, Y. Fan, O. J. Rojas, *ACS Nano* **2019**, *13*, 2927.
17. L. Qiu, J. Z. Liu, S. L. Y. Chang, Y. Wu, D. Li, *Nat. Commun.* **2012**, *3*, 1241.
18. D. Li, X. Bu, Z. Xu, Y. Luo, H. Bai, *Adv. Mater.* **2020**, *32*, 2001222.
19. Y. Shao, M. F. El-Kady, C.-W. Lin, G. Zhu, K. L. Marsh, J. Y. Hwang, Q. Zhang, Y. Li, H. Wang, R. B. Kaner, *Adv. Mater.* **2016**, *28*, 6719.
20. X. Zhang, Z. Ju, L. M. Housel, L. Wang, Y. Zhu, G. Singh, N. Sadique, K. J. Takeuchi, E. S. Takeuchi, A. C. Marschilok, G. Yu, *Nano Lett.* **2019**, *19*, 8255.


KOPRI 극지연구소

21. X. Yang, Q. sun, C. Zhao, X. Gao, K. R. Adair, Y. Liu, J. Luo, X. Lin, J. Liang, H. Huang, L. Zhang, R. Yang, S. Lu, R. Li, X. Sun, *Nano Energy* **2019**, *61*, 567.

22. N. Wang, X. Zhang, Z. Ju, X. Yu, Y. Wang, Y. Du, Z. Bai, S. Dou, G. Yu, *Nat. Commun.* **2021**, *12*, 4519.

23. O. Lorain, P. Thiebaud, E. Badorc, Y. Aurelle, *Water. Res.* **2001**, *35*, 541.

24. Y. Choi, H.-I. Yoon, C. Lee, L. Vetráková, D. Heger, K. Kim, J. Kim, *Environ. Sci. Technol.* **2018**, *52*, 5378.

25. N. T. H. Le, J. Ju, B. Kim, M. S. Kim, C. Lee, S. Kim, W. Choi, K. Kim, J. Kim, *Chem. Eng. J.* **2020**, *388*, 124226.

26. K. Kim, H. Y. Chung, B. Kim, G. Wong, A. Q. K. Nguyen, S. Kim, J. Kim, *Environ. Sci. Technol.* **2020**, *54*, 16204.

27. Watanabe, T. Otsuka, M. Harada, T. Okada, *J. Phys. Chem. C* **2014**, *118*, 15723.

28. C. Robinson, C. S. Boxe, M. I. Guzman, A. J. Colussi, M. R. Hoffmann, *J. Phys. Chem. B* **2006**, *110*, 7613.

29. N. Takenaka, M. Tanaka, K. Okitsu, H. Bandow, *J. Phys. Chem. A* **2006**, *110*, 10628.

30. V. I. Lozinsky, R. V. Ivanov, E. V. Kalinina, G. I. Timofeeva, A. R. Khokhlov, *Macromol. Rapid Commun.* **2001**, *22*, 1441.

31. S. Ahmed, S. Fujita, K. Matsumura, *Nanoscale* **2016**, *8*, 15888.

32. M. Faraday, *Philos. Mag.* **1859**, *17*, 162.

33. Y. Furukawa, *J. Cryst. Growth* **1987**, *82*, 665.

34. T. Kling, F. Kling, D. Donadio, *J. Phys. Chem. C* **2018**, *122*, 24780.

35. Y. Furukawa, M. Yamamoto, T. Kuroda, *J. Cryst. Growth* **1987**, *82*, 665.

36. V. Sadtchenko, G. E. Ewing, *J. Chem. Phys.* **2002**, *116*, 4686.

37. M. M. Conde, C. Vega and A. Patrykiejew, *J. Chem. Phys.* **2008**, *129*, 014702.

38. D. T. Limmer, D. Chandler, *J. Chem. Phys.* **2014**, *141*, 18C505.

39. I. Pickering, M. Paleico, Y. A. P. Sirkin, D. A. Scherlis, M. H. Factorovich, *J. Phys. Chem. B* **2018**, *122*, 4880.

40. Wei, P. B. Miranda, Y. R. Shen, *Phys. Rev. Lett.* **2001**, *86*, 1554.

41. H. Asakawa, G. Sazaki, K. Nagashima, S. Nakatsubo, Y. Furukawa, *Cryst. Growth Des.* **2015**, *15*, 3339.

42. I. Y. Choi, J. Lee, H. Ahn, J. Lee, H. C. Choi, M. J. Park, *Angew. Chem. Int. Ed.* **2015**, *54*, 10497.

43. K. Kim, H. Ahn, M. J. Park, *ACS Appl. Mater. Interface* **2017**, *9*, 30278.

KOPRI 극지연구소

44. D. Barpuzary, K. Kim, M. J. Park, *ACS Nano* **2019**, *13*, 3953.

45. J. Huang, R. B. Kaner, *J. Am. Chem. Soc.* **2004**, *126*, 851.

46. Y. E. Yagci, M. Antonietti, H. G. G. Börner, *Macromol. Rapid Commun.* **2006**, *27*, 1660.

47. E. Dmitrieva, L. Dunsch, *J. Phys. Chem. B* **2011**, *115*, 6401.

48. T. Abdiryim, Z. Xiao-Gang, R. Jama, *Mater. Chem. Phys.* **2005**, *90*, 367.

49. L. Wang, Q. Yao, H. Bi, F. Huang, Q. Wang, L. Chen, *J. Mater. Chem. A* **2015**, *3*, 7086.

50. Q. Yao, Q. Wang, L. Wang, Y. Wang, J. Sun, H. Zeng, Z. Jin, X. Huang, L. Chen, *J. Mater. Chem. A* **2014**, *2*, 2634.

51. L. Wang, Q. Yao, H. Bi, F. Huang, Q. Wang, L. Chen, *J. Mater. Chem. A* **2015**, *3*, 7086.

52. F. Liu, S. Luo, D. Liu, W. Chen, Y. Huang, L. Dong, L. Wang, *ACS Appl. Mater. Interfaces* **2017**, *9*, 33791.

53. V. Vohra, K. Kawashima, T. Kakara, T. Koganezawa, I. Osaka, K. Takimiya, H. Murata, *Nat. Photonics* **2015**, *9*, 403.

KOPRI
극지연구소

## FIGURES

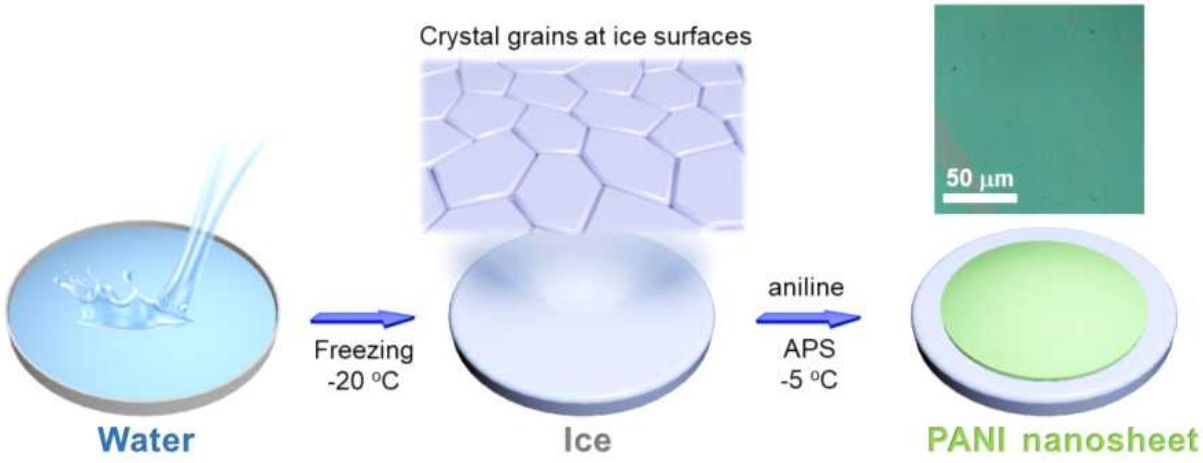
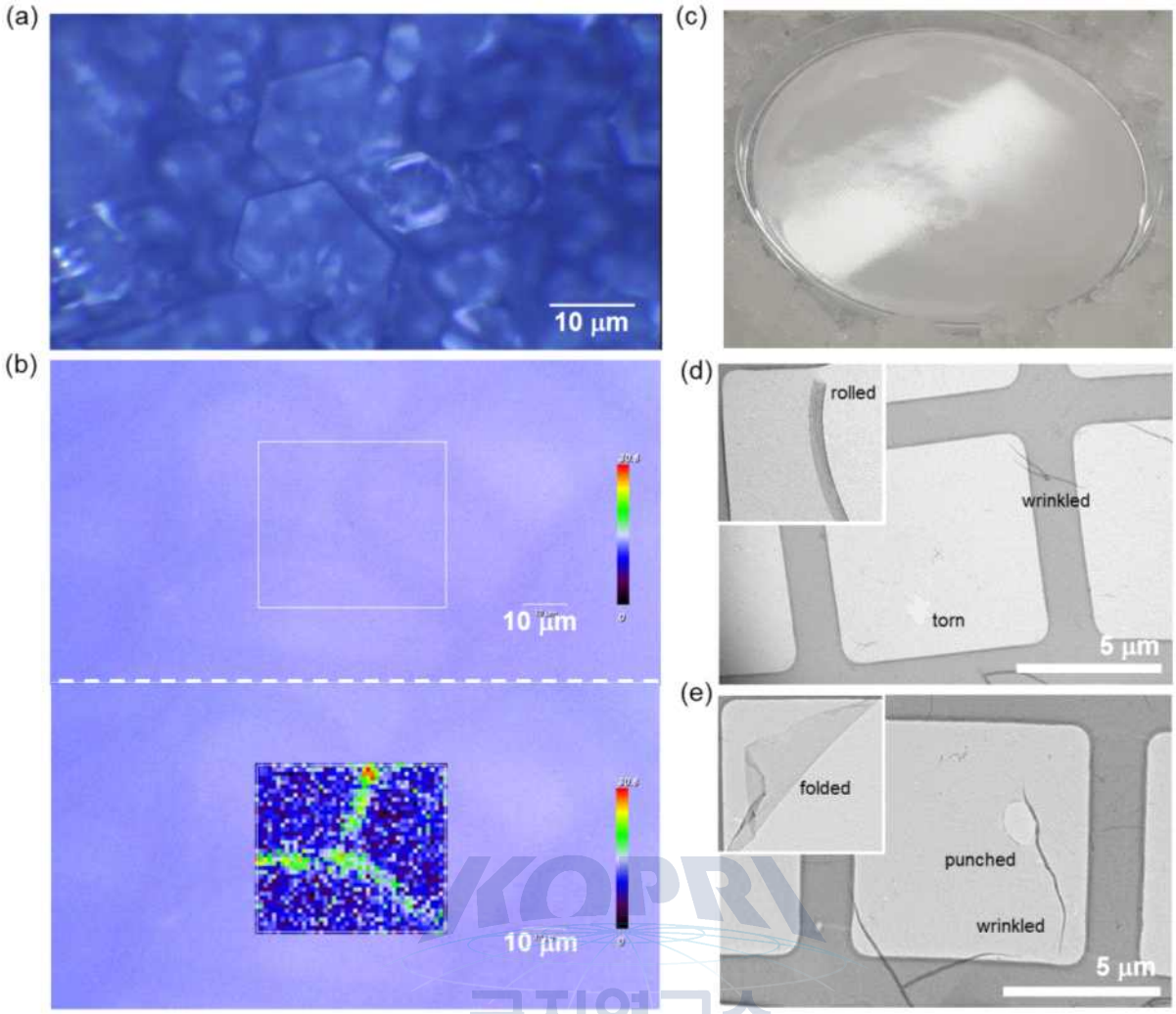



Fig. 1. Schematic illustration of synthesis of PANI nanosheets on ice surfaces with controlled ice crystallinity.

KOPRI
극지연구소




KOPRI
극지연구소

Fig. 2. Optical micrographs of (a) pure ice and (b) PEG-ice surfaces. Image shown at bottom of (b) represents PEG-map obtained using Raman spectroscopy. (c) Digital photograph of PEG-ice showing smooth surface. TEM images of PANI with sheet-like morphology formed on (d) pure ice and (e) PEG-ice.

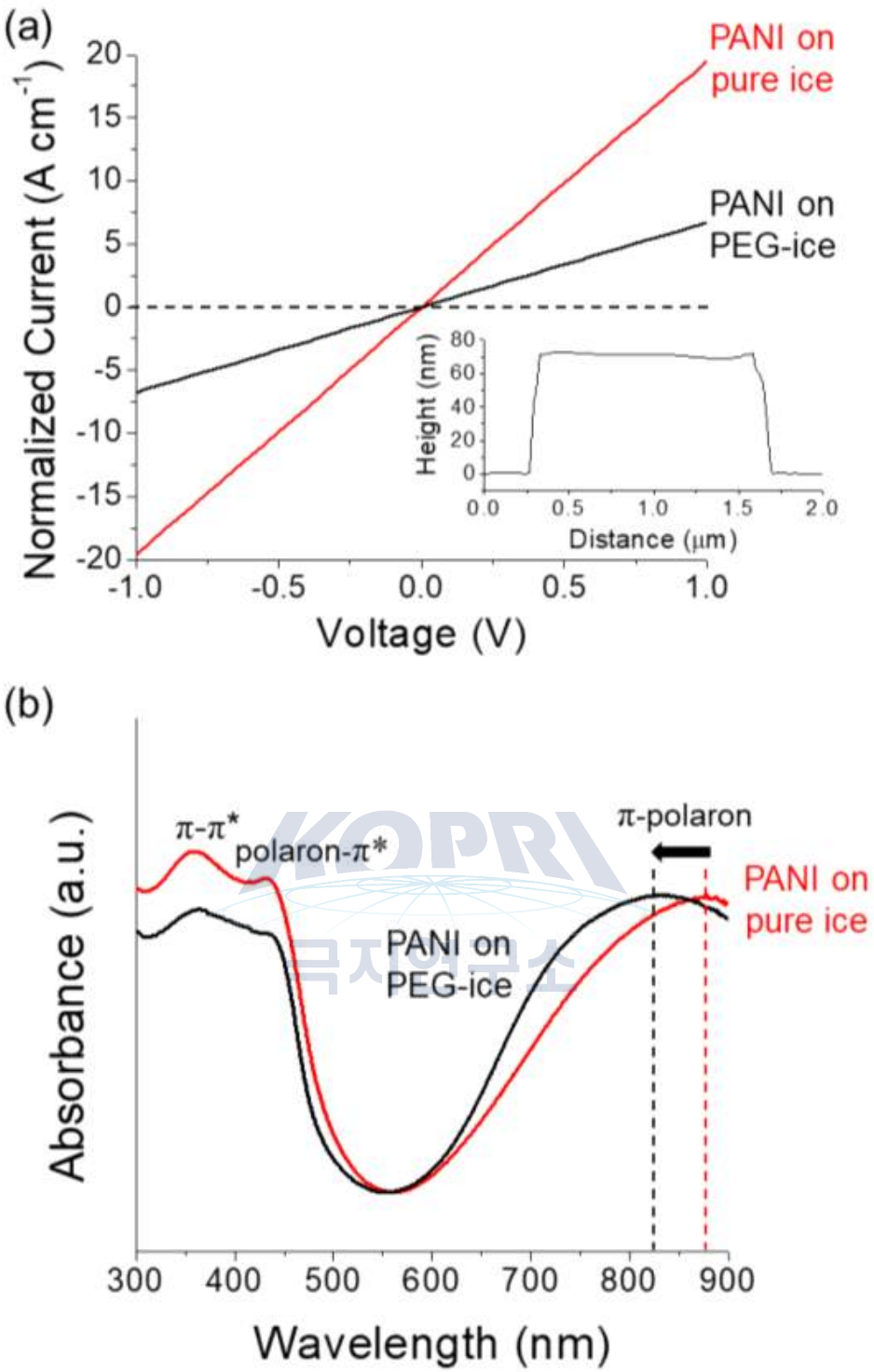



Fig. 3. (a) Normalized currents of PANI nanosheets formed on pure ice and PEG-ice for voltage sweep in range of -1 V to 1V. Thickness of each film as estimated using SPM was ~ 70 nm. (b) UV-visible spectra of ice-templated PANI nanosheets formed using pure ice and PEG-ice.

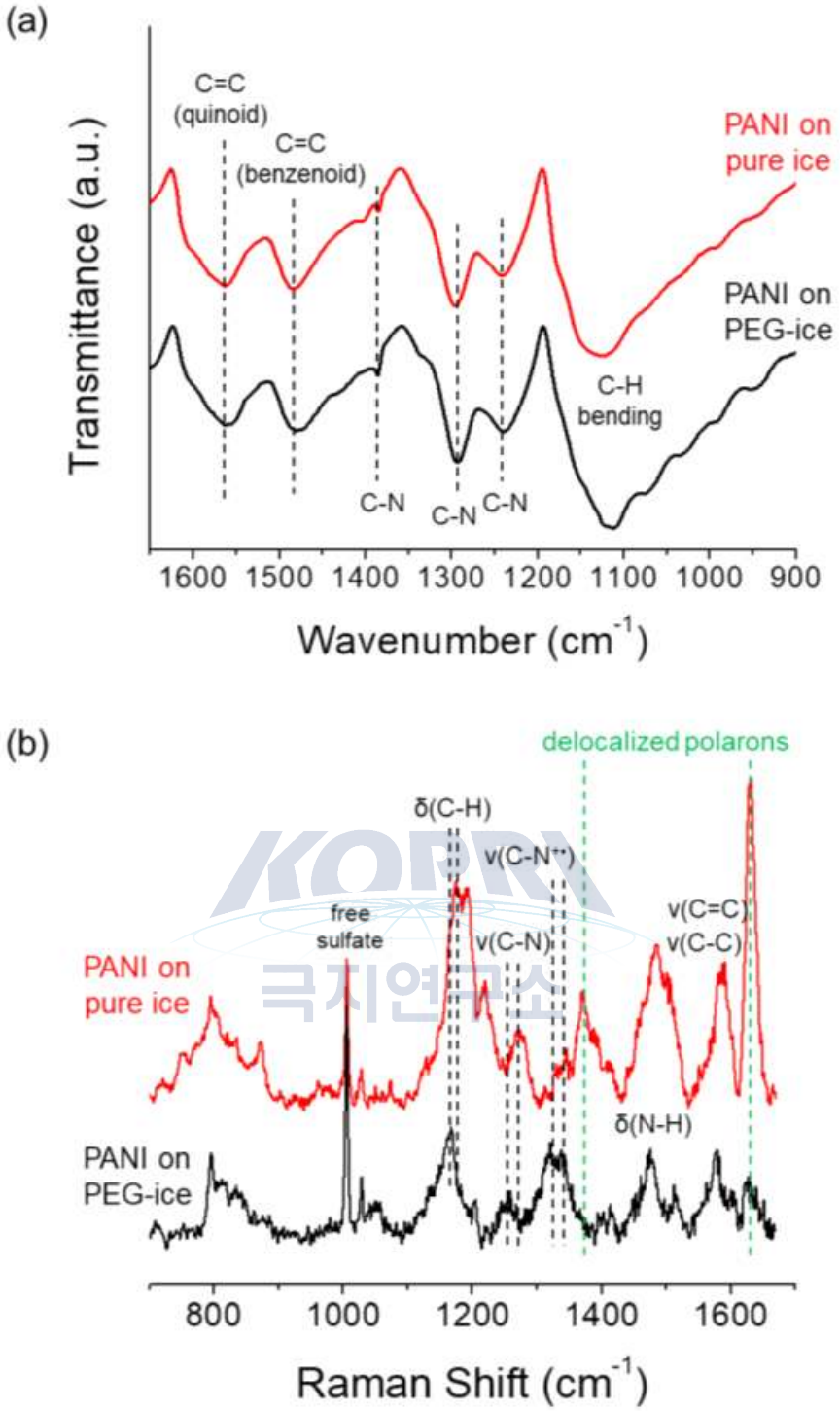



Fig. 4. (a) FT-IR spectra and (b) low-temperature in-situ Raman spectra of PANI nanosheets formed on pure ice and PEG-ice.

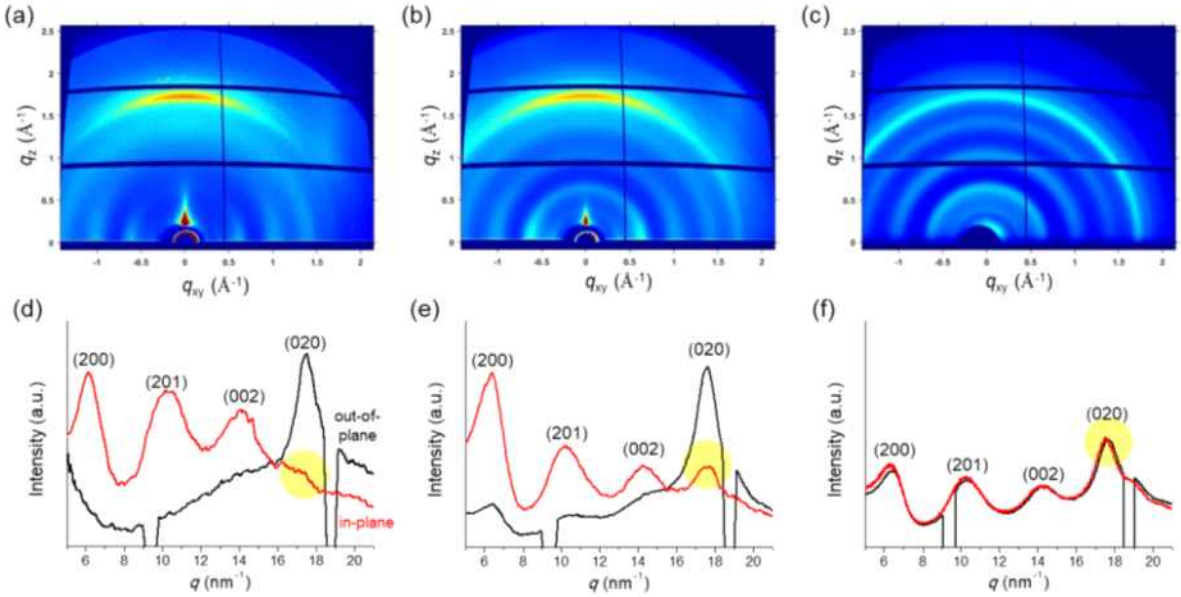



Fig. 5. 2D GIXS patterns and 1D scattering profiles of PANI nanosheets formed on (a, d) pure ice and (b, e) PEG-ice and (c, f) those of conventional PANI. In-plane (020) peaks are shaded to highlight difference in π-π stacking intensities along in-plane direction.

KOPRI
극지연구소

# 제 8 절. Activation of peroxymonosulfate by bicarbonate and acceleration of the reaction by freezing⑧

Yong-Yoon Ahn[1], Jungwon Kim[2], and Kitae Kim[1,3]

[1]Korea Polar Research Institute (KOPRI)

[2]Department of Environmental Science and Biotechnology, Hallym University

[3]Department of Polar Science, University of Science of Technology (UST)

## Abstract

This study demonstrates the positive effects of dissolved bicarbonate and carbonate anions on peroxymonosulfate (PMS) induced oxidation and the remarkable acceleration of the reaction by freezing. More than 90% of the initial 4-chlorophenol (4-CP) decomposed in the frozen case, whereas only less than 20% of the 4-CP was removed in the aqueous case in the same time period. This accelerated reaction is attributed to the freeze-concentration of the dissolved substrates (i.e., PMS, bicarbonate, and pollutants) in the quasi-liquid layer at the ice grain boundaries between ice crystals. The reaction between bicarbonate and PMS was found to be unique because none of the effects were observed in the phosphate and hydroxide cooperated system with freezing, although the base activation of PMS could participate under basic conditions (pH > 9). Based on electron paramagnetic resonance spectroscopy measurements and comparison with the photo-excited Rose Bengal system as a reference system for singlet oxygen ($^1O_2$) generation, $^1O_2$ was found to have a minor effect on the oxidation of 4-CP in the frozen bicarbonate-PMS system. While, direct electron transfer from the target organic substrate to the PMS was suggested as a major mechanism of 4-CP oxidation, because the selected target organic substrates were decomposed with different tendencies, and the consumption of PMS was accelerated by the presence of an electron donating compound. The results show the potential applicability of the freezing phenomenon, which occurs naturally in the mid-latitude and polar area, to help a decomposition of water dissolved organic pollutants by the imitation of the natural purification process.

⑧ 본 연구는 본 과제(PE21120)와 해양수산부 “극지 유래 생물자원을 활용한 항생제 후보물질 개발(15250103, KOPRI Grant PM21030)”의 지원으로 수행되었으며, 연구 결과는 *Sci. Total Environ.* 2021, 785, 147369에 출간되었다.

## 1. Introduction

The significance of temperature in chemical reactions is well known. Specifically, decreasing the temperature decreases the chemical reaction rate. Conversely, the acceleration of certain chemical reactions in the ice phase, which proceed relatively slowly in the aqueous phase, has been identified and studied.[1] These reactions include oxidation of nitrite by dissolved oxygen,[2,3] redox reactions between chromate and phenolic compounds,[4] chromate with arsenite,[5] chromate reduction by hydrogen peroxide,[6] reduction of bromate by humic substances,[7] oxidation of inorganic mercury,[8] and inorganic peroxide derived oxidation.[9,10] Two main circumstances have been postulated to cause acceleration of the reaction in the ice phase; (i) the freeze-concentration effect, and (ii) the freezing-potential effect.[1,2] The freeze-concentration effect is introduced by the rejection of solutes into the liquid-like region of the ice grain boundary, which is called quasi-liquid layer, from the growing ice crystal. Therefore, the concentrations of solutes in the ice grain boundary are higher than those in the original solution. However, none of the solutes migrate from the ice lattice to the liquid phase with the same degree and tendency; thus, the separation of cations and anions results in electric potential differences, namely, the freezing-potential effect.[11] In addition, the catalytic effect of the ice surface and convection during freezing have also been suggested as reasons for acceleration, but the influences of these factors are likely minor relative to those of the two abovementioned features.

KOPRI 극지연구소

Peroxymonosulfate (PMS) is an inorganic oxidant and is widely used in sanitizers, swimming pool cleaners, etchants, and bleaching agents under the commercial name of CAROAT or OXONE. In advanced oxidation processes (AOP), PMS has been used as a precursor of strong oxidizing agents because the homolytic cleavage of the peroxide bond of PMS generates $SO_4^{\bullet -}$ and $^{\bullet}OH$ which have redox potentials of 2.4 and 2.7 $V_{NHE}$ respectively (note that the redox potential of PMS is 1.8 VNHE).[12-14] PMS activation increases the oxidation capability of PMS, and the development of a strategy to activate PMS has become a subject of intensive research for water treatment.[15] For instance, PMS can be activated by inserting energy in the form of light,[16] heat,[17] or ultrasound,[18] or via a catalytic reaction using transition metals and noble metals,[19] carbon materials,[20] or a combination of them, such as a photocatalytic reaction,[21] or electrolysis.[22] Besides, recent studies showed that the carbonate and bicarbonate can assist metal-catalyzed PMS systems with the degradation of dye compounds.[23,24] Furthermore, Yang et al. reported that bicarbonate ions attack PMS by nucleophilic interaction and increase the Acid Orange 7 decolorization performance.[25] In the paper, the influence of bicarbonate was identified only in PMS, and no effect of bicarbonate was observed for hydrogen peroxide ($H_2O_2$) and peroxydisulfate (PDS). The vulnerability of PMS to nucleophilic substances is attributed to

the asymmetric chemical structure of PMS.

Bicarbonate is one of the most abundant anion species in natural environments. It has been reported that the bicarbonate concentration of groundwater can vary from 0.7 to 10 mM depending on the regional conditions.[26] The concentration of bicarbonate is affected by the pH and the partial pressure of carbon dioxide in the atmosphere. Therefore, it can significantly affect water treatment systems. In general, the role of background species such as bicarbonate in AOPs has been considered to be retardation because they consume reactive species that are generated by the activation process, and consequently abate the oxidation efficiency.[27-33] However, in some cases, the increased removal of organic substances by adding (bi)carbonate to the system has been reported.[34-36] The reason for this improvement has been identified as the generation of a selective secondary oxidant, i.e., the weakened secondary oxidant attacks the target organic compound in a more concentrate manner, whereas a strong oxidant (e.g., $^{\bullet}OH$) can easily be diminished due to its non-selective character. For example, Jiang et al. reported the activation of PDS by bicarbonate in the oxidation of pharmaceuticals, and estimated that the main oxidants are approximately 51.4% singlet oxygen ($^1O_2$) and 48.6% peroxymonocarbonate ($HCO_4^-$).[35] Yang et al. reported the positive effect of bicarbonate on the oxidation of organic compounds by PMS, and speculated that $HOOCO_2^-$ species ($HCO_4^-$) can engage in oxidation.[37] Furthermore, carbonate radicals ($CO_3^{\bullet -}$) can be presumed to be involved in the bicarbonate derived reaction, but there is little information about the involvement of $CO_3^{\bullet -}$ in the bicarbonate-PMS system.[36] In fact, we found only limited research on the positive effects of bicarbonate on oxidation, whereas numerous articles have reported negative effects of bicarbonate on AOP systems utilizing PMS.[27-33]

In this study, we investigated the reaction of PMS activated by bicarbonate in a frozen solution. We selected 4-chlorophenol (4-CP) as a test organic compound because of its recalcitrant characteristics and toxicity toward aquatic environments.[38] The reaction of PMS and bicarbonate likely caused an oxidative attack on the 4-CP that was accompanied by PMS decomposition, and this reaction was promoted by the freezing process. Because the freezing process obviously enhances the activation of PMS by bicarbonate, we attempted to determine the reason for this enhancement as it is not common knowledge. The oxidation mechanism was investigated by testing plausible scenarios including base activation and the generation of single oxygen molecules and radical species. We also investigated the characteristics of the reaction such as reactivity toward various substrates and the tendency to consume PMS. Although various methods to activate the PMS have been developed, the freezing process does not require an additional input of energy when operated in a cold region.

## 2. Chemicals and methods

### 2.1. Chemicals

The chemical reagents used in this study include the following: peroxymonosulfate compound (Sigma-Aldrich, OXONE®), 4-chlorophenol (Sigma-Aldrich), 4-nitrophenol (Sigma-Aldrich), benzoic acid (Sigma-Aldrich), 4-hydroxybenzoic acid (Sigma-Aldrich), phenol (Sigma-Aldrich), hydroquinone (Sigma-Aldrich), furfuryl alcohol (Sigma-Aldrich), Rose Bengal (Sigma-Aldrich), p-benzoquinone (Sigma-Aldrich), sodium bicarbonate (Sigma-Aldrich), sodium carbonate (Sigma-Aldrich), sodium phosphate monobasic monohydrate (Sigma-Aldrich), sodium phosphate dibasic heptahydrate (Sigma-Aldrich), sodium phosphate (Sigma-Aldrich), sodium hydroxide solution (Sigma-Aldrich), perchloric acid (Sigma-Aldrich), hydrogen peroxide solution 30 w.t.% (Sigma-Aldrich), methanol (Supelco), acetonitrile (Supelco), formic acid (Sigma-Aldrich), phosphoric acid (Sigma-Aldrich), cresol-red (Sigma-Aldrich), 5-tert-butoxycarbonyl-5-methyl-1-pyrroline-N-oxide (BMPO, ENZO Life Science, Inc.), and 2,2,6,6,-tetramethylpiperidine (TEMP, Sigma-Aldrich). All chemicals were of reagent grade and were used as received without any further purification. The entire chemical solutions used in this study were prepared with ultrapure deionized water (18.2 MΩ • cm) which was produced by a Milli-Q Water Purification System (Millipore).

KOPRI 극지연구소

### 2.2. Experimental procedure

The test solution was prepared in a 100 mL glass beaker. The 100 mM of PMS, $NaHCO_3$ and $Na_2CO_3$ stock solutions were added into the beaker to obtain the desired concentration and initial pH value. NaOH and $HClO_4$ solutions were used if the initial pH was not controlled by the addition of the stock solution. Then, 10 mL of the solution was poured into a 15 mL polypropylene conical tube. Normally, we prepared eight conical tubes, four of which were immersed in an ethanol-circulated cooling bath (operating in -20 ℃), whereas the remaining four were kept in the atmosphere. The number of conical tubes can be selected according to the time sampling points. These preparation procedures were implemented as fast as possible (approximately 20~30s was required), and we assigned the starting point at this moment (i.e., t = 0). After, the conical tube containing the frozen solution was withdrawn from the cooling bath and then put into the 30 ℃ warm water to thaw the ice for conducting chemical analyses. We confirmed that the 4-CP degradation was not derived from the thawing process (Figure S1). At least two runs of each experiment were performed to confirm the data reproducibility.

### 2.3. Analytical methods

The concentration of 4-CP was analyzed using a High-Pressure-Liquid-Chromatography (HPLC) (Agilent, 1260 Infinity II). A variable wavelength detector (G7114 1260VWD) was employed and the detection wavelength was set to 230 nm. A Poroshell 120 EC-C18 column (4.6 mm × 150 mm) was used for separation. The 0.1% (v/v) phosphoric acid and neat acetonitrile were introduced into the pump module (G7111A 1260 Quat Pump VL) to implement isocratic elution (60/40 volume ratio). The oxidation by-products were analyzed using a HPLC (Thermo Fisher Scientific, Vanquish) combined with a quadrupole-orbitrap mass spectrometer (Thermo Fisher Scientific, Q Exactive Focus). The separation was performed on a Hypersil GOLD$^{TM}$ aQ column with a mobile phase composed of 0.1% (v/v) of formic acid (dissolved in LC-MS grade water) and neat acetonitrile (LC-MS grade) at a flow rate of 0.3 mL/min. Mass detection was carried out in a negative electrospray ionization (ESI) mode, and the operating parameters were set as follows: detection range = 50 to 550 m/z with a resolution of 70,000, spray voltage = 2.50 kV, capillary temperature = 320 ℃, sheath gas flow rate = 40 a.u., auxiliary gas flow rate = 10 a.u., auxiliary gas heater temperature = 300 ℃, S lens RF level = 50.0, maximum injection time = 200 ms, and an automatic gain control (AGC) target = $1\times10^6$. UV-vis spectroscopy (Shimadzu, UV-2600) was used to determine the PMS concentration. The PMS concentration was analyzed using the method proposed by Liang et al., which is based on iodometry [39]. The on-site detection of concentrated PMS and bicarbonate in frozen solution was conducted using a confocal Raman microscope (Renishaw, InVia Qontor). Liquid sample (25 μL) were dropped onto a silica sample holder (8 mm × 8 mm × 2 mm) and mounted on a temperature-controlled microscope sage (Linkam Scientific, THMS600). The freezing rate was -1.5 ℃/min and the temperature was maintained at -20 ℃. The temperature controller was operated using liquid nitrogen and an electrical heating plate. A monochromatic laser (λ = 532 nm DPSS) was used to introduce Raman-Stoke scattering. The distance from the prism to the 2400 l/mm grating was 8.3 cm. Electron paramagnetic resonance spectroscopy measurements were conducted by using EMXnano (Bruker). The experimental conditions were as follows: Microwave Frequency = 9.64 GHz, Microwave Power = 1 mW, Modulation Frequency = 100 kHz, Modulation Amplitude = 1 G, and Sweep Time = 48 s with continuous-wave-EPR (CW-EPR) mode.

## 3. Result and discussion

### 3.1. Degradation of 4-CP in the bicarbonate-PMS system

Figure 1a shows the degradation of 4-CP by the bicarbonate-PMS system (under

aqueous conditions) with the initial PMS dose (black symbols). In the case of a 2 mM PMS dose (at aqueous case), more than half of the initial 4-CP was removed during the 4 h reaction time, where the initial pH was 9. When the PMS dose was decreased to 0.1 mM, the degradation of 4-CP slowed down, i.e., 40%, 20%, and less than 1% of the initial 4-CP decomposed at PMS dose of 1, 0.5, and 0.1 mM, respectively, within 4 h. In addition to the PMS concentration, the 4-CP degradation rate also depends on the concentration of the carbonate species (i.e., the total concentration of $HCO_3^-$ and $CO_3^{2-}$), as shown in Figure 1b. It was found that the absence of PMS or bicarbonate caused no degradation of 4-CP, which was followed by a low concentration trend (Figure S2). Furthermore, reduction of at most 20% of the initial PMS concentration was observed during the reaction in the presence of bicarbonate, whereas no PMS decomposition was detected in the absence of bicarbonate (Figure S3a). Thus, PMS was activated by bicarbonate, and was responsible for the degradation of 4-CP. This phenomenon agrees well with the recent findings that bicarbonate can be a PMS activator,[34-36] although bicarbonate acts as a scavenger of reactive species, therefore, inhibits the oxidation performance in many cases.[27-33]

On the other hand, a drastic improvement in 4-CP degradation was found in the ice phase (Figure 1a; blue symbols). For instance, freezing the solution at -20 ℃ in an ethanol bath resulted in the removal of almost all the 4-CP within 2 h with an initial PMS concentration of 2 mM, while only 50% of the initial 4-CP was decomposed in its aqueous counterpart (Figure 1a; black symbols). In parallel with this trend, the PMS decomposition rate increased, indicating that 4-CP degradation is highly correlated with PMS consumption (Figure S3b). According to this, a positive correlation between the initial concentrations of PMS and bicarbonate on 4-CP decomposition rate was also found in the frozen case. From these results, it is clear that the freezing process enhanced 4-CP degradation relative to that under aqueous conditions (Figure 1).

Because of the arise of freeze-concentration phenomenon during the freezing process, the positive correlation between the PMS (or bicarbonate) concentration and 4-CP removal implies that the freeze-concentration effect is responsible for the acceleration of 4-CP degradation in frozen solution (note that the chemical reaction rate depends on the concentration of the reactants). In this regard, we conducted in-situ measurement of the frozen solution using Raman spectroscopy with a temperature-controllable microscope stage (Linkam, FDCS196). Figure 2a shows an optical microscope image of the frozen bicarbonate-PMS system focusing on its ice grain boundary, which is an unfrozen region between the ice crystal, along with the Raman spectrum at the marked point. The rainbow scale expression was employed to display the intensity of the Raman scattering light; namely, the red and violet dots represent high and low signals at the position, respectively.

Here, the signal at 984 nm was selected for representative intensity of dots. It is obvious that the red and green dots are aligned along the grain boundary, whereas the bulk of the ice crystal exhibit violet and black dots. In the representative spectrum, the appearance of a specific signal indicates the presence of a particular species, i.e., v = 984 $cm^{-1}$ likely corresponds to the symmetric S-O stretching vibration and v = 1025 $cm^{-1}$ probably originated from the C-OH stretching mode of $HCO_3^-$.[10,40,41] To confirm these features, we obtained the signals of only PMS or bicarbonate and consequently confirmed that the signals at 883, 984, and 1062 $cm^{-1}$ assigned the PMS whereas that at 1025 $cm^{-1}$ assigned the bicarbonate (Figure S4 and S5). Evidently, the high intensity of v = 984 $cm^{-1}$ (i.e., $SO_4^{2-}$) was concentrated along the ice grain boundary line of the frozen PMS system (Figure S4). A similar distribution pattern of v = 1020 $cm^{-1}$ (i.e., $HCO_3^-$) also manifested when only bicarbonate present (Figure S5). The absence of PMS and bicarbonate yielded no specific peak even in the center of the grain boundary (Figure S6). Therefore, we can conclude that the dissolved substrates are accumulate into the ice grain boundary.

We also investigated the influence of the freezing temperature to demonstrate the freeze-concentration effect on the system (Figure 2b). The point at which freezing began differed along the operated temperature. When the solution was frozen at -10 ℃, the aqueous phase maintained more than 30 min and the concentration of 4-CP was also retained. This indicates that the oxidation is not initiated before freezing. Similar behavior was observed at -20 ℃; at this temperature, approximately 10 min was needed before freezing began. In fact, the temperature affects both the speed at which freezing occurs and the size of the ice crystals that form.[9] It is emphasized that when the solution was frozen in liquid nitrogen (-196℃), the reaction was evidently retarded owing to the elimination of quasi-liquid layer by amorphously crystallized water at extremely low temperatures. Hence, we can conclude that the freeze-concentration of PMS and bicarbonate occurs in the ice grain boundaries and is responsible for the increased 4-CP oxidation with respect to aqueous case.

### 3.2. Participation of base-mediated PMS activation in bicarbonate-PMS system

A previous study revealed that PMS spontaneously decomposes in an alkaline environment and that the self-decay is maximized around pH 9.4 (note that the $pK_{a2}$ of PMS is 9.4 and that the peroxide bond of $HSO_5^-$ is readily attacked by nucleophilic $SO_5^{2-}$).[37] Consequently, the reactions produced $SO_4^{2-}$ and $O_2$ (i.e., $HSO_5^- + SO_5^{2-} \rightarrow HSO_6^- + SO_4^{2-}$ and $HSO_6^- + OH^- \rightarrow H_2O + SO_4^{2-} + O_2$).[42] In addition, some research has shown that PMS under basic conditions can degrade organic dye compounds and trichlorophenol.[43,44] Therefore, we examined the influence of base activation as well as the stability of PMS in our system in the aqueous and frozen cases, because our PMS

activation system usually conducted at initial pH of 9. Figure 3 demonstrates the degradation of 4-CP in various pH ranges, which are controlled by three different reagents: carbonate ($HCO_3^-/CO_3^{2-}$), phosphate ($H_2PO_4^-/HPO_4^{2-}/PO_4^{3-}$), and hydroxide ($OH^-$). Overall, the degradation of 4-CP in all aqueous cases did not exceed 15% of the initial 4-CP concentration at pH 9, and it reached nearly half of that at pH 10 during the 4 h reaction period. Besides, the performance degradation of the NaOH adjusted system was the lowest among the three cases (Figure 3c). It is noted that PMS decomposition induces a pH shift toward acidic pH values due to H+ generation.[43] Apparently, the NaOH adjusted system was sensitively affected by the transformation of PMS (note that the pH was around 7.8 after the reaction when the initial pH was 10; data not shown), while carbonate and phosphate adjusted systems exhibited relatively stable pH variations (with a decrease of 0.5 ~ 1 during 4 h of reaction) due to their pH buffering capacities. In addition, there was only a slight loss of PMS in all reagent cases under aqueous conditions on our time scale: the PMS decomposition ratio was not exceeded up of 20% even at an initial pH of 10 (Figure S7, aqueous cases). Presumably, this PMS decay rate is similar to the previous result if the low ionic strength in our case is considered.[37] Accordingly, it is obvious that the base condition affects the PMS system, but this influence is not significant when the pH of the solution is less than 9 under our experimental conditions.

On the other hand, not only the influence of the pH, but also the type of pH adjusting reagent were clearly discriminated in the freezing cases (we need to mention that the initial pH is the value before freezing) (Figure 3; white symbols). In the carbonate case (frozen, Figure 3a), 4-CP remains at 65%, 40%, 10%, and < 1% of the initial concentration at pH 7, 8, 9, and 10, respectively. It should be emphasized that negligible 4-CP removal appears near a neutral pH when phosphate and NaOH were used for pH adjustment (Figure 3b, 3c). However, the 4-CP removal reaches 40% when the pH increases to 9 in those two cases. Remarkably, 4-CP is fully eliminated at pH 10 regardless of the reagent type. These results might indicate that the base activation of PMS in the system contributed to the 4-CP removal and improved with freezing. In fact, an acidic solution becomes more acidic during freezing because the local concentration of the acid increases .[45] Similarly, it is plausible that an accumulation of $OH^-$ occurred during freezing,[46] thereby reinforcing the base activation of PMS and improving the degradation efficiency. To describe this, we employed cresol-red (CR) as pH indicator with which to make in-situ estimation of the pH of the ice. We need to mention that the color of CR was disappeared during freezing when PMS exist in CR solution, due to its oxidation property (data was not shown). For this reason, we prepared bicarbonate solution with an initial pH 9 without PMS. As shown at Figure 3d, the initial color of CR solution was light pink: however, this changed to light yellow when the solution was completely frozen. The temperature

dependence of protonation is not likely significant at this case because the $pK_a$ at 253K is known to be 8.7;[45] therefore, we believe that the frozen solution has a pH of less than 8.7. Thus, the accumulation of $OH^-$ is not the main reason for the increased PMS activation in the ice. Furthermore, the apparent degradation of 4-CP was also found in the neutral conditions of bicarbonate-PMS system, whereas reactivity in the phosphate and NaOH was marginal (Figure 3a, 3b, and 3c). Based on the observation, it is likely that some different kinds of chemical reactions occur in the bicarbonate PMS system that do not occur in the phosphate and NaOH systems. In fact, several researchers have reported that the carbonate species in the system can activate PMS to improve the degradation of organic compounds.[25,34,36] In this regard, the identification of reactive species is needed to reveal the reaction mechanism.

### 3.3 Identification of reactive species

As mentioned above, molecular oxygen can be generated during PMS decomposition. In previous research, singlet oxygen ($^1O_2$) formation via the self-decay of peroxy-acids above their $pK_a$ value was identified.[47] In addition, according to Zhou et al., the generation of 1O2 from the reaction of PMS with benzoquinone derived from the intermediate of phenolic compound decomposition was proposed to be the oxidant responsible for organic compound degradation (note that the carbonyl moiety (C=O) has been found to accelerate $^1O_2$ production from PMS at basic pH).[48,49] We observed a trend similar to that of Zhou et al., which is the biphasic kinetics of phenol degradation at room temperature (Figure S10). Therefore, considering the participation of $^1O_2$ in this stage is quite reasonable. However, electron paramagnetic resonance (EPR) data indicate that the role of $^1O_2$ in 4-CP degradation is doubtful. As shown in Figure 4a, we monitored the EPR signal of TEMPO, which was derived from the spin probes TEMP by $^1O_2$ in our experimental condition, in the bicarbonate-PMS system and base activated (by NaOH) PMS system (Figure 4a). Apparently, the signal intensity is lower in the bicarbonate-PMS system than in the NaOH-PMS system. Because 4-CP was more efficiently degraded in the bicarbonate-PMS system than in the NaOH-PMS system (Figure 3), the EPR results indicate that $^1O_2$ plays a minor role in the 4-CP degradation in the bicarbonate-PMS system. The insignificance of $^1O_2$ in the 4-CP degradation in our system was also found by comparison with the reference system. Photo-excited Rose Bengal (RB) is a well-known photo-sensitized $^1O_2$ generation system, so we employed this system to account for the role of $^1O_2$.[50] As shown in Figure 4b, the degradation of 4-CP was negligible in the photo-excited RB system, while 60% of the 4-CP disappeared in the frozen bicarbonate-PMS system. We confirmed the significant degradation of furfuryl alcohol (FFA), which reacts well with $^1O_2$ ($k = 1.2\times10^8\ M^{-1}s^{-1}$[51]), in the photo-RB system; therefore, $^1O_2$ likely to arose from photo-excited

RB. We need to mention that we adjusted the experimental conditions of the photo-RB system, in which the FFA degradation rate become similar to that in the frozen bicarbonate-PMS case. In parallel with this, the FFA degradation was comparable to (but slightly slower than) the 4-CP degradation in the frozen bicarbonate-PMS system, which means that $^1O_2$ is not likely a dominant oxidant in the frozen bicarbonate-PMS system.

Peroxymonocarbonate ($HCO_4^-$) was proposed as another reactive species in the bicarbonate mediated PMS activation. The reactivity of $HCO_4^-$ is weaker (1.8 $V_{NHE}$) than conventional oxidizing reagents such as $^{\bullet}OH$ (2.7 $V_{NHE}$), but numerous papers have suggested that $HCO_4^-$ can oxidize a variety of organic compounds.[52-54] Generally, it has been reported that $H_2O_2$ and $HCO_3^-$ are in chemical equilibrium with $HCO_4^-$—, so we employed the $HCO_3^-$-$H_2O_2$ system to estimate the influence of $HCO_4^-$ on the reaction of the bicarbonate-PMS system. However, when we mimicked the experiment of Yang et. al.,[53] we observed no disappearance of 4-CP (Figure 4c), whereas the phenol, which was chosen as target organic pollutant by Yang et. al., was decomposed within 120 min. Therefore, we speculate that the influence of $HCO_4^-$ on the 4-CP degradation in the frozen bicarbonate-PMS system is negligible.

### 3.4 Characteristic of the oxidation in the frozen bicarbonate-PMS system

One of the major characteristics of oxidants is their reactivity. Figure 5 shows the selective oxidation efficacy of the bicarbonate-PMS system. In general, it is known that the split of the peroxide bond in PMS by one-electron transfer results in $SO_4^{\bullet -}$ generation. The rate constants between $SO_4^{\bullet -}$ and the test organic compounds at room temperature are reported as follows: $1.2\times10^9$ (benzoic acid), $2.5\times10^9$ (4-hydroxybenzoic acid), $8.8\times10^9$ (phenol), $8.7\times10^9$ (4-chlorophenol),[55] and $6.83\times10^8$ (4-nitrophenol).[56] Based on the reaction rate constants, we anticipate that the selected organic compounds can be degraded by $SO_4^{\bullet -}$ with only slight differences. However, as shown in Figure 5, the degradation rates of selected organic compounds differ significantly from those in the frozen bicarbonate-PMS system. For instance, benzoic acid was negligibly decomposed, while 4-hydroxybenzoic acid was diminished within 40 min, although the reactivity of the two compounds with $SO_4^{\bullet -}$ was on the order of ~$10^9$. We also confirmed the marginal influence of the addition of an excess of radical quenching agents (Figure S8). Furthermore, we did not observe a typical signal of spin trapping reagent (5-tert-butoxycarbonyl-5-methyl-1-pyrroline-N-oxide, BMPO) in the EPR spectrum whereas, the benchmark system (i.e., UV/$H_2O_2$ as the $^{\bullet}OH$ system and UV/$S_2O_8^{2-}$ as the $SO_4^{\bullet -}$ system) showed clear features of radical signals (Figure S9). Hence, radical species such as $SO_4^{\bullet -}$ and $^{\bullet}OH$ were not likely to be reactive species responsible for the oxidation of organic compounds. In addition, we found that 4-hydroxybenzoic acid degraded

faster than 4-CP and phenol, which are substituents that have lover electron-withdrawing effects than $-CO_2H$ on the aromatic ring. In addition, even though the Hammett constant of 4-nitrophenol (with respect to phenol, $\sigma^+$=0.79) is higher than that of 4-chlorophenol ($\sigma^+$=0.11),[57] it degraded slightly faster than 4-CP in the frozen bicarbonate-PMS system. These findings indicate that the reaction does not rely on the electrophilicity of the aromatic ring. Although we cannot delve into the characteristic of substrate dependence in more detail, it should be emphasized that the oxidation accelerated in the concentrated region in the ice, which requires clarification of the unusual chemical reaction. It is noted that the degradation of selected substrates by bicarbonate-PMS with a reaction time of 1 h was marginal in the aqueous solution, except for that of phenol (Figure S10).

On the other hand, the PMS consumption was strongly related to the degree of organic compound degradation (Figure 6). The decomposition of PMS in the absence of an organic substrate was comparable to that of benzoic acid, which showed no degradation by the bicarbonate-PMS system. Meanwhile, 4-CP and 4-nitrophenol were moderately degraded PMS, and phenol and 4-hydroxybenzoic acid exhibited fast PMS decomposition. Especially, the addition of hydroquinone resulted in the elimination of PMS within 2 h (Figure S11). Therefore, we speculated that the electron donating performance of the target organic substrate is closely related to the PMS consumption rate, so direct electron transfer from the electron donor to the acceptor presumably contributed to the reaction. On the other hand, the 40% PMS decomposition in the None case in Figure 6 was probably caused by the base activation of PMS, which means the generation of $^1O_2$ from the decomposition of PMS (the presence of $^1O_2$ was identified from the EPR experiment). Phenol and hydroquinone apparently accelerated the PMS decomposition in aqueous condition (Figure S12) and were previously reported to be activators to generate $^1O_2$ from PMS.[49] So, this circumstance can concomitantly contribute to the high decomposition of PMS in the phenol and hydroxyquinone cases with respect to the benzoic acid and 4-nitrophenol cases, which are not PMS activator to produce $^1O_2$.

Parallel to the influence of the target substrate on the PMS decomposition, we found that the increase in bicarbonate dosage also increased the PMS and 4-CP degradation, as shown in Figure 1b and S3. Also, the absence of bicarbonate showed a very limited 4-CP degradation when the pH was adjusted by phosphate and hydroxide (Figure 3). All of those reactions became significant in the frozen case rather than the aqueous case (note that freezing induced the freeze-concentration as shown Figure 2a). In addition, the radical quenching reagent did not inherently degrade 4-CP, and there was no specific EPR signal for $^{\bullet}OH$, $SO_4^{\bullet-}$ and $O2^{\bullet-}$; therefore, the oxidation mechanism was not likely to have proceeded via a radical species (Figure S8, S9). With regard to those circumstances, we concluded that electron transfer from the target organic compound to the PMS is likely a

primary procedure for oxidation in these cases, as suggested in previous reports,[9,10] and bicarbonate ion helps this transfer process. The probability of collision between molecules can be increased during freeze-concentration, promoting electron transfer between reactants. A previous report showed that the coupling reaction between phenolic compounds is more dominant in ice crystals than in aqueous counterparts.[58] Similarly, we found that the biphenyl compound, as well as doubly carboxylate compound and sulfonated compound, were more highly evolved in the frozen case, whereas the abundances of some ring-opened compounds were higher in the aqueous case than in the frozen case (Figure S13). Notably, the generation tendencies of some chlorinated intermediates (e.g., chlorocatechol; measured m/z = 142.98924) were similar in the aqueous and frozen cases, so they likely share the same degradation pathways in the early stages of the reaction.

## 4. Conclusion

We investigated the decomposition of 4-CP by a bicarbonate-PMS system and the acceleration of the reaction by freezing. The positive relationship between 4-CP degradation and the concentration of reagents shows that PMS can be activated by bicarbonate. Raman spectroscopy measurements and temperature-dependent experiments suggested that the enhanced 4-CP degradation efficiency in the frozen bicarbonate-PMS system can be ascribed to the freeze-concentration effect. Although the base activation of PMS can affect the degradation of 4-CP, which was induced by a bicarbonate species, the reaction between bicarbonate and PMS was apparent because of the lack of an effect on phosphate and hydroxide system under circumneutral conditions. In addition, observation of the color of CR showed that the pH of ice decreased; therefore, the accumulation of $OH^-$ during the freezing process was not found to be the main reason for the increased PMS activation. The dominant reactive species in the bicarbonate-PMS system was systematically investigated, and a direct electron transfer from organic substances to PMS was proposed to be the main oxidation mechanism. The bicarbonate-PMS reaction was more strongly influenced by the reactant concentrations than the temperature; although the latter is generally an important factor in the reaction. Hence, the bicarbonate-PMS reaction accelerated in the highly concentrated brine in the grain boundary of ice. However, the detailed mechanisms of the reaction of bicarbonate-PMS and that at the concentrated grain boundary are not yet fully understood. Though the mechanism of bicarbonate-PMS has been discussed in some studies, there are still many ambiguities on this issue. The question of how bicarbonate promotes the electron transfer from PMS to the target organic compound remains open and should be studied further. In addition, to reveal the unique properties of chemical reactions during freezing, we will further analyze its characteristics

KOPRI 극지연구소

and utility by using various chemical systems.

We also need to mention the environmental implications of the freezing process. Water freezes naturally in cold regions where no external resources are required to make ice. This feature is an advantage of frozen bicarbonate-PMS system, in terms of other processes that induce the PMS activation; heat, ultrasound, and ultra-violet light are energy consuming process that utilize resources to generate the energy required. Furthermore, catalyst-mediated PMS activation processes need post treatment to separate nanomaterials or transition metal ions from the system while the frozen bicarbonate-PMS system does not because all its reagents are natural (e.g., bicarbonate and sulfate). In this regard, our process can be considered as eco-friendly water treatment technology, particularly when it is used in cold areas such as a high latitude region or a mid-latitude in winter. Finally, the frozen bicarbonate-PMS system can degrade various organic pollutants and can thus be expected to function as a potent water treatment system.

KOPRI
극지연구소

## REFERENCES


1. O'Concubhair, R., J.R. Sodeau, The Effect of Freezing on Reactions with Environmental Impact, Acc. *Chem. Res. 46* (2013) 2716-2724
2. Takenaka, N., A. Ueda, T. Daimon, H. Bandow, T. Dohmaru, Y. Maeda, Acceleration Mechanism of Chemical Reaction by Freezing: The Reaction of Nitrous Acid with Dissolved Oxygen, *J. Phys. Chem. 100* (1996) 13874-13884
3. Takenaka, N., A. Ueda, Y. Maeda, Acceleration of the rate of nitrite oxidation by freezing in aqueous solution, *Nature 358* (1992) 736-738
4. Ju, J., J. Kim, Ľ. Vetráková, J. Seo, D. Heger, C. Lee, H.-I. Yoon, K. Kim, J. Kim, Accelerated redox reaction between chromate and phenolic pollutants during freezing, *J. Hazard. Mater. 329* (2017) 330-338
5. Kim, K., W. Choi, Enhanced Redox Conversion of Chromate and Arsenite in Ice, *Environ. Sci. Technol. 45* (2011) 2202-2208
6. Kim, K., J. Kim, A.D. Bokare, W. Choi, H.-I. Yoon, J. Kim, Enhanced Removal of Hexavalent Chromium in the Presence of H2O2 in Frozen Aqueous Solutions, *Environ. Sci. Technol. 49* (2015) 10937-10944
7. Min, D.W., W. Choi, Accelerated Reduction of Bromate in Frozen Solution, *Environ. Sci. Technol. 51* (2017) 8368-8375
8. O'Concubhair, R., D. O'Sullivan, J.R. Sodeau, Dark Oxidation of Dissolved Gaseous Mercury in Polar Ice Mimics, *Environ. Sci. Technol. 46* (2012) 4829-4836
9. Choi, Y., H.-I. Yoon, C. Lee, L.u. Vetráková, D. Heger, K. Kim, J. Kim, Activation of Periodate by Freezing for the Degradation of Aqueous Organic Pollutants, *Environ. Sci. Technol. 52* (2018) 5378-5385
10. Le, N.T.H., J. Ju, B. Kim, M.S. Kim, C. Lee, S. Kim, W. Choi, K. Kim, J. Kim, Freezing-enhanced non-radical oxidation of organic pollutants by peroxymonosulfate, *Chem. Eng. J. 388* (2020) 124226
11. Workman, E.J., S.E. Reynolds, Electrical Phenomena Occurring during the Freezing of Dilute Aqueous Solutions and Their Possible Relationship to Thunderstorm Electricity, *Phys. Rev. 78* (1950) 254-259
12. Ghanbari, F., M. Moradi, Application of peroxymonosulfate and its activation methods for degradation of environmental organic pollutants: Review, *Chem. Eng. J. 310* (2017) 41-62
13. Lee, J., U. von Gunten, J.-H. Kim, Persulfate-Based Advanced Oxidation: Critical Assessment of Opportunities and Roadblocks, *Environ. Sci. Technol. 54* (2020) 3064-3081


KOPRI 극지연구소

14. Wang, J., S. Wang, Activation of persulfate (PS) and peroxymonosulfate (PMS) and application for the degradation of emerging contaminants, *Chem. Eng. J. 334* (2018) 1502-1517

15. Ahn, Y.-Y., E. Yun, Heterogeneous metals and metal-free carbon materials for oxidative degradation through persulfate activation: A review of heterogeneous catalytic activation of persulfate related to oxidation mechanism, *Korean J. Chem. Eng. 36* (2019) 1767-1779

16. Xu, Y., Z. Lin, Y. Wang, H. Zhang, The UV/peroxymonosulfate process for the mineralization of artificial sweetener sucralose, *Chem. Eng. J. 317* (2017) 561-569

17. Huang, X., X. Zhou, J. Zhou, Z. Huang, S. Liu, G. Qian, N. Gao, Bromate inhibition by reduced graphene oxide in thermal/PMS process, *Water Res. 122* (2017) 701-707

18. Grčić, I., S. Papić, N. Koprivanac, I. Kovačić, Kinetic modeling and synergy quantification in sono and photooxidative treatment of simulated dyehouse effluent, *Water Res. 46* (2012) 5683-5695

19. Ahn, Y.-Y., H. Bae, H.-I. Kim, S.-H. Kim, J.-H. Kim, S.-G. Lee, J. Lee, Surface-loaded metal nanoparticles for peroxymonosulfate activation: Efficiency and mechanism reconnaissance, *Appl. Catal. B: Environ. 241* (2019) 561-569

20. Wang, G., S. Chen, X. Quan, H. Yu, Y. Zhang, Enhanced activation of peroxymonosulfate by nitrogen doped porous carbon for effective removal of organic pollutants, *Carbon 115* (2017) 730-739

21. Jo, Y., C. Kim, G.-H. Moon, J. Lee, T. An, W. Choi, Activation of peroxymonosulfate on visible light irradiated TiO2 via a charge transfer complex path, *Chem. Eng. J. 346* (2018) 249-257

22. Wang, K., D. Huang, W. Wang, Y. Ji, J. Niu, Enhanced perfluorooctanoic acid degradation by electrochemical activation of peroxymonosulfate in aqueous solution, *Envir. Inter. 137* (2020) 105562

23. Huang, Z., Y. Yao, J. Lu, C. Chen, W. Lu, S. Huang, W. Chen, The consortium of heterogeneous cobalt phthalocyanine catalyst and bicarbonate ion as a novel platform for contaminants elimination based on peroxymonosulfate activation, *J. Hazard. Mater. 301* (2016) 214-221

24. Dai, D., Z. Yang, Y. Yao, L. Chen, G. Jia, L. Luo, Highly efficient removal of organic contaminants based on peroxymonosulfate activation by iron phthalocyanine: mechanism and the bicarbonate ion enhancement effect, *Catal. Sci. Technol. 7* (2017) 934-942

25. Yang, S., P. Wang, X. Yang, L. Shan, W. Zhang, X. Shao, R. Niu, Degradation

KOPRI 극지연구소

efficiencies of azo dye Acid Orange 7 by the interaction of heat, UV and anions with common oxidants: Persulfate, peroxymonosulfate and hydrogen peroxide, *J. Hazard. Mater. 179* (2010) 552-558

26. Wilkin, R.T., D.C. DiGiulio, Geochemical Impacts to Groundwater from Geologic Carbon Sequestration: Controls on pH and Inorganic Carbon Concentrations from Reaction Path and Kinetic Modeling, *Environ. Sci. Technol. 44* (2010) 4821-4827
27. Yang, J.-F., L.-M. Yang, S.-B. Zhang, L.-H. Ou, C.-B. Liu, L.-Y. Zheng, Y.-F. Yang, G.-G. Ying, S.-L. Luo, Degradation of azole fungicide fluconazole in aqueous solution by thermally activated persulfate, *Chem. Eng. J. 321* (2017) 113-122
28. Mora, V.C., J.A. Rosso, G. Carrillo Le Roux, D.O. Mártire, M.C. Gonzalez, Thermally activated peroxydisulfate in the presence of additives: A clean method for the degradation of pollutants, *Chemosphere 75* (2009) 1405-1409
29. Qian, Y., X. Guo, Y. Zhang, Y. Peng, P. Sun, C.-H. Huang, J. Niu, X. Zhou, J.C. Crittenden, Perfluorooctanoic Acid Degradation Using UV - Persulfate Process: Modeling of the Degradation and Chlorate Formation, *Environ. Sci. Technol. 50* (2016) 772-781
30. Lee, M.-Y., W.-L. Wang, Q.-Y. Wu, N. Huang, Z.-B. Xu, H.-Y. Hu, Degradation of dodecyl dimethyl benzyl ammonium chloride (DDBAC) as a non-oxidizing biocide in reverse osmosis system using UV/persulfate: Kinetics, degradation pathways, and toxicity evaluation, *Chem. Eng. J. 352* (2018) 283-292
31. Ma, J., Y. Yang, X. Jiang, Z. Xie, X. Li, C. Chen, H. Chen, Impacts of inorganic anions and natural organic matter on thermally activated persulfate oxidation of BTEX in water, *Chemosphere 190* (2018) 296-306
32. Luo, C., J. Jiang, J. Ma, S. Pang, Y. Liu, Y. Song, C. Guan, J. Li, Y. Jin, D. Wu, Oxidation of the odorous compound 2,4,6-trichloroanisole by UV activated persulfate: Kinetics, products, and pathways, *Water Res. 96* (2016) 12-21
33. Chen, L., T. Cai, C. Cheng, Z. Xiong, D. Ding, Degradation of acetamiprid in UV/H2O2 and UV/persulfate systems: A comparative study, *Chem. Eng. J. 351* (2018) 1137-1146
34. Nie, M., W. Zhang, C. Yan, W. Xu, L. Wu, Y. Ye, Y. Hu, W. Dong, Enhanced removal of organic contaminants in water by the combination of peroxymonosulfate and carbonate, *Sci. Total Environ. 647* (2019) 734-743
35. Jiang, M., J. Lu, Y. Ji, D. Kong, Bicarbonate-activated persulfate oxidation of acetaminophen, *Water Res. 116* (2017) 324-331
36. Sun, Y., H. Xie, C. Zhou, Y. Wu, M. Pu, J. Niu, The role of carbonate in sulfamethoxazole degradation by peroxymonosulfate without catalyst and the

generation of carbonate racial, *J. Hazard. Mater. 398* (2020) 122827

37. Yang, Y., G. Banerjee, G.W. Brudvig, J.-H. Kim, J.J. Pignatello, Oxidation of Organic Compounds in Water by Unactivated Peroxymonosulfate, *Environ. Sci. Technol. 52* (2018) 5911-5919
38. Michałowicz, J., W. Duda, Phenols – Sources and toxicity, *Pol. J. of Environ. Stud. 16* (2007) 347-362
39. Liang, C., C.-F. Huang, N. Mohanty, R.M. Kurakalva, A rapid spectrophotometric determination of persulfate anion in ISCO, *Chemosphere 73* (2008) 1540-1543
40. Wang, W., Y. Liu, T. Xue, J. Li, D. Chen, T. Qi, Mechanism and kinetics of titanium hydrolysis in concentrated titanyl sulfate solution based on infrared and Raman spectra, *Chem. Eng. Sci. 134* (2015) 196-204
41. Perkins, R.S., J.D. Garber, Raman Spectroscopy of Iron in Aqueous Carbonate Solutions, *J. Solution Chem. 32* (2003) 265-272
42. Ball, D.L., J.O. Edwards, The Kinetics and Mechanism of the Decomposition of Caro's Acid. I, *J. Am. Chem. Soc. 78* (1956) 1125-1129
43. Qi, C., X. Liu, J. Ma, C. Lin, X. Li, H. Zhang, Activation of peroxymonosulfate by base: Implications for the degradation of organic pollutants, *Chemosphere 151* (2016) 280-288
44. Yang, F., Y. Huang, C. Fang, Y. Xue, L. Ai, J. Liu, Z. Wang, Peroxymonosulfate/base process in saline wastewater treatment: The fight between alkalinity and chloride ions, *Chemosphere 199* (2018) 84-88
45. Heger, D., J. Klánová, P. Klán, Enhanced Protonation of Cresol Red in Acidic Aqueous Solutions Caused by Freezing, *J. Phys. Chem. B 110* (2006) 1277-1287
46. Takenaka, N., M. Tanaka, K. Okitsu, H. Bandow, Rise in the pH of an Unfrozen Solution in Ice Due to the Presence of NaCl and Promotion of Decomposition of Gallic Acids Owing to a Change in the pH, *J. Phys. Chem. A 110* (2006) 10628-10632
47. Evans, D.F., M.W. Upton, Studies on singlet oxygen in aqueous solution. Part 3. The decomposition of peroxy-acids, *J. Chem. Soc., Dalton Trans.* (1985) 1151-1153
48. Zhou, Y., J. Jiang, Y. Gao, S.-Y. Pang, Y. Yang, J. Ma, J. Gu, J. Li, Z. Wang, L.-H. Wang, L.-P. Yuan, Y. Yang, Activation of peroxymonosulfate by phenols: Important role of quinone intermediates and involvement of singlet oxygen, *Water Res. 125* (2017) 209-218
49. Zhou, Y., J. Jiang, Y. Gao, J. Ma, S.-Y. Pang, J. Li, X.-T. Lu, L.-P. Yuan, Activation of Peroxymonosulfate by Benzoquinone: A Novel Nonradical Oxidation Process, *Environ. Sci. Technol. 49* (2015) 12941-12950

KOPRI 극지연구소

50. Yun, E.-T., J.H. Lee, J. Kim, H.-D. Park, J. Lee, Identifying the Nonradical Mechanism in the Peroxymonosulfate Activation Process: Singlet Oxygenation Versus Mediated Electron Transfer, *Environ. Sci. Technol. 52* (2018) 7032-7042

51. Scully, F.E., J. Hoigné, Rate constants for reactions of singlet oxygen with phenols and other compounds in water, *Chemosphere 16* (1987) 681-694

52. Xu, A., X. Li, H. Xiong, G. Yin, Efficient degradation of organic pollutants in aqueous solution with bicarbonate-activated hydrogen peroxide, *Chemosphere 82* (2011) 1190-1195

53. Yang, X., Y. Duan, J. Wang, H. Wang, H. Liu, D.L. Sedlak, Impact of Peroxymonocarbonate on the Transformation of Organic Contaminants during Hydrogen Peroxide in Situ Chemical Oxidation, *Environ. Sci.Technol. Lett. 6* (2019) 781-786

54. Richardson, D.E., H. Yao, K.M. Frank, D.A. Bennett, Equilibria, Kinetics, and Mechanism in the Bicarbonate Activation of Hydrogen Peroxide: Oxidation of Sulfides by Peroxymonocarbonate, *Journal of the American Chemical Society 122* (2000) 1729-1739

55. Ziajka, J., K.J. Rudzinski, Autoxidation of SIV inhibited by chlorophenols reacting with sulfate radicals *J. Environ. Chem. 4* (2007) 355-363

56. Rudziński, K.J., Aqueous Reactions of Sulfate Radical-Anions with Nitrophenols in Atmospheric Context, *Atmosphere 10* (2019) 795

57. Lee, Y., J. Yoon, U. von Gunten, Kinetics of the Oxidation of Phenols and Phenolic Endocrine Disruptors during Water Treatment with Ferrate (Fe(VI)), *Environmental Science & Technology 39* (2005) 8978-8984

58. Klánová, J., P. Klán, J. Nosek, I. Holoubek, Environmental Ice Photochemistry: Monochlorophenols, *Environ. Sci. Technol. 37* (2003) 1568-1574

KOPRI 극지연구소

FIGURES

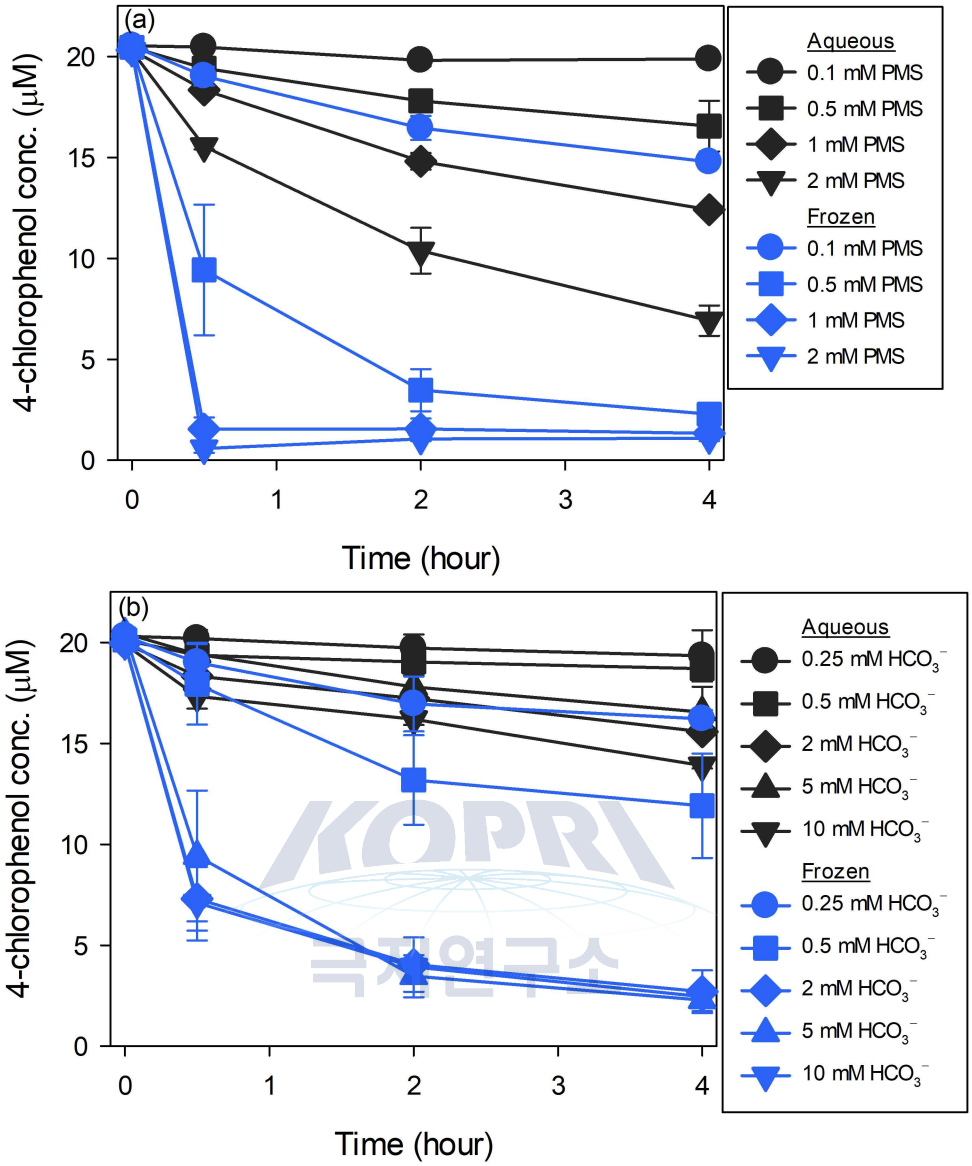



Fig. 1. 4-CP concentration profile versus elapsed time in the bicarbonate-PMS system with (a) various PMS concentrations and (b) various bicarbonate concentrations. $[4\text{-CP}]_0$ = 0.02 mM; $[HCO_3^-]_0$ = 5 mM (at (a)); $[PMS]_0$ = 0.5 mM (at (b)); $pH_i$ = 9; Temperature = 25 ℃ (aqueous condition) and -20 ℃ (frozen condition).

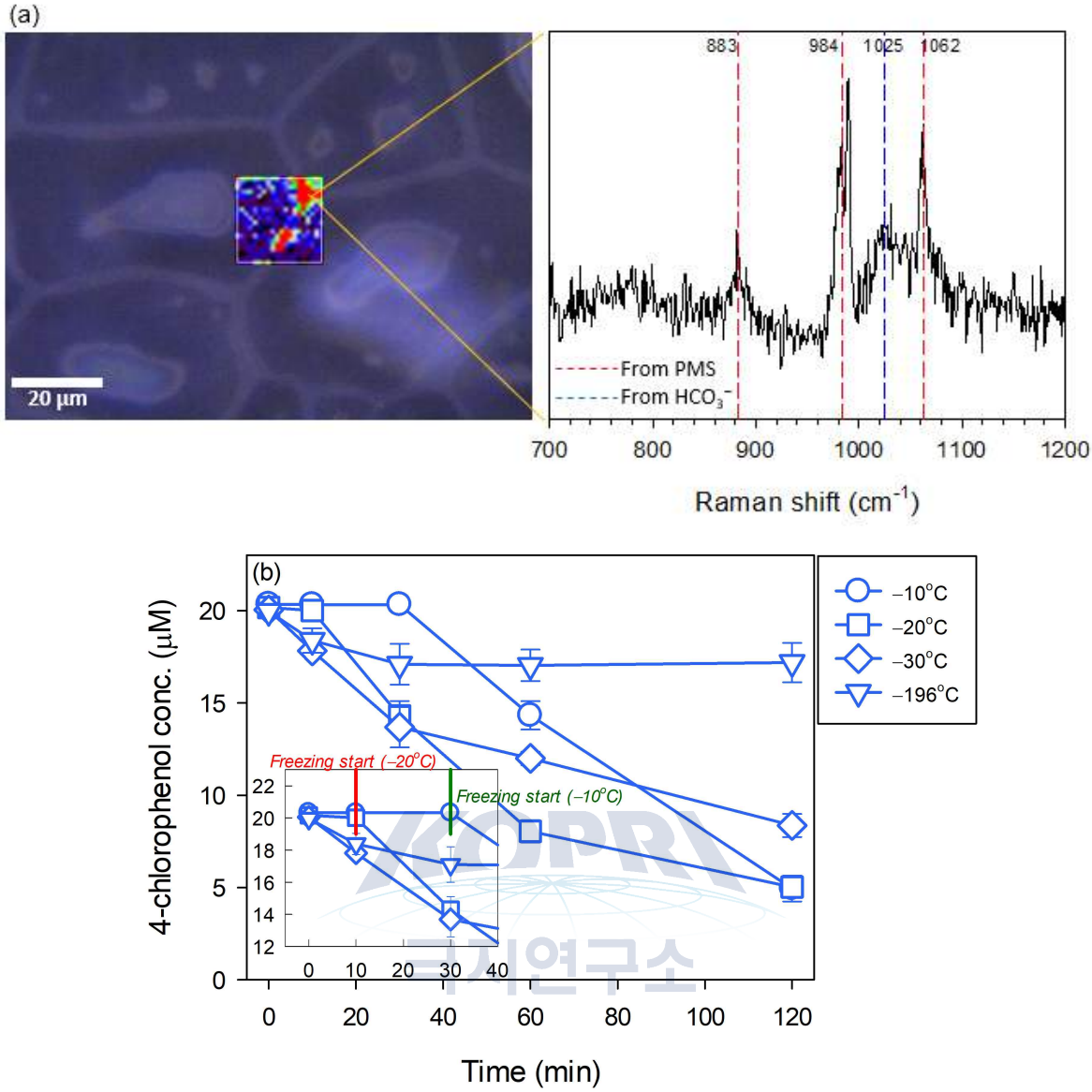



Fig. 2. (a) Microscope image of ice grain boundary and representative Raman spectrum of the frozen bicarbonate-PMS solution. The signal at 984 $cm^{-1}$ was selected to show the map image. Cooling speed = -2℃/min; terminal temperature = -20℃; $[PMS]_0$ = 5 mM; $[HCO_3^-]_0$ = 10 mM. (b) 4-CP concentration profile at different freezing temperatures. Temperatures of -10, -20, and -30℃ were obtained via use of an ethanol bath and that of -196℃ was obtained using liquid $N_2$. $[4\text{-CP}]_0$ = 0.02 mM; $[PMS]_0$ = 0.5 mM; $[HCO_3^-]_0$ = 5 mM; $pH_i$ = 9.

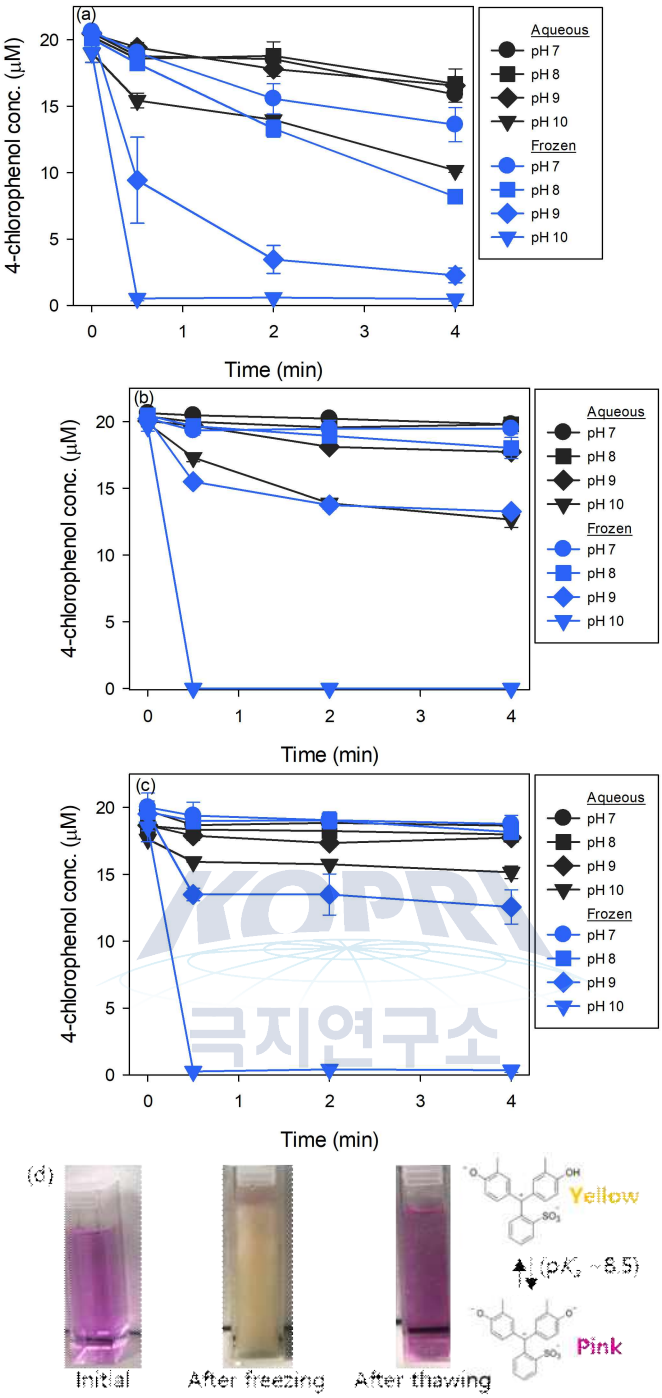



Fig. 3. 4-CP degradation by PMS. The solution pH was adjusted by (a) carbonate, (b) phosphate, and (c) hydroxide anion. $[4\text{-CP}]_0$ = 0.02 mM; $[PMS]_0$ = 0.5 mM; $[anion]_0$ = 5 mM; temperature = 25 ℃ (aqueous) and -20 ℃ (frozen). (d) The color of cresol-red in the bicarbonate solution. $[HCO_3^-]_0$ = 5 mM; $pH_i$ = 9; Freezing temperature = -20 ℃.

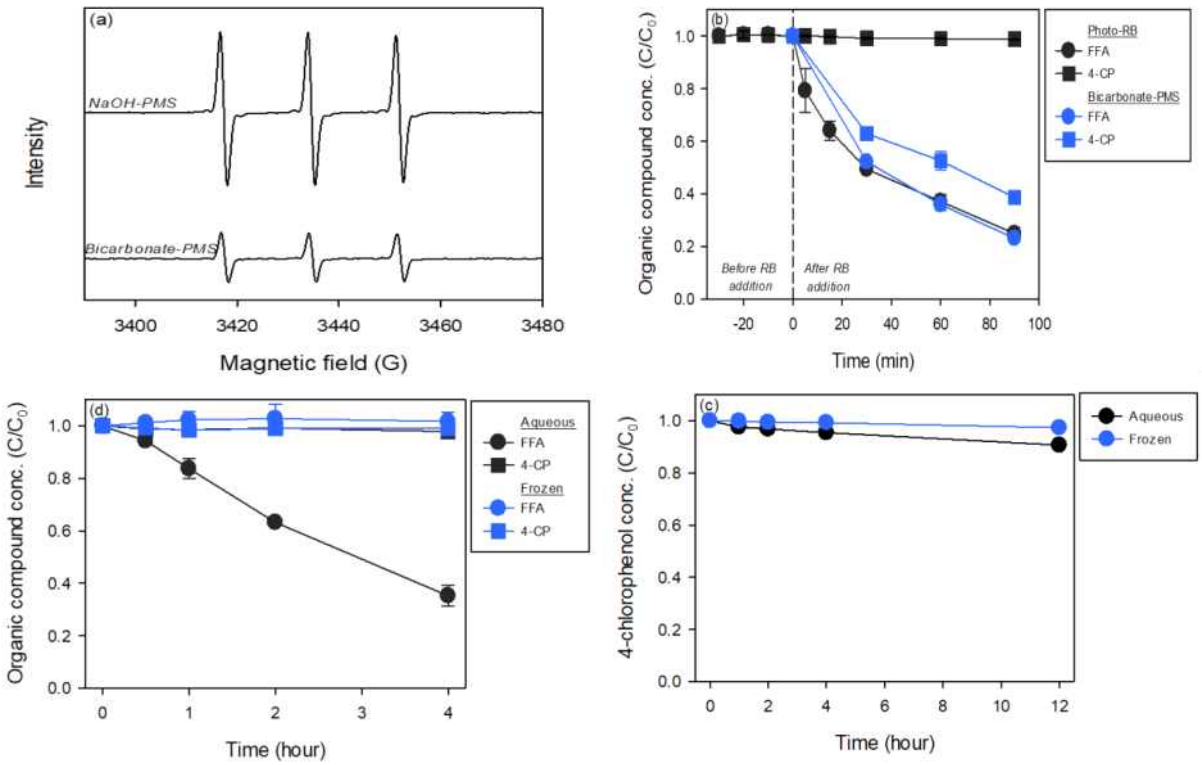



Fig. 4. (a) EPR signal of TEMPO of the frozen PMS solution. NaOH was infused into the PMS solution to make the pH the same as that of the bicarbonate-PMS. $[TEMP]_0$ = 1 mM; $[PMS]_0$ = 0.5 mM; $[HCO_3^-]_0$ = 5 mM (bicarbonate-PMS); $[NaOH]_0$ = 0.325 mM (NaOH-PMS); $pH_i$ = 9; Temperature = -20℃. (b) Degradation of organic pollutants in the photo-excited RB and frozen bicarbonate-PMS. In RB systems: $[RB]_0$ = 0.5 μM; $[HCO_3^-]_0$ = 1 mM, In PMS system: $[PMS]_0$ = 0.5 mM; $[HCO_3^-]_0$ = 5 mM; [organic substrate]$_0$ = 0.05 mM; pHi = 9. (c) Degradation of 4-CP in the bicarbonate activated hydrogen peroxide system. $[H_2O_2]_0$ = 200 mM; $[HCO_3^-]_0$ = 100 mM; $[4\text{-CP}]_0$ = 0.2 mM; $pH_i$ = 9. (d) Degradation of organic pollutants in the bicarbonate-PDS system. $[PDS]_0$ = 5 mM; $[HCO_3^-]_0$ = 5 mM; [organic substrate]$_0$ = 0.05 mM; $pH_i$ = 9; temperature = 25 ℃ (aqueous) and -20 ℃ (frozen).

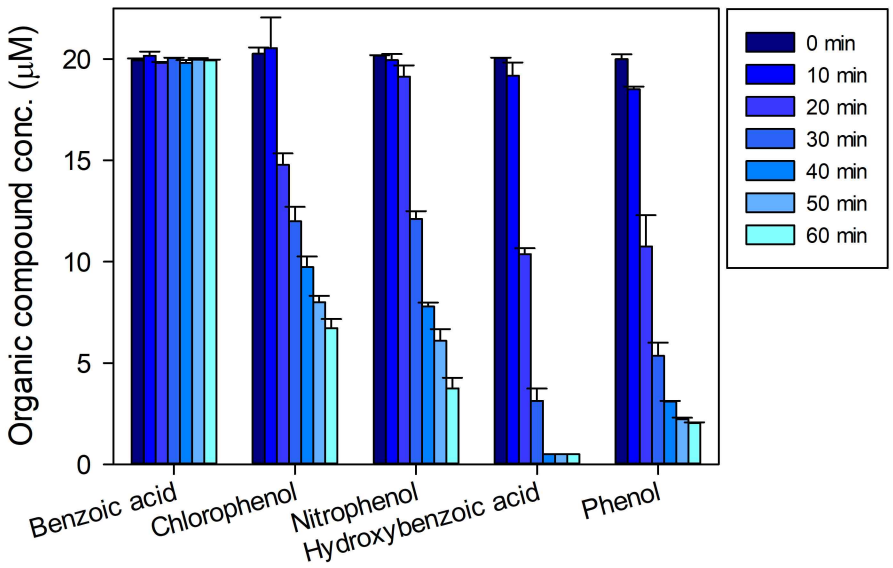



Fig. 5. Degradation of various selected organic compounds in the frozen bicarbonate-PMS system. $[PMS]_0$ = 0.5 mM; $[HCO_3^-]_0$ = 5 mM; [organic substrate]$_0$ = 0.02 mM; $pH_i$ = 9; temperature = -20 ℃.

KOPRI
극지연구소

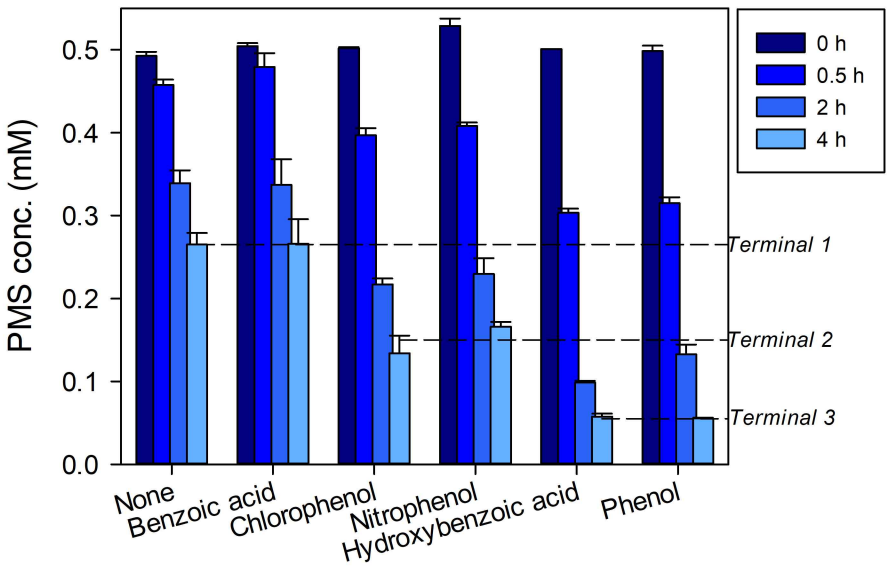



Fig. 6. PMS concentrations obtained using various target organic substrates in the bicarbonate-PMS system with freezing. $[PMS]_0$ = 0.5 mM; $[HCO_3^-]_0$ = 5 mM; [organic substrate]$_0$ = 0.02 mM; $pH_i$ = 9; temperature = -20 ℃.

KOPRI
극지연구소

# 제 9 절. Proton Transport and Related Chemical Processes of Ice⑨

Du Hyeong Lee[1] and Heon Kang[2]

[1]Korea Polar Research Institute, 26 Songdomirae-ro

[2]Department of Chemistry and The Research Institute of Basic Sciences, Seoul National University

## Abstract

Excess protons play a key role in the chemical reactions of ice because of their exceptional mobility, even when the diffusion of atoms and molecules is suppressed in ice at low temperatures. This article reviews the current state of knowledge on the properties of excess protons in ice, with a focus on the involvement of protons in chemical reactions. The mechanism of efficient proton transport in ice, which involves a proton-hopping relay along the hydrogen-bond ice network and the reorientation of water, is discussed and compared with the inefficient transport of hydroxide in ice. Distinctly different properties of protons residing in the ice interior and on the ice surface are emphasized. Recent observations of the spontaneous occurrence of reactions in ice at low temperatures, which include the dissociation of protic acids and the hydrolysis of acidic oxides, are discussed with regard to the kinetic and thermodynamic effects of mobile protons on the promotion of unique chemical processes of ice.

## 1. Introduction

Ice is ubiquitous in the cryosphere environment of Earth and in outer space and provides important media for chemical reactions that occur in nature at low temperatures. Famous examples include the heterogeneous reactions on the polar stratospheric ice particles that lead to the seasonal depletion of the ozone layer.[1] Astronomical observations using infrared (IR) telescopes and laboratory simulation experiments support the possibility that simple chemical species are transformed into more complex molecules on ice particles in interstellar space.[2-3] In early studies on these processes, empirical observation was usually a higher priority than obtaining a basic chemical understanding of the observed phenomena. Fundamental principles that underlie these ice-related chemical processes are of interest, but the current level of understanding of the chemistry of ice is very limited, compared

⑨ 본 연구는 본 과제(PE21120)와 해양수산부 지원사업(15250103, KOPRI Grant PM21030)의 일환으로 수행되었으며, 결과는 *J. Phys. Chem. C* 2021, 125, 8270-8281에 출간되었다.

with the vast knowledge regarding reactions in the aqueous or gas phase, which has been accumulated for a long time.

According to a basic knowledge of chemical kinetics, cold ice can be considered an adverse environment for reactions to occur, because reagent molecules are trapped immobile in a solid ice lattice, and the rate of diffusion of the molecules is reduced by several orders of magnitude compared with that in liquid water. In addition, there is insufficient thermal energy to surmount the reaction activation barrier. However, a notable exception is the "excess" proton (also called $H^+$ ion, hydronium, or positive ionic defect) in ice. Excess protons efficiently migrate in ice via the Grotthuss mechanism, which involves a proton-hopping relay along the hydrogen-bonded water chain of the ice network.4-5 This process makes the protons uniquely mobile species in ice at low temperatures, where the diffusion of atoms and molecules is extremely suppressed. The general mechanism for the transport of protons in ice has been well established through extensive studies.4-5 However, considerable uncertainties and confusion still exist in the literature regarding the details of the proton-transport mechanism as well as the properties of excess protons in ice. The present review focuses on these issues. It discusses the current level of understanding of the static and dynamic properties of excess protons in ice, with an emphasis on the roles of protons in the chemical reactions of ice. The remainder of this paper is organized as follows. Section 2 presents a brief history of studies on proton-transport phenomena in ice and discusses recent developments. Section 3 highlights the different properties of protons residing in ice and on its surface. Section 4 addresses the chemical reactions and their connection with the mobile protons of ice. Section 5 presents a summary and concluding remarks.

Excellent reviews have been published on the chemical processes of ice surfaces. These reviews are primarily focused on the structure of ice surfaces and adsorbate - surface interactions;[6] surface chemical properties of frozen water films and sulfuric acid films;7 adsorption and ionization of hydrogen chloride on ice surfaces;[8] elementary steps of reactions on ice surfaces;[9] theoretical studies on heterogeneous reactions related to atmospheric ozone depletion;[10] structure, molecular diffusivity, and reactions on ice surfaces;[11] reactive scattering processes of low-energy ion beams on ice surfaces;[12-13] and adsorption, diffusion, and reactions on amorphous solid water (ASW) films relevant to cosmic dust grains.[14-15] The previous studies have mainly investigated the processes that occur on the surface of ice partly because chemical reactions occur more easily on the surface, where the molecular diffusivity is higher than that in the interior of ice. Additionally, various surface spectroscopic techniques are available for the analysis of the chemical states of ice surfaces in ultrahigh-vacuum (UHV) environments.

When the ice temperature increases close to the melting point, a quasi-liquid layer (QLL)

may form on the ice surface, as well as a liquid-phase compartment at the interface between the ice grain boundaries.[4-5,16] Such distinctly different microscopic environments of ice can act as a host for diverse types of reactions and have many interesting effects, such as accelerated reaction rates and new pathways due to the freeze-concentration effect in the liquid compartment,[17-20] as well as the synthesis of new materials on the QLL-covered ice surface.[21] These high-temperature chemical processes are important issues in environmental research related to terrestrial, oceanic, and atmospheric ices.[17,22-23] Such subjects are beyond the scope of the present review, and interested readers are referred to excellent reviews annotated above. The present review is restricted to ice processes occurring at low temperatures (typically below 160 K), at which an ice surface has a solid-like property without a QLL. Additionally, an ice sample can be prepared and maintained under UHV conditions at these low temperatures, which is an important advantage for conducting experiments on ice samples in the absence of impurities owing to the adsorption of environmental gases.

Recent progress in the studies on proton behaviors and chemical reactions of ice would not have been possible without parallel development in the studies on other related phenomena of ice, e.g., the morphology of vapor-deposited ice films,[24-26] the phase transition of ASW to crystalline ice,[24-25,27-32] the diffusion of molecules in ice,[33-34] the mixing and segregating behaviors of foreign additives,[35-48] the structure of the ice film/metal interface,[49-52] and the roughening transition of thin ice films on metal substrates.[24,53-56] A majority of credible information about these phenomena has been accumulated during the past two decades through extensive experimental studies that employ a thin-film growing technique and spectroscopic analysis of ice samples under UHV conditions. During the investigation of chemical processes of ice, unwanted side processes related to these phenomena may concomitantly occur for ice samples and interfere with the observation, depending on the temperature and preparation conditions of the samples. Therefore, knowledge of these processes is essential for discriminating their effects from experimental observations or avoiding them via careful design of the experiment.

## 2. Proton transport in ice

The transport phenomena of excess protons in ice have been a subject of interest in the physics and chemistry of ice for a long time. In the late 1950s, Eigen and De Maeyer[57-58] studied the proton transport phenomena in ice and liquid water and concluded that the proton mobility in ice is higher than that in liquid water, probably by one to two orders of magnitude, based on the measurements of the electrical conductivity of ice available at that time. They attributed the high proton mobility in ice to efficient proton jumps along the

hydrogen-bonded network of an ice crystal, in contrast to the structural diffusion of protons in an aqueous solution, which involves the rearrangement of the protonated water complex as the rate-determining step. The electrical conductivity measurements for ice were subjected to a large uncertainty because of the contribution of complicating factors of unknown magnitudes, including the ice - electrode interfacial phenomena.[57] This led to the reports of very different conclusions regarding the proton mobility in ice in other investigations.[4-5,59-60] Around the same time, Jaccard[61-63] and Onsager[64] developed the theory of charge conduction in ice based on the properties of ionic and Bjerrum (orientational) defects in ice.[65] According to this molecular-level theory, charge conduction occurs through a combination of ionic defect transfer, which involves successive proton jumps along the hydrogen-bond network of ice, and Bjerrum defect transfer, which involves the reorientation of water molecules. Figure 1 illustrates this proton-transport mechanism. A proton-hopping relay occurs along the water chain with proper hydrogen-bond polarization (Figure 1a), but the proton transfer path is interrupted by the trapping of a proton at the Bjerrum L defect (Figure 1b). The reorientation of water releases a proton from the trap (Figure 1c), and proton transfer in the ice resumes (Figure 1d). For the next proton to pass through the same path, the hydrogen-bond polarization direction of the water chain must be returned to its original state via Bjerrum defect transfer (not shown). This elegant theory has provided a basis for interpreting the conductivity and dielectric relaxation measurements for ice and yielded information about the mobility and relative charge of ionic and Bjerrum defects.[5]

In the 1980s, Devlin and coworkers[67-69] used IR spectroscopy to study proton-transport phenomena in ice. They investigated the H/D isotopic exchange process of $D_2O$-doped $H_2O$-ice films and observed that intact $D_2O$ molecules undergo stepwise conversion to coupled $(HOD)_2$ units and ultimately to individual isolated HOD molecules. The results provided clear molecular-level evidence that proton conduction in ice occurs through proton hopping and water reorientation steps ("hop-and-turn" mechanism). In addition, they concluded that excess protons are trapped by Bjerrum defects in the ice lattice at a low temperature, and the protons become mobile upon thermal activation of Bjerrum defect motion at a temperature above ~120 K.[69] There have been opposing experimental observations regarding proton mobility in ice also;[59,70] however, as discussed in section 3, these results most likely resulted from the ice surface phenomena rather than reflecting the properties of protons in the bulk phase, according to further investigations.[59,71] Two decades later, Lee et al.[71-73] confirmed the proton mobility and transport mechanism by conducting surface spectroscopic measurements for thin ice films, which revealed that excess protons migrate through an ice film via the hop-and-turn mechanism at temperatures above 125 K. The study also indicated that a small portion of protons may be transmitted through the

ice film via a hopping relay process without water reorientation at temperatures below 100 K.[73]

Huppert and coworkers.[74-76] studied proton transport in ice by conducting time-resolved fluorescence experiments for ice samples containing excess protons and proton-sensitive fluorescent molecules. They found that the diffusion rate of protons in ice at temperatures of 235 - 270 K is 10 times faster than that in liquid water at 295 K. The diffusion coefficient exhibits a weak temperature dependence in this range, with an activation energy of $E_a < 1$ kJ/mol. The proton-hopping time was estimated to be approximately 0.2 ps. Surprisingly, this value is in accordance with the conclusion drawn by Eigen and De Maeyer in the 1950s from the electrical conductivity measurements of ice despite the large uncertainty in the measurements.[57] In the range of 175 - 235 K, the diffusion coefficient varied significantly with changes in the temperature with $E_a \approx 30$ kJ/mol, indicating that water reorientation is the rate-determining step of proton diffusion.[76] Quasi-elastic neutron scattering (QENS) experiments performed by the same group revealed a good correspondence between the proton-hopping times estimated from the time-resolved fluorescence experiments and the neutron scattering experiments.[77] Timmer et al.[78] studied proton transport from photoacids to bases embedded in ice using femtosecond pump-probe spectroscopy. They observed that proton transfer occurs in two distinct timescales: a fast (~1 ps) transfer across a short distance independent of temperature at 240 - 270 K and a slow (~300 ps at 270 K) transfer across a longer distance with strong temperature dependence. The fast proton-transfer processes observed in the foregoing time-resolved spectroscopic experiments may correspond to proton-hopping events along the water wire between the proton donor and acceptor. The length of the proton-conducting wire in these experiments may be short and dependent on the sample preparation conditions. The slow transfer processes with strong temperature dependence may result from the rate-determining behavior of other steps of the proton-transport mechanism, such as Bjerrum defect migration and rearrangement of the hydration structures of proton donors and acceptors.

Theoretical studies using quantum mechanical (QM) calculations and molecular dynamics (MD) simulations have provided valuable insights into the structure, energy, and dynamics of excess protons in ice. Ohmine and coworkers[79-80] investigated the potential energy surfaces associated with proton transfer in ice using ab initio calculations combined with an empirical method (called the QM/MM method). In ice (in contrast to liquid water), a stable hydrated proton structure is not formed, because of the structural constraints of the ice lattice. Thus, excess protons are not trapped in a deep energy minimum in an ice crystal but transferred along the ice network on small energy barriers.[79] The stretching and shrinking motions of intermolecular O - O distances of the ice structure around the excess

proton are mutually coupled to facilitate sequential proton transfers in a concerted fashion. Recent MD simulations[66,81-82] indicated that proton transfer occurs on a timescale of ~1 ps with an Arrhenius energy barrier of 1.5 kJ/mol. The rate of proton diffusion decreases with a decrease in the temperature, for example, by a factor of 20 when the temperature decreases from 270 to 50 K.[81] These trends are in accordance with the results of real-time spectroscopic measurements.[74-76,78]

The proton transport in ASW was also studied by theoretical calculations.[83-84] The local trapping structure of excess protons in ASW somewhat resembles the hydronium structures in liquid water but has evolved to a network with enhanced directionality.[83] Excess protons undergo sporadic jumps between these structures through a water bridge. QM/effective fragment potential (EFP) calculations at the B3LYP level revealed that the average proton-hopping time is approximately 0.3 ps in ASW at 160 K and increases to 0.05 ps at 300 K.[84] The energy barrier for the proton hopping is approximately 2.7 kJ/mol.[84]

Although the major features of the proton transport phenomena in ice have been well established through extensive experimental and theoretical studies, there are uncertain features that need further clarification. In the following, two specific issues are discussed. (1) Does proton hopping occur in ice even at very low temperatures? (2) How different or similar are the transport mechanisms of hydronium and hydroxide? The first question arises from the consideration that proton hopping along the ice network is assisted by geometrical relaxation in the ice structure.[79] In this case, the effective mass of the proton transfer is expected to be large, and the proton may be less mobile at very low temperatures. MD simulations indicate that the proton-hopping rate in ice $I_h$ is significantly reduced as the temperature decreases from 270 to 50 K, and it becomes almost zero in ice $I_c$ at 50 K.[81] Lee et al.[85] investigated this issue by performing experiments to measure the proton-transfer efficiency from a donor ($H_3O^+$) to an acceptor ($NH_3$) embedded in ASW at temperatures of 10−80 K. The proton-transport distance was controlled by changing the separation distance between the donor and the acceptor in the samples. They observed that protons migrated across a distance of approximately 10 water molecules on average. Importantly, the proton-transfer efficiency did not change significantly from 80 to 10 K. The results indicate that proton hopping occurs at temperatures as low as 10 K and that its efficiency is not significantly affected by the lattice temperature.

In the experiment performed by Lee et al.,[85] the transient mobility of excess protons in ASW was observed; a mobile proton is released from a stable hydronium structure by the external stimulus of ammonia adsorption on the ASW film surface.[85] One might question the idling mobility of excess protons in a perfectly crystalline ice, but this would only be a hypothetical question because excess protons are almost always trapped at defects in real ice at low temperatures.[68-69,86-87] There was a report about the observation of idling mobility

of protons in a neutral ice $I_h$ lattice at 5 K in QENS experiments,[88] but this claim was refuted by further investigations.[89]

The second issue addresses the assumption of the "mirror image" transport mechanisms of hydronium and hydroxide in ice, i.e., hydroxide moves through sequential "proton hole" transfers in analogy to hydronium transport through proton-hopping events.[4-5] Recent studies indicate that fundamentally different molecular mechanisms may operate for the transport of hydronium and hydroxide in ice.[84,90-93] Moon et al.[90] examined the migratory behaviors of $H_3O^+$ and $OH^-$ in ASW at ~80 K and observed that the migration distance of $H_3O^+$ is much longer (<23 ML) than that of $OH^-$ (<5 ML). Lee et al.[93] measured the migration speeds of $H_3O^+$ and $OH^-$ from the interior of an ASW film sample to its surface. The H/D exchange reactions that these ions underwent along the passage through a $D_2O$-ASW film were also monitored. The study revealed that hydronium migrates through ASW faster than hydroxide to appear on the sample surface at temperatures of >140 K during a gradual increase in the sample temperature, in contrast to the slower appearance of hydroxide on the surface at >155 K. Furthermore, hydronium undergoes extensive H/D exchange with $D_2O$, whereas hydroxide does not. Figure 2 shows the extent of the H/D exchange reactions for hydronium and hydroxide observed in these experiments.[93] Hydroniums and water molecules detected on the surface had virtually identical H/(H + D) ratios (HDRs) at all the investigated temperatures (Figure 2a), indicating efficient H/D exchange between hydronium and water molecules during the hydronium migration via proton transfer. In contrast, the HDR of surface hydroxide was far higher than that of surface water at 154 - 168 K (Figure 2b). Using this HDR value, the probability that hydroxide undergoes proton-hole transfer during passage through one monolayer of $D_2O$ is estimated to be <4% at 160 K.[93] This shows that hydroxide moves exclusively via molecular hydroxide diffusion rather than proton-hole transfer.

Different proposals were also reported for the transport mechanism of negative charge carriers in ice. Recently, Watanabe and coworkers[94-96] studied the behavior of OH radicals produced by ultraviolet (UV) photolysis of ASW. When the ASW films grown on a metal substrate were exposed to both UV photons and low energy electrons at 10−50 K, negative current was measured at the metal substrate along with a decrease in OH radical population at the ASW surface. They proposed that the negative current results from electron attachment to OH radicals and the transport of resultant $OH^-$ ions through ASW via a proton-hole transfer mechanism. The negative current, however, may originate from multiple sources in these experiments, including electron transmission through ASW,[97-98] electron attachment to OH radicals and defect structures in ASW, as well as the proposed $OH^-$ transport. These various possibilities weaken the proposal of $OH^-$ transport via a proton-hole transfer mechanism. Compelling evidence of this mechanism would be the

direct observation of hydroxide diffusion and the H/D exchange of hydroxides and water molecules in the ice, but to our best knowledge, these processes have not yet been reported for ASW or crystalline ice at low temperatures (e.g., below 90 K).

Uddin et al.[84] investigated the origin of the different transport mechanisms of hydronium and hydroxide by performing QM/EFP-MD calculations for the transport of these ions in a condensed-phase water model. The calculated free-energy barrier of proton transfer for hydronium is significantly lower (by ~5.4 kJ/mol) in height and narrower (by 0.02 nm) in width than that of proton transfer to hydroxide (i.e., proton-hole transfer). These differences in the potential energy surface strongly affect the transport dynamics of the two species and significantly reduce the efficiency of proton transfer for hydroxide at low temperatures. For example, hydroxide hardly undergoes proton transfer with water at 160 K within 100 ps, whereas 80% of hydronium does so within 1 ps. At 300 K, the proton transfer to hydroxide is still relatively suppressed, and the average time for proton transfer to hydroxide is two orders of magnitude longer than that of hydronium (~5 ps vs. ~0.04 ps). These theoretical results agree with the experimental results observed for ASW at 154 - 168 K (Figure 2).[93] Furthermore, the studies suggest that molecular hydroxide transport may play a significant role for hydroxide diffusion in aqueous solutions also.[84]

## 3. Protons at surface

Protons residing at the surface of ice can influence a variety of ice surface phenomena, including the electrical conductivity, charge imbalance, and acid - base properties of the ice surface. Recent studies have shown that excess protons tend to accumulate at the ice surface rather than disperse uniformly in the bulk phase.[71-73,99-105] Additionally, the surface-residing protons exhibit significantly different properties from those in the interior. Historically, insufficient information about these properties has been a major problem that hampers accurate measurement of proton conductivity for ice samples.[5,59,70] Evidence that excess protons have a propensity for ice surfaces has been obtained from several different experimental observations over the past two decades. Cowin et al.[70] deposited very low-energy (1 eV) beams of $H_3O^+$ ions onto an ice film surface and observed that hydronium ions did not migrate from the ice surface to the interior over a wide range of temperatures (30 - 190 K). This observation was initially interpreted as a lack of proton mobility through the ice. Later, on the basis of LES experiments for ice film samples, Lee et al.[71-72] reinterpreted the observation as an indication of the thermodynamic affinity of protons for ice surfaces, rather than the immobility of protons through the ice. Further evidence came from the observation of asymmetric proton-transport behavior between the ice surface and interior, i.e., protons spontaneously migrate from the ice interior to the

surface, but the reverse migration does not occur.[73,99] Figure 3 shows the surface-segregating behavior of excess protons observed in TPD, LES, and reactive ion scattering (RIS) experiments for "hydronium-sandwich" ice films.[99] Upon gradual heating of the sample, protons migrate from the ice film interior to its surface to be detected as surface hydroniums at temperature above ~154 K (Figure 3b). Efficient H/D exchange between the hydronium and water molecules is indicated by the correlation between the isotopomeric compositions of hydroniums (Figure 3b) and water molecules (Figures 3a and 3c). Lilach et al.[100] observed a similar surface-segregative behavior for hydroniums that were generated by the dissociation of water at the interface of an ice film and a Pt(111) substrate.

Devlin and coworkers[101-102] measured the H/D exchange rate at the surface of ice nanocrystals by monitoring changes in the populations of dangling H and D bonds using IR spectroscopy. The results indicate that the proton activity for inducing H/D exchange between $H_2O$ and $D_2O$ at the ice surface is enhanced by a factor of approximately 20 compared with that in the ice interior.[102] More recently, Kato et al.[103] simultaneously measured the H/D exchange rates at the surface and in the interior of a pure ice film using isothermal desorption and reflection absorption IR spectroscopy (RAIRS), respectively. The proton activity at the topmost surface was increased by more than three orders of magnitude compared with that in the bulk. Because the proton activity is proportional to both the proton concentration and the mobility, and (as will be discussed shortly) the proton mobility is substantially lower on the ice surface than in the interior,[107] the enhanced proton activity at the surface is consistent with proton segregation at the surface.[102-103] The ratio of the proton concentration at the surface to that in the interior may be substantially higher than the corresponding ratio of the observed proton activity.[103]

The surface propensity of excess protons is well supported by theoretical calculations.[66,102,104-105,108-110] Density functional theory (DFT) calculations indicate that the hydronium structure is energetically stabilized at the ice surface compared with that in the tetrahedral ice lattice.[102,104,108-110] The calculated surface segregation energy of hydronium varies sensitively with respect to the local structure of the ice surface, particularly the spatial arrangement of dangling surface hydrogens, in a wide range of 20 - 80 kJ $mol^{-1}$.[104] Hydroxide is also stabilized at the ice surface with a comparable magnitude of surface segregation energy.[104] In contrast, water molecules are destabilized at the ice surface. It follows that the degree of autoionization of the ice surface is correspondingly higher than that of a bulk ice crystal. The autoionization constant of an ice surface cannot be accurately determined at present. Studies on the H/D exchange rates of ice nanoparticles with adsorbed $H_2S$ suggest that the autoionization constant of the ice surface may be on the same order of magnitude as the ionization constant of $H_2S$.[102]

In the foregoing studies, similar surface-segregative properties of protons were observed for different forms of ice samples (thin films,[71-73,99-100,103] nanocrystals,[101-102] ice models[66,102,104-105,108-110]) and different sources of protons (soft-landed hydroniums,[70] dissociation of acids,[71-72,99,101] dissociation of interfacial water,[100] and autoionization of ice[101-103]). These observations strongly indicate that the affinity of protons for ice surfaces is a thermodynamic property that is generally applicable to various ice conditions.

The depth distribution of surface-residing protons is an interesting subject, and it may be related to the depth of the ice surface region where the acidity is higher than that in the bulk ice.[82] Lee et al.[111] studied the depth distribution of excess protons generated by the ionization of HCl into $H^+$ and $Cl^-$ at an ASW surface. Both $H^+$ and $Cl^-$ ions have a thermodynamic propensity to reside on the ice surface.99 A negative voltage was observed for the space-charge layer (SCL) formed at the ASW surface, which indicates that $H^+$ penetrates deeper toward the interior than $Cl^-$, thereby generating a net negative charge at the outermost surface.[111] Assuming that $Cl^-$ remained at the surface,[47] the average depth of $H^+$ in the ASW surface was estimated to be $d(H^+) = 2.9 \pm 1$ ML.[111] Similar measurements for the SCL produced by adding CsOH on an ASW surface indicated that the average depth of $OH^-$ was $d(OH^-) = 1.0 \pm 0.3$ ML. Therefore, protons are distributed over a wider depth than hydroxide, although both species prefer to reside at the surface. This difference was explained by the higher mobility of $H^+$ compared with $OH^-$ and the entropy of $H^+$ diffusion in the ice.[111-112]

The thermodynamic affinity of protons for ice surfaces influences the dynamics of proton transport on the surface. Because of the energetic stability of a surface hydronium structure, a proton cannot diffuse freely on the surface but experiences a substantial barrier in moving between the hydronium structures. This situation is illustrated in Figure 4 by a sketch of the potential-energy profile of proton diffusion along the ice surface. The barrier height for surface proton diffusion is expected to be on the order of 10 kJ $mol^{-1}$ and vary substantially depending on the local surface structure, according to MD simulation results indicating that the surface segregation energy of hydronium is in the range of 20 - 80 kJ $mol^{-1}$.[104] The experimental activation energy for proton diffusion on a polycrystalline ice surface was 10  3 kJ $mol^{-1}$, as estimated from the Arrhenius behavior of the rate coefficients for the H/D exchange reaction of the ice surface at temperatures of 90 - 110 K.107 In this experiment, the H/D exchange rate was measured for an ice surface with preformed hydroniums, to eliminate the effect of the heat of acid ionization on proton diffusion and measure only the temperature effect.[107] These theoretical and experimental studies indicate that proton diffusion on the ice surface has very different characteristics from that inside the ice crystal, where it occurs over barriers with low and uniform heights (~1 kJ/mol).[66,74-76,81-82] Consequently, the proton mobility on the ice surface is

KOPRI 극지연구소

significantly lower than that inside the ice crystal and decreases rapidly as the temperature decreases.[66,104,107]

We close this section by briefly mentioning the contributions of the increased surface population of protons and their reduced mobility to the proton activity on the ice surface. Studies on the H/D exchange process of ice in the temperature range of 110 - 160 K indicate that the proton activity on ice surfaces is higher than that in the ice interior,[101-103] indicating that proton accumulation at the ice surface overwhelms the reduced mobility of surface protons at these temperatures. Whether this trend extends to higher temperatures is an interesting question related to the relative efficiencies of the surface and bulk reactions of ice particles in the atmosphere.[17,22-23] The degree of proton accumulation at the ice surface is expected to decrease with the increasing temperature, according to the Boltzmann factor. However, high temperatures activate surface proton diffusion. The opposite temperature dependences of the two effects make it difficult to predict the proton activity of the ice surface at high temperatures, which requires experimental verification.

## 4. Spontaneous chemical reactions

Although molecular diffusion is suppressed in ice at low temperatures, certain types of reactions can occur spontaneously in the ice or on its surface. Reported examples include the dissociation of strong (HCl, HBr, $HNO_3$, and $H_2SO_4$)[7-8,10,113-114] and weak protic acids (HF, halogen-substituted acetic acids)[112,115-118] and the hydrolysis of acidic oxides ($SO_2$ and NO2).[108-109,119-122] These reactions occur at ice temperatures of 8 - 150 K when reactant molecules are adsorbed on the ice surface or co-deposited with water molecules to form an ice mixture. A feature in common for these reactions is that they involve proton transfer with ice. For example, the dissociation of acids releases excess protons into the ice lattice. QM/EFP calculations[109] indicate that the hydrolysis of $SO_2$ on ice surfaces proceeds through transition states that involve proton transfer between the $SO_2$ adsorbate and ice. Experimental studies[109,120-122] show that the reactions of $SO_2$ and $NO_2$ on ice surfaces produce various protonated species as a result of facile proton transfer, and these species are kinetically isolated on the ice surface as metastable products at low temperatures. The facile proton transfer in these reactions indicates that proton mobility plays a crucial role in removing the kinetic constraint of the reactions imposed by molecular immobility in the ice lattice.

Remarkably, for certain reactions, the reaction yield is higher in ice at a low temperature than in an aqueous solution at room temperature,[112,115-118] indicating that the reaction becomes thermodynamically more favorable, not to mention kinetically feasible, in the ice. This effect is clearly manifested by the enhanced dissociation of weak acids in ice, as

opposed to their nondissociation in aqueous solutions. Ayotte et al.[115-116,118] observed that the adsorption of HF on the surface of an ASW film or dissolution within an ASW film at 40 - 80 K yielded strong continuous absorbance ("Zundel continuum") across the 1000 - 3275 $cm^{-1}$ region in the RAIR spectrum, which is the hallmark spectroscopic signature of hydrated protons.[123] Additionally, extensive H/D-isotope scrambling occurred in the ASW sample. These features indicate extensive ionic dissociation of HF in ASW and on its surface, although HF is a weak acid in an aqueous solution. Park et al.[112,117] reported that a series of fluoroacetic acids ($CH_xF_{3-x}COOH$; x = 0 - 2), which are weak acids, dissociated almost completely in ASW at 8 - 140 K, according to RAIRS detection of molecular and dissociated forms of the acids. Figure 5 shows the RAIR spectra of the acids dissolved in $D_2O$-ASW at 70 - 80 K, along with the spectra of pure acids. As indicated by the spectra of monofluoroacetic acid (MFA), difluoroacetic acid (DFA), and trifluoroacetic acid (TFA), the ν(O−H) band of the molecular carboxylic acid appeared for a pure acid sample (black traces) but disappeared when the acid was dissolved in ASW (red traces). In addition, the shape of the ν(C=O) band of the molecular carboxylic acid changed to that of the carboxylate anion in ASW. These changes indicate the complete dissociation of MFA, DFA, and TFA in ASW. That is, they behave as strong acids in ASW.

In contrast, the ν(O−H) and ν(C=O) bands of formic acid (FA) and acetic acid (AA) did not change significantly between the pure acid and acid-$D_2O$ mixture samples (Figures 5d and 5e), indicating that these acids do not dissociate in ASW. Interestingly, FA underwent efficient H/D exchange between molecular FA and $D_2O$-ASW, similar to the proton exchange equilibrium of weak acids in an aqueous solution.[112] These observations indicate that the boundary for acid dissociation and nondissociation in ASW is located between MFA ($pK_a$ = 2.82) and FA ($pK_a$ = 3.75), where the number in the parentheses is the acid dissociation constant for the aqueous solution. This suggests that the acid dissociation constant increases by a factor of ~$10^3$ in ASW compared with that in an aqueous solution at room temperature.[112]

The enhanced dissociation of weak acids in ASW indicates the thermodynamic effect of proton mobility for increasing the reaction yield. Park et al.[112] explained this observation in terms of an interesting proposition that the acid equilibrium is forward-shifted by the entropy of mobile protons injected from the acid into the ice. The excess proton diffuses into a large volume of the ice because of its high mobility.[85,117] The diffusion of proton increases the configurational entropy of the system according to the relationship $\Delta S_{conf} = kB\ln W$, where $kB$ is the Boltzmann constant and $W$ represents the number of positions accessible by a proton in the volume of proton diffusion in the ice. The entropy increase lowers the free energy of acid dissociation and shifts the equilibrium in the forward direction. It is noted that $\Delta S_{conf}$ is an extra quantity added to the residual entropy of ice,

and the Grotthuss proton diffusion does not change the residual entropy of the lattice. The authors estimated $\Delta S_{conf}$ to be approximately 63 J $mol^{-1}$ $K^{-1}$ for acid dissociation in an ASW sample prepared in corresponding experiments.[117] From the thermodynamic relationship between the entropy and the equilibrium constant, they showed that $\Delta S_{conf}$ can increase the acid dissociation constant in ASW by a factor of ~$10^3$, which agrees well with the experimental results for fluoroacetic acids.

$\Delta S_{conf}$ is unusually large compared with other entropies of molecular solids (e.g., residual entropy of ice $I_h$ = 3.4 J $mol^{-1}$ $K^{-1}$) and is comparable in magnitude to the entropy of gas (e.g., entropy of water vaporization = 109 J $mol^{-1}$1 $K^{-1}$). Therefore, $\Delta S_{conf}$ can significantly affect the thermodynamics of the reactions in ASW or crystalline ice. $\Delta S_{conf}$ is expected to be larger in crystalline ice than in ASW because of the longer proton-diffusion path in the former. This entropic effect can be pronounced when the enthalpy of the reaction is nearly thermoneutral, as in the case of dissociation of fluoroacetic acids in an aqueous environment.[124] If we consider that proton mobility is an intrinsic property of ice, we can imagine that this entropic effect operates for a wide range of physical and chemical phenomena of ice that involve proton transfer. Lee et al.[125] suggested that a similar entropic effect may promote the crystallization of ASW doped with acid impurities.

KOPRI 극지연구소

## 5. Summary and concluding remarks

Fundamental research on the chemical processes of ice is a relatively new area of study, and the discovery of additional interesting features is anticipated as further studies are performed in this area. Experimental and theoretical studies clearly indicate uniquely high mobility of excess protons in ice, which is attributed to a transport mechanism that involves a proton-hopping relay along the ice network and Bjerrum defect transfer. IR spectroscopic studies on the H/D exchange process of ice, ultrafast time-resolved spectroscopic studies on proton transport dynamics, and surface science studies on ice films containing excess protons have provided further detailed information about the proton-transport phenomena and the properties of excess protons in ice and on ice surfaces. A few reaction types investigated to date indicate that proton mobility plays a crucial role in the occurrence of chemical reactions in ice at low temperatures.

The proton-hopping relay along the ice network occurs with a low barrier (~1 kJ/mol) on a subpicosecond timescale. Therefore, an excess proton can move in ice even at very low temperatures across a limited length of water chain of the ice network that fulfills the structural requirement for proton tunneling. However, the excess protons are typically trapped in the defects of the ice lattice, rendering them immobile. The reorientation of water molecules at high temperatures releases the protons from the traps and resumes the

proton-transfer relay. These combined processes make protons migrate over a long distance, and the proton transport exhibits strong temperature dependence and a substantial activation barrier.

The protons at the ice surface exhibit significantly different properties from those in the interior of ice. Excess protons tend to accumulate at the surface rather than spread uniformly in the bulk crystal. The thermodynamic affinity of protons for ice surfaces results from the energetic stabilization of the hydronium structure at the surface. The stabilization also generates a substantial energy barrier for proton movement along the surface and significantly reduces the proton mobility. The activation energy for proton surface diffusion was estimated to be on the order of 10 kJ $mol^{-1}$. Because of the surface-accumulated protons, the electrical and chemical properties of the ice surface are expected to differ significantly from those of bulk ice.

In contrast to efficient proton transport in ice, hydroxide transport is relatively inefficient. Hydroxides can only move through the diffusion of molecular hydroxides without proton transfer. Therefore, at very low temperatures, excess protons are the only mobile charge carriers in ice, and the main role of hydroxides for electrical conductivity and chemical reactivity is to inhibit the activity of protons. Both protons and hydroxides have a propensity for the ice surface, but protons are distributed deeper into the ice interior than hydroxides.

Proton mobility is a key factor in the occurrence of chemical reactions in ice at low temperatures. The proton assists the reaction both kinetically and thermodynamically. Proton transfer between the reactant molecule and the ice lattice is kinetically feasible, even when the diffusion of molecules is suppressed. Furthermore, proton diffusion in ice generates a large amount of configurational entropy, which lowers the free energy of the proton-transfer reaction and shifts the equilibrium in the forward direction. This thermodynamic effect is clearly manifested by the dissociation of weak acids in ASW at low temperatures, in contrast to the nondissociation of these acids in aqueous solutions. In addition to efficient proton transfer, an important characteristic of reactions for ice is the strong kinetic constraint imposed on the reaction by the extremely low molecular diffusivity of ice.[9] Thus, reactions in ice or on ice surfaces do not proceed to the final thermodynamic products but are halted at intermediate stages. This often leads to the formation of protonated species as metastable products, which are produced by efficient proton transfer accompanied by kinetic trapping in cold ice environments.[9,109,120-122]

The facile occurrence of proton-transfer reactions implies that the acid - base reaction may be an important chemical process in cryogenic ice environments. For example, in the study of chemical reactions of ice particles in interstellar space, it has been assumed that the reactions are driven by external energy input, such as UV absorption, cosmic particle

bombardment, and thermal processing.[2-3] However, one can also imagine that spontaneous acid–base reactions may occur under interstellar ice conditions, even without external energy input. Excess protons may be generated by the photolysis of ice particles under ionizing radiation or by the injection of cosmic protons into the ice. The excess protons can be stored as hydronium ion in the ice and utilized for subsequent chemical reactions.[86-87] Moon et al.[126] proposed that such hydronium ion may act as an “invisible” acid for the reactions of interstellar ice particles. The acid–base reaction between hydronium ions and ammonia molecules trapped in the ice may explain the origin of the mysteriously large abundance of ammonium ions detected in interstellar molecular clouds.

Moving forward, it will be interesting to investigate whether the knowledge of the ice processes at low temperatures (<160 K) will be applicable to elucidate the corresponding processes occurring in terrestrial and atmospheric ice at higher temperatures. The transport mechanism, high mobility, and surface-segregative property of excess protons discussed herein are considered the intrinsic properties of the ice lattice and thus are not expected to drastically change at high temperatures. Therefore, this review will advance the research related to the chemistry of ice at various temperatures, although the microscopic environment of ice may differ at different temperatures.

KOPRI
극지연구소

## REFERENCES


1. Molina, M. J.; Tso, T. L.; Molina, L. T.; Wang, F. C. Y. Antarctic Stratospheric Chemistry of Chlorine Nitrate, Hydrogen-Chloride and Ice: Release of Active Chlorine. *Science* **1987**, *238*, 1253-1257.
2. Greenberg, J. M. Cosmic Dust and Our Origins. *Surf. Sci.* **2002**, *500*, 793-822.
3. van Dishoeck, E. F. ISO Spectroscopy of Gas and Dust: From Molecular Clouds to Protoplanetary Disks. *Annu. Rev. Astron. Astrophys.* **2004**, *42*, 119-167.
4. Hobbs, P. V. *Ice Physics*; Clarendon Press: Oxford, **1974**.
5. Petrenko, V. F.; Whitworth, R. W. *Physics of Ice*; Oxford University Press: Oxford, **1999**.
6. Devlin, J. P.; Buch, V. Surface of Ice as Viewed from Combined Spectroscopic and Computer Modeling Studies. *J. Phys. Chem.* 1995, *99*, 16534-16548.
7. Roberts, J. T. Chemistry at the Surfaces of Ice and Sulfuric Acid: Toward an Understanding of Adsorption at Molecular Solids. *Acc. Chem. Res.* **1998**, *31*, 415-421.
8. Buch, V.; Sadlej, J.; Aytemiz-Uras, N.; Devlin, J. P. Solvation and Ionization Stages of HCl on Ice Nanocrystals. *J. Phys. Chem. A* **2002**, *106*, 9374-9389.
9. Kang, H. Chemistry of Ice Surfaces. Elementary Reaction Steps on Ice Studied by Reactive Ion Scattering. *Acc. Chem. Res.* **2005**, *38*, 893-900.
10. Bianco, R.; Hynes, J. T. Heterogeneous Reactions Important in Atmospheric Ozone Depletion: A Theoretical Perspective. *Acc. Chem. Res.* **2006**, *39*, 159-165.
11. Park, S. C.; Moon, E. S.; Kang, H. Some Fundamental Properties and Reactions of Ice Surfaces at Low Temperatures. *Phys. Chem. Chem. Phys.* **2010**, *12*, 12000-12011.
12. Cyriac, J.; Pradeep, T.; Kang, H.; Souda, R.; Cooks, R. G. Low-Energy Ionic Collisions at Molecular Solids. *Chem. Rev.* **2012**, *112*, 5356-5411.
13. Bag, S.; Bhuin, R. G.; Natarajan, G.; Pradeep, T. Probing Molecular Solids with Low-Energy Ions. *Annu. Rev. Anal. Chem.* **2013**, *6*, 97-118.
14. Watanabe, N.; Kouchi, A. Ice Surface Reactions: A Key to Chemical Evolution in Space. Prog. *Surf. Sci.* **2008**, *83*, 439-489.
15. Hama, T.; Watanabe, N. Surface Processes on Interstellar Amorphous Solid Water: Adsorption, Diffusion, Tunneling Reactions, and Nuclear-Spin Conversion. *Chem. Rev.* **2013**, *113*, 8783-8839.
16. Slater, B.; Michaelides, A. Surface Premelting of Water Ice. *Nat. Rev. Chem* **2019**, *3*, 172-188.
17. Bartels-Rausch, T., et al. A Review of Air-Ice Chemical and Physical Interactions


KOPRI 극지연구소

(AICI): Liquids, Quasi-Liquids, and Solids in Snow. *Atmos. Chem. Phys.* **2014**, *14*, 1587-1633.

18. Takenaka, N.; Ueda, A.; Maeda, Y. Acceleration of the Rate of Nitrite Oxidation by Freezing in Aqueous-Solution. *Nature* **1992**, *358*, 736-738.
19. O'Sullivan, D.; Sodeau, J. R. Freeze-Induced Reactions: Formation of Iodine-Bromine Interhalogen Species from Aqueous Halide Ion Solutions. *J. Phys. Chem. A* **2010**, *114*, 12208-12215.
20. Kim, K.; Menacherry, S. P. M.; Kim, J.; Chung, H. Y.; Jeong, D.; Saiz-Lopez, A.; Choi, W. Simultaneous and Synergic Production of Bioavailable Iron and Reactive Iodine Species in Ice. *Environ. Sci. Technol.* **2019**, *53*, 7355-7362.
21. Kim, K.; Park, M. J. Ice-Assisted Synthesis of Functional Nanomaterials: The Use of Quasi-Liquid Layers as Nanoreactors and Reaction Accelerators. *Nanoscale* **2020**, *12*, 14320-14338.
22. Abbatt, J. P. D. Interactions of Atmospheric Trace Gases with Ice Surfaces: Adsorption and Reaction. *Chem. Rev.* **2003**, *103*, 4783-4800.
23. Huthwelker, T.; Ammann, M.; Peter, T. The Uptake of Acidic Gases on Ice. *Chem. Rev.* **2006**, *106*, 1375-1444.
24. Hodgson, A.; Haq, S. Water Adsorption and the Wetting of Metal Surfaces. *Surf. Sci. Rep.* **2009**, *64*, 381-451.
25. Smith, R. S.; Petrik, N. G.; Kimmel, G. A.; Kay, B. D. Thermal and Nonthermal Physiochemical Processes in Nanoscale Films of Amorphous Solid Water. *Acc. Chem. Res.* **2012**, *45*, 33-42.
26. Stevenson, K. P.; Kimmel, G. A.; Dohnalek, Z.; Smith, R. S.; Kay, B. D. Controlling the Morphology of Amorphous Solid Water. *Science* **1999**, *283*, 1505-1507.
27. Smith, R. S.; Huang, C.; Wong, E.; Kay, B. D. The Molecular Volcano: Abrupt CCl4 Desorption Driven by the Crystallization of Amorphous Solid Water. *Phys. Rev. Lett.* **1997**, *79*, 909.
28. Souda, R. Glass Transition and Intermixing of Amorphous Water and Methanol. *Phys. Rev. Lett.* **2004**, *93*, 235502.
29. Safarik, D. J.; Mullins, C. B. The Nucleation Rate of Crystalline Ice in Amorphous Solid Water. *J. Chem. Phys.* **2004**, *121*, 6003-6010.
30. Backus, E. H. G.; Grecea, M. L.; Kleyn, A. W.; Bonn, M. Surface Crystallization of Amorphous Solid Water. *Phys. Rev. Lett.* **2004**, *92*, 236101.
31. McClure, S. M.; Barlow, E. T.; Akin, M. C.; Tanaka, P. L.; Safarik, D. J.; Truskett, T. M.; Mullins, C. B. Effect of Dilute Nitric Acid on Crystallization and Fracture of

KOPRI 극지연구소

Amorphous Solid Water Films. *J. Phys. Chem. C* **2007**, *111*, 10438-10447.

32. Hama, T.; Ishizuka, S.; Yamazaki, T.; Kimura, Y.; Kouchi, A.; Watanabe, N.; Sugimoto, T.; Pirronello, V. Fast Crystalline Ice Formation at Extremely Low Temperature through Water/Neon Matrix Sublimation. *Phys. Chem. Chem. Phys.* **2017**, *19*, 17677-17684.
33. George, S. M.; Livingston, F. E. Dynamic Ice Surface in the Polar Stratosphere. *Surf. Rev. Lett.* **1997**, *4*, 771-780.
34. McClure, S. M.; Barlow, E. T.; Akin, M. C.; Safarik, D. J.; Truskett, T. M.; Mullins, C. B. Transport in Amorphous Solid Water Films: Implications for Self-Diffusivity. *J. Phys. Chem. B* **2006**, *110*, 17987-17997.
35. Gunster, J.; Krischok, S.; Kempter, V.; Stultz, J.; Goodman, D. W. Characterization of Coadsorbed Molecular Species in a Multilayer Solvent Environment on Insulating Surfaces. *Surf. Rev. Lett.* **2002**, *9*, 1511-1551.
36. Guo, J. H.; Luo, Y.; Augustsson, A.; Kashtanov, S.; Rubensson, J. E.; Shuh, D. K.; Agren, H.; Nordgren, J. Molecular Structure of Alcohol-Water Mixtures. *Phys. Rev. Lett.* **2003**, *91*, 157401.
37. Souda, R. Solvation of Octane at Water- and Methanol-Ice Surfaces and Surfactant Effect of Methanol at Octane-Water Interface Studied by Temperature-Programmed TOF-SIMS. *J. Phys. Chem. B* **2004**, *108*, 12159-12163.
38. Souda, R. A Temperature-Programed Time-of-Flight Secondary Ion Mass Spectroscopy Study of Intermixing of Amorphous Ethanol and Heavy-Water Films at 15-200 K. *J. Chem. Phys.* **2005**, *122*, 134711.
39. Souda, R. Interaction of Water with LiCl, LiBr, and LiI in the Deeply Supercooled Region. *J. Chem. Phys.* **2007**, *127*, 214505.
40. Souda, R. Hydration of Ammonia, Methylamine, and Methanol in Amorphous Solid Water. *Chem. Phys. Lett.* **2016**, *645*, 27-31.
41. Borodin, A.; Höfft, O.; Kahnert, U.; Kempter, V.; Allouche, A. Electron Spectroscopy (UPS(HeI and II) and Metastable Impact Electron Spectroscopy (MIES)) Applied to Molecular Surfaces: The Interaction of Atoms and Molecules With Solid Water. *Vacuum* **2004**, *73*, 15-24.
42. Bahr, S.; Borodin, A.; Hofft, O.; Kempter, V.; Allouche, A. Interaction of Formic Acid with Solid Water. *J. Chem. Phys.* **2005**, *122*, 234704.
43. Hofft, O.; Kahnert, U.; Bahr, S.; Kempter, V. Interaction of NaI with Solid Water and Methanol. *J. Phys. Chem. B* **2006**, *110*, 17115-17120.
44. Cyriac, J.; Pradeep, T. Probing Difference in Diffusivity of Chloromethanes through

Water Ice in the Temperature Range of 110-150 K. *J. Phys. Chem. C* **2007**, *111*, 8557-8565.

45. Cyriac, J.; Pradeep, T. Interaction of Carboxylic Acids and Water Ice Probed by Argon Ion Induced Chemical Sputtering. *J. Phys. Chem. C* **2008**, *112*, 1604-1611.
46. Kumar, G. N.; Cyriac, J.; Bag, S.; Pradeep, T. Low Energy Ion Scattering Investigations of N-Butanol-Ice System in the Temperature Range of 110-150 K. *J. Phys. Chem. C* **2009**, *113*, 14258-14263.
47. Kim, J. H.; Kim, Y. K.; Kang, H. Interaction of NaF, NaCl, and NaBr with Amorphous Ice Films. Salt Dissolution and Ion Separation at the Ice Surface. *J. Phys. Chem. C* **2007**, *111*, 8030-8036.
48. Kim, J. H.; Kim, Y. K.; Kang, H. Hydrolysis of Sodium Atoms on Water-Ice Films. Characterization of Reaction Products and Interfacial Distribution of Sodium and Hydroxide Ions. *J. Phys. Chem. C* **2009**, *113*, 321-327.
49. McBride, F.; Hodgson, A. Water and Its Partially Dissociated Fragments at Metal Surfaces. *Int. Rev. Phys. Chem.* **2017**, *36*, 1-38.
50. Sugimoto, T.; Aiga, N.; Otsuki, Y.; Watanabe, K.; Matsumoto, Y. Emergent High-Tc Ferroelectric Ordering of Strongly Correlated and Frustrated Protons in a Heteroepitaxial Ice Film. *Nature Physics* **2016**, *12*, 1063-1068.
51. Sugimoto, T.; Matsumoto, Y. Orientational Ordering in Heteroepitaxial Water Ice on Metal Surfaces. *Phys. Chem. Chem. Phys.* **2020**, *22*, 16453-16466.
52. Kim, Y.; Noh, C.; Jung, Y.; Kang, H. The Nature of Hydrated Protons on Platinum Surfaces. *Chem. Eur. J.* **2017**, *23*, 17566-17575.
53. Kimmel, G. A.; Petrik, N. G.; Dohnalek, Z.; Kay, B. D. Crystalline Ice Growth on Pt(111): Observation of a Hydrophobic Water Monolayer. *Phys. Rev. Lett.* **2005**, *95*, 166102.
54. Zimbitas, G.; Haq, S.; Hodgson, A. The Structure and Crystallization of Thin Water Films on Pt(111). *J. Chem. Phys.* **2005**, *123*, 174701.
55. Thurmer, K.; Bartelt, N. C. Nucleation-Limited Dewetting of Ice Films on Pt(111). *Phys. Rev. Lett.* **2008**, *100*, 186101.
56. Thurmer, K.; Nie, S. Formation of Hexagonal and Cubic Ice During Low-Temperature Growth. *Proc. Natl. Acad. Sci. U.S.A.* **2013**, *110*, 11757-11762.
57. Eigen, M.; De Maeyer, L. Self-Dissociation and Protonic Charge Transport in Water and Ice. *Proc. R. Soc. A* **1958**, *247*, 505-533.
58. Eigen, M. Proton Transfer, Acid-Base Catalysis, and Enzymatic Hydrolysis. Part I: Elementary Processes. *Angew. Chem. Int. Ed.* **1964**, *3*, 1-19.

59. Maidique, M. A.; Hippel, A. V.; Westphal, W. B. Transfer of Protons through Pure Ice Ih Single Crystals. III. Extrinsic Versus Intrinsic Polarization; Surface Versus Volume Conduction. *J. Chem. Phys.* **1971**, *54*, 150-160.

60. Kunst, M.; Warman, J. M. Nanosecond Time-Resolved Conductivity Studies of Pulse-Ionized Ice. 2. The Mobility and Trapping of Protons. *J. Phys. Chem.* **1983**, *87*, 4093-4095.

61. Jaccard, C. Etude Theorique Et Experimentale Des Proprietes De La Glace. *Helv. Phys. Acta* **1959**, *32*, 89-128.

62. Jaccard, C. Thermodynamics of Irreversible Processes Applied to Ice. *Phys. Konden. Mater.* **1964**, *3*, 99-118.

63. Jaccard, C. Mechanism of the Electrical Conductivity in Ice. *Ann. N.Y. Acad. Sci.* **1965**, *125*, 390-400.

64. Onsager, L.; Dupuis, M. The Electrical Properties of Ice. In *Electrolytes*, Pesce, B., Ed. Pergamon Press: Oxford, **1962**; pp 27-46.

65. Bjerrum, N. Structure and Properties of Ice. *Science* **1952**, *115*, 385-390.

66. Park, K.; Lin, W.; Paesani, F. Fast and Slow Proton Transfer in Ice: The Role of the Quasi-Liquid Layer and Hydrogen-Bond Network. *J. Phys. Chem. B* **2014**, *118*, 8081-8089.

67. Ritzhaupt, G.; Thornton, C.; Devlin, J. P. Infrared-Spectrum of $D_2O$ Vibrationally Decoupled in $H_2O$ Ice $I_c$. Chem. *Phys. Lett.* **1978**, *59*, 420-422.

68. Collier, W. B.; Ritzhaupt, G.; Devlin, J. P. Spectroscopically Evaluated Rates and Energies for Proton-Transfer and Bjerrum Defect Migration in Cubic Ice. *J. Phys. Chem.* **1984**, *88*, 363-368.

69. Wooldridge, P. J.; Devlin, J. P. Proton Trapping and Defect Energetics in Ice from FT-IR Monitoring of Photoinduced Isotopic Exchange of Isolated $D_2O$. *J. Chem. Phys.* **1988**, *88*, 3086-3091.

70. Cowin, J. P.; Tsekouras, A. A.; Iedema, M. J.; Wu, K.; Ellison, G. B. Immobility of Protons in Ice from 30 to 190 K. *Nature* **1999**, *398*, 405-407.

71. Moon, E. S.; Lee, C. W.; Kang, H. Proton Mobility in Thin Ice Films: A Revisit. *Phys. Chem. Chem. Phys.* **2008**, *10*, 4814-4816.

72. Lee, C. W.; Lee, P. R.; Kang, H. Protons at Ice Surfaces. Angew. *Chem. Int. Ed.* **2006**, *45*, 5529-5533.

73. Lee, C. W.; Lee, P. R.; Kim, Y. K.; Kang, H. Mechanistic Study of Proton Transfer and H/D Exchange in Ice Films at Low Temperatures (100-140 K). *J. Chem. Phys.* **2007**, *127*, 084701.

KOPRI 극지연구소

74. Uritski, A.; Presiado, I.; Huppert, D. Indication of a Very Large Proton Diffusion in Ice $I_h$. *J. Phys. Chem. C* **2008**, *112*, 11991-12002.

75. Uritski, A.; Presiado, I.; Huppert, D. Indication of a Very Large Proton Diffusion in Ice $I_h$. III. Fluorescence Quenching of 1-Naphthol Derivatives. *J. Phys. Chem. A* **2009**, *113*, 959-974.

76. Uritski, A.; Presiado, I.; Erez, Y.; Gepshtein, R.; Huppert, D. Temperature Dependence of Proton Diffusion in $I_h$ Ice. *J. Phys. Chem. C* **2009**, *113*, 10285-10296.

77. Presiado, I.; Lal, J.; Mamontov, E.; Kolesnikov, A. I.; Huppert, D. Fast Proton Hopping Detection in Ice $I_h$ by Quasi-Elastic Neutron Scattering. *J. Phys. Chem. C* **2011**, *115*, 10245-10251.

78. Timmer, R. L. A.; Cox, M. J.; Bakker, H. J. Direct Observation of Proton Transfer in Ice $I_h$ Using Femtosecond Spectroscopy. *J. Phys. Chem. A* **2010**, *114*, 2091-2101.

79. Kobayashi, C.; Saito, S. J.; Ohmine, I. Mechanism of Fast Proton Transfer in Ice: Potential Energy Surface and Reaction Coordinate Analyses. *J. Chem. Phys.* **2000**, *113*, 9090-9100.

80. Kobayashi, C.; Saito, S.; Ohmine, I. Mechanism of Proton Transfer in Ice. II. Hydration, Modes, and Transport. *J. Chem. Phys.* **2001**, *115*, 4742-4749.

81. Sakti, A. W.; Nishimura, Y.; Chou, C. P.; Nakai, H. Density-Functional Tight-Binding Molecular Dynamics Simulations of Excess Proton Diffusion in Ice $I_h$ , Ice $I_c$, Ice III, and Melted Ice VI Phases. *J. Phys. Chem. A* **2018**, *122*, 33-40.

82. Vacha, R.; Buch, V.; Milet, A.; Devlin, P.; Jungwirth, P. Autoionization at the Surface of Neat Water: Is the Top Layer pH Neutral, Basic, or Acidic? *Phys. Chem. Chem. Phys.* **2007**, *9*, 4736-4747.

83. Tahat, A.; Marti, J. Dynamical Aspects of Intermolecular Proton Transfer in Liquid Water and Low-Density Amorphous Ices. *Phys. Rev. E* **2014**, *89*, 052130.

84. Uddin, N.; Kim, J.; Sung, B. J.; Choi, T. H.; Choi, C. H.; Kang, H. Comparative Proton Transfer Efficiencies of Hydronium and Hydroxide in Aqueous Solution: Proton Transfer vs Brownian Motion. *J. Phys. Chem. B* **2014**, *118*, 13671-13678.

85. Lee, D. H.; Kang, H.; Kang, H. Tunneling Diffusion of Excess Protons in Amorphous Solid Water at 10 and 80 K. *J. Phys. Chem. C* **2019**, *123*, 3657-3663.

86. Moon, E. S.; Lee, C. W.; Kim, J. K.; Park, S. C.; Kang, H. UV-induced Protonation of Molecules Adsorbed on Ice Surfaces at Low Temperature. *J. Chem. Phys.* **2008**, *128*, 191101

87. Moon, E.-S.; Kang, H. Metastable Hydronium Ions in UV-irradiated Ice. *J. Chem. Phys.* **2012**, *137*, 204704.

88. Bove, L. E.; Klotz, S.; Paciaroni, A.; Sacchetti, F. Anomalous Proton Dynamics in Ice at Low Temperatures. *Phys. Rev. Lett.* **2009**, *103*, 165901.

89. Kolesnikov, A. I.; Ehlers, G.; Mamontov, E.; Podlesnyak, A. Ice $I_h$ Revisited: No Proton Tunneling Observed in a Quasielastic Neutron Scattering Experiment. *Phys. Rev. B* **2018**, *98*, 064301.

90. Moon, E.-s.; Kim, Y.; Shin, S.; Kang, H. Asymmetric Transport Efficiencies of Positive and Negative Ion Defects in Amorphous Ice. *Phys. Rev. Lett.* **2012**, *108*, 226103.

91. Kim, S.; Park, E.; Kang, H. Segregation of Hydroxide Ions to an Ice Surface. *J. Chem. Phys.* **2011**, *135*, 074703.

92. Kim, J. H.; Kim, Y. K.; Kang, H. Proton Transfer and H/D Isotopic Exchange of Water Molecules Mediated by Hydroxide Ions on Ice Film Surfaces. *J. Chem. Phys.* **2009**, *131*, 044705.

93. Lee, D. H.; Choi, C. H.; Choi, T. H.; Sung, B. J.; Kang, H. Asymmetric Transport Mechanisms of Hydronium and Hydroxide Ions in Amorphous Solid Water: Hydroxide Goes Brownian While Hydronium Hops. *J. Phys. Chem. Lett.* **2014**, *5*, 2568-2572.

94. Watanabe, N.; Sameera, W. M. C.; Hidaka, H.; Miyazaki, A.; Kouchi, A. Ultraviolet-Photon Exposure Stimulates Negative Current Conductivity in Amorphous Ice Below 50 K. *Chem. Phys. Lett.* **2019**, *737*, 136820.

95. Tsuge, M.; Watanabe, N. Behavior of Hydroxyl Radicals on Water Ice at Low Temperatures. *Acc. Chem. Res.* **2021**, *54*, 471-480.

96. Kitajima, K.; Nakai, Y.; Sameera, W. M. C.; Tsuge, M.; Miyazaki, A.; Hidaka, H.; Kouchi, A.; Watanabe, N. Delivery of Electrons by Proton-Hole Transfer in Ice at 10 K: Role of Surface OH Radicals. *J. Phys. Chem. Lett.* **2021**, *12*, 704-710.

97. Sagi, R.; Akerman, M.; Ramakrishnan, S.; Asscher, M. Temperature Effect on Transport, Charging, and Binding of Low-Energy Electrons Interacting with Amorphous Solid Water Films. *J. Phys. Chem. C* **2018**, *122*, 9985-9996.

98. Bang, J.; Kang, H. Transmission and Trapping of Low-Energy (1-10 eV) Electrons in Crystalline Ice Films. *J. Phys. Chem. C* **2020**, *124*, 15862-15869.

99. Park, E.; Lee, D. H.; Kim, S.; Kang, H. Transport and Surface Accumulation of Hydroniums and Chlorides in an Ice Film. A High Temperature (140-180 K) Study. *J. Phys. Chem. C* **2012**, *116*, 21828-21835.

100. Lilach, Y.; Iedema, M. J.; Cowin, J. P. Proton Segregation on a Growing Ice Interface. *Surf. Sci.* **2008**, *602*, 2886-2893.

101. Uras-Aytemiz, N.; Joyce, C.; Devlin, J. P. Protonic and Bjerrum Defect Activity near

the Surface of Ice at T < 145 K. *J. Chem. Phys.* **2001**, *115*, 9835-9842.

102. Buch, V.; Milet, A.; Vácha, R.; Jungwirth, P.; Devlin, J. P. Water Surface Is Acidic. *Proc. Natl. Acad. Sci. U.S.A.* **2007**, *104*, 7342-7347.

103. Kato, F.; Sugimoto, T.; Matsumoto, Y. Direct Experimental Evidence for Markedly Enhanced Surface Proton Activity Inherent to Water Ice. *J. Phys. Chem. Lett.* **2020**, *11*, 2524-2529.

104. Watkins, M.; VandeVondele, J.; Slater, B. Point Defects at the Ice (0001) Surface. *Proc. Natl. Acad. Sci. U.S.A.* **2010**, *107*, 12429-12434.

105. Watkins, M.; Pan, D.; Wang, E. G.; Michaelides, A.; VandeVondele, J.; Slater, B. Large Variation of Vacancy Formation Energies in the Surface of Crystalline Ice. *Nat. Mater.* **2011**, *10*, 794-798.

106. Kang, H. Reactive Ion Scattering of Low Energy $Cs^+$ from Surfaces. A Technique for Surface Molecular Analysis. *Bull. Korean Chem. Soc.* **2011**, *32*, 389-398.

107. Moon, E. S.; Yoon, J.; Kang, H. Energy Barrier of Proton Transfer at Ice Surfaces. *J. Chem. Phys.* **2010**, *133*, 044709.

108. Jagoda-Cwiklik, B.; Devlin, J.; Buch, V. Spectroscopic and Computational Evidence for $SO_2$ Ionization on 128 K Ice Surface. *Phys. Chem. Chem. Phys.* **2008**, *10*, 4678-4684.

109. Bang, J.; Shoaib, M. A.; Choi, C. H.; Kang, H. Efficient Thermal Reactions of Sulfur Dioxide on Ice Surfaces at Low Temperature: A Combined Experimental and Theoretical Study. *ACS Earth Space Chem.* **2017**, *1*, 503-510.

110. Shoaib, M. A.; Choi, C. H. Adsorptions of Formic and Acetic Acids on Ice Surface: Surface Binding Configurations and a Possibility of Interfacial Proton Transfer. *J. Phys. Chem. C* **2013**, *117*, 4181-4188.

111. Lee, D. H.; Bang, J.; Kang, H. Surface Charge Layer of Amorphous Solid Water with Adsorbed Acid or Base: Asymmetric Depth Distributions of $H^+$ and $OH^-$ Ions. *J. Phys. Chem. C* **2016**, *120*, 12051-12058.

112. Park, Y.; Shin, S.; Kang, H. Entropy-Driven Spontaneous Reaction in Cryogenic Ice: Dissociation of Fluoroacetic Acids. *J. Phys. Chem. Lett.* **2018**, 4282-4286.

113. Marchand, P.; Marcotte, G.; Ayotte, P. Spectroscopic Study of $HNO_3$ Dissociation on Ice. *J. Phys. Chem. A* **2012**, *116*, 12112-12122.

114. Marcotte, G.; Ayotte, P.; Bendounan, A.; Sirotti, F.; Laffon, C.; Parent, P. Dissociative Adsorption of Nitric Acid at the Surface of Amorphous Solid Water Revealed by X-Ray Absorption Spectroscopy. *J. Phys. Chem. Lett.* **2013**, *4*, 2643-2648.

115. Ayotte, P.; Hébert, M.; Marchand, P. Why Is Hydrofluoric Acid a Weak Acid? *J. Chem. Phys.* **2005**, *123*, 184501.

KOPRI 극지연구소

116. Ayotte, P.; Rafiei, Z.; Porzio, F.; Marchand, P. Dissociative Adsorption of Hydrogen Fluoride onto Amorphous Solid Water. *J. Chem. Phys.* **2009**, *131*, 124517.

117. Shin, S.; Park, Y.; Kim, Y.; Kang, H. Dissociation of Trifluoroacetic Acid in Amorphous Solid Water: Charge-Delocalized Hydroniums and Zundel Continuum Absorption. *J. Phys. Chem. C* **2017**, *121*, 12842-12848.

118. Ayotte, P.; Plessis, S.; Marchand, P. Trapping Proton Transfer Intermediates in the Disordered Hydrogen-Bonded Network of Cryogenic Hydrofluoric Acid Solutions. *Phys. Chem. Chem. Phys.* **2008**, *10*, 4785-4792.

119. Loeffler, M. J.; Hudson, R. L. Thermally-Induced Chemistry and the Jovian Icy Satellites: A Laboratory Study of the Formation of Sulfur Oxyanions. Geophys. *Res. Lett.* **2010**, *37*, L19201.

120. Kim, Y. K.; Kim, S. K.; Kim, J. H.; Kang, H. Kinetic Isolation of Reaction Intermediates on Ice Surfaces. Precursor States of $SO_2$ Hydrolysis. *J. Phys. Chem. C* **2009**, *113*, 16863-16865.

121. Kim, S.-K.; Kang, H. Efficient Conversion of Nitrogen Dioxide into Nitrous Acid on Ice Surfaces. *J. Phys. Chem. Lett.* **2010**, *1*, 3085-3089.

122. Bang, J.; Lee, D. H.; Kim, S. K.; Kang, H. Reaction of Nitrogen Dioxide with Ice Surface at Low Temperature (<= 170 K). *J. Phys. Chem. C* **2015**, *119*, 22016-22024.

123. Zundel, G. Hydrogen Bonds with Large Proton Polarizability and Proton Transfer Processes in Electrochemistry and Biology. *Adv. Chem. Phys.* **2000**, *111*, 1-217.

124. Stewart, R. *The Proton: Applications to Organic Chemistry*; Academic Press: Orlando, **1985**.

125. Lee, D. H.; Kang, H. Acid-Promoted Crystallization of Amorphous Solid Water. *J. Phys. Chem. C* **2018**, *122*, 24164-24170.

126. Moon, E. S.; Kang, H.; Oba, Y.; Watanabe, N.; Kouchi, A. Direct Evidence for Ammonium Ion Formation in Ice through Ultraviolet-Induced Acid-Base Reaction of $NH_3$ with $H_3O^+$. *Astrophys. J.* **2010**, *713*, 906-911.

## FIGURES

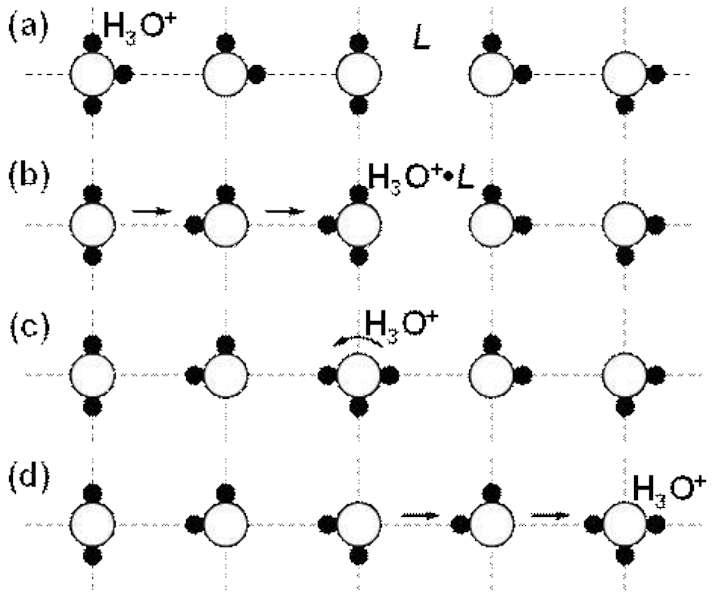



Fig. 1. Pictorial illustration of the proton-transport mechanism in ice. The ice lattice is represented by a straightened-out chain of water molecules ("square ice" model) for convenience. The hydrogen bond is indicated by the dotted lines. (a) $H_3O^+$ indicates a hydronium structure with extra proton attached to water molecule, and L indicates a Bjerrum orientational defect. (b) Hydronium moves via successive jumps of excess protons (straight arrows) along the water chain until a proton is trapped by forming a stable $H_3O^+$ • L defect complex. (c) Reorientation of water in the complex (circle arrow) releases a proton and (d) resumes a proton-hopping relay. The actual mechanism for the trapping and release of a proton at a Bjerrum L defect is more complex than that drawn in this figure. A proton is trapped as a result of electrostatic stabilization of the $H_3O^+$ • L structure in the ice lattice,[5,66] but this process is difficult to illustrate in the one-dimensional chain model. Additionally, a Bjerrum defect is moved by the reorientation of water, but this process is inaccurately represented by hydronium reorientation in the figure.

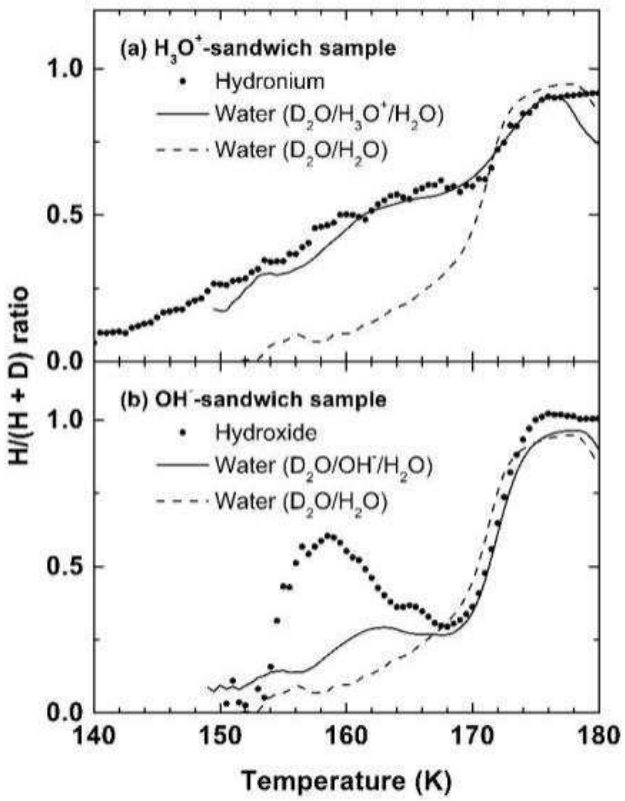



Fig. 2. (a) HDRs of hydronium (black circles) and water (solid line) measured on the surface of a "hydronium-sandwich" ASW film, in which $H_3O^+$ and $Cl^-$ (produced by ionization of HCl) are initially trapped between the bottom $H_2O$ layer and the top $D_2O$ layer [$D_2O$ (~30 ML)/$H^+$ + $Cl^-$/$H_2O$ (≥110 ML)/Pt(111)]. The virtually identical HDRs for hydronium and water above ~150 K indicate efficient H/D exchange due to proton transfer. The broken line indicates the HDR of water molecules measured on the surface of a pure ASW film [$D_2O$ (~30 ML)/$H_2O$ (≥110 ML)/Pt(111)], where the H/D exchange reaction is not catalyzed by hydronium. (b) HDRs for hydroxide (black circle) and water (solid line) on the surface of a hydroxide-sandwich ASW film [$D_2O$ (~30 ML)/$OH^-$ + Na+/$H_2O$ (≥110 ML)/Pt(111)]. The HDR of hydroxide is significantly higher than that of water at 154 - 168 K owing to molecular hydroxide diffusion. The sample temperature was increased at a rate of 0.5 K $s^{-1}$. The surface populations and isotopomeric compositions of hydroniums and hydroxides were measured by means of low-energy sputtering (LES). In this technique, ions present at the ice surface are desorbed by the collisions of $Cs^+$ projectiles with the surface at low energy and the desorbed ions are detected by a mass spectrometer.[9] The collision energy is controlled to be only slightly above the desorption threshold of the ions to minimize molecular fragmentation and suppress secondary ion emission. The isotopomeric composition of water molecules was measured by means of temperature-programmed desorption (TPD). Reproduced with permission from ref. 93. Copyright 2014 American Chemical Society.

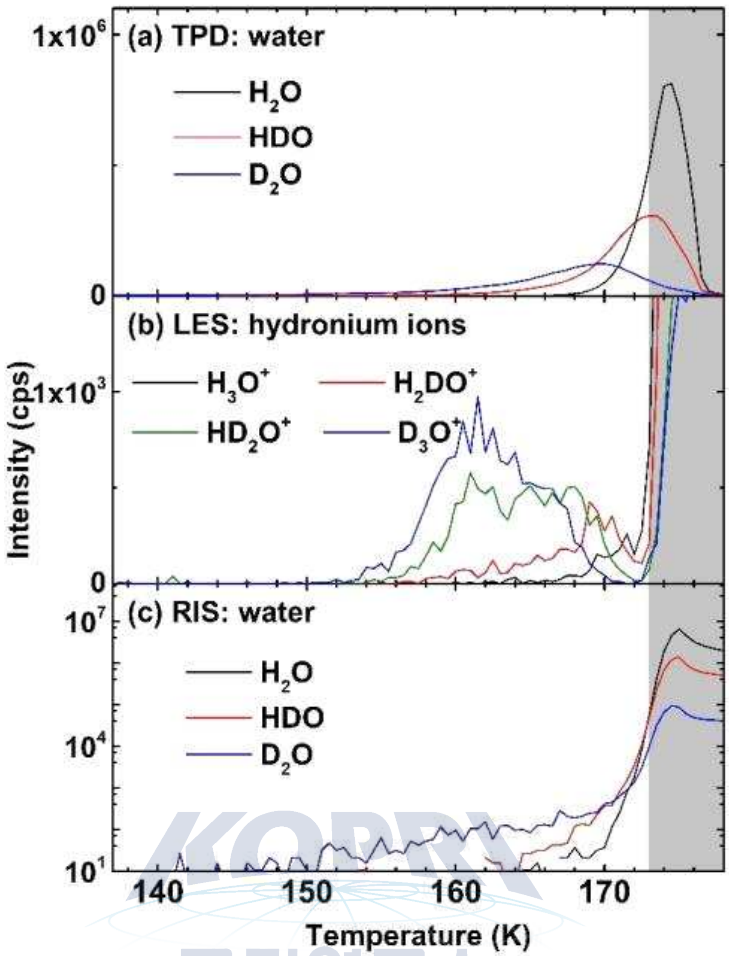



Fig. 3. Results of TPD, LES, and RIS measurements for a "hydronium-sandwich" ice film [$D_2O$ (~70 ML)/$H^+$ + $Cl^-$ (0.3 ML)/$H_2O$ (~120 ML)/Pt(111)] during an increase in the temperature from 138 to 178 K. The ordinate scale indicates the mass spectrometric signal intensity (count per second) for each experiment. (a) TPD curves of water isotopomers. (b) LES signals of various hydronium isotopomers appearing on the surface. (c) RIS measurement of water isotopomers on the surface. In RIS, $Cs^+$ projectiles pick up molecules on the surface during the scattering process, and the resultant $Cs^+$ - molecule complex is identified by a mass spectrometer.[9,106] The RIS signal is presented on a logarithmic scale. A roughing transition of the ice film occurred above ~173 K (shaded region), which destroyed the film structure.[24,53-55] The TPD (a) and RIS (c) curves show changes in the isotopomeric composition of surface water molecules caused by diffusional mixing and H/D exchange reactions. The LES curves (b) indicate that hydroniums migrated from the film interior to the surface at a temperature above ~154 K. The temperature ramping rate was 0.5 degree $s^{-1}$ for all the spectra. The $Cs^+$ beam energy for the LES and RIS measurements was 35 eV. Reproduced with permission from ref. 99. Copyright 2012 American Chemical Society.

KORRI 극지연구소

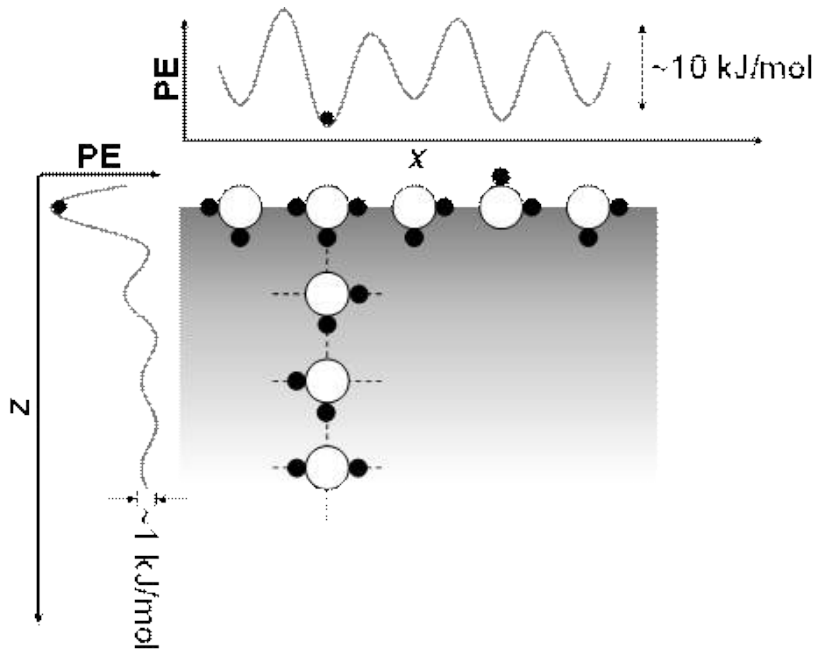



Fig. 4. Illustration of the potential energy (PE) profiles for the migration of excess proton along the ice surface (x direction) and toward the ice interior (z direction). The ice lattice is represented by a square ice model for simplicity. A dot in the potential well indicates the location of an excess proton. The energetic stabilization of a surface hydronium structure makes excess protons reside preferentially at the surface and experience a large barrier for diffusion along the surface.

KOPRI
극지연구소

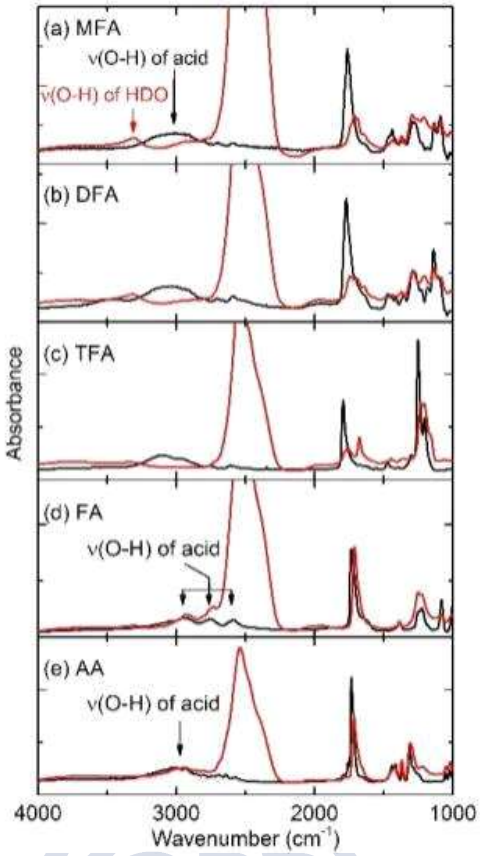



Fig. 5. RAIR spectra of pure acid films (black traces) and acid-$D_2O$ mixture films (red traces), which are shown overlapped for each acid for better visualization of the dissociation or nondissociation behavior of the acids. In each set of spectra, the spectral intensities are rescaled to equalize the molar amounts of acid in the pure and mixture films. The intense bulk ν(O - D) band (~2540 $cm^{-1}$) of $D_2O$ is truncated. (a) Spectra of a pure MFA and MFA-$D_2O$ mixture (4% MFA in molar ratio) at 80 K. (b) Spectra of a pure DFA and DFA-$D_2O$ (6% DFA) mixture at 70 K. (c) Spectra of a pure TFA and TFA-$D_2O$ (4% TFA) mixture at 70 K. (d) Spectra of a pure FA and FA-$D_2O$ (6% FA) mixture at 80 K. (e) Spectra of a pure AA and AA-$D_2O$ (4% AA) mixture at 80 K. Differences between the spectra in (a - c) and those in (d, e) are clearly visible. For MFA (a), DFA(b), and TFA(c), the ν(O−H) band of molecular carboxylic acid almost disappears for the mixture film, indicating acid dissociation. This differs from the case of FA (d) and AA (e), where the ν(O−H) band of molecular acid remains after dissolution in $D_2O$ at 70 - 80 K. Additionally, for MFA, DFA and TFA, the ν(C=O) band of a pure acid film and that of a mixture film differ significantly, in both intensity and shape. The sharp ν(C=O) band shape of the molecular carboxylic group at ~1770 $cm^{-1}$ changes to the ν(C=O) band shape of the carboxylate anion in the range of 1600 - 1800 $cm^{-1}$ for the mixture film. For non-dissociating FA and AA, the shape of the ν(C=O) band does not change significantly. Reproduced with permission from Supporting Information of ref. 112. Copyright 2018 American Chemical Society.

# 제 10 절. Freezing-enhanced Oxidation of Iodide by Hydrogen Peroxide in the Presence of Antifreeze Proteins from the Arctic Yeast Leucosporidium sp.AY30⑩

Bomi Kim[1,2], Hackwon Do[1], Bo-Mi Kim[1], Jun Hyuck Lee[1,2], Sanghee Kim[1], Eun Jae Kim[1], Jungeun Lee[1], Sung Mi Cho[1], Kitae Kim[1,2]

[1]Korea Polar Research Institute

[2]Department of Polar Sciences, University of Science and Technology (UST)

## Abstract

Ice-binding proteins (IBPs), originating from Arctic or Antarctic microorganisms, have freeze-inhibiting characteristics, allowing these organisms to survive in polar regions. Despite their significance in polar environments, the mechanism through which IBPs affect the chemical reactions in ice by controlling ice crystal formation has not yet been reported. In this study, a new mechanism for iodide ($I^-$) activation into triiodide ($I_3^-$), which is the abundant iodine species in seawater, by using hydrogen peroxide ($H_2O_2$) in a frozen solution with IBPs was developed. A significant enhancement of $I^-$ activation into $I_3^-$ was observed in the presence of Arctic-yeast-originating extracellular ice-binding glycoprotein (LeIBP) isolated from Leucosporidium sp.AY30, and a further increase in the $I_3^-$ concentration was observed with the introduction of $H_2O_2$ to the frozen solution (25 times higher than in the aqueous solution after 24 h of reaction). The reaction in the ice increased with an increase in LeIBP concentration. The in-situ pH measurement in ice using cresol red (CR) revealed protons accumulated in the ice grain boundaries by LeIBP. However, the presence of LeIBP did not influence the acidity of the ice. The enhanced freeze concentration effect of $H_2O_2$ by LeIBP indicated that larger ice granules were formed in the presence of LeIBP. The results suggest that LeIBP affects the formation and morphology of ice granules, which reduces the total volume of ice boundaries throughout the ice. This leads to an increased local concentration of $I^-$ and $H_2O_2$ within the ice grain boundaries. IBP-assisted production of gaseous iodine in a frozen environment provides a previously unrecognized formation mechanism of active iodine species in the polar regions.

⑩ 이 연구는 본 과제(PE22120)의 지원을 받았으며 또한 "극지 유래 생물자원을 활용한 항생제 후보물질 개발(15250103, KOPRI Grant PM21030)"과제의 일환으로 진행되었다. 연구 결과는 *Environ. Res.* 2022, 212, 113233에 출판되었다.

## 1. Introduction

Reactive halogens play a significant role in the global climate and atmospheric environment. Gaseous halogen molecules include gaseous iodine, particularly those present in ice-covered marine boundary layers, and are interest in polar atmospheric chemistry. Reactive halogens deplete ozone through catalytic cycles, affect the oxidative capacity of the atmosphere, and contribute to new particle formation (Abbatt et al., 2012; Pratt et al., 2013; Saiz-Lopez et al., 2012; Saiz-Lopez et al., 2008; Saiz-Lopez and von Glasow, 2012; Schroeder et al., 1998; Simpson et al., 2015; Simpson et al., 2007; von Glasow, 2008). The mechanisms of iodine production in the polar atmosphere are less understood than those of chlorine and bromine production (Frieß et al., 2010; Saiz-Lopez et al., 2007). Iodide ion ($I^-$) undergoes the oxidation reaction (Eq. 1) under acidic conditions, forming triiodide ion ($I_3^-$) and releasing iodine gas molecules ($I_2$) into the air in equilibrium with $I_3^-$ (Eq. 2) (O'Sullivan & Sodeau, 2010).

$$O_2\ (aq) + 4\ H^+ + 6I^- \rightarrow 2H_2O + 2I_3^- \quad (1)$$

$$I_3^- \leftrightarrow I_2 + I^- \quad (2)$$

This reaction is known to be extremely slow in aqueous solutions; however, some oxidizing agents, such as hydrogen peroxide ($H_2O_2$), can increase the $I_2$ production rate through the reaction given in Eq. 3 (Couto et al., 2006).

$$3I^- + H_2O_2 + 2H^+ \leftrightarrow I_3^- + 2H_2O \quad (3)$$

Hydroperoxides in the atmosphere, including $H_2O_2$, increase the tropospheric oxidization capacity of $HO_x$ radicals and ozone precursors in the remote upper troposphere (Barth et al., 2007; Grannas et al., 2007). Heterogeneous reactions between gaseous-phase species and halides on the ice-covered surfaces are important in halogen chemistry. The air above and within the snowpack in the high and middle latitudes has significant impacts on atmospheric oxidant concentrations because these surfaces are photochemically reactive across the snow-air interface (Dominé & Shepson, 2002; Grannas et al., 2007; Hutterli et al., 2004; Hutterli et al., 2001). Natural ice media in polar regions (snowpack, glacier, sea ice) cause unique chemical reactions that are different from those in aqueous solutions. Snow and ice contain a variety of solutes, including salts and polar microorganisms that release antifreeze proteins and affect ice crystal formation. These solutes are concentrated in liquid-like grain boundary regions or brine channels in ice as generated by the crystalline ice network (Bartels-Rausch et al., 2014; O'Concubhair & Sodeau, 2013), accelerating the chemical reactions between these solutes (i.e., freeze concentration effect).

Previous studies have suggested that polar atmospheric components such as nitric oxide (Kim et al., 2017), sulfur oxide (Le et al., 2020), and halogen gas molecules, including iodide (Kim et al., 2016), are released into the atmosphere by different reactions of aqueous solutions to polar surfaces and sea ice because of freeze concentration effects. Natural conditions, including local temperature (Mason et al., 2015) and the wide pH range of ice media [in the Arctic, snow surface is pH 3 - 4 (Nawrot et al., 2016), fresh snow pH is 4.6 - 6.1 (Caritat et al., 2005), melt pond pH is 6 - 7 (Bates et al., 2014)] can also affect the freeze concentration and chemical reactions in ice. Thus, the acceleration of chemical reactions in ice media is key to understanding the reaction mechanisms of the cryosphere; however, the research on this topic is still limited.

Anti-freeze proteins or ice-binding proteins (IBPs) originating from polar microorganisms influence ice nuclei formation and the growth of ice crystals. Because of their inhibitory effects on ice growth and recrystallization, IBPs play a significant role in the survival of microorganisms and the protection of stem cells and blood cells in cold environments (DeVries & Wohlschlag, 1969). IBPs are extracted from natural polar organisms, such as fish, plants (Griffith & Yaish, 2004), insects (Doucet et al., 2002), and bacteria (Kawahara et al., 2007; Kawahara et al., 2004; Raymond et al., 2008; Raymond et al., 2007) that live in subzero temperatures, because these organisms can synthesize antifreeze enzymes. The extracellular ice-binding glycoprotein (LeIBP) isolated from the Arctic yeast Leucosporidium sp. AY30 (Lee et al., 2012a) has hyperactive ice-binding properties, including thermal hysteresis and ice recrystallization inhibition (Park et al., 2012). LeIBP, the one of the well characterized ice binding protein, have been found inside the ice core and affected on ice crystals and ice microstructures. Therefore, in the presence of IBPs, chemical reactions in ice due to freeze concentration effects are expected to change, although there are no studies reporting these changes.

In this study, we investigated how the presence of LeIBP affects ice crystal formation and iodide activation (i.e., oxidation of $I^-$ to $I_3^-$) with $H_2O_2$ in ice. Experimental conditions (slow cooling rate during freezing at low initial pH) were simulated in the laboratory to examine the reaction trend in polar environments. The effects of various experimental factors on freezing - enhanced iodide oxidation were studied to understand the chemical process in frozen solutions, and the freeze concentration effects was visualized using Raman spectroscope.

## 2. Materials and methods

### 2.1. Chemicals and ice-binding protein

Potassium iodide (KI, reagent grade, ≥98%, as iodide source), perchloric acid ($HClO_4$,

ACS reagent, 60%), o-cresolsulfonephthalein sodium salt (CR, cresol red indicator, $C_{21}H_{17}NaO_5S$, ≥95%), methanol ($CH_3OH$, reagent grade), glucose ($C_6H_{12}O_6$, anhydrous, 96%, for yeast extract - peptone - dextrose medium (YPD)), and bovine serum albumin (BSA, lyophilized powder, ≥96%) were purchased from Sigma - Aldrich, Inc. (St. Louis, MO, USA) at analytical grades. Hydrogen peroxide ($H_2O_2$, 34.5%) and sodium hydroxide solution (NaOH, 1 N) were purchased from Samchun Chemicals (Seoul, South Korea). All aqueous solutions were prepared using ultrapure deionized water (R ≥ 18.0 MΩ · cm) prepared using a Barnstead purification system. The methylotrophic Pichia pastoris X33 (for LeIBP expression) was purchased from Invitrogen (Carlsburg, CA, USA), and the pPICZαA vector was used for expression in the P.pastoris system.

LeIBP was prepared for pilot-scale production as explained in the report by Lee et al (2013). Initially, LeIBP originating from Glaciozyma sp. was recombinantly matured in the methylotrophic yeast Pichia pastoris X33 cells containing the pPICZαA vector, then grown at 25 ℃ for two days in YPD for the expression of the LeIBP gene. LeIBP was induced by adding 5 mL of methanol per day for six days. After centrifugation (8000 × g for 10 min), the supernatant was passed through a 0.2-μm filter (Nalge Nunc, Rochester, NY, USA), loaded onto the Q-Sepharose FF column (GE Healthcare, Little Chalfont, UK), and eluted with 50 mM Tris-HCl buffer (pH 8.0) with a salt gradient of 0 to 1 M NaCl for ion exchange chromatography. For further separation, a Superdex 200 size exclusion column (Amersham Pharmacia) was used. Purified LeIBP was confirmed using gel electrophoresis. The molecular weight of the isolated protein was ~25 kDa.

KORI 극지연구소

### 2.2. Experimental procedure

The chemical stock solutions ([KI] = 10 mM and [$H_2O_2$] = 10 mM) were added to deionized water in a beaker to determine the desired initial concentrations for the experiment (usually [KI] = 1 mM and [$H_2O_2$] = 0.5 mM), and the initial pH of the solution was adjusted using $HClO_4$ or NaOH solution (pH = 4.0). The LeIBP stock solution (200 ppm) was prepared by dispersing the LeIBP powder in deionized water (pH = 7.0) without buffer solutions; the concentration was 100 ppm in the sample solution. The sample solution (total volume 5 mL) was transferred to conical tubes and immersed in an ethanol bath (-20 °C) for freezing. The samples were thawed at regular time intervals (0, 1, 2, 6, and 24 h) in lukewarm water (30-40 °C) for further analysis. A reaction time of zero was set after immersing the conical tube in an ethanol bath. The experiments were performed in triplicate under given conditions to confirm reproducibility.

### 2.3. Chemical analysis

Quantitative analysis of $I_3^-$ concentrations (denoted as $[I_3^-]$) was performed using a UV−Vis spectrometer (Cary 4000, Agilent) to monitor the absorbance of the aqueous sample. The concentrations were calculated using Beer-Lambert law with the molar absorption coefficient of $\varepsilon$ = 26,400 $M^{-1}$ $cm^{-1}$ at 353 nm (Awtrey & Connick, 1951).

The pH of the frozen sample (more precisely, the pH value in the ice grain boundary region) was estimated by measuring the UV - Vis absorption spectra of CR (Krausková et al., 2016). CR exhibits different maximum absorption wavelengths (λmax) depending on the pH value of both the aqueous solution and frozen solution. The sample solutions mixed with 10 $\mu$M of CR solution were added into a 4-mL rectangular cuvette and then frozen in an ethanol bath at -20 °C. After 1 h of freezing, the absorption spectrum was measured using a UV−Vis spectrometer without melting.

Raman imaging and chemical mapping of the frozen samples were performed to confirm the freeze concentration effect of each reagent. The Raman signals from concentrated chemicals in the ice grain boundaries were investigated in-situ using confocal Raman spectroscopy (Renishaw inVia Qontor) combined with a temperature-controlled stage (Linkam Scientific THMS600). A monochromatic 532-nm laser was used as the excitation source. An aqueous sample containing $H_2O_2$ (1 mM) and LeIBP (100 ppm) was dropped onto the temperature-controlled stage, and the temperature was decreased to -20 °C (cooling rate: -2.0 °C /min). Chemical mapping was performed by measuring the intensity of the characteristic Raman peaks of $H_2O_2$ (880 $cm^{-1}$ for O−O stretching vibration mode (Giguére & Srinivasan, 1974)) and visualized on the optical image of the ice grain boundaries using a rainbow color scale.

## 3. Results and discussion

### 3.1. Iodide oxidation in the presence of LeIBP in aqueous and frozen solution

The oxidation of $I^-$ to $I_3^-$ in the presence of LeIBP was investigated in aqueous and frozen solutions (Fig. 1a). The activation of $I^-$ with $H_2O_2$ resulted in a significantly accelerated reaction in both the aqueous and ice phases. The chemical reaction occurred according to Eq. 3 with $H_2O_2$ as the oxidant; Eq. 3 is typically more than ten times faster than Eq. 1 in aqueous solutions. Meanwhile, the freeze concentration of $I^-$ and $H_2O_2$ leads to a higher production rate in the ice phase. The reaction in Eq. 3 in the presence of LeIBP was faster than that in the absence of LeIBP. The final (after 24 h) $[I_3^-]$ was nearly three times higher (57.5 $\mu$M) than when LeIBP was absent. This suggests that LeIBP promotes the formation of $I_3^-$ in ice; even when the experiments were conducted

under dark conditions, a greater amount of $I_3^-$ was formed in the presence of LeIBP than in the experiments conducted under light conditions (Kim et al., 2016). $I_3^-$ production in ice occurs concurrently with the solidification of the solutions (within 30 min) in the presence of LeIBP and $H_2O_2$, which suggests that LeIBP accelerates the rate of chemical reactions in ice.

The effect of each chemical involved in the reaction was examined to compare the $I_3^-$ production in aqueous and frozen solutions after the 24 h reaction (Fig. 1b). Oxidative formation of $I_3^-$ (Eq. 1) occurred extremely slowly in the aqueous solution ($I^-$ in aqueous solution, 0.47 $\mu$M after 24 h), whereas the reaction was considerably accelerated in the frozen solution ($I^-$ in ice, 10.15 $\mu$M after 24 h) due to the freeze concentration effect (Kim et al., 2016; Kim et al., 2019). The presence of $I^-$ in the ice crystal grain boundaries increased the concentration; thus, the oxidation from $I^-$ to $I_3^-$ in the frozen solution was faster than that in the aqueous phase. However, low $I_3^-$ formation in the frozen solution was observed in the presence of LeIBP without $H_2O_2$. After the 24 h reaction, the $I_3^-$ formation in the presence of LeIBP was slightly lower (6.02 $\mu$M) than that in the absence of LeIBP (10.15 $\mu$M) in the frozen solution. Since halides are known to be highly reactive and interact with proteins specifically and non-specifically (Skitchenko et al., 2020), we infer that these interactions inhibit iodide oxidation (Eq. 1). The iodide solution containing $H_2O_2$ produced $I_3^-$ in the aqueous phase (14.00 $\mu$M). In the presence of LeIBP and $H_2O_2$ in the iodide solution, the production of $I_3^-$ in ice was 25 times higher than that in the aqueous solution. The amount of $I_3^-$ after 24 h freeze was three times that in the absence of LeIBP. The results suggest that the reduced production of $I_3^-$ in the aqueous solution is caused by the interaction between iodide and LeIBP, as well as the presence of only iodides and LeIBP in the solution. Iodide oxidation by $H_2O_2$ also occurs in ice, and the reaction is further enhanced by the freeze concentration in the presence of LeIBP. Circular dichroism (CD) analysis was performed to ensure the stability and antifreezing activity of LeIBP in the experimental conditions (Fig. S1). The results indicated that the secondary structure of LeIBP had no change at pH 4.0 and in the presence of $H_2O_2$. Based on these results, we propose that iodide activation in the presence of LeIBP and $H_2O_2$ is enhanced through the abiotic processes.

### 3.2. Iodide oxidation by hydrogen peroxide with LeIBP in various conditions

Figure 2 summarizes the $I_3^-$ production under different experimental conditions in the aqueous solution and ice (i.e., various concentrations of iodide, $H_2O_2$, and LeIBP). The amount of $I_3^-$ in ice was higher than that in the aqueous solution under all test conditions. The production of $I_3^-$ implies the presence of $I_2$ in equilibrium (Eq. 2); however, gaseous $I_2$ detection in the UV-VIS spectrum was limited under the various experimental conditions

(Fig. S2). The gaseous $I_2$ trapped in the frozen solution was emitted to the air.

The [$I_3^-$] after the 24 h reaction is directly proportional to the initial iodide concentration (Fig. 2a). Even if [$H_2O_2$] is fixed (0.5 mM), the production of $I_3^-$ increases in proportion to the initial iodide concentration due to freezing because the reaction under acidic conditions occurs according to Eq. 1. $I_3^-$ production in ice was observed at a low initial [$I^-$] (0.05 mM) in the presence of LeIBP. These results suggest that $I_3^-$ formation does not occur in aqueous solutions at low [$I^-$] however, it can occur in the presence of LeIBP in naturally formed ice media (i.e., in polar regions). [$I_3^-$] in a frozen solution tends to be proportional to the $H_2O_2$ concentration (denoted as [$H_2O_2$]). However, even if [$H_2O_2$] exceeds [$I^-$], it has similar (~30 $\mu$M) concentrations in the aqueous solution, whereas [$I_3^-$] increases further in ice (Fig. 2b). In frozen solutions, even if traces of $H_2O_2$ (0.01 mM) were present, the reaction would proceed; only 50 $\mu$M of $H_2O_2$ generated $I_3^-$ in the ice. This result indicates that $H_2O_2$ in the polar atmosphere facilitates iodine oxidation in ice media. On the contrary, the higher the concentration of LeIBP, the lower the generation of $I_3^-$ in the aqueous solution (Fig. 2c), which is similar to the result shown in Fig 1b, caused by the increased interaction of iodide with proteins (Skitchenko et al., 2020). Conversely, [$I_3^-$] was the highest at 100 ppm of LeIBP in ice, which suggests that LeIBP itself does not enhance iodide activation; rather, both LeIBP and $H_2O_2$ in ice with iodide accelerates the reaction via the freeze concentration effect. Freezing was conducted with BSA as a negative control, and no significant enhancement in the reaction was observed (Fig. S3).

### 3.3. pH shift in frozen samples and pH effect on iodide oxidation

The reaction in Eq. 1 assumes that acidic conditions and proton involvement are essential, and it is known that a high pH suppresses the reaction. Therefore, the pH dependence of the reaction in ice was studied using the non-negative least squares minimization method (Kim et al., 2019). The pH within the ice grain boundaries typically differs from the pH of the aqueous solution owing to the freezing potential (Gross et al., 1975); even the pH value of the ice grain boundaries becomes strongly acidic because of the protons expelled from the bulk ice crystal during freezing (Watanabe et al., 2014). As a result, ice grain boundaries have appropriate conditions for iodide activation. The absorption spectra of CR were measured in the aqueous and frozen solutions (Fig. 3). In this experiment, the pH of the $H_2O_2$ solution was compared with that of the iodide solution because the $I_3^-$ spectrum (generated by iodide) interferes with that of the CR. The pH values of the frozen solutions were strongly acidic under the experimental conditions. There was no significant difference between the pH value of two samples; frozen $H_2O_2$ solution pH = 1.40 and frozen $H_2O_2$ solution with LeIBP pH = 1.28. In other words, proton enrichment within the ice grain boundaries is supported by freezing, regardless of LeIBP

presence (slightly more acidic with LeIBP). Therefore, enhanced $I_3^-$ production in the frozen solution is affected by increased acidity due to proton enrichment by freezing, as well as the increase in the concentration of other solutes.

The production of $I_3^-$ after the 24 h reaction in a broad pH range was quantified in the presence of LeIBP (Fig. 4). Independent of the presence of LeIBP, a strong dependence on pH was observed in iodide solutions without $H_2O_2$; as pH increased, $I_3^-$ production decreased (Fig. 4a, b). At neutral pH conditions (pH 6−8), no $I_3^-$ production was detected either in the aqueous or the ice phase, similarly to previously reported results (Kim et al., 2016). However, the production increased in both phases when $H_2O_2$ was present (Fig. 4c). The reaction occurred in the frozen solution at pH 6−8 and progressed to Eq. 3, owing to the freeze concentration effect. The presence of LeIBP and $H_2O_2$ in the frozen solution (Fig. 4d) increased the productivity of $I_3^-$ even under basic conditions (pH 8). The amount of $I_3^-$ production was 115 times greater than that in ice where $H_2O_2$ and LeIBP do not exist (0.25 $\mu$M in iodide frozen solution vs. 28.9 $\mu$M in iodide frozen solution with $H_2O_2$ and LeIBP). These results suggest that the presence of LeIBP enables iodide activation under various pH conditions in the ecosystem, as well as under conditions where conventional iodide activation does not occur.

### 3.4. Effect of LeIBP on ice crystal formation

To verify the feasibility of the correlation between the LeIBP operation and enhanced iodide activation reaction, we measured the changes in size and shape of the ice granules in the presence of LeIBP using optical images (Fig. 5). In the absence of LeIBP, the ice grain boundaries were formed throughout the frozen $H_2O_2$ solution with relatively small ice granules (Fig. 5a). Freezing with BSA, a protein known to have no antifreeze effect (Park et al., 2012), revealed no significant change in the formation of ice crystals (Fig. 5b). In contrast, the size of ice granules increased by five times, and each ice granule presented an unusual shape closer to a rectangle than a hexagon in the presence of LeIBP (Fig. 5c). This experiment confirmed the unique properties of LeIBP. Unlike BSA, LeIBP attaches irreversibly to the ice nuclei, hindering their growth and recrystallization. This mechanism reduces the number of growing ice nuclei in the entire solution; therefore, the ice granules growing from several ice nuclei form relatively larger granules. The unique formation of larger ice granules reduces the total volume of ice grain boundaries in the frozen solution and increases the freeze concentration effect. Notably, LeIBP does not directly participate in chemical reactions; it only changes in the morphology of the ice granule and the total volume of bulk ice crystals in frozen solution, resulting in a change in the solute concentration within the ice grain boundaries. Moreover, LeIBP, along with other hyperactive IBPs, binds to multiple ice planes, preferentially to the basal and primary prism

planes (Lee et al., 2012b). As a result, the final structure of ice granules frozen with LeIBP is rectangular rather than hexagonal. In addition, the shape of ice grain boundaries presented in Figure 5(c) shows the rough surfaces caused by the inhibition mechanism of adsorbed LeIBP on the ice crystal lattice. LeIBPs, which act like other hyperactive IBPs, conferred steric hindrance to ice binding. Therefore, the ice granule bound by LeIBP had a rough boundary rather than straight shape after the ice crystal growth. The formation of ice crystals related to the cooling rate duration freezing was also confirmed (Fig. S4). When freezing occurred rapidly, only small ice seeds were formed, and bulk ice crystals were not developed by the ice nucleation inhibition of LeIBP. However, when the cooling rate was reduced, similar to the conditions in nature, the ice granule approached the rectangle shape, as shown in Figure 5(c).

### 3.5. In-Situ Raman mapping of H2O2 in ice grain boundaries in the presence of LeIBP

Freeze concentration enhancement by LeIBP was visualized via confocal Raman microscopy using an $H_2O_2$ solution. After being dropped on the temperature-controlled stage, the aqueous solution was cooled to -20 °C. The Raman intensity of $H_2O_2$ (880 $cm^{-1}$ for O−O stretching vibration mode) was measured to confirm the freeze concentration of $H_2O_2$ in the presence of LeIBP. The concentration of $H_2O_2$ was visualized on the optical image of the ice grain boundaries using a rainbow color scale. In the frozen $H_2O_2$ solution (Fig. 6a, 6b), only weak signals were detected within the ice grain boundaries, while the mapping images in the presence of LeIBP indicated a higher $H_2O_2$ signal in the ice grain boundaries (Fig. 6c, 6d). In Fig. 6d, the $H_2O_2$ signal was rarely detected on ice granules, in contrast to the ice grain boundaries. This indicates the increase in $I_3^-$ production in the presence of LeIBP and changes in the local concentration within the ice grain boundaries due to the formation of larger ice granules by LeIBP. This result is consistent with other previous studies, which reported that the local concentration of solutes in the ice-grain boundary region could be enhanced by tens of orders of magnitude from their respective aqueous concentrations (Kim et al., 2016; Menacherry et al., 2018). The proportion of the iodide ions trapped in the ice lattice was somewhat small (<3% of the initial concentration of iodide ions), which suggested the preferential concentration of iodide ions in the ice grain boundaries.

## 4. Conclusion

This study demonstrates how the oxidative reaction of iodide ions to iodine gas molecules is regulated in the presence of LeIBP. We observed a significant enhancement in

the oxidation of $I^-$ to $I_3^-$ by $H_2O_2$ when LeIBP was present in ice. We found that the rate of reaction was varied by freezing under weakly acidic conditions similar to those in natural ice media, as confirmed and visualized by in-situ measurement techniques. The presence of LeIBP has a varying effect on the freeze concentration, which has a significant impact on chemical reactions in ice. This acceleration is accomplished by the confinement of solutes (such as $H_2O_2$) and proton accumulation in ice grain boundaries. Antifreeze substances, including LeIBPs, typically bind to the surface of ice crystals to interfere with ice nucleation and crystal growth. LeIBP itself does not participate in a chemical reaction in ice but changes the local concentration within the ice grain boundaries. We observed no significant changes in the pH of ice due to the presence of LeIBP, while LeIBP was strongly involved in the concentration of $H_2O_2$ within the ice grain boundaries. This result suggests that LeIBP influences the formation of ice crystals and increases the freezing concentration with a slow cooling rate during freezing at low initial pH, thereby increasing the reaction rate of iodine oxidation. LeIBP has an extracellular ice-binding properties and it affect the formation of ice crystals; therefore, the result of this study can be used to explain the effect of coexisting biological groups (i.e., polar microorganisms) on ice-associated reactions related to polar atmospheric molecules, especially related with the reactive halogen gas emissions from sea ice to the polar atmosphere. These results can be applied not only to iodine compounds but also to other halogens and gas molecules generated in ice media in the polar atmosphere.

KOPRI 극지연구소

## REFERENCES


1. Abbatt, J. P. D., Thomas, J. L., Abrahamsson, K., Boxe, C., Granfors, A., Jones, A. E., King, M. D., Saiz-Lopez, A., Shepson, P. B., Sodeau, J., Toohey, D. W., Toubin, C., von Glasow, R., Wren, S. N., Yang, X., **2012**. Halogen activation via interactions with environmental ice and snow in the polar lower troposphere and other regions. *Atmos. Chem. Phys.* 12, 6237-6271.
2. Awtrey, A. D., Connick, R. E., **1951**. Rate law and mechanism of the reaction of iodine with tetrathionate ion. *J. Am. Chem. Soc.* 73, 4546-4549.
3. Bartels-Rausch, T., Jacobi, H. W., Kahan, T. F., Thomas, J. L., Thomson, E. S., Abbatt, J. P. D., Ammann, M., Blackford, J. R., Bluhm, H., Boxe, C., Domine, F., Frey, M. M., Gladich, I., Guzmán, M. I., Heger, D., Huthwelker, T., Klán, P., Kuhs, W. F., Kuo, M. H., Maus, S., Moussa, S. G., McNeill, V. F., Newberg, J. T., Pettersson, J. B. C., Roeselová, M., Sodeau, J. R., **2014**. A review of air - ice chemical and physical interactions (AICI): liquids, quasi-liquids, and solids in snow. *Atmos. Chem. Phys.* 14, 1587-1633.
4. Barth, M. C., Kim, S. W., Wang, C., Pickering, K. E., Ott, L. E., Stenchikov, G., Leriche, M., Cautenet, S., Pinty, J. P., Barthe, C., Mari, C., Helsdon, J. H., Farley, R. D., Fridlind, A. M., Ackerman, A. S., Spiridonov, V., Telenta, B., **2007**. Cloud-scale model intercomparison of chemical constituent transport in deep convection. *Atmos. Chem. Phys.* 7, 4709-4731.
5. Bates, N. R., Garley, R., Frey, K. E., Shake, K. L., Mathis, J. T., **2014**. Sea-ice melt $CO_2$ - carbonate chemistry in the western Arctic Ocean: meltwater contributions to air - sea $CO_2$ gas exchange, mixed-layer properties and rates of net community production under sea ice. *Biogeosciences.* 11, 6769-6789.
6. Caritat, P. d., Hall, G., Gìslason, S., Belsey, W., Braun, M., Goloubeva, N., Olsen, H., Scheie, J., Vaive, J., **2005**. Chemical composition of arctic snow: Concentration levels and regional distribution of major elements. *Sci. Total Environ.* 336, 183-199.
7. Couto, A. B., de Souza, D. C., Sartori, E. R., Jacob, P., Klockow, D., Neves, E. A., **2006.** The catalytic cycle of oxidation of iodide ion in the oxygen/nitrous acid/nitric oxide system and its potential for analytical applications. *Anal. Lett.* 39, 2763-2774.
8. DeVries, A. L., Wohlschlag, D. E., **1969**. Freezing resistance in some Antarctic fishes. *Science*, 163, 1073-1075.
9. Dominé, F., Shepson, P. B., **2002**. Air-Snow interactions and atmospheric chemistry. *Science* , 297, 1506-1510.
10. Doucet, D., Tyshenko, M. G., Davies, P. L., Walker, V. K., **2002**. A family of


KOPRI 극지연구소

expressed antifreeze protein genes from the moth, Choristoneura fumiferana. *Eur. J. Biochem.* 269, 38-46.

11. Frieß, U., Deutschmann, T., Gilfedder, B. S., Weller, R., Platt, U., **2010.** Iodine monoxide in the Antarctic snowpack. *Atmos. Chem. Phys.* 10, 2439-2456.
12. Giguére, P. A., Srinivasan, T. K. K., **1974**. A Raman study of $H_2O_2$ and $D_2O_2$ vapor. *J. Raman Spectrosc.* 2, 125-132.
13. Grannas, A. M., Jones, A. E., Dibb, J., Ammann, M., Anastasio, C., Beine, H. J., Bergin, M., Bottenheim, J., Boxe, C. S., Carver, G., Chen, G., Crawford, J. H., Dominé, F., Frey, M. M., Guzmán, M. I., Heard, D. E., Helmig, D., Hoffmann, M. R., Honrath, R. E., Huey, L. G., Hutterli, M., Jacobi, H. W., Klán, P., Lefer, B., McConnell, J., Plane, J., Sander, R., Savarino, J., Shepson, P. B., Simpson, W. R., Sodeau, J. R., von Glasow, R., Weller, R., Wolff, E. W., Zhu, T., **2007**. An overview of snow photochemistry: evidence, mechanisms and impacts. *Atmos. Chem. Phys.* 7, 4329-4373.
14. Griffith, M., Yaish, M. W., **2004**. Antifreeze proteins in overwintering plants: a tale of two activities. *Trends Plant Sci.* 9, 399-405.
15. Gross, G. W., Wu, C. h., Bryant, L., McKee, C., **1975**. Concentration dependent solute redistribution at the ice/water phase boundary. II. Experimental investigation. *J. Chem. Phys.* 62, 3085-3092.
16. Hutterli, M. A., McConnell, J. R., Chen, G., Bales, R. C., Davis, D. D., Lenschow, D. H., **2004**. Formaldehyde and hydrogen peroxide in air, snow and interstitial air at South Pole. *Atmos. Environ.* 38, 5439-5450.
17. Hutterli, M. A., McConnell, J. R., Stewart, R. W., Jacobi, H. W., Bales, R. C., **2001**. Impact of temperature-driven cycling of hydrogen peroxide ($H_2O_2$) between air and snow on the planetary boundary layer. *J. Geophys. Res.* 106, 15395-15404.
18. Kawahara, H., Iwanaka, Y., Higa, S., Muryoi, N., Sato, M., Honda, M., Omura, H., Obata, H., **2007.** A novel, intracellular antifreeze protein in an antarctic bacterium, Flavobacterium xanthum. *Cryo letters.* 28, 39-49.
19. Kawahara, H., Nakano, Y., Omiya, K., Muryoi, N., Nishikawa, J., Obata, H., **200**4. Production of two types of ice crystal-controlling proteins in Antarctic bacterium. *J. Biosci. Bioeng.* 98, 220-223.
20. Kim, K., Chung, H. Y., Ju, J., Kim, J., **2017**. Freezing-enhanced reduction of chromate by nitrite. Sci. *Total Environ.* 590-591, 107-113.
21. Kim, K., Ju, J., Kim, B., Chung, H. Y., Vetráková, L., Heger, D., Saiz-Lopez, A., Choi, W., Kim, J., **2019**. Nitrite-induced activation of iodate into molecular iodine in frozen solution. Environ. *Sci. Technol.* 53, 4892-4900.

KOPRI 극지연구소

22. Kim, K., Yabushita, A., Okumura, M., Saiz-Lopez, A., Cuevas, C. A., Blaszczak-Boxe, C. S., Min, D. W., Yoon, H.-I., Choi, W., **2016.** Production of molecular iodine and tri-iodide in the frozen solution of iodide: implication for polar atmosphere. *Environ. Sci. Technol.* 50, 1280-1287.

23. Krausková, Ľ., Procházková, J., Klašková, M., Filipová, L., Chaloupková, R., Malý, S., Damborský, J., Heger, D., **2016**. Suppression of protein inactivation during freezing by minimizing pH changes using ionic cryoprotectants. *Int. J. Pharm.* 509, 41-49.

24. Le, N. T. H., Ju, J., Kim, B., Kim, M. S., Lee, C., Kim, S., Choi, W., Kim, K., Kim, J., **2020.** Freezing-enhanced non-radical oxidation of organic pollutants by peroxymonosulfate. *Chem. Eng. J.* 388, 124226.

25. Lee, J. H., Lee, S. G., Do, H., Park, J. C., Kim, E., Choe, Y. H., Han, S. J., Kim, H. J., **2013**. Optimization of the pilot-scale production of an ice-binding protein by fed-batch culture of Pichia pastoris. Appl. *Microbiol. Biotechnol.* 97, 3383-3393.

26. Lee, J. H., Park, A. K., Do, H., Park, K. S., Moh, S. H., Chi, Y. M., Kim, H. J., **2012a**. Structural basis for antifreeze activity of ice-binding protein from arctic yeast. *J. Biol. Chem.* 287, 11460-11468.

27. Lee, S. G., Koh, H. Y., Lee, J. H., Kang, S. H., Kim, H. J., **2012b**. Cryopreservative effects of the recombinant ice-binding protein from the arctic yeast Leucosporidium sp. on red blood cells. *Appl. Biochem. Biotechnol.* 167, 824-834.

28. Mason, R. H., Si, M., Chou, C., Irish, V. E., Dickie, R., Elizondo, P., Wong, R., Brintnell, M., Elsasser, M., Lassar, W. M., Pierce, K. M., Leaitch, W. R., MacDonald, A. M., Platt, A., Toom-Sauntry, D., Sarda-Estève, R., Schiller, C. L., Suski, K. J., Hill, T. C. J., Abbatt, J. P. D., Huffman, J. A., DeMott, P. J., and Bertram, A. K. **2016**, Size-resolved measurements of ice nucleating particles at six locations in North America and one in Europe. *Atmos. Chem. Phys.,* 16, 1637 - 1651.

29. Menacherry, S. P. M.; Kim, K.; Lee, W.; Choi, C. H.; Choi, W. Ligand-specific dissolution of iron oxides in frozen solutions. *Environ. Sci. Technol.* **2018**, 52, 13766 - 13773.

30. Nawrot, A. P., Migała, K., Luks, B., Pakszys, P., Głowacki, P., **2016**. Chemistry of snow cover and acidic snowfall during a season with a high level of air pollution on the Hans Glacier, Spitsbergen. *Polar Science.* 10, 249-261.

31. O'Driscoll, P., Minogue, N., Takenaka, N., Sodeau, J., **2008**. Release of nitric oxide and iodine to the atmosphere from the freezing of sea-salt aerosol components. *J. Phys. Chem. A.* 112, 1677-1682.

32. O'Concubhair, R., Sodeau, J. R., **2013**. The Effect of freezing on reactions with

environmental impact. *Acc. Chem. Res.* 46, 2716-2724.

33. O'Sullivan, D., Sodeau, J. R., **2010**. Freeze-Induced Reactions: Formation of iodine–bromine interhalogen species from aqueous halide ion solutions. *J. Phys. Chem. A.* 114, 12208-12215.

34. Park, K. S., Do, H., Lee, J. H., Park, S. I., Kim, E., Kim, S. J., Kang, S. H., Kim, H. J., **2012**. Characterization of the ice-binding protein from Arctic yeast Leucosporidium sp. AY30. *Cryobiology.* 64, 286-296.

35. Pratt, K. A., Custard, K. D., Shepson, P. B., Douglas, T. A., Pöhler, D., General, S., Zielcke, J., Simpson, W. R., Platt, U., Tanner, D. J., Gregory Huey, L., Carlsen, M., Stirm, B. H., **2013**. Photochemical production of molecular bromine in Arctic surface snowpacks. *Nat. Geosci.* 6, 351-356.

36. Raymond, J. A., Christner, B. C., Schuster, S. C., **2008**. A bacterial ice-binding protein from the Vostok ice core. *Extremophiles.* 12, 713-717.

37. Raymond, J. A., Fritsen, C., Shen, K., **2007**. An ice-binding protein from an Antarctic sea ice bacterium. *FEMS Microbiol. Ecol.* 61, 214-221.

38. Saiz-Lopez, A., Mahajan, A. S., Salmon, R. A., Bauguitte, S. J.-B., Jones, A. E., Roscoe, H. K., Plane, J. M. C., **2007**. Boundary layer halogens in coastal Antarctica. *Science*, 317, 348-351.

39. Saiz-Lopez, A., Plane, J. M. C., Baker, A. R., Carpenter, L. J., von Glasow, R., Gómez Martín, J. C., McFiggans, G., Saunders, R. W., **2012**. Atmospheric chemistry of iodine. *Chem.* Rev. 112, 1773-1804.

40. Saiz-Lopez, A., Plane, J. M. C., Mahajan, A. S., Anderson, P. S., Bauguitte, S. J. B., Jones, A. E., Roscoe, H. K., Salmon, R. A., Bloss, W. J., Lee, J. D., Heard, D. E., **2008**. On the vertical distribution of boundary layer halogens over coastal Antarctica: implications for $O_3$, $HO_x$, $NO_x$ and the Hg lifetime. Atmos. *Chem. Phys.* 8, 887-900.

41. Saiz-Lopez, A., von Glasow, R., **2012.** Reactive halogen chemistry in the troposphere. *Chem. Soc.* Rev. 41, 6448-6472.

42. Schroeder, W. H., Anlauf, K. G., Barrie, L. A., Lu, J. Y., Steffen, A., Schneeberger, D. R., Berg, T., **1998**. Arctic springtime depletion of mercury. *Nature*. 394, 331-332.

43. Simpson, W. R., Brown, S. S., Saiz-Lopez, A., Thornton, J. A., von Glasow, R., **2015**. Tropospheric halogen chemistry: sources, cycling, and impacts. *Chem.* Rev. 115, 4035-4062.

44. Simpson, W. R., von Glasow, R., Riedel, K., Anderson, P., Ariya, P., Bottenheim, J., Burrows, J., Carpenter, L. J., Frieß, U., Goodsite, M. E., Heard, D., Hutterli, M., Jacobi, H. W., Kaleschke, L., Neff, B., Plane, J., Platt, U., Richter, A., Roscoe, H., Sander, R.,

Shepson, P., Sodeau, J., Steffen, A., Wagner, T., Wolff, E., 2007. Halogens and their role in polar boundary-layer ozone depletion. Atmos. *Chem. Phys.* 7, 4375-4418.

45. Skitchenko, R. K., Usoltsev, D., Uspenskaya, M., Kajava, A. V., Guskov, A., 2020. Census of halide-binding sites in protein structures. Bioinformatics. 36, 3064-3071.

46. von Glasow, R., 2008. Sun, sea and ozone destruction. *Nature*. 453, 1195-1196.

47. Watanabe, H., Otsuka, T., Harada, M., Okada, T., 2014. Imbalance between anion and cation distribution at ice interface with liquid phase in frozen electrolyte as evaluated by fluorometric measurements of pH. J. Phys. *Chem. C*. 118, 15723-15731.

KOPRI
극지연구소

## FIGURES

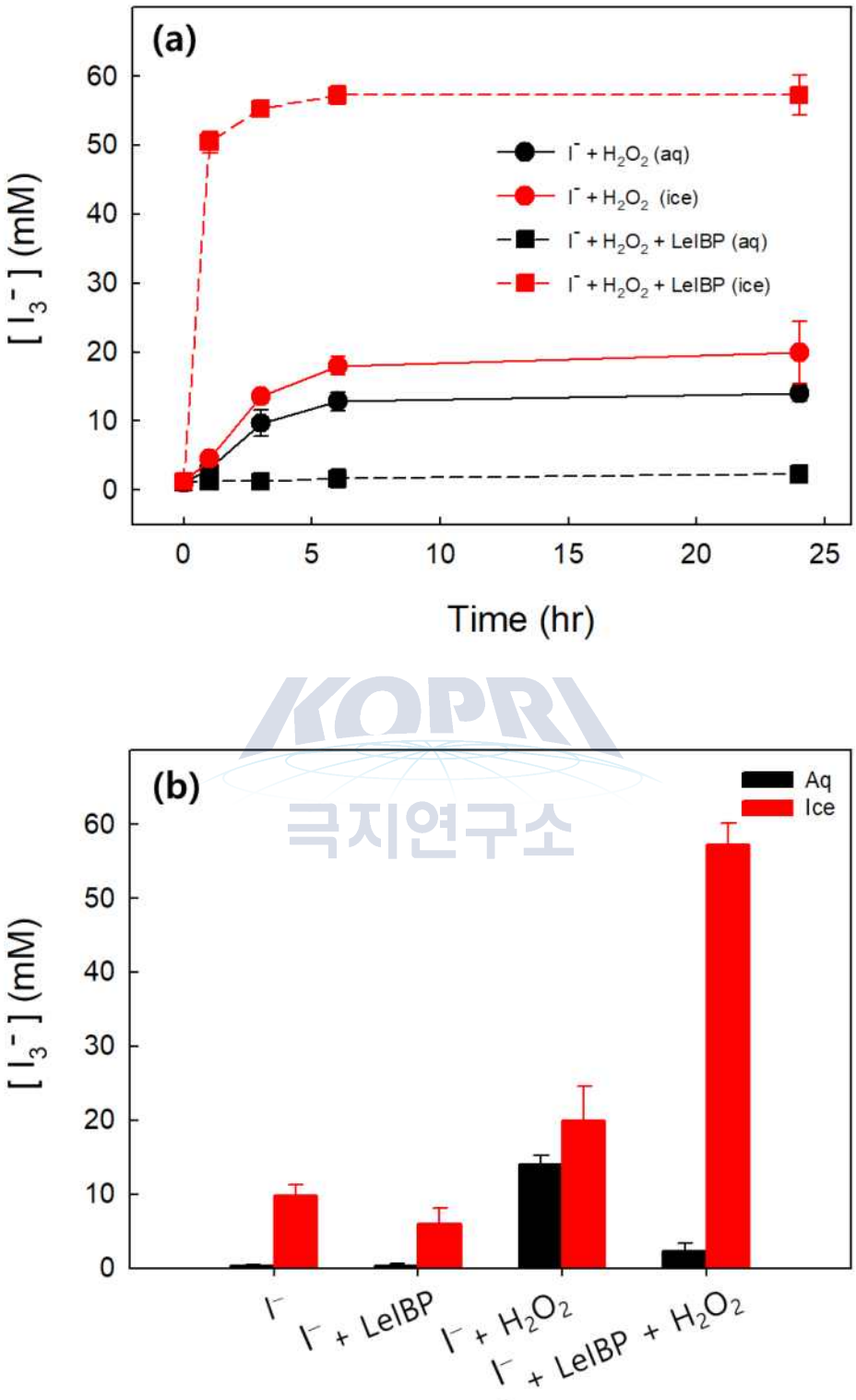



Fig. 1. Iodide oxidation with $H_2O_2$ in aqueous phase and ice in the presence of LeIBP. (a) Time profile of $I_3^-$ production in aqueous phase (at 25 °C) or in ice (at -20 °C). (b) Production of $I_3^-$ in aqueous phase or ice after the 24 h reaction. Initial conditions: $[I^-]$ = 1 mM, $[H_2O_2]$ = 0.5 mM, LeIBP = 100 ppm, pH = 4.0.

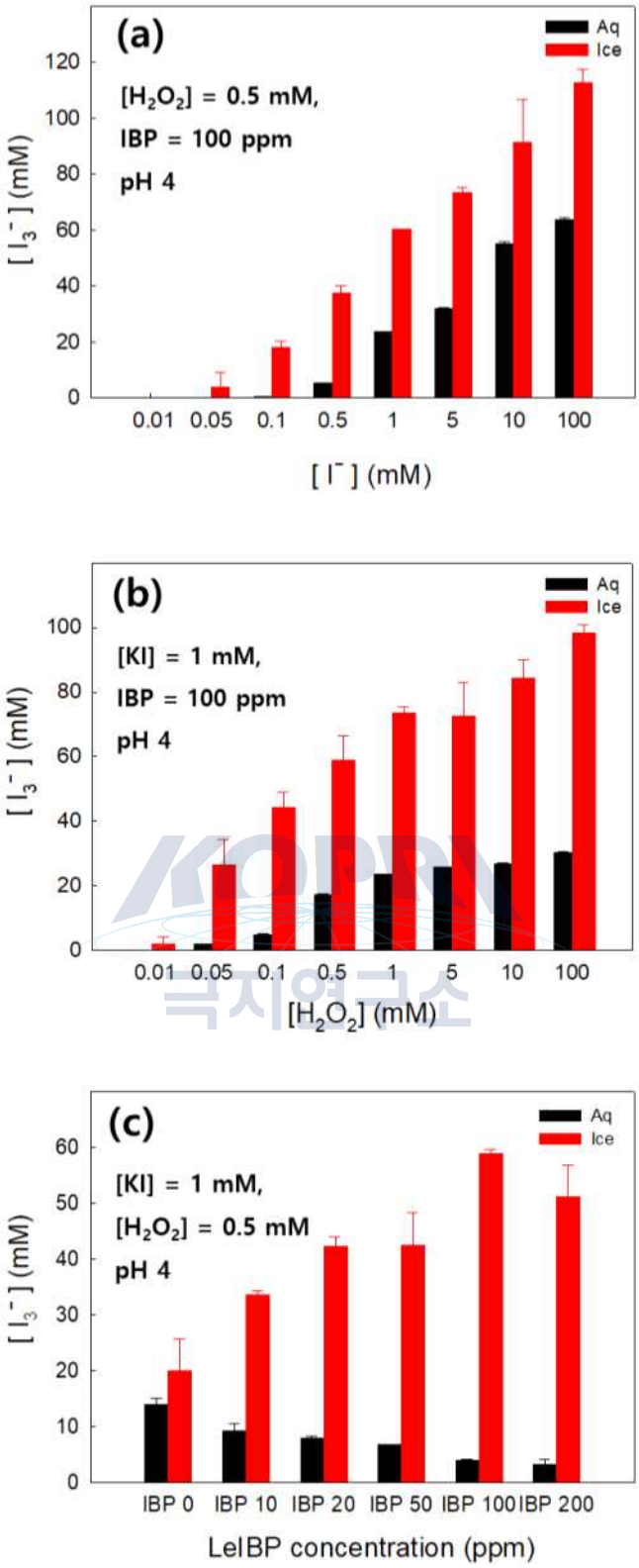



Fig. 2. $I_3^-$ production in aqueous phase (at 25 °C) or ice (at -20 °C) after the 24 h reaction under various conditions, against (a) [$I^-$], (b) [$H_2O_2$], and (c) LeIBP concentration.

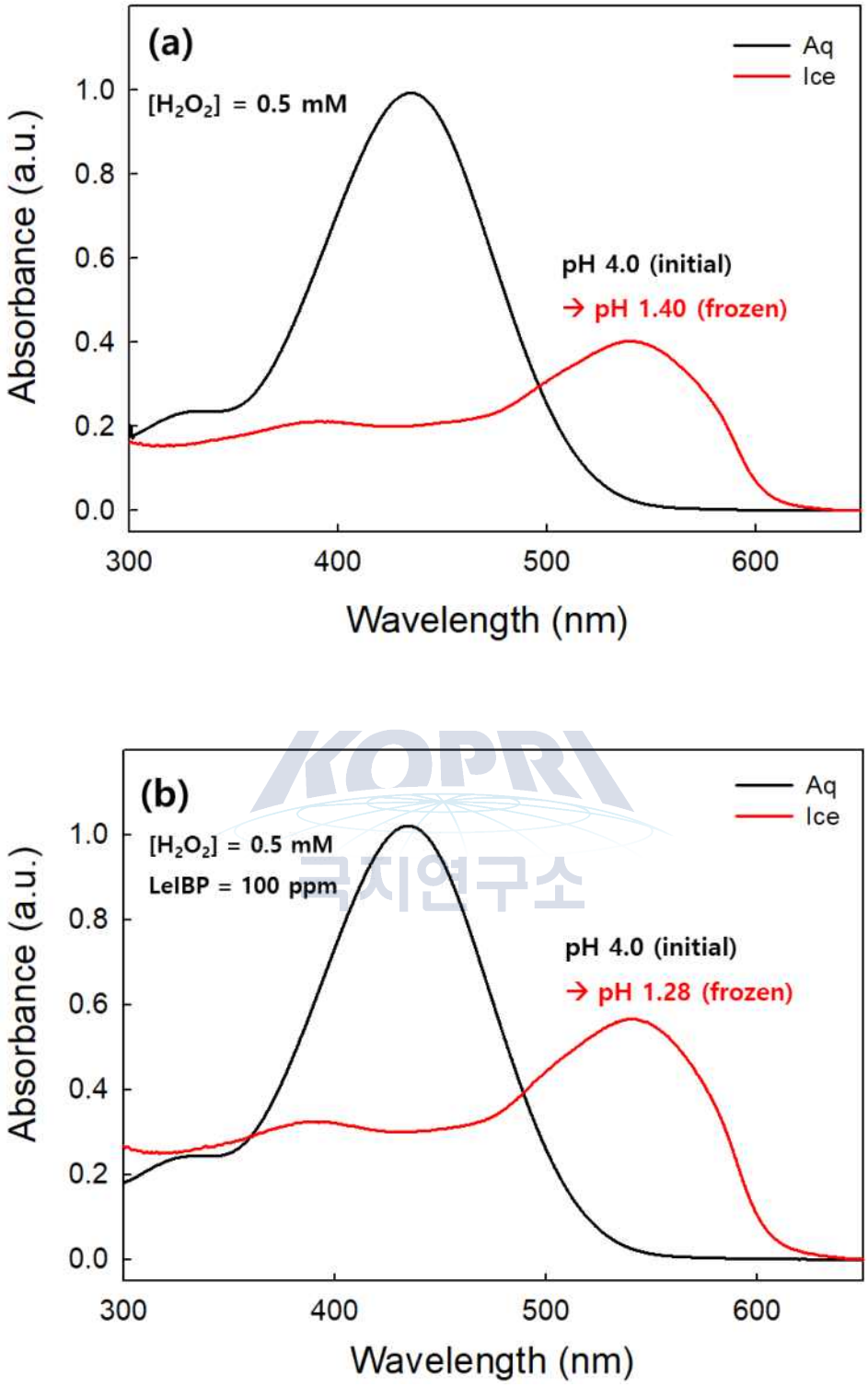



Fig. 3. Change in UV - Vis absorption spectra of CR before and after freezing of (a) $H_2O_2$ solution, (b) $H_2O_2$ with LeIBP solution. Initial condition conditions: freezing temperature = -20 °C, freezing time = 1 h, [$H_2O_2$] = 0.5 mM, LeIBP = 100 ppm, [CR] = 10 μM, initial pH 4.0.

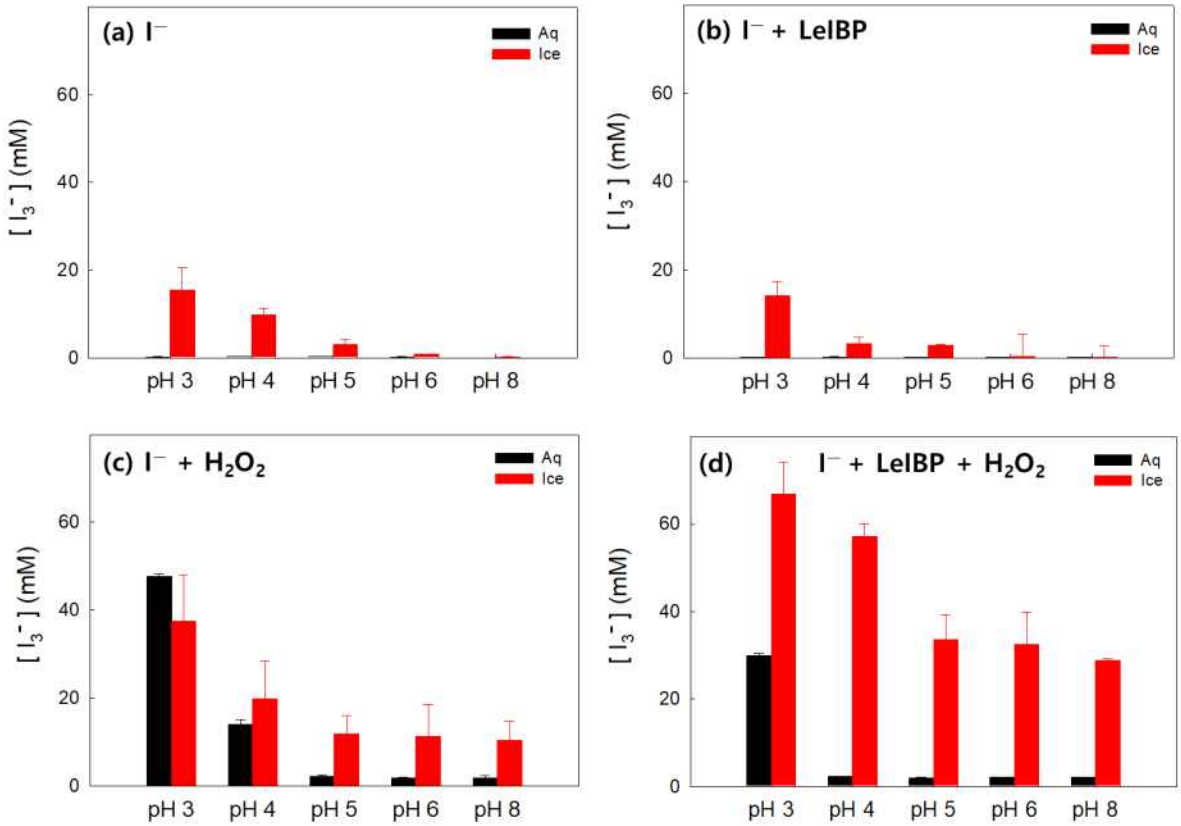



Fig. 4. $I_3^-$ production in aqueous phase (at 25 °C) or ice (at -20 °C) after 24 h reaction in (a) iodide solution, (b) iodide solution with LeIBP, (c) iodide solution with $H_2O_2$, and (d) iodide solution with LeIBP and $H_2O_2$, under different pH conditions. Initial condition: $[I^-]$ = 1 mM, $[H_2O_2]$ = 0.5 mM, LeIBP = 100 ppm.

KOPRI 극지연구소

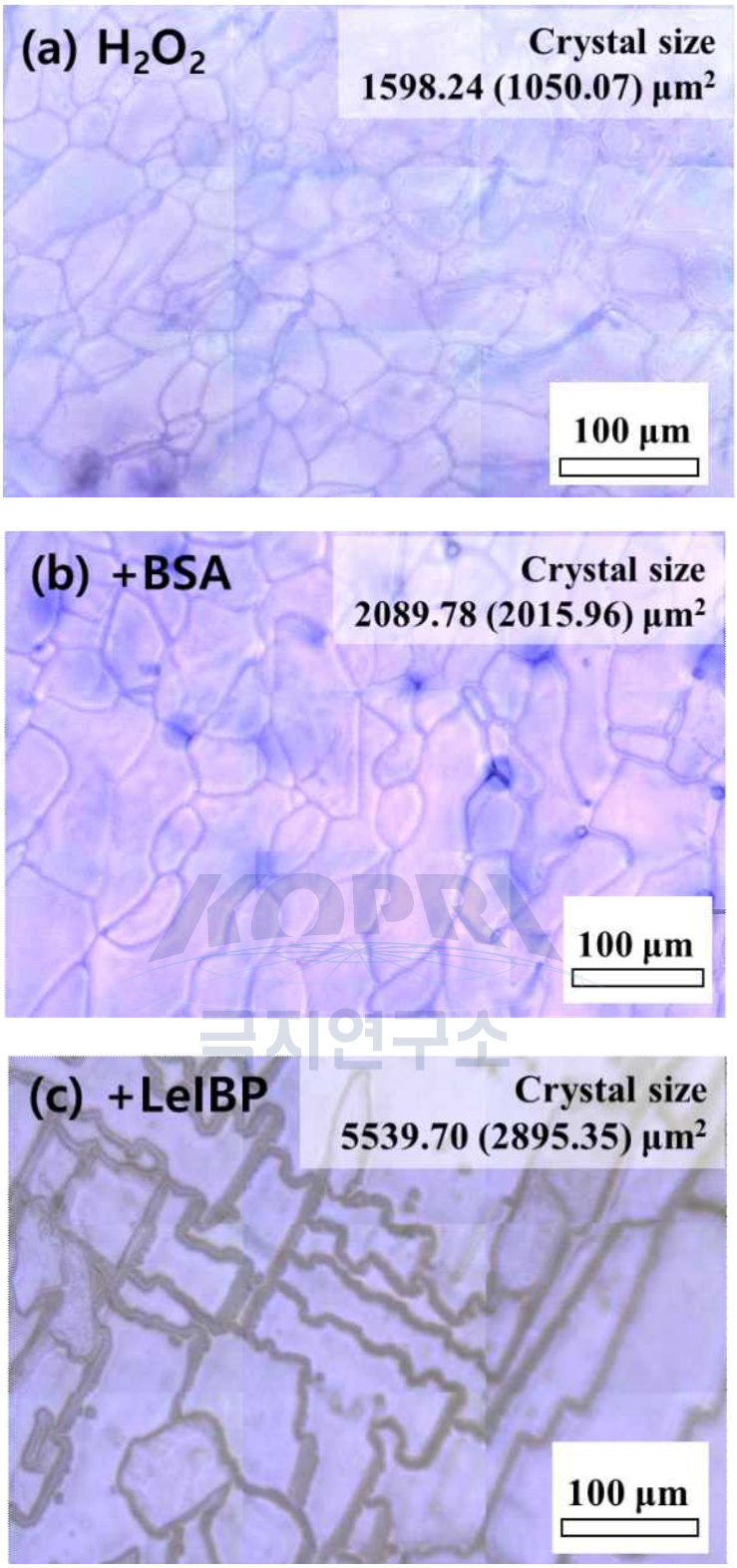



Fig. 5. Optical images of the ice granules of (a) $H_2O_2$ frozen solution, (b) $H_2O_2$ frozen solution with BSA, and (c) $H_2O_2$ frozen solution with LeIBP. Initial condition: [$H_2O_2$] = 0.5 mM, LeIBP = 100 ppm, BSA = 100 ppm, pH 4.0, cooling temperature: -20 °C

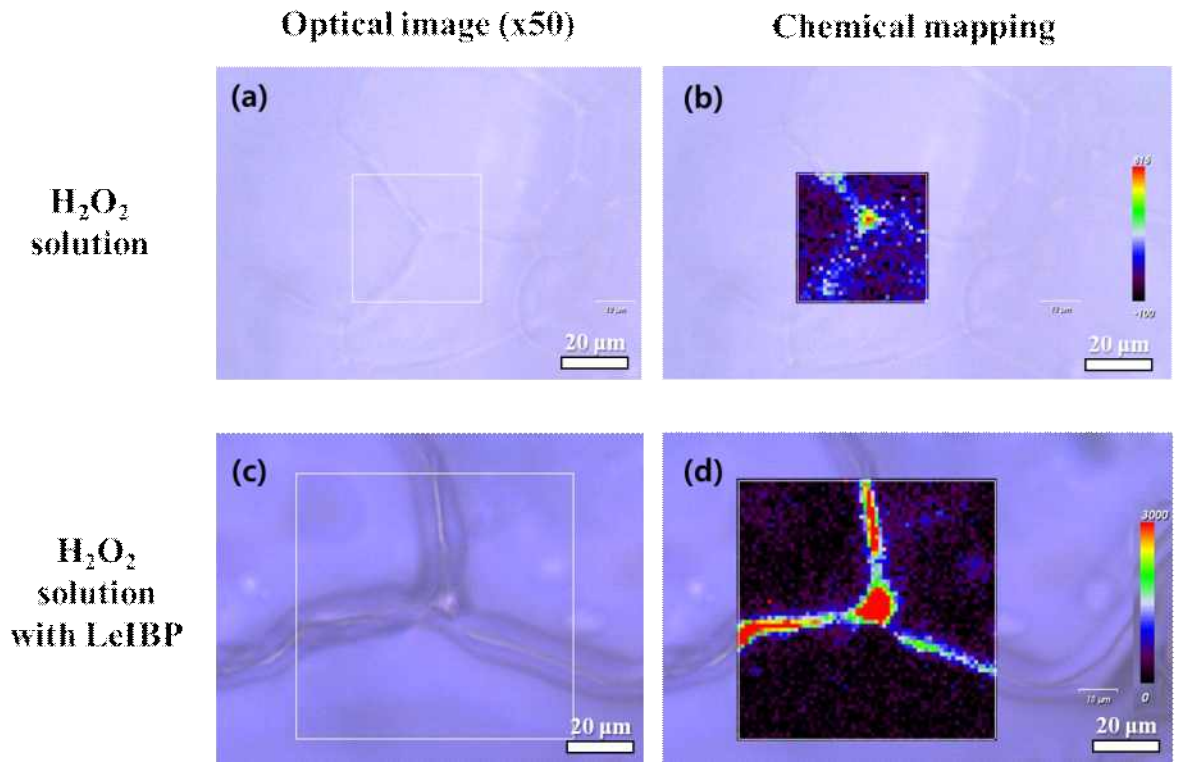



Fig. 6. Optical image of the frozen (a, b) $H_2O_2$ solution, (c, d) $H_2O_2$ with LeIBP and their spatial distribution based on the Raman peak intensity at 880 $cm^{-1}$, for O−O stretching vibration mode from $H_2O_2$. The signal intensity was ordered using a rainbow color scale. (black: low à red: high). Initial condition: [$H_2O_2$] = 1 mM, LeIBP 100 ppm, pH 4.0, cooling temperature: -20 °C

KOPRI 극지연구소

# 제 11 절. Importance of rigidity of ice-binding protein (FfIBP) for hyperthermal hysteresis activity and microbial survival⑪

Jisub Hwang[1,2], Bomi Kim[1,2], Min Ju Lee[1], Eun Jae Kim[3], Sung Mi Cho[3], Sung Gu Lee[1,2], Se Jong Han[2,3], Kitae Kim[1,2], Jun Hyuck Lee[1,2], and Hackwon Do[1,2]

[1]Research Unit of Cryogenic Novel Material, Korea Polar Research Institute
[2]Department of Polar Sciences, University of Science and Technology
[3]Division of Life Sciences, Korea Polar Research Institute

## 1. Introduction

Ice grows from ice crystal seeds and expands its size as temperature drops. The ice size can be increased even under diminutive temperature fluctuations—known as ice recrystallization.[1,2] The ice formation and growth in the inner and outer layers of cells causes physical damage as well as osmotic shock to an organism in sub-zero environments[3-5]. Therefore, organisms from the polar region produce ice-binding proteins (IBPs) to protect themselves from freeze-induced damage as cold adaptation and/or avoidance mechanisms amico.[6]

Unlike general enzymes, IBPs have unique properties, i.e., binding to ice, and this interaction results in the inhibition of ice growth at low temperatures by covering the potential binding sites for water molecules on the crystal surface.[7] The magnitude of the interaction strength can primarily be evaluated by the thermal hysteresis (TH) activity and an ice recrystallization inhibition assay.[8] TH activity is represented by a numerical value defining the gap between the freezing and melting points. Based on TH activity, IBPs can be divided into two groups: moderately active or hyperactive IBPs. Moderately active IBPs have been found in fish and plants with a TH activity of ~0.5 °C at the maximum protein concentrations measured, whereas the hyperactive proteins from bacteria and insects show activity up to 5 °C at the maximum concentration.[9-13] Two factors are common for hyperactive proteins: a common motif at the ice-binding site (IBS) and a wide range of IBSes.[14] For example, the hyperactive TmAFP from Tenebrio molitor and sbwAFP from the spruce budworm (Choristoneura occidentalis) contain regular Thr-X-Thr motifs at the IBS, whereas MpAFP from Marinomonas primoryensis contains the Thr-X-Asn motif.[9,15,16]

⑪ 이 연구는 해양수산부 “극지 유래 생물자원을 활용한 항생제 후보물질 개발” 과제(15250103, PM21030) 및 PE21160, 본 과제(PE22120), PE21300 과제 지원으로 수행되었으며 그 결과는 다음의 논문으로 출판되었음: *Int. J. Biol. Macromol.* 2022, 204, 485-499.

These regularly spaced residues can be assembled with an ice lattice, probably via the hydration of water molecules. In addition, these hyperactive IBPs are formed by the association of parallel β-strands in a helical pattern. This parallel β-sheet is beneficial for hyperactive IBPs to interact with an extended ice surface. Furthermore, truncated CfAFP (from C. fumiferana) showed reduced TH activity, whereas long wild-type CfAFP had a higher activity, indicating that the area of IBP interacting with ice is vital for hyper-TH activity.[14]

The binding mechanism between IBPs and ice has been established using multiple methods[17], and the dominant theory states that IBPs interact with ice via water-mediated interactions involved in hydrogen bonding and hydrophobic effects coordinating water molecules at the IBS. In other words, residues on the IBP surface play a role in arranging the water molecules, which mimics the arrangement of water molecules on ice.[18-20] Thus, well-arranged and rigid residues at IBSes complementary to ice water would be important to increase the ice-binding strength of IBPs, as shown in the hyperactive IBPs. However, although intensive biochemical and structural investigations of IBPs have been conducted for decades, limited information regards the correlation between the structural stability and TH activity as well as the implication of hyperactive IBPs for microbial survival in cold environments.

Previously, our lab investigated two IBPs, FfIBP from the Antarctic bacterium Flavobacterium frigoris PS1 and LeIBP from the Arctic yeast Glaciozyma sp.[10,21-23] Although the two IBPs share a highly sequential and tertiary structure similarity, the TH activity of FfIBP was 10 times higher than LeIBP. The residue composition (e.g., T-A(G)-X-T/N motif at the IBS) and broader surface area at the IBS were thought to be important factors for the hyperactivity of FfIBP.[10] However, although the chimeric protein mFfIBP, which swapped the capping head region with LeIBP, has highly identical residues at the IBS similar to FfIBP, it showed only moderate TH activity and lower stability than FfIBP. Based on this observation, we hypothesized that the capping head region is important for TH activity by stabilizing the overall structure.

We here report that the capping head region of β-helical IBPs is involved in protein stabilization that can be correlated to the hyper TH activity. Hyperactive IBPs have either FfIBP like capping head region or disulfide bond in the ice interacting strands for protein stabilization. Importantly, we show that polar microorganisms utilize the hyper-active and membrane-anchored IBPs that promote the formation of brine pockets to reduce the salt concentration in the sub-zero environments.

## 2. Results and discussion

### 2.1. Capping head region-dependent TH activity

Although the ice crystal plane where FfIBP can bind has not been identified experimentally, the docking experiment and the dendritic pattern perpendicular to the c-axis at the freezing point clearly indicate that FfIBP binds to the basal plane.[10,21] To facilitate the interaction between FfIBP and ice, FfIBP comprises T-X-A-T(N) motifs at the IBS, which are flat with parallel β-strands.[21] In particular, the residues forming the motifs T79-X-A-T82 on β2, T263-X-A-T266 on β17, and T245-X-A-T248 on β15 (X: Val or Ile) matched the regularly spaced water molecules on the basal plane of ice crystals (Fig. 1A).[21] This positional combination of motifs was also found in the hyperactive IBPs for favorable contact with either the hydration water or water from ice and is thought to be an important factor for hyper-TH activity.[11,14,24]

We generated chimeric protein (mFfIBP), whose sequence was a combination of capping region (a.a. 62 - 109) from LeIBP and body region (a.a 2 - 61 and 110 - 255) from FfIBP, and determined the crystal structure at 2Å resolution (PDB code: 4NU3).[21] The structural comparison of FfIBP with mFfIBP showed that the mFfIBP body region (61 - 92 and 130 - 276) was similar to FfIBP with a root-mean-square deviation (RMSD) of 0.30 for Cα and near identical for residues of β2, β15, and β17 at the IBS (Fig. 1C and S1 Fig. and S2 Fig.). The only difference between FfIBP and mFfIBP is the capping head region. Although the IBSes of both proteins are similar, their activity is different. The TH activity of FfIBP is close to 2.5 °C at 50 μM concentration.[10] In contrast, the TH activity of mFfIBP was three times less than that of FfIBP, indicating that the composition of the residues at the IBS was not a sufficient criterion for hyperactivity, and some other factor(s) from the capping head region may be influencing TH activity. The capping head region-dependent TH activity was consistent with the single mutation C107S in the capping head region. Breaking the disulfide bond by mutation shows decreased activity, indicating that rigidity in the capping region may be an essential factor in maintaining the hyperactivity of FfIBP (Fig. 1D and S3 Fig.).

### 2.2. Residual fluctuation at IBS caused by capping head region

As seen in the hyperactive IBPs, regularly spaced motifs seem critical for hyperactivity.[25] Water molecules on the basal plane of ice, where the hyperactive IBPs mainly interact, were spaced 4.5 Å vertically and 10.5 Å horizontally. At the IBS of FfIBP, the distance between T79 - T245 and T82 - N248 was 9.7 Å and 8.9 Å (Cβ), respectively, and the distances between T79 - T82 and T245 - N248 were close to 10 Å (Cβ) for both, which stereo-specifically matches to the basal plane of the ice (S4 Fig.).[21] In addition, the

electrostatic potential was analyzed using the Adaptive Poisson- Boltzmann Solver to understand the ice-binding mechanism of FfIBP.[26] The analysis revealed that the IBS of FfIBP consists of mainly non-polar residues, while negatively charged residues from the motifs are locally distributed (Fig. 1B). This hydrophobic surface with spaced hydroxyl groups from the motifs is considered an important feature of IBS for stabilizing the hydration water layer ordering, which is associated with its ice-binding function. Consistent with this observation, careful investigation regarding the hydration water layer on IBS found the hexagonally latticed waters around the residues from the motifs after solvation and energy minimization during simulation.[27] The reduced activity of mFfIBP or C107S is probably due to the disturbance of these hydration waters on the IBS, which stems from the capping head region of FfIBP. Based on this idea, we hypothesized that the immobility of FfIBP is important for interaction with solid ice. To test this hypothesis, we performed molecular dynamics (MD) simulations using FfIBP, C107S, and mFfIBP structures.

First, the RMSD and residual root-mean-square fluctuation (RMSF) were calculated for each system to measure the spatial fluctuation of residues at the IBS from the MD simulation at 300 K. The mean RMSD of FfIBP during simulation was below 0.9 Å with a low standard deviation (0.108 Å), whereas the RMSD values of mFfIBP and C107S were close to or higher than 1 Å as 1.23 Å and 1.18 Å, respectively. In contrast to the FfIBP, the RMSD values of mFfIBP and C107S continued to increase over time, indicating higher fluctuations in residue positions around the starting points (Fig. 2A). Furthermore, the RMSD difference was caused by residual movement in the capping head region of the IBPs in both cases.

A comparison of FfIBP with mFfIBP indicated that the a.a. 70 - 80 region of mFfIBP was more mobile, as indicated by the high value of fluctuation in the simulation data (Fig. 2B). Superimposition of the frames extracted from mFfIBP simulation every 10 ns exhibited notable flexibility at the small turn region (70-PAAAY-75). This alanine-rich region was barely connected via hydrophobic interaction between Ala73 and Tyr104 in the crystal structure. The simulation results indicated that the interaction between the two residues is broken, and the PAAAY region could be freely flipped out toward the IBS. This would generate steric hindrance which may interfere with the IBS's access to the ice, resulting in loss of TH activity (Fig. 3B). Notably, the capping head region fluctuation was also observed in the C107S system. The distance of alpha-carbons between C107 and C124 of FfIBP is close to 3.7 Å, which does not change during simulation. However, breaking of disulfide bond by mutation (C107S) resulted in a great increment of the distance from 3.7 Å to 8.3 Å (at 50 ns) between Ca of two cysteines and displacements of the Cys124. This fluctuation at the unstructured loop influenced the movement on the 98-ITGAA-102 region that corresponds to the PAAAY region of mFfIBP. Together, the switching of the capping

head region or breaking the disulfide bond (C107 – C124) resulted in an increased fluctuation of the entire capping region of IBP, specifically the small turn region facing the IBS (Fig. 3C).

Next, we investigated how the movement of the capping head region reflects at the IBS. The investigation of the residual movement in the IBS implies that a mutation in the capping head region distorts the position of residues. The distance of the grid-like position of the hydroxyl residues was measured from the simulation data. The average distance between T79 and T245 of FfIBP was 10.36 Å during the entire simulation, which is almost identical to the vertical distance of water molecules on ice. However, the mFfIBP and C107S showed the increased distance as mean distances of 11.25 Å and 11.20 Å, respectively (Fig. 4A and S3 Table). It is also worth noting that the distance between T79 – T82 of FfIBP was steady with a low standard deviation during the simulation, whereas that of mFfIBP and C107S increased with time, indicating the increased movement of residues (Fig. 4A). However, the distances which involved N248 (i.e., T82 – N248 and T245 – N248 for FfIBP and C107S; T55 – N228 and T225 – N228 for mFfIBP) were similar to those of FfIBP. Therefore, T79 was the most affected residue from the capping head region fluctuation with a tendency to move toward the head capping head region (Fig. 4A).

Since the arrangement of the hydration water molecules in regular intervals is essential and is thought to play an important role in facilitating IBP binding, we analyzed the side-chain dihedral angle distributions of motifs interacting with the hydration water. The dihedral angles (χ1) of T79 (T52 of mFfIBP), T82 (T55 of mFfIBP), T245 (T225 of mFfIBP), and N248 (N228 of mFfIBP) were measured and compared.[28] The dihedral angle distributions showed that the side chain of T79 of FfIBP is steady, as indicated by a major peak at 60° with low deviation, whereas the T52 of mFfIBP and T79 of C107S changed the dihedral angles with high deviation. In a comparison of T82s, although FfIBP and mFfIBP exhibited similar distribution angles at 180° as major peaks, a minor peak could also be seen at 60° for mFfIBP (T55). Moreover, unlike the FfIBP and mFfIBP, the T82 of C107 showed dominant rotamers at different angles. These distribution differences were also seen in the T245 and T248. In case of the T245, the preferred orientation of FfIBP was 60°, whereas the mFfIBP and C107S changed the orientation approximately to 160° and 180°, respectively. Moreover, major peaks for N248 distribution were not changed among IBPs, but the minor peaks for the mFfIBP and C107S were increased at 180° (Fig. 4B). The distance of two residues and the rotamer distribution analysis indicate that the fluctuation of the capping head region alters the movement of residue as well as the side-chain conformation that are essential for the arrangement of hydration water molecules on IBS. Together, these results indicate that the capping head region with the disulfide bond of FfIBP influences the immobilization of the residues at the IBS.

### 2.3. Morphology of ice crystals in the presence of IBPs

The ice morphology and growth rate were checked at a freezing point during the TH activity measurement. FfIBP effectively and consistently inhibited ice growth until the ice burst rapidly. Dendritic burst formation is a typical phenomenon of hyperactive IBPs because it mainly binds to the basal plane such that the ice grows to the A-axis.[29-33] However, mFfIBP and C107S failed to inhibit the ice growth, even at higher concentrations (Fig. 5). This observation provides convincing insights regarding the low TH activity of mFfIBP and C107S. Other differences in the presence of mFfIBP and C107S were ice morphologies. Ice forms truncated bipyramidal structures in the presence of mFfIBP, whereas ice with C107S shows hexagrams. The hexagram formation changed at a higher concentration of C107S, similar to the ice morphology in the presence of FfIBP. The residue composition on IBS of mFfIBP and C107S were well fitted to corresponding residues on IBS of FfIBP. However, the increase in residue mobility might have disrupted or weakened the bonding between the protein and ice, resulting in differences in the ice growth rate and morphologies of FfIBP, mFfIBP, and C107S (Fig. 5).

### 2.4. Common characteristics of hyperactive IBPs or AFPs

To generalize our findings, we analyzed the structural characteristics of the IBPs. Although the IBPs share the same function of adsorption to ice, their structures are diverse.[34] Among them, a particular IBP family with the DUF3494 domain has been consistently found in polar microorganisms. The members of this DUF3494 IBP family include: FfIBP (PDB:4NU2), LeIBP (PDB:3UYV), ColAFP (PDB:3WPY), TisAFP6 (PDB:3VN3), EfcIBP (PDB:6EIO), CfAFP-501 (PDB:1M8M), CfAFP-337 (PDB:1L0S), SfIBP_1 (PDB:6BG8), and AnpIBP (PDB:7BWX).[31] The structural analysis of the IBPs indicated that the DUF3494 IBP family can be divided into two subgroups based on the folding of the capping head region and the presence of disulfide bonds (which always resulted in hyperactive IBPs, except for TisAFP8).[19,31] For example, the hyperactive ColAFP from Colwellia sp. SLW05 has similar folding in the capping head region to FfIBP with disulfide bonds, whereas other DUF3494 IBPs showing moderate TH activity do not have a disulfide bond or capping head region (e.g., EfcIBP and AnpIBP)[33,35] (Fig. 6). Notably, the SfIBP_1 with distinctly different folding on the capping head region from the two subgroups has TH activity between moderate and hyperactivity, indicating that the folding of the capping head region is probably a distinguishable factor for TH activity.[31]

Furthermore, in this study, although the hyperactive IBPs do not belong to the DUF3494 IBP family, they have intramolecular disulfide bonds in the intervals of the β-strands at the IBSes. The disulfide bond among the strands stabilizes the overall structure and helps to maintain the rigidity of regularly spaced residues. Therefore, these hyperactive IBPs

probably evolved by integrating the disulfide bonds to stabilize the structure, resulting in hyperactivity. In contrast, the hyperactive MpAFP, which does not have a disulfide bond, instead has calcium ions between β-strands for the regular interval of residues. This contradicts the importance of rigid and regularly spaced residues for hyperactivity (Fig. 6).[15]

The data we present here indicate that the stability of regularly spaced residues at the IBS stemming from the capping head region is an essential factor for the hyperactivity of FfIBP, which had been less of a focus for TH activity, whereas the composition of hydrophilic residues and shape of the IBS received attention. Furthermore, generalizing our findings to the DUF3494 IBP family and β-helical hyperactive IBPs suggests that either the capping head region or integrated disulfide bond(s) of IBPs seem to be an important factor for hyper-TH activity.

### 2.5. FfIBP is a membrane-anchored protein

To explore the benefits of IBP with hyper-TH activity for bacteria, we first analyzed the FfIBP sequence. The sequence analysis of FfIBP by SignalP 5.0[36] predicted that FfIBP has a lipoprotein signal sequence at the N-terminal end of the coding sequence with 99% possibility, followed by a cysteine. The signal sequence has the most conserved amino acid (leucine) in the lipobox and cleaves between the LMTN and CSND sequences of the 20th amino acid (S5 Table). This sequential feature indicates FfIBP is anchored to membranes via N-terminal lipids.

To prove that FfIBP is a membrane-anchored protein based on signal sequence analysis, we cloned the full-length ffibp coding sequence in the pET-21b vector to generate C-terminal His-tagged IBPs. IBP-induced cells were then analyzed for protein expression by western blotting probed with a His-tag antibody. Subsequently, we investigated the subcellular localization of FfIBP by fractionation. Consistent with the sequential predictions, FfIBP was detected only in the membrane fraction (Fig. 7A).

In addition, IPTG-induced cells were incubated with 6×His-tag specific fluorescent dye (NTA-Atto 550) and checked for protein localization using a fluorescence microscope. The fluorescence signal was present in the bacterial cells harboring pET21b, FfIBP, mFfIBP, and C107S, whereas no fluorescent signal was observed in the cells containing empty pET-21b (Fig. 7B). Moreover, the reduced fluorescent signal image revealed that the fluorescent signal came from the membrane fraction. It is noteworthy that the fluorescence dye NTA-Atto 550 is not membrane permeable. Together, these results confirm FfIBP is a membrane-anchored protein that is most similar to the membrane of Flavobacterium frigoris PS1 in its natural state.

## 2.6. Benefits of hyperactive IBPs for microorganisms inhabiting ice

To better understand how microorganisms with IBP on their membrane surface survive in a cold environment, the recovery rate of cells after repeated freezing and thawing processes was measured. The proteins were expressed on the cell surface and the protein expression for each cell was confirmed by checking the fluorescence level before the experiment. The 1st round of freeze-thaw cycles resulted in a steep decline in the recovery rates of all strains, indicating high fragility of the cells. However, differences could be observed among the strains. After the 1st freeze-thaw cycle, the colony forming units (CFUs) of viable bacteria with the empty vector were $3.5 \times 10^4$ on average, whereas for the strains with FfIBP, mFfIBP, and C107S, CFUs were over $7.2 \times 10^5$, $1.7 \times 10^6$, and $2.1 \times 10^5$, respectively. Strains with FfIBP had a 20 times higher survival rate than the empty vector strain. Most cells with empty vectors died in the 2nd freeze-thaw cycle (CFU $< 1 \times 10^2$), whereas the CFUs of strains with FfIBP, mFfIBP, and C107S were $8.5 \times 10^4$, $4.0 \times 10^3$, and $5.9 \times 10^2$, respectively. These results indicate that the cells with IBPs having high TH activity were resistant to the repetitive freeze-thaw cycles compared to the cells without IBP (Fig. 8A).

Although the same process and conditions were used for protein expression and incubation for tagging a specific fluorescence dye, the intensity of the fluorescence for each cell type was different (as shown in Fig. 7). For instance, some cells had no fluorescence, indicating variability in the protein contents of each cell, potentially because of the different IPTG-induction times for each cell. Because FfIBP contributes to bacterial cell survival in the freeze-thaw cycle, we speculated that strains with higher FfIBP content (high Atto fluorescence intensity) survive better than those with low or no protein content. Consistent with our hypothesis, the percentage of cells with FfIBP (cells with fluorescence/total cells) increased from ~20% up to 65% after the 3rd cycle, indicating that the strains with high FfIBP content has a higher survival rate to the repeated freeze-thaw process than the stains without/low FfIBP (Fig. 8B). This could also explain the low survival rate of strains compared to those with FfIBP in the 1st round of the freeze-thaw cycle.

Next, we mimicked the natural conditions to understand the detailed mechanism of bacterial survival with IBPs in ice. Cells with or without membrane-anchored IBPs were frozen in a chamber, and the morphological phenomena of ice were compared. As shown in Fig. 9 and S5 Fig, the cells (fluorescein isothiocyanate [FITC]-stained) without IBP or with mFfIBP (moderately active) showed high fluorescence intensity at the triangular junction of ice granules, indicating concentrated cells. In contrast, the cells with FfIBP or C107S were distributed in the ice and formed small brine pockets in the granule boundary with low fluorescence intensity. Smaller granules were also found in the ice cubes. Under freezing temperatures, the ice nuclei formed randomly and grew until the space was filled

with ice. During this process, the cells were pushed by growing ice granules and concentrated in the triangular junction where the three ice granules were in contact. However, cells with hyperactive IBPs could attach to the ice surface and create brine pockets in the ice granule boundary. These brine pockets contained less concentrated cells and facilitated cellular distribution throughout the ice cubes. This is probably because the hyperactive IBPs bind to the multiple planes of ice and immobilize the bacteria from flowing through the quasi-liquid layer (QLL). Therefore, cells with hyperactive IBPs can be deconcentrated in ice and expand the overall living area.

To understand the beneficial effect of brine pockets on the ecological conditions of the FfIBP sample, we estimated the salt concentration of the ice cubes with cells using Raman spectroscopy. Previously, the OH stretching band of water was chosen to measure the dynamic properties and the effect of ions.[37] The intramolecular OH bonds are influenced by local conditions, including the presence of ions. In the aqueous solutions, “disordered” vibration from OH-Cl was dominantly exhibited at the 3,400 - 3,600 $cm^{-1}$ region of the Raman spectrum rather than the “ordered” vibration at 3,140 $cm^{-1}$ from accumulated water (i.e., ice) or ion-free conditions. Therefore, the salt concentration of the area of interest in the frozen sample can be estimated by calculating the Raman intensity ratio of 3,140/3,430 $cm^{-1}$. The intensity ratio of the QLL region where NaCl was mainly gathered was 1.87 in the presence of 50 mM NaCl solution, and it decreased as NaCl concentration increased (S6 Fig.). The average ratio (3,140/3,430 $cm^{-1}$) of the 10 QLL regions with FfIBP was 1.42, which was higher than the empty sample (1.30), indicating that the salt concentration of the FfIBP sample in the QLL region was lower than the empty sample. In addition, the brine pocket region with FfIBP is adjacent to 1.66, whereas the empty sample is 2.08, which is close to the ratio of the ice granule region (2.07). The increased number of brine pockets and smaller ice granules probably helped expand the area of the QLL region and reduced the salt concentration. These results suggest that cells with FfIBP undergo mild salt concentration in QLL and brine pockets under freezing conditions, whereas those without FfIBP experience extreme conditions (high salt at QLL; or ice in the brine or bubble region).

## 2.7. Discussion

Many IBPs have been found in plants, animals, insects, fungi, and bacteria.[38] Structural and biochemical investigations helped us understand the ice-binding mechanisms of these proteins. Although uncertainty remains regarding the ice-binding mechanism due to the structural diversity of IBPs[32,34], numerous studies indicate that IBPs interact with ice via the "ice-like waters" that are layers of water molecules on IBS.[15,27] These water molecules can be arranged by interactions involving hydrogen bonding and hydrophobic effects to

facilitate the interaction with ice. FfIBP also has a hydrophobic surface with spaced hydroxyl groups from the motifs, which is not only considered crucial for locating the polygonally arranged ice-like water molecules on IBS, but is also directly related to the TH activity (Fig. 1B).[27]

IBPs are divided into two categories based on their TH activity: moderate and hyperactive IBPs. However, the mechanism underlying these differences in activity is yet to be elucidated clearly. Here, we report hyperactive FfIBP has a unique capping head region with a disulfide bond, which stabilizes the protein and reduces the movement of residues at the IBS. The movement of residues on IBPs can be negatively correlated with TH activity. Replacing the capping region or breaking the disulfide bond on the capping region caused incremental fluctuation of residue T79 and orientation of side chains of residues on IBS, destabilizing the hydration water layer and decreasing the TH activity.

The correlation between structural stability and TH activity can be found in other IBPs. Unlike moderate IBPs, hyperactive IBPs either have disulfide bond(s) between the β-strands or FfIBP-like-capping head region. The disulfide bond(s) maintains regular space among strands, which minimizes residual fluctuation in the IBS and most likely increases the strength with a long-range interaction time between the IBP and ice, resulting in hyperactivity. Thus, structural stability constitutes another condition for IBP to be hyperactive. These novel insights into the complexities of the ice-binding mechanism of IBPs will provide new evidence for distinguishing IBPs into moderate and hyperactive IBPs, predicting information on the activity of uncharacterized IBPs and ideas for the generation of artificial IBPs for hyperactivity.

Another key finding from this study is the role of membrane-anchored hyperactive IBPs in cold environments. All previously characterized DUF3494 IBP family members are secreted and thought to secure the area by inhibiting ice growth toward the bacterial habitat (S5 Table).[39,40] The reason that only secretory IBPs have been discovered is probably that researchers initially screened IBPs from the bacterial secretome. Unlike these IBPs, FfIBP is a membrane-anchored protein not yet characterized. Bacteria with FfIBP can effectively survive freeze-thaw cycles. Experiments mimicking natural conditions indicate FfIBP induces the formation of brine pockets by preventing the migration of bacteria in the QLL (Fig. 9 and 11). The number of brine pockets depends on the TH activity. Multiple ice-binding sites—characteristic features of hyperactive IBPs—probably help bacteria bind to various planes on the ice boundary and generate brine pockets starting from the ice-bound bacteria (Fig. 11). The generation of brine pockets could be beneficial for the short- and long-term survival of bacteria. An increase in brine pocket domains reduces salt concentration in QLL and brine pockets, protecting bacteria from osmotic shock during the freezing process.[41] The freezing process accompanies increases in

solute concentrations in the liquid-like layer of ice. The high salt concentration outside the cell induces the migration of the water through biological membranes, and microorganism living in this condition has to adapt their physiology to maintain high osmotic pressure. Especially the rapid change in salt concentration occurring in the freezing process is harsher for the microorganism. Therefore, maintaining the low salt concentration in the extended QLL or brine pocket will help the organisms in living in the polar region.

Another advantage of brine pockets is nutrient acquisition by bacteria. The polar microorganisms in the ice experience a nutrient limitation.[42] This distribution of trapped bacteria with a low population in the habitat is probably beneficial for the bacteria to reduce the nutrient consumption for long-term survival compared to the concentrated population in the brine pocket (Fig. 11). We also found that many uncovered or uncharacterized IBPs from bacteria from the cold environment have a lipoprotein signal peptide sequence at the N-terminus. This observation indicates that the survival mechanism with membrane-anchored IBPs and generation of brine pockets, as suggested in this study, is another example of the cold-adaptation mechanism of microorganisms from the polar region.

In conclusion, the data in this study provide a detailed molecular and mechanistic understanding of the relationship between residual rigidity and TH activity. The rigidity of IBP stemming from the capping head region, especially the disulfide bond, can immobilize the residues at the IBS to increase the protein-ice interaction strength, as indicated by hyper-TH activity. Furthermore, cells with IBPs on the membrane surface survive better than cells without IBPs by generating brine pockets to expand the living space in a TH activity-dependent manner. This study thus identified a previously unknown survival mechanism using membrane-anchored IBPs responsible for polar microorganism survival in a cold environment.

## 3. Materials and methods

### 3.1. Purification of IBPs

Recombinant FfIBP and mFfIBP were obtained as previously described.[10,21] The FfIBP gene in the pCold vector was transformed into BL21(DE3) cells. Overnight seed culture from a single cell was inoculated into 4 L Luria - Bertani (LB) broth supplemented with ampicillin. Once the culture reached an OD600 of 0.8, 1 mM IPTG was added to induce protein expression for 36 h at 10 °C. Cells were harvested by centrifugation, and the proteins were purified by His-tag purification followed by FPLC using a HiLoad® 16/600 Superdex® 200 pg column. Similar protein expression and purification methods were applied to the C107S mutant construct. For mFfIBP protein production, a pET28a vector was used,

and protein production was induced at 25 °C (S1 Table).

### 3.2. Circular dichroism analysis

The secondary structure composition of the FfIBP, mFfIBP and C107S were messured by using circular dichroism analysis. The far-UV CD was performed on a Chirascan CD spectrometer (Applied Photophysics Ltd., Leatherhead, UK) between 200 and 260 nm by using a quartz cuvette with 1 mm path length at 293 K. Five scans were recorded, the baseline spectra (buffer alone) were subtracted and the results were averaged followed by smoothing of the data. Buffer used for the proteins was 20 mM Tris pH 8.5, 150 mM NaCl.

### 3.3. Structure determination and models for MD simulation

The structure of C107S was determined by X-ray crystallography. The purified protein was crystallized by the hanging drop vapor diffusion method with a precipitant solution composed of sodium citrate pH 4.6 and 2.9 M NaCl. The crystal was diffracted at 2.0 Å, and the structure phase was obtained by molecular replacement using the FfIBP crystal structure (PDB code: 4NU2). The refined C107S structure was almost identical to FfIBP, as indicated by the RMSD value of 0.158, except for the disulfide bond. The detailed data after refinement are listed in S2 Table (PDB CODE: 7EHK). The crystal structures of FfIBP (PDB: 4NU2, 2.1 Å resolution), C107S, and chimeric mFfIBP (PDB: 4NU3, 1.4 Å resolution) (chain A) were used as models for the MD simulations. Water molecules and ions obtained from the crystallographic studies were removed.

### 3.4. MD simulation

The protein structures were subjected to MD simulations using the GROMACS v2020.4 with the CHARMM 27 force field topologies and parameters.[43,44] Process and syntax followed the GROMACS documentation and the Galaxy platform.[44] The system was solvated with a TIP4P water model in a cubic box and neutralized with 0.15 M NaCl. The sides of the cubic box had dimensions of 4 nm for each system, and the model was located at the center of the box before the simulation. One thousand steps of steepest descent followed by 50,000 steps of the adopted basis Newton-Raphson method were performed for minimization. Two equilibrations steps – isothermal-isochoric ensemble (NVT; the number of particles (N), simulation cell volume (V), and temperature (T)) and the isothermal-isobaric ensemble (NPT; pressure (P)) – were performed for 4 ns before the production step. In addition, a leap-frog algorithm for integrating Newton motion equation and a smooth particle mesh Ewald (SPME) method for electrostatic and van der Waals interactions were applied [45]. MD was performed at 300 K with a 1 fs time step

for 50 ns (simulated 2 ns.gro trajectory output files, which were continuously restarted by the res-files, were combined into the final 50 ns) under the NPT ensemble. The GROMACS v2020.4 and parameter sets were used to run MD under. GROMACS was used to analyze the trajectory files for RMSD, RMSF, the distances between residues, and the side-chain distribution. The VMD and Pymol programs were used for figure generation.

### 3.5. TH activity

The ice morphology at freezing points was obtained during the measurement of the TH activity of IBPs, as described previously.[10] Briefly, the sample was placed on holes of an aluminum disk on the stage and frozen rapidly at approximately -20 °C using a nanoliter osmometer (Otago Osmometers, Dunedin, New Zealand). The temperature was raised slowly until a single ice crystal remained (melting temperature). Then, the temperature was lowered again slowly (~0.5 °C/min) until the ice crystal grew (freezing temperature). The morphology of the ice crystals at the freezing point was observed under a microscope. Images were taken using a Canon Power Shot 620. Measurements were performed in 20 mM Tris-HCl (pH 8.5) and 150 mM NaCl buffer at various sample concentrations.

### 3.6. Expression and localization of IBPs

Genes for IBPs (full-length FfIBP, mFfIBP, and C107S) were cloned into pET-21b at the NdeI restriction enzyme site using the LIC cloning method[46] to generate C-terminal His-tagged IBPs. BL21(DE3) cells were transformed with cloned vectors. ITPG (1 mM) was added to the culture medium at an OD600 of 0.5 and incubated for 20 h to induce protein expression. The cells were then washed three times with phosphate-buffered saline (PBS) or 150 mM NaCl three times and incubated with His-tag specific fluorescence dye (Ni-NTA-Atto 550; Sigma-Aldrich, St. Louis, MO, USA) for 15 min. The unbound fluorescence dye was washed twice with PBS or 150 mM NaCl. The protein expression levels and localization were analyzed using a microplate reader (EnVision 2013 multilabel Reader; Perkin Elmer, Waltham, MA, USA) or under a laser confocal microscope (LSM-800; Zeiss, Oberkochen, Germany).

### 3.7. Subcellular fractionation

Subcellular fractionation was followed by a combination of cold osmotic shock and sonication methods, named PureFrac.[47] IPTG-induced cells were washed twice with PBS and centrifuged, and the supernatant was discarded. The cell pellet was resuspended in a spheroplast buffer (0.1 M Tris-HCl, pH 8.0, 500 mM sucrose, and 0.5 mM EDTA), incubated for 5 min, and the supernatant was carefully discarded after centrifugation. The

pellet was then resuspended in cold 1 mM $MgCl_2$, incubated for 15 s on ice, and 20 mM $MgSO_4$ was added to the periplasmic fraction. The pelleted cells were resuspended in buffer (50 mM Tris-acetate, pH 8.0, 2.5 mM EDTA) and sonicated on ice. The lysed cells were centrifuged at 16,000 rpm for 40 min, and the supernatant and pellets were separated into cytoplasmic and membrane fractions, respectively.

### 3.8. Western blotting

Samples from subcellular fractionation were loaded onto an SDS-PAGE gel, and the proteins were semi-dry transferred to a PVDF membrane. The membrane with proteins was blocked with skim milk overnight at 4 °C. After blocking, the membrane was incubated with a His-probe antibody (SC-53073; SANTA CRUZ, Santa Cruz, CA, USA) at a 1:2,000 dilution and the m-IgGk BP-HRP (SC-516102; Santa Cruz) at a 1:20,000 dilution in TBST. SuperSignal™ West Femto (Thermo Fisher, Waltham, MA, USA) was the chemiluminescent substrate.

### 3.9. Recovery rate of bacteria

The protective effects of IBPs on bacteria from the freeze-thaw cycle were measured by calculating CFUs. First, cells were washed, resuspended in 150 mM NaCl solution, and the $OD_{600}$ was adjusted to 1.0, representing approximately $1 \times 10^9$ CFUs for all samples. Next, the cells were frozen at -80 °C without a cryoprotectant. After one day, the frozen cells were thawed on ice for 30 min and transferred to 25 °C. The serial dilutions of the samples were plated on LB agar plates for CFU calculation in the 1st round of the freeze-thaw cycle. The thawed cells were re-frozen and then thawed again using a similar process as the 2nd freeze-thaw cycle next day. A similar process was used to calculate the recovery rate for the 3rd freeze-thaw cycle.

### 3.10. Brine pocket formation using laser confocal microscopy

The protective effects of IBPs on bacterial cells were analyzed using a laser confocal microscope (LSM-800; Zeiss) equipped with a Linkam THMS 600 stage (Linkam Scientific Instruments, Tadworth, UK) controlled by Linksys software. IPTG-induced bacterial cells were washed twice with PBS and resuspended in 150 mM NaCl solution in the same volume of the culture medium. Then, the cells were mixed with water containing 100 nM FITC in a 1:1 ratio, placed in a square chamber fitted to the Linkam THMS 600 stage, and frozen. The freezing process was performed in three steps: the temperature was first decreased from 25 °C to 0 °C at a rate of -5 °C/min, then decreased to -5 °C at a rate of 1 °C/min, and finally to -20 °C at a rate of -0.2 °C/min. The temperature was maintained

for 30 s between the steps for latent heat. The FITC (detection wavelength 490 - 700 nm) and electronically switchable illumination and detection (ESID) channels were observed using an LSM-800 with an LD ×50 objective (N/A = 0.55) with a 488 nm laser as the excitation source. A GaAsP-PMT detector for the FITC channel and photodiode ESID detector for the ESID channel were used.

### 3.11. Raman spectroscopy of brine pocket and QLL

Confocal Raman spectroscopy (inVia Qontor; Renishaw, Wotton-under-Edge, UK) was used to investigate the relative salt concentrations in the brine pockets. An aqueous NaCl solution with different salt concentrations was dropped onto a temperature-controlled stage, followed by a reduction rate of -0.2 °C/min to -20 °C. The detailed freezing process with cells was similar to that used in processing the samples for laser confocal microscopy, except for adding FITC. After the temperature reached -20 ºC, the ice granules, brine pockets, and QLL regions were scanned from 2,868 to 3,693 $cm^{-1}$. The spectra from 10 areas were scanned five times and averaged. A 532 nm laser was used as the excitation source. The salt concentration of the aqueous solution was estimated to proximate the brine pocket, and the QLL region was measured by Raman spectroscopy, as shown previously.[37]

KOPRI 극지연구소

## REFERENCES


1. H.J. Kim, J.H. Lee, Y.B. Hur, C.W. Lee, S.H. Park, B.W. Koo, Marine antifreeze proteins: Structure, function, and application to cryopreservation as a potential cryoprotectant, *Mar. Drugs*. 15 (**2017**).
2. C.A. Knight, A.L. DeVries, L.D. Oolman, Fish antifreeze protein and the freezing and recrystallization of ice, *Nature*. 308 (**1984**) 295 - 296.
3. K. Muldrew, L.E. McGann, Mechanisms of intracellular ice formation, *Biophys. J.* 57 (**1990**) 525 - 532.
4. P. Mazur, S. Seki, I.L. Pinn, F.W. Kleinhans, K. Edashige, Extra- and intracellular ice formation in mouse oocytes, *Cryobiology*. 51 (**2005**) 29 - 53.
5. K.E. Zachariassen, E. Kristiansen, Ice nucleation and antinucleation in nature, *Cryobiology*. 41 (**2000**) 257 - 279.
6. S. D'Amico, T. Collins, J.C. Marx, G. Feller, C. Gerday, Psychrophilic microorganisms: Challenges for life, *EMBO Rep.* 7 (**2006**) 385 - 389.
7. A.L. DeVries, Antifreeze glycopeptides and peptides: Interactions with ice and water, *Methods Enzymol.* 127 (**1986**) 293 - 303.
8. E. Kristiansen, K.E. Zachariassen, The mechanism by which fish antifreeze proteins cause thermal hysteresis, *Cryobiology*. 51 (**2005**) 262 - 280.
9. Y.C. Liou, A. Tocilj, P.L. Davies, Z. Jia, Mimicry of ice structure by surface hydroxyls and water of a β-helix antifreeze protein, *Nature*. 406 (**2000**) 322 - 324.
10. H. Do, J.H. Lee, S.G. Lee, H.J. Kim, Crystallization and preliminary X-ray crystallographic analysis of an ice-binding protein (FfIBP) from Flavobacterium frigoris PS1, Acta Crystallogr. *Sect. F Struct. Biol. Cryst. Commun.* 68 (**2012**) 806 - 809.
11. L.A. Graham, Y.C. Liou, V.K. Walker, P.L. Davies, Hyperactive antifreeze protein from beetles, *Nature*. 388 (**1997**) 727 - 728.
12. C.B. Marshall, A. Chakrabartty, P.L. Davies, Hyperactive antifreeze protein from winter flounder is a very long rod-like dimer of α-helices, *J. Biol. Chem.* 280 (**2005**) 17920 - 17929.
13. F.H. Lin, T. Sun, G.L. Fletcher, P.L. Davies, Thermolabile antifreeze protein produced in Escherichia coli for structural analysis, *Protein Expr. Purif.* 82 (**2012**) 75 - 82.
14. E.K. Leinala, P.L. Davies, D. Doucet, M.G. Tyshenko, V.K. Walker, Z. Jia, A β-helical antifreeze protein isoform with increased activity. Structural and functional insights, *J. Biol. Chem.* 277 (**2002**) 33349 - 33352.


KORDI 극지연구소

15. C.P. Garnham, R.L. Campbell, P.L. Davies, Anchored clathrate waters bind antifreeze proteins to ice, *Proc. Natl Acad. Sci. U. S. A.* 108 (**2011**) 7363 – 7367.

16. S.P. Graether, M.J. Kuiper, S.M. Gagné, V.K. Walker, Z. Jia, B.D. Sykes, P.L. Davies, β-Helix structure and ice-binding properties of a hyperactive antifreeze protein from an insect, *Nature*. 406 (**2000**) 325 – 328.

17. A. Cheng, K.M. Merz, Ice-binding mechanism of winter flounder antifreeze proteins, *Biophys. J.* 73 (**1997**) 2851 – 2873.

18. M.J. Kuiper, C.J. Morton, S.E. Abraham, A. Gray-Weale, The biological function of an insect antifreeze protein simulated by *molecular dynamics, eLife*. 4 (**2015**).

19. J. Cheng, Y. Hanada, A. Miura, S. Tsuda, H. Kondo, Hydrophobic ice-binding sites confer hyperactivity of an antifreeze protein from a snow mold fungus, *Biochem. J.* 473 (**2016**) 4011 – 4026.

20. S.M. Marks, A.J. Patel, Antifreeze protein hydration waters: Unstructured unless bound to ice, *Proc. Natl Acad. Sci. U. S. A.* 115 (**2018**) 8244 – 8246.

21. H. Do, S.J. Kim, H.J. Kim, J.H. Lee, Structure-based characterization and antifreeze properties of a hyperactive ice-binding protein from the Antarctic bacterium Flavobacterium frigoris PS1, Acta Crystallogr. *D Biol. Crystallogr.* 70 (**2014**) 1061 – 1073.

22. K.S. Park, H. Do, J.H. Lee, S.I. Park, E.J. Kim, S.J. Kim, S.H. Kang, H.J. Kim, Characterization of the ice-binding protein from *Arctic yeast Leucosporidium sp. AY30, Cryobiology*. 64 (**2012**) 286 – 296.

23. J.H. Lee, A.K. Park, H. Do, K.S. Park, S.H. Moh, Y.M. Chi, H.J. Kim, Structural basis for antifreeze activity of ice-binding protein from arctic yeast, *J. Biol. Chem.* 287 (**2012**) 11460 – 11468.

24. A. Hudait, N. Odendahl, Y. Qiu, F. Paesani, V. Molinero, Ice-nucleating and antifreeze proteins recognize ice through a diversity of anchored clathrate and ice-like motifs, *J. Am. Chem. Soc.* 140 (**2018**) 4905 – 4912.

25. S. Chakraborty, B. Jana, Optimum number of anchored clathrate water and its instantaneous fluctuations dictate ice plane recognition specificities of insect antifreeze protein, *J. Phys. Chem.* B. 122 (**2018**) 3056 – 3067.

26. E. Jurrus, D. Engel, K. Star, K. Monson, J. Brandi, L.E. Felberg, D.H. Brookes, L. Wilson, J. Chen, K. Liles, M. Chun, P. Li, D.W. Gohara, T. Dolinsky, R. Konecny, D.R. Koes, J.E. Nielsen, T. Head-Gordon, W. Geng, R. Krasny, G.W. Wei, M.J. Holst, J.A. McCammon, N.A. Baker, Improvements to the APBS biomolecular solvation software suite, *Protein Sci.* 27 (**2018**) 112 – 128.

KOPRI 극지연구소

27. A. Yamauchi, T. Arai, H. Kondo, Y.C. Sasaki, S. Tsuda, An ice-binding protein from an Antarctic ascomycete is fine-tuned to bind to specific water molecules located in the ice prism planes, *Biomolecules*. 10 (**2020**) 1 – 15.

28. A.Q. Zhou, C.S. O'Hern, L. Regan, The power of hard-sphere models: Explaining side-chain dihedral angle distributions of thr and val, *Biophys. J.* 102 (**2012**) 2345 – 2352.

29. Y. Celik, L.A. Graham, Y.F. Mok, M. Bar, P.L. Davies, I. Braslavsky, Superheating of ice crystals in antifreeze protein solutions, *Proc. Natl Acad. Sci. U. S. A.* 107 (**2010**) 5423 – 5428.

30. A.J. Scotter, C.B. Marshall, L.A. Graham, J.A. Gilbert, C.P. Garnham, P.L. Davies, The basis for hyperactivity of antifreeze proteins, *Cryobiology*. 53 (**2006**) 229 – 239.

31. T.D.R. Vance, L.A. Graham, P.L. Davies, An ice-binding and tandem beta-sandwich domain-containing protein in Shewanella frigidimarina is a potential new type of ice adhesin, *FEBS Journal*. 285 (**2018**) 1511 – 1527.

32. M. Bayer-Giraldi, G. Sazaki, K. Nagashima, S. Kipfstuhl, D.A. Vorontsov, Y. Furukawa, Growth suppression of ice crystal basal face in the presence of a moderate ice-binding protein does not confer hyperactivity, *Proc. Natl Acad. Sci. U. S. A.* 115 (**2018**) 7479 – 7484.

33. Y. Hanada, Y. Nishimiya, A. Miura, S. Tsuda, H. Kondo, Hyperactive antifreeze protein from an Antarctic sea ice bacterium Colwellia sp. has a compound ice-binding site without repetitive sequences, *FEBS Journal*. 281 (**2014**) 3576 – 3590.

34. P.L. Davies, Ice-binding proteins: A remarkable diversity of structures for stopping and starting ice growth, *Trends Biochem. Sci.* 39 (**2014**) 548 – 555.

35. M. Mangiagalli, G. Sarusi, A. Kaleda, M. Bar Dolev, V. Nardone, V.F. Vena, I. Braslavsky, M. Lotti, M. Nardini, Structure of a bacterial ice binding protein with two faces of interaction with ice, *FEBS Journal*. 285 (**2018**) 1653 – 1666.

36. J.J. Almagro Armenteros, K.D. Tsirigos, C.K. Sønderby, T.N. Petersen, O. Winther, S. Brunak, G. von Heijne, H. Nielsen, SignalP 5.0 improves signal peptide predictions using deep neural networks, *Nat. Biotechnol.* 37 (**2019**) 420 – 423.

37. I. Duričković, M. Marchetti, R. Claverie, P. Bourson, J.M. Chassot, M.D. Fontana, Experimental study of NaCl aqueous solutions by raman spectroscopy: Towards a new optical sensor, *Appl. Spectrosc.* 64 (**2010**) 853 – 857.

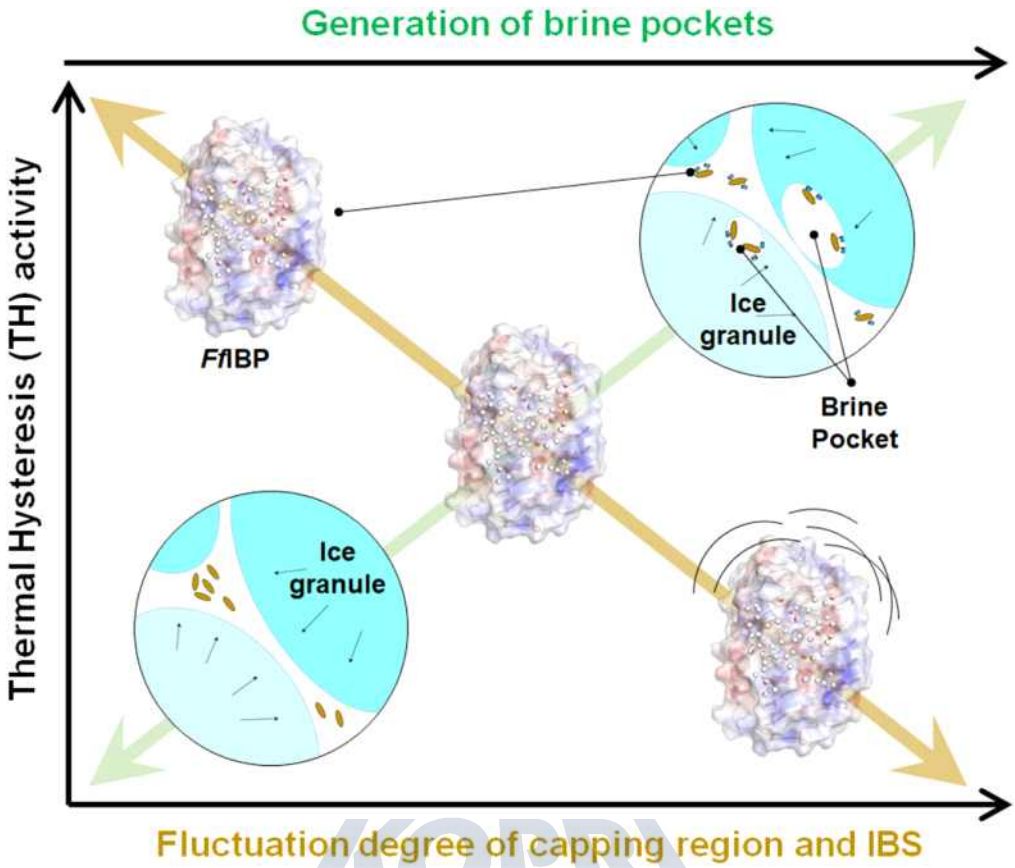
38. I.K. Voets, From ice-binding proteins to bio-inspired antifreeze materials, *Soft Matter*. 13 (**2017**) 4808 – 4823.

39. H.J. Kim, J.H. Lee, H. Do, W. Jung, Production of antifreeze proteins by *cold-adapted*

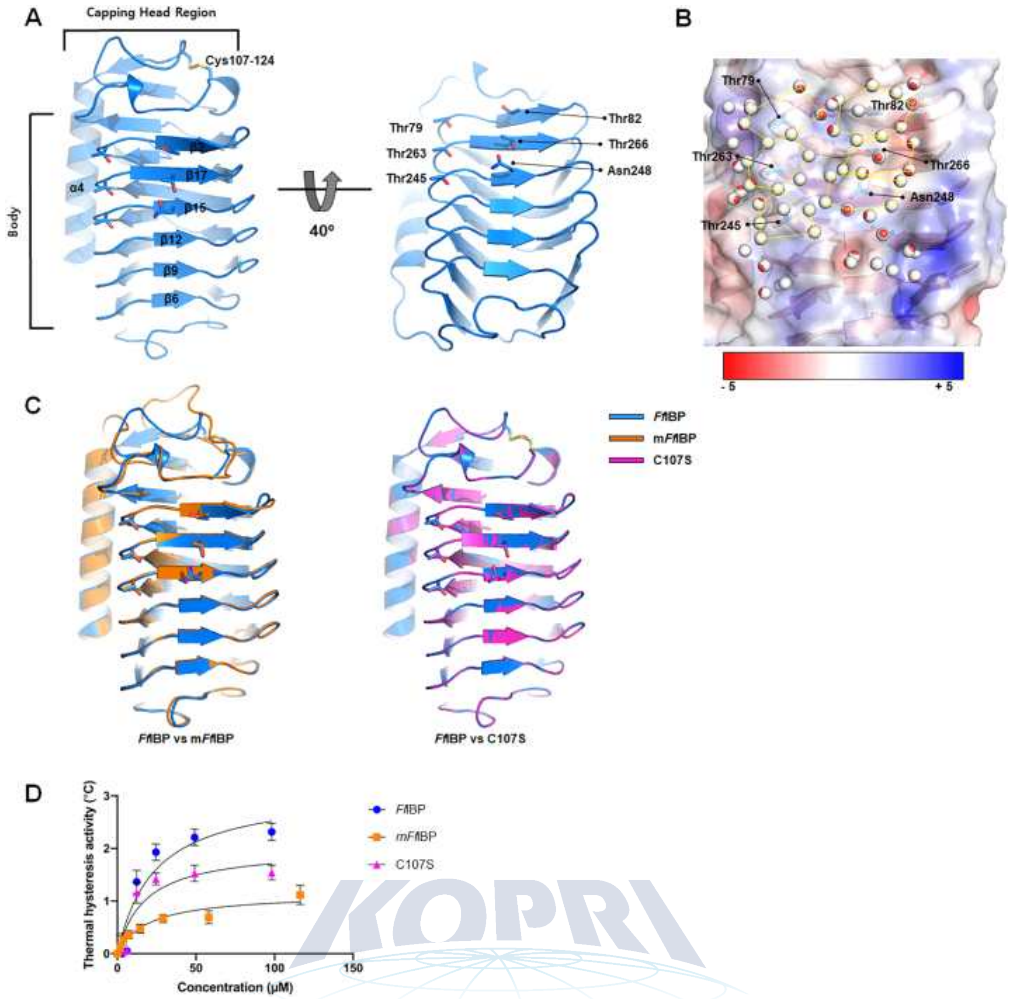
*yeasts,* 2014.

40. K. Junge, J.T. Staley, Extremophiles Handbook, *Extrem. Handb.* (2011).
41. M. Ewert, J.W. Deming, Bacterial responses to fluctuations and extremes in temperature and brine salinity at the surface of Arctic winter sea ice, *FEMS Microbiol. Ecol.* 89 (2014) 476 - 489.
42. H. Kuosa, H. Kaartokallio, Experimental evidence on nutrient and substrate limitation of Baltic Sea sea-ice algae and bacteria, *Hydrobiologia.* 554 (2006) 1 - 10.
43. M.J. Abraham, T. Murtola, R. Schulz, S. Páll, J.C. Smith, B. Hess, E. Lindahl, Gromacs: High performance molecular simulations through multi-level parallelism from laptops to supercomputers, *SoftwareX.* 1 - 2 (2015) 19 - 25.
44. E. Afgan, D. Baker, B. Batut, M. Van Den Beek, D. Bouvier, M. Cech, J. Chilton, D. Clements, N. Coraor, B.A. Grüning, A. Guerler, J. Hillman-Jackson, S. Hiltemann, V. Jalili, H. Rasche, N. Soranzo, J. Goecks, J. Taylor, A. Nekrutenko, D. Blankenberg, The Galaxy platform for accessible, reproducible and collaborative biomedical analyses: 2018 update, *Nucleic Acids Res.* 46 (2018) W537 - W544.
45. U. Essmann, L. Perera, M.L. Berkowitz, T. Darden, H. Lee, L.G. Pedersen, A smooth particle mesh Ewald method, *J. Chem. Phys.* 103 (1995) 8577 - 8593.
46. J.Y. Jeong, H.S. Yim, J.Y. Ryu, H.S. Lee, J.H. Lee, D.S. Seen, S.G. Kang, One-step sequence- and ligation-independent cloning as a rapid and versatile cloning method for functional genomics Studies, *Appl. Environ. Microbiol.* 78 (2012) 5440 - 5443.
47. G. Malherbe, D.P. Humphreys, E. Davé, A robust fractionation method for protein subcellular localization studies in Escherichia coli, *BioTechniques.* 66 (2019) 171 - 178.

## SCHEMES AND FIGURES




Scheme 1. Schematic illustration of the negative correlation between fluctuation and TH activity of FfIBP and mechanistic insights into cold adaptation for hyperactive FfIBP anchored on microorganism membrane. FfIBP is shown in surface presentation, and the ordered hydration water layer around the IBS is shown with sphere (white for hydrogen and red for oxygen). Brine pocket formation (large white ovals) caused by FfIBPs attached to the microorganism (small brown ovals) is shown in a circle.




KOPRI
극지연구소

Fig. 1. Structure and activity comparison of FfIBP with derivatives. (A) Cartoon view of FfIBP with forward-facing IBS. Ice-binding motifs on β2, β17, and β15 are represented with sticks with CPK coloring. (B) Structure superposition of FfIBP with mFfIBP and C107S. (C) TH activity of FfIBP, mFfIBP, and C107S at different concentrations.

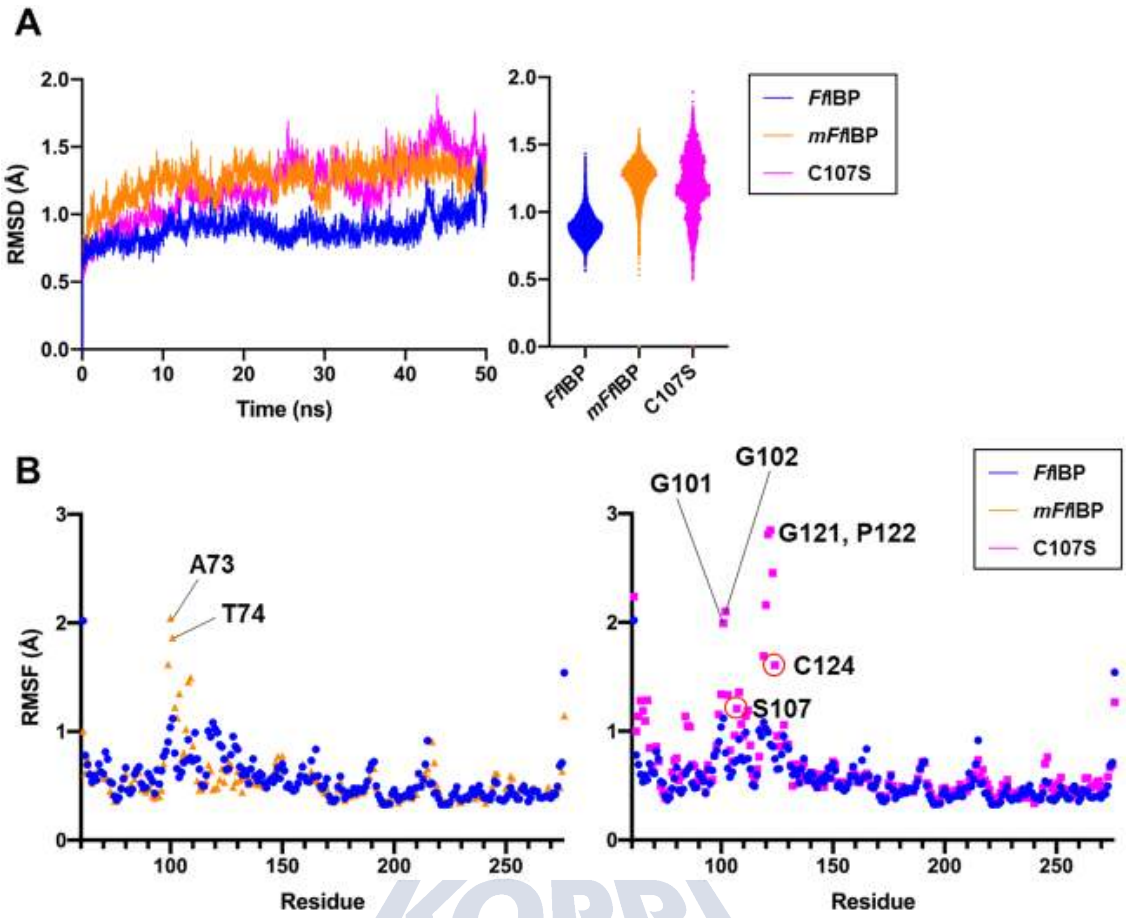



Fig. 2. MD simulation and residual fluctuation. (A) Backbone RMSDs (Cα) for FfIBP (blue), mFfIBP (orange), and C107S (magenta). (B) Backbone RMSF (Cα) of each residue as a function of the atom location along with the proteins.

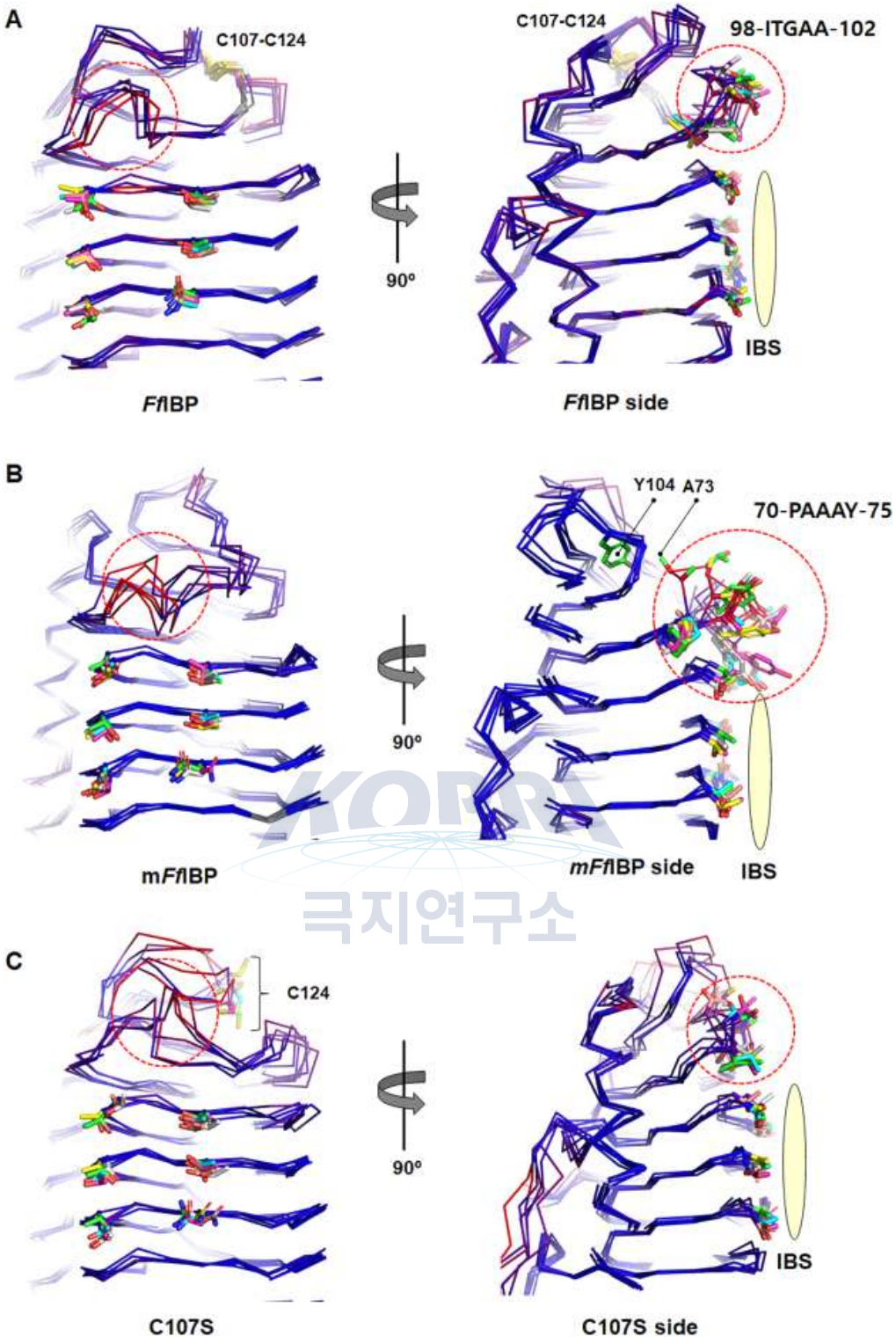



Fig. 3. The superposition of the initial structure and frames extracted from FfIBP (A), mFfIBP (B), and C107S (C) simulation system. The initial structure was used as a target, and every 10 ns frame was aligned as mobile. Each mobile/target atom-pair was colored by distance. Dark blue indicates good alignment, while red means higher deviations. The motifs on IBS and the capping head region residues of 98-ITGAA-102 of FfIBP and C107 and 70-PAAAY-75 of mFfIBP are represented by sticks with different color codes. The IBS is shown with a light yellow oval.

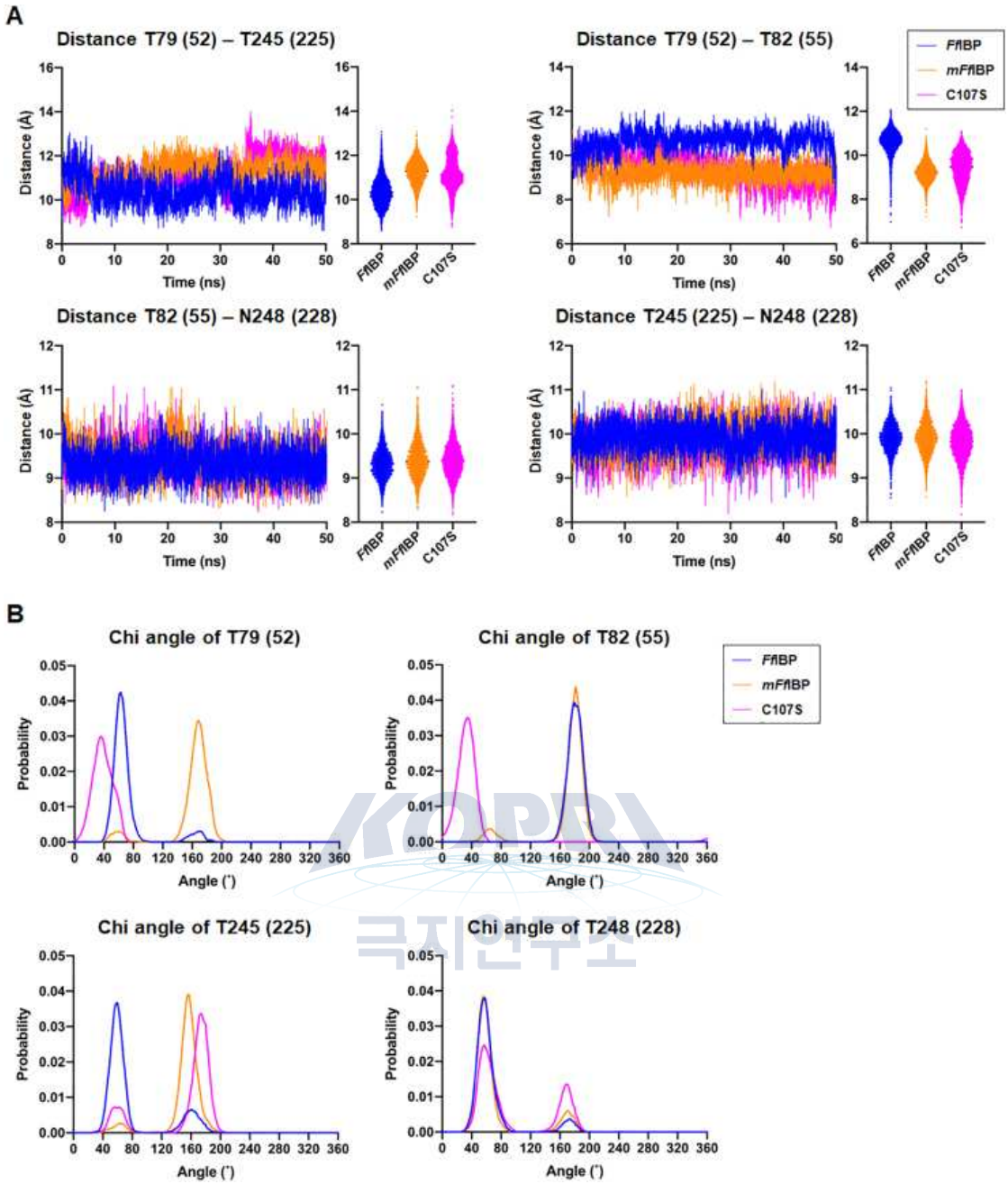



Fig. 4. Capping head region-dependent movement during MD simulations. (A) Distance (C β) of two residues at IBS and magnitude of fluctuation for WT (blue), mFfIBP (orange), and C107S (magenta) during MD simulations. Distances between the residues (T79 - T245), (T79 - T82), (T82 - N248), and (T245 - N248) for FfIBP and C107S and (T52 - T225), (T52 - T55), (T55 - N228), and (T225 - N228) for mFfIBP were measured during the simulation. The mean distances and distribution of each combination of residues are shown on the right panel with the same color code. The distances were calculated from the trajectory files taken every 10 ps from MD simulation. (B) Side-chain dihedral angle distribution (χ1) of T79, T82, T245, and N248 of FfIBP and C107S, and T52, T55, T225, and N228 of mFfIBP. Dihedral angle of N-Ca-Cα-CG2 for Thr and N-Ca-Cα-CG for Asn were measured, and the probability was displayed as a function of angle. Corresponding residues in mFfIBP were shown in brackets.

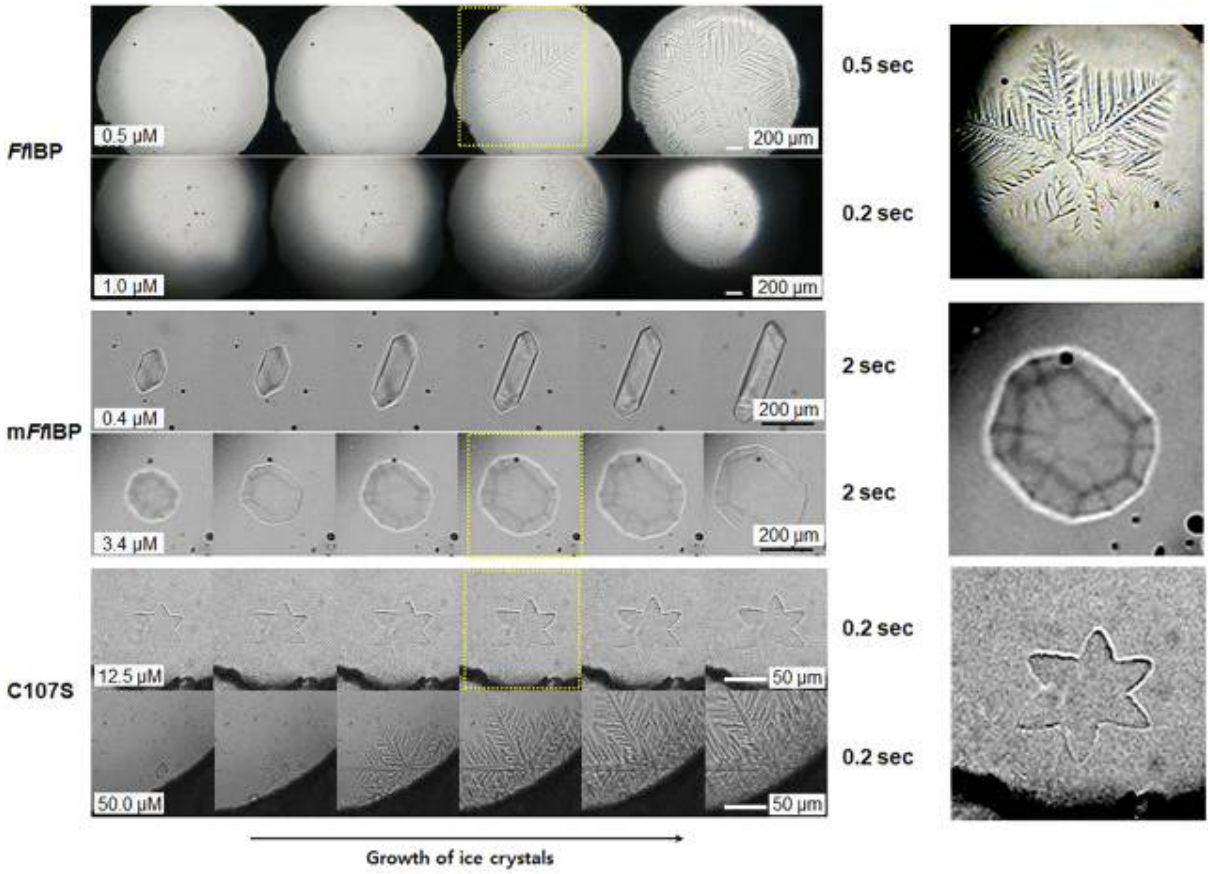



Fig. 5. Ice morphology at different concentrations at the freezing points of FfIBP, mFfIBP, and C107S. FfIBP effectively and consistently inhibited the growth of ice until the ice burst, whereas mFfIBP failed even at higher concentrations. The pictures were taken during the TH measurement. The time interval is indicated on the right side of the pictures. Photographs were taken using a Canon Power Shot 620. (Right panel) Magnified view of each ice crystal from yellow square. The scale bars represent 200 μm, 200 μm, and 50 μm for FfIBP, mFfIBP, and C107S, respectively.

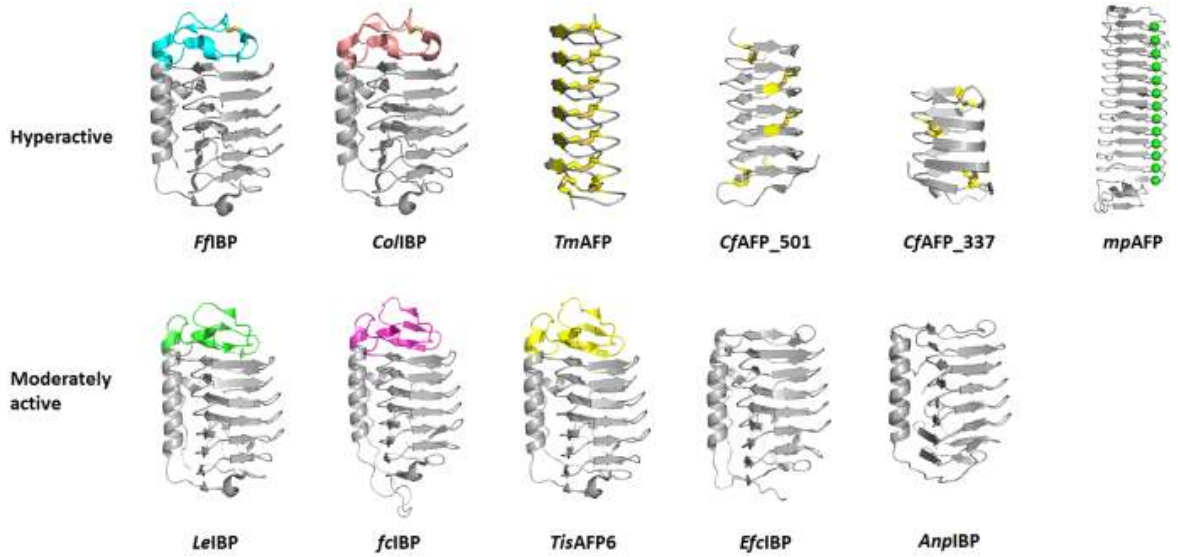



Fig. 6. Representations of the overall structure of hyperactive and moderately active IBPs. The disulfide bond(s) on the capping head region or in the intermolecular β-strands of the hyperactive IBPs are represented with bold yellow sticks. The moderately active IBPs either have a LeIBP-like capping head region or no capping head region. The capping head regions of IBPs are highlighted with different color codes. The green spheres on the structure of MpAFP represent calcium ions.

KOPRI
극지연구소

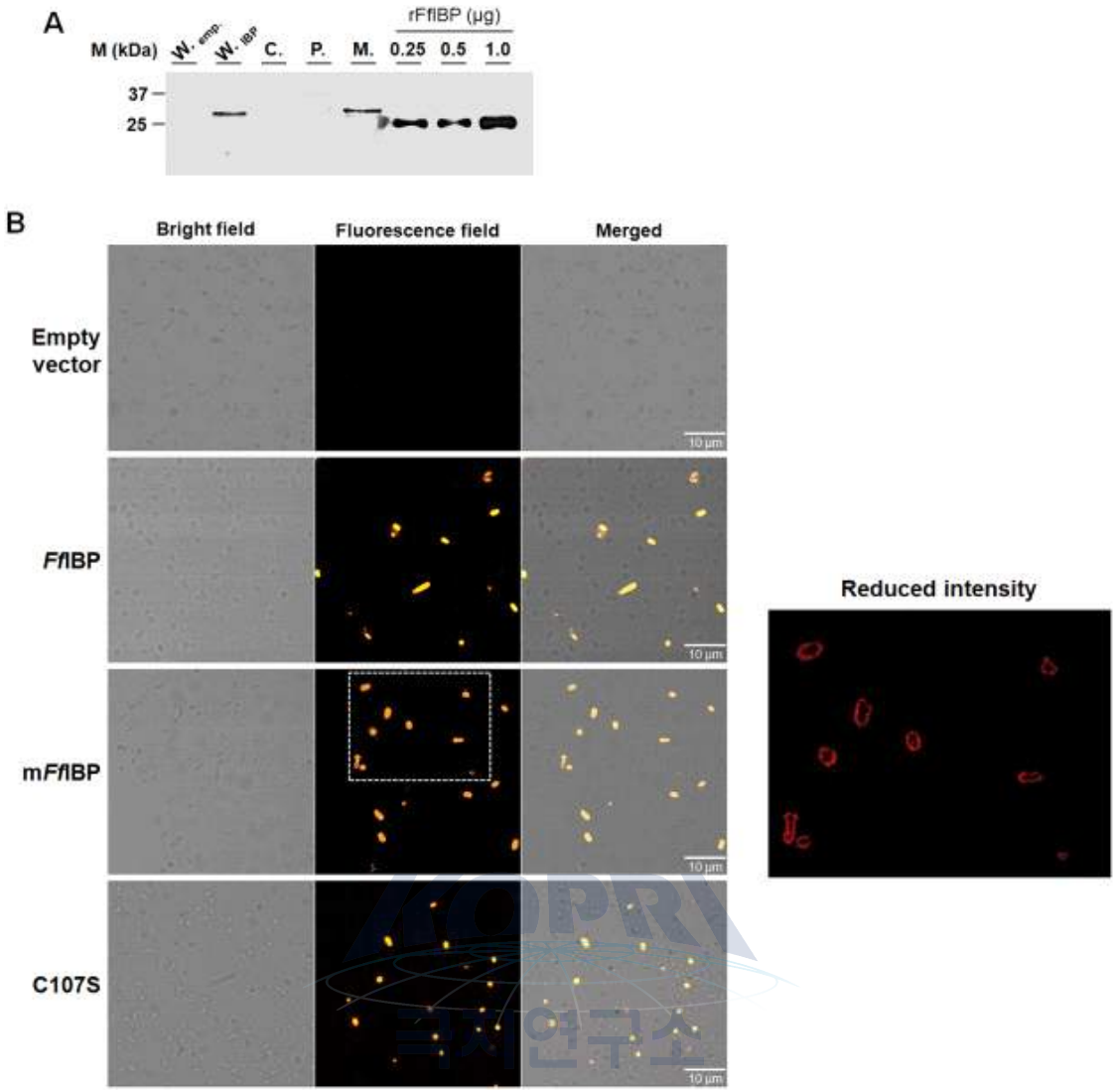
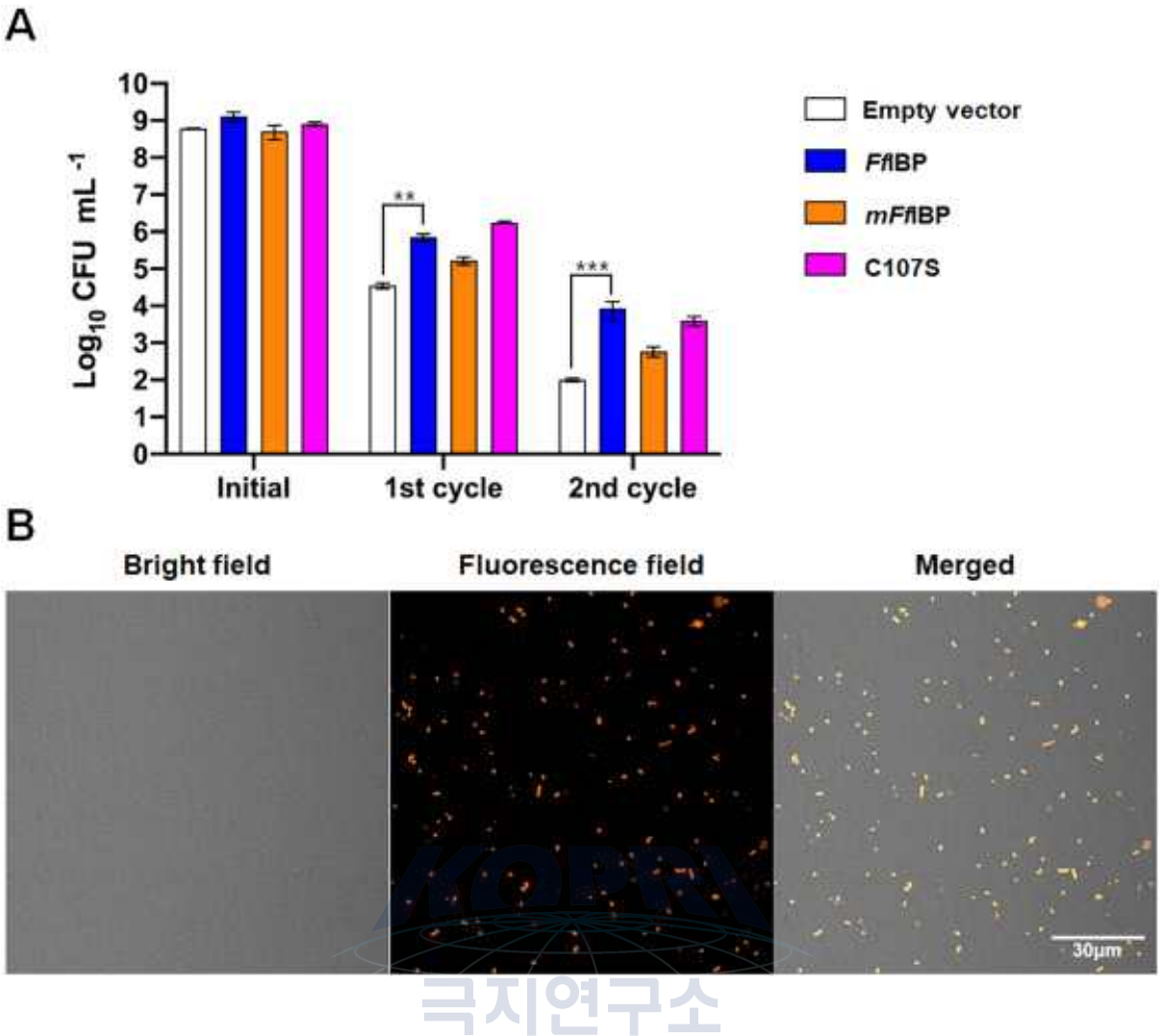



Fig. 7. Expression and identification of the subcellular localization of FfIBP in bacteria. (A) Western immunoblot analysis of FfIBP from bacterial cell fractions detected by His-tag antibodies. Cell fractions are shown above the lanes: W., whole cell; C., cytoplasm; P., periplasm; M., membrane fractions. The whole cells with empty vector (W. emp.) were considered as a negative control. Different amounts of recombinant FfIBP (amino acids 27 - 276) with His-tag were used as a positive control [11]. (B) Confocal microscopy images of cells harboring empty, FfIBP, mFfIBP, and C107S vectors. Protein-expressing bacteria were incubated with Ni-NTA-ATTO 550, washed, and examined under fluorescence microscope LSM800. Scale bars represent 10 μm. The image from the mFfIBP sample with low laser intensity was shown in the right panel to identify the specific localization of IBPs.




KOPRI
극지연구소

Fig. 8. CFUs of bacteria (empty, FfIBP, mFfIBP, and C107S) after freeze-thaw cycles. (A) The CFUs of each sample were measured after the freeze-thaw cycle to calculate the live cells. Protein-expressing cells were washed with 150 mM NaCl and the CFU was adjusted to $10^9$ for the initial amount of cells. The data was plotted from three individual measurements. (B) The cells with FfIBP that survived the 3rd freeze-thaw cycle. Cells were treated with Atto 550 for the IBP identification. Scale bar represents 10 μm.

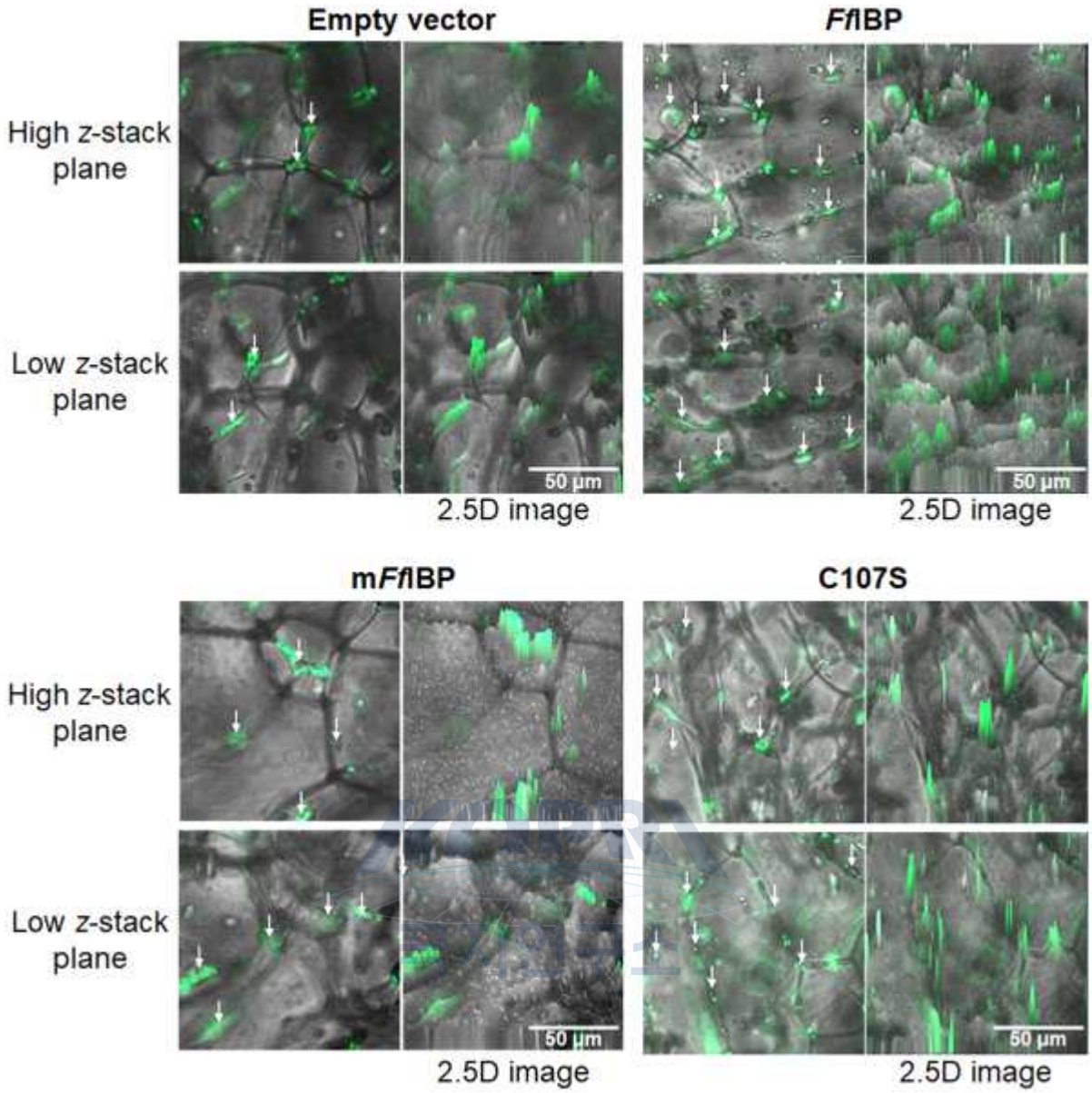
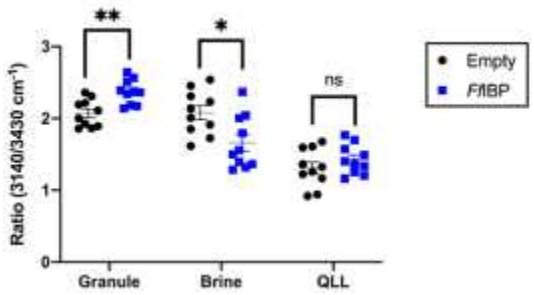



Fig. 9. Confocal microscopy of ice-trapped bacterial cells. Bacteria were frozen in a 1 cm × 1 cm chamber and observed using a fluorescence microscope. The intensity of fluorescence was indicated vertically in the 2.5-dimension (2.5D) images on the right of each image. Different levels along the z-axis were observed in the same system (lower panel). Images shown are merged bright field and fluorescence field images. Concentrated cells, either in the triangular junction of ice or brine pockets, are indicated with white arrows. Scale bar represents 50 μm.




| Strain with | Peak ratio (3140/3430 cm$^{-1}$) | | |
|---|---|---|---|
| | Ice granule | Brine | QLL |
| Empty | 2.07 | 2.08 | 1.30 |
| *Ff*IBP | 2.36 | 1.66 | 1.42 |

Fig. 10. Peak ratio of Raman spectroscopy (3,140/3,430 cm$^{-1}$). The 10 ice granules, brine pockets, and QLL region areas were scanned five times and averaged. The averaged data indicated on the right correspond to the data in the graph. a single asterisk [*] indicates $p < 0.05$, and double asterisks [**] indicate $p < 0.01$) by unpaired t-test). ns: not significant.

KOPRI
극지연구소

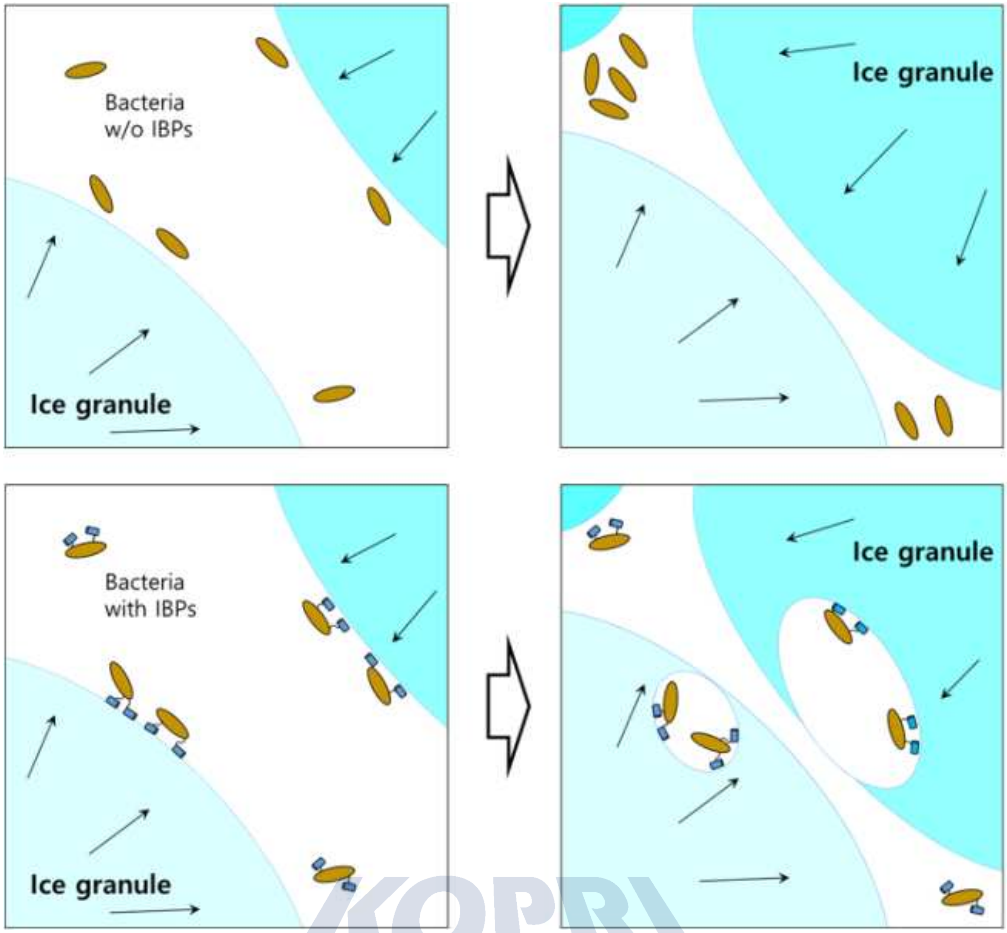



Fig. 11. Proposed survival mechanism of bacteria with membrane-anchored IBP. (Top) Bacteria without IBPs on the ice surface were flown into the triangular junction of ice granules and concentrated with salt. (Bottom) Bacteria with IBPs bound to the ice surface using the IBPs inhibit ice growth and form brine pockets as individual habitats. The ice granules are shown in cyan color. The bacteria and IBPs are indicated with brown ovals and blue cylinders, respectively.

KOPRI 극지연구소

# 제 12 절. Ice-templated synthesis of tungsten oxide nanosheets and their application in arsenite oxidation⑫

Anh Quoc Khuong Nguyen[1], Kitae Kim[2,3] Yong-Yoon Ahn[4], Minsun Kim[5], Gonu Kim[6], Jeong Tae Lee[1], Soonhyun Kim[4] , Jungwon Kim[6],

[1]Department of Chemistry, Hallym University
[2]Korea Polar Research Institute (KOPRI)
[3]Department of Polar Sciences, University of Science and Technology (UST)
[4]Division of Energy Technology, Daegu Gyeongbuk Institute of Science and Technology (DGIST)
[5]Department of Chemistry and Biology, Korea Science Academy of KAIST
[6]Department of Environmental Sciences and Biotechnology, Hallym University

## Abstract

Tungsten oxide ($WO_3$) nanosheets were prepared as catalysts to activate hydrogen peroxide ($H_2O_2$) in arsenite (As(III)) oxidation. Ice particles were employed as templates to synthesize the $WO_3$ nanosheets, enabling easy template removal via melting. Transmission electron microscopy and atomic force microscopy revealed that the obtained $WO_3$ nanosheets were plate-like, with lateral sizes ranging from dozens of nanometers to hundreds of nanometers and thicknesses of <10 nm. Compared to that of the $WO_3$ nanoparticle/$H_2O_2$ system, a higher efficiency of As(III) oxidation was observed in the $WO_3$ nanosheet/$H_2O_2$ system. Electron spin resonance spectroscopy, radical quenching studies, and As(III) oxidation experiments under anoxic conditions suggested that the hydroperoxyl radical ($HO_2^{\bullet}$) acted as the primary oxidant. The $WO_3$ nanosheets possessed numerous surface hydroxyl groups and electrophilic metal centers, enhancing the production of $HO_2^{\bullet}$ via $H_2O_2$ activation. Various anions commonly present in As(III)-contaminated water exhibited little effect on As(III) oxidation in the $WO_3$ nanosheet/$H_2O_2$ system. The high oxidation efficiency was maintained by adding $H_2O_2$ when it was depleted, suggesting that the catalytic activity of the $WO_3$ nanosheets did not deteriorate after multiple catalytic cycles.

## 1. Introduction

Arsenic (As) pollution is one of the most severe environmental issues worldwide[1,2]. >200

① 연구는 본 과제(PE22120)로 수행되었으며, 결과는 *Sci. Total Environ.*. 2023, 20, 865에 출간되었다.

million people are exposed to water containing high levels of As, with many affected by As-related diseases, such as cancers, skin and cardiovascular diseases, neurological disorders, and diabetes[3,4]. Most As species exist as arsenite (As(III)) and arsenate (As(V)) in aqueous environments; As(III) is more harmful and challenging to remove than As(V)[5]. As removal processes typically comprise two successive steps, i.e., chemical oxidation of As(III) to As(V) and physical removal of As(V) via adsorption, coagulation, and precipitation[6,7]. Various oxidants and catalysts, including ozone[8], hypochlorite, permanganate[9], peroxymonosulfate[10], manganese oxide[11], iron (hydro)oxides[12], and iron - manganese oxides[13], have been employed in As(III) oxidation. Recently, a catalytic method using a metal oxide (e.g., $TiO_2$[14], $CeO_2$, $Ce_{0.25}Ti_{0.75}O_2$[15], Fe - Ce oxide[16], or Fe - Mn oxide[17]) and $H_2O_2$ was proposed as a practical candidate for As(III) oxidation based on its high efficiency. In previous studies, metal oxide nanoparticles were used as catalysts in the oxidation of As(III) via $H_2O_2$ activation.

Two-dimensional (2D) metal oxides have received increasing attention as efficient catalysts due to their large surface areas, high electrical conductivities, and high hydrophilicities[18,19,20,21]. For instance, ruthenium oxide ($RuO_2$) nanosheets exhibited higher activities than those of $RuO_2$ nanoparticles in degrading phenolic compounds via peroxymonosulfate activation[22]. Fenton-like oxidations of phenolic compounds on copper oxide (CuO) and hematite ($\alpha$-$Fe_2O_3$) nanosheets were more effective than those on the corresponding nanoparticles[23,24] (the Fenton reaction is the conversion of $H_2O_2$ to hydroxyl radicals ($^{\bullet}OH$) in the presence of $Fe^{2+}$ ($Fe^{2+} + H_2O_2 \rightarrow Fe^{3+} + {}^{\bullet}OH + OH^-$)[25], and the Fenton-like reaction is the conversion of inorganic oxidants (e.g., $H_2O_2$[26], peroxymonosulfate[27], peroxydisulfate[28], and periodate[29]) to more reactive radical species using other homogeneous and heterogeneous catalysts (not $Fe^{2+}$)). Among the various morphologies of tungsten trioxide hydrates ($WO_3 \cdot 2H_2O$), ultrathin nanosheets exhibited the highest efficiencies in degrading rhodamine B under light irradiation[30].

As 2D metal oxides often display superior catalytic activities compared to those of spherical metal oxides, various techniques have been developed to synthesize 2D metal oxides, including physical exfoliation, chemical vapor deposition, and wet chemical synthesis[31,32]. However, each method has its advantages and disadvantages. The exfoliation method, using scotch tape, a ball-milling machine, or an ultrasonicator, is low-cost and scalable, but a suitable layered metal oxide is required as a precursor, and the products synthesized using this method are not uniform. The vapor deposition method can control the thicknesses of the 2D metal oxides, but its large-scale application is limited by its low productivity and the required high temperature and inert atmosphere[33,34,35,36]. Wet chemical methods, including hydrothermal, solvothermal, and template syntheses, can produce high-quality 2D metal oxides in large quantities at low costs[33,37,38], but removing the

surfactants or templates used in the synthetic process is challenging[39,40,41].

Wet chemical synthesis using ice as a template is a promising method of fabricating 2D materials because the ice template can be easily removed via melting. A thin water layer with a thickness of <15 nm, which is denoted the quasi-liquid layer (QLL), generally exists on the surface of ice[42,43]. As chemical reactions can only occur in the QLL on the ice surface[44,45], using ice as a template can produce very thin materials. 2D conducting polymers, such as polyaniline[46], poly(3,4-ethylenedioxythiophene):poly(styrenesulfonate)[47], and polypyrrole[48], were synthesized via oxidative reactions on ice surfaces. In addition, 2D $TiO_2$ was successfully prepared via the hydrolysis of titanium isopropoxide between organic solvents and ice particles[49]. However, few 2D materials have been synthesized using ice templates, and their main applications have been in the field of energy storage, e.g., supercapacitors and batteries.

In this study, $WO_3$ nanosheets were prepared via a wet chemical method using ice particles as templates to overcome the major limitation of template-based wet chemical synthesis (i.e., the challenge of template removal). The catalytic activity of the $WO_3$ nanosheets in As(III) oxidation in the presence of $H_2O_2$ was compared with those of $WO_3$ and $TiO_2$ nanoparticles. The mechanism of oxidation in the $WO_3$ nanosheet/$H_2O_2$ system was investigated in detail. Furthermore, the effects of anions such as fluoride, chloride, nitrate, and bicarbonate on the kinetics of As(III) oxidation were examined. Finally, the reusability of the $WO_3$ nanosheets was evaluated over multiple cycles of As(III) oxidation.

KOPRI 극지연구소

## 2. Experimental

### 2.1. Materials and chemicals

The materials and chemicals used in this study include: tungsten(VI) ethoxide ($W(OC_2H_5)_6$), sodium tungstate dihydrate ($Na_2WO_4 \cdot 2H_2O$), tungsten(VI) oxide ($WO_3$), titanium(IV) oxide ($TiO_2$, Aeroxide P25 and Hombikat UV100), iron(II) perchlorate hydrate ($Fe(ClO_4)_2 \cdot xH_2O$), hydrochloric acid (HCl), hydrogen peroxide ($H_2O_2$), sodium (meta)arsenite (As(III), $NaAsO_2$), sodium arsenate dibasic heptahydrate (As(V), $Na_2HAsO_4 \cdot 7H_2O$), ascorbic acid ($C_6H_8O_6$), tert-butyl alcohol ($(CH_3)_3COH$), dichloromethane ($CH_2Cl_2$), ethanol ($C_2H_5OH$), methanol ($CH_3OH$), sodium fluoride (NaF), sodium chloride (NaCl), sodium nitrate ($NaNO_3$), sodium bicarbonate ($NaHCO_3$), sodium phosphate monobasic dihydrate ($NaH_2PO_4 \cdot 2H_2O$), sodium phosphate dibasic heptahydrate ($Na_2HPO_4 \cdot 7H_2O$), N,N-diethyl-p-phenylenediamine (DPD, $C_{10}H_{16}N_2$), sulfuric acid ($H_2SO_4$), peroxidase from horseradish, molybdate reagent solution, 5-tert-butoxycarbonyl-5-methyl-1-pyrroline-N-oxide (BMPO, $C_{10}H_{17}NO_3$), coumarin ($C_9H_6O_2$), potassium dioxide ($KO_2$), dimethyl sulfoxide ($C_2H_6SO$), perchloric acid ($HClO_4$), and argon (Ar). Detailed information on the chemicals and materials used in this study is provided in Table S1. All solutions and suspensions were prepared using deionized

water (resistivity = 18.3 MΩ·cm), which was produced using a water purification system (Millipore Milli-Q Direct 8).

### 2.2. Syntheses of the $WO_3$ nanosheets and nanoparticles

The $WO_3$ nanosheets were fabricated via a sol-gel reaction at the interfacial region between an organic solvent (hydrophobic phase) and ice particles (hydrophilic phase). More precisely, most synthetic reactions occur in the quasi-liquid layers (QLLs, liquid) on ice crystals (solid). The synthetic procedure is shown in Fig. 1. First, tungsten(VI) ethoxide (0.25 g, tungsten precursor) was placed in a beaker containing 200 mL of dichloromethane (organic solvent). The bulk ice was crushed into small ice particles using an ice breaker, and the ice particles (100 g) were added to the tungsten solution, which was stirred for 1 min. The tungsten(VI) ethoxide was hydrolyzed by the water molecules (i.e., the QLL) to form $W(OH)_6$ (Eq. (1)), and $WO_3$ nanosheets were then formed via the condensation of $W(OH)_6$ (Eq. (2))[10,73].

$$W(OC_2H_5)_6 + 6H_2O \rightarrow W(OH)_6 + 6C_2H_5OH \quad (1)$$

$$nW(OH)_6 \rightarrow (WO3)_n + 3nH_2O \quad (2)$$

After the reaction, the dichloromethane was drained from the beaker, and 100 mL of ethanol was then added to the beaker to completely remove the residual dichloromethane on the surfaces of the $WO_3$ nanosheets. The $WO_3$ nanosheets were collected via filtration, washed with deionized water, and dried at 50 °C for 10 h.

$WO_3$ nanoparticles were synthesized using an acidification method[65]. Sodium tungstate dihydrate (2.5 g) was dissolved in 100 mL of deionized water, and an HCl solution (5%) was added dropwise to the sodium tungstate solution under vigorous stirring until $WO_3$ nanoparticles were precipitated. These $WO_3$ nanoparticles were collected, washed, and dried in the same manner as the $WO_3$ nanosheets.

### 2.3. Characterizations of the WO3 nanosheets and nanoparticles

X-ray diffraction (XRD) patterns of the $WO_3$ nanosheets and nanoparticles were measured using an X-ray diffractometer (Malvern Panalytical X'Pert Pro MPD) with Cu K α radiation (λ = 1.54 Å) at 40 kV (accelerating voltage) and 30 mA (applied current). The scanning rate was 1.6°/min with a step size of 0.013° in the 2Θ range 5° - 90°. The $WO_3$ nanosheets and nanoparticles were observed via atomic force microscopy (AFM) using a multimode system (Bruker) coupled with a controller (Bruker NanoScope V), and the observations were conducted in the tapping mode using an AFM probe (Bruker TESP-V2, tip radius: 10 nm, typical resonant frequency: 320 kHz, and spring constant: 42 $N \cdot m^{-1}$).

The morphologies and elemental compositions of the $WO_3$ nanosheets were examined using field emission transmission electron microscopy (FE-TEM, JEOL JEM-2100F) combined with energy-dispersive X-ray (EDX) spectroscopy.

The surface areas of the $WO_3$ nanosheets and nanoparticles were measured using a gas sorption surface area analyzer (Quantachrome Instruments Quadrasorb evo). Thermogravimetric analysis (TGA) was performed from room temperature to 700 °C at a heating rate of 5 °C/min under a nitrogen atmosphere using a thermogravimetric instrument (TA Instruments Q500). The surface characteristics of the $WO_3$ nanosheets and nanoparticles were explored using X-ray photoelectron spectroscopy (XPS, Thermo Scientific K-Alpha). A monochromatic Al Kα line (1486.6 eV) was used as the excitation source, and the binding energies were calibrated based on the C 1s peak (284.8 eV). The zeta potentials of the $WO_3$ nanosheets and $TiO_2$ nanoparticles were measured using an electrophoretic light scattering spectrophotometer (Malvern Panalytical Zetasizer).

### 2.4. As(III) oxidation experiments

The catalyst powder (25 mg) was added to deionized water (47.8 mL) and dispersed by sonication for 3 min. An aliquot of an As(III) stock solution (10 mM, 2 mL) was added to the catalyst suspension to yield an initial As(III) concentration of 400 μM. As most As(III)-contaminated water and wastewater samples are highly acidic[37,39,53], the pH of the catalyst suspension was adjusted to 2.5 using an $HClO_4$ solution. Subsequently, an aliquot of an $H_2O_2$ stock solution (0.5 M, 0.2 mL) was added to induce catalytic As(III) oxidation. The initial concentration of $H_2O_2$ in the catalyst suspension was 2 mM. A 100 mL glass beaker, which was covered with aluminum foil to prevent photochemical reactions under ambient light, was used as the reactor. The reaction time started when $H_2O_2$ was added to the catalyst suspension. Sample aliquots (1.5 mL) were withdrawn from the reactor at predetermined intervals and filtered through 0.1 μm polytetrafluoroethylene filters (Millipore) to remove catalyst particles.

The catalytic activity in As(III) oxidation in the presence of $H_2O_2$ was evaluated by measuring the production of As(V) with reaction time. The concentration of As(V) was measured using the molybdene blue method[41]. Ascorbic acid (0.57 M, 0.1 mL) and molybdate reagent (0.2 mL) solutions were added to a 15 mL conical tube containing 4 mL of the diluted sample. This solution was then vigorously mixed for 1 min and maintained in darkness for 1 h. The absorbance of the sample was measured at 870 nm using a UV-visible spectrophotometer (Shimadzu UV-2600). Sodium arsenate dibasic heptahydrate was used as the As(V) source to prepare a standard calibration curve. The As(III) oxidation experiments were performed in duplicate or triplicate under identical experimental conditions, and the results are presented as average values and standard deviations.

### 2.5. Reactive oxygen species measurements

The concentration of hydrogen peroxide ($H_2O_2$) was determined using the N,N-diethyl-p-phenylenediamine (DPD) method[57]. Briefly, 3 mL of the diluted sample was mixed with 0.4 mL of phosphate buffer solution (0.5 M, $NaH_2PO_4 \cdot 2H_2O$ + $Na_2HPO_4 \cdot 7H_2O$ at pH 6.0), 0.05 mL of DPD solution (1 g/100 mL of 0.1 M $H_2SO_4$), and 0.05 mL of peroxidase solution (0.1 g/100 mL). The conical tube containing the mixture was vigorously shaken for 1 min, and its absorbance was then measured at 551 nm using a UV - visible spectrophotometer (Shimadzu UV-2600).

Electron spin resonance (ESR) spectroscopy was performed using an ESR spectrometer (Bruker EMXnano) to identify the radical species generated within the system. 5-tert-butoxycarbonyl-5-methyl-1-pyrroline-N-oxide (BMPO) was used as a spin-trapping reagent to yield stable BMPO-radical adducts[56]. The operating parameters of the ESR spectrometer were as follows: microwave power = 1 mW, microwave frequency = 9.6294 GHz, modulation amplitude = 1 G, modulation frequency = 100 kHz, sweep time = 10 s, and scan number = 10.

The production of hydroxyl radicals ($^{\bullet}OH$) was selectively monitored using fluorescence spectroscopy with coumarin as a chemical probe. 7-Hydroxycoumarin, with fluorescence emission centered at 460 nm, is generated as a product of the reaction between $^{\bullet}OH$ and coumarin[87]. The intensity of the fluorescence emission of 7-hydroxycoumarin was measured under 332 nm light excitation using a spectrofluorometer (Shimadzu RF-5301).

## 3. Results and Discussion

### 3.1. Characterizations of the $WO_3$ nanosheets and nanoparticles

The XRD patterns of the $WO_3$ nanosheets synthesized using an ice template and $WO_3$ nanoparticles obtained by an acidification method were measured (Fig. 2). No clear peaks were observed in the XRD patterns, suggesting the amorphous natures of the samples. After calcination at 400 °C for 3 h, the XRD patterns of the $WO_3$ nanosheets and nanoparticles showed distinct peaks owing to the increased crystallinities of the samples. The XRD patterns of the calcined $WO_3$ nanosheets and nanoparticles were similar to that of commercial $WO_3$ nanoparticles. The dominant diffraction peaks at $2\Theta$ = 23.1, 23.6, 24.3, 26.6, 28.8, 33.3, 34.1, 41.7, 49.9, and 55.8° represent the (002), (020), (200), (120), (112), (022), (202), (222), (140), and (420) crystal planes of the monoclinic $WO_3$ phase, respectively (JCPDS No. 43 - 1035)[60,61]. These results confirm that the materials synthesized without calcination are amorphous $WO_3$. Fig. 3 shows the AFM images and the thicknesses of the $WO_3$ nanosheets and nanoparticles. The thicknesses of the $WO_3$ nanosheets were in the range 4 - 10 nm, depending on the number of layers (Fig. 3a and b). On the other hand,

the thicknesses of the $WO_3$ nanoparticles were 40–50 nm (Fig. 3c and d), which were significantly larger than those of the $WO_3$ nanosheets. As shown in the TEM images (Fig. 4), the $WO_3$ nanosheets exhibited plate-like morphologies, with lateral sizes ranging from dozens of nanometers to hundreds of nanometers. Most $WO_3$ nanosheets overlapped (Fig. 4a and b), and several $WO_3$ nanosheets existed as few-layer nanosheets (Fig. 4c and d). The presence of tungsten and oxygen in the $WO_3$ nanosheets was confirmed by the elemental mapping images, and the distribution of tungsten overlapped precisely with that of oxygen (Fig. 4e–j).

### 3.2. Oxidation of As(III) using the $WO_3$ nanosheets in the presence of $H_2O_2$

The catalytic activity of the $WO_3$ nanosheets in the oxidation of As(III) was investigated in the presence of $H_2O_2$ (Fig. 5). When $H_2O_2$ was added to the suspension of the $WO_3$ nanosheets containing 400 μM As(III), the production of As(V) gradually increased with reaction time, reaching 400 μM after 1 h. However, the oxidation of As(III) was negligible in the control systems, wherein $WO_3$ nanosheets or $H_2O_2$ were absent (Fig. 5a). The concentration of $H_2O_2$ decreased only when the $WO_3$ nanosheets were present (Fig. 5b). These results indicate that As(III) is oxidized to As(V) via the $WO_3$-catalyzed activation of $H_2O_2$.

$H_2O_2$ was consumed rapidly by the $WO_3$ nanosheets in the presence of As(III). However, when As(III) was completely oxidized to As(V) (after 1 h), the rate of $H_2O_2$ decomposition was significantly reduced. This behavior differs from those within other catalyst/oxidant systems (e.g., pyrite/$H_2O_2$, $Fe^0$/persulfate, $LaCoO_3$/peroxymonosulfate, $Fe_3O_4$–$CeO_2$/$H_2O_2$, and Fe–C/peroxydisulfate systems), wherein the oxidants continuously decompose after pollutant degradation is complete[62,63,64,65,66]. The significantly reduced rate of $H_2O_2$ decomposition after the complete oxidation of As(III) minimizes $H_2O_2$ consumption in the $WO_3$ nanosheet/$H_2O_2$ system and improves its economic viability.

The oxidation of As(III) using the $WO_3$ nanosheets was also compared with that using the $WO_3$ nanoparticles (Fig. 5c). The $WO_3$ nanosheets synthesized using the ice template were superior to the $WO_3$ nanoparticles synthesized using the acidification method and commercial $WO_3$ nanoparticles in terms of the oxidation of As(III) in the presence of $H_2O_2$. As(III) oxidation was completed within 1 h using the $WO_3$ nanosheets, 2 h using the $WO_3$ nanoparticles synthesized using the acidification method, and 3 h using the commercial $WO_3$ nanoparticles. Moreover, the activities of the amorphous $WO_3$ nanosheets and nanoparticles in As(III) oxidation were reduced after calcination, becoming similar to that of the commercial crystalline $WO_3$ nanoparticles. This suggests that the high activity of the $WO_3$ synthesized in this study may be related to its amorphous characteristics.

### 3.3. Reason of the higher activity of the $WO_3$ nanosheets compared to that of the $WO_3$ nanoparticles

The surface areas of metal oxides generally decrease with increasing crystallinity[67,68]. The surface areas of the amorphous $WO_3$ nanosheets (21.7 $m^2$ $g^{-1}$) and nanoparticles (27.7 $m^2$ $g^{-1}$) were higher than those of the commercial crystalline $WO_3$ nanoparticles (9.4 $m^2$ $g^{-1}$). Similarly, the amorphous $WO_3$ nanosheets and nanoparticles showed higher activities than those of the crystalline $WO_3$ nanoparticles. However, the $WO_3$ nanosheets, with smaller surface areas, exhibited higher efficiencies in As(III) oxidation than those of the $WO_3$ nanoparticles, suggesting that surface area may not be the sole reason for the efficiency.

The reactions between metal oxides and $H_2O_2$ generate metal peroxo complexes (>M−OH + $H_2O_2$ → >M−OOH + $H_2O$), which can further produce hydroperoxyl radicals ($HO_2^{\bullet}$) via electron transfer from the –OOH groups to the metal centers (Eq. (3))[14,69]. In addition, $H_2O_2$ can be adsorbed on the surfaces of metal oxides via hydrogen bonding (>M−OH + $H_2O_2$ → >M−OH···$H_2O_2$). The subsequent homolytic cleavage of the O–O bond in $H_2O_2$ by the metal center produces hydroxyl radicals ($^{\bullet}OH$) (Eq. (4))[70,71].

$$>Mx-OOH \rightarrow >M(x-1)-{}^{\bullet}OOH \quad (3)$$

$$>M-OH\cdots H_2O_2 \rightarrow >M-OH+2{}^{\bullet}OH \quad (4)$$

KORRI 극지연구소

As the complexation and adsorption of $H_2O_2$ occur via interactions with the surface hydroxyl groups on $WO_3$, the number of surface hydroxyl groups rather than the surface area should intrinsically determine the production of reactive oxygen species, such as $HO_2^{\bullet}$ and $^{\bullet}OH$.

TGA is often used to estimate the quantities of surface hydroxyl groups on metal oxides[72]. Fig. 6 shows the TGA curves of the $WO_3$ nanoparticles and nanosheets. Complete dehydration of the $WO_3$ nanoparticles was observed at 440 °C, whereas that of the $WO_3$ nanosheets was observed at 470 °C. Although the total weight loss of the $WO_3$ nanosheets (8.6%) was similar to that of the $WO_3$ nanoparticles (8.7%), the shapes of the TGA curves were significantly different. The weight loss at temperatures of <250 °C is due to the release of water molecules physically adsorbed on the $WO_3$ surface (surface $H_2O$). On the other hand, temperatures of >250 °C induce dissociation of the surface hydroxyl groups of $WO_3$ (>W−OH + >W−OH → >W−O−W< + $H_2O$)[73,74,75,76]. The weight loss at >250 °C (i.e., the weight loss due to the removal of >W−OH) observed for the $WO_3$ nanosheets was higher than that observed for the $WO_3$ nanoparticles (Table 1), suggesting that the $WO_3$ nanosheets bear more surface hydroxyl groups than the $WO_3$ nanoparticles.

The surface chemical compositions and electronic states of the $WO_3$ nanoparticles and

nanosheets were investigated using XPS (Fig. 7). The spectrum of the $WO_3$ nanoparticles displays two peaks at 36.0 and 38.1 eV corresponding to the binding energies of W $4f_{7/2}$ and W $4f_{5/2}$ in $W^{6+}$, respectively (Fig. 7a). In the spectrum of the $WO_3$ nanosheets, the peaks representing W $4f_{7/2}$ and W $4f_{5/2}$ are observed at 36.8 and 38.9 eV, respectively (Fig. 7b). The higher binding energies indicate that the W metal centers of the $WO_3$ nanosheets have higher electron affinities[77,78,79], facilitating electron transfer from the –OOH groups to the W metal centers (>W^VI−OOH → >W^V−•OOH) and the subsequent production of $HO_2^{\bullet}$.

The O 1s spectrum of the $WO_3$ nanoparticles can be deconvoluted into three peaks at 530.8, 532.1, and 532.9 eV, which are assigned to the oxygen atoms in the lattice (lattice O), surface hydroxyl groups (>W−OH), and water molecules adsorbed on the surface (surface $H_2O$), respectively[80,81,82] (Fig. 7c). Similar peaks are observed at 529.8, 530.9, and 532.0 eV in the O 1s spectrum of the $WO_3$ nanosheets (Fig. 7d). The relative quantities of the oxygen species (i.e., lattice O, >W−OH, and surface $H_2O$) on the surfaces of the $WO_3$ nanoparticles and nanosheets were calculated based on the ratios of their peak areas (Table 2). Most oxygen species on the surfaces of the $WO_3$ nanoparticles and nanosheets are lattice O. In terms of non-lattice O, the $WO_3$ nanosheets exhibit a higher ratio of >W−OH but a lower ratio of surface $H_2O$ compared to those of the $WO_3$ nanoparticles, indicating that the non-lattice O primarily exists as >W−OH on the $WO_3$ nanosheets, but as surface $H_2O$ on the $WO_3$ nanoparticles. This is consistent with the results of TGA (Fig. 6), confirming that the $WO_3$ nanosheets bear more surface hydroxyl groups than the $WO_3$ nanoparticles.

The higher number of surface hydroxyl groups on the $WO_3$ nanosheets favors the production of reactive oxygen species because these hydroxyl groups induce the complexation and adsorption of $H_2O_2$ as the first step in producing $HO_2^{\bullet}$ and $^{\bullet}OH$, as shown in Eq. (3) and Eq. (4). In addition, the W metal centers in the $WO_3$ nanosheets can easily withdraw electrons from the –OOH groups in the metal peroxo complexes (>M−OOH) because the $W^{6+}$ in the $WO_3$ nanosheets is relatively electrophilic. The higher electron-withdrawing ability of $W^{6+}$ in the $WO_3$ nanosheets facilitates the production of $HO_2^{\bullet}$ via Eq. (3) and enhances the oxidation of As(III).

### 3.4. Mechanistic investigation of As(III) oxidation in the $WO_3$ nanosheet/$H_2O_2$ system

Activation of $H_2O_2$ on the surfaces of metal oxides generates $^{\bullet}OH$[70,71] and $HO_2^{\bullet}$[14,69]. Quenching experiments were performed to investigate the primary radical species involved in As(III) oxidation in the $WO_3$ nanosheet/$H_2O_2$ system (Fig. 8). Tert-butyl alcohol and ascorbic acid were used as $^{\bullet}OH$($k = 6.0 \times 10^8\ M^{-1}\ s^{-1}$)[83] and $HO_2^{\bullet}$ ($k = 1.25 \times 10^6\ M^{-1}\ s^{-}$

$^{1)}$[84] scavengers, respectively. The oxidation of As(III) was completely inhibited in the presence of ascorbic acid (Fig. 8a). However, the presence of tert-butyl alcohol had a negligible effect on the rate of As(III) oxidation (Fig. 8b). This result implies that $HO_2^{\bullet}$ is the dominant radical in As(III) oxidation in the $WO_3$ nanosheet/$H_2O_2$ system.

ESR spectroscopy was employed to identify the reactive oxygen species produced in the $WO_3$ nanosheet/$H_2O_2$ system (Fig. 9). BMPO was used as the spin-trapping agent. The characteristic peaks of BMPO - $HO_2^{\bullet}$, which were the same as those generated by a $KO_2$ solution (a mixture of $KO_2$ in dimethyl sulfoxide and BMPO in water), were observed in the spectrum of the suspension of the $WO_3$ nanosheets after adding $H_2O_2$. In contrast, the typical ESR signals representing BMPO - $^{\bullet}OH$ (i.e., quartet signals with relative intensities of 1:2:2:1) were not observed[85,86]. The negligible production of $^{\bullet}OH$ in the $WO_3$ nanosheet/$H_2O_2$ system was also verified using a fluorescence technique (Fig. S1 and Text S1). The effect of oxygen on As(III) oxidation in the $WO_3$ nanosheet/$H_2O_2$ system was also studied. Argon was continuously purged to remove oxygen; however, the kinetics of As(III) oxidation were not altered by argon purging (Fig. S2). These results verify that $HO_2^{\bullet}$ is the primary oxidant in As(III) oxidation in the $WO_3$ nanosheet/$H_2O_2$ system.

### 3.5. Practical viability of the $WO_3$ nanosheet/$H_2O_2$ system in As(III) oxidation

Most As(III)-contaminated water and wastewater samples are highly acidic and contain high concentrations of anions[53,54,55]. Therefore, the effects of various anions, such as fluoride ($F^-$), chloride ($Cl^-$), nitrate ($NO_3^-$), and bicarbonate ($HCO_3^-$), on the oxidation of As(III) in the $WO_3$ nanosheet/$H_2O_2$ system were investigated. As shown in Fig. 10a, all tested anions had little effect on As(III) oxidation. The reactivities of $HO_2^{\bullet}$ toward $F^-$, $Cl^-$, and $NO_3^-$ are very low[84], and therefore, $HO_2^{\bullet}$ produced in the $WO_3$ nanosheet/$H_2O_2$ system selectively reacts with As(III). Although $HCO_3^-$ can moderately react with $HO_2^{\bullet}$ ($k = 1.5 \times 10^6\ M^{-1}\ s^{-1}$)[84], the secondary carbonate radicals ($CO_3^{\bullet -}$) produced from the oxidation of $HCO_3^-$ can react with As(III) at a rate similar to that of $HO_2^{\bullet}$ ($E^0(CO_3^{\bullet -}/CO_3^{2-}) = 1.57\ V_{NHE}$ and $E^0(HO_2^{\bullet}/H_2O_2) = 1.46\ V_{NHE}$)[87].

The inhibition of As(III) oxidation by anions is frequently reported in other systems, such as a glucose-derived carbon/$SO_3^{2-}$ system[88], an electrocatalytic system with an $MnO_2$/$TiO_2$ nanotube anode[89], a CuNSi/$SO_3^{2-}$ system[90], and a photocatalytic system with a $ZnFe_2O_4$/g-$C_3N_4$ composite[91]. Fig. 10b shows the oxidation of As(III) in the suspension of $TiO_2$ nanoparticles (Aeroxide P25) with $H_2O_2$ in the absence or presence of $F^-$. In contrast to catalysis using the $WO_3$ nanosheets, the presence of $F^-$ significantly inhibited As(III) oxidation when Aeroxide P25 $TiO_2$ was used as the catalyst. The inhibitory effect of $F^-$ on As(III) oxidation was also observed when using other $TiO_2$ nanoparticles (Hombikat UV100) (Fig. S3). In this respect, $WO_3$ is a superior catalyst to $TiO_2$ in the oxidation of

As(III) via $H_2O_2$ activation.

The effect of $F^-$ on As(III) oxidation is likely due to the different surface charges of the catalysts. The zeta potential measurements show that the surface charge of the $WO_3$ nanosheets is negative under acidic conditions, whereas that of the $TiO_2$ nanoparticles is positive (Fig. 10c). The positively charged $TiO_2$ nanoparticles attract $F^-$, inducing ligand exchange between $F^-$ and the surface hydroxyl groups (>Ti−OH + $F^-$ → >Ti−F + $OH^-$)[92,93]. The substitution of surface hydroxyl groups by $F^-$ reduces the production of reactive oxygen species and hinders As(III) oxidation. However, the negatively charged $WO_3$ nanosheets repel $F^-$, which prevents ligand exchange between $F^-$ and the surface hydroxyl groups. Therefore, the presence of $F^-$ had a minor effect on As(III) oxidation in the $WO_3$ nanosheet/$H_2O_2$ system.

We compared the catalytic activity of the $WO_3$ nanosheets in As(III) oxidation in the presence of $H_2O_2$ to those of other heterogeneous catalysts in the presence of $H_2O_2$. The results are expressed in terms of the first-order rate constants (k) of oxidation (Table S2). However, this comparison should be considered only a rough estimate because the reaction parameters, such as the As(III) concentration, catalyst dose, $H_2O_2$ concentration, and solution pH, are different in each study. Generally, the $WO_3$ nanosheet catalyst synthesized in this study (k = 0.062 $min^{-1}$) displays a similar activity to those of ferrous materials (k of $Fe^{3+}$@B. subtilis spore = 0.026 $min^{-1}$[194], k of Fe(III)-amidoximated PAN = 0.053 $min^{-1}$[195], k of Fe-Ce oxide = 0.055 $min^{-1}$[116], k of Fe-Mn oxide = 0.055 $min^{-1}$[117], and k of $Fe^0$ = 0.011 $min^{-1}$[196]) but a higher activity compared to those of nonferrous materials (k of $WO_3$ (Aldrich) = 0.015 $min^{-1}$, k of $TiO_2$ (Aeroxide P25) = 0.002 $min^{-1}$, k of $TiO_2$ (Hombikat UV100) = 0.004 $min^{-1}$, k of Mn-doped $La_2O_2CO_3$ = 0.007 $min^{-1}$[197], k of $CeO_2$ = 0.008 $min^{-1}$, and k of $Ce_{0.25}Ti_{0.75}O_2$ = 0.050 $min^{-1}$[115]). $H_2O_2$ can induce the dissolution of Fe ions on the surfaces of ferrous materials[14]. Therefore, high concentrations of Fe ions are leached from ferrous materials after the catalytic activation of $H_2O_2$, resulting in decreased efficiencies of As(III) oxidation[95,96,117,116]. In this respect, even compared to ferrous materials, the $WO_3$ nanosheets are sufficiently competitive as $H_2O_2$ activators for the oxidation of As(III) in water.

As(III) oxidation in the $WO_3$ nanosheet/$H_2O_2$ system was performed repeatedly to assess the stability and reusability of the $WO_3$ nanosheet catalyst as an $H_2O_2$ activator (Fig. 11). The As(III) solution was injected repeatedly into the reactor at the beginning of each cycle, and the initial $WO_3$ nanosheets were reused without surface cleaning. When $H_2O_2$ was added only at the beginning of the first cycle, the rate of As(III) oxidation remained high until the fourth cycle but was drastically reduced in the fifth cycle due to $H_2O_2$ consumption. No oxidation occurred in the eighth cycle because $H_2O_2$ was depleted during the seventh cycle (Fig. 11a and b). When $H_2O_2$ was injected at intervals of four cycles,

complete As(III) oxidation was observed for up to twelve cycles without a decrease in the As(III) oxidation rate (Fig. 11c and d). In addition, the XPS spectra and XRD patterns of the $WO_3$ nanosheets changed little after multiple cycles of As(III) oxidation (Fig. S4 and S5). These results suggest that the $WO_3$ nanosheet catalyst shows excellent stability and reusability. This strategy (i.e., adding $H_2O_2$ at regular intervals) improves the practical viability of the $WO_3$ nanosheet/$H_2O_2$ system for use in treating large volumes of As(III)-contaminated water.

## 4. Conclusions

This study developed an efficient and stable approach for use in As(III) oxidation, employing $WO_3$ nanosheets as catalysts in the presence of $H_2O_2$. The $WO_3$ nanosheets were synthesized via a wet chemical method, with ice particles as easily removable templates. Compared with those of the $WO_3$ nanoparticles, the $WO_3$ nanosheets synthesized in this study exhibited higher efficiencies in As(III) oxidation. The higher number of hydroxyl groups on the surface of the $WO_3$ nanosheet and the higher electron affinity of the W metal center contribute synergistically to the increased $HO_2^{\bullet}$ generation for As(III) oxidation. Unlike other catalyst/oxidant systems, consumption of the oxidant ($H_2O_2$) proceeded rapidly only in the presence of the target pollutant (As(III)) in the $WO_3$ nanosheet/$H_2O_2$ system. The presence of anions, which generally inhibited As(III) oxidation in other systems, had little effect in the $WO_3$ nanosheet/$H_2O_2$ system. Moreover, the catalytic activity of the $WO_3$ nanosheets did not deteriorate after multiple catalytic cycles. Owing to features such as high efficiency and stability, minimized $H_2O_2$ consumption, and lack of interference by background anions, the $WO_3$ nanosheets synthesized using the ice template can be practically used as $H_2O_2$ activators for the oxidation of As(III) in water. This synthetic strategy could be extended to develop various high-performance 2D metal oxide catalysts.

KOPRI 극지연구소

## REFERENCES


[1] Christen, K., 2001. The arsenic threat worsens. *Environ. Sci. Technol.* 35, 286 - 291.

[2] Podgorski, J., Berg, M., 2020. Global threat of arsenic in groundwater. *Science* 368, 845 - 850.

[3] Naujokas, M.F., Anderson, B., Ahsan, H., Aposhian, H.V., Graziano, J.H., Thompson, C., Suk, W.A., 2013. The broad scope of health effects from chronic arsenic exposure: update on a worldwide public health problem. *Environ. Health Perspect.* 121, 295 - 302.

[4] Rahaman, S., Rahman, M., Mise, N., Sikder, T., Ichihara, G., Uddin, K., Kurasaki, M., Ichihara, S., 2021. Environmental arsenic exposure and its contribution to human diseases, toxicity mechanism and management. *Environ. Pollut.* 289, 117940.

[5] Sharma, V.K., Sohn, M., 2009. Aquatic arsenic: toxicity, speciation, transformations, and remediation. *Environ. Int.* 35, 743 - 759.

[6] Liu, R., Qu, J., 2021. Review on heterogeneous oxidation and adsorption for arsenic removal from drinking water. *J. Environ. Sci.* 110, 178 - 188.

[7] Montefalcon, M.F.V., Chiong III, M.R., Resurreccion, A.C., Garcia-Segura, S., Ocon, J.D., 2020. Arsenic removal by advanced electrocoagulation processes: the role of oxidants generated and kinetic modeling. *Catalysts* 10, 928.

[8] Jasim, S.Y., Mohseni, M., 2019. Ozone application for arsenic and manganese treatment at the City of White Rock, BC, Canada. Ozone: *Sci. Eng.* 41, 322 - 331.

[9] van Genuchten, C.M., Ahmad, A., 2020. Groundwater As removal by As(III), Fe(II), and Mn(II) co-oxidation: contrasting As removal pathways with $O_2$, NaOCl, and $KMnO_4$. *Environ. Sci. Technol.* 54, 15454 - 15464.

[10] Wang, Z., Bush, R.T., Sullivan, L.A., Chen, C., Liu, J., 2014. Selective oxidation of arsenite by peroxymonosulfate with high utilization efficiency of oxidant. *Environ. Sci. Technol.* 48, 3978 - 3985.

[11] Gude, J.C.J., Rietveld, L.C., van Halem, D., 2017. As(III) oxidation by $MnO_2$ during groundwater treatment. *Water Res.* 111, 41 - 51.

[12] Zhao, Z., Guan, M., Zeng, H., Chen, P., 2018. Adsorption and oxidation of As(III) on iron (hydro)oxides. *Water Environ. Res.* 90, 483 - 489.

[13] Hu, H., Zhang, Q., Wang, C., Chen, M., Chen, M., 2022. Mechanochemically synthesized Fe - Mn binary oxides for efficient As(III) removal: insight into the origin of synergy action from mutual Fe and Mn doping. *J. Hazard. Mater.* 424, 127708.

[14] Kim, D.-h., Bokare, A.D., Koo, M.s., Choi, W., 2015. Heterogeneous catalytic oxidation of As(III) on nonferrous metal oxides in the presence of $H_2O_2$. *Environ. Sci. Technol.* 49, 3506 - 3513.

[15] Shan, C., Liu, H., Hua, M., Pan, B., 2020. Enhanced Fenton-like oxidation of As(III) over Ce - Ti binary oxide: a new strategy to tune catalytic activity via balancing

bimolecular adsorption energies. *Environ. Sci. Technol.*54, 5893 – 5901.

[16] Wen, Z., Zhang, Y., Dai, C., Sun, Z., 2015. Nanocasted synthesis of magnetic mesoporous iron cerium bimetal oxides (MMIC) as an efficient heterogeneous Fenton-like catalyst for oxidation of arsenite. *J. Hazard. Mater.* 287, 225 – 233.

[17] Wen, Z., Lu, J., Zhang, Y., Cheng, G., Guo, S., Wei, P., Ming, Y.-a., Wang, Y., Chen, R., 2020. Simultaneous oxidation and immobilization of arsenite from water by nanosized magnetic mesoporous iron manganese bimetal oxides (Nanosized-MMIM): synergistic effect and interface catalysis. *Chem. Eng. J.* 391, 123578.

[18] Baruah, K., Deb, P., 2021. Electrochemically active site-rich nanocomposites of two dimensional materials as anode catalysts for direct oxidation fuel cells: new age beyond graphene. *Nanoscale Adv.* 3, 3681 – 3707.

[19] Jia, Y., Yi, X., Li, Z., Zhang, L., Yu, B., Zhang, J., Wang, X., Jia, X., 2020. Recent advance in biosensing applications based on two-dimensional transition metal oxide nanomaterials. *Talanta* 219, 121308.

[20] Kalantar-zadeh, K., Ou, J.Z., Daeneke, T., Mitchell, A., Sasaki, T., Fuhrer, M.S., 2016. Two dimensional and layered transition metal oxides. *Appl. Mater. Today* 5, 73 – 89.

[21] Kumar, K.S., Choudhary, N., Jung, Y., Thomas, J., 2018. Recent advances in two-dimensional nanomaterials for supercapacitor electrode applications. *ACS Energy Lett.* 3, 482 – 495.

[22] Lim, J., Lee, J.M., Kim, C., Hwang, S.-J., Lee, J., Choi, W., 2019. Two-dimensional $RuO_2$ nanosheets as robust catalysts for peroxymonosulfate activation. *Environ. Sci.: Nano* 6, 2084 – 2093.

[23] Fang, M., Zheng, R., Wu, Y., Yue, D., Qian, X., Zhao, Y., Bian, Z., 2019. CuO nanosheet as a recyclable Fenton-like catalyst prepared from simulated Cu(II) waste effluents by alkaline $H_2O_2$ reaction. *Environ. Sci.: Nano* 6, 105 – 114.

[24] Shao, P., Ren, Z., Tian, J., Gao, S., Luo, X., Shi, W., Yan, B., Li, J., Cui, F., 2017. Silica hydrogel mediated dissolution-recrystallization strategy for synthesis of ultrathin α-$Fe_2O_3$ nanosheets with highly exposed (110) facets: a superior photocatalyst for degradation of bisphenol S. *Chem. Eng. J.* 323, 64 – 73.

[25] Fenton, H.J.H., 1894. LXXIII.-Oxidation of tartaric acid in presence of iron. *J. Chem. Soc. Trans.* 65, 899 – 910.

[26] Bokare, A.D., Choi, W., 2014. Review of iron-free Fenton-like systems for activating H2O2 in advanced oxidation processes. *J. Hazard. Mater.* 275, 121 – 135.

[27] Sun, Q., Wang, X., Liu, Y., Xia, S., Zhao, J., 2022. Activation of peroxymonosulfate by a floating oxygen vacancies- $CuFe_2O_4$ photocatalyst under visible light for efficient degradation of sulfamethazine. *Sci. Total Environ.* 824, 153630.

[28] Zhou, T., Han, Y., Xiang, W., Wang, C., Wu, X., Mao, J., Huang, M., 2022. Revealing

the heterogeneous activation mechanism of peroxydisulfate by CuO: the critical role of surface binding organic substrates. *Sci. Total Environ.* 802, 149833.

[29] Zong, Y., Zhang, H., Shao, Y., Ji, W., Zeng, Y., Xu, L., Wu, D., 2022. Surface-mediated periodate activation by nano zero-valent iron for the enhanced abatement of organic contaminants. *J. Hazard. Mater.* 423, 126991.

[30] Fang, X., Yao, M., Guo, L., Xu, Y., Zhou, W., Zhuo, M., Shi, C., Liu, L., Wang, L., Li, X., Chen, W., 2017. One-step, solventless, and scalable mechanosynthesis of $WO_3 \cdot 2H_2O$ ultrathin narrow nanosheets with superior UV−vis-light-driven photocatalytic activity. *ACS Sustain. Chem. Eng.* 5, 10735 - 10743.

[31] Mei, J., Liao, T., Sun, Z., 2018. Two-dimensional metal oxide nanosheets for rechargeable batteries. *J. Energy Chem.* 27, 117 - 127.

[32] Zhang, H., 2015. Ultrathin two-dimensional nanomaterials. *ACS Nano* 9, 9451 - 9469.

[33] Mei, J., Liao, T., Kou, L., Sun, Z., 2017. Two-dimensional metal oxide nanomaterials for next generation rechargeable batteries. *Adv. Mater.* 29, 1700176.

[34] Tan, C., Zhang, H., 2015. Wet-chemical synthesis and applications of non-layer structured two-dimensional nanomaterials. *Nat. Commun.* 6, 7873.

[35] Wang, D., Zhou, W., Zhang, R., Zeng, J., Du, Y., Qi, S., Cong, C., Ding, C., Huang, X., Wen, G., Yu, T., 2018. Mass production of large-sized, nonlayered 2D nanosheets: their directed synthesis by a rapid "gel-blowing" strategy, and applications in Li/Na storage and catalysis. *Adv. Mater.* 30, 1803569.

[36] Xiao, X., Song, H., Lin, S., Zhou, Y., Zhan, X., Hu, Z., Zhang, Q., Sun, J., Yang, B., Li, T., Jiao, L., Zhou, J., Tang, J., Gogotsi, Y., 2016. Scalable salt-templated synthesis of two-dimensional transition metal oxides. *Nat. Commun.* 7, 11296.

[37] Nosheen, F., Wasfi, N., Aslam, S., Anwar, T., Hussain, S., Hussain, N., Shah, S.N., Shaheen, N., Ashraf, A., Zhu, Y., Wang, H., Ma, J., Zhang, Z., Hu, W., 2020. Ultrathin Pd-based nanosheets: syntheses, properties and applications. *Nanoscale* 12, 4219 - 4237.

[38] Zhang, J., Ye, S., Sun, Y., Zhou, F., Song, J., Qu, J., 2020. Soft-template assisted synthesis of hexagonal antimonene and bismuthene in colloidal solutions. *Nanoscale* 12, 20945 - 20951.

[39] Quinson, J., Dworzak, A., Simonsen, S.B., Kuhn, L.T., Jensen, K.M.Ø., Zana, A., Oezaslan, M., Kirkensgaard, J.J.K., Arenz, M., 2021. Surfactant-free synthesis of size controlled platinum nanoparticles: insights from in situ studies. *Appl. Surf. Sci.* 549, 149263.

[40] Tan, H.T., Sun, W., Wang, L., Yan, Q., 2016. 2D transition metal oxides/hydroxides for energy-storage applications. *ChemNanoMat* 2, 562 - 577.

[41] Zhong, J., Zeng, Y., Yin, Z., Zhang, M., Yan, D., Su, Z., Chen, P., Fu, M., Ye, D., 2021. *J. Mater. Chem. A* 9, 6890 - 6897.

KOPRI 극지연구소

[42] Conde, M.M., Vega, C., Patrykiejew, A., 2008. The thickness of a liquid layer on the free surface of ice as obtained from computer simulation. *J. Chem. Phys.* 129, 014702.

[43] Sadtchenko, V., Ewing, G.E., 2002. Interfacial melting of thin ice films: an infrared study. *J. Chem. Phys.* 116, 4686 - 4697.

[44] Kim, K., Chung, H.Y., Kim, B., Wong, G., Nguyen, A.Q.K., Kim, S., Kim, J., 2020. Freezing-induced simultaneous reduction of chromate and production of molecular iodine: mechanism, kinetics, and practical implications. *Environ. Sci. Technol.* 54, 16204 - 16211.

[45] Kim, K., Le, N.T.H., Nguyen, A.Q.K., Ahn, Y.-Y., Kim, B., Shin, G., Choi, W., Kim, J., 2022. Freezing-induced activation of the binary chloride-Oxone system to free chlorine and its application in water treatment. *Chem. Eng. J.* 428, 131134.

[46] Choi, I.Y., Lee, J., Ahn, H., Lee, J., Choi, H.C., Park, M.J., 2015. High-conductivity two dimensional polyaniline nanosheets developed on ice surfaces. *Angew. Chem. Int. Edit.* 54, 10497 - 10501.

[47] Barpuzary, D., Kim, K., Park, M.J., 2019. Two-dimensional growth of large-area conjugated polymers on ice surfaces: high conductivity and photoelectrochemical applications. *ACS Nano* 13, 3953 - 3963.

[48] Bai, N., Xu, Z., Tian, Y., Gai, L., Jiang, H., Marcus, K., Liang, K., 2017. Tailorable polypyrrole nanofilms with exceptional electrochemical performance for all-solid-state flexible supercapacitors. *Electrochim. Acta* 249, 360 - 368.

[49] Kim, G., Jo, C., Kim, W., Chun, J., Yoon, S., Lee, J., Choi, W., 2013. TiO2 nanodisks designed for Li-ion batteries: a novel strategy for obtaining an ultrathin and high surface area anode material at the ice interface. *Energy Environ. Sci.* 6, 2932 - 2938.

[50] Cantalini, C., Atashbar, M.Z., Li, Y., Ghantasala, M.K., Santucci, S., Wlodarski, W., Passacantando, M., 1999. Characterization of sol-gel prepared WO3 thin films as a gas sensor. *J. Vac. Sci. Technol. A* 17, 1873 - 1879.

[51] Takase, A., Miyakawa, K., 1991. Raman study on sol-gel derived tungsten oxides from tungsten ethoxide. *Jpn. J. Appl. Phys.* 30, L1508 - L1511.

[52] Senguttuvan, T.D., Srivastava, V., Tawal, J.S., Mishra, M., Srivastava, S., Jain, K., 2010. Gas sensing properties of nanocrystalline tungsten oxide synthesized by acid precipitation method. *Sens. Actuator B: Chem.* 150, 384 - 388.

[53] Kong, L., Peng, X., Hu, X., 2017. Mechanisms of UV-light promoted removal of As(V) by sulfide from strongly acidic wastewater. Environ. Sci. Technol. 51, 12583 - 12591.

[54] Lee, Y., Ren, Y., Cui, M., Ma, J., Han, Z., Kwon, O., Ko, J., Khim, J., 2021. Rare earth real wastewater treatment by pilot scale using new concept continuous treatment process. *Chemosphere* 279, 130523.

[55] Nordstrom, D.K., Alpers, C.N., 1999. Negative pH, efflorescent mineralogy, and

consequences for environmental restoration at the Iron Mountain Superfund site, California. *Proc. Natl. Acad. Sci. U. S. A.* 96, 3455 - 3462.

[56] Lenoble, V., Deluchat, V., Serpaud, B., Bollinger, J.-C., 2003. Arsenite oxidation and arsenate determination by the molybdene blue method. *Talanta* 61, 267 - 276.

[57] Bader, H., Sturzenegger, V., Hoigné, J., 1988. Photometric method for the determination of low concentrations of hydrogen peroxide by the peroxidase catalyzed oxidation of N,N diethyl-p-phenylenediamine (DPD). *Water Res.* 22, 1109 - 1115.

[58] Phan, H.T.B., Nguyen, A.Q.K., Ahn, Y.-Y., Kim, K., Kim, S., Kim, J., 2022. Visible light-induced degradation of propranolol with peroxymonosulfate as an oxidant and a radical precursor. *Sep. Purif. Technol.* 289, 120764.

[59] Yoo, H.Y., Kim, M.S., Shin, H., Lim, J., 2022. Peroxymonosulfate activation by black $TiO_2$ nanotube arrays under solar light: switching the activation mechanism and enhancing catalytic activity and stability. *J. Hazard. Mater.* 433, 128796.

[60] Priya, A., Arunachalam, P., Selvi, A., Madhavan, J., Al-Mayouf, A.M., 2018. Synthesis of $BiFeWO_6/WO_3$ nanocomposite and its enhanced photocatalytic activity towards degradation of dye under irradiation of light. *Colloids Surf. A Physicochem. Eng. Asp.* 559, 83 - 91.

[61] Shi, H., Yang, S., Han, C., Niu, Z., Li, H., Huang, X., Ma, J., 2019. Fabrication of $Ag/Ag_3PO_4/WO_3$ ternary nanoparticles as superior photocatalyst for phenol degradation under visible light irradiation. *Solid State Sci.* 96, 105967.

[62] Guo, H., Zhou, X., Zhang, Y., Yao, Q., Qian, Y., Chu, H., Chen, J., 2020a. Carbamazepine degradation by heterogeneous activation of peroxymonosulfate with lanthanum cobaltite perovskite: performance, mechanism and toxicity. *J. Environ. Sci.* 91, 10 - 21.

[63] Li, X., Qin, Y., Jia, Y., Wang, R., Ye, Z., Zhou, M., 2022. Persulfate activation by novel iron carbon composites for organic contaminant removal: performance, mechanism, and DFT calculations. *Sep. Purif. Technol.* 281, 119962.

[64] Peng, S., Feng, Y., Liu, Y., Wu, D., 2018. Applicability study on the degradation of acetaminophen via an $H_2O_2$/PDS-based advanced oxidation process using pyrite. *Chemosphere* 212, 438 - 446.

[65] Xu, L., Wang, J., 2012. *Environ. Sci. Technol.* 46, 10145 - 10153.

[66] Yun, E.-T., Yoo, H.-Y., Bae, H., Kim, H.-I., Lee, J., 2017. Exploring the role of persulfate in the activation process: radical precursor versus electron acceptor. *Environ. Sci. Technol.* 51, 10090 - 10099.

[67] Cui, Z., Zeng, D., Tang, T., Liu, J., Xie, C., 2010. Processing－structure－property relationships of $Bi_2WO_6$ nanostructures as visible-light-driven photocatalyst. *J. Hazard. Mater.* 183, 211 - 217.

[68] Singh, R., Dutta, S., 2018. Synthesis and characterization of solar photoactive TiO2 nanoparticles with enhanced structural and optical properties. *Adv. Powder Technol.* 29, 211 – 219.

[69] Kitajima, N., Fukuzumi, S.-i., Ono, Y., 1978. Formation of superoxide ion during the decomposition of hydrogen peroxide on supported metal oxides. *J. Phys. Chem.* 82, 1505 – 1509.

[70] Lousada, C.M., Johansson, A.J., Brinck, T., Jonsson, M., 2012. Mechanism of H2O2 decomposition on transition metal oxide surfaces. *J. Phys. Chem. C* 116, 9533 – 9543.

[71] Lousada, C.M., Jonsson, M., 2010. Kinetics, mechanism, and activation energy of $H_2O_2$ decomposition on the surface of $ZrO_2$. *J. Phys. Chem. C* 114, 11202 – 11208.

[72] Chen, C.-C., Hu, S.-H., Fu, Y.-P., 2015. Effects of surface hydroxyl group density on the photocatalytic activity of $Fe^{3+}$-doped $TiO_2$. *J. Alloys Compd.* 632, 326 – 334.

[73] Agrawal, A., Habibi, H., 1989. Effect of heat treatment on the structure, composition and electrochromic properties of evaporated tungsten oxide films: I. *Thin Solid Films* 169, 257 – 270.

[74] Deepa, M., Srivastava, A.K., Agnihotry, S.A., 2006. Influence of annealing on electrochromic performance of template assisted, electrochemically grown, nanostructured assembly of tungsten oxide. *Acta Mater.* 54, 4583 – 4595.

[75] Enferadi-Kerenkan, A., Ello, A.S., Do, T.-O., 2017. Synthesis, organo-functionalization, and catalytic properties of tungsten oxide nanoparticles as heterogeneous catalyst for oxidative cleavage of oleic acid as a model fatty acid into diacids. *Ind. Eng. Chem. Res.* 56, 10639 – 10647.

[76] Schlotter, P., Pickelmann, L., 1982. The xerogel structure of thermally evaporated tungsten oxide layers. *J. Electron. Mater.* 11, 207 – 236.

[77] Liu, J., Xu, S.-M., Li, Y., Zhang, R., Shao, M., 2020. Facet engineering of $WO_3$ arrays toward highly efficient and stable photoelectrochemical hydrogen generation from natural seawater. *Appl. Catal. B Environ.* 264, 118540.

[78] Yu, S.Q., Ling, Y.H., Wang, R.G., Zhang, J., Qin, F., Zhang, Z.J., 2018. Constructing superhydrophobic $WO_3$@$TiO_2$ nanoflake surface beyond amorphous alloy against electrochemical corrosion on iron steel. *Appl. Surf. Sci.* 436, 527 – 535.

[79] Zhang, N., Li, X., Liu, Y., Long, R., Li, M., Chen, S., Qi, Z., Wang, C., Song, L., Jiang, J., Xiong, Y., 2017. Defective tungsten oxide hydrate nanosheets for boosting aerobic coupling of amines: synergistic catalysis by oxygen vacancies and Brønsted acid sites. *Small* 13, 1701354.

[80] Meng, Z., Fujii, A., Hashishin, T., Wada, N., Sanada, T., Tamaki, J., Kojima, K., Haneoka, H., Suzuki, T., 2015. Morphological and crystal structural control of tungsten trioxide for highly sensitive $NO_2$ gas sensors. *J. Mater. Chem. C* 3, 1134 – 1141.

[81] Wang, H., Ren, X., Liu, Z., Jiang, D., Lv, B., 2019a. Bubble-template synthesis of $WO_3 \cdot 0.5H_2O$ hollow spheres as a high-activity catalyst for catalytic oxidation of benzyl alcohol to benzaldehyde. *CrystEngComm* 21, 1026 - 1033.

[82] Yin, M., Yu, L., Liu, S., 2017. *J. Alloys Compd.* 696, 490 - 497.

[83] Buxton, G.V., Greenstock, C.L., Helman, W.P., Ross, A.B., 1988. Critical review of rate constants for reactions of hydrated electrons, hydrogen atoms and hydroxyl radicals ($\cdot OH/\cdot O^-$) in aqueous solution. *J. Phys. Chem. Ref. Data* 17, 513 - 886.

[84] Bielski, B.H.J., Cabelli, D.E., Arudi, R.L., Ross, A.B., 1985. Reactivity of HO2/O2− radicals in aqueous solution. *J. Phys. Chem. Ref. Data* 14, 1041 - 1100.

[85] Guo, K., Zheng, S., Zhang, X., Zhao, L., Ji, S., Chen, C., Wu, Z., Wang, D., Fang, J., 2020b. Roles of bromine radicals and hydroxyl radicals in the degradation of micropollutants by the UV/bromine process. *Environ. Sci. Technol.*54, 6415 - 6426.

[86] Wang, J., Quan, X., Chen, S., Yu, H., Chen, Y., 2019b. Performing homogeneous catalytic ozonation using heterogeneous $Mn^{2+}$-bonded oxidized carbon nanotubes by self-driven pH variation induced reversible desorption and adsorption of $Mn^{2+}$. *Environ. Sci.: Nano* 6, 1932 - 1940.

[87] Armstrong, D.A., Huie, R.E., Koppenol, W.H., Lymar, S.V., Merényi, G., Neta, P., Ruscic, B., Stanbury, D.M., Steenken, S., Wardman, P., 2015. Standard electrode potentials involving radicals in aqueous solution: inorganic radicals (IUPAC Technical Report). *Pure Appl. Chem.* 87, 1139 - 1150.

[88] Zhang, Y., Yang, W., Zhang, K., Kumaravel, A., Zhang, Y., 2021. Sulfite activation by glucose derived carbon catalysts for As(III) oxidation: the role of ketonic functional groups and conductivity. *Environ. Sci. Technol.* 55, 11961 - 11969.

[89] Xiong, Y., Liu, X., Zhang, T.C., Yuan, S., 2021. *ACS Appl. Nano Mater.* 4, 7404 - 7415.

[90] Ding, W., Huang, X., Zhang, W., Wu, F., Li, J., 2019. Sulfite activation by a low-leaching silica supported copper catalyst for oxidation of As(III) in water at circumneutral pH. *Chem. Eng. J.* 359, 1518 - 1526.

[91] Lei, D., Xue, J., Peng, X., Li, S., Bi, Q., Tang, C., Zhang, L., 2021. Oxalate enhanced synergistic removal of chromium(VI) and arsenic(III) over $ZnFe_2O_4$/g-$C_3N_4$: Z-scheme charge transfer pathway and photo-Fenton like reaction. *Appl. Catal. B Environ.* 282, 119578.

[92] Kim, J., Monllor-Satoca, D., Choi, W., 2012. Simultaneous production of hydrogen with the degradation of organic pollutants using $TiO_2$ photocatalyst modified with dual surface components. *Energy Environ. Sci.* 5, 7647 - 7656.

[93] Ryu, J., Kim, W., Kim, J., Ju, J., Kim, J., 2017. Is surface fluorination of TiO2 effective for water purification? The degradation vs. mineralization of phenolic pollutants. *Catal. Today* 282, 24 - 30.

[94] Qin, Y., Faheem, A., Jia, G., Hu, Y., 2020. Self-assembled $Fe^{3+}$@spores as a sustainable heterogeneous Fenton catalyst for arsenite removal. *J. Environ. Chem. Eng.* 8, 104485.

[95] Gao, L., Hao, M., Bu, F., Ji, C., Qu, R., Sun, C., Zhang, Y., 2020. As(III) removal by Fe(III) amidoximated PAN in the presence of $H_2O_2$ through simultaneous oxidation and adsorption. *Water Supply* 20, 565 - 573.

[96] Kang, Y.-G., Yoon, H., Lee, W., Kim, E.-j., Chang, Y.-S., 2018. Comparative study of peroxide oxidants activated by nZVI: removal of 1,4-dioxane and arsenic(III) in contaminated waters. *Chem. Eng. J.* 334, 2511 - 2519.

[97] Su, J., Lyu, T., Cooper, M., Mortimer, R.J.G., Pan, G., 2021. Efficient arsenic removal by a bifunctional heterogeneous catalyst through simultaneous hydrogen peroxide ($H_2O_2$) catalytic oxidation and adsorption. *J. Clean. Prod.* 325, 129329.

KOPRI
극지연구소

## FIGURES

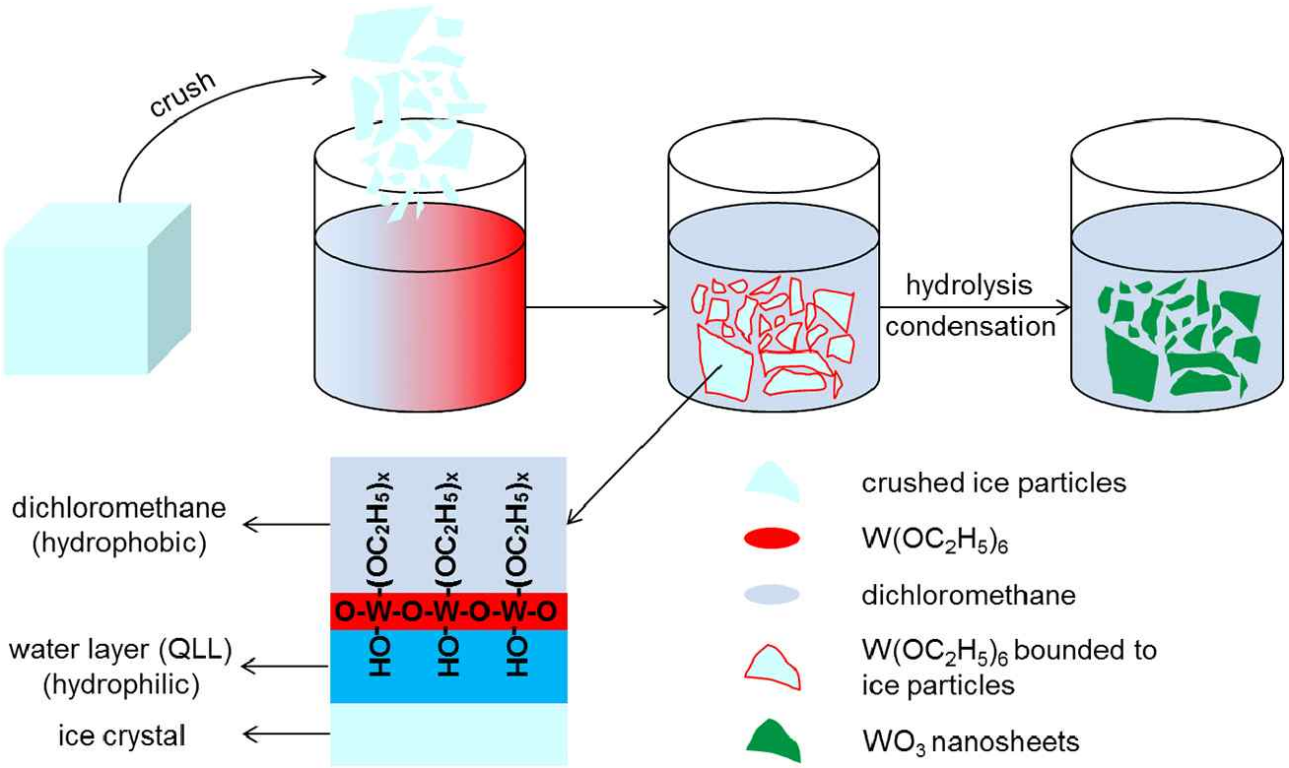



Fig. 1. Schematic diagram of the synthesis of $WO_3$ nanosheets using an ice particle template.

KOPRI
극지연구소

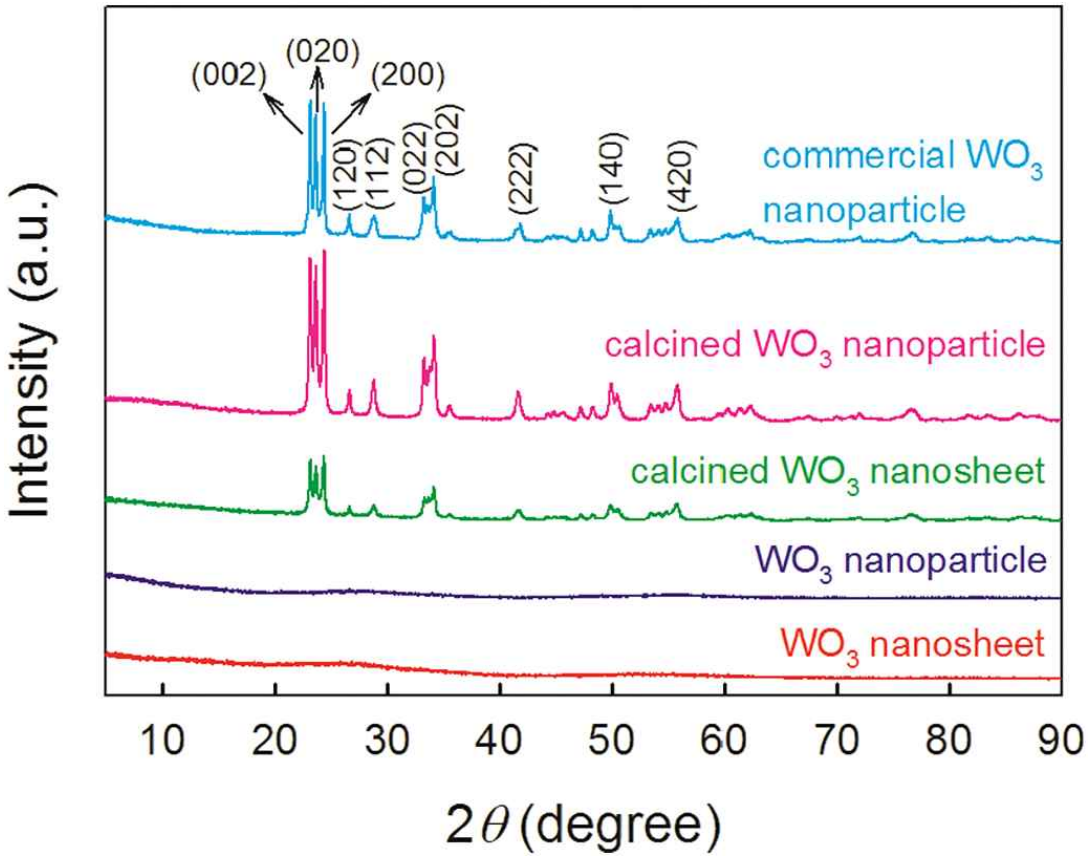



Fig. 2. XRD patterns of the $WO_3$ nanosheets, $WO_3$ nanoparticles, calcined WOS nanosheets, calcined $WO_3$ nanoparticles, and commercial $WO_3$ nanoparticles

KOPRI
극지연구소

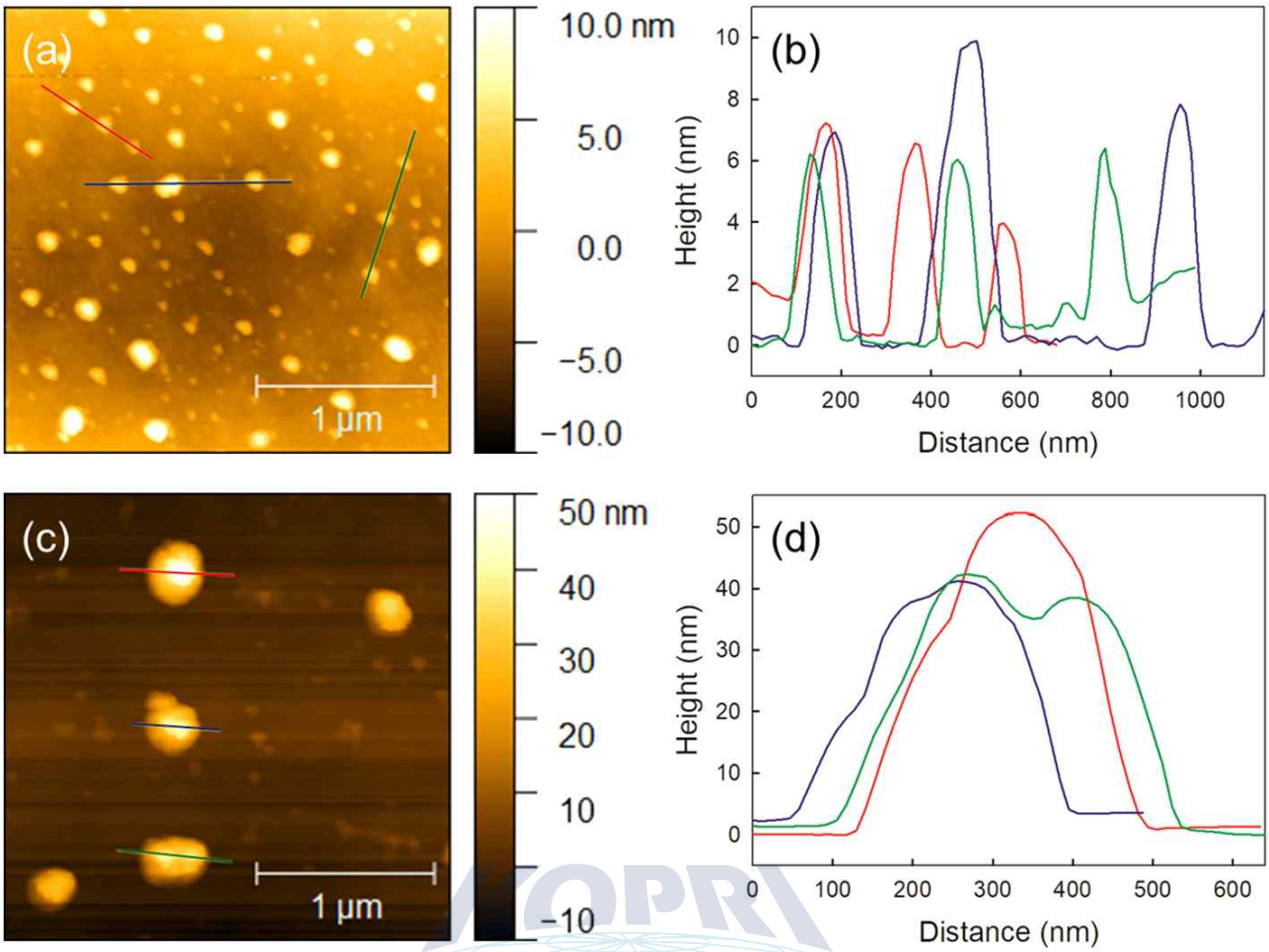



Fig. 3. AFM images and thicknesses of the (a and b) WO3 nanosheets and (c and d) nanoparticles.

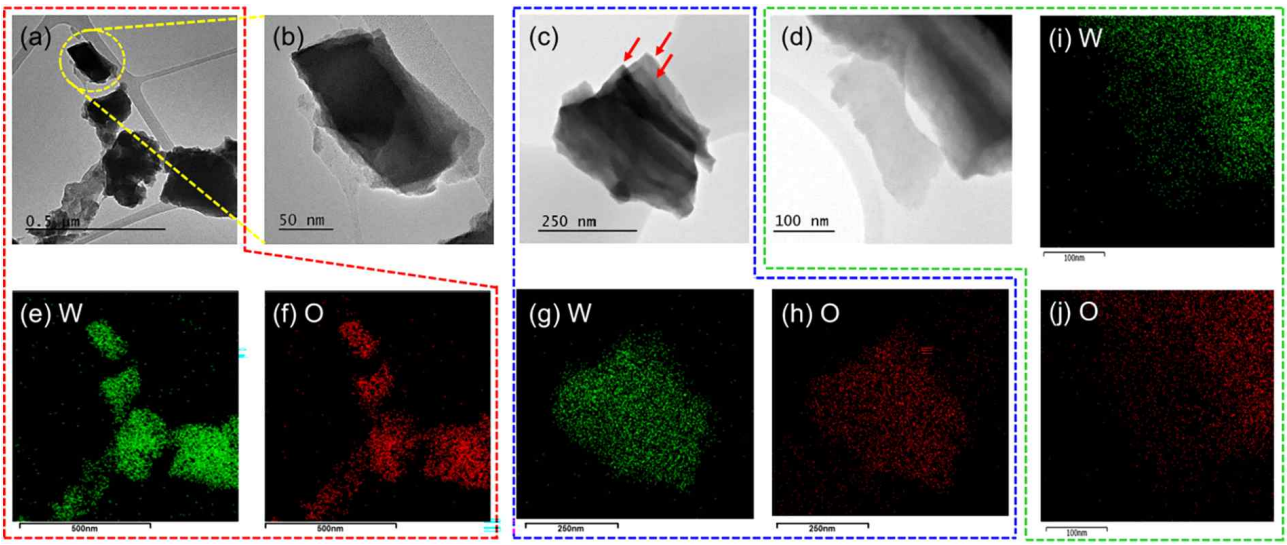



Fig. 4. (a-d) TEM images of the $WO_3$ nanosheets and elemental mapping images of (e, g, and I) W and (f, h, and j) O. The arrows shown in panel (c) indicate the edges of the few-layer $WO_3$ nanosheets.

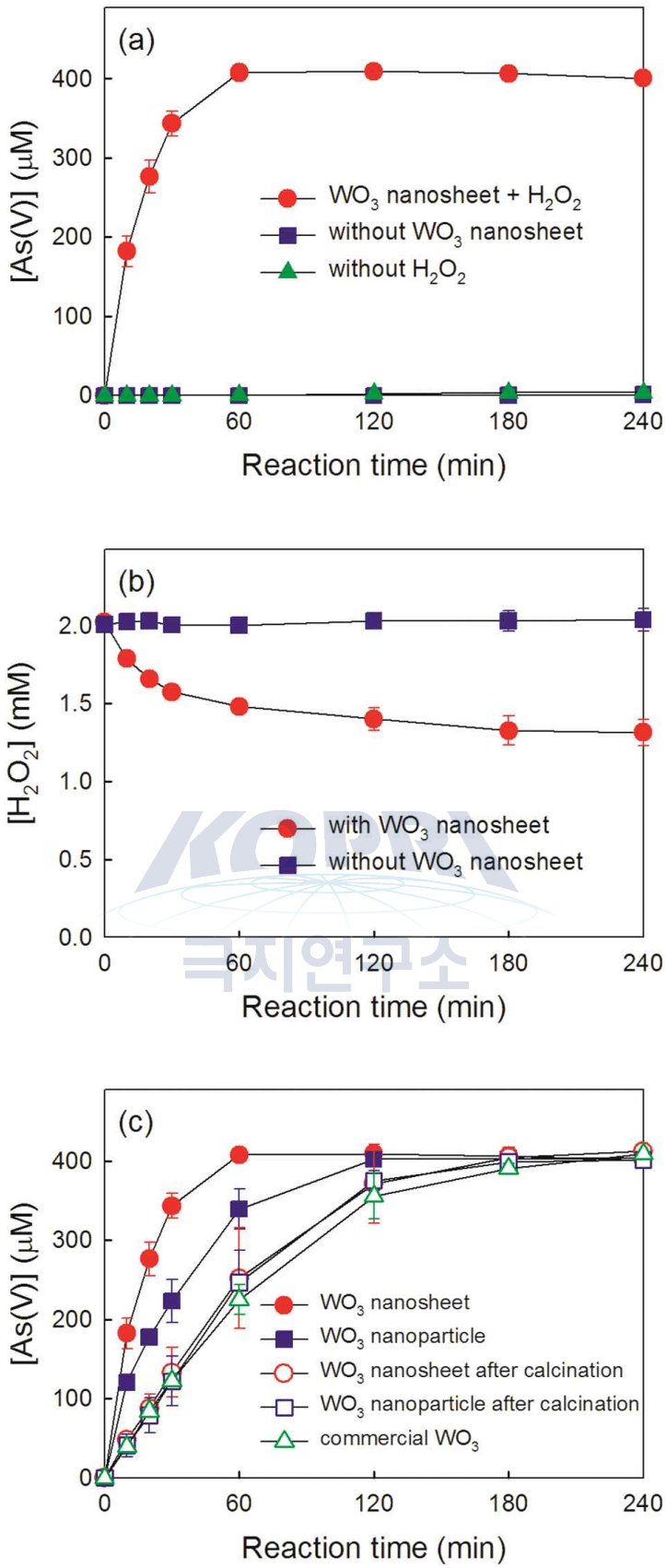



Fig. 5. Time profiles of the (a) As(V) and (b) $H_2O_2$ concentrations during As(III) oxidation in the $WO_3$ nanosheet/$H_2O_2$ system. (c) Production of As(V) in the presence of $H_2O_2$ using different catalysts. Experimental conditions: [catalyst] = 0.5 g/L, [As(III)]= 400 μM, [$H_2O_2$] = 2 mM, and pH=2.5.

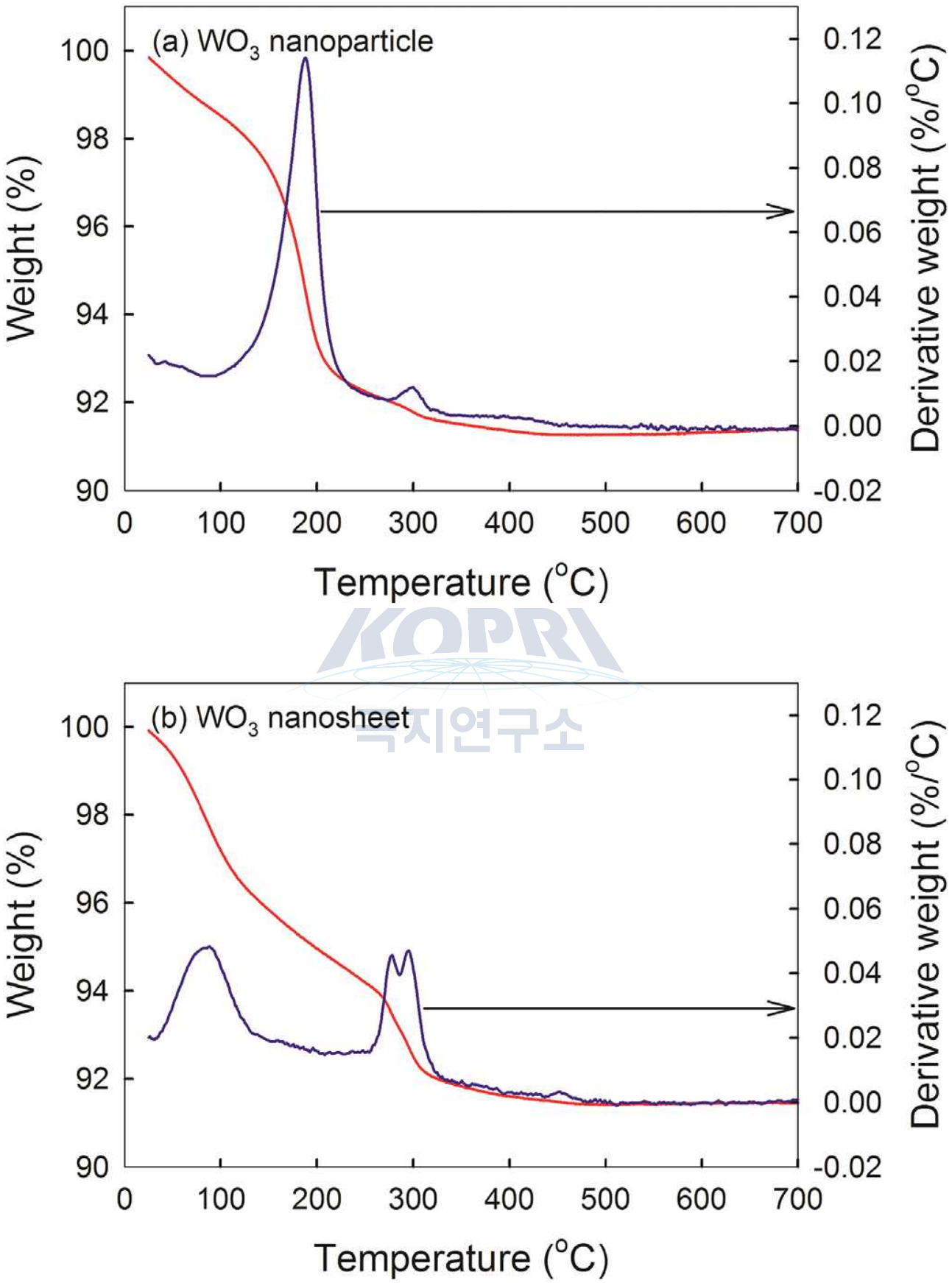



Fig. 6. TGA curves of the (a) $WO_3$ nanoparticles and (b) nanosheets.

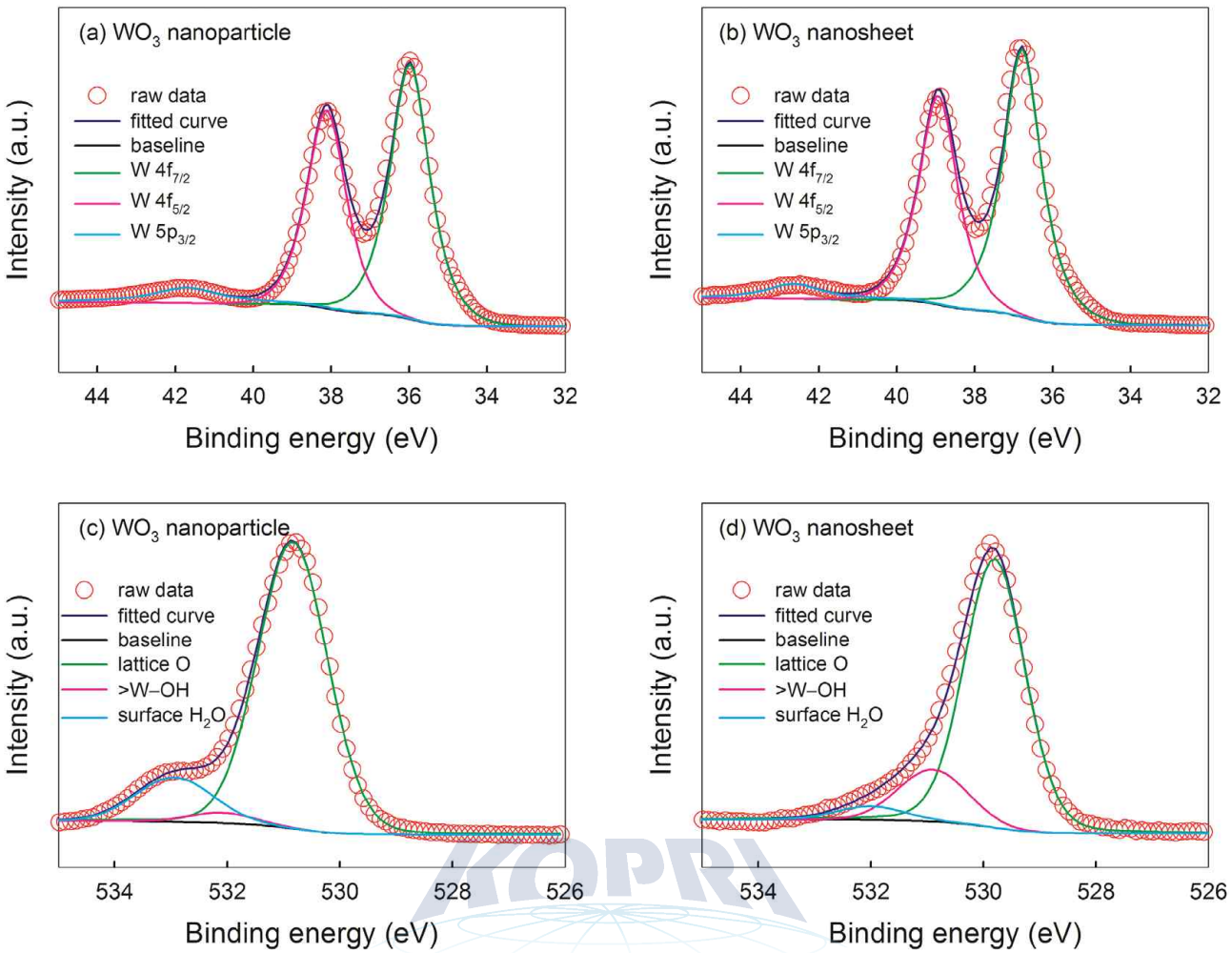



Fig. 7. (a and b) W 4f and (c and d) O 1s XPS spectra of the $WO_3$ nanoparticles and nanosheets.

KOPRI 극지연구소

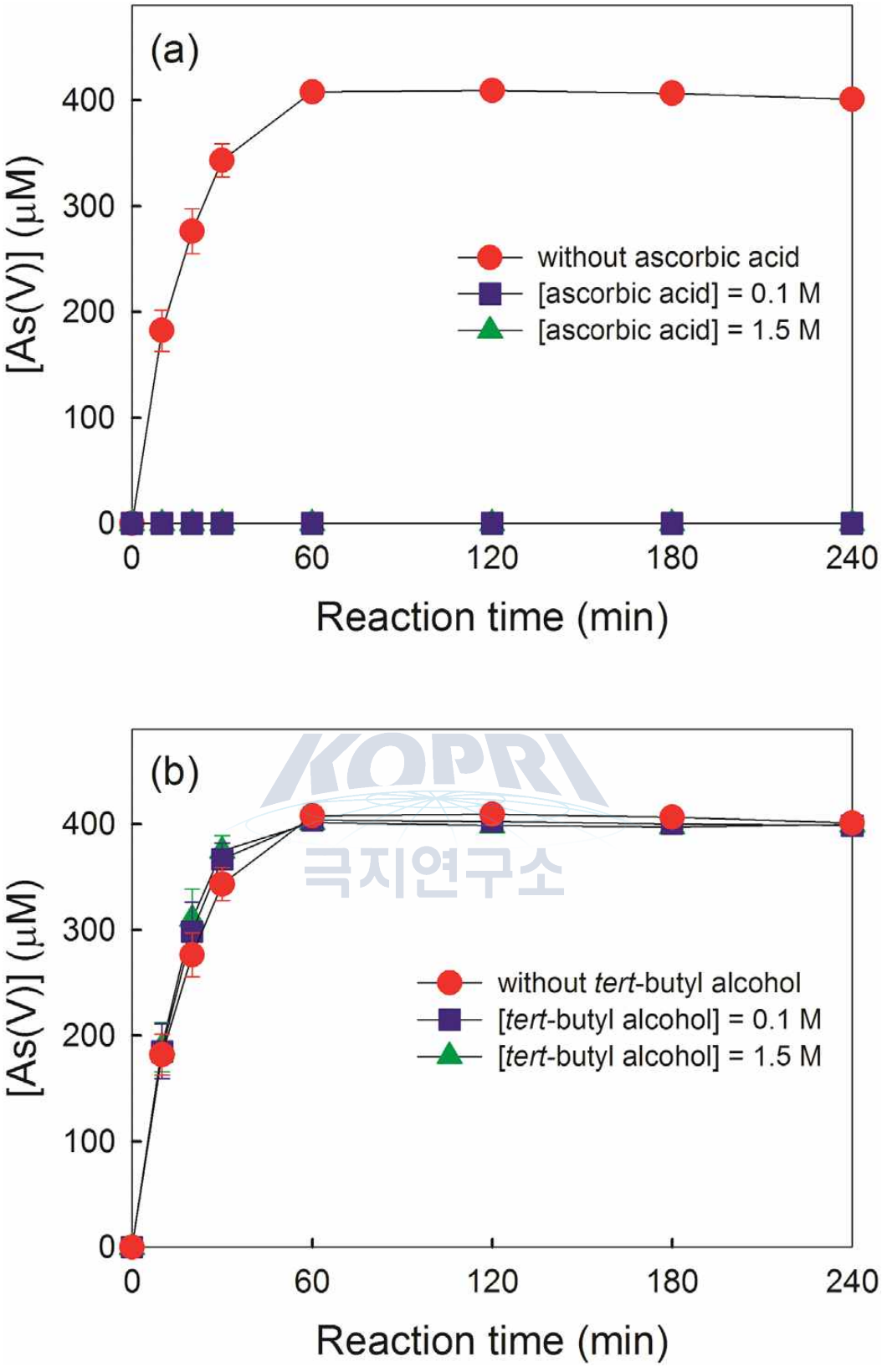



Fig. 8. Effects of (a) ascorbic acid ($HO_2^{\bullet}$ scavenger) and (b) tert-butyl alcohol ($^{\bullet}OH$ scavenger) on As(III) oxidation in the WO3 nanosheet/$H_2O_2$ system. Experimental conditions: [catalyst] = 0.5 g/L, [As(III)] = 400 μM, [$H_2O_2$] = 2 mM, [ascorbic acid] in panel (a)=[tert-butyl alcohol] in panel (b)=0.1 or 1.5 M, and pH = 2.5.

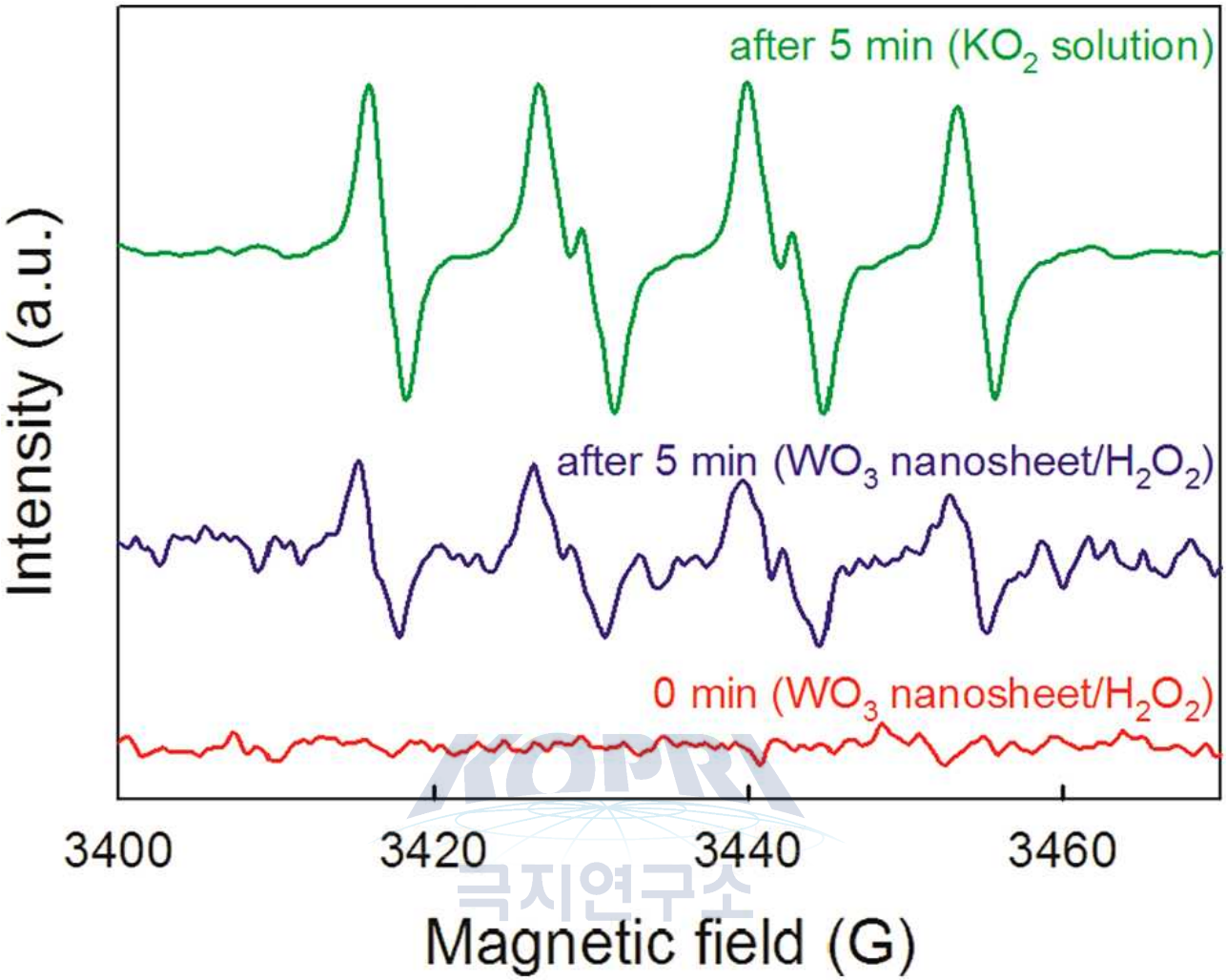



Fig. 9. ESR spectra of the BMPO-radical adducts produced in the $WO_3$ nanosheet/$H_2O_2$ system and $KO_2$ solution. Experimental conditions: [catalyst] = 0.5 g/L, [$H_2O_2$] = 2 mM, [$KO_2$] = 2 g/L, [BMPO]=5 mM, and pH=2.5.

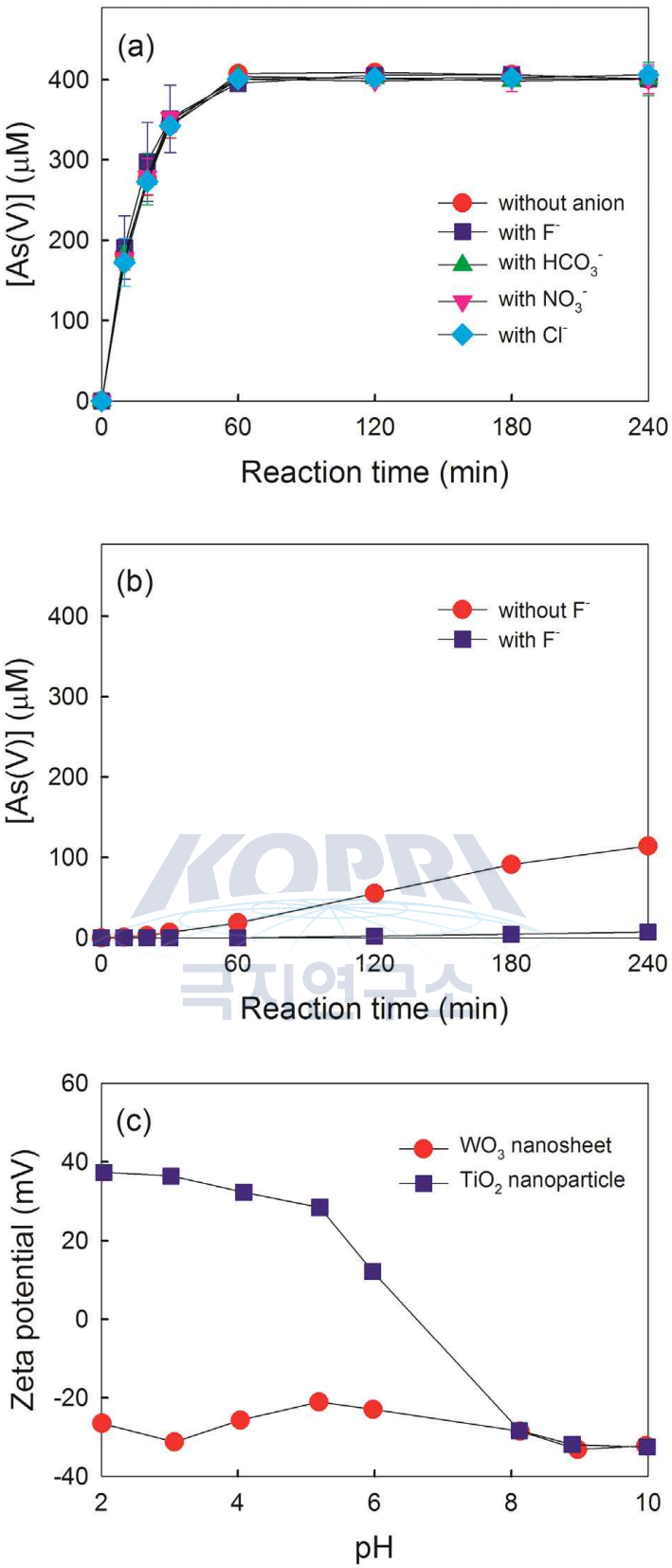



Fig. 10. Effects of various anions on the kinetics of As(III) oxidation in the (a) $WO_3$ nanosheet/$H_2O_2$ system and (b) $TiO_2$ nanoparticle (Aeroxide P25)/$H_2O_2$ system.(c) Zeta potentials of the $WO_3$ nanosheets and $TiO_2$ nanoparticles (Aeroxide P25) as functions of pH. Experimental conditions in panels (a) and (b): [catalyst]= 0.5 g/L, [As(III)] = 400 μM, [H2O2] = 2 mM, [anion] = 10 mM, and pH= 2.5.

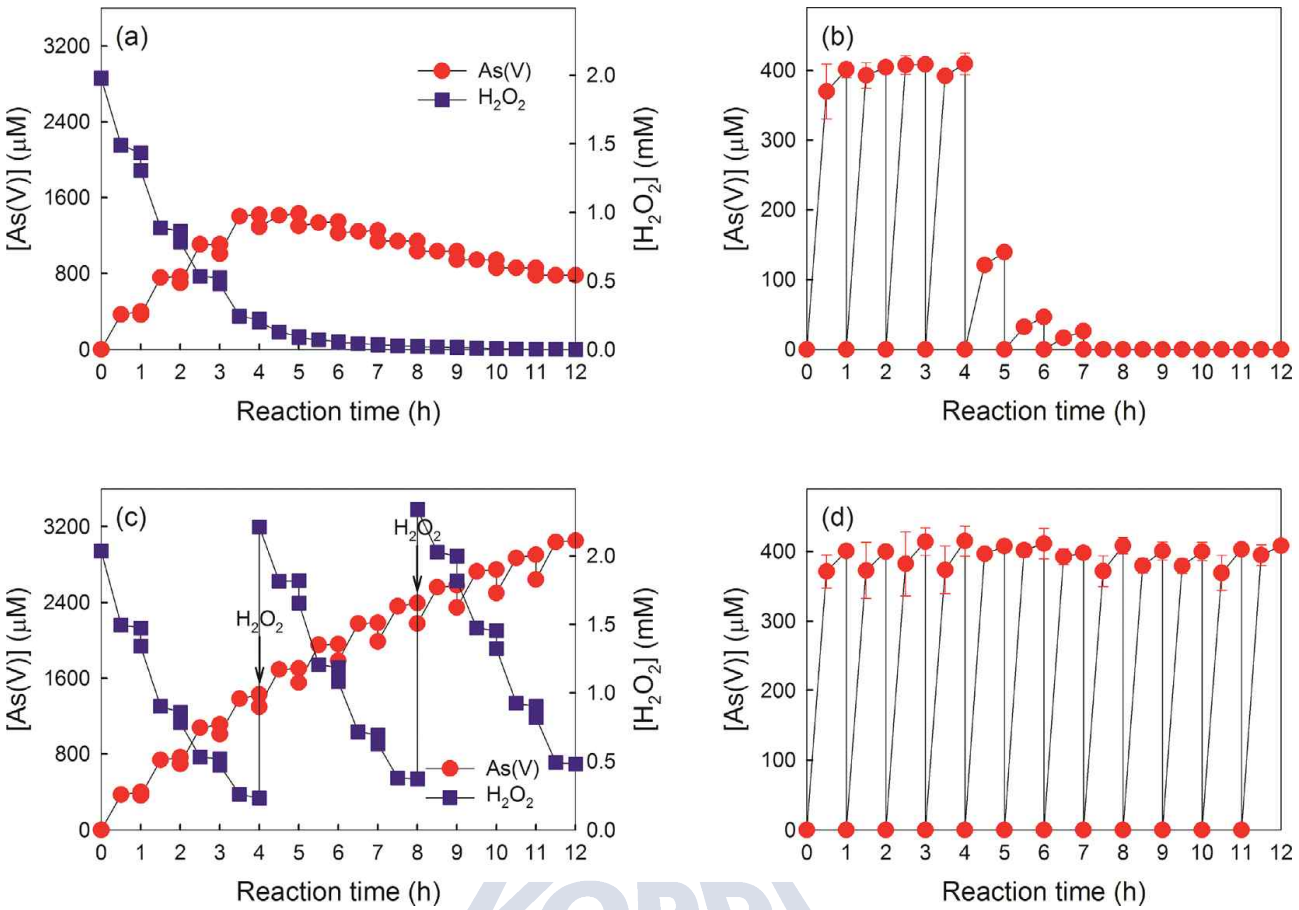



Fig. 11. Repeated cycles of As(III) oxidation in the $WO_3$ nanosheet/$H_2O_2$ system (a and b) without and (c and d) with the injection of additional $H_2O_2$. Experimental conditions: [catalyst] = 0.5 g/L, initial [As(III)] = injected [As(III)]= 400 μM, initial $[H_2O_2]$ = injected $[H_2O_2]$ in panels (c) and (d) = 2 mM, and pH = 2.5. In panels (b) and (d), the concentrations of As(V) are calculated by subtracting the initial concentration of As(V) in each cycle from the final concentration of As(V) in each cycle.

KOPRI 극지연구소

# 제 13 절. Frozen Clay Minerals as a Potential Source of Bioavailable Iron and Magnetite⑬

Hyun Young Chung[1, 2], Jaewoo Jung[3], Kiho Yang[4], Jungwon Kim[5] and Kitae Kim[1, 2*]

[1]Korea Polar Research Institute
[2]University of Science and Technology
[3]Korea Institute of Ocean Science & Technology
[4]Pusan National University
[5]Hallym University

## Abstract

Iron (Fe) is an essential micronutrient that affects biological production. Iron-containing clay minerals are an important source of bioavailable iron. However, the dissolution of iron-containing clay minerals at temperatures below the freezing point has not been investigated. Here, we demonstrate the enhanced reductive dissolution of iron from a clay mineral in ice in the presence of iodide ($I^-$) as the electron donor. The accelerated production of dissolved iron in the frozen state was irreversible, and the freeze concentration effect was considered the main driving force. Furthermore, the formation of magnetite ($Fe_3O_4$) after the freezing process was observed using transmission electron microscopy analysis. Our results suggest a new mechanism of accelerated abiotic reduction of Fe(III) in clay minerals, which may release bioavailable iron, Fe(II), and reactive iodine species into the natural environment. We also propose a novel process for magnetite formation in ice. The freezing process can serve as a source of bioavailable iron or act as a sink, leading to the formation of magnetite.

## 1. Introduction

Chemical reactions are known to accelerate at high temperatures, as described by the Arrhenius equation. However, in contrast to this general phenomenon, some reactions can be enhanced in a frozen state. Therefore, the significance of ice as a medium for chemical transformations has gradually been accepted. Snowpacks in polar regions play an important role in formaldehyde production and affect the oxidative capacity of the atmosphere.[1] Ice has also been suggested to play a key role in the destruction of ozone in the stratosphere in polar regions.[2] The transformation of halogen species, including iodine and bromine, into

⑬ 본 연구는 본 과제(PE23120) 및 (KOPRI PM23030, KIMST 15250103)로 수행되었으며, 결과는 *Environ. Sci. Technol.* 2023, 57, 19805 - 19816에 출간되었다.

reactive forms in sea ice or snowpacks and their release into the atmosphere in polar regions have also been reported.[3-5] With regard to chemical reactions with minerals, the chemical weathering of granite proceeds in both a frozen state and the aqueous phase.[6] Moreover, iron oxide dissolution can be enhanced in ice in the presence of organic acids.[7] The freeze concentration effect, producing an increased concentration of solutes at ice grain boundaries during ice formation, has been suggested as the main cause of these enhanced chemical reactions in ice.[1]

Iron is the fourth most abundant element in the earth's continental crust, comprising 6.7% by weight.[8] Iron is also important in biochemical processes being used as an electron transfer agent in metabolic processes such as photosynthesis and respiration.[9] The high solubility of Fe(II) compared to Fe(III) results in enhanced bioavailability of this oxidation state, which can be readily utilized by living organisms.[10] However, in environments rich in oxygen, iron typically exists as ferric iron, Fe(III).[11] To overcome the deficiency in bioavailable iron, microorganisms release siderophores, which are iron-chelating compounds.[12] Plants also release chelating organic compounds known as phytosiderophores to increase iron solubility.[13] Fe(II) is also crucial in marine environments because it constitutes an essential micronutrient for the growth and metabolism of organisms.[14] Therefore, despite its abundance, iron can be a limiting factor for organisms, depending on environmental circumstances. Fe(III) reduction to Fe(II) is generally coupled with the remineralization of organic matter, which is oxidized in the surface sediments of marine and freshwater environments.[15] Primary productivity in particular is limited by the insufficient iron availability in high-nutrient low-chlorophyll (HNLC) regions.[16,17] Previous studies on oceanic iron inputs have focused on aeolian dust, iron-rich sediments in shallow water, and minerals of hydrothermal origin.[18] It was also reported that ice sheets and icebergs can release bioavailable iron to the oceans in Antarctica.[19,20] The influx of iron predominantly originates from atmospheric deposition of iron-rich dust in open marine environments.[21] Iron-containing dust becomes more soluble during transport and undergoes substantial atmospheric processing.[22] However, the sources and mechanisms of Fe(II) entering oceans are not yet fully understood. Assuming an equilibrium between iron supply and consumption by phytoplankton,[23] there still appears to be a ~10% deficiency in supply for phytoplankton assimilation.

Iron-bearing clay minerals are ubiquitous in the environment, ranging from the atmosphere to soil and sediments.[24,25] Dithionite has been extensively employed as a chemical reductant for investigating the redox cycling of iron in clay minerals.[26] In natural environments, microbial activities can reduce iron in clay minerals,[27] and the microbial dissolution of clay minerals containing iron has been intensively studied due to their status as an important iron source for microbial metabolism.[28] Microbes can reduce iron in clay

minerals by modifying the surface properties and grain sizes of iron-rich smectites,[29] and organic matter such as humic substances can serve as an electron shuttle for facilitating these processes.[30] When Fe(II) is dissolved in atmospheric dust, the mineral composition of the dust affects the amount of released Fe(II).[31] Specifically, a higher content of clay minerals substantially contributes to iron dissolution from atmospheric dust (despite their low iron content) owing to their higher iron solubility compared to that of iron oxides.[32] The composition of dust tends to become enriched with clay minerals as the dust is transported farther away from the source region since heavier quartz particles more easily fall out of the atmosphere.[33] The effects of solar radiation, acidity, and temperature on the dissolution of clay minerals in the atmosphere have been investigated,[34] and the reduction of Fe(III) containing clay minerals has been studied at various temperatures ranging from room temperature (25 °C) to temperatures of up to 115 °C;[35] however, this phenomenon has not yet been investigated at freezing temperatures. It has recently been suggested that Fe(II) can be released from iron-containing dust trapped in ice and snow via the freeze-concentration effect.[7] Furthermore, it is known that biogeochemical reactions at low temperatures can modify mineral structure and chemistry,[36] which are generally sensitive to redox conditions in the system.[37] Previous studies have reported that physicochemical changes in bioreduced clay minerals increase the amount of residual Fe(II) in the clay structure and solution form of iron, suggesting that the release of Fe(II) from sediments could be a consequence of microbial structural Fe(III) reduction in clay minerals.[38] However, none of these prior studies have considered the dissolution of iron-bearing clay minerals accompanying the abiotic dissolution of iron during the freezing process.

Iodine species in polar regions play important roles such as controlling oxidative capacity in the atmosphere, ozone depletion events, oxidation of mercury, and formation of ultrafine aerosol particles as cloud condensation nuclei.[39] In spite of the presence of reactive oxygen species in seawater and aerosols, the predominant forms of iodine species found in aerosols and seawater are iodide ($I^-$) and iodate ($IO_3^-$).[40,41] Iodine species found in snow, sea ice, seawater, surface water, and atmospheric aerosols mainly consist of $I^-$ and $IO_3^-$. Both iron-containing clay minerals and iodide are ubiquitous in various environments, making their coexistence fairly common. The concentration of iodine in rain and snow falls within the range of 0.5 - 20 μg $L^{-1}$.[42] Iodide has been detected in atmospheric aerosols across a variety of environments and may be present across a wide range of nanomolar concentrations.[39,43] It has been reported that snowpack in Antarctica can contain several nanomolar concentrations of total iodine.[5] Iodide concentrations ranging from a few to several tens of nanomolar have been found in the sea ice of the Antarctic Ocean.[44] The average concentration of total iodide in seawater has been reported as 58 μg $L^{-1}$.[42] Recently, the active redox transformation between iron oxide and iodide in a frozen state

has been reported.[45] Here, we used iodide as a model reductant to function as an electron donor for the dissolution of iron-containing clay minerals. Nontronite, a representative Fe-rich smectite clay mineral and the most reducible clay mineral, was used as an iron source.[46] The high reducibility of nontronite is related to its expandability and layer charge.[47] Unlike previous studies, we conducted our experiments under aerobic conditions. Our findings may demonstrate the feasibility of iron dissolution in glacial and atmospheric environments and suggest a new pathway for iron supply to the HNLC regions.

## 2. Materials and Methods

### 2.1. Materials

Nontronite (NAu-2) ($M^{+}_{0.72}(Si_{7.55}A_{l0.45})-(Fe_{3.83}Mg_{0.05})O_{20}(OH)_4$), purchased from the source clay repository of the Clay Minerals Society (CMS) located at Purdue University, Indiana, USA, was used as an Fe-containing clay mineral. NAu-2 contains 23.4% total Fe content, and Fe in its structure is almost entirely Fe(III) (99.4%).[48] Fe(III) mostly exists as octahedral Fe(III), with a small amount of tetrahedral Fe(III) in NAu-2.[49] Mössbauer spectroscopy and X-ray diffraction analyses revealed that NAu-2 consisted of pure nontronite.[50] Clay fractions (less than 0.2 μm) were separated using gravitational settling in a distilled water column and then freeze-dried to produce a homogeneous clay mineral without any impurities. Potassium iodide (KI; BioUltra, ≥99.5%; Sigma-Aldrich) was used to provide iodide to the samples. Sulfuric acid ($H_2SO_4$; ACS reagent, 95.0 - 98.0%; Sigma-Aldrich) was used to adjust the pH of the samples. The ferrozine reagent was prepared by adding $10^{-2}$ mol $L^{-1}$ PDT disulfonate monosodium salt hydrate ($C_{20}H_{13}N_4NaO_6S_2 \cdot xH_2O$; 97%; Sigma-Aldrich) to $10^{-1}$ mol $L^{-1}$ ammonium acetate ($CH_3COONH_4$; BioXtra, ≥98%; Sigma-Aldrich) solution. Iron(II) sulfate heptahydrate ($FeSO_4 \cdot 7H_2O$; ≥99.0%; Sigma-Aldrich) was used to calibrate when analyzing Fe(II) and total iron. The iron standard for ICP (no. 43149; Supelco, Sigma-Aldrich) was used as a certified reference material (CRM) for inductively coupled plasma atomic emission spectroscopy (ICP-OES) analysis. When the CRM was diluted to contain 8.71 μM total iron, the average concentration was 8.95 ± 0.12 μM. The calculated accuracy for the test was 2.76%. Deionized water (DW) used in this experiment was prepared using a Barnstead water purification system and checked before using it to determine whether it had 18.2 MΩ·cm of resistivity. As reactors, 15 mL conical centrifuge tubes (VWR, Radnor, PA, USA) were used. A disposable Advantec PTFE 0.20 μm syringe filter and Henke-Ject 10 mL (12 mL) syringe were used to remove the particles from the aqueous and thawed ice samples after the reactions. At acidic pHs, the particles tend to aggregate and form larger particles due to the electrostatic attraction between hydrogen ions and the negatively charged

KOPRI 극지연구소

surfaces of the particles.[51] Therefore, clay particles can aggregate to larger than 0.2 μm during filtering. Three solution samples containing 0.2 g $L^{-1}$ NAu-2 were prepared and filtered immediately to test whether the filter size was adequate to effectively eliminate NAu-2 particles. Filtrate sample analysis using ICP-OES showed an average iron concentration of 0.007 ± 0.007 μM. This was significantly lower than that in the experiments conducted in this study, indicating the effective removal of NAu-2 particles by a 0.2 μm filter.

### 2.2. Batch Experiment

Bulk solution samples were prepared by mixing nontronite and DW with a concentrated potassium iodide solution in a beaker. The initial pH of the sample containing 0.2 g $L^{-1}$ nontronite and 200 μM $I^-$ was 8.68. In this experiment, the control denotes the sample prepared without $I^-$, and other conditions were equal ([NAu-2] = 0.2 g L - 1, adjusted to pH 3) to identify the effect of $I^-$. The experimental conditions followed previous studies investigating the dissolution of iron oxides induced by freezing processes.[45,52] After adjusting the pH of the samples to the desired pH, the samples were dispensed into the reactor so that each aliquot contained 10 mL of sample. The ice samples were placed in an ethanol-circulating cryogenic bath (precooled at −20 °C) to be frozen. Aqueous samples were stored at room temperature. In this experiment, time zero (t = 0) was defined as the point at which the temperature of the sample was controlled. After the reaction, the ice samples were thawed in a beaker filled with lukewarm water (30 - 40 °C) on a hot plate. The ice samples were thoroughly thawed for <10 min. An aliquot (1 mL) was extracted from each sample, transferred to unused tubes before filtering, and kept at −70 °C for electron microscopy analyses. The residue was filtered using a syringe filter, and the filtrate was analyzed as follows. The batch experiment was conducted in triplicates for reproducibility. All graphs, except for the full spectra of iodine species analyzed using UV/vis spectroscopy, were plotted with error bars representing triplicate measurements.

### 2.3. Chemical and Microscopic Analyses

A pH meter (Orion 3-Star; Thermo Fisher Scientific, Waltham, MA, USA) was used to measure the pH when adjusting the pH of the solution samples. The $I^-$ concentration was analyzed using an ion chromatography system (Aquion, Dionex, Thermo Fisher Scientific, Waltham, MA, USA) equipped with an AERS 500 suppressor, an AS 23 4 mm column, and an AG 23 guard column. The eluent was prepared to contain 0.8 mM sodium bicarbonate ($NaHCO_3$) and 4.5 mM sodium carbonate ($Na_2CO_3$) and flown at 1.0 mL $min^{-1}$. The $I^-$ peak was also observed by using a UV/vis spectrophotometer (Cary 8454, Agilent Technologies, Santa Clara, CA, USA) at a wavelength of approximately 424 nm. A 1 cm

path length cell was used in all analyses using a UV/vis spectrophotometer. $I_3^-$ and $I_2$ peaks were also observed at 353 and 460 nm using a UV/vis spectrophotometer. The concentrations of $I_3^-$ and $I_2$ in the solution were calculated from the absorbance at the peak ($\varepsilon m$ = 26,400 and 746 $M^{-1}$ $cm^{-1}$, respectively).[53] For $Fe(II)_{aq}$ concentration analysis, 50 µL of ferrozine reagent was added to 1.5 mL of sample, and the absorbance was obtained at 562 nm after 1 h of color development in the dark. Total dissolved Fe ($Fe(II)_{aq}$ + $Fe(III)_{aq}$) concentrations were determined with ICP-OES (ICAP 7600; Thermo Fisher Scientific, Bremen, Germany). Microscopy (Lens HC PLAN 10 × 20 BR, L 50×/0.50; Leica, Wetzlar, Germany) was used to observe ice grain boundary images. A temperature-controlled stage (FTIR 600; Linkam Scientific, Salfords, UK) and a water circulating system were used to freeze the sample and maintain the temperature at −20 °C during the observation.

### 2.4. Electron Microscopy Analyses

A drop of the suspension was deposited on a Formvar-covered copper grid (200 mesh; Ted Pella, Redding, CA, USA) and dried overnight at room temperature.[54] During sample preparation, all procedures were performed on a clean bench to minimize contamination. TEM images were obtained using a Talos F200X TEM equipped with energy-dispersive X-ray spectroscopy (EDS; Talos F200X, Thermo Fisher Scientific) in scanning transmission electron microscopy (STEM) mode. Lattice fringe images were obtained at high magnification (×50,000) to determine the dissolution reprecipitation of Fe-bearing minerals. Bragg's reflections for the NAu-2 structure were measured by selected area electron diffraction (SAED) patterns.

## 3. Results and Discussion

### 3.1. Enhanced Reductive Dissolution of Fe(III) from Nontronite in Ice

After 24 h, 0.89 (±0.05) µM total dissolved Fe and 0.60 (±0.07) µM Fe(II) were extracted from the dissolution of nontronite in the aqueous phase of control samples (Figure 1). The dissolution of total Fe and Fe(II) was not considerably different between the aqueous samples to which $I^-$ was added and the control samples (1.04 ± 0.01 µM total Fe and 0.37 ± 0.01 µM Fe(II), respectively). However, the dissolution of total Fe (3.79 ± 0.10 µM) and Fe(II) (2.65 ± 0.07 µM) was significantly enhanced in the ice samples when $I^-$ was added. NAu-2 utilized in the experiment comprised 23.4% (w/w) of total iron within its structure, with nearly all of it existing as Fe(III) (99.4%). Consequently, 0.2 g $L^{-1}$ NAu-2 implies a total iron content of approximately 46.8 ppm. In ice samples containing 200 ppm of NAu-2 and 200 µM iodide at pH 3, approximately 0.21 ppm of total iron and 0.15 ppm of soluble

Fe(II) are generated. These calculations indicate that the described freezing process results in the production of approximately 0.45% soluble total iron and 0.32% Fe(II). Despite the low yield of dissolved iron, the reductive dissolution of iron from nontronite was obviously enhanced in ice samples compared to aqueous samples. It should be noted that the samples at t = 0 consisted of the aqueous samples that were immediately filtered because ice samples could not be frozen at this point, and thus no comparison between ice samples and aqueous samples was made at 0 h (t = 0). Without the addition of $I^-$, no significant increase in Fe dissolution was observed in ice samples (1.00 ± 0.03 μM total Fe and 0.37 ± 0.02 μM Fe(II)). In the first hour of the reaction, the dissolution of total Fe and Fe(II) from nontronite in the ice samples in the presence of iodide increased rapidly compared to that in the aqueous samples. When $I^-$ was added, approximately 3.6 times the total Fe and 7.2 times the Fe(II) were dissolved in ice compared to that in aqueous solutions (after 24 h). Although initial nontronite contained a negligible amount of Fe(II),[49] the form of most of the dissolved Fe in filtrate from nontronite in ice samples was reduced form of Fe (Fe(II), approximately 74% of total dissolved Fe). The production of dissolved Fe(II) and total Fe gradually increased, and the solution became almost complete within 12 h of the beginning of the reaction (Figure 1). In contrast, the production of $I_3^-$ and $I_2$ and the decrease in $I^-$ continued after 12 h (Figure 2). Thus, the reaction of iodide oxidation to $I_3^-$ and $I_2$ proceeded independently of the reductive dissolution of nontronite after 12 h. The cessation of the reduction before all Fe(III) of nontronite is exhausted is related to the inhibition of electron transfer from iodide, induced by resorbed Fe(II) or the formation of magnetite on the NAu-2 surface.[50] Fe(II) sorption or precipitation at the surface of nontronite released from the reduction of Fe(III) can inhibit further reduction.[55]

Tests were conducted to examine the relationship between pH and the dissolution of iron as well as the transformation of iodine species. Dissolved total iron concentration in the experiment conducted at pH 4 was approximately 1 order of magnitude lower than that at pH 3 (Figure S1a). After 24 h at pH 4, 0.08 ± 0.00 and 0.23 ± 0.01 μM of total iron were released in aqueous and ice samples, respectively. Dissolved ferrous iron concentrations were below the detection limit (0.3 μmol/L) of the analytic method.[56] The transformation was negligible in aqueous samples (Figure S1b). The transformation of iodine species (iodide to tri-iodide and molecular iodine) was also observed in ice samples (Figure S1c). After adjusting the pH of the solution containing NAu-2 and iodide to pH 2, the concentrations of dissolved total iron and ferrous iron increased to 6.02 ± 0.64 and 4.85 ± 0.66 μM, respectively, following 24 h of freezing experiments (Figure S2a,b). In aqueous samples, the concentrations of dissolved total iron and ferrous iron were found to be 3.45 ± 0.07 and 3.08 ± 0.00 μM, respectively. The transformation of iodide to tri-iodide and

molecular iodine was minimal in aqueous samples (Figure S2c), while a significant increase in the generation of tri-iodide and molecular iodine was present in ice samples (Figure S2d). To summarize these outcomes, the concentrations of dissolved total iron and ferrous iron were represented by using a bar graph after 24 h of experiments (Figure 3). The results indicate that the dissolution of both total iron and ferrous iron from nontronite increased at low pH. These results are consistent with previous studies that reported the decreased dissolution of iron with increasing pH.[57] It was expected that a trace amount of iron would be dissolved from NAu-2 at pH levels above 5. To test the dependence of iodide concentrations on iron dissolution, initial iodide concentrations were controlled within a range of 0–200 μM. The dissolution of total iron and ferrous iron from NAu-2 was clearly enhanced in ice samples compared to aqueous samples (Figure 4). The reductive dissolution increased with higher concentrations of iodide. It should be noted that the dissolution of iron was observed, even in the absence of iodide (Figure 4). NAu-2 used in the experiment contains 23.4% (w/w) total iron, of which 99.4% is in the form of Fe(III). Therefore, 0.2 g $L^{-1}$ NAu-2 contains 0.0468 g L–1 (46.8 ppm) total iron. Of this, 99.4% (46.5 ppm) is Fe(III), and 0.6% (0.2808 ppm) is Fe(II). In the experiment where $[I^-]$initial = 0 μM, the observed value of 0.37 μM (20.66 ppb) Fe(II) is below the initially present value of 280.8 ppb of Fe(II) in 0.2 g $L^{-1}$ NAu-2. Therefore, it can be concluded that at $[I^-]$initial = 0 μM, simple rather than reductive dissolution of Fe(II) and Fe(III) present in NAu-2 occurred. When a small amount of iodide was added, the dissolution of iron somewhat decreased. To explore the potential of lower concentrations of both nontronite and iodide, an experiment was conducted with initial NAu-2 and iodide concentrations of 2 mg $L^{-1}$ and 2 μM, respectively. Even at these low initial concentrations, the dissolution of iron from nontronite was accelerated in ice samples compared to aqueous samples (Figure S4). This finding is consistent with the results obtained from experiments conducted with relatively high concentrations of both NAu-2 and iodide. A tendency for enhanced dissolution of iron in ice samples compared to aqueous samples was observed even at low initial concentrations of nontronite and iodide.

## 3.2. Mechanisms of the Reductive Dissolution and Freeze Concentration Effect

There are two mechanisms for the reduction of Fe(III) in clay minerals: solid-state and reductive dissolution–precipitation.[46] In solid-state reduction, changes in clay minerals are small and completely reversible by the reoxidation of reduced clay minerals.[58] This reduction occurs without any significant dissolution of the clay structure or release of iron.[46] In contrast, dissolution and reprecipitation of clay minerals release iron,

accompanying the formation of solids by reprecipitation.[59] In this regard, the reduction of Fe(III) in nontronite can be regarded as dissolution–precipitation rather than solid-state reduction, which can release Fe(II) into the natural environment. Mineral particles containing iron dissolve through three distinct processes: dissolution promoted by protons, dissolution controlled by ligands, and dissolution driven by reduction.[31] In proton-promoted dissolution, higher concentrations of protons can weaken the bonds between iron and oxygen (Fe–O) within the crystal lattice, which facilitates dissolution of iron.[60] Therefore, the proton-promoted dissolution can dissolve iron originally present in NAu-2 into the form of Fe(III) or Fe(II). In contrast, the reductive dissolution of NAu-2 induced by $I^-$ occurs in five steps: (i) mass transport of solutes ($H^+$ and $I^-$) to the surface of nontronite; (ii) adsorption or complex formation of $H^+$ and $I^-$ at the surface; (iii) chemical reactions at the surface [electron transfer from $I^-$ to Fe(III) and the reduction of Fe(III) to Fe(II)]; (iv) detachment of the reduced Fe(II) from the surface; and (v) mass transport of the detached Fe(II) into the bulk solution.[61] During the third step of the dissolution of nontronite, oxidized $I^-$ ($I^\bullet$) reacts with $I^-$ in the solution, generating a diiodine radical ($I_2^{\bullet -}$).[62] The reaction between 2 mol of $I_2^{\bullet -}$ produces 1 mol of tri-iodide ($I_3^-$) and 1 mol of $I^-$.[62] The overall chemical reaction between Fe(III) and $I^-$ is shown in eq 1.[62,63]

$$2Fe^{3+}+3I^- \rightarrow 2Fe^{2+}+I_3^- \quad (1)$$

KOPRI 극지연구소

In addition to the reductive dissolution by iodide, Fe(III) detached from NAu-2 during proton-promoted dissolution can undergo a reaction with iodide to generate Fe(II). The reaction between Fe(III) and $I^-$ is first order for the Fe(III) concentration and is second order for the $I^-$ concentration (eq 2).[63]

$$R=k[H^+][I^-]^2 \quad (2)$$

The surfaces of clay minerals can adsorb protons from the solution at low pH and become positive (pH-dependent charge), and this positive charge at the surface can increase the adsorption of $I^-$ to the clay mineral.[64]

The effect of temperature on the dissolution rate of clay minerals should be distinguished between these two facets: (i) the effect of temperature on the rate of dissolution according to the Arrhenius equation and (ii) the effect of temperature on the adsorption of protons on the surface of clay minerals.[65] Because clay mineral dissolution depends on the surface process, the effect of pH on the dissolution rate is controlled by adsorbed protons on the surface, not directly by the pH of the solution.[66] The surface coverage of protons can differ at different temperatures even under the same solution pH.[66] In this respect, the adsorption

of $H^+$ and $I^-$ on the surface of nontronite affects the dissolution rate. Solutes are known to extrude outward from bulk ice and concentrate at the ice grain boundary, which remains in a liquid state when the solution is frozen.[67] Owing to this freeze concentration effect, the concentration of solutes at the ice grain boundary increases by approximately 3–5 orders of magnitude.[67] To investigate the effect of the freeze concentration on nontronite dissolution, we examined an optical image of a frozen solution containing nontronite particles. When freezing the solution in the temperature-controlled stage, it was observed that nontronite can also be concentrated along the ice grain boundary, not only the solutes (Figure 5). In this experiment, the ice grain boundaries formed were several dozen micrometers in size. The nontronite used in this experiment (<0.2 μm) is small enough to penetrate the ice grain boundaries. Therefore, the enhanced production of Fe(II) and reactive iodine species in ice was due to the freeze concentration effect and the accompanying increases in $H^+$ and $I^-$ concentrations on the surface of nontronite at the ice grain boundaries.

## 3.3. Accelerated Transformations of Iodine Species in Ice

Iodide can be slowly oxidized to tri-iodide in an aqueous solution in the presence of oxygen (eq 3).[68] However, it has been previously reported that the reaction can be accelerated in an acidic frozen solution.[4] This enhanced reaction in the ice phase can happen under both dark and light conditions.

KOPRI 극지연구소

$$O_{2(aq)}+4H^+ +6I^- \rightarrow 2H_2O+2I_3^- \quad (3)$$

Since DW used in this experiment was not controlled to remove the dissolved gas (including $O_2$), dissolved $O_2$ probably affected the oxidation of $I^-$ to $I_3^-$. The $I^-$ concentrations of frozen samples gradually decreased, whereas they were relatively constant in aqueous samples at approximately 200 μM (the initial concentration) after 24 h of reaction (Figure 2a,b). Peaks of $I^-$ and $I_3^-$ were observed at 226 and 353 nm, respectively (Figure 2b,d). Although the peak of $I_2$ was not precisely shaped at 460 nm, the absorbance of the samples at 460 nm was distinguishable for individual samples (Figure 2d). The peak at 288 nm represents the coexistence of $I_3^-$ and $I_2$ in the samples. The concentrations of $I_3^-$ and $I_2$ increased substantially in frozen samples, whereas $I_3^-$ or $I_2$ production was not significant in the aqueous samples (Figure 2c). The freeze concentration effect of oxygen and solutes at the ice grain boundary has been suggested in a previous study.[67] Therefore, the accelerated oxidation of $I^-$ in the ice samples can be ascribed to the concentrations of oxygen, $I^-$, and hydrogen ions at the ice grain boundaries.

## 3.4. Irreversibility of Reactive Iodine Species Generated from Iodide

To identify the reversibility of the transformation reactions between iodide and generated tri-iodide and molecular iodine ($I_2$), we carried out further observations with ice samples after 24 h of reaction time. After the ice sample was thawed and filtered, a quartz cell for the UV/vis spectrophotometer containing the sample was kept at room temperature to observe the changes in the spectra of $I^-$, $I_3^-$, and $I_2$. The cell was not sealed to evaporate the sample naturally. After 4, 8, 12, and 24 h of evaporation, the sample was analyzed using a UV/vis spectrophotometer. There was no significant difference between the $I^-$ peaks at 226 nm from 0 to 12 h, and the peak increased slightly after 24 h (Figure 6a). In other words, there was no actual change in the $I^-$ concentration, and the concentration increased slightly after 24 h, only because the sample evaporated. On the other hand, the peaks of $I_3^-$ and $I_2$ shown from 250 to 500 nm gradually decreased over time (Figure 6b). According to eq 4, which represents the equilibrium between the iodine species, generated $I_3^-$ from the oxidation of $I^-$ can be retransformed to $I_2$ in the presence of $I^-$.[53] Therefore, the detection of $I_3^-$ from the oxidation of $I^-$ implies the presence of $I_2$ by equilibrium.

$$I_2 + I^- \leftrightarrow I_3^- \quad K = 700 \tag{4}$$

The generated gaseous $I_2$ in ice can be emitted into the atmosphere when the frozen solution is thawed.[4] We checked the color change of the sample to identify the evaporation of the iodine species. At the first time, after 24 h of reaction on ice, the thawed sample appeared faint yellow, indicating the existence of $I_3^-$ in the solution (Figure 6c). However, the yellow color of the solution faded after the solution was left to evaporate for 24 h at room temperature (Figure 6d). Thus, the diminished color represents the decreased concentration of $I_3^-$ in the solution, which implies the generation of gaseous $I_2$ at equilibrium. In a previous study, the emission of $I_2$ gas into the atmosphere which is generated from the oxidation of $I^-$ and equilibrium with $I_3^-$ (which is induced by freezing) was observed using cavity ring-down spectroscopy (CRDS).[4] In this experiment, we also determined that $I_3^-$ generated from $I^-$ was transformed into $I_2$ by equilibrium, and there was no return to $I^-$. The generated gaseous $I_2$ gradually evaporated; thus, the UV/vis spectrophotometer peaks of $I_3^-$ and $I_2$ in the solution eventually decreased (Figure 6b). Therefore, reactive iodine generated from the oxidation of $I^-$ in ice can be emitted into the atmosphere.

## 3.5. Abiotic Formation of Magnetite in Ice

In the TEM analysis, the unaltered nontronite sample exhibited a bulky texture and

layered crystals (Figure 7a). Each crystal of nontronite is difficult to be resolved abiotically.[59] However, flakes were produced from the dissolution of nontronite after freezing with the addition of $H^+$ and $I^-$ (Figure 7b). As a result of dissolution in the presence of $H^+$ and $I^-$, abrasion of nontronite was observed in the SAED pattern analysis, as indicated by the extinction of the reflection at 0.13 nm and diffused ring patterns (Figure 7b). Moreover, the presence of nanosized iron oxide particles was unexpectedly observed after 24 h of freezing (Figure 7c,d). In the SAED pattern analysis (Figure 7e) and EDS spectra analysis (Figure 7f), it was identified as magnetite.[69] In addition to the reductive dissolution of Fe(III) in nontronite, Fe(III) in the octahedral sheet of nontronite can also be released into the solution in an Fe(III) form in an acid solution,[70] even though cation dissolution from nontronite at low pH follows the order interlayer > tetrahedral > octahedral sheet.[71] Moreover, after 24 h of freezing, a broad shoulder of high-charge nontronite was observed at 9.0 2Θ (corresponding to 9.8 Å), providing further evidence for the clay structure modification through dissolution (Figure 8).[72] The XRD results from the freezing experiments after 12 and 24 h revealed peaks at approximately 10 Å for the (001) plane, indicating a decrease in the nontronite's d-spacing compared to the initial sample's value of 13.4 Å. This decrease suggests that the freezing process led to reductive dissolution of structural Fe, resulting in the modification of the clay structure.[38] TEM images (Figure 7b) and the results of dissolved iron (Figure 1) also support the alteration of the clay structure and the reductive dissolution of structural iron in NAu-2. In aqueous solutions, magnetite (Fe3O4) nanoparticles can be chemically formed by mixing Fe(III) and $I^-$ under alkaline pH conditions (eqs 5 and 6).[73]

$$3Fe^{3+}+I^- \rightarrow 2Fe^{3+}+Fe^{2+}+1/2I_2 \quad (5)$$

$$2Fe^{3+}+Fe^{2+}+8OH^- \rightarrow Fe_3O_4+4H_2O \quad (6)$$

Two theories are commonly proposed to explain the conventional synthesis of magnetite: coprecipitation of ferrous and ferric ions, or partial oxidation of ferrous ions.[74,75] The pH condition of the experiments reported here is too low to induce the oxidation of ferrous ions. The coprecipitation and accompanying magnetite formation in aqueous solutions proceed through two stages, consisting of a short burst of nucleation followed by slow growth of the nuclei.[76] In aqueous solutions at room or higher temperatures, nucleation occurs when the solutes are concentrated and the concentration reaches a critical supersaturation. Once nucleation occurs, the solutes disperse to the surface, and the crystals undergo gradual growth. It has been suggested that cryogenic mineral formation occurs as a result of the concentration of solutes at the ice grain boundaries.[77] During the freezing process, the concentrations of ferric and ferrous ions can increase at the ice grain

boundaries, leading to supersaturation and the generation of nuclei. Although the reaction of magnetite formation between Fe(III) and $I^-$ is favored under alkaline pH conditions, the nuclei formation induced by supersaturation can be boosted in ice. After nucleation, nontronite particles can serve as a site for magnetite particle growth. Magnetite forms as concentrated solutes at the ice grain boundaries, and the released Fe(III) and the reduced Fe(II) resulting from the dissolution of nontronite are adsorbed at the surface of nontronite.[78] As ice crystals grow, the existing nontronite and newly formed magnetite aggregate and increase the particle size (Figure 7). In our experiment, magnetite formation was observed only in the ice samples rather than in the aqueous samples. The small size of the magnetite nanoparticles could potentially allow them to pass through the 0.2 μm filter. However, the formed magnetite is attached to the nontronite particles (Figure 7c), which would be expected to enable their removal by filtering despite their small size. Furthermore, the majority of iron present in the filtrate is in the form of ferrous ions (Figure 1). Thus, even if magnetite were to pass through the filter, the quantity would likely be minimal. Previously, significant modifications of clay minerals, such as release of a soluble form of Fe from the reductive dissolution of smectite[79] and changes in physicochemical properties of smectite including dewatering[80] have been reported in many laboratory-based studies with mesophilic (30 °C) and thermophilic (70 °C) reactions. It has been reported that microbial activities can transform nontronite into secondary minerals such as siderite, vivianite, and Illite.[46] However, no reactions of this type below the freezing point have been reported. The freezing process can bypass kinetic and thermodynamic barriers when nontronite dissolves and magnetite is formed. Our results suggest a new mechanism for the formation of secondary-phase minerals accompanied by the dissolution of clay minerals in ice. These findings suggest that freezing processes may have a noteworthy role in the geochemical cycling of iron and iodine and constitute a previously overlooked factor.

## 3.6. Environmental Implications

Over the past few decades, the dissolution of iron-containing dust has been recognized as an important source of bioavailable iron.[16,81] Although the dissolution of iron from clay minerals is dependent on temperature, the impact of temperatures below the freezing point has not hitherto been identified.[82,83] It has been established that solutes can become concentrated at ice grain boundaries; however, this is not the case for all solutes. The behavior of a particular substance can vary significantly depending on its coexistence with other materials, resulting in its presence within bulk ice or aggregation at ice grain boundaries.[84] The present study for the first time reveals the importance of a freezing

procedure that enhances the reductive dissolution of iron in clay minerals, the transformation of iodine species, and the formation of magnetite. Most of the iron in the nontronite used in our experiment exists as ferric, which is a form of iron less available to organisms. However, a significant amount of reduction of ferric iron in nontronite occurred through chemical reactions in ice when $I^-$ was added. The production and release of reactive iodine species ($I_3^-$ and $I_2$) in ice accompanied by reductive dissolution were also observed. Reductive dissolution of Fe(III)-containing clay minerals with microbial activity has been intensively investigated.[50] Previous studies have focused on the microbial reduction of ferric iron in clay minerals occurring in soil, terrestrial sediment, and marine sediment.[46] In the atmosphere, photoirradiation during the daytime and the presence of acids such as nitric acid enhance the reductive dissolution of dust particles.[85] Smectite in the form of dust particles was also identified in the troposphere and stratosphere.[86] The pH of sea salt aerosols in the atmosphere was measured and found to range from alkaline to pH 1.[87] It has been suggested that the pH of iron-containing aerosols can decrease to pH 1–2 in the presence of acid anions such as $SO_2$ or $HNO_3$.[88,89] Therefore, our research suggests a new mechanism for the reductive dissolution of iron from clay minerals during freezing that is feasible in the atmosphere. Further, environmental conditions with high acidity and ice formation also exist in polar regions. Snowpacks in Antarctica typically exhibit acidic conditions, and a pH of approximately 3.3 has been reported.[90] It was also reported that the pH of streamwater in Antarctica can range from pH 3.2 to 4.5 in the presence of acid mine drainage.[91] The Antarctic acid mine drainage regions have conditions conducive to these reactions, including the presence of ice and clay minerals, the potential influx of iodide from the ocean, and a pH that can be as low as 3. Iodine flux from the ocean to the atmosphere has been reported and is generated from coastal algae and photochemical reactions.[39] The outcomes of our experiments suggest that chemical reactions with the ice medium could be a possible source of bioavailable iron. The generated reactive iodine species could contribute to atmospheric cloud properties and radiative forcing involving the formation of new particles.[92] Thus, these new findings can be applied to ice or snow near seawater in polar regions or in the atmosphere. The release of bioavailable iron in a cryogenic environment is consistent with the reported presence of labile and bioavailable iron in the catchments of the Greenland and Antarctic ice sheets.[20] It has been assumed that the nanoparticulates of clays and ferrihydrite in runoff were formed from microbially reduced iron in the subglacial environment.[20] However, our results imply an alternative explanation for the missing supply of ferrous iron to oceans that has not previously been considered. The reduced ferrous iron generated from nontronite dissolution in ice can be used as electron acceptors in metabolism or redox reactions in natural chemical reactions.[93] The reductive dissolution of iron oxides, such as maghemite and goethite, can be enhanced

KOPRI 극지연구소

in ice; this may increase the concentration of ferrous iron in polar regions.[52] In this study, it was revealed that abiotic reductive dissolution of ferrous iron from iron-containing clay minerals and magnetite formation occurred during ice-freezing reactions. When ferrous iron is leached from clay minerals, it becomes bioavailable iron, which can be readily used by organisms. However, when this iron reverts to solid magnetite, it again becomes inaccessible to biological uptake. Therefore, the formation of magnetite during the freezing process can be considered to be a previously unrecognized missing sink for iron. Consequently, the role of ice-freezing reactions as regulators of the sink and/or source of iron under natural conditions was verified. Due to their small size, clay minerals can be transported over long distances in the atmosphere. As dust particles linger in the atmosphere, the dissolution of soluble iron tends to increase. Consequently, clay minerals in atmospheric dust play a crucial role as a source of the iron supply to the oceans. It is widely recognized that photochemical reduction in dust aerosols can result in significant concentrations of Fe(II).[94] Our findings suggest that the freezing process can serve as a mechanism for the release of bioavailable iron. The enhanced reductive dissolution of iron from clay minerals during freezing and the subsequent generation of reactive iodine species have implications for atmospheric processes and the formation of new particles. Therefore, the freezing process may contribute to bioavailable iron input into marine ecosystems, explaining a potential missing source of bioavailable iron in oceans. Further research is needed to determine whether the enhanced iron reductive dissolution, iodide transformation, and magnetite formation observed under laboratory conditions occur in natural environments and to investigate their environmental impacts.

## REFERENCES


(1) Sumner, A. L.; Shepson, P. B., Snowpack production of formaldehyde and its effect on the Arctic troposphere. Nature **1999**, 398 (6724), 230 - 233.

(2) Prather, M. J., More rapid polar ozone depletion through the reaction of HOCl with HCl on polar stratospheric clouds. Nature **1992**, 355 (6360), 534 - 537.

(3) Abbatt, J.; Thomas, J. L.; Abrahamsson, K.; Boxe, C.; Granfors, A.; Jones, A.; King, M.; Saiz-Lopez, A.; Shepson, P.; Sodeau, J. H., Halogen activation via interactions with environmental ice and snow in the polar lower troposphere and other regions. Atmos. Chem. Phys. **2012**, 12 (14), 6237 - 6271.

(4) Kim, K.; Yabushita, A.; Okumura, M.; Saiz-Lopez, A.; Cuevas, C. A.; Blaszczak-Boxe, C. S.; Min, D. W.; Yoon, H.-I.; Choi, W., Production of molecular iodine and tri-iodide in the frozen solution of iodide: implication for polar atmosphere. Environ. Sci. Technol. **2016**, 50 (3), 1280 - 1287.

(5) Frieß, U.; Deutschmann, T.; Gilfedder, B. S.; Weller, R.; Platt, U., Iodine monoxide in the Antarctic snowpack. Atmos. Chem. Phys. **2010**, 10 (5), 2439 - 2456.

(6) Chung, H. Y.; Jung, J.; Lee, D. H.; Kim, S.; Lee, M. K.; Lee, J. I.; Yoo, K.-C.; Lee, Y. I.; Kim, K., Chemical Weathering of Granite in Ice and Its Implication for Weathering in Polar Regions. Minerals **2020**, 10 (2), 185.

(7) Kim, K.; Choi, W.; Hoffmann, M. R.; Yoon, H.-I.; Park, B.-K., Photoreductive dissolution of iron oxides trapped in ice and its environmental implications. Environ. Sci. Technol. **2010**, 44 (11), 4142 - 4148.

(8) Hawkesworth, C. J.; Kemp, A., Evolution of the continental crust. Nature **2006**, 443 (7113), 811 - 817.

(9) Weber, K. A.; Achenbach, L. A.; Coates, J. D., Microorganisms pumping iron: anaerobic microbial iron oxidation and reduction. Nat. Rev. Microbiol. **2006**, 4 (10), 752 - 764.

(10) Huang, J.; Jones, A.; Waite, T. D.; Chen, Y.; Huang, X.; Rosso, K. M.; Kappler, A.; Mansor, M.; Tratnyek, P. G.; Zhang, H., Fe(II) redox chemistry in the environment. Chem. Rev. **2021**, 121 (13), 8161 - 8233.

(11) Waldron, K. J.; Robinson, N. J., How do bacterial cells ensure that metalloproteins get the correct metal? Nat. Rev. Microbiol. **2009**, 7 (1), 25 - 35.

(12) Kramer, J.; Özkaya, Ö.; Kümmerli, R., Bacterial siderophores in community and host interactions. Nat. Rev. Microbiol. **2020**, 18 (3), 152 - 163.

(13) Palmer, C. M.; Guerinot, M. L., Facing the challenges of Cu, Fe and Zn homeostasis in plants. Nat. Chem. Biol. **2009**, 5 (5), 333 - 340.

(14) De Baar, H. J.; De Jong, J. T.; Bakker, D. C.; Löscher, B. M.; Veth, C.; Bathmann, U.; Smetacek, V., Importance of iron for plankton blooms and carbon dioxide drawdown in the Southern Ocean. Nature **1995**, 373 (6513), 412 - 415.

(15) Kappler, A.; Bryce, C.; Mansor, M.; Lueder, U.; Byrne, J. M.; Swanner, E. D., An evolving view on biogeochemical cycling of iron. Nat. Rev. Microbiol. **2021**, 19, 360 - 374.

(16) Martin, J. H.; Gordon, R. M.; Fitzwater, S. E., Iron in Antarctic waters. Nature **1990**, 345 (6271), 156 - 158.

(17) Duggen, S.; Olgun, N.; Croot, P.; Hoffmann, L.; Dietze, H.; Delmelle, P.; Teschner, C., The role of airborne volcanic ash for the surface ocean biogeochemical iron-cycle: a review. Biogeosciences **2010**, 7 (3), 827 - 844.

(18) Tagliabue, A.; Bowie, A. R.; Boyd, P. W.; Buck, K. N.; Johnson, K. S.; Saito, M. A., The integral role of iron in ocean biogeochemistry. Nature **2017**, 543 (7643), 51 - 59.

(19) Duprat, L. P.; Bigg, G. R.; Wilton, D. J., Enhanced Southern Ocean marine productivity due to fertilization by giant icebergs. Nat. Geosci. **2016**, 9 (3), 219 - 221.

(20) Hawkings, J. R.; Wadham, J. L.; Tranter, M.; Raiswell, R.; Benning, L. G.; Statham, P. J.; Tedstone, A.; Nienow, P.; Lee, K.; Telling, J., Ice sheets as a significant source of highly reactive nanoparticulate iron to the oceans. Nat. Commun. **2014**, 5 (1), 3929.

(21) Jickells, T.; An, Z.; Andersen, K. K.; Baker, A.; Bergametti, G.; Brooks, N.; Cao, J.; Boyd, P.; Duce, R.; Hunter, K., Global iron connections between desert dust, ocean biogeochemistry, and climate. Science **2005**, 308 (5718), 67 - 71.

(22) Mahowald, N. M.; Hamilton, D. S.; Mackey, K. R.; Moore, J. K.; Baker, A. R.; Scanza, R. A.; Zhang, Y., Aerosol trace metal leaching and impacts on marine microorganisms. Nat. Commun. **2018**, 9 (1), 2614.

(23) Fung, I. Y.; Meyn, S. K.; Tegen, I.; Doney, S. C.; John, J. G.; Bishop, J. K., Iron supply and demand in the upper ocean. Global Biogeochem. Cycles **2000**, 14 (1), 281 - 295.

(24) Atkinson, J. D.; Murray, B. J.; Woodhouse, M. T.; Whale, T. F.; Baustian, K. J.; Carslaw, K. S.; Dobbie, S.; O'Sullivan, D.; Malkin, T. L., The importance of feldspar for ice nucleation by mineral dust in mixed-phase clouds. Nature **2013**, 498 (7454), 355 - 358.

(25) Lalonde, K.; Mucci, A.; Ouellet, A.; Gélinas, Y., Preservation of organic matter in sediments promoted by iron. Nature **2012**, 483 (7388), 198 - 200.

(26) Fan, Q.; Wang, L.; Fu, Y.; Li, Q.; Liu, Y.; Wang, Z.; Zhu, H., Iron redox cycling in layered clay minerals and its impact on contaminant dynamics: A review. Sci. Total Environ. **2023**, 855, 159003.

(27) Yong, S. N.; Lim, S.; Ho, C. L.; Chieng, S.; Kuan, S. H., Mechanisms of microbial-based iron reduction of clay minerals: Current understanding and latest developments. Appl. Clay Sci. **2022**, 228, 106653.

(28) Vorhies, J. S.; Gaines, R. R., Microbial dissolution of clay minerals as a source of iron and silica in marine sediments. Nat. Geosci. **2009**, 2 (3), 221 - 225.

(29) Liu, G.; Qiu, S.; Liu, B.; Pu, Y.; Gao, Z.; Wang, J.; Jin, R.; Zhou, J., Microbial reduction of Fe(III)-bearing clay minerals in the presence of humic acids. Sci. Rep. **2017**, 7 (1), 45354.

(30) Liu, D.; Zhang, Q.; Wu, L.; Zeng, Q.; Dong, H.; Bishop, M. E.; Wang, H., Humic acid-enhanced illite and talc formation associated with microbial reduction of Fe(III) in nontronite. Chem. Geol. **2016**, 447, 199 - 207.

(31) Fu, H.; Cwiertny, D. M.; Carmichael, G. R.; Scherer, M. M.; Grassian, V. H., Photoreductive dissolution of Fe-containing mineral dust particles in acidic media. J. Geophys. Res.: Atmos. **2010**, 115 (D11), D11304.

(32) Journet, E.; Desboeufs, K. V.; Caquineau, S.; Colin, J. L., Mineralogy as a critical factor of dust iron solubility. Geophys. Res. Lett. **2008**, 35 (7), L07805.

KOPRI 극지연구소

(33) Usher, C. R.; Michel, A. E.; Grassian, V. H., Reactions on mineral dust. Chem. Rev. **2003**, 103 (12), 4883 - 4940.

(34) Hettiarachchi, E.; Reynolds, R. L.; Goldstein, H. L.; Moskowitz, B.; Rubasinghege, G., Bioavailable iron production in airborne mineral dust: Controls by chemical composition and solar flux. Atmos. Environ. **2019**, 205, 90 - 102.

(35) Kashefi, K.; Shelobolina, E. S.; Elliott, W. C.; Lovley, D. R., Growth of thermophilic and hyperthermophilic Fe(III)-reducing microorganisms on a ferruginous smectite as the sole electron acceptor. Appl. Environ. Microbiol. **2008**, 74 (1), 251 - 258.

(36) Jung, J.; Yoo, K.-C.; Rosenheim, B. E.; Conway, T. M.; Lee, J. I.; Yoon, H. I.; Hwang, C. Y.; Yang, K.; Subt, C.; Kim, J., Microbial Fe(III) reduction as a potential iron source from Holocene sediments beneath Larsen Ice Shelf. Nat. Commun. **2019**, 10 (1), 5786.

(37) Gorski, C. A.; Klüpfel, L. E.; Voegelin, A.; Sander, M.; Hofstetter, T. B., Redox properties of structural Fe in clay minerals: 3. Relationships between smectite redox and structural properties. Environ. Sci. Technol. **2013**, 47 (23), 13477 - 13485.

(38) Koo, T.-h.; Jang, Y.-n.; Kogure, T.; Kim, J. H.; Park, B. C.; Sunwoo, D.; Kim, J.-w., Structural and chemical modification of nontronite associated with microbial Fe(III) reduction: Indicators of “illitization”. Chem. Geol. **2014**, 377, 87 - 95.

(39) Saiz-Lopez, A.; Plane, J. M.; Baker, A. R.; Carpenter, L. J.; von Glasow, R.; Gómez Martín, J. C.; McFiggans, G.; Saunders, R. W., Atmospheric chemistry of iodine. Chem. Rev. **2012**, 112 (3), 1773 - 1804.

(40) Gómez Martín, J. C.; Saiz-Lopez, A.; Cuevas, C. A.; Baker, A. R.; Fernández, R. P., On the speciation of iodine in marine aerosol. J. Geophys. Res.: Atmos. **2022**, 127 (4), e2021JD036081.

(41) Chance, R.; Tinel, L.; Sarkar, A.; Sinha, A. K.; Mahajan, A. S.; Chacko, R.; Sabu, P.; Roy, R.; Jickells, T. D.; Stevens, D. P., Surface Inorganic Iodine Speciation in the Indian and Southern Oceans From 12° N to 70° S. Front. Mar. Sci. **2020**, 7, 621.

(42) Fuge, R.; Johnson, C. C., The geochemistry of iodine—a review. Environ. Geochem. Health **1986**, 8, 31 - 54.

(43) Pechtl, S.; Schmitz, G.; von Glasow, R., Modelling iodide-iodate speciation in atmospheric aerosol: Contributions of inorganic and organic iodine chemistry. Atmos. Chem. Phys. **2007**, 7 (5), 1381 - 1393.

(44) Atkinson, H. M.; Huang, R.-J.; Chance, R.; Roscoe, H. K.; Hughes, C.; Davison, B.; Schönhardt, A.; Mahajan, A. S.; Saiz-Lopez, A.; Hoffmann, T., Iodine emissions from the sea ice of the Weddell Sea. Atmos. Chem. Phys. **2012**, 12 (22), 11229 - 11244.

(45) Kim, K.; Menacherry, S. P. M.; Kim, J.; Chung, H. Y.; Jeong, D.; Saiz-Lopez, A.; Choi, W., Simultaneous and synergic production of bioavailable iron and reactive iodine

species in ice. Environ. Sci. Technol. **2019**, 53 (13), 7355 - 7362.

(46) Dong, H.; Jaisi, D. P.; Kim, J.; Zhang, G., Microbe-clay mineral interactions. Am. Mineral. **2009**, 94 (11 - 12), 1505 - 1519.

(47) Ghadiri, M.; Chrzanowski, W.; Rohanizadeh, R., Biomedical applications of cationic clay minerals. RSC Adv. **2015**, 5 (37), 29467 - 29481.

(48) Jaisi, D. P.; Kukkadapu, R. K.; Eberl, D. D.; Dong, H., Control of Fe(III) site occupancy on the rate and extent of microbial reduction of Fe(III) in nontronite. Geochim. Cosmochim. Acta **2005**, 69 (23), 5429 - 5440.

(49) Schaefer, M. V.; Gorski, C. A.; Scherer, M. M., Spectroscopic evidence for interfacial Fe(II)-Fe(III) electron transfer in a clay mineral. Environ. Sci. Technol. **2011**, 45 (2), 540 - 545.

(50) Jaisi, D. P.; Dong, H.; Liu, C., Influence of biogenic Fe(II) on the extent of microbial reduction of Fe(III) in clay minerals nontronite, illite, and chlorite. Geochim. Cosmochim. Acta **2007**, 71 (5), 1145 - 1158.

(51) Kottsova, A. K.; Mirzaie Yegane, M.; Tchistiakov, A. A.; Zitha, P. L., Effect of electrostatic interaction on the retention and remobilization of colloidal particles in porous media. Colloids Surf., A **2021**, 617, 126371.

(52) Jeong, D.; Kim, K.; Min, D. W.; Choi, W., Freezing-enhanced dissolution of iron oxides: effects of inorganic acid anions. Environ. Sci. Technol. **2015**, 49 (21), 12816 - 12822.

(53) O'Sullivan, D.; Sodeau, J. R., Freeze-induced reactions: Formation of iodine-bromine interhalogen species from aqueous halide ion solutions. J. Phys. Chem. A **2010**, 114 (46), 12208 - 12215.

(54) Mavrocordatos, D.; Fortin, D., Quantitative characterization of biotic iron oxides by analytical electron microscopy. Am. Mineral. **2002**, 87 (7), 940 - 946.

(55) Roden, E. E.; Urrutia, M. M., Influence of biogenic Fe(II) on bacterial crystalline Fe(III) oxide reduction. Geomicrobiol. J. **2002**, 19 (2), 209 - 251.

(56) Viollier, E.; Inglett, P.; Hunter, K.; Roychoudhury, A.; Van Cappellen, P., The ferrozine method revisited: Fe(II)/Fe(III) determination in natural waters. Appl. Geochem. **2000**, 15 (6), 785 - 790.

(57) Jeong, D.; Kim, K.; Choi, W., Accelerated dissolution of iron oxides in ice. Atmos. Chem. Phys. **2012**, 12 (22), 11125 - 11133.

(58) Lee, K.; Kostka, J. E.; Stucki, J. W., Comparisons of structural Fe reduction in smectites by bacteria and dithionite: An infrared spectroscopic study. Clays Clay Miner. **2006**, 54 (2), 195 - 208.

(59) Dong, H.; Kostka, J. E.; Kim, J., Microscopic evidence for microbial dissolution of smectite. Clays Clay Miner. **2003**, 51 (5), 502 - 512.

KOPRI 극지연구소

(60) Cwiertny, D. M.; Baltrusaitis, J.; Hunter, G. J.; Laskin, A.; Scherer, M. M.; Grassian, V. H., Characterization and acid-mobilization study of iron-containing mineral dust source materials. J. Geophys. Res.: Atmos. **2008**, 113, D05202.

(61) Wieland, E.; Wehrli, B.; Stumm, W., The coordination chemistry of weathering: III. A generalization on the dissolution rates of minerals. Geochim. Cosmochim. Acta **1988**, 52 (8), 1969 - 1978.

(62) Kim, K.; Ju, J.; Kim, B.; Chung, H. Y.; Vetráková, L.; Heger, D.; Saiz-Lopez, A.; Choi, W.; Kim, J., Nitrite-induced activation of iodate into molecular iodine in frozen solution. Environ. Sci. Technol. **2019**, 53 (9), 4892 - 4900.

(63) Laurence, G.; Ellis, K., Oxidation of iodide ion by iron(III) ion in aqueous solution. J. Chem. Soc., Dalton Trans. **1972**, (20), 2229 - 2233.

(64) Johnson, D. W.; Cole, D. W., Anion mobility in soils: relevance to nutrient transport from forest ecosystems. Environ. Int. **1980**, 3 (1), 79 - 90.

(65) Amram, K.; Ganor, J., The combined effect of pH and temperature on smectite dissolution rate under acidic conditions. Geochim. Cosmochim. Acta **2005**, 69 (10), 2535 - 2546.

(66) Cama, J.; Metz, V.; Ganor, J., The effect of pH and temperature on kaolinite dissolution rate under acidic conditions. Geochim. Cosmochim. Acta **2002**, 66 (22), 3913 - 3926.

(67) Takenaka, N.; Ueda, A.; Daimon, T.; Bandow, H.; Dohmaru, T.; Maeda, Y., Acceleration mechanism of chemical reaction by freezing: The reaction of nitrous acid with dissolved oxygen. J. Phys. Chem. **1996**, 100 (32), 13874 - 13884.

(68) Couto, A. B.; de Souza, D. C.; Sartori, E. R.; Jacob, P.; Klockow, D.; Neves, E. A., The catalytic cycle of oxidation of iodide ion in the oxygen/nitrous acid/nitric oxide system and its potential for analytical applications. Anal. Lett. **2006**, 39 (15), 2763 - 2774.

(69) Galateanu, B.; Bunea, M.-C.; Stanescu, P.; Vasile, E.; Casarica, A.; Iovu, H.; Hermenean, A.; Zaharia, C.; Costache, M., In vitro studies of bacterial cellulose and magnetic nanoparticles smart nanocomposites for efficient chronic wounds healing. Stem Cells Int. **2015**, 2015, 1 - 10.

(70) Luca, V.; MacLachlan, D. J., Site occupancy in nontronite studied by acid dissolution and Mössbauer spectroscopy. Clays Clay Miner. **1992**, 40 (1), 1 - 7.

(71) Gainey, S.; Hausrath, E.; Hurowitz, J.; Milliken, R., Nontronite dissolution rates and implications for Mars. Geochim. Cosmochim. Acta **2014**, 126, 192 - 211.

(72) Liu, D.; Dong, H.; Zhao, L.; Wang, H., Smectite reduction by Shewanella species as facilitated by cystine and cysteine. Geomicrobiol. J. **2014**, 31 (1), 53 - 63.

(73) Atta, A. M.; Al-Lohedan, H. A.; Al-Hussain, S. A., Synthesis of stabilized

KOPRI 극지연구소

myrrh-capped hydrocolloidal magnetite nanoparticles. Molecules **2014**, 19 (8), 11263 - 11278.

(74) Altan, C. L.; Lenders, J. J.; Bomans, P. H.; de With, G.; Friedrich, H.; Bucak, S.; Sommerdijk, N. A., Partial oxidation as a rational approach to kinetic control in bioinspired magnetite synthesis. Chem. - Eur. J. **2015**, 21 (16), 6150 - 6156.

(75) Wu, W.; He, Q.; Jiang, C., Magnetic iron oxide nanoparticles: synthesis and surface functionalization strategies. Nanoscale Res. Lett. **2008**, 3, 397.

(76) Laurent, S.; Forge, D.; Port, M.; Roch, A.; Robic, C.; Vander Elst, L.; Muller, R. N., Magnetic iron oxide nanoparticles: synthesis, stabilization, vectorization, physicochemical characterizations, and biological applications. Chem. Rev. **2008**, 108 (6), 2064 - 2110.

(77) Žák, K.; Onac, B. P.; Kadebskaya, O. I.; Filippi, M.; Dublyansky, Y.; Luetscher, M., Cryogenic mineral formation in caves. Ice Caves; Elsevier, **2018**, pp 123 - 162.

(78) Ahn, T.; Kim, J. H.; Yang, H.-M.; Lee, J. W.; Kim, J.-D., Formation pathways of magnetite nanoparticles by coprecipitation method. J. Phys. Chem. C **2012**, 116 (10), 6069 - 6076.

(79) Liu, C.; Zachara, J. M.; Foster, N. S.; Strickland, J., Kinetics of reductive dissolution of hematite by bioreduced anthraquinone-2,6-disulfonate. Environ. Sci. Technol. **2007**, 41 (22), 7730 - 7735.

(80) Bruce, C. H., Smectite dehydration—its relation to structural development and hydrocarbon accumulation in northern Gulf of Mexico basin. AAPG Bull. **1984**, 68 (6), 673 - 683.

(81) Maher, B.; Prospero, J.; Mackie, D.; Gaiero, D.; Hesse, P.; Balkanski, Y., Global connections between aeolian dust, climate and ocean biogeochemistry at the present day and at the last glacial maximum. Earth-Sci. Rev. **2010**, 99 (1 - 2), 61 - 97.

(82) Xie, T.; Lu, S.; Rao, L.; Zhang, L.; Wang, X.; Wang, W.; Wang, Q., Dissolution factors and oxidative potential of acid soluble irons from chlorite mineral particles. Atmos. Environ. **2021**, 255, 118436.

(83) Jung, J.; Chung, H. Y.; Ko, Y.; Moon, I.; Suh, Y. J.; Kim, K., A microbial driver of clay mineral weathering and bioavailable Fe source under low-temperature conditions. Front. Microbiol. **2022**, 13, 980078.

(84) Krausková, L'.; Procházková, J.; Klašková, M.; Filipová, L.; Chaloupková, R.; Malý, S.; Damborský, J.; Heger, D., Suppression of protein inactivation during freezing by minimizing pH changes using ionic cryoprotectants. Int. J. Pharm. **2016**, 509 (1 - 2), 41 - 49.

(85) Gankanda, A.; Grassian, V. H., Nitrate photochemistry on laboratory proxies of mineral dust aerosol: wavelength dependence and action spectra. J. Phys. Chem. C **2014**, 118

KOPRI 극지연구소

(50), 29117 - 29125.

(86) Rietmeijer, F. J., CM-like interplanetary dust particles in lower stratosphere during 1989 October and 1991 June/July. Meteorit. Planet. Sci. **1996**, 31 (2), 278 - 288.

(87) Kerkweg, A.; Jöckel, P.; Pozzer, A.; Tost, H.; Sander, R.; Schulz, M.; Stier, P.; Vignati, E.; Wilson, J.; Lelieveld, J., Consistent simulation of bromine chemistry from the marine boundary layer to the stratosphere—Part 1: Model description, sea salt aerosols and pH. Atmos. Chem. Phys. **2008**, 8 (19), 5899 - 5917.

(88) Meskhidze, N.; Chameides, W. L.; Nenes, A.; Chen, G., Iron mobilization in mineral dust: Can anthropogenic $SO_2$ emissions affect ocean productivity? Geophys. Res. Lett. **2003**, 30 (21), 2085.

(89) Zhu, X.; Prospero, J.; Millero, F., Diel variability of soluble Fe(II) and soluble total Fe in North African dust in the trade winds at Barbados. J. Geophys. Res.: Atmos. **1997**, 102 (D17), 21297 - 21305.

(90) Hodson, A. J.; Sabacka, M.; Dayal, A.; Edwards, A.; Cook, J.; Convey, P.; Redeker, K.; Pearce, D., Marked seasonal changes in the microbial production, community composition, and biogeochemistry of glacial snowpack ecosystems in the maritime Antarctic. J. Geophys. Res.: Biogeosci. **2021**, 126 (7), e2020JG005706.

(91) Dold, B.; Gonzalez-Toril, E.; Aguilera, A.; Lopez-Pamo, E.; Cisternas, M.; Bucchi, F.; Amils, R., Acid rock drainage and rock weathering in Antarctica: important sources for iron cycling in the Southern Ocean. Environ. Sci. Technol. **2013**, 47 (12), 6129 - 6136.

(92) Raso, A. R.; Custard, K. D.; May, N. W.; Tanner, D.; Newburn, M. K.; Walker, L.; Moore, R. J.; Huey, L. G.; Alexander, L.; Shepson, P. B., Active molecular iodine photochemistry in the Arctic. Proc. Natl. Acad. Sci. U.S.A. **2017**, 114 (38), 10053 - 10058.

(93) Bird, L. J.; Bonnefoy, V.; Newman, D. K., Bioenergetic challenges of microbial iron metabolisms. Trends Microbiol. **2011**, 19 (7), 330 - 340.

(94) Rubasinghege, G.; Elzey, S.; Baltrusaitis, J.; Jayaweera, P. M.; Grassian, V. H., Reactions on atmospheric dust particles: Surface photochemistry and size-dependent nanoscale redox chemistry. J. Phys. Chem. Lett. **2010**, 1 (11), 1729 - 1737.

KOPRI 극지연구소

## FIGURES

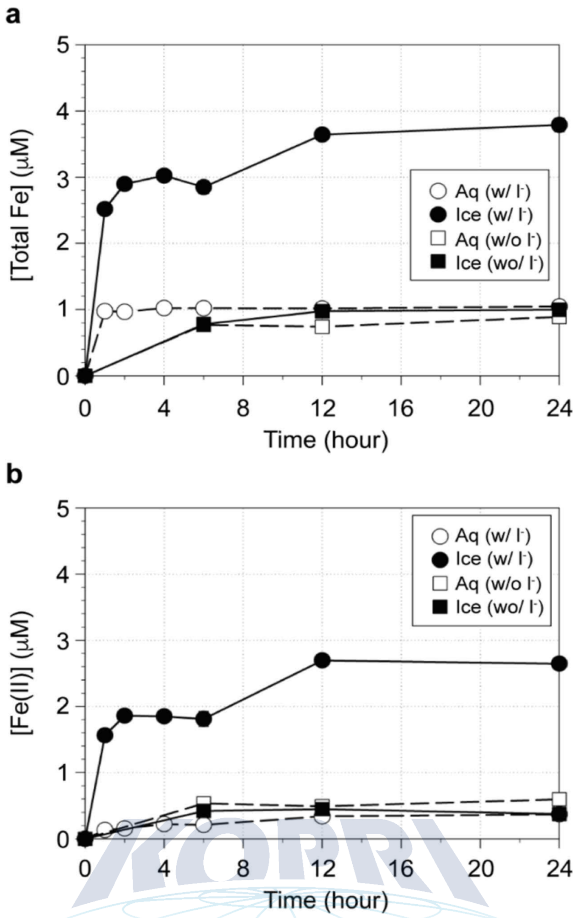



**Figure 1.** Time profiles of dissolved Fe concentrations in aqueous and ice samples with or without iodide. Filled markers represent the data of frozen samples whereas open markers show that of aqueous samples. Circles denote the data of the samples with the addition of $I^-$. Squares represent the data of control samples (without $I^-$). (a) Concentration of total Fe and (b) Fe(II) in filtrates. Experimental conditions: [NAu-2] = 0.2 g $L^{-1}$, [$I^-$] = 0 or 200 μM, pH 3, T = 25 or −20 °C.

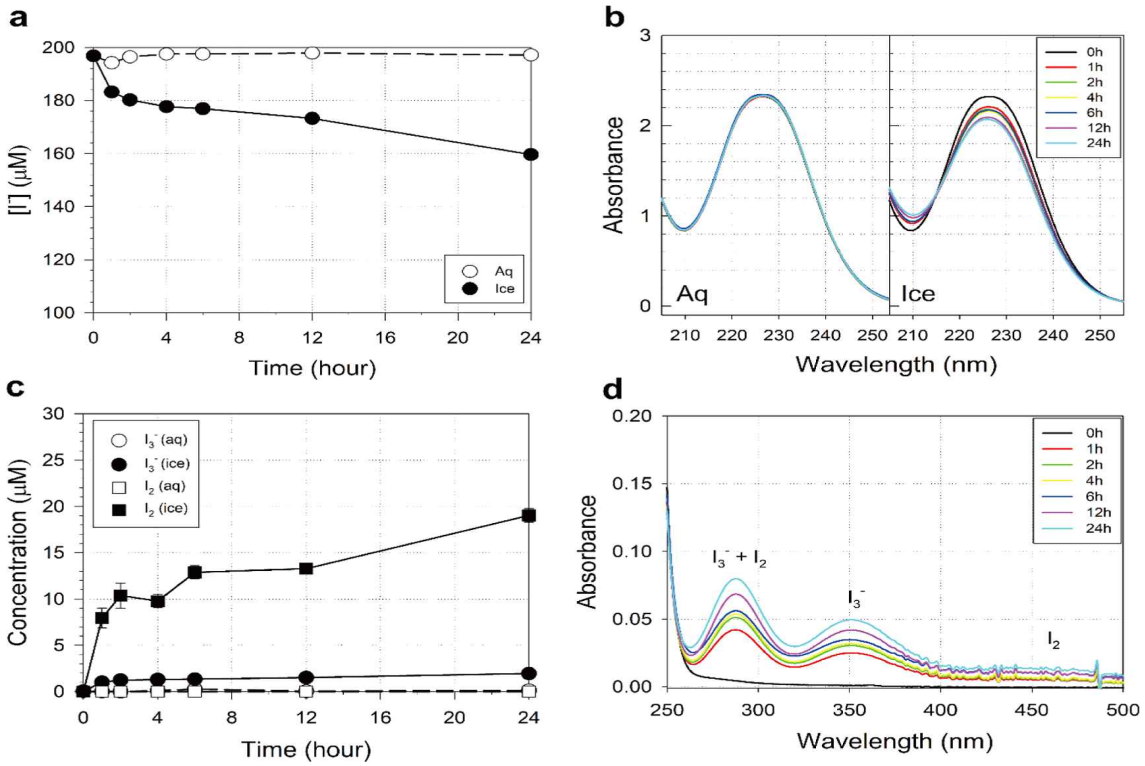



**Figure 2.** Results of the transformation of iodine species. (a) $I^-$ concentrations of aqueous and ice samples measured using the ICP system, (b) UV/vis spectrum of $I^-$ in aqueous and ice samples around 226 nm, (c) $I_3^-$ and $I_2$ concentrations calculated from the absorbance analyzed using a UV/vis spectrophotometer in aqueous and ice samples, and (d) UV/vis spectra of $I_3^-$ and $I_2$ in ice samples. Experimental conditions: [NAu-2] = 0.2 g $L^{-1}$, [$I^-$] = 200 μM, pH 3 (adjusted with $H_2SO_4$), T = 25 or −20 °C.

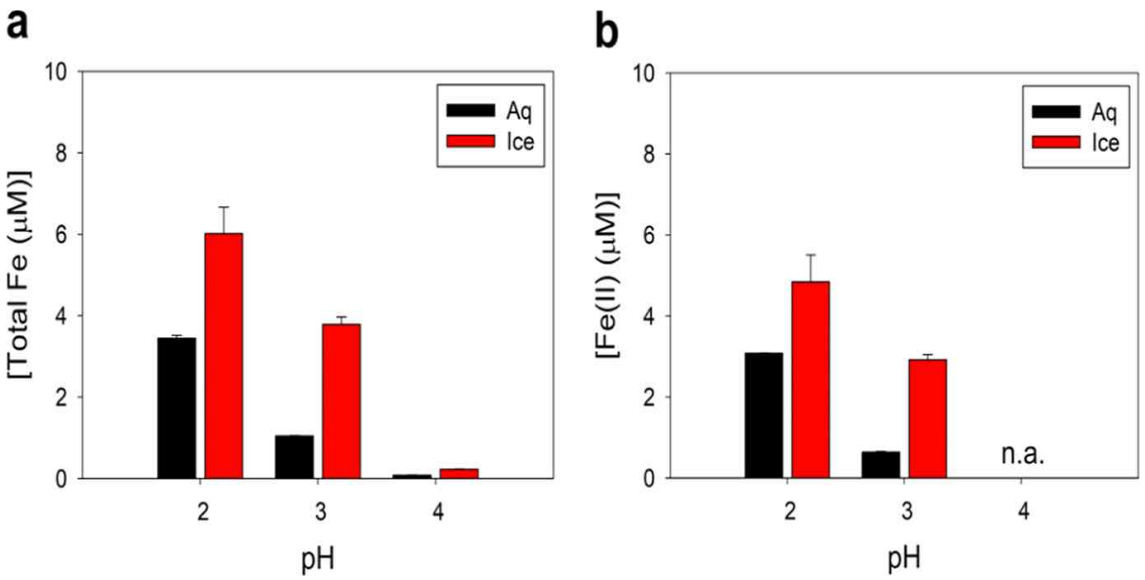



**Figure 3.** pH dependence of dissolved total iron and ferrous iron concentrations in aqueous and ice samples. Red bars represent frozen samples and black bars represent aqueous samples. (a) Concentration of total Fe and (b) Fe(II) in filtrates. Experimental conditions: [NAu-2] = 0.2 g $L^{-1}$, [I - ] = 200 μM, pH = 2 - 4, T = 25 or −20 °C.

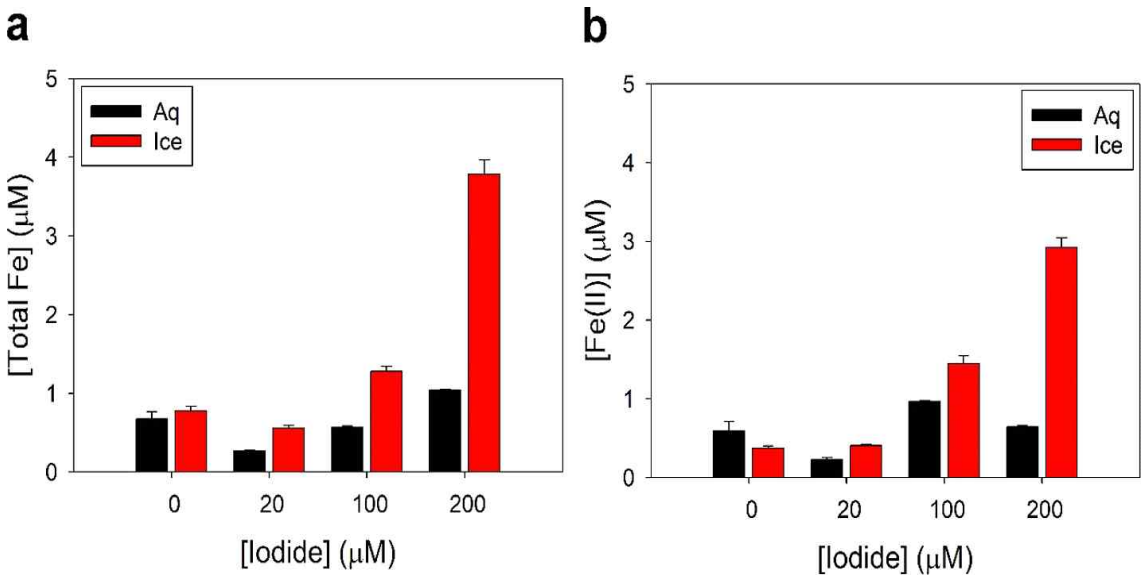



**Figure 4.** Iodide dependence of dissolved total iron and ferrous iron concentrations in aqueous and ice samples. Red bars represent frozen samples and black bars represent aqueous samples. (a) Concentration of total Fe and (b) Fe(II) in filtrates. Experimental conditions: [NAu-2] = 0.2 g $L^{-1}$, [$I^-$] = 0 - 200 μM, pH = 3, T = 25 or −20 °C.

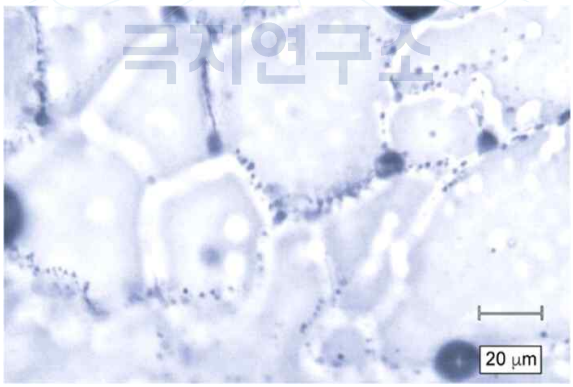



**Figure 5.** Optical image of concentrated NAu-2 particles at the ice grain boundaries. Experimental conditions: [NAu-2] = 0.2 g $L^{-1}$, [DW] = 10 mL, freezing rate: −2 °C $min^{-1}$, observed temperature: −20 °C.

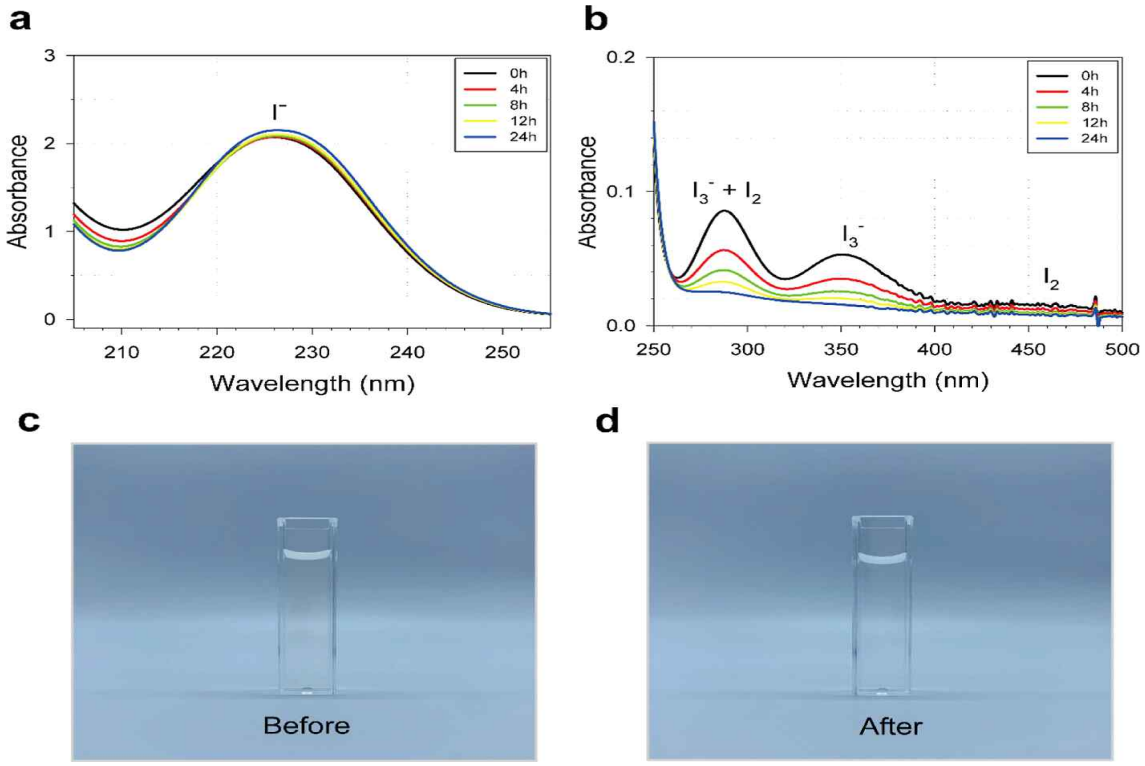



**Figure 6.** Changes of UV/vis spectra of iodine species and color of the ice sample taken after 24 h of reaction and filtering. Experimental conditions were as follows: [NAu-2] = 0.2 g $L^{-1}$, [$I^-$] = 200 μM, pH 3 (adjusted with $H_2SO_4$), T = −20 °C. (a) UV/vis spectra depicting $I^-$ around 226 nm and (b) UV/vis spectra of $I_3^-$ and $I_2$. The absorbance at 353 nm represents $I_3^-$ concentrations, the absorbance at 460 nm represents $I_2$ concentrations, and the absorbance at 288 nm represents the combined spectra of $I_3^-$ and $I_2$. (c) Image of the thawed and filtered ice sample after 24 h of freezing experiment and (d) image after leaving the sample in (c) to evaporate at room temperature for 24 h.

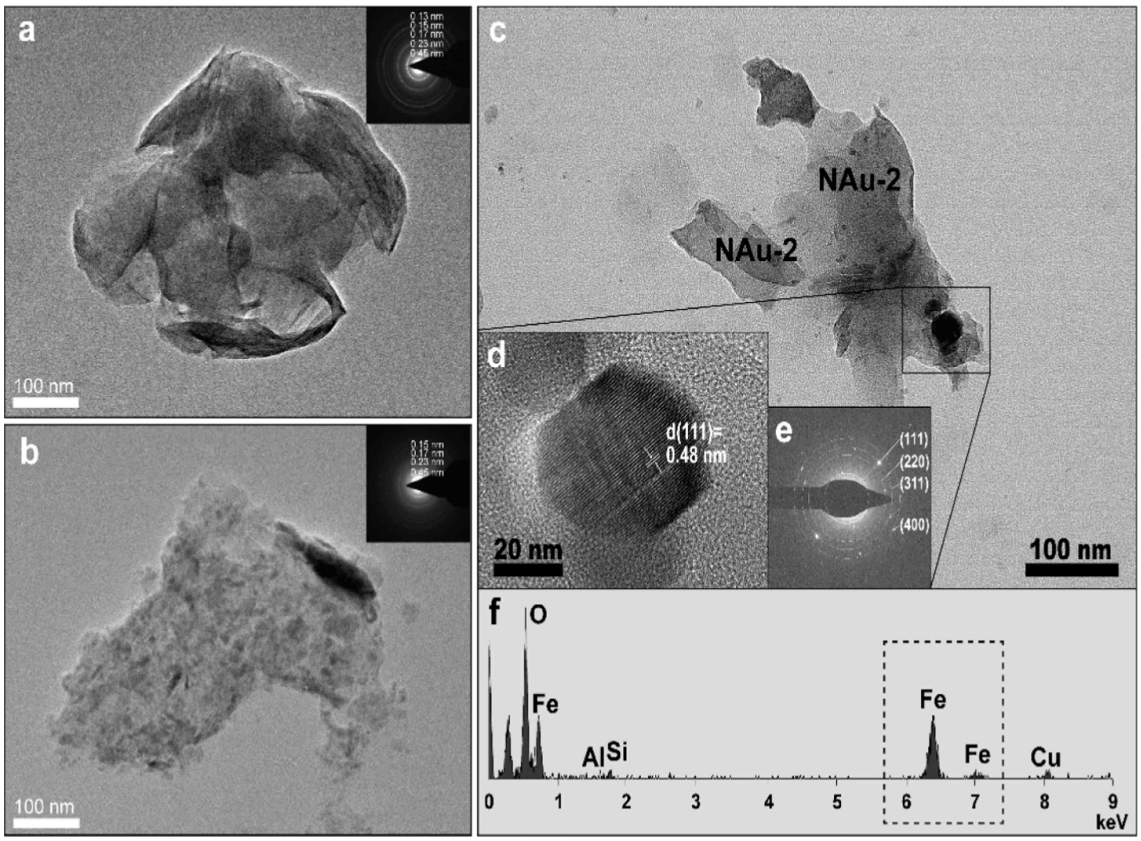



**Figure 7.** TEM images of NAu-2 and magnetite particles with the corresponding SAED patterns and EDS spectra. (a) TEM image and SAED pattern of initial NAu-2, (b) TEM image and SAED pattern of NAu-2 after 24 h of freezing experiment, (c) TEM image of NAu-2 and magnetite after 24 h of freezing experiment, (d) magnified TEM image of magnetite nanoparticulate, (e) corresponding SAED pattern, and (f) EDS spectra.

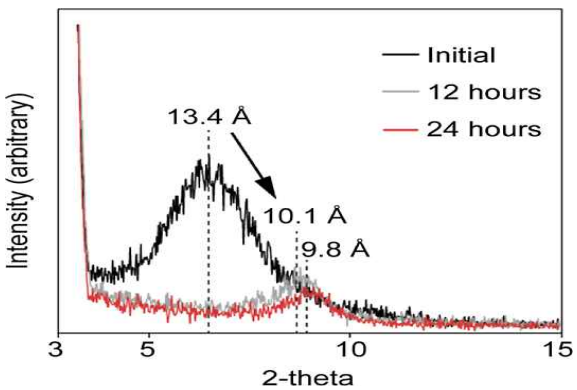



**Figure 8.** X-ray diffraction profiles of initial NAu-2 and NAu-2 after 12 and 24 h of freezing.

# 제 14 절. Detoxification of arsenite by iodide in frozen solution⑭

Quoc Anh Nguyen[1,2], Bomi Kim[1,2], Hyun Young Chung[1,2], Yong-Yoon Ahn[1], Kitae Kim[1,2]

[1]Korea Polar Research Institute (KOPRI), Incheon 21990, Republic of Korea
[2]Department of Polar Sciences, University of Science and Technology (UST), Incheon 21990, Republic of Korea

## Abstract

The oxidation of arsenite (As(III)) to arsenate (As(V)) has received significant attention because it helps mitigate the hazardous and adverse effects of As(III) and subsequently improves the effectiveness of arsenic removal. This study developed an efficient freezing technology for the oxidative transformation of As(III) based on iodide ($I^-$). For a sample containing a very low concentration of 20 μM As(III) and 200 μM $I^-$ frozen at −20 °C, approximately 19 μM As(V) was formed after reaction for 0.5 h at pH 3. This rapid conversion has never been achieved in previous studies. However, As(V) was not generated in water at 25 °C. The acceleration of the oxidation of As(III) by $I^-$ in ice may be attributed to the freeze-concentration effect. During freezing, all components (i.e., As(III), $I^-$, and protons) are highly concentrated in the ice grain boundary regions, resulting in thermodynamically and kinetically favorable conditions for the redox reaction between As(III) and $I^-$. The efficiency of the oxidation of As(III) using $I^-$ increased at high $I^-$ concentrations and low pH values. The low freezing temperature (below −20 °C) hindered the oxidative transformation of As(III) by $I^-$. The efficiency of the oxidation of As(III) significantly increased using a fixed initial concentration of $I^-$ by subjecting the system to six freezing - melting cycles. The outcomes of this study suggest the possibility of the self-detoxification of As(III) in the natural environment, indicating the potential for developing an eco-friendly method for the treatment of As(III)-contaminated areas in regions with a cold climate. It also demonstrates radical remediation to almost completely remove a very small amount of As(III) that was input in As(III)-contaminated wastewater detoxification, a benchmark that existing methods have been unable to achieve.

⑭ 본 연구는 본 과제(PE23120)로 수행되었으며, 결과는 *Chemosphere,* 2023, 340, 139903 에 출간되었다.

## 1. Introduction

Arsenic, a carcinogenic element, is naturally present in various environmental components owing to factors such as weathering, volcanic activities, and the dissolution of As-containing minerals (Jacukowicz-Sobala et al., 2020; Zhang et al., 2020). Additionally, anthropogenic activities, such as the application of fertilizers (Jayasumana et al., 2015), wood preservatives (Takahashi et al., 2018), and pesticides (Paltseva et al., 2018), significantly contribute to the release of As into the environment. Among the four species of As with different oxidation states – namely, arsine ($AsH_3$), arsenic (As (0)), arsenite (As(III)), and arsenate (As(V)) – the latter two, inorganic As(III) and As(V), are primarily detected in aquatic environments (Demirel et al., 2022; Nicomel et al., 2015). As(III) is more detrimental than As(V) owing to its high toxicity and mobility (Coelho et al., 2020; Smith et al., 2018). Therefore, the preliminary oxidation of As(III) to As(V) is necessary to temporarily minimize the hazardous and adverse effects due to As(III). Furthermore, it helps improve the efficiency of As degradation processes. Several current remediation processes that pre-oxidize As(III) include coagulation (Eslami et al., 2019; Wang et al., 2019), membrane technology (Sen et al., 2010), sorption (Liu et al., 2018), ion exchange (Bashir et al., 2019), and photocatalytic oxidation (Farhan et al., 2023). Although these methods are frequently applied for As removal, tests carried out with low initial concentrations of the order of several micromolar per liter of As(III) showed low oxidation efficiency (Sorlini and Gialdini, 2010). In contrast, the photochemical oxidation of As(III) attained high efficiency, but it requires a high energy input as well as a catalyst to facilitate the photochemistry of As(III) (Bissen and Frimmel, 2003). Therefore, benign, financially sustainable systems that oxidize As(III) for large-scale applications are currently being developed (Farhan et al., 2023). Recently, owing to the thawing permafrost, the enrichment of As has been documented in snow/ice-covered regions (Antarctica; Arctic) (Bhardwaj et al., 2023; Farías et al., 2007; Hong et al., 2004; Krachler et al., 2009; Perryman et al., 2020; Schwanck et al., 2016). Therefore, raising awareness regarding the characteristics and effects of As on these regions is important. Additionally, the development of a cost-effective and environmentally friendly freezing technique for As(III) oxidation is imperative.

Iodide ($I^-$) has a significant impact on seawater owing to its high reactivity compared to iodate ($IO_3^-$) and its equilibrium with hypoiodous acid (HIO), which leads to the formation of reactive iodine species. These reactive iodine species play significant roles in determining the chemistry and oxidizing capacity of the troposphere, particularly tropospheric ozone depletion events (Saiz-Lopez et al., 2016) and the transformation of gaseous elemental mercury ($Hg^0$) to reactive gaseous mercury ($Hg^{2+}$). The concentration of $I^-$ in seawater ranges from tens of nanomolar at high latitudes to several hundreds of

nanomolar in tropical and coastal seas, thereby dominating both the atmospheric iodine concentrations and the oceanic dry deposition of ozone via the reaction $I^- + O_3 \rightarrow IOOO^-$ (Carpenter et al., 2021). However, the abiotic chemical mechanisms and kinetics of iodide with heavy metals during freezing remain unclear and must be investigated in detail.

Based on the extensive research conducted in recent years, the freezing process at temperatures below the freezing point can significantly enhance the rate of redox reactions compared with that in water at temperatures above the freezing point. For instance, the complete removal of furfuryl alcohol (FFA), which is an organic pollutant, using inorganic periodate ($IO_4^-$) was considerable in ice media but negligible in aqueous media (Choi et al., 2018). Hexavalent chromium (Cr(VI)) is reduced to trivalent chromium (Cr(III)) by reducing agents, such as $H_2O_2$ and $I^-$, to a more considerable degree in ice than it does in water (Kim et al., 2015, 2020). Furthermore, the formation of organoiodine compounds in the ferric/$I^-$/humic acid system was more pronounced in ice than in water (Du et al., 2022). This phenomenon is explained by the freeze-concentration effect (Ahn et al., 2022; Han et al., 2021; Kim et al., 2022; Min and Choi, 2017; Nguyen et al., 2021). Specifically, during the freezing process, ice grain boundary regions with sizes in the range of several micrometers are formed. Simultaneously, all components evacuate from the ice lattice and converge on the ice grain boundary regions, leading to a significant increase in the concentration of components and a decrease in the activation energy of chemical reactions (Bartels-Rausch et al., 2014; Takenaka et al., 1996; Takenaka and Bandow, 2007). Additionally, the pH changes after freezing due to the accumulation of protons ($H^+$) in acidic environments or hydroxides ($OH^-$) in basic environments within the ice grain boundary regions (Heger et al., 2006; Okada et al., 2019).

Although the photochemistry of $I^-$-induced As(III) under 254 nm ultraviolet (UV) illumination has been reported (Yeo and Choi, 2009), the mechanism of chemical transformation in ice media remains unclear. In this study, we investigated the oxidative conversion of As(III) to As(V) using $I^-$ in both water and ice. The efficiency of As(III) oxidation using $I^-$ was examined by varying the experimental parameters. Furthermore, a detailed discussion regarding the mechanism of oxidation of As(III) with $I^-$ is provided. Finally, a practical application and the novelty of the As(III)/$I^-$/freezing system are demonstrated.

## 2. Materials and Methods

### 2.1. Chemicals

The following chemicals were used in this study: sodium (meta)arsenite ($NaAsO_2$, Aldrich, ≥90%), sodium arsenate dibasic heptahydrate ($Na_2HAsO_4.7H_2O$, Aldrich, ≥

98%), l-ascorbic acid ($C_6H_8O_6$, Aldrich, ≥99%), molybdate reagent solution (Supelco), potassium iodide (KI, Aldrich, ≥99%), perchloric acid ($HClO_4$, Aldrich, 60%), sodium hydroxide (NaOH, Aldrich, 1 N), and cresol red (CR; $C_{21}H_{18}O_5S$, Aldrich, 95%). All solutions in this experiment were prepared using deionized water (18.2 MΩ cm), which was purified using a Barnstead water purification system (Mili-Q Direct 16).

### 2.2. Experimental procedure

Two working solutions of As(III) and $I^-$ were prepared in this study. Generally, the concentrations of As(III) and $I^-$ were set to 20 and 200 μM, respectively. The solutions were prepared by adding aliquots of their respective stock solutions to deionized water in a 250 mL volumetric flask. The pH of the solutions was adjusted according to the desired value, typically to pH 3, using either a 60% $HClO_4$ or a 1 N NaOH solution. A Thermo Scientific Orion 2-Star Benchtop pH meter was used for pH measurements. Samples (5 mL) containing both As(III) and $I^-$ were transferred to 15 mL VWR centrifuge tubes. These tubes were then immersed in a temperature controller set to the desired temperature, and ethanol was used as the coolant. In most cases, the temperature was set to 25 or −20 °C when reacting in water or ice, respectively. The time-zero was defined as the moment when the tubes were placed in the ethanol bath, and the temperature was maintained at −20 °C. At each observed reaction time interval, the tubes were withdrawn from the temperature controller and immediately placed in a beaker containing lukewarm water at 30 °C for 1 min. These steps were performed to ensure that the frozen samples were completely thawed before the analysis. Freezing-melting cycles were reproduced by alternately freezing samples (10 mL) containing both 100 μM As(III) and 200 μM $I^-$ at pH 3 at −20 °C for 1 h and melting the samples in lukewarm water at 30 °C for 0.5 h. All experiments were conducted in triplicate to confirm data reproducibility.

### 2.3. Chemical Analyses

A spectrophotometric method was used to quantitatively measure the concentrations of As(V), $I_2$, and $I_3^-$. The molybdenum blue method was employed for measuring the As(V) concentration (Lenoble et al., 2003). Specifically, 1 mL of sample was added to a 15 mL polypropylene centrifuge tube, which contained 3 mL of deionized water, 0.2 mL of molybdate reagent solution, and 0.2 mL of l-ascorbic acid (2 g/L). The mixed samples were vortexed, maintained in the dark for 4 h, and then transferred to a 3 mL cuvette for further analysis. The maximum absorbance values of the samples were measured at 870 nm using a UV - visible spectrophotometer (Shimadzu UV-2600). A linear relationship between the absorbance value and the concentration of As(V) was established using the As(V) calibration curve ($r^2$ = 0.9999). To measure the $I_2$ and $I_3^-$ concentrations, the

absorbance values at 460 and 353 nm, respectively, were recorded using a UV–visible spectrophotometer (Shimadzu UV-2600). The concentrations of $I_2$ and $I_3^-$ were calculated using Beer–Lambert's law with a path length of 1 cm for the cuvette and the molar absorption coefficients ($\epsilon$) of $I_2$ (746 $M^{-1}$ $cm^{-1}$) and $I_3^-$ (26,400 $M^{-1}$ $cm^{-1}$) (Awtrey and Connick, 1951).

The pH of the ice grain boundary region in the frozen sample was estimated by recording the UV–visible absorption spectra of CR, which is an acid–base indicator (Krausková et al., 2016; Vetráková et al., 2017). The CR spectra demonstrate three different maximum absorption peaks at wavelengths ($\lambda_{max}$) of 518, 434, and 573 nm, depending on the pH (Heger et al., 2006). Therefore, 3 mL of the aqueous sample containing As(III), $I^-$, and CR ([As(III)] = 20 μM, [$I^-$] = 200 μM, and [CR] = 6.7 μM at pH 3) was transferred into a 4 mL plastic rectangular cuvette and introduced into the temperature controller preset at −20 °C for 1 h. The frozen sample was then withdrawn, and the UV–visible absorption spectra were immediately measured without thawing. Frozen deionized water was used as the baseline for measuring the frozen sample.

The distribution and concentration changes of As(V) generated in the ice grain boundary regions of the frozen sample were visualized using a confocal Raman spectroscope (Renishaw inVia Qontor), which was connected to a microscope stage. A constant temperature of −20 °C was maintained using a temperature controller (Linkam Scientific THMS600). Aqueous samples (0.1 mL), including As(III) only ([As(III)] = 1 mM at pH 3) and the mixture of As(III) and $I^-$ ([As(III)] = 1 mM, [$I^-$] = 1 mM at pH 3), were placed in the sample holder at the temperature-controlled stage. Liquid nitrogen was used as a coolant to lower the temperature from 25 to −20 °C at a rate of −2 °C/min. The As(V) distribution and concentration in the confined liquid region were mapped by measuring the intensity of the characteristic As(V) peak (As(V)–O stretching mode) at 780 $cm^{-1}$ using a monochromatic 532 nm laser as the excitation source (Xu et al., 2010; Yang et al., 2019).

## 3. Results and Discussion

### 3.1. As(III) oxidation by $I^-$ in water and ice

The process of the oxidation of As(III) by $I^-$ in the frozen solution at −20 °C was compared with that in an aqueous solution at 25 °C under the experimental conditions of [As(III)] = 20 μM, [$I^-$] = 200 μM, and pH 3 (Fig. 1). From Fig. 1(a), in the presence of $I^-$, a significant amount of As(V) is formed under frozen conditions, whereas this phenomenon is not observed in water. In particular, approximately 100% of As(III) was oxidized after 0.5 h of reaction in the ice phase. However, the oxidation of As(III) was not observed in the aqueous phase during the reaction time. In the absence of $I^-$, As(V) was not detected in water or ice. This suggests that the dissolved oxygen-mediated As(III) oxidation cannot

be considered in this study (i.e., $2HAs^{(III)}O_2 + 2H_2O + O_2 \rightarrow 2H_2As^{(V)}O_4^- + 2H^+$; $E^0$ = 0.83 V, as shown in Eq. (S5) in Supplementary Material). Fig. 1(b) illustrates the time profiles of the $I_2$ and $I_3^-$ concentrations in the samples containing As(III) and $I^-$ in both the aqueous and ice phases. The generation of $I_2$ and $I_3^-$ in aqueous media was negligible. Notably, the production of $I_3^-$ gradually increased after 0.5 h of reaction, and $I_2$ was not generated during freezing. These results reveal that the oxidation of As(III) in the ice phase preferentially occurred compared to that in the aqueous phase. Additionally, $I_3^-$ can act as an oxidant for As(III) oxidation in frozen solution. This conjecture is confirmed by the observation of the two peaks corresponding to the maximum absorptions at 288 and 353 nm, indicating the generation of $I_3^-$ (Fig. S1, Supplementary Material) (Awtrey and Connick, 1951). From Fig. S1, the intensity of the two characteristic $I_3^-$ peaks was negligible in the case of the $I^-$ solution ($[I^-]$ = 200 μM at pH 3) with and without freezing after 6 h. A similar propensity was observed in the As(III)/$I^-$ system at 25 °C after 6 h. However, after adding 200 μM $I^-$ to 20 μM As(III) at pH 3, followed by the cooling of the resulting mixture to −20 °C, the two characteristic peaks of $I_3^-$ were clearly observed after 1 h of reaction. Furthermore, the two typical peaks of $I_3^-$ gradually increased in intensity throughout the duration of the tested reaction. These findings are consistent with previous results. Notably, although the two $I_3^-$ peaks were not observed after 0.5 h of reaction in the ice phase, the total content of As(III) was oxidized. This is because both As(III) and $I^-$ are well-known reducing agents. Hence, from a thermodynamic perspective, no chemical reaction occurs between them. However, in the frozen state, $I_3^-$ can be formed via the chemical interaction between $I^-$, dissolved oxygen, and the protons present in the liquid boundaries, with As(III) acting as a catalyst. The amount of $I_3^-$ that was generated after 0.5 h is sufficient to completely oxidize 20 μM As(III). Considering the mechanism of this process, the conversion of $I^-$ into $I_3^-$ is assumed to initially occur in an acidic environment (reaction (1)). Subsequently, $I_3^-$ serves as the major oxidizing agent and enables the thermodynamic and kinetic transformations of As(III) into As(V) via electron transfer (reaction (2)). In most cases, the presence of $I_2$ and the characteristic $I_2$ peak at the maximum absorption wavelength of 460 nm (Awtrey and Connick, 1951) (Fig. S1, Supplementary Material) were not detected during freezing. This suggests that among the two products derived from $I^-$ (i.e., $I_2$ and $I_3^-$), the production of $I_3^-$ predominated (reaction (1)), and the oxidation of As(III) was primarily driven by $I_3^-$ (reaction (2)). Notably, the oxidation of $I^-$ by dissolved oxygen (reaction (1)) was considerably slow when only 200 μM $I^-$ was frozen at pH 3 after 6 h of reaction, despite the positive reaction potential of $E^0$ = 0.694 $V_{NHE}$ (Eq. (S6), Supplementary Material). Specifically, the two characteristic $I_3^-$ peaks were not observed (Fig. S1, Supplementary Material). However, chemical reaction (1) was significantly accelerated in the presence of

As(III). From the viewpoint of kinetics, this could be explained by considering that, with the support of As (III) serving as a catalyst, the conversion of $I^-$ into $I_3^-$ preferably proceeds via a transition state involving the formation of the $As^{(III)}$–$I^-$ complex with lower activation energy. Therefore, this facilitates the formation of $I_3^-$ via the oxidation of $I^-$ in $As^{(III)}$ - $I^-$ by the dissolved oxygen. From a thermodynamic viewpoint, this could be understood by considering that the redox reaction between As(III) and $I_3^-$ is thermodynamically spontaneous, with a positive driving force of $E^0$ = 0.136 $V_{NHE}$ (Eq. (S3), Supplementary Material) under the experimental conditions used in the test. This reaction disturbs the dynamic equilibrium (1) by decreasing the concentration of $I_3^-$. Consequently, equilibrium (1) shifts in the direction of the generation of $I_3^-$ to offset the change in the $I_3^-$ concentration in accordance with Le Chatelier's principle. This led us to conclude that As(III) acts as a reductant as well as a catalyst to accelerate the rate of $I_3^-$ formation in this study.

$$O_2 + 4H^+ + 6I^- \rightarrow 2H_2O + 2I_3^- \quad (1)$$

$$I_3^- + HAs^{(III)}O_2 + 2H_2O \rightarrow H_2As^{(V)}O_4^- + 3H^+ + 3I^- \quad (2)$$

### 3.2. Freeze-concentration effect

Based on reaction (2), indicating the relationship between the driving force of the total reaction (2) and the concentration of the substances in chemical equation (2) (Eq. (S3), Supplementary Material), the oxidative transformation of As(III) to As(V) by $I^-$ primarily depends on the concentration of $I_3^-$. Meanwhile, the generation of $I_3^-$ is more beneficial at higher concentrations of initial $I^-$ and dissolved $O_2$ at lower pH (reaction (1) and Eq. (S6), Supplementary Material). Therefore, increasing the initial concentration of $I^-$ and/or decreasing the pH may help enhance the conversion rate of As(III) using $I^-$. In addition, freezing plays a significant role in the oxidation of As(III) by $I^-$. When a sample is frozen in an acidic environment, the protons have been reported to be eliminated from ice crystals. Furthermore, they gradually enter the boundaries of the ice grains. This creates a more acidic environment, which favors the oxidation of As(III) by $I^-$ by lowering the activation energy (Heger et al., 2006). Moreover, the enrichment of As(III) and $I^-$ in the ice grain boundary regions has a synergistic effect on $I^-$–mediated As(III) oxidation, owing to the increase in the number of effective collisions between As(III) and $I_3^-$ for their redox reactions.

The spatial distribution and concentration changes of As(V) produced in the ice grain boundary regions were monitored in situ, without melting, using confocal Raman spectroscopy (Fig. 2). To visually delineate the formation of the ice grain boundary regions upon freezing, a sample solution containing only As(III) was frozen. A significant difference was observed between the two compartments composed of ice crystals and liquid regions

(i.e., ice grain boundary regions) surrounded by ice crystals (Fig. 2(a)). The estimated size of the ice grain boundary regions was in the range of a few micrometers. During freezing, we measured the relative Raman intensities of the As(V) peak corresponding to the characteristic Raman As(V) - O stretching mode at 780 $cm^{-1}$ to demonstrate the redox reaction between As(III) and $I^-$ occurring in the ice grain boundary regions (Mulvihill et al., 2008). The relative concentration of generated As(V), which is proportional to the relative intensity of the As(V) peak, is shown on a rainbow scale, wherein the concentration increases when the color changes from black (indicating the lowest concentration) to red (indicating the highest concentration) (Fig. 2(b) vs Fig. 2(c)). As shown in Fig. 2(a), the colors black and blue are mainly observed in the ice grain boundary regions. This result revealed that As(V) was not present in the ice grain boundaries. However, after the initial 1 h of reaction, red areas appeared. Moreover, the density of the red areas increased after an additional 1 h of reaction in the frozen state at the ice grain boundary regions (Fig. 2(b) vs Fig. 2(c)). These observations confirmed that As(V) is the final product of the As(III)/$I^-$/freezing system. The distribution of As(V) was observed in the ice grain boundaries, indicating that As(III) and $I^-$ first accumulated in these active sites. The redox reaction between As(III) and $I_3^-$ then spontaneously occurred within the ice grain boundary regions rather than within the ice lattices.

To obtain conclusive evidence of the freezing-induced pH shift, we used CR as an acid - base indicator to quantitatively measure the decrease in pH caused by freezing using the UV - visible spectra (Krausková et al., 2016; Newberg, 2018; Vetráková et al., 2017) (Fig. 3). For an aqueous CR solution, three different absorption peak maxima were observed depending on the pH, mainly owing to protonation and deprotonation (di-protonated CR: $H_2A$, mono-protonated CR: $HA^-$ and deprotonated CR: $A^{2-}$) (Heger et al., 2006). Fig. 3 shows the shift in the UV - visible spectra of CR in both the aqueous and ice phases in the sample containing As(III), $I^-$ and CR. Significantly, only one peak was recorded at 434 nm for the aqueous sample, as the CR formed at pH 3 mainly comprised $HA^-$ ($\lambda_{max}$ = 434 nm). Notably, when the aqueous sample was frozen for 1 h, the intensity of the $HA^-$ peak decreased, and a new peak emerged at 518 nm, corresponding to $H_2A$ (El Nahhal et al., 2012). This indicates that the $HA^-$ anions gradually migrated into the ice grain boundary regions during freezing, and several $HA^-$ anions gained protons owing to a decrease in pH, thereby forming $H_2A$ molecules ($HA^- + H^+ \rightarrow H_2A$). The pH of the ice grain boundary regions was estimated by applying the Henderson - Hasselbalch equation ($pH = pK_{a1} + \log [HA^-]/[H_2A]$, where $pK_{a1}$ = 1.1) (Dean, 1992). The ratio, $[HA^-]/[H_2A]$, was determined as ~0.85 using the non-negative least squares minimization method (Ju et al., 2017). The calculated pH value of the ice grain boundary regions was approximately 1.03 under the experimental conditions of [As(III)] = 20 μM, $[I^-]$ = 200 μM, [CR] = 6.7 μM

and pH 3 at −20 °C. Therefore, freezing indirectly helps create a highly acidic environment that is kinetically favorable for $I^-$-mediated As(III) oxidation.

To demonstrate the impact of the freeze-concentration effect on the chemical transformation of As(III) by $I^-$, the kinetics of the formation of As(V) was measured in water at [As(III)] = 20 μM, [$I^-$] = 2 or 20 mM and pH 1, 2, or 3 (Fig. 4). The As(V) was not observed to have formed upon increasing the concentration of $I^-$ tenfold (from 200 μM to 2 mM) or hundredfold (from 200 μM to 20 mM). A similar trend was observed upon decreasing the pH value by one (from pH 3 to 2) or two units (from pH 3 to 1). Notably, when the concentration of $I^-$ was increased tenfold ([$I^-$] = 2 mM), and the pH value was decreased by one unit (to pH 2), a small amount of As(V) was generated (approximately 2 μM). However, when the concentration of $I^-$ was increased hundredfold ([$I^-$] = 20 mM), and the pH value was decreased by two units (to pH 1) after 4 h of reaction, the concentration of As(V) approximately quadrupled (~8 μM). To further understand this result, the UV - visible spectra of an $I^-$ solution with a high concentration and low pH ([$I^-$] = 20 mM; pH 1) were recorded for the duration of the reaction (Fig. S2, Supplementary Material). The spectra show that the intensities of the characteristic peaks corresponding to maximum absorptions of $I_3^-$ at 288 and 353 nm (Pursell and Pursell, 2016) decreased after 2 h. The intensities of these two peaks gradually increased after 4 h. This emphasizes the significance of the ice grain boundary regions in creating an environment of highly concentrated protons and dissolved oxygen. These conditions thermodynamically and kinetically facilitate the generation of $I_3^-$ (reaction (1)), which is predominantly responsible for transforming As(III) into As(V) via chemical reaction (2). The acceleration of the oxidation of As(III) by $I^-$ in the ice grain boundary regions during freezing is attributed to the synergistic effects of both $I^-$ anions and protons rather than the individual contributions of either $I^-$ anions or protons.

### 3.3. Freezing-induced As(III) oxidation by $I^-$ under various conditions

In the next stage, the impact of various experimental factors (i.e., $I^-$ concentration, pH, and freezing temperature) on the oxidative transformation of As(III) by $I^-$ was investigated in the aqueous and ice phases to determine the highest efficiency for this process (Fig. 5). Notably, the efficiency of this process is proportional to the formation rate of As(V). For aqueous samples with $I^-$ concentrations in the range of 50 - 300 μM, a similar trend was observed (Fig. 5(a)). As(V) was not generated under the given conditions ([$I^-$] = 50 - 300 μM, [As(III)] = 20 μM and reaction time = 4 h at pH 3) in water, as the aforementioned conditions were not thermodynamically and kinetically favorable for the formation of $I_3^-$, which was the oxidant source for the oxidation of As(III). In contrast, the generation of As(V) (i.e., As(III) oxidation) was significantly enhanced in the frozen samples after 4 h of

reaction by increasing the concentration of $I^-$. No significant difference was observed in the As(V) concentrations when $[I^-] \geq 200$ μM ([As(V)] = 3.93 μM at $[I^-]$ = 50 μM, [As(V)] = 5.64 μM at $[I^-]$ = 100 μM, [As(V)] = 19.07 μM at $[I^-]$ = 200 μM and [As(V)] = 19.30 μM at $[I^-]$ = 300 μM). Therefore, in this study, the highest process efficiency was achieved with 200 μM $I_3^-$ for the complete oxidation of 20 μM As(III) at pH 3. This was attributed to the increase in the concentration of $I_3^-$ that was generated in the ice grain boundary regions during freezing when the $I^-$ concentration was increased, thereby increasing the rate at which As(III) is oxidized over that of $I^-$.

Fig. 5(b) shows a comparison of the generation rate of As(V) formed via the oxidation of 20 μM As(III) by 200 μM $I^-$ between the aqueous and ice phases in the pH range 2 - 9 after 4 h of reaction. Generally, the chemical removal of As(III) by $I^-$ was not observed in water at any of the tested pH values (i.e., the pH range of 2 - 9). In contrast, the production of As(V) gradually increased as the pH values decreased from 5 to 3 owing to freezing ([As(V)] = 3.01 μM at pH 5, [As(V)] = 3.99 μM at pH 4 and [As(V)] = 19.07 μM at pH 3). These results further confirm the role of protons in the accelerated oxidation of As(III) by $I^-$. Furthermore, the amount of As(V) generated at pH 2 was small compared with that at pH 3, and As(V) was not released at pH 9 even when the sample was cooled to −20 °C. When a sample in a basic environment is frozen, a higher number of $OH^-$ anions gather at the ice grain boundary regions, resulting in a more basic environment (Takenaka et al., 2006). However, based on reaction (1), the presence of protons accelerates the formation of $I_3^-$, leading to the suppression of the formation of As(V) at pH 9. Specifically, $I_3^-$ and As(V) were not generated at pH 9 during the time the reaction was monitored (Fig. S3(c), Supplementary Material). Notably, the maximum absorption peaks of $I_3^-$ at 288 and 353 nm (Pursell and Pursell, 2016) were not detected for the oxidation of As(III) at pH 4 and 5 compared with the case of oxidation at pH 3 in the ice phase (Fig. S3(a) vs Fig. S3(b), Supplementary Material). Therefore, all the formed $I_3^-$ anions instantaneously and completely reacted with As(III) in the ice grain boundary regions during 4 h of the reaction. Therefore, this finding indicates that by creating a highly acidic environment in the ice grain boundary regions, all three components (i.e., As(III), $I^-$, and protons) exhibit a synergistic effect on the $I^-$-mediated As(III) oxidation efficiency.

The temperature dependence of the oxidation of 20 μM As(III) by 200 μM $I^-$ at pH 3 was studied for 4 h at various freezing temperatures of −10, −15, −20, −25, −30, and −196 °C (Fig. 5(c)). To evaluate the influence of the frozen state on the oxidation efficiency of As(III) using $I^-$, liquid nitrogen was used to attain the temperature of −196 °C. The concentration of As(V) reached approximately zero at −196 °C. This is because the use of liquid nitrogen as a coolant to establish a permafrost environment in which the temperature was maintained at −196 °C, caused the sample to rapidly freeze.

Ice crystals immediately formed and their formation was complete. Therefore, ice grain boundary regions were absent. All constituents (i.e., As(III), $I^-$, and protons) were trapped in the ice lattices and were unable to move into the ice grain boundary regions. Consequently, no chemical reaction occurred in this case. To evaluate the influence of the size of ice grain boundary regions on the oxidation of As(III) based on $I^-$, samples were frozen at various freezing temperatures ranging from −10 to −30 °C. Generally, the maximum rate at which As(V) was formed via $I^-$-mediated As(III) oxidation was achieved at −20 °C. In the freezing temperature range of −20 to −30 °C, the formation of As(V) is hindered by the $I^-$-mediated conversion of As(III) owing to the increasing speed of ice crystal formation. Lowering the freezing temperature results in an increase in the rate of ice crystal formation and reduces the size of the ice grain boundary regions. As a result, sufficient time was not available for the migration of components (i.e., As(III), $I^-$, protons) into the ice grain boundary regions, and therefore, the freeze-concentration effect was suppressed. In contrast, when the temperature was lowered to −10 °C, the sample started to freeze, causing the size of the ice grain boundaries to gradually decrease. The size continuously decreased until reaching a specific temperature, at which the rate of chemical reactions was maximized (−20 °C in this study). Notably, the smaller the size of the ice grain boundaries, the higher the concentration of the components at those sites. Consequently, the concentration of As(V) increased as the temperature decreased from −10 to −20 °C. Therefore, the freezing process indirectly enhances the rate of redox reactions in general, particularly in the As(III)/$I^-$ system, by creating a favorable reaction space for reactants. The highest efficiency of the As(III)/$I^-$/freezing system was achieved at −20 °C wherein 20 μM As(III) was completely oxidized by 200 μM $I^-$ at pH 3.

### 3.4. Practical application of As(III)/$I^-$/freezing system for the oxidation of As(III) and production of $I_3^-$ through freezing - melting cycles

$I^-$ is ubiquitously present in various natural environments. In particular, the average concentration of $I^-$ is approximately 20 μg/L in untreated water (Moran et al., 2002) and up to 100 μg/L in drinking water (Richardson et al., 2008). Additionally, the expansion of shale gas and hydraulic fracturing have facilitated the production of a significant amount of $I^-$ in wastewater, with concentrations reaching as much as 54 mg/L in the hydraulic fracturing process of wastewater (Harkness et al., 2015; Liberatore et al., 2017; Parker et al., 2014). In the presence of strong oxidizers in wastewater (such as ozone, chlorine, and monochloramine), $I^-$ can be preferentially oxidized into highly reactive iodine species (such as $I_2$, $I_3^-$, hypoiodous acid, and radicals) (Li et al., 2020). During chlorination, iodinated organic compounds can be formed, which is significantly toxic to the environment (Li et al., 2020). $I_2$ and iodine radicals in the troposphere are known to play a significant role in

inducing climate change. This is because they affect cloud generation and radiative balance through the production of new aerosol particles (Gilfedder et al., 2007).

The use of a considerable amount of $I^-$ to oxidize As(III) to As(V) in wastewater provides a cost-effective and environmentally friendly strategy to significantly reduce the generation of toxic species from $I^-$ and As(III). In this study, we evaluated the maximum efficiency of the oxidation process of a large amount of As(III) using a constant amount of $I^-$ throughout the freezing–melting cycles (Fig. 6). As previously mentioned, the optimal conditions for fully oxidizing 20 μM As(III) were 200 μM $I^-$ and pH 3 using the freezing method. Based on chemical equation (2), the input source $I^-$ is recovered after the oxidation of As(III) by $I^-$. Consequently, the concentration of $I^-$ was significantly conserved after the reaction. However, the production of $I_3^-$ is limited by the dissolved oxygen present in the ice grain boundary regions. Notably, when dissolved oxygen is continuously added to the ice grain boundary regions as a result of the freezing–melting cycles that annually occur in polar regions, the self-detoxification process of As(III) to As(V) using $I^-$ is feasible. To test this hypothesis, an aqueous sample containing 100 μM As(III) (increased fivefold) and 200 μM $I^-$ (unchanged) at pH 3 was subjected to six freezing–melting cycles (1 h of freezing and 0.5 h of melting alternately) with the supplementation of dissolved oxygen to the ice grain boundary regions. The production of As(V) via the oxidation of As(III) by $I^-$ gradually increased after each freezing–melting cycle, and 100% As(III) was converted into As(V) after a minimum of six freezing–melting cycles were completed. The use of this As(III)/$I^-$/freezing system provides an effective pathway for As(III) treatment in industrial wastewater and is a significant strategy for the self-purification of As(III) by $I^-$ in cold regions. Freezing–melting cycles are known to annually occur under daylight conditions in cold regions, and the ice grain boundary regions are considered reactive sites that collect a wide variety of contaminants (Huthwelker et al., 2006).

## 4. Conclusions

We studied and compared the oxidative conversion of As(III) by $I^-$ in water and ice. The formation of As(V) via the oxidation of As(III) by $I^-$ was achieved in the frozen state owing to the freeze-concentration effect. The freezing process created favorable conditions for the accumulation of all components (i.e., As(III), $I^-$, and protons) in the grain boundary regions of the ice, thereby thermodynamically and kinetically favoring the occurrence of the redox reaction between As(III) and $I^-$. Additionally, the recovery of $I^-$ (the input source), which is required for the oxidation of a significant amount of As(III), was achieved using freezing–melting cycles, which continuously occur in polar regions. This finding is vital for the self-detoxification of As(III) in the natural environment, specifically in polar regions.

The $I^-$-mediated As(III) oxidation can be feasibly applied in the treatment of As(III)-contaminated wastewater in cold climate regions. From an economic perspective, this system is viable as electricity is not required for the freezing process in cold regions. Furthermore, future research should focus on taking advantage of the As(III)/$I^-$/freezing system as a subsequent stage to eliminate the very low concentration of As(III) remaining in the wastewater, which is a drawback of existing methods. However, a comparison of the exact cost difference between the traditional As(III) oxidation process and the freezing As(III)//$I^-$ process is difficult because the relationship between the oxidation efficiency and cost depends on the type and volume of As(III)-contaminated wastewater. The precise cost evaluation of the As(III)/$I^-$/freezing system would require field experiments using various freezing systems under different experimental conditions to be conducted. Additionally, the effect of other anions present in As(III)-contaminated wastewater on the efficiency of the As(III)/$I^-$/freezing system would have to be investigated. All of these factors will be explored in our future studies.

KOPRI
극지연구소

## REFERENCES


Ahn, Y.Y., Kim, J., Kim, K., 2022. Frozen hydrogen peroxide and nitrite solution: theacceleration of benzoic acid oxidation via the decreased pH in ice. Environ. Sci.Technol. 56 (4), 2323 – 2333.

Awtrey, A.D., Connick, R.E., 1951. The absorption spectra of $I_2$, $I_3^-$, $I^-$, $IO_3^-$, $S_4O_6^{2-}$ and $S_2O_3^{2-}$. Heat of the reaction $I_3^- = I_2 + I^-$. J. Am. Chem. Soc. 73 (4), 1842 – 1843.

Bartels-Rausch, T., Jacobi, H.W., Kahan, T.F., Thomas, J.L., Thomson, E.S., Abbatt, J.P.D., Ammann, M., Blackford, J.R., Bluhm, H., Boxe, C., Domine, F., Frey, M.M.,Gladich, I., Guzman, ´ M.I., Heger, D., Huthwelker, T., Kl´an, P., Kuhs, W.F., Kuo, M.H.,Maus, S., Moussa, S.G., McNeill, V.F., Newberg, J.T., Pettersson, J.B.C.,Roeselova, ´ M., Sodeau, J.R., 2014. A review of air-ice chemical and physicalinteractions (AICI): liquids, quasi-liquids, and solids in snow. Atmos. Chem. Phys. 14(3), 1587 – 1633.

Bashir, A., Malik, L.A., Ahad, S., Manzoor, T., Bhat, M.A., Dar, G.N., Pandith, A.H., 2019.Removal of heavy metal ions from aqueous system by ion-exchange and biosorptionmethods. Environ. Chem. Lett. 17 (2), 729 – 754.

Bhardwaj, L.K., Sharma, S., Jindal, T., 2023. Estimation of physico-chemical and heavymetals in the lakes of grovnes & broknes peninsula, larsemann hill, east Antarctica.Chem. Afr. 1 – 18.

Bissen, M., Frimmel, F.H., 2003. Arsenic-a review. Part II: oxidation of arsenic and itsremoval in water treatment. Acta Hydrochim. Hydrobiol. 31 (2), 97 – 107.

Carpenter, L.J., Chance, R.J., Sherwen, T., Adams, T.J., Ball, S.M., Evans, M.J.,Hepach, H., Hollis, L.D.J., Hughes, C., Jickells, T.D., Mahajan, A., Stevens, D.P.,Tinel, L., Wadley, M.R., 2021. Marine iodine emissions in a changing world. Proc. R.Soc. A: Math. Phys. Eng. Sci. 477 (2247), 20200824.

Choi, Y., Yoon, H.I., Lee, C., Vetr´akov´a, L., Heger, D., Kim, K., Kim, J., 2018. Activationof periodate by freezing for the degradation of aqueous organic pollutants. Environ.Sci. Technol. 52 (9), 5378 – 5385.

Coelho, D.G., Marinato, C.S., de Matos, L.P., de Andrade, H.M., da Silva, V.M., SantosNeves, P.H., Araújo, S.C., Oliveira, J.A., 2020. Is arsenite more toxic than arsenate in plants? Ecotoxicology 29 (2), 196 – 202.

Dean, J., 1992. Lange's Handbook of Chemistry, fourteenth ed. McGraw-Hill, New York.

Demirel, T., Özmen, F.K., Yavuz, Y., Koparal, A.S., 2022. The effect of electrocoagulation(EC) on total arsenic, arsenite ($As^{3+}$) and arsenate ($As^{5+}$) species removal from model groundwater investigating toxicity and sludge characteristic. Appl. Water Sci. 12 (6), 1 – 13.

Du, J., Kim, K., Min, D.W., Choi, W., 2022. Freeze – thaw cycle-enhanced transformationof iodide to organoiodine compounds in the presence of natural organic matter and

Fe(III). Environ. Sci. Technol. 56 (2), 1007 – 1016.

El Nahhal, I.M., Zourab, S.M., Kodeh, F.S., Babonneau, F., Hegazy, W., 2012. Sol – gelencapsulation of cresol red in presence of surfactants. J. Sol. Gel Sci. Technol. 62 (2),117 – 125.

Eslami, H., Ehrampoush, M.H., Esmaeili, A., Salmani, M.H., Ebrahimi, A.A., Ghaneian, M.T., Falahzadeh, H., Fard, R.F., 2019. Enhanced coagulation process by Fe–Mn bimetal nano–oxides in combination with inorganic polymer coagulants forimproving As(V) removal from contaminated water. J. Clean. Prod. 208, 384 – 392.

Farhan, A., Zulfiqar, M., Samiah Rashid, E.U., Nawaz, S., Iqbal, H.M.N., Jesionowski, T., Bilal, M., Zdarta, J., 2023. Removal of toxic metals from water by nanocompositesthrough advanced remediation processes and photocatalytic oxidation. Curr. Pollut. Rep. 1 – 21.

Farías, S., Smichowski, P., Vélez, D., Montoro, R., Curtosi, A., Vodopívez, C., 2007. Totaland inorganic arsenic in Antarctic macroalgae. Chemosphere 69 (7), 1017 – 1024.

Gilfedder, B.S., Petri, M., Biester, H., 2007. Iodine speciation in rain and snow:implications for the atmospheric iodine sink. J. Geophys. Res. Atmos. 112 (D7), D07301.

Han, T.U., Kim, J., Kim, K., 2021. Use of spent coffee ground as a reducing agent forenhanced reduction of chromate by freezing process. J. Ind. Eng. Chem. 100,310 – 316.

Harkness, J.S., Dwyer, G.S., Warner, N.R., Parker, K.M., Mitch, W.A., Vengosh, A., 2015.Iodide, bromide, and ammonium in hydraulic fracturing and oil and gaswastewaters: environmental implications. Environ. Sci. Technol. 49 (3), 1955 – 1963.

Heger, D., Klánová, J., Kl´an, P., 2006. Enhanced protonation of cresol red in acidicaqueous solutions caused by freezing. J. Phys. Chem. B 110 (3), 1277 – 1287.

Hong, S., Barbante, C., Boutron, C., Gabrielli, P., Gaspari, V., Cescon, P., Thompson, L.,Ferrari, C., Francou, B., Maurice–Bourgoin, L., 2004. Atmospheric heavy metals intropical South America during the past 22000 years recorded in a high altitude icecore from Sajama, Bolivia. J. Environ. Monit. 6 (4), 322 – 326.

Huthwelker, T., Ammann, M., Peter, T., 2006. The uptake of acidic gases on ice. Chem. Rev. 106 (4), 1375 – 1444.

Jacukowicz–Sobala, I., Ociński, D., Mazur, P., Stanisławska, E., Kociołek–Balawejder, E., 2020. Cu(II)–Fe(III) oxide doped anion exchangers – Multifunctional composites forarsenite removal from water via As(III) adsorption and oxidation. J. Hazard Mater. 394, 122527.

Jayasumana, C., Fonseka, S., Fernando, A., Jayalath, K., Amarasinghe, M.,Siribaddana, S., Gunatilake, S., Paranagama, P., 2015. Phosphate fertilizer is a mainsource of arsenic in areas affected with chronic kidney disease of unknown etiology in Sri Lanka.

SpringerPlus 4 (1), 90.

Ju, J., Kim, J., Vetráková, Ľ. Seo, J., Heger, D., Lee, C., Yoon, H.I., Kim, K., Kim, J., 2017. Accelerated redox reaction between chromate and phenolic pollutants during freezing. J. Hazard Mater. 329, 330 – 338.

Kim, K., Chung, H.Y., Kim, B., Wong, G., Nguyen, A.Q.K., Kim, S., Kim, J., 2020.Freezing-induced simultaneous reduction of chromate and production of molecullariodine: mechanism, kinetics, and practical implications. Environ. Sci. Technol. 54(24), 16204 – 16211.

Kim, K., Kim, J., Bokare, A.D., Choi, W., Yoon, H.I., Kim, J., 2015. Enhanced removal ofhexavalent chromium in the presence of H2O2 in frozen aqueous solutions. Environ. Sci. Technol. 49 (18), 10937 – 10944.

Kim, K., Le, N.T.H., Nguyen, A.Q.K., Ahn, Y.Y., Kim, B., Shin, G., Choi, W., Kim, J., 2022.Freezing-induced activation of the binary chloride-oxone system to free chlorine and its application in water treatment. Chem. Eng. J. 428, 131134.

Krachler, M., Zheng, J., Fisher, D., Shotyk, W., 2009. Global atmospheric as and Bicontamination preserved in 3000 year old Arctic ice. Global Biogeochem. Cycles 23(3), GB3011.

Krausková, Ľ., Procházková, J., Klašková, M., Filipová, L., Chaloupková, R., Malý, S., Damborský, J., Heger, D., 2016. Suppression of protein inactivation during freezingby minimizing pH changes using ionic cryoprotectants. Int. J. Pharm. 509 (1 – 2),41 – 49.

Lenoble, V., Deluchat, V., Serpaud, B., Bollinger, J.C., 2003. Arsenite oxidation andarsenate determination by the molybdene blue method. Talanta 61 (3), 267 – 276.

Li, J., Jiang, J., Pang, S.Y., Cao, Y., Zhou, Y., Guan, C., 2020. Oxidation of iodide andhypoiodous acid by non-chlorinated water treatment oxidants and formation ofiodinated organic compounds: a review. Chem. Eng. J. 386, 123822.

Liberatore, H.K., Plewa, M.J., Wagner, E.D., Vanbriesen, J.M., Burnett, D.B., Cizmas, L.H., Richardson, S.D., 2017. Identification and comparative mammalian cellcytotoxicity of new iodo-phenolic disinfection byproducts in chloraminated oil andgas wastewaters. Environ. Sci. Technol. Lett. 4 (11), 475 – 480.

Liu, B., Jian, M., Wang, H., Zhang, G., Liu, R., Zhang, X., Qu, J., 2018. Comparing adsorption of arsenic and antimony from single-solute and bi-solute aqueous systems onto ZIF-8. Colloids Surf. A Physicochem. Eng. Asp. 538, 164 – 172.

Min, D.W., Choi, W., 2017. Accelerated reduction of bromate in frozen solution. Environ.Sci. Technol. 51 (15), 8368 – 8375.

Moran, J.E., Oktay, S.D., Santschi, P.H., 2002. Sources of iodine and iodine 129 in rivers. Water Resour. Res. 38 (8), 24, 1.

Mulvihill, M., Tao, A., Benjauthrit, K., Arnold, J., Yang, P., 2008. Surface-enhanced Raman

spectroscopy for trace arsenic detection in contaminated water. Angew.Chem. Int. Ed. 47 (34), 6456 – 6460.

Newberg, J.T., 2018. Equilibrium shifts upon freezing. Fluid Phase Equil. 478, 82 – 89.

Nguyen, Q.A., Kim, B., Chung, H.Y., Nguyen, A.Q.K., Kim, J., Kim, K., 2021. Reductivetransformation of hexavalent chromium by ferrous ions in a frozen environment: mechanism, kinetics, and environmental implications. Ecotoxicol. Environ. Saf. 208, 111735.

Nicomel, N.R., Leus, K., Folens, K., Van Der Voort, P., Du Laing, G., 2015. Technologies for arsenic removal from water: current status and future perspectives. Int. J. Environ. Res. Publ. Health 13 (1), 62.

Okada, Y., Uyama, M., Harada, M., Okada, T., 2019. Quasichemical approach to pH shiftsin frozen phosphate buffers. Ind. Eng. Chem. Res. 58 (39), 18422 – 18431.

Paltseva, A., Cheng, Z., Deeb, M., Groffman, P.M., Shaw, R.K., Maddaloni, M., 2018.Accumulation of arsenic and lead in garden-grown vegetables: factors and mitigation strategies. Sci. Total Environ. 640 – 641, 273 – 283.

Parker, K.M., Zeng, T., Harkness, J., Vengosh, A., Mitch, W.A., 2014. Enhanced formation of disinfection byproducts in shale gas wastewater-impacted drinking water supplies. Environ. Sci. Technol. 48 (19), 11161 – 11169.

Perryman, C.R., Wirsing, J., Bennett, K.A., Brennick, O., Perry, A.L., Williamson, N.,Ernakovich, J.G., 2020. Heavy metals in the Arctic: distribution and enrichment offive metals in Alaskan soils. PLoS One 15 (6), e0233297.

Pursell, J.L., Pursell, C.J., 2016. Host-guest inclusion complexation of α-cyclodextrin and triiodide examined using UV-Vis spectrophotometry. J. Phys. Chem. A 120 (13),2144 – 2149.

Richardson, S.D., Fasano, F., Ellington, J.J., Crumley, F.G., Buettner, K.M., Evans, J.J.,Blount, B.C., Silva, L.K., Waite, T.J., Luther, G.W., Mckague, A.B., Miltner, R.J.,Wagner, E.D., Plewa, M.J., 2008. Occurrence and mammalian cell toxicity ofiodinated disinfection byproducts in drinking water. Environ. Sci. Technol. 42 (22),8330 – 8338.

Saiz-Lopez, A., Plane, J.M.C., Cuevas, C.A., Mahajan, A.S., Lamarque, J.F., Kinnison, D.E., 2016. Nighttime atmospheric chemistry of iodine. Atmos. Chem. Phys. 16 (24),15593 – 15604.

Schwanck, F., Simões, J.C., Handley, M., Mayewski, P.A., Bernardo, R.T., Aquino, F.E., 2016. Anomalously high arsenic concentration in a West Antarctic ice core and its relationship to copper mining in Chile. Atmos. Environ. 125, 257 – 264.

Sen, M., Manna, A., Pal, P., 2010. Removal of arsenic from contaminated groundwater by membrane-integrated hybrid treatment system. J. Membr. Sci. 354 (1 – 2), 108 – 113.

Smith, R., Knight, R., Fendorf, S., 2018. Overpumping leads to California groundwater arsenic threat. Nat. Commun. 9 (1), 2089.

Sorlini, S., Gialdini, F., 2010. Conventional oxidation treatments for the removal of arsenic with chlorine dioxide, hypochlorite, potassium permanganate and monochloramine. Water Res. 44 (19), 5653 – 5659.

Takahashi, N., Yoshida, T., Kojima, S., Yamaguchi, S., Ohtsuka, R., Takeda, M.,Kosaka, T., Harada, T., 2018. Pathological and clinical pathological changes induced by four-week, repeated-dose, oral administration of the wood preservative chromated copper arsenate in Wistar rats. Toxicol. Pathol. 46 (3), 312 – 323.

Takenaka, N., Bandow, H., 2007. Chemical kinetics of reactions in the unfrozen solutionof ice. J. Phys. Chem. A 111 (36), 8780 – 8786.

Takenaka, N., Tanaka, M., Okitsu, K., Bandow, H., 2006. Rise in the pH of an unfrozen solution in ice due to the presence of NaCl and promotion of decomposition of gallic acids owing to a change in the pH. J. Phys. Chem. A 110 (36), 10628 – 10632.

Takenaka, N., Ueda, A., Daimon, T., Bandow, H., Dohmaru, T., Maeda, Y., 1996. Acceleration mechanism of chemical reaction by freezing: the reaction of nitrous acid with dissolved oxygen. J. Phys. Chem. 100 (32), 13874 – 13884.

Vetráková, Ľ., Vykoukal, V., Heger, D., 2017. Comparing the acidities of aqueous, frozen,and freeze-dried phosphate buffers: is there a “pH memory” effect? Int. J. Pharm. 530 (1 – 2), 316 – 325.

Wang, Y., Lv, C., Xiao, L., Fu, G., Liu, Y., Ye, S., Chen, Y., 2019. Arsenic removal from alkaline leaching solution using Fe (III) precipitation. Environ. Technol. 40 (13),1714 – 1720.

Xu, Z., Hao, J., Li, F., Meng, X., 2010. Surface-enhanced Raman spectroscopy of arsenate and arsenite using Ag nanofilm prepared by modified mirror reaction. J. Colloid Interface Sci. 347 (1), 90 – 95.

Yang, M., Liamtsau, V., Fan, C., Sylvers, K.L., McGoron, A.J., Liu, G., Fu, F., Cai, Y., 2019. Arsenic speciation on silver nanofilms by surface-enhanced Raman spectroscopy.Anal. Chem. 91 (13), 8280 – 8288.

Yeo, J., Choi, W., 2009. Iodide-mediated photooxidation of arsenite under 254 nm irradiation. Environ. Sci. Technol. 43 (10), 3784 – 3788.

Zhang, Y., Jiang, X., Zhang, J., Xia, Y., Qiu, J., Wang, T., Qiu, Y., Qin, X., Wang, B., Zou, Z., Chen, C., 2020. Heterozygous disruption of beclin 1 mitigates arsenite induced neurobehavioral deficits via reshaping gut microbiota-brain axis. J. Hazard Mater. 398, 12274

KIGAM 극지연구소

FIGURES

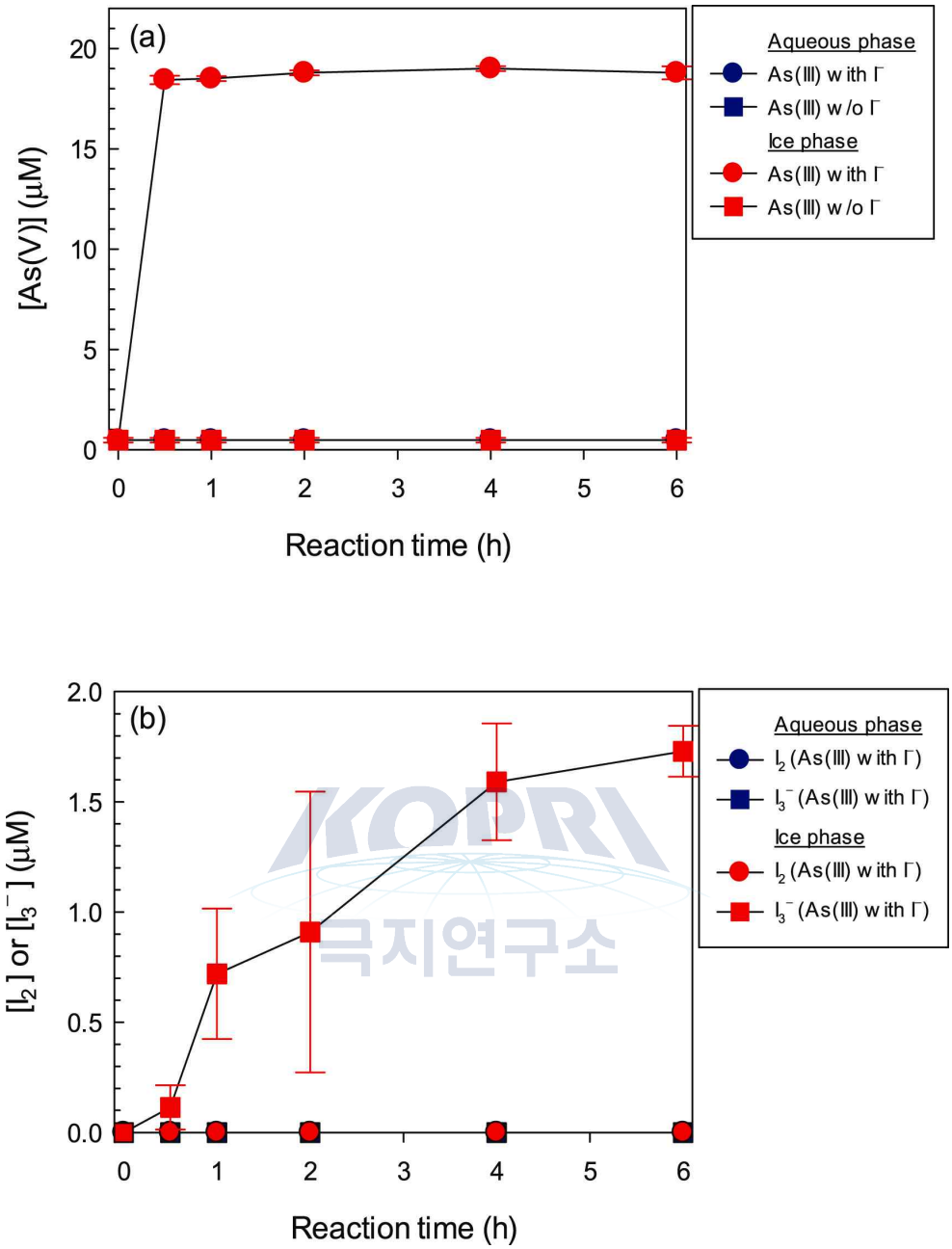



**Figure 1.** Generation of (a) As(V) and (b) $I_2$ and $I_3^-$ via the oxidation of As(III) by $I^-$ in water and ice. Experimental conditions: [As(III)] = 20 μM, [$I^-$] = 200 μM, pH 3, and reaction temperature = 25 or −20 °C.

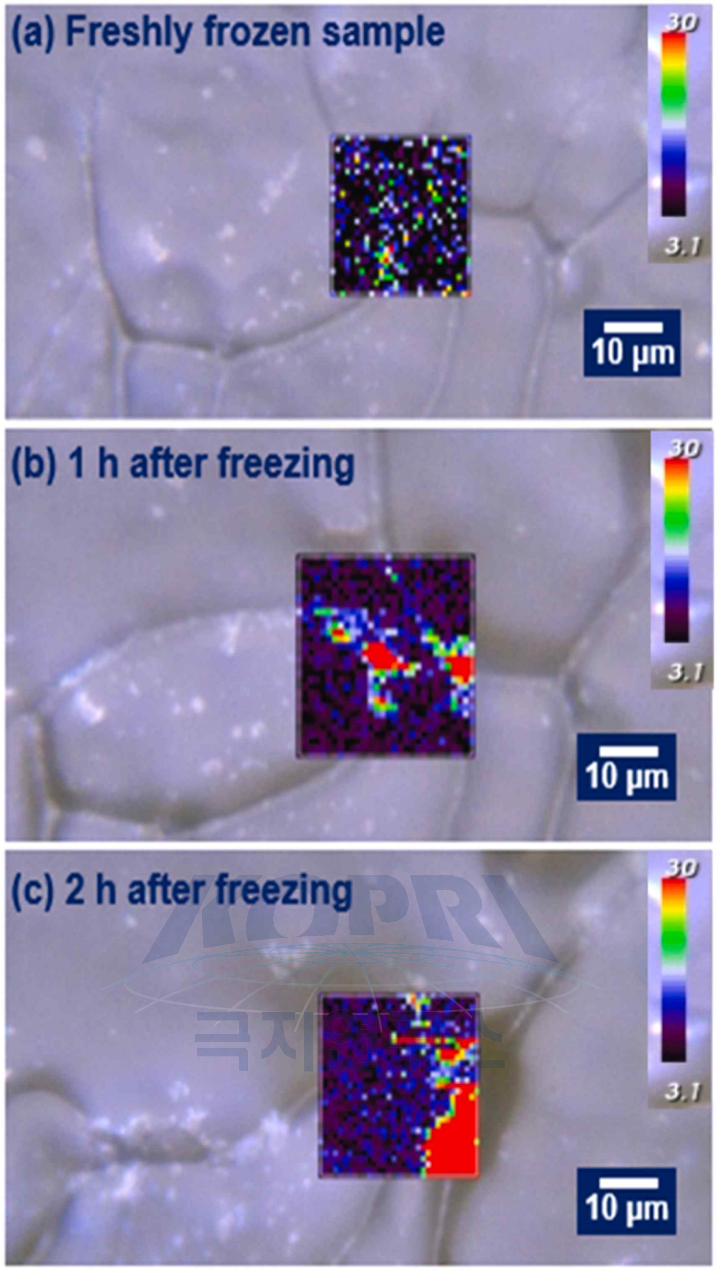



**Figure 2.** (a) Optical image of the unfrozen solution of ice containing only As(III). Local concentrations of As(V) in the unfrozen solution of ice after additional time: (b) 1 and (c) 2 h. Experimental conditions: [As(III)] = 1 mM, [$I^-$] = 1 mM, and pH 3. In (a), the temperature decreased from 0 to −20 °C at the rate of −2 °C/min. In (b) and (c), the temperature remained unchanged at −20 °C.

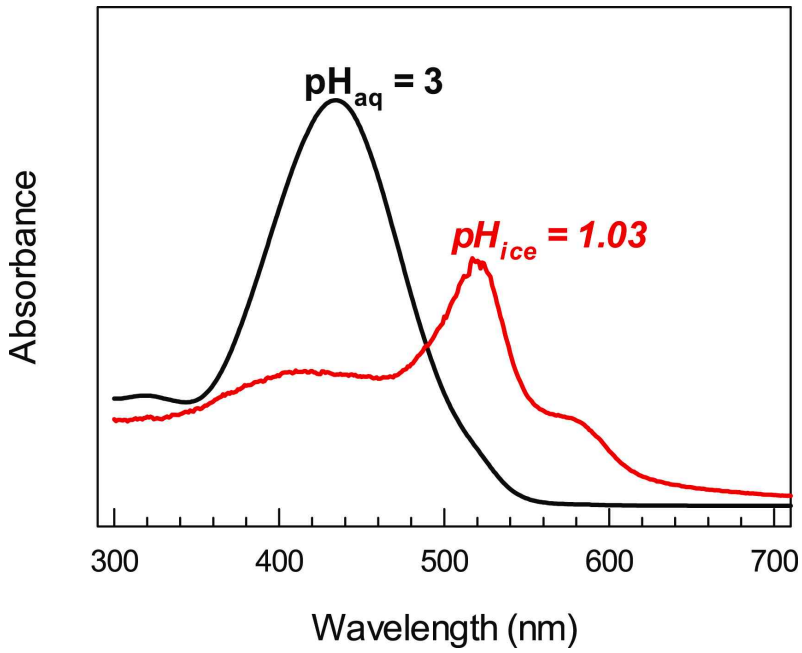



**Figure 3.** Change in UV–visible absorption spectra of CR via freezing. Experimental conditions: [As(III)] = 20 μM, [$I^-$] = 200 μM, [CR] = 6.7 μM, pH 3, reaction temperature = −20 °C, and freezing time = 1 h.

KOPRI 극지연구소

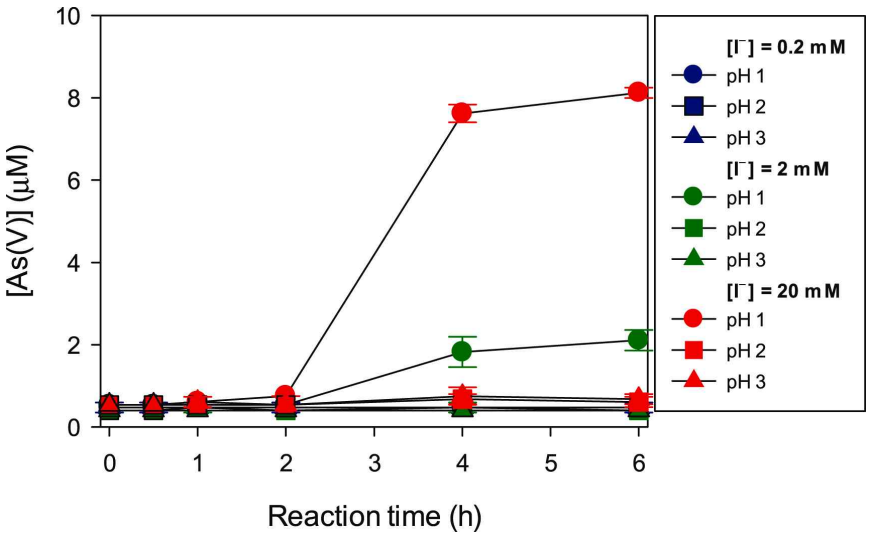



**Figure 4.** Effects of the increase in the $I^-$ concentration and/or decrease in pH on the oxidation of As(III) in an aqueous solution. Experimental conditions: [As(III)] = 20 μM, [$I^-$] = 200 μM or 2 or 20 mM, pH = 1, 2, or 3, and reaction temperature = 25 °C.

KOPRI
극지연구소

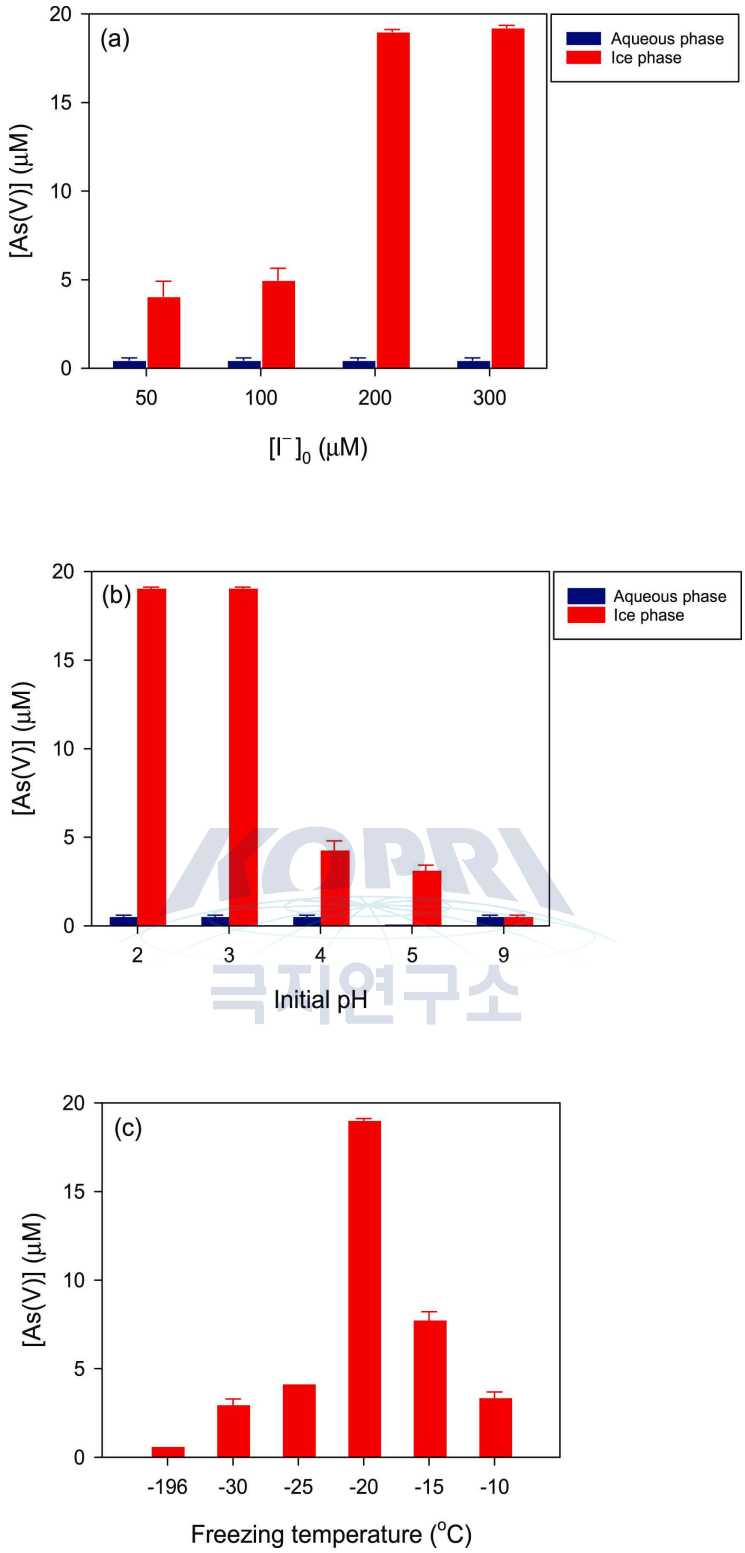



**Figure 5.** Effects of (a) $I^-$ concentration, (b) pH, and (c) temperature on the oxidation of As(III) by $I^-$ in water and ice. Experimental conditions: [As(III)] = 20 μM, [$I^-$] = 200 μM for parts (b) and (c), pH 3 for parts (a) and (c), reaction temperature = 25 or −20 °C for parts (a) and (b) and reaction time = 4 h.

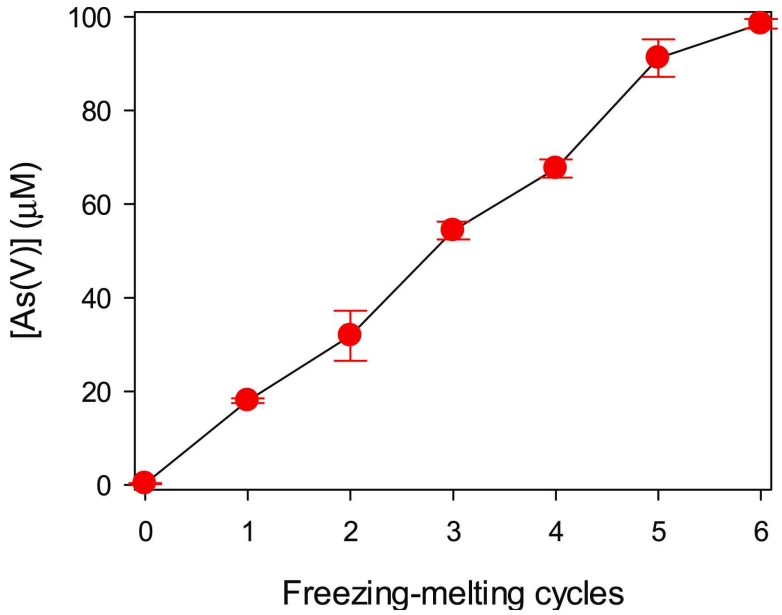



**Figure 6.** Generation of As(V) from the $I^-$-induced As(III) oxidation using the freezing - melting cycles. Experimental conditions: [As(III)] = 100 μM, [$I^-$] = 200 μM, pH 3, and reaction temperature = −20 °C.

KOPRI
극지연구소

# 제 15 절. Catalytic behavior of nitrous acid for acetaminophen transformation during the freezing process⑮

Yong-Yoon Ahn[1], Jungwon Kim[2], Kitae Kim[1,3]

[1]Korea Polar Research Institute (KOPRI)
[2]Department of Environmental Science and Biotechnology, Hallym University
[3]Department of Polar Science, University of Science of Technology (UST)

## Abstract

This study demonstrates the transformation of acetaminophen by reactive nitrous acid in a frozen solution and its abnormal stoichiometry. The chemical reaction between acetaminophen and nitrous acid (AAP/$NO_2^-$ system) was negligible in the aqueous solution; however, the reaction rapidly progressed if the solution started to freeze. The ultrahigh performance liquid chromatography-electrospray ionization tandem mass spectrometry measurements showed that polymerized acetaminophen and nitrated acetaminophen were formed in the proceeding reaction. Electron paramagnetic resonance spectroscopy measurements showed that nitrous acid oxidized acetaminophen via a one-electron transfer reaction producing acetaminophen-derived radical species, which is the cause of acetaminophen polymerization. We demonstrated that a relatively smaller dose of nitrite than acetaminophen caused significant acetaminophen degradation in the frozen AAP/$NO_2^-$ system and revealed that the dissolved oxygen content notably affected acetaminophen degradation. We showed that the reaction occurs in a natural Arctic lake matrix (nitrite and acetaminophen spiked). Considering that the freezing phenomenon is common in the natural environment, our research provides a possible scenario for the freezing chemistry of nitrite and pharmaceuticals in environmental chemistry.

## 1. Introduction

Recently, we proposes a freezing-induced bottom-up humification scenario of phenolic compounds in a nitrite ($NO_2^-$) solution.[1] This interesting phenomenon is relevant to the environmental chemistry in the cold region because the organic nitrogen is solely synthesized from the inorganic nitrogen species (e.g., $NO_2^-$) through the freezing of water. The chemical reaction was initiated via one-electron abstraction of nitrosonium ion from phenolic compounds to generate phenolic radicals, and subsequently, polymerization

⑮ 본 연구는 본 과제(PE23120)로 수행되었으며, 결과는 *J. Hazard. Mater* 2023, 456, 131652에 출간되었다.

progressed to generate fulvic-like acids and humic-like acids. Notably, the reaction was not significant in the aqueous phase, but it clearly progressed along with the growing ice crystals. In particular, a $NO_2^-$ dose of only 5 μM, which is 20 times less than the concentration of the starting substrate catechol (phenolic monomer), induced a 50% conversion of catechol to polymeric substances in 6 h during freezing. This abnormal stoichiometry presumably can be a key mechanism in freezing-induced humification scenario, but a revealing detailed reaction mechanism is lack in the research and should be clarified. In fact, it is known that $HNO_2$ has a catalytic effect on metal oxidation or aromatic nitration if a small amount of $HNO_2$ is added to the concentrated nitric acid solution (eq. 1 to 3).[2]

$$HNO_2 + H^+ \leftrightarrow NO^+ + H_2O \quad (1)$$

$$ArH + NO^+ \rightarrow ArNO + H^+ \quad (2)$$

$$ArNO + HNO_3 \rightarrow ArNO_2 + HNO_2 \quad (3)$$

Here, ArOH, ArNO, and $ArNO_2$ refer to phenolic substances, nitroso-compounds, and nitro-compounds, respectively. Throughout the equation (1) to (3), the $HNO_2$ is consumed by ArH to generate ArNO, but the oxidation of ArNO by nitric acid produces $HNO_2$ again. Thus, in this case, catalytic behavior of $HNO_2$ is based on the continuous supply from the regeneration. However, this reaction only progresses in an extremely acidic condition and the decreasing temperature inhibit the reaction.[3]

In general, the rates of chemical reactions are accelerated when the temperature is increased. Also, chemical reactions depend on the concentration of the reacting species. These two empirical relationships can be established from that the molecules must collide properly to react. In this manner, although the temperature in ice is lower than that in the room-temperature, the increase in the chemical reaction during the freezing process can be understood by the concentration of reacting species in the niche of ice crystals because the growing ice crystals expel the solutes. The concentration of solutes, such as ions, gas, and protons/hydroxides in ice is referred to as the freeze concentration effect.[4] Accordingly, an extremely enhanced nitrite-to-nitrate transformation during the freezing of water was identified previously.[5] As mentioned above, the freeze concentration effect was suspected as the major reason for this phenomenon. However, the unexpectedly high acceleration factor (ca. 100,000) of $NO_2^-$ oxidation during the freezing of the aqueous solution was not explained by the freeze concentration effect only.[6] It should be noted that if the only factor for the chemical reaction during freezing is the freeze concentration, the enhanced reaction should be observed in any type of chemical reactant. However, only some reactions that are dependent on specific conditions, such as the solution pH and components, are accelerated by freezing. It is worth noting that freezing can alter the pH of a solution, since the separation of anions and cations during freezing can lead to the migration of

$H_3O^+$ and $OH^-$ in the liquid-like region of ice.[7, 8] In previous study, we suggest that the chemical reaction of $NO_2^-$ is highly affected by the speciation of $NO_2^-$ to $HNO_2$ by the pH drop in ice.[9] Since the $HNO_2$ is more reactive than $NO_2^-$, it sufficiently generates a very strong reagent peroxynitrous acid (HOONO; a very unstable isomer of $HNO_3$) from the reaction with hydrogen peroxide and accelerated the benzoic acid transformation which is inert to the attack of $HNO_2$.

Owing to its photochemical property and inherent reactivity, $NO_2^-$ is an important species related to hydrocarbon transformation in the atmosphere.[10-12] The pKa value of $NO_2^-$ to $HNO_2$ is generally taken as 3.27 at 298 K, but a range of 2.3 to 5.2 has been reported.[13] In addition, the presence of the other pKa value of $HNO_2$ to nitrous acidium cation ($H_2ONO^+$) of 1.7 has been reported in the literature, which generates nitrosonium ion ($NO^+$) when $H_2ONO^+$ is dehydrated.[14] $HNO_2$ and $H_2ONO^+$ are effective reagents for the nitration and nitrosation of aromatic compounds. They also act as oxidizing reagents for phenolic compounds. However, the reaction mechanism of the catalytic effect of $HNO_2$ during freezing process is not clearly understood yet, and the $NO_2^-$ mediated chemical reaction in ice needs to be investigated thoroughly.

Acetaminophen (AAP), which is also known as paracetamol, has been reported as one of the most consumed pharmaceuticals in the world.[15-18] AAP is a safe drug when consumed appropriately; however, AAP overdosage can be fatal.[19] The impact of AAP on the aquatic ecosystem is poorly understood, but it is remarkable that AAP is one of the most frequently detected anthropogenic compounds in U.S. streams.[20] Furthermore, AAP comprises the largest proportion of pharmaceuticals detected in the Arctic region of Kongsfjorden.[21] Even at the Antarctic coast, AAP is emitted to the sea from Antarctic stations due to human activity such as scientific research and tourism.[22] Due to the tremendous production and continuous emission of AAP, it is apparently persistent in the environment and becomes a concern for aquatic and marine life.[23] According to Guiloski et al., AAP is an endocrine disruptor when male fish undergo subchronic exposure.[24] In addition, it should be noted that the potential risk of AAP not only depends on its own toxicity, but also on the transformed substances like its metabolites.[25] Accordingly, the freezing-induced transformation of AAP could have impact on the polar environment.

In this study, we investigated the $NO_2^-$ mediated chemical transformation of AAP during freezing to better understand the unique abnormal stoichiometry of $NO_2^-$ during freezing. We compared the AAP transformations in aqueous and frozen systems and surveyed the compounds produced by the chemical reaction between $HNO_2$ and AAP, and suggested how the reaction could progress. We then tested the influence of $NO_2^-$ dose and compared the effect of selected oxidants on AAP transformation. The influence of dissolved oxygen (DO) and reactivity of organic substrates on $HNO_2$ regeneration were also considered to

understand the catalytic behavior of $HNO_2$ during the freezing process. In addition, we demonstrated AAP transformation by $NO_2^-$ in a natural Arctic lake water matrix, which was collected from the Tvillingvatnet in Svalbard, Norway (78°54.94′N, 11°52.54′E).

## 2. Experimental Section

### 2.1. Chemicals

The chemical reagents used in this study included sodium nitrite (Sigma-Aldrich), sodium nitrate (Sigma-Aldrich), perchloric acid (Sigma-Aldrich), acetaminophen (Sigma-Aldrich), phenol (Sigma-Aldrich), caffeine (Sigma-Aldrich), ibuprofen (Sigma-Aldrich), carbamazepine (Sigma-Aldrich), L-ascorbic acid (Sigma-Aldrich), 4-chlorophenol (Sigma-Aldrich), 1,2-hydroxybenzene (Sigma-Aldrich), 1,4-hydroxybenzene (Sigma-Aldrich), sodium hypochlorite solution (Sigma-Aldrich), potassium persulfate (Sigma-Aldrich), peroxymonosulfate compound (Sigma-Aldrich, OXONE), hydrogen peroxide solution (30 wt%, Sigma-Aldrich), phosphoric acid (Sigma-Aldrich), methanol (Supelco), acetonitrile (Supelco), formic acid (Sigma-Aldrich), sodium formate (Sigma-Aldrich), sodium bicarbonate (Sigma-Aldrich), sodium carbonate (Sigma-Aldrich), 5-tert-butoxycarbonyl-5-methyl-1-pyrroline-N-oxide (BMPO, ENZO Life Science, Inc.), cresol red (Sigma-Aldrich), hydrochloric acid (Sigma-Aldrich), nitric acid (Sigma-Aldrich), and sulfuric acid (Sigma-Aldrich). All chemicals were of reagent grade and used as received without any further purification. The chemical solutions used in this study were prepared with ultrapure deionized water (18.2 MΩ·cm), which was produced using a Milli-Q Water Purification System (Millipore).

### 2.2. Experimental procedure

The test solution was prepared in a 100 mL glass beaker. AAP and 100 mM of $NaNO_2$ stock solutions (10 mM) were added to a beaker to obtain the desired concentrations. The $HClO_4$ solutions were then added to obtain the initial pH values. Next, 10 mL of this solution was poured into a 15 mL polypropylene conical tube sealed with a cap and placed in an ethanol cooling bath, which was precooled to the desired temperatures (-20 °C and 20 °C). The number of conical tubes was selected by the time sampling points. These preparation procedures were conducted as quickly as possible (approximately 30 s was required), and we assigned the moment at which the conical tubes were immersed in the cooling bath as the starting point (i.e., t = 0). The frozen conical tube was withdrawn from the cooling bath at a particular time and placed in a lukewarm water bath at 30 °C to thaw the ice for chemical analysis. We need to mention here that thawing in a lukewarm water bath had negligible effect on the AAP transformation; AAP degradation was similar

regardless of the thawing temperature, and a yellowish color was clearly observed prior to the thawing process. After thawing, the samples were immediately analyzed. Each experiment was performed at least twice to confirm data reproducibility. When we needed to freeze the solution using the air-cooling system, the 10 ml solution contained petri dishes (open to the air) were placed in a custom-made low-temperature chamber, which operated at -20 °C with marginal temperature variation from the programmed value.

### 2.3. Analytical methods

High-pressure liquid chromatography (HPLC) (Agilent, 1260 Infinity II) was used to analyze the organic substances in this study. The organic substances were identified by examining the retention time (Poroshell 120 EC-C18 column (4.6 mm × 150 mm) was used) and the light-absorbance with respect to them (using a variable wavelength detector (G7114 1260VWD)). In the analysis, 0.1% (v/v) phosphoric acid and acetonitrile were used as the eluents.

Nitrite and nitrate concentrations were measured using an ion chromatograph (Dionex ICS-1100) with a suppressor (Dionex AERS 500), column (Dionex IonPac AS23), and conductivity detector. Sodium carbonate and bicarbonate solutions (0.477 and 0.067 g in 1 L, respectively) were used for elution.

The AAP transformation products were analyzed using UHPLC (Thermo Fisher Scientific, Vanquish) combined with a quadrupole-orbitrap mass spectrometer (Thermo Fisher Scientific, Q Exactive Focus). Separation was performed using a Hypersil GOLD$^{TM}$ aQ column. The mobile phase was a mixture of ammonium acetate solution (5 mM; A) and acetonitrile/ammonium acetate solution (9:1 volume ratio; B) at a flow rate of 0.3 mL/min. Gradient elution was programmed as follows: 5% B for 0-2 min, 5-100% B for 2-14 min, 100% B for 14-17 min, and 100-5% B for 17-21 min. Mass detection was carried out in negative electrospray ionization (ESI) mode, and the operating parameters were set as follows: a detection range of 60 to 660 m/z, with a resolution of 70,000, spray voltage of -2.50 kV, capillary temperature of 320 °C, sheath gas flow rate of 40 a.u., auxiliary gas flow rate of 10 a.u., auxiliary gas heater temperature of 300 °C, S lens RF level of 50.0, maximum injection time of 200 ms, and an automatic gain control (AGC) target of $1\times10^{6}$. The obtained total ion current (TIC) signals were analyzed using the Free Style 1.5$^{TM}$ (Thermo Fisher Scientific) and Compound Discoverer 3.2$^{TM}$ (Thermo Fisher Scientific) software with Chemspider and mzCloud databases to identify and confirm the detected by-products.

Electron paramagnetic resonance spectroscopy (EPR) measurements were conducted using an EMXnano (Bruker). The experimental conditions were as follows: microwave frequency = 9.64 GHz, microwave power = 1 mW, modulation frequency = 100 kHz, modulation

amplitude = 1 G, and sweep time = 240 s in continuous-wave-EPR (CW-EPR) mode.

Total organic carbon (TOC) was measured using a TOC analyzer (TOC-LCPH, Shimadzu).

Dissolved oxygen was measured using an ORION STAR A216 module (Thermo Scientific) with a dissolved oxygen probe (ORION 083005MD, Thermo Scientific).

The Potential difference in ice was monitored by the open circuit potential measurement using the electrochemical workstations (AUT302N, Metrohm). The data collection was performed by NOVA 2.1 software (Metrohm).

## 3. Result and discussion

### 3.1. Acetaminophen degradation in the frozen nitrite solution

The concentration changes in AAP in the AAP/$NO_2^-$ system were monitored in varying operation temperature (Figure 1a). The AAP concentration did not change under the 20℃ condition (i.e., aqueous phase). However, a prominent chemical reaction was observed under all the frozen conditions (i.e., -5℃, -10℃, and -20℃). Notably, solidification started to occur at different time points along the operation temperature, and the AAP concentration remained at the original level when the sample did not start to freeze. At solidification, rapid AAP degradation was observed regardless of the freezing temperature, but the tendency for a slowed degradation differed depending on the conditions. It is remarkable that the freezing temperature affected the freezing speed: the growing speed of ice crystals was higher at a lower freezing temperature. Consequently, the solutes are concentrated much faster at lower freezing temperature.[26-29] Thus, the different AAP degradation rates at the various freezing temperatures probably resulted from the influence of the inner structure of the ice. Especially at -20℃ condition (red symbols), approximately 75% of the AAP was rapidly transformed within 30 min, and the transformation ratio reached 90% within 4 h, as the reaction slowed down (Figure 1a). Accordingly, we observed that the dissolved oxygen (DO) in the system decreased with the elapsed reaction time (Figure 1b). Clearly, this chemical reaction was not found when the $NO_2^-$ was not in the solution, so the $NO_2^-$ is the essential component in the freezing-induced AAP transformation. In addition, we also identified that the increase of nitrate ($NO_3^-$) concentration was accompanied as the chemical reaction progressed in the AAP/$NO_2^-$ system (Figure 1c). We consider that the generation of $NO_3^-$ was associated with $NO_2^-$ transformation,[6] but its generation tendency was different depending on whether AAP was present or absent (Figure 1c and 1d). The concentration of $NO_3^-$ was only 25 μM in the AAP/$NO_2^-$ system, whereas it reached 80 μM when AAP was absent. This probably indicates that nitrosation[30] or nitration[31] of AAP occurs during the process.

Figure 2 shows the identified acetaminophen transformation byproducts after 30 min of freezing at -20℃. The color represents the relative intensity of each compound which is measured by the mass spectroscopy. Here, we need to note that the displayed intensities are the relative value between the experimental conditions (namely, x axis) at the designated m/z value (namely, y axis). In addition, because the chemical reaction proceeds far more quickly if there is a greater supply of reactants (increase in nitrite dose), the comparison between the variations in nitrite dose gives us information about the reaction progress. Thus, we can speculate on the stepwise information by aligning the red colors (i.e., relatively intense signals) in Figure 2. As expected from Figure 1c and 1d, we can detect not only nitro-acetaminophen (m/z 195; C8H7O4N2) and dinitro-acetaminophen (m/z 240; C8H6O6N3), but also nitrated dimer and quinone-like compounds (m/z 344, 389, 225, and 148). Interestingly, we found that dimerized AAP substances appeared at the early stage of the transformation, and nitrated compounds were detected later (AAP dimer: m/z 299, AAP trimer: m/z 448). This feature well corresponds with the intensity change in the reaction time. According to the reconnaissance literature,[32-35] oxidized AAP readily combines to form a polymer, and our results revealed that polymerizations between AAP were a more preliminary step to nitration. Based on the MS/MS analysis, we believe that the dimerized quinone-like substances, which showed the highest signals at 25 μM of nitrite, were not nitrated yet. Thus, it is likely that the nitroacetaminophen monomer originated from the dissociation of dimerized substances after nitration. The knowledge on environmental implication of those transformed AAP derivatives is limited until present. But it is remarkable that the LD50 toxicity values (intraperitoneal injections in mouse) of N-Acetyl-p-benzoquinone imine (m/z 148) was 20 mg/kg whereas the value of AAP was 500 mg/kg.[25]

### 3.2. Analysis of nitrous acid mediated oxidation

As supported by Figure 2, the coupling reaction between AAP occurred at the early stage of the AAP transformation. The detection of polymerized AAP compounds indicates that the AAP induced radical species should occur from the oxidation of AAP during freezing by a one-electron transfer reaction, as was proposed in a previous research.[34] To measure the production of acetaminophen-derived radical species, we employed the spin-trapping reagent 5-tert-butoxycarbonly-5-methyl-1-pyrroline-N-oxide (BMPO) and tested the EPR experiment. The concentrations of the reactants were set higher than the other experimental conditions, but this is reasonable for imitation in the ice grain boundary region where the freeze concentration occur.[27] In addition, a high-concentrated condition was required to obtain the high signal intensity.[1] As shown in Figure 3, there was no identifiable signal when AAP and $NO_2^-$ were not present together. We speculate that the

observed signal in the case of AAP-$NO_2^-$ was caused from the acetaminophen-derived radical species because the similar EPR signal was detected when the AAP/BMPO mixture (without $HNO_2$) was illuminated under UV light (note that the AAP-derived radical species can be produced by UV illumination[36]). Thus, we infer that $HNO_2$ oxidized AAP by one-electron transfer to produce AAP radicals and that dimerized AAP species were produced by the termination reaction between AAP radicals.

The concentration of reactive nitrogen species in the system should be related to the $NO_2^-$ concentration and solution pH (note that the $NO_2^-$ converted to the $HNO_2$ and $H_2ONO^+$ that are responded to the solution pH). Apparently, the AAP conversion was enhanced with a decrease in pH because the portion of the $HNO_2$ in nitrite solution should be increased in pH decrease (Figure 4a, red symbols). In aqueous condition, the overall AAP degradation was negligible, but approximately 10% of the AAP degradation was found at pH 3 (Figure 4b, dark blue circles). Besides, the degradation rate of AAP in the aqueous solution markedly increased when the solution pH was adjusted to 1. It is noteworthy that the pH of ice can be decreased when a slightly acidic solution is frozen.[37] This phenomenon can be explained by the fact that ions in ice have different tendencies to incorporate into the ice crystal, leading to charge inconsistencies. The highly mobile $H_3O^+$ and $OH^-$ ions then compensate for these inconsistencies in the ice.[7] Accordingly, we observed a color shift of cresol red (pH indicating compound) when cresol red was dissolved in the AAP/$NO_2^-$ system: The estimated pH in ice is 1.034.[9] Thus, enhanced AAP degradation in ice was ascribed to the pH drop during freezing. However, if this is the case, pH buffering reagents probably can prevent AAP transformation because AAP degradation is triggered by the nitrous acid generation that resulted from the pH decrease by freezing. Figure 4b shows the effect of the buffering reagent on AAP degradation. Although the buffering reagent did not significantly inhibit AAP degradation during the freezing process, the amount of AAP degradation clearly responded to the concentration of the buffering reagent. In addition, the degradation rate of AAP at pH 3 (aqueous condition) increased with increasing $NO_2^-$ concentration. Thus, the accelerated AAP transformation during freezing was mainly derived from two factors: (i) the speciation of $NO_2^-$ to $HNO_2$ by the pH decrease in ice and (ii) the concentration of reactants in the ice grain boundary.

In many cases, background anion species can affect the chemical reaction in ice. Furthermore, the physical environment in ice can be changed by the ion constituents in the solution.[6, 38] Thus, we tested the effect of background anion species by switching the type of pH-adjusting reagent (i.e., HCl, $HNO_3$, and $H_2SO_4$). However, there were no prominent differences between the pH-adjusting reagents, but only a marginal difference was found. Hence, we concluded that the type of acid was negligible in the system.

On the other hand, freezing potential can be established during the freezing of a dilute

salt solution.[38] This can alter the thermodynamic properties of the incorporated reactants in ice and eventually affect the chemical reaction.[4] Hence, we monitored the potential difference between two separate points in the frozen system. The working and auxiliary electrodes consist of 50-mm-long stainless steel wires with a diameter of 10 μm. The working electrode was immersed in the center of the reactor (a cylindrical jacket beaker, 100 mL), and the auxiliary electrode was placed at the edge of the reactor. The cooling fluid flowed through the jacket beaker to control the temperature. The temperature was initially set to 10℃ and was gradually decreased to -10℃ during the measurement process. We compared three different conditions, namely only $HClO_4$ solution (pH 4), $NO_2^-$ in $HClO_4$ solution, and AAP/$NO_2^-$ in $HClO_4$ solution. Overall, potential difference between the electrodes was established rapidly as the solidification began. In addition, potential at the working electrode decreased. We speculated that accumulated anions on the working electrode resulted in the decreased potential there. However, the potential difference was restored despite the system remaining in ice form. This could be ascribed to that ice is a protonic conductor.[39] However, since we did not observe significant differences in characteristics across the three different conditions, the freezing potential possibly did not have a significant effect on the transformation of AAP in ice. Nevertheless, many studies have suggested that chemical reaction in ice can be influenced by the shift of redox potential. How the thermodynamic properties in ice can be change is not clear yet, and further studies would be required to reveal the phenomenon more accurately.

In addition, we tested the influence of ice surface on the oxidation of AAP by nitrite. Ten ice pellets (each produced by freezing 5 mL of pure water; disc shape, diameter ~ 35 mm, and thickness ~ 5 mm) were immersed in 50 mL of AAP/$NO_2^-$ solution, which was pre-cooled to 0℃. In the 50 mL solution, the initial concentration of both AAP and $NO_2^-$ was 200 μM, and 2000 μM $HClO_4$ was added to maintain an acidic pH. During the reaction, the ice-water was gently stirred at 80 rpm using a 10-mm-long magnetic bar. At every time point, we melted all ice pellets by increasing the temperature 20℃ to measure the degradation of AAP. Hence, the total volume of solution became 100 mL at this time. Here, since the AAP was not significantly degraded, the ice surface was not a major factor for AAP transformation in ice.

### 3.3. Catalytic behavior of nitrous acid

Figure 5a compares the amount of AAP decreased under frozen and aqueous conditions with varying nitrite concentration at a reaction time of 30 min. When the solution was not frozen, the amount did not change regardless of the injected nitrite concentration. However, significant degradation of AAP was observed in the frozen samples. Remarkably, AAP was degraded more than the injected nitrite amount (see 10, 25, and 50 μM nitrite dose in

Figure 5a). At the case of 10 μM nitrite dose, approximately 50 μM of AAP was disappeared: the reduced AAP concentration was five times higher than the injected nitrite concentration (note that AAP conversion was negligible in the absence of nitrite). When the nitrite dose increased over 100 μM, the comparable AAP concentrations were remained in the ice (i.e., 25-30 μM AAP was detected). Notably, the AAP almost disappeared when the injected nitrite was dominant over the initial AAP concentration, such as 10 and 4 times over the initial concentration of AAP (10, and 25 μM AAP dose, respectively; Figure 5b). Hence, nitrite is an evident source of reactive species in the system, but probably it does not react in a one-by-one ratio with AAP, as shown in Figures 5a and 5b.

To confirm whether the abnormal stoichiometry of nitrite occurs in the aqueous solution, we examined the AAP degradation under varying reactant doses while keeping the AAP:$NO_2^-$ ratio constantly set at 10:1 (Figure 5c). The AAP degradation rate clearly depends on the concentration of the reactant. Remarkably, we can observe the abnormal stoichiometry of nitrite: at the AAP 1000/$NO_2^-$ 100 μM ratio, approximately 30% of the total AAP was decomposed, despite the initial nitrite concentration being only 10% of the initial AAP concentration. However, the progress was much slower and the transformation efficiency was lower compared to the frozen condition (It should be noted that the condition of AAP 1 mM and $NO_2^-$ 100 μM in pH 1 is quite an extreme situation in natural environments). This suggests that freezing can significantly enhance the catalytic behavior of nitrite in transforming AAP, even at relatively low concentrations of the reactants and mild pH condition.

The reactivity of the oxidant also affects the conversion of AAP during freezing. Accordingly, we demonstrated the effect of selected oxidants on AAP degradation (Figure 5d). We selected those oxidants based on the previous studies: (i) HOCl and $S_2O_8^{2-}$ were exploited for AAP degradation.[33-35] (ii) increased freezing-induced chemical reaction of Cr(VI) conversion by $H_2O_2$,[40] and organic compound degradation by $HSO_5^-$[41, 42] were reported. However, although $H_2O_2$, $S_2O_8^{2-}$, and $HSO_5^-$ have high oxidation potentials (1.78, 1.82, and 2.01 $V_{NHE}$)[43], they showed negligible reactivity toward AAP regardless of the freezing or aqueous conditions (Figure 5d). In contrast, HOCl (1.36 $V_{NHE}$)[43] markedly degraded AAP and accelerated the reaction under frozen conditions. HOCl reacts with aromatic substances mostly by electrophilic substitutions.[44] Further, we clearly identified the nitrated compounds in the AAP/$NO_2^-$ system (Figure 2). We found a similar intermediate generation trend between the HOCl and $NO_2^-$ systems. Thus, electrophilic substitution is likely the dominant reaction pathway in frozen chemical systems. However, we emphasize that the degradation tendency of AAP in oxidant dose is apparently different between the HOCl and $NO_2^-$ cases. In the HOCl case, the degradation of AAP was linearly related to the HOCl concentration; approximately 10, 40, and 90 μM of AAP decreased at 10, 50, and

100 μM of HOCl, respectively (Figure 5d), whereas 50, 75, and 70 μM of AAP decreased in the $NO_2^-$ case (Figure 5a). This abnormal stoichiometry in the $NO_2^-$ case plausibly indicates that the regeneration of $HNO_2$ occurs in the system because $HNO_2$ regeneration could have the same effect as a high dose of nitrite. However, the plateau of the AAP degradation (Figure 5a) cannot be interpreted solely by the regeneration of $HNO_2$ alone. As shown in Figure 1, DO plays a vital role in this phenomenon.

Figure 6 shows the influence of the initial DO concentration on the frozen AAP/$NO_2^-$ system. The initial DO concentration was controlled by varying the $N_2$ purging time. Clearly, we can observe the significance of the initial DO content on AAP degradation in the frozen AAP/$NO_2^-$ system, that is, 50, 30, and 10 μM of AAP remained at 2, 5, and 8 ppm of DO, respectively (Figure 6a). Accordingly, $NO_2^-$ and $NO_3^-$ concentrations were also affected by the initial DO concentration (Figure 6b and 6c). According to previous research, DO oxidizes $HNO_2$, as described by Eq. (4).[6]

$$2HNO_2 + O_2 \rightarrow 2NO_3^- + 2H^+ \quad (4)$$

If eq. (4) is significant, which means that $O_2$ and AAP compete with $HNO_2$, so low DO content likely results in effective $HNO_2$ derived AAP degradation. In contrast, the AAP degradation decreased with the initial DO concentration, so we inferred that $O_2$ simultaneously participates in the regeneration of $HNO_2$ and $NO_3^-$ production. In a previous study, it was proposed that the methylcatechol nitration can proceed not only by the direct role of $HNO_2$ but also by the participation of $O_2$ in the reaction pathway, that is, dissolved $O_2$ oxidizes the NO radical to $NO_2$ radical, which is produced from the oxidation of phenolic compounds by $HNO_2$, and the combination of NO with $NO_2$ restores the consumed $HNO_2$ (Eq. 5 to 8).[10]

$$HNO_2 + ArOH \leftrightarrow [NO]^+\text{--}ArOH + OH^- \quad (5)$$

$$[NO]^+\text{--}ArOH \leftrightarrow ArO + NO + H^+ \quad (6)$$

$$2NO + O_2 \rightarrow 2NO_2 \quad (7)$$

$$NO_2 + NO + H_2O \rightarrow 2HNO_2 \quad (8)$$

Similarly, the reaction between $HNO_2$ and AAP probably generates NO and AAP radicals (e.g., C8H8NO2).[45] The termination of radicals then generates polymerized AAP compounds, quinone-like substances, and nitrated AAP compounds (Figure 2). Here, the NO radical behaves as a nitrating reagent and source of $HNO_2$. We also need to mention that the pH in ice is highly acidic, as mentioned above (ca. 1.034). Consequently, $HNO_2$ can be converted to $H_2ONO^+$ (pKa = 1.7), which is a highly reactive nitrating agent. In this context, $H_2ONO^+$ can get dehydrated to $NO^+$ and oxidize AAP via a one-electron transfer process (Eq. 9 to 10).[1]

$$ArOH + NO^+ \rightarrow ArO + NO + H^+ \quad (9)$$

$$ArO \rightarrow \text{polymerization} \quad (10)$$

Accordingly, NO is generated from the reduction of $NO^+$, which can subsequently lead to the regeneration of $HNO_2$, as described in Eq. 7 and 8, and produce polymerized AAP.

The $HNO_2$ mediated catalytic oxidation is anticipated to occur not only in AAP degradation but also in the reaction of other species. We conducted the freezing-induced $NO_2^-$ system with various organic compounds (Figure 7). Hydroquinone, catechol, and vitamin C (ascorbic acid) showed the apparent catalytic behavior of $HNO_2$ in ice chemistry because their concentrations decreased more larger than that of the injected $NO_2^-$. Phenol, 4-chlorophenol, and furfuryl alcohol exhibited lower reactivity than hydroquinone, catechol, and vitamin C. This indicates that the reactivity between organic substances and $HNO_2$ should be considered. The low transformation efficiency of phenol is consistent with previous research showing that the catechol conversion efficiency was much higher than that of phenol.[1] Thus, it can be assumed that the secondary functional group on phenol (e.g., acetamido or second hydroxyl group) strongly influences the polymerization reactivity of phenolic compounds. It is noted that the reactivities of phenolic compounds depend on the property of functional group: electron donating group provide the substrate more prone to the oxidation.[46] Caffeine, carbamazepine, and ibuprofen showed no reactivity toward frozen chemical system. These compounds cannot be oxidized by $HNO_2$. Based on the experimental results of DO effect and the selectivity in various organic substances, we conclude that the catalytic behavior of $HNO_2$ is affected by the reducing capability of organic substance and dissolved oxygen concentration.

## 4. Conclusion

In this study, we suggested that the substantial chemical transformation of AAP via nitrous acid mediated oxidation can occur if it is frozen. Furthermore, the reaction proceeds with catalytic behavior of nitrous acid via its regeneration. Nitrite is one of the most common natural species. Owing to the chemical properties of nitrite, it is also artificially produced in factories and used in food preservatives, chemical precursors for dye production, medicine, and fertilizers. Thus, it can be markedly concentrated in industrial areas and spread to the natural water environment. The nitrite concentration in snow surface reported as few-μM levles, but the concentration increases up to μM range in seawater.[47, 48] In addition, considering that the freezing phenomenon is common in natural environments, such as the polar region and middle latitudes in winter, the freezing chemistry of nitrite could be significant in environmental chemistry. As demonstrated in this study, a small amount of nitrite could transform pharmaceutical compounds if the solution is slightly acidic and frozen. We have only limited information about the environmental impact of transformed products (TPs), and we must consider the fate of

TPs in those ways, namely, how they can be produced and how they behave.[33, 34]

Anthropogenic chemicals (such as pharmaceuticals and their metabolites) are a concern when they are exposed to the natural environment due to the potential negative influences of the original and derived substances. While the Arctic area is normally thought to be pollution-free due to its remoteness from the populated region, many studies have warned that anthropogenic compounds have been discovered in this region.[21] Furthermore, as the freezing-thawing cycle enhances the chemical transformation according to recent research,[49] transported anthropogenic substances can be converted into their derivatives in this cold region. Among the various anthropogenic compounds, AAP has been reported as one of the most consumed pharmaceuticals in the world.[15-18] In addition, the average observed AAP concentration throughout the Arctic Ocean's coast in Ny-Alesund in Svalbard, Norway was 60 μg/L.[21] This can potentially spread out in the Arctic region with the help of sea currents and contaminate the Arctic region following the scenario mentioned above. Hence, in further study, the proof for the relevance between freezing chemistry and pharmaceutical TPs in Arctic ocean, and also consideration on their environmental implication are required.

KOPRI
극지연구소

## REFERENCES


[1] Min, D.W., K. Kim, K.H. Lui, B. Kim, S. Kim, J. Cho, W. Choi, Abiotic Formation of Humic-Like Substances through Freezing-Accelerated Reaction of Phenolic Compounds and Nitrite, Environmental Science & Technology 53 (2019) 7410-7418

[2] Ridd, J.H., The range of radical processes in nitration by nitric acid, Chemical Society Reviews 20 (1991) 149-165

[3] Albright, L.F., R.V.C. Carr, R.J. Schmitt, Nitration: An Overview of Recent Developments and Processes, in Nitration. 1996, American Chemical Society. p. 1-9.

[4] O'Concubhair, R., J.R. Sodeau, The Effect of Freezing on Reactions with Environmental Impact, Accounts of Chemical Research 46 (2013) 2716-2724

[5] Takenaka, N., A. Ueda, Y. Maeda, Acceleration of the rate of nitrite oxidation by freezing in aqueous solution, Nature 358 (1992) 736-738

[6] Takenaka, N., A. Ueda, T. Daimon, H. Bandow, T. Dohmaru, Y. Maeda, Acceleration Mechanism of Chemical Reaction by Freezing:? The Reaction of Nitrous Acid with Dissolved Oxygen, The Journal of Physical Chemistry 100 (1996) 13874-13884

[7] Bronshteyn, V.L., A.A. Chernov, Freezing potentials arising on solidification of dilute aqueous solutions of electrolytes, Journal of Crystal Growth 112 (1991) 129-145

[8] Imrichová, K., L. Veselý, T.M. Gasser, T. Loerting, V. Neděla, D. Heger, Vitrification and increase of basicity in between ice Ih crystals in rapidly frozen dilute NaCl aqueous solutions, The Journal of Chemical Physics 151 (2019) 014503

[9] Ahn, Y.-Y., J. Kim, K. Kim, Frozen Hydrogen Peroxide and Nitrite Solution: The Acceleration of Benzoic Acid Oxidation via the Decreased pH in Ice, Environmental Science & Technology 56 (2022) 2323-2333

[10] Vidović, K., D. Lašič Jurković, M. Šala, A. Kroflič, I. Grgić, Nighttime Aqueous-Phase Formation of Nitrocatechols in the Atmospheric Condensed Phase, Environmental Science & Technology 52 (2018) 9722-9730

[11] Kroflič, A., M. Huš, M. Grilc, I. Grgić, Underappreciated and Complex Role of Nitrous Acid in Aromatic Nitration under Mild Environmental Conditions: The Case of Activated Methoxyphenols, Environmental Science & Technology 52 (2018) 13756-13765

[12] Kroflič, A., M. Grilc, I. Grgić, Unraveling Pathways of Guaiacol Nitration in Atmospheric Waters: Nitrite, A Source of Reactive Nitronium Ion in the Atmosphere, Environmental Science & Technology 49 (2015) 9150-9158

[13] Riordan, E., N. Minogue, D. Healy, P. O'Driscol, J.R. Sodeau, Spectroscopic and Optimization Modeling Study of Nitrous Acid in Aqueous Solution, The Journal of Physical Chemistry A 109 (2005) 779-786

[14] Anastasio, C., L. Chu, Photochemistry of Nitrous Acid (HONO) and Nitrous Acidium

Ion ($H_2ONO^+$) in Aqueous Solution and Ice, Environmental Science & Technology 43 (2009) 1108-1114

[15] Phong Vo, H.N., G.K. Le, T.M. Hong Nguyen, X.-T. Bui, K.H. Nguyen, E.R. Rene, T.D.H. Vo, N.-D. Thanh Cao, R. Mohan, Acetaminophen micropollutant: Historical and current occurrences, toxicity, removal strategies and transformation pathways in different environments, Chemosphere 236 (2019) 124391

[16] Rodríguez-Morales, A.J., J.A. Cardona-Ospina, M.M. Murillo-Muñoz, Gastroenterologists, Hepatologists, COVID-19 and the Use of Acetaminophen, Clinical Gastroenterology and Hepatology 18 (2020) 2142-2143

[17] Reinstadler, V., V. Ausweger, A.-L. Grabher, M. Kreidl, S. Huber, J. Grander, S. Haslacher, K. Singer, M. Schlapp-Hackl, M. Sorg, H. Erber, H. Oberacher, Monitoring drug consumption in Innsbruck during coronavirus disease 2019 (COVID-19) lockdown by wastewater analysis, Science of The Total Environment 757 (2021) 144006

[18] Romano, S., H. Galante, D. Figueira, Z. Mendes, A.T. Rodrigues, Time-trend analysis of medicine sales and shortages during COVID-19 outbreak: Data from community pharmacies, Research in Social and Administrative Pharmacy 17 (2021) 1876-1881

[19] Bessems, J.G.M., N.P.E. Vermeulen, Paracetamol (Acetaminophen)-Induced Toxicity: Molecular and Biochemical Mechanisms, Analogues and Protective Approaches, Critical Reviews in Toxicology 31 (2001) 55-138

[20] Kolpin, D.W., E.T. Furlong, M.T. Meyer, E.M. Thurman, S.D. Zaugg, L.B. Barber, H.T. Buxton, Pharmaceuticals, Hormones, and Other Organic Wastewater Contaminants in U.S. Streams, 1999~2000: A National Reconnaissance, Environmental Science & Technology 36 (2002) 1202-1211

[21] Choi, Y., K. Kim, D. Kim, H.-b. Moon, J. Jeon, Ny-Ålesund-oriented organic pollutants in sewage effluent and receiving seawater in the Arctic region of Kongsfjorden, Environmental Pollution 258 (2020) 113792

[22] Perfetti-Bolaño, A., K. Muñoz, A.S. Kolok, A. Araneda, R.O. Barra, Analysis of the contribution of locally derived wastewater to the occurrence of Pharmaceuticals and Personal Care Products in Antarctic coastal waters, Science of The Total Environment 851 (2022) 158116

[23] Ebele, A.J., M. Abou-Elwafa Abdallah, S. Harrad, Pharmaceuticals and personal care products (PPCPs) in the freshwater aquatic environment, Emerging Contaminants 3 (2017) 1-16

[24] Guiloski, I.C., J.L.C. Ribas, L.D.S. Piancini, A.C. Dagostim, S.M. Cirio, L.F. Fávaro, S.L. Boschen, M.M. Cestari, C. da Cunha, H.C. Silva de Assis, Paracetamol causes endocrine disruption and hepatotoxicity in male fish Rhamdia quelen after subchronic exposure, Environmental Toxicology and Pharmacology 53 (2017) 111-120

KOPRI 극지연구소

[25] Dahlin, D.C., S.D. Nelson, Synthesis, decomposition kinetics, and preliminary toxicological studies of pure N-acetyl-p-benzoquinone imine, a proposed toxic metabolite of acetaminophen, Journal of Medicinal Chemistry 25 (1982) 885-886

[26] Choi, Y., H.-I. Yoon, C. Lee, L.u. Vetráková, D. Heger, K. Kim, J. Kim, Activation of Periodate by Freezing for the Degradation of Aqueous Organic Pollutants, Environ. Sci. Technol. 52 (2018) 5378-5385

[27] Ju, J., J. Kim, J. Vetráková, J. Seo, D. Heger, C. Lee, H.-I. Yoon, K. Kim, J. Kim, Accelerated redox reaction between chromate and phenolic pollutants during freezing, Journal of Hazardous Materials 329 (2017) 330-338

[28] Heger, D., J. Jirkovský, P. Klán, Aggregation of Methylene Blue in Frozen Aqueous Solutions Studied by Absorption Spectroscopy, The Journal of Physical Chemistry A 109 (2005) 6702-6709

[29] Kim, K., W. Choi, Enhanced Redox Conversion of Chromate and Arsenite in Ice, Environmental Science & Technology 45 (2011) 2202-2208

[30] Helaleh, M.I.H., T. Korenaga, Fluorometric determination of nitrite with acetaminophen, Microchemical Journal 64 (2000) 241-246

[31] Vione, D., V. Maurino, C. Minero, D. Borghesi, M. Lucchiari, E. Pelizzetti, New Processes in the Environmental Chemistry of Nitrite. 2. The Role of Hydrogen Peroxide, Environmental Science & Technology 37 (2003) 4635-4641

[32] Lu, J., Q. Huang, L. Mao, Removal of Acetaminophen Using Enzyme-Mediated Oxidative Coupling Processes: I. Reaction Rates and Pathways, Environmental Science & Technology 43 (2009) 7062-7067

[33] Bedner, M., W.A. MacCrehan, Transformation of Acetaminophen by Chlorination Produces the Toxicants 1,4-Benzoquinone and N-Acetyl-p-benzoquinone Imine, Environmental Science & Technology 40 (2006) 516-522

[34] Li, W., X. Zhang, J. Han, Formation of Larger Molecular Weight Disinfection Byproducts from Acetaminophen in Chlorine Disinfection, Environmental Science & Technology 56 (2022) 16929-16939

[35] Jiang, M., J. Lu, Y. Ji, D. Kong, Bicarbonate-activated persulfate oxidation of acetaminophen, Water Res. 116 (2017) 324-331

[36] Pozdnyakov, I.P., X. Zhang, T.A. Maksimova, V.V. Yanshole, F. Wu, V.P. Grivin, V.F. Plyusnin, Wavelength-dependent photochemistry of acetaminophen in aqueous solutions, Journal of Photochemistry and Photobiology A: Chemistry 274 (2014) 117-123

[37] Heger, D., J. Klánová, P. Klán, Enhanced Protonation of Cresol Red in Acidic Aqueous Solutions Caused by Freezing, The Journal of Physical Chemistry B 110 (2006) 1277-1287

[38] Wilson, P.W., A.D.J. Haymet, Workman-Reynolds Freezing Potential Measurements

KOPRI 극지연구소

between Ice and Dilute Salt Solutions for Single Ice Crystal Faces, The Journal of Physical Chemistry B 112 (2008) 11750-11755

[39] Khusnatdinov, N.N., V.F. Petrenko, Experimental Study of Ice Electrolysis under UV Irradiation, The Journal of Physical Chemistry B 101 (1997) 6208-6211

[40] Kim, K., J. Kim, A.D. Bokare, W. Choi, H.-I. Yoon, J. Kim, Enhanced Removal of Hexavalent Chromium in the Presence of H2O2 in Frozen Aqueous Solutions, Environmental Science & Technology 49 (2015) 10937-10944

[41] Ahn, Y.-Y., J. Kim, K. Kim, Activation of peroxymonosulfate by bicarbonate and acceleration of the reaction by freezing, Science of The Total Environment 785 (2021) 147369

[42] Le, N.T.H., J. Ju, B. Kim, M.S. Kim, C. Lee, S. Kim, W. Choi, K. Kim, J. Kim, Freezing-enhanced non-radical oxidation of organic pollutants by peroxymonosulfate, Chemical Engineering Journal 388 (2020) 124226

[43] Połczyński, P., R. Jurczakowski, W. Grochala, Stabilization and strong oxidizing properties of Ag(ii) in a fluorine-free solvent, Chemical Communications 49 (2013) 7480-7482

[44] Deborde, M., U. von Gunten, Reactions of chlorine with inorganic and organic compounds during water treatment-Kinetics and mechanisms: A critical review, Water Research 42 (2008) 13-51

[45] Khalafi, L., M. Rafiee, Kinetic study of the oxidation and nitration of catechols in the presence of nitrous acid ionization equilibria, Journal of Hazardous Materials 174 (2010) 801-806

[46] Lee, Y., J. Yoon, U. von Gunten, Kinetics of the Oxidation of Phenols and Phenolic Endocrine Disruptors during Water Treatment with Ferrate (Fe(VI)), Environmental Science & Technology 39 (2005) 8978-8984

[47] Jacobi, H.-W., J. Kleffmann, G. Villena, P. Wiesen, M. King, J. France, C. Anastasio, R. Staebler, Role of Nitrite in the Photochemical Formation of Radicals in the Snow, Environmental Science & Technology 48 (2014) 165-172

[48] Ito, K., Y. Takayama, N. Makabe, R. Mitsui, T. Hirokawa, Ion chromatography for determination of nitrite and nitrate in seawater using monolithic ODS columns, Journal of Chromatography A 1083 (2005) 63-67

[49] Du, J., K. Kim, D.W. Min, W. Choi, Freeze-Thaw Cycle-Enhanced Transformation of Iodide to Organoiodine Compounds in the Presence of Natural Organic Matter and Fe(III), Environmental Science & Technology 56 (2022) 1007-1016

KOPRI 극지연구소

## FIGURES

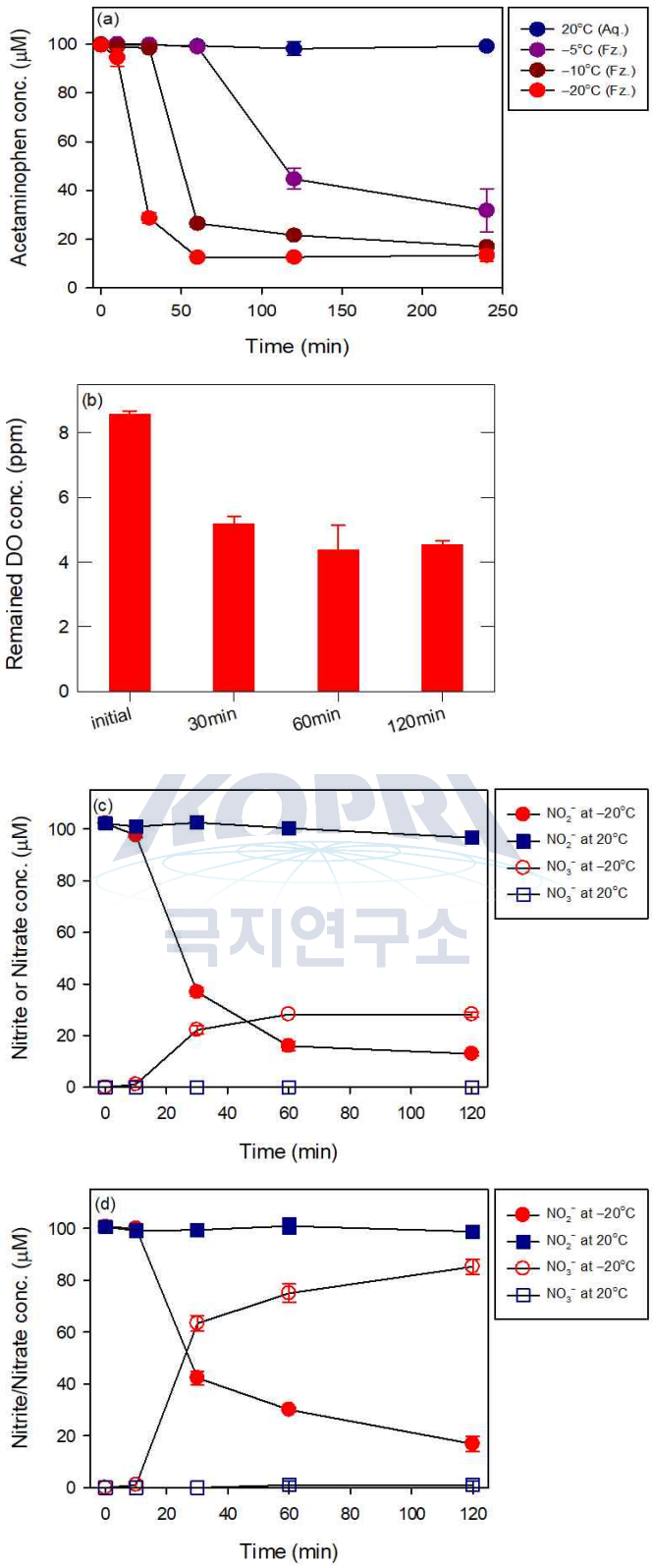



**Figure 1.** (a) The time-profile of AAP concentration in varying temperature. (b) the remained dissolved oxygen in the AAP/$NO_2^-$ system at -20℃ condition. (c) The time-profile of nitrite and nitrate in the AAP/$NO_2^-$ system at the -20℃ condition. (d) The time-profile of nitrite and nitrate in the AAP absent system at the -20℃ condition. Experimental condition: $[AAP]_0$ = 100 μM; $[NaNO_2]_0$ = 100 μM; pHi = 4 ($HClO_4$ adjust).

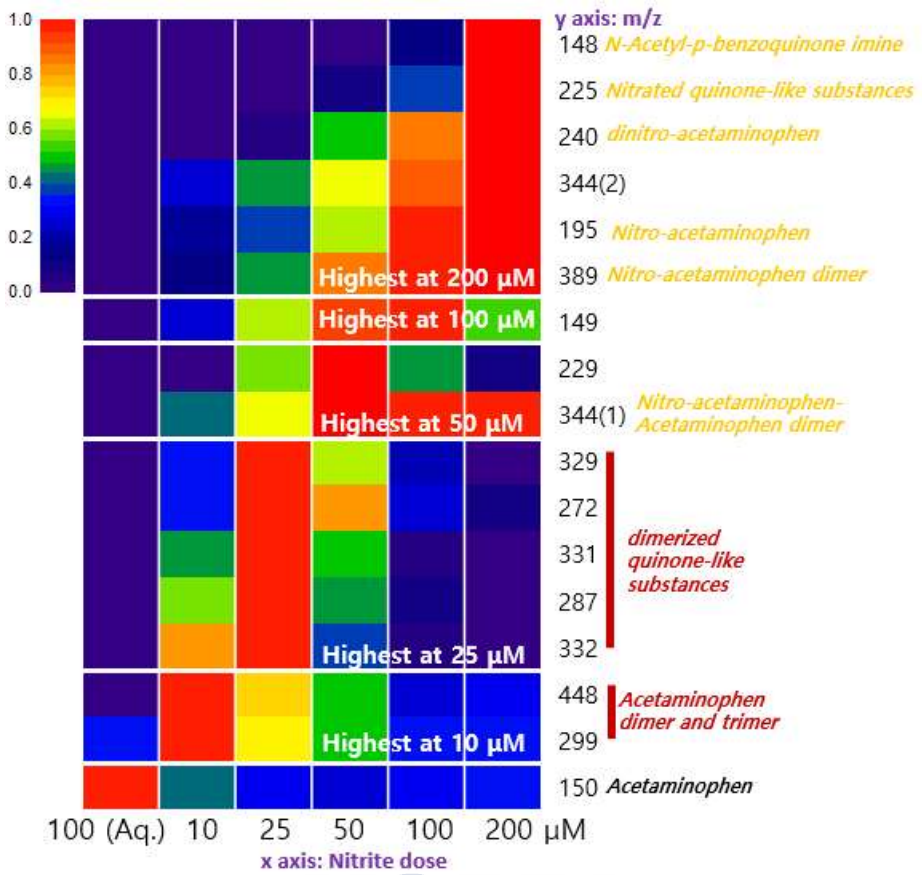



**Figure 2.** The AAP transformation byproducts in the frozen nitrite solution. Experimental condition: $[AAP]_0$ = 100 µM; $[NaNO_2]_0$ = 100 µM; pHi = 4 ($HClO_4$ adjust); Temperature = 20℃ (Aq.) / -20℃ (Fz.); Reaction time = 30 min.

KOPRI 극지연구소

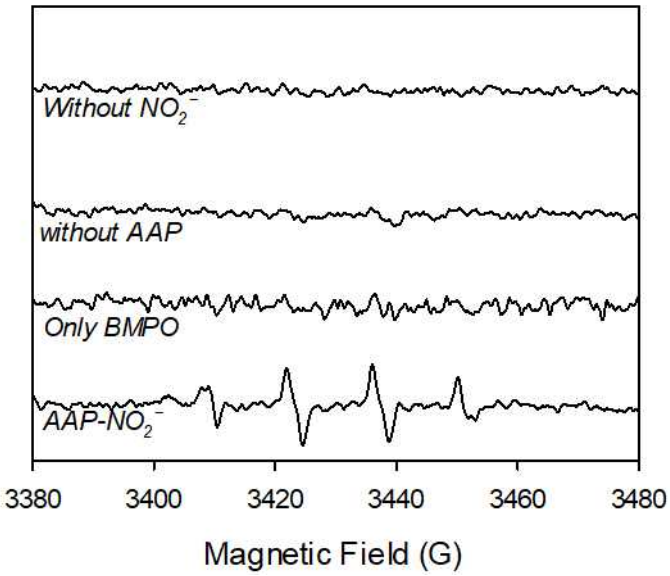



**Figure 3.** The detection of radical species through an EPR experiment. Experimental condition: $[AAP]_0$ = 10 mM; $[NaNO_2]_0$ = 10 mM; $[BMPO]_0$ = 20 mM; pHi = 2 ($HClO_4$ adjust); room temperature.

KOPRI
극지연구소

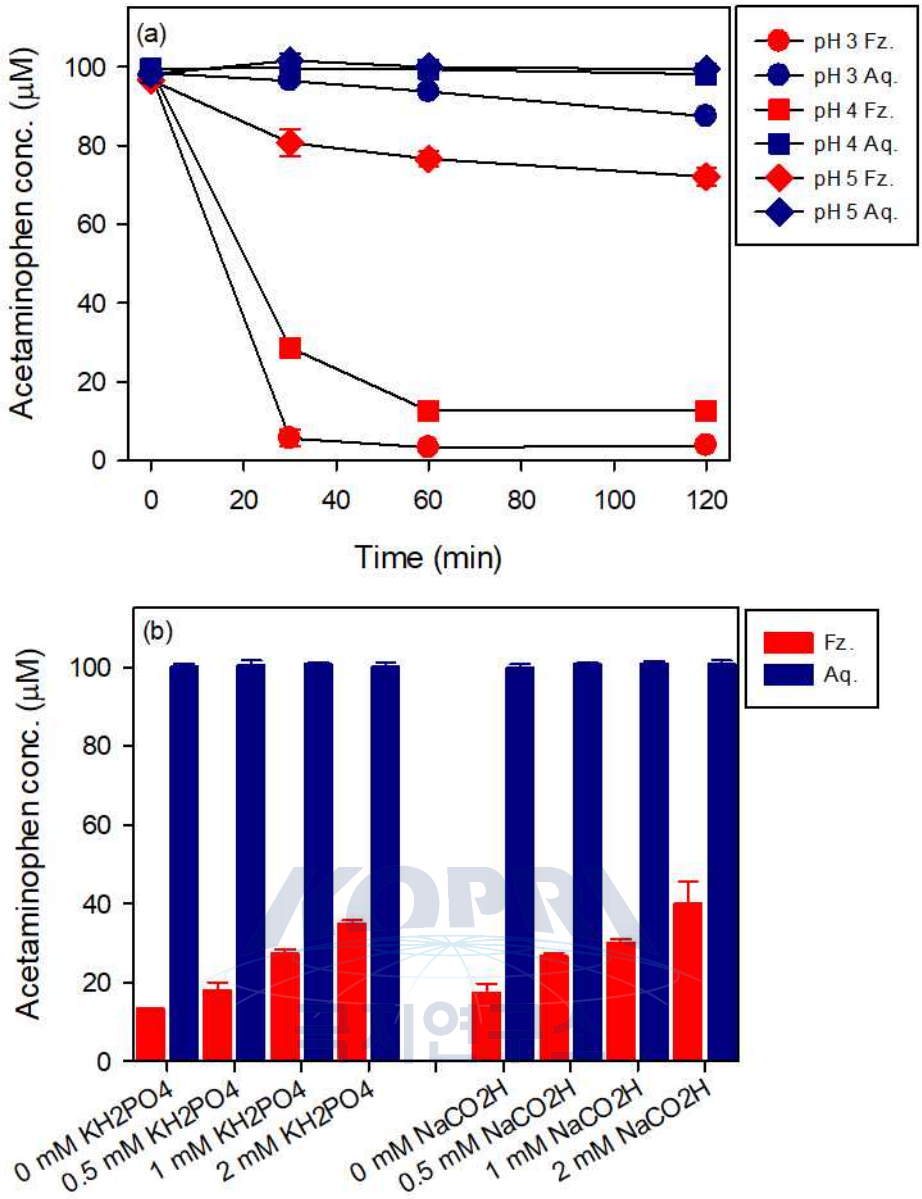



**Figure 4.** (a) The pH dependence of the AAP/$NO_2^-$ system. Experimental condition: $[AAP]_0$ = 100 μM; $[NaNO_2]_0$ = 100 μM; Temperature = 20℃ (Aq.) / -20℃ (Fz.). The initial pH was adjusted by the addition of $HClO_4$. (b) The effect of buffering reagent concentration on the AAP/$NO_2^-$ system. Experimental condition: $[AAP]_0$ = 100 μM; $[NaNO_2]_0$ = 100 μM; Temperature = 20℃ (Aq.) / -20℃ (Fz.). The initial pH was adjusted to 4 using phosphoric acid and formic acid with respect to the buffer anion.

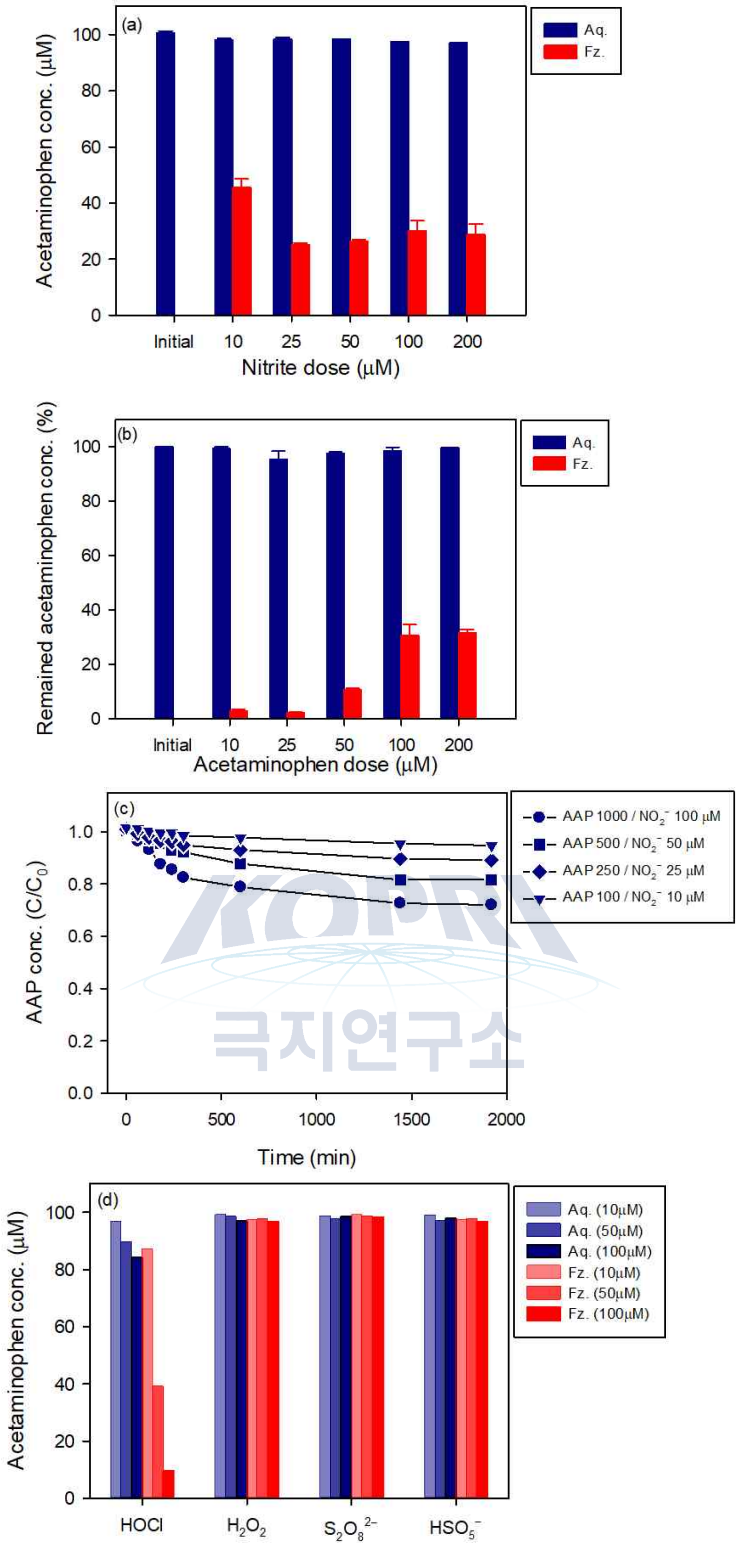



**Figure 5.** (a) The nitrite dose dependence of the AAP/$NO_2^-$ system, and (b) The AAP dose dependence of the AAP/$NO_2^-$ system. Experimental condition: $[AAP]_0$ = 100 μM; $[NaNO_2]_0$ = 100 μM; pHi = 4 ($HClO_4$ adjust); Reaction time = 30 min; Temperature = 20℃ (Aq.) / -20℃ (Fz.). (c) The AAP degradation in pH 1 aqueous solution. Experimental condition: pHi = 1 ($HClO_4$ adjust); Temperature = 20℃. (d) The effect of a selected oxidant on the degradation of AAP. Experimental condition: $[AAP]_0$ = 100 μM; pHi = 4 ($HClO_4$ adjust); Reaction time = 30 min; Temperature = 20℃ (Aq.) / -20℃ (Fz.).

KOPRI 극지연구소

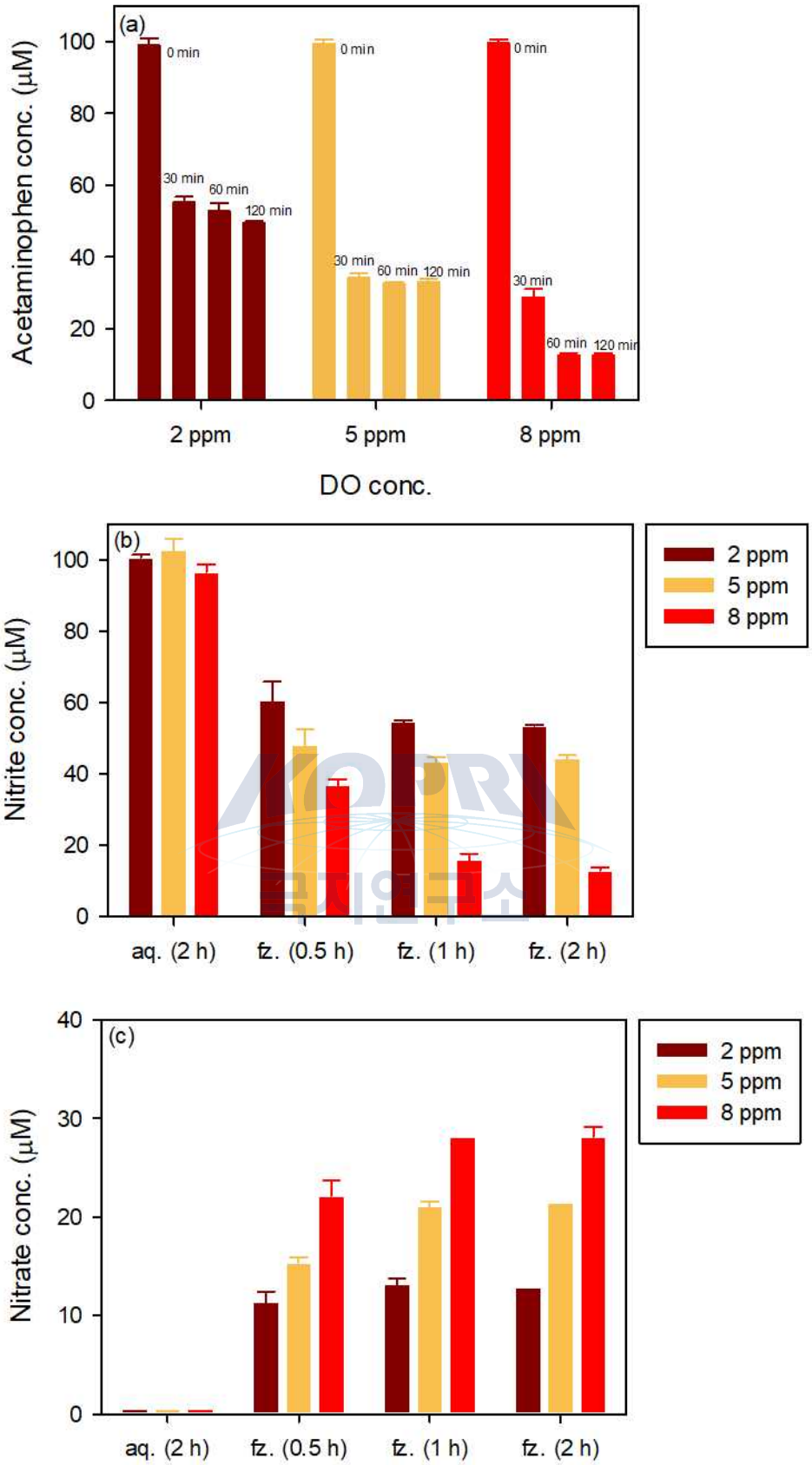



**Figure 6.** (a) The effect of AAP degradation on the initial dissolved oxygen concentration in the AAP/$NO_2^-$ system. (b) The nitrite concentration that remained. (c) The generated nitrate concentration. Experimental condition: $[Acetaminophen]_0$ = 100 μM; $[NaNO_2]_0$ = 100 μM; pHi = 4 ($HClO_4$ adjust); Temperature = 20℃ (Aq.) / -20℃ (Fz.).

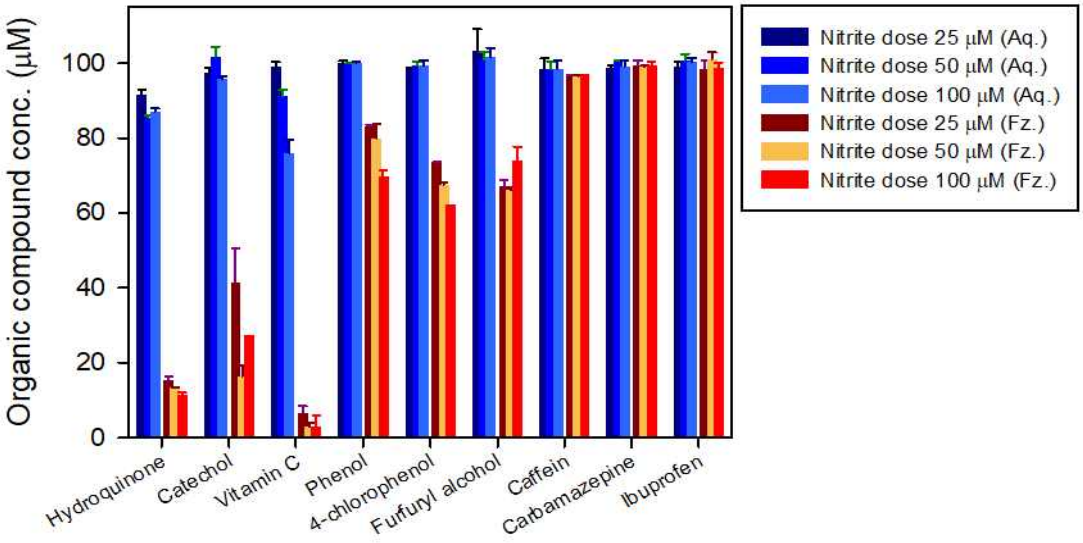



**Figure 7.** The reactivity of the frozen nitrite system in various organic substances. Experimental condition: $[Organic\ compound]_0$ = 100 μM; pHi = 4 ($HClO_4$ adjust); Reaction time = 60 min; Temperature = 20℃ (Aq.) / -20℃ (Fz.).

KOPRI
극지연구소

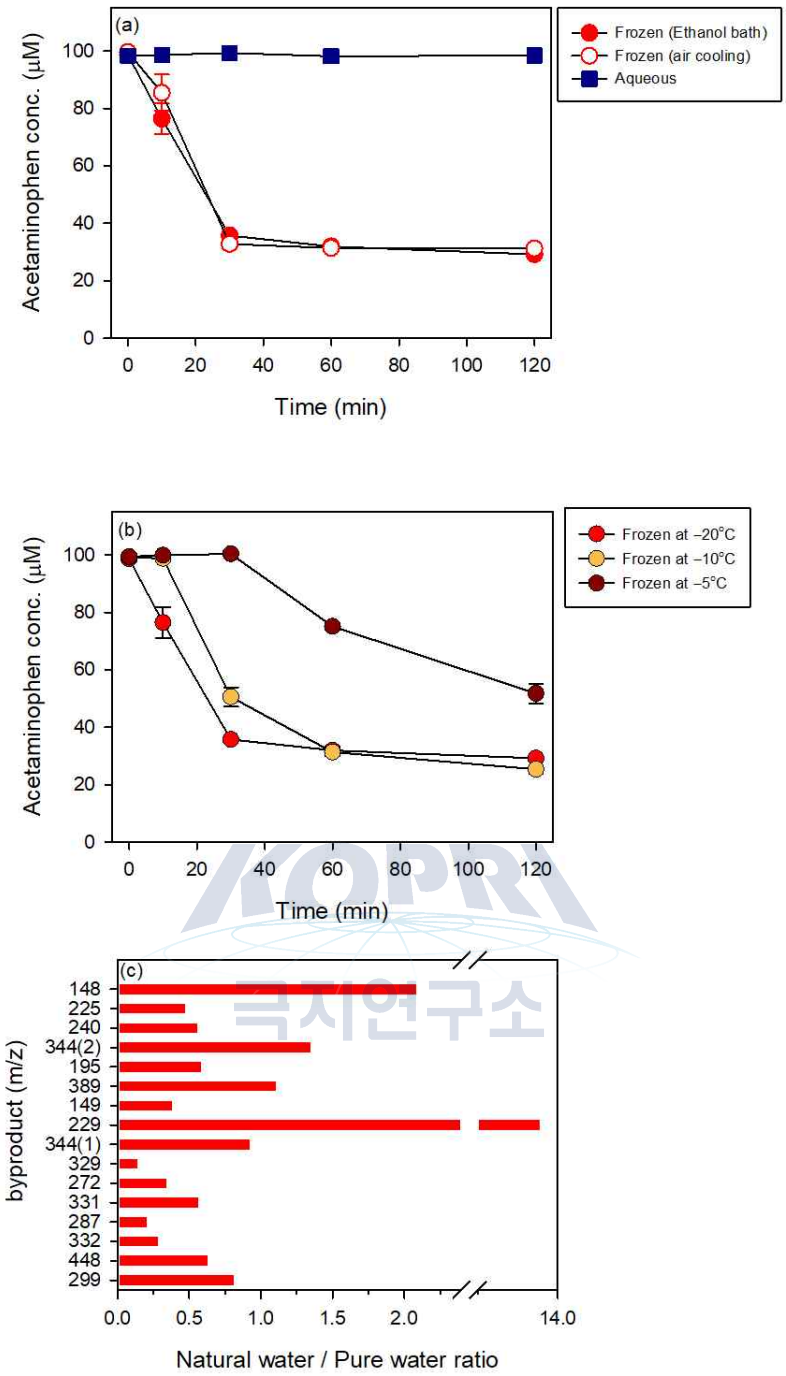



**Figure 8.** Time-profile of AAP concentration in the AAP/$NO_2^-$ system with a natural lake water matrix. (a) Cooling in the ethanol bath and ambient air condition. (b) Various temperature ranges in the ethanol bath cooling system. (c) Comparison of byproduct intensity between the natural water and pure water system; here, a value < 1.0 implied low intensity in the natural water system, and a value > 1.0 implied high intensity in the natural water system. Experimental condition: $[AAP]_0$ = 100 μM; $[NaNO_2]_0$ = 100 μM; pHi = 4 ($HClO_4$ adjust); Temperature Aq. = 20℃ / Fz. = -20℃; Reaction time = 30 min.

# 제 16 절. Production of Molecular Iodine via a Redox Reaction between Iodate and Organic Compounds in Ice⑯

Kitae Kim[1,2], Bomi Kim[1,2], Yong-Yoon Ahn[1], Khen Duy Tran[3], Hanh Thi My Truong[3], Jungwon Kim[3,*]

[1]Korea Polar Research Institute (KOPRI), Incheon 21990, Republic of Korea
[2]Department of Polar Sciences, University of Science and Technology (UST), Incheon 21990, Republic of Korea
[3]Department of Environmental Sciences and Biotechnology, Hallym University, Chuncheon, Gangwon-do 24252, Republic of Korea

## Abstract

The abiotic mechanism of molecular iodine ($I_2$) production from iodate ($IO_3^-$) remains largely unknown. Here, we demonstrate the production of $I_2$ in the presence of $IO_3^-$ and organic compounds in ice. When the solution containing $IO_3^-$ (100 μM) and furfuryl alcohol (100 μM) at pH 3.0 was frozen at −20 °C, 13.1 μM of $I_2$ was produced with complete degradation of furfuryl alcohol after 20 min. However, there was little change in the $IO_3^-$ and furfuryl alcohol concentrations in water at 25 °C. The production of $I_2$ in ice is due to the freeze concentration effect, which induces the accumulation of $IO_3^-$, furfuryl alcohol, and protons in the ice grain boundaries. This behavior facilitated the production of $I_2$ via a redox reaction between $IO_3^-$ and organic compounds. The production of $I_2$ increased with increasing furfuryl alcohol concentration and decreasing pH. However, freezing temperature had a minor effect on the maximum production of $I_2$. The production of $I_2$ is highly dependent on the type of organic compounds. It was higher for organic compounds with higher electron-donating properties. This study suggests a new mechanism for $I_2$ production, which is helpful for predicting precisely the atmospheric $I_2$ budget in cold regions.

## 1. Introduction

Molecular iodine ($I_2$) has a major impact on the global environment by inducing catalytic ozone ($O_3$) destruction, oxidation of organic and inorganic compounds, and formation of ultrafine particles (cloud condensation nuclei). (1) Although it has been suggested that

⑯ 본 연구는 본 과제(PE23120)로 수행되었으며, 결과는 *J. Phys. Chem. A* 2023, 127, 2830−2838에 출간되었다.

biological processes (i.e., the oxidative stress of marine algae) are primarily responsible for the production of $I_2$ from iodide ($I^-$), (2−4) various abiotic mechanisms of $I_2$ production have also been introduced. The chemical reaction between potassium iodide and dinitrogen tetroxide ($2KI + N_2O_4 \rightarrow 2KNO_2 + I_2$), (5) photochemical oxidation of $I^-$ ($4I^- + O_2 + 2H_2O + h\nu \rightarrow 2I_2 + 4OH^-$), (6) thermal oxidation of $I^-$ ($2I^- + 2H^+ + 0.5O_2 + \text{heat} \rightarrow I_2 + H_2O$), (7) and Dushman reaction ($IO_3^- + 5I^- + 6H^+ \rightarrow 3I_2 + 3H_2O$) (8) contribute to the atmospheric $I_2$ budget. Despite extensive studies, the previously reported biotic and abiotic mechanisms cannot completely account for the total $I_2$ budget. The missing mechanism for $I_2$ production from inorganic iodine species, such as $I^-$ and $IO_3^-$, remains. (9,10)

Recently, the importance of ice media in the production of $I_2$ has emerged. The production of $I_2$ in the presence of $I^-$ and $O_2$ was considerably enhanced when the aqueous solution was frozen under both dark and light-irradiation conditions. (11) Freezing accelerated the production of $I_2$ via the chemical reaction of $I^-$ with iron oxides, chromate, or ferric ions. (12−14) Although the production of $I_2$ via $NO_2^-$-mediated oxidation of $I^-$ was negligible in water, it was clearly observed in ice. (15−17) The freeze concentration effect is considered to be the main reason for the noteworthy enhanced production of $I_2$ from $I^-$ in ice. At temperatures between the freezing and eutectic points, frozen solutions contain both solid and liquid phases, which are referred to as bulk ice crystals and ice grain boundaries, respectively. (18) Substrates (solutes and gases) accumulate in the ice grain boundaries (liquid phase) as the ice crystals (solid phase) grow during the freezing process. (19−21) In addition, the pH of the solution changes after freezing; usually, an acidic solution becomes more acidic by $H^+$ accumulation and a basic solution becomes more basic by $OH^-$ accumulation in the ice grain boundaries. (22,23) Under these conditions, the considerably increased concentrations of substrates in the ice grain boundary region can enhance the production of $I_2$ by accelerating the redox reaction between $I^-$ and oxidants (e.g., $O_2$, iron oxides, chromate, $Fe^{3+}$, and $NO_2^-$). In addition, the freezing-induced pH decrease in the acidic solution converts $NO_2^-$ into more oxidizing forms, such as nitrous acid ($HNO_2$) and nitrous acidium ion ($H_2ONO^+$), (24) which synergistically act to further increase the production of $I_2$ in the presence of $NO_2^-$ and $I^-$ in ice.

In most previous studies of freezing-induced $I_2$ production, $I^-$ was used as the starting substrate. However, the concentration of $I^-$ in real environments is low. As inorganic iodine primarily exists as $IO_3^-$, (25,26) the $I_2$ production route from $IO_3^-$ has a greater impact. Nevertheless, the kinetics and mechanism of conversion of $IO_3^-$ to $I_2$ are largely unknown. We first reported the conversion of $IO_3^-$ to $I_2$ in ice, wherein $NO_2^-$ was used as a reductant ($2IO_3^- + 5HNO_2 \rightarrow I_2 + 5NO_3^- + 3H^+ + H_2O$). (27) Aside from $NO_2^-$, various inorganic and organic compounds could induce the conversion of $IO_3^-$ to $I_2$ by acting as reductants in ice. Identifying compounds that convert $IO_3^-$ to $I_2$ in ice is important for

predicting more precisely the atmospheric $I_2$ budget. It has recently been reported that some organic compounds, such as humic acid, fulvic acid, formic acid, methanol, ethanol, formaldehyde, and acetaldehyde, can act as reductants in ice. Therefore, the reduction of bromate to bromide by the aforementioned organic compounds ($BrO_3^- + 6H^+ + 6e^- \rightarrow Br^- + 3H_2O$) proceeded rapidly in ice. (28)

In this study, we investigated the production of $I_2$ via the redox reaction between $IO_3^-$ and organic compounds in ice and compared it with that in water. The reason for the enhanced production of $I_2$ in ice was suggested based on chemical analyses of the ice grain boundary region. In addition, the effects of the reaction parameters on $I_2$ production in ice were investigated and discussed. Finally, the environmental implications of this study were discussed.

## 2. Experimental Section

### 2.1. Chemicals

The chemicals were used as received without further purification. They include potassium iodate ($KIO_3$, Sigma-Aldrich, ≥ 99.5%), potassium iodide (KI, Junsei, ≥ 99.5%), furfuryl alcohol ($C_5H_6O_2$, Aldrich, ≥ 98.0%), tryptophan ($C_{11}H_{12}N_2O_2$, Sigma-Aldrich, ≥ 98.0%), cimetidine ($C_{10}H_{16}N_6S$, Sigma, ≥ 98.0%), ranitidine hydrochloride ($C_{13}H_{22}N_4O_3S{\cdot}HCl$, Sigma, ≥ 98.0%), phenol ($C_6H_6O$, Sigma-Aldrich, ≥ 99.0%), bisphenol A ($C_{15}H_{16}O_2$, Aldrich, ≥ 99.0%), acetic acid ($C_2H_4O_2$, Sigma-Aldrich, ≥ 99.7%), formic acid ($CH_2O_2$, Sigma-Aldrich, ≥ 96.0%), cresol red ($C_{21}H_{18}O_5S$, Sigma-Aldrich, ≥ 95.0%), perchloric acid ($HClO_4$, Aldrich, 1M), sodium hydroxide (NaOH, Supelco, 1M), acetonitrile ($C_2H_3N$, J.T. Baker, ≥ 99.9%), phosphoric acid ($H_3PO_4$, Junsei, 85%), sodium bicarbonate ($NaHCO_3$, Sigma-Aldrich, ≥ 99.7%), and sodium carbonate ($Na_2CO_3$, Sigma-Aldrich, ≥ 99.5%). All experimental solutions were prepared in ultrapure deionized water (18.3 MΩ·cm), which was produced using a Millipore water purification system (Milli-Q Direct 8).

### 2.2. Experimental procedure

Aliquots of chemical stock solutions (usually 10 mL of $IO_3^-$ (1 mM) and 10 mL of furfuryl alcohol (1 mM)) were added to deionized water (80 mL) in a beaker to yield the desired initial concentration (usually [$IO_3^-$] = 100 μM and [furfuryl alcohol] = 100 μM). The pH of the solution was adjusted using an $HClO_4$ or NaOH solution (usually pH 3.0). Ten milliliters of the aqueous solution containing $IO_3^-$ and furfuryl alcohol was transferred to a 15 mL polypropylene conical tube (Corning). Conical tubes (usually seven) containing aqueous solution were placed in a conical tube holder made of stainless steel. Thereafter, the conical tube holder was placed in a temperature-controlled cooling bath containing

ethanol as the coolant (Jeio Tech RW-0540G), which was precooled to the desired temperature (usually −20 °C). This point was considered the start of the reaction. At predetermined time intervals (10 min, 20 min, 30 min, 1, 2, 3, and 4 h), the conical tube containing the frozen sample was removed from the temperature-controlled cooling bath and placed in a tepid water bath at 35 °C for 2 min. Thereafter, melted samples were analyzed. Experiments were performed in water at 25 °C as a control. All kinetic experiments were performed two or more times under identical experimental conditions, and the results are presented as the average value ± standard deviation.

### 2.3. Chemical Analyses

The concentrations of organic compounds (furfuryl alcohol, tryptophan, cimetidine, ranitidine, phenol, and bisphenol A) in the samples were analyzed using high-performance liquid chromatography (Agilent 1120). Separation was performed on a Zorbax 300SB C-18 column (4.6 mm × 150 mm) using a binary mixture of acetonitrile and 0.1% (v/v) phosphoric acid as the eluent at a flow rate of 1.0 mL/min. The composition of the eluent (acetonitrile:0.1% phosphoric acid) and the detection wavelength were 15:85 (v/v) and 218 nm for furfuryl alcohol, 10:90 (v/v) and 220 nm for tryptophan, 5:95 (v/v) and 218 nm for cimetidine, 5:95 (v/v) and 230 nm for ranitidine, 30:70 (v/v) and 270 nm for phenol, and 30:70 (v/v) and 229 nm for bisphenol A. The concentrations of $I^-$, $IO_3^-$, acetate ($CH_3CO_2^-$), and formate ($HCO_2^-$) were measured using an ion chromatograph (Dionex ICS-1100) equipped with a suppressor (Dionex AERS 500), column (Dionex IonPac AS14, 4 mm × 250 mm), and conductivity detector. The eluent was a binary mixture of sodium bicarbonate (1 mM) and sodium carbonate (3.5 mM), at a flow rate of 1.0 mL/min. The production of $I_2$ was calculated based on the absorbance of the sample at 460 nm ($\varepsilon$ = 746 $M^{-1}$ $cm^{-1}$). (29) A UV–visible spectrophotometer (Shimadzu UV-2600) was used to measure the absorbance value.

The change in pH of the sample after freezing was monitored using a colorimetric method. Cresol red was used as an acid–base indicator. (22) The pH of the frozen solution was estimated by computing the concentration ratio of the monoprotonated form to the diprotonated form from the UV–visible absorption spectrum of cresol red after freezing. (30) The detailed method for the pH measurement of the frozen sample is described in Text S1. Confocal Raman spectroscopy was used to identify the spatial distributions of furfuryl alcohol and $IO_3^-$ in ice. Twenty microliters of an aqueous solution containing furfuryl alcohol (10 mM) or $IO_3^-$ (10 mM) at pH 3.0 was loaded on a temperature-controlled stage (Linkam Scientific THMS600). The droplet was frozen by decreasing the temperature of the stage from 0 to −20 °C at a rate of −2 °C/min. The Raman signal intensities of furfuryl alcohol and $IO_3^-$ were measured under 532 nm

monochromatic laser excitation using a confocal Raman spectrometer (Renishaw inVia Qontor). The relative concentrations of furfuryl alcohol and $IO_3^-$ in ice (i.e., in bulk ice crystals and ice grain boundaries) were visualized based on the Raman intensities at 1504 $cm^{-1}$ for furfuryl alcohol and 770 $cm^{-1}$ for $IO_3^-$.

## 3. Results and Discussion

### 3.1. $I_2$ Production in the Presence of $IO_3^-$ and Furfuryl Alcohol in Water and Ice

The production of $I_2$ in the presence of $IO_3^-$ and organic compounds in ice was measured and compared to that in water. For these experiments, furfuryl alcohol was used as a model organic compound, and ice- and water-phase reactions were performed at −20 and 25 °C, respectively. The concentrations of furfuryl alcohol and $IO_3^-$ did not change in water at [$IO_3^-$] = 100 μM, [furfuryl alcohol] = 100 μM, and pH 3.0 (Figures 1a and b). However, when the solution containing $IO_3^-$ and furfuryl alcohol was frozen, the concentrations of $IO_3^-$ and furfuryl alcohol decreased with increasing reaction time. In addition, the production of $I_2$ and $I^-$ was observed with nearly 100% iodine mass balance (Figures 1c and d). The control experiment without $IO_3^-$ in ice induced negligible degradation of furfuryl alcohol (Figure 1c). Similarly, $IO_3^-$ was not converted to $I_2$ or $I^-$ in the absence of furfuryl alcohol in ice (Figure 1d). The results of the control experiments indicate that the production of $I_2$ and $I^-$ (also the degradation of furfuryl alcohol) in ice proceeds via a redox reaction between $IO_3^-$ and furfuryl alcohol (reactions 1 and 2). The concentration of $I_2$ increased in the initial period (up to 20 min), and decreased thereafter. In contrast, the concentration of $I^-$ continued to increase after 20 min. This behavior was likely due to the conversion of $I_2$ to $I^-$ in ice (reaction 3) because the concentration of $IO_3^-$ was little changed after 20 min. Although furfuryl alcohol was completely degraded after 20 min, the degradation products remained in the ice (Figure 1c). Based on the results of the liquid chromatography - mass spectrometry (LC-MS) analysis and previous studies on furfuryl alcohol oxidation, (31,32) the structures of the degradation products are presented in Table S1. Here, the reduction of $I_2$ by degradation products (reaction 3) should be more favored than that of $IO_3^-$ by degradation products (reactions 1 and 2).

$$2IO_3^- + 12H^+ + 10e^- \text{ (furfuryl alcohol)} \rightarrow I_2 + 6H_2O \quad (1)$$

$$IO_3^- + 6H^+ + 6e^- \text{(furfuryl alcohol)} \rightarrow I^- + 3H_2O \quad (2)$$

$$I_2 + 2e^- \text{(degradation products)} \rightarrow 2I^- \quad (3)$$

### 3.2. Mechanistic Investigations of $I_2$ Production in Ice

It has been established that the concentration of substrates increases and the pH of an acidic solution decreases during freezing because of the freeze concentration

effect. (19,22) However, the degree of the freeze concentration effect depends considerably on substrate type. Some substrates are preferentially trapped in ice crystals during freezing. (33) Therefore, the spatial distributions of $IO_3^-$ and furfuryl alcohol in ice were investigated using confocal Raman spectroscopy (Figure 2). The black and red lines in Figure 2a indicate the Raman signals measured in the bulk ice crystal and ice grain boundary, respectively, of the frozen $IO_3^-$ solution. The Raman peak at 770 $cm^{-1}$ corresponding to the I–O stretching vibration in $IO_3^-$ was observed in the ice grain boundary; (34) however, it was not in the bulk ice crystal (Figure 2a). The relative concentrations of $IO_3^-$ in the ice were visualized by measuring the Raman signal intensity at 770 $cm^{-1}$. High signal intensities (red, yellow, and green) were observed in the ice grain boundary region, and low signal intensities (black, purple, and blue) were observed in the bulk ice crystal region (Figure 2b). The Raman spectrum of furfuryl alcohol exhibits several peaks from 1000 to 1600 $cm^{-1}$ due to intramolecular vibrations. (35) These peaks were observed only in the ice grain boundary region (Figure 2c). When the relative concentrations of furfuryl alcohol in ice were measured based on the Raman signal intensity at 1504 $cm^{-1}$, which was attributed to the C=C stretching vibration in furfuryl alcohol, (35) accumulation of furfuryl alcohol in the ice grain boundary region (red, yellow, and green) was also observed (Figure 2d). The Raman spectroscopy results show that both $IO_3^-$ and furfuryl alcohol are highly concentrated in the ice grain boundaries after freezing.

We also investigated how much the pH decreased after freezing the solution of $IO_3^-$ and furfuryl alcohol using cresol red as an acid–base indicator (Figure 3), which exists in three different forms depending on the pH. The absorption peaks of deprotonated, monoprotonated, and diprotonated forms are found near 573, 434, and 518 nm, respectively. (22) As the monoprotonated form is dominant at pH 3.0 ($pK_{a1}$ of cresol red = 1.10 and $pK_{a2}$ of cresol red = 8.15), (22) the absorption peak of the aqueous solution containing $IO_3^-$, furfuryl alcohol, and cresol red at pH 3.0 (i.e., before freezing) was observed at 434 nm. However, the absorption peak shifted to 524 nm after freezing. This result indicated that the monoprotonated form changed to the diprotonated form in ice. This speciation change of cresol red in ice is evidence that supports the pH decrease caused by freezing. Based on the Henderson–Hasselbalch equation (pH = $pK_{a1}$ + log[monoprotonated form]/[diprotonated form]) and the concentration ratio of the monoprotonated form to diprotonated form (1.26:1) which was computed from Figure 3, the pH of the frozen solution containing $IO_3^-$ and furfuryl alcohol was estimated to be approximately 1.2.

The increase in $IO_3^-$ and furfuryl alcohol concentrations and the decrease in pH after freezing synergistically facilitate the production of $I_2$ because the redox reaction between $IO_3^-$ and furfuryl alcohol is favored at higher concentrations of $IO_3^-$ and furfuryl alcohol and lower pH (reaction 1). To provide evidence of freeze-concentration effect-induced

$I_2$ production in the presence of $IO_3^-$ and furfuryl alcohol, the effect of the increase in $IO_3^-$ and furfuryl alcohol concentrations on $I_2$ production was investigated in water at pH 1.2 (Figure 4). The production of $I_2$ was negligible in the presence of 1 mM $IO_3^-$ and 1 mM furfuryl alcohol in water at pH 3.0 (Figure S1), indicating that highly acidic conditions are essential for $I_2$ production. $I_2$ was not produced at [$IO_3^-$] = 100 μM and [furfuryl alcohol] = 100 μM at pH = 1.2 (Figure 4a). When the concentration of furfuryl alcohol was increased 10-fold ([furfuryl alcohol] = 1 mM) at [$IO_3^-$] = 100 μM, the production of $I_2$ was observed (Figure 4b). The 10-fold increase in $IO_3^-$ concentration ([$IO_3^-$] = 1 mM) at [furfuryl alcohol] = 100 μM also induced the production of $I_2$ (Figure 4c). However, the production of $I_2$ was very low in both cases. When both $IO_3^-$ and furfuryl alcohol concentrations increased 10-fold ([$IO_3^-$] = 1 mM and [furfuryl alcohol] = 1 mM), the production of $I_2$ drastically increased (Figure 4d). These experimental results confirm that all three components in our system (i.e., $IO_3^-$, furfuryl alcohol, and $H^+$) act synergistically to enhance the production of $I_2$.

### 3.3. Effects of Reaction Parameters on the Freezing-Induced Production of $I_2$

The effects of reaction parameters such as furfuryl alcohol concentration, pH of the solution before freezing, and freezing temperature on the production of $I_2$ were investigated. The time-dependent concentrations of furfuryl alcohol were also monitored as a function of the $IO_3^-$ concentration, pH of the solution before freezing, and freezing temperature (Figure 5). The production of $I_2$ in ice increased with increasing furfuryl alcohol concentration (Figure 5a). The degradation of furfuryl alcohol in ice was also accelerated with increasing $IO_3^-$ concentration (Figure 5b). These results imply that the production of $I_2$ accompanied by the degradation of furfuryl alcohol in ice proceeds via a redox reaction between $IO_3^-$ as an oxidant and furfuryl alcohol as a reductant.

Figures 5c and d show the pH-dependent kinetics of $I_2$ production and furfuryl alcohol degradation, respectively. The production of $I_2$ increased with decreasing pH. Accordingly, the degradation of furfuryl alcohol was favored under more acidic conditions. When a more acidic aqueous solution is frozen, the pH of the frozen solution is lower. A lower pH provides favorable conditions for the redox reaction between $IO_3^-$ and furfuryl alcohol because $H^+$ is required for reactions 1 and 2. This phenomenon can explain the higher production of $I_2$ with a higher degradation efficiency of furfuryl alcohol at lower pH.

We also investigated the effect of freezing temperature on the production of $I_2$ and the degradation of furfuryl alcohol in ice (Figures 5e and f). The production of $I_2$ accompanied by the degradation of furfuryl alcohol was observed at all freezing temperatures tested (−10 to −30 °C). Both the production rate of $I_2$ and the degradation rate of furfuryl alcohol increased with decreasing freezing temperature because the accumulation of $IO_3^-$, furfuryl

alcohol, and $H^+$ in the ice grain boundary (the growth of bulk ice crystals) was faster at lower freezing temperatures. However, the maximum production of $I_2$ was similar without regard to the freezing temperature (14.1 μM at −10 °C, 13.1 μM at −20 °C, and 14.8 μM at −30 °C). Notably, the decomposition rate of $I_2$ was very slow at −30 °C, unlike the cases at −10 and −20 °C. This is because the reduction of $I_2$ by the degradation products (reaction 3) in ice is markedly retarded when the ice grain boundary disappears by solidification. (36) The ice grain boundaries were clearly observed when the solution containing $IO_3^-$ and furfuryl alcohol was frozen for 30 min at −10 and −20 °C. However, a significant proportion of the ice grain boundaries disappeared after 30 min of freezing at −30 °C (Figure S2).

### 3.4. Environmental Implications

To investigate the effect of the inflow of organic compounds during the freeze–thaw cycling processes on $I_2$ production from $IO_3^-$, furfuryl alcohol (100 μM) was injected into the sample after melting the frozen solution, and the melted solution was refrozen (Figure 6). When furfuryl alcohol was added only prior to the first freezing process, the production of $I_2$ decreased after 20 min (Figure 1d). However, the additional injection of furfuryl alcohol between the freeze and thaw cycling processes maintained the production of $I_2$ longer. The maximum production of $I_2$ (23.3 μM) was observed after the third freezing process (i.e., after 1.5 h) (Figure 6a). This result implies that freeze–thaw cycling processes by seasonal and day/night temperature variations with the inflow of organic compounds can enhance the production of $I_2$ in the presence of $IO_3^-$ in ice. When $IO_3^-$ was depleted (i.e., from the fourth freezing process), the degradation of furfuryl alcohol stopped (Figure 6b). This result confirms that $IO_3^-$ is required for the degradation of furfuryl alcohol in ice.

We also examined which organic compound was more efficient in $I_2$ production from $IO_3^-$ in ice (Figure 7). In addition to furfuryl alcohol, three pharmaceutical compounds (tryptophan, cimetidine, and ranitidine), two phenolic compounds (phenol and bisphenol A), and two organic acids (acetic and formic acids) were tested. In water, both the production of $I_2$ and degradation of organic compounds were negligible for all organic compounds tested (data not shown). Although the production of $I_2$ from $IO_3^-$ in ice varied significantly depending on the type of organic compound, a general trend in $I_2$ production was observed. The production of $I_2$ was higher when the degradation of the organic compounds was faster. The presence of pharmaceutical compounds produced a large amount of $I_2$ with the rapid degradation of pharmaceutical compounds (Figures 7b–d). However, the production of $I_2$ was low in the presence of phenolic compounds (Figures 7e and f) and negligible in the presence of organic acids (Figures 7g and h). Pharmaceuticals containing furan, imidazole,

and pyrrole moieties are vulnerable to electrophilic attack (i.e., they have high electron-donating properties). (37,38) Therefore, these pharmaceuticals can work as effective electron donors to produce more $I_2$ by reducing $IO_3^-$ rapidly in ice.

It has recently been reported that various pharmaceuticals are found in sewage effluent (up to hundreds of micromoles) and receiving seawater (up to dozens of nanomoles) in the Arctic region. (39) In addition, high concentrations of pharmaceuticals (up to hundreds of nanomoles) are frequently found in surface water. (40) The concentrations of $IO_3^-$ reach hundreds of nanomoles in most places, including the polar regions, seawater, and surface water. (41,42) Thus, the redox reaction between $IO_3^-$ and pharmaceutical compounds in ice can occur frequently and contribute to the production of $I_2$ in midlatitudes during the winter season and in polar regions.

## 4. Conclusions

$I_2$ plays a key role in several environmental processes. However, abiotic production of $I_2$ from inorganic iodine species, particularly $IO_3^-$, has been little studied. In this study, we investigated the production of $I_2$ via a redox reaction between $IO_3^-$ and organic compounds in ice. Although the production of $I_2$ in the presence of $IO_3^-$ and furfuryl alcohol was negligible in water at 25 °C, it proceeded rapidly during freezing at −20 °C. This phenomenon is due to the freeze concentration effect, which favors the redox reaction by increasing the concentrations of $IO_3^-$ and furfuryl alcohol and decreasing the pH. There was a close correlation between $I_2$ production and organic compound degradation in ice. Consequently, among various organic compounds, pharmaceutical compounds, which are easily degradable (highly electron-donating), showed high efficiency for $I_2$ production in the presence of $IO_3^-$ in ice. Higher concentrations of reactive iodine species than the predicted concentrations were measured in specific areas. (9,10) The proposed mechanism can help reduce the interval between measured and predicted concentrations of reactive iodine species in the atmosphere. However, some concerns about the influence of the proposed mechanism in real environments still exist because the production of $I_2$ from $IO_3^-$ in ice is available under acidic conditions (pH $\leq$ 5.0) and in the presence of specific organic compounds. There are more abundant organic compounds that could reduce $IO_3^-$ rapidly in ice in real environments. Further investigations (i.e., finding abundant organic compounds that are efficient for $I_2$ production in ice, with modeling studies on their contribution to the global $I_2$ budget) need to be performed.

KOPRI 극지연구소

## REFERENCES


(1) Saiz-Lopez, A.; Plane, J. M. C.; Baker, A. R.; Carpenter, L. J.; vonGlasow, R.; Gómez Martín, J. C.; McFiggans, G.; Saunders, R. W. Atmospheric chemistry of iodine. Chem. Rev. 2012, 112, 1773−1804.

(2) Saiz-Lopez, A.; Plane, J. M. C. Novel iodine chemistry in themarine boundary layer. Geophys. Res. Lett. 2004, 31, L04112.

(3) Palmer, C. J.; Anders, T. L.; Carpenter, L. J.; Küpper, F. C.; McFiggans, G. B. Iodine and halocarbon response of Laminariadigitata to oxidative stress and links to atmospheric new particle production. Environ. Chem. 2005, 2, 282−290.

(4) Küpper, F. C.; Carpenter, L. J.; McFiggans, G. B.; Palmer, C. J.; Waite, T. J.; Boneberg, E.-M.; Woitsch, S.; Weiller, M.; Abela, R.;Grolimund, D.; et al. Iodide accumulation provides kelp with aninorganic antioxidant impacting atmospheric chemistry. Proc. Natl. Acad. Sci. U. S. A. 2008, 105, 6954−6958.

(5) O'Neill, E.; Hinrichs, R. Z. Production of molecular iodine fromthe heterogeneous reaction of nitrogen dioxide with solid potassiumiodide. J. Geophys. Res. 2011, 116, D01301.

(6) Möller, A.; Lovrlc, M.; Scholz, F. Evidence for the occasionalappearance of molecular iodine in sea water. Int. J. Environ. Anal.Chem. 1996, 63, 99−106.

(7) Wren, J. C.; Ball, J. M.; Glowa, G. A. The chemistry of iodine incontainment. Nucl. Technol. 2000, 129, 297−325.

(8) Truesdale, V. W. On the feasibility of some photochemicalreactions of iodide in seawater. Mar. Chem. 2007, 104, 266−281.

(9) Gálvez, O.; Baeza-Romero, M. T.; Sanz, M.; Saiz-Lopez, A. Photolysis of frozen iodate salts as a source of active iodine in thepolar environment. Atmos. Chem. Phys. 2016, 16, 12703−12713.

(10) Saiz-Lopez, A.; Blaszczak-Boxe, C. S.; Carpenter, L. J. Amechanism for biologically induced iodine emissions from sea ice.Atmos. Chem. Phys. 2015, 15, 9731−9746.

(11) Kim, K.; Yabushita, A.; Okumura, M.; Saiz-Lopez, A.; Cuevas,C. A.; Blaszczak-Boxe, C. S.; Min, D. W.; Yoon, H.-I.; Choi, W.Production of molecular iodine and tri-iodide in the frozen solution of iodide: implication for polar atmosphere. Environ. Sci. Technol. 2016, 50, 1280−1287.

(12) Kim, K.; Chung, H. Y.; Kim, B.; Wong, G.; Nguyen, A. Q. K.;Kim, S.; Kim, J. Freezing-induced simultaneous reduction of chromateand production of molecular iodine: mechanism, kinetics, and practical implications. Environ. Sci. Technol. 2020, 54, 16204−16211.

(13) Kim, K.; Menacherry, S. P. M.; Kim, J.; Chung, H. Y.; Jeong,D.; Saiz-Lopez, A.; Choi, W. Simultaneous and synergic production of bioavailable iron and reactive iodine


KOPRI 극지연구소

species in Ice. Environ. Sci.Technol. 2019, 53, 7355－7362.
(14) Du, J.; Kim, K.; Min, D. W.; Choi, W. Freeze-thaw cycle enhanced transformation of iodide to organoiodine compounds in the presence of natural organic matter and Fe(III). Environ. Sci. Technol. 2022, 56, 1007－1016.
(15) O'Driscoll, P.; Lang, K.; Minogue, N.; Sodeau, J. Freezing halide ion solutions and the release of interhalogens to the atmosphere. J. Phys. Chem. A 2006, 110, 4615－4618.
(16) O'Sullivan, D.; Sodeau, J. R. Freeze-induced reactions:formation of iodine-bromine interhalogen species from aqueous halide ion solutions. J. Phys. Chem. A 2010, 114, 12208－12215.
(17) O'Driscoll, P.; Minogue, N.; Takenaka, N.; Sodeau, J. Release of nitric oxide and iodine to the atmosphere from the freezing of seasalt aerosol components. J. Phys. Chem. A 2008, 112, 1677－1682.
(18) Bartels-Rausch, T.; Jacobi, H.-W.; Kahan, T. F.; Thomas, J. L.;Thomson, E. S.; Abbatt, J. P. D.; Ammann, M.; Blackford, J. R.; Bluhm, H.; Boxe, C.; et al. A review of air-ice chemical and physical interactions (AICI): liquids, quasi-liquids, and solids in snow. Atmos. Chem. Phys. 2014, 14, 1587－1633.
(19) Heger, D.; Jirkovsky', J.; Klán, P. Aggregation of methylene blue in frozen aqueous solutions studied by absorption spectroscopy. J.Phys. Chem. A 2005, 109, 6702－6709.
(20) Takenaka, N.; Ueda, A.; Daimon, T.; Bandow, H.; Dohmaru, T.; Maeda, Y. Acceleration mechanism of chemical reaction by freezing: The reaction of nitrous acid with dissolved oxygen. J. Phys.Chem. 1996, 100, 13874－13884.
(21) Dubowski, Y.; Hoffmann, M. R. Photochemical transformations in ice: Implications for the fate of chemical species. Geophys. Res. Lett.2000, 27, 3321－3324.
(22) Heger, D.; Klánová, J.; Klán, P. Enhanced protonation of cresol red in acidic aqueous solutions caused by freezing. J. Phys. Chem. B2006, 110, 1277－1287.
(23) Newberg, J. T. Equilibrium shifts upon freezing. Fluid Phase Equilib. 2018, 478, 82－89.
(24) Riordan, E.; Minogue, N.; Healy, D.; O'Driscoll, P.; Sodeau, J.R. Spectroscopic and optimization modeling study of nitrous acid inaqueous solution. J. Phys. Chem. A 2005, 109, 779－786.
(25) Suorsa, V.; Otaki, M.; Zhang, W.; Virkanen, J.; Koivula, R. A simple method for quantifying iodate and iodide fractions in solution using Ag+-impregnated activated carbon. J. Radioanal. Nucl. Chem.2020, 324, 135－142.
(26) McTaggart, A. R.; Butler, E. C. V.; Haddad, P. R.; Middleton, J.H. Iodide and iodate concentrations in eastern Australian subtropicalwaters, with iodide by ion chromatography. Mar. Chem. 1994, 47,159－172.
(27) Kim, K.; Ju, J.; Kim, B.; Chung, H. Y.; Vetrákova, L'.; Heger, D.; Saiz-Lopez, A.; Choi, W.; Kim, J. Nitrite-induced activation ofiodate into molecular iodine in frozen

solution. Environ. Sci. Technol. 2019, 53, 4892−4900.

(28) Min, D. W.; Choi, W. Accelerated reduction of bromate in frozen solution. Environ. Sci. Technol. 2017, 51, 8368−8375.

(29) Awtrey, A. D.; Connick, R. E. The absorption spectra of $I_2$, $I_3^-$,$I^-$, $IO_3^-$, $S_4O_6^=$ and $S_2O_3^=$. Heat of the reaction $I_3^-$ = $I_2$ + $I^-$. J. Am. Chem. Soc. 1951, 73, 1842−1843.

(30) Ju, J.; Kim, J.; Vetráková, L'.; Seo, J.; Heger, D.; Lee, C.; Yoon, H.-I.; Kim, K.; Kim, J. Accelerated redox reaction between chromate and phenolic pollutants during freezing. J. Hazard. Mater. 2017, 329,330−338.

(31) Panzarasa, G. Just add luminol to turn the spotlight on Radziszewski amidation. ACS Omega 2018, 3, 13179−13182.

(32) Braun, A. M.; Dahn, H.; Gassmann, E.; Gerothanassis, I.; Jakob,L.; Kateva, J.; Martinez, C. G.; Oliveros, E. (2 + 4)-cycloaddition with singlet oxygen. $^{17}O$-investigation of the reactivity of furfuryl alcoholendoperoxide. Photochem. Photobiol. 1999, 70, 868−874.

(33) Takenaka, N.; Tanaka, M.; Okitsu, K.; Bandow, H. Rise in the pH of an unfrozen solution in ice due to the presence of NaCl and promotion of decomposition of gallic acids owing to a change in thepH. J. Phys. Chem. A 2006, 110, 10628−10632.

(34) Durig, J. R.; Bonner, O. D.; Breazeale, W. H. Raman studies of iodic acid and sodium iodate. J. Phys. Chem. 1965, 69, 3886−3892.

(35) Kim, T.; Assary, R. S.; Curtiss, L. A.; Marshall, C. L.; Stair, P. C. Vibrational properties of levulinic acid and furan derivatives: Raman spectroscopy and theoretical calculations. J. Raman Spectrosc. 2011,42, 2069−2076.

(36) Kim, K.; Kim, J.; Bokare, A. D.; Choi, W.; Yoon, H.-I.; Kim, J. Enhanced removal of hexavalent chromium in the presence of $H_2O_2$ in frozen aqueous solutions. Environ. Sci. Technol. 2015, 49, 10937−10944.

(37) Bokare, A. D.; Choi, W. Singlet-oxygen generation in alkaline periodate solution. Environ. Sci. Technol. 2015, 49, 14392−14400.

(38) Kim, H.; Kim, W.; Mackeyev, Y.; Lee, G.-S.; Kim, H.-J.;Tachikawa, T.; Hong, S.; Lee, S.; Kim, J.; Wilson, L. J.; et al. Selective oxidative degradation of organic pollutants by singlet oxygen-mediated photosensitization: Tin porphyrin versus $C_{60}$ aminofullerenesystems. Environ. Sci. Technol. 2012, 46, 9606−9613.

(39) Choi, Y.; Kim, K.; Kim, D.; Moon, H.-b.; Jeon, J. Ny-Ålesund oriented organic pollutants in sewage effluent and receiving seawater in the Arctic region of Kongsfjorden. Environ. Pollut. 2020, 258, 113792.

(40) da Silva, B. F.; Jelic, A.; López-Serna, R.; Mozeto, A. A.; Petrovic, M.; Barceló, D. Occurrence and distribution of pharmaceuticals in surface water, suspended solids and sediments of the Ebroriver basin, Spain. Chemosphere 2011, 85, 1331−1339.

(41) Atkinson, H. M.; Huang, R.-J.; Chance, R.; Roscoe, H. K.;Hughes, C.; Davison, B.; Schönhardt, A.; Mahajan, A. S.; Saiz-Lopez,A.; Hoffmann, T.; et al. Iodine emissions from the sea ice of the Weddell Sea. Atmos. Chem. Phys. 2012, 12, 11229－11244.

(42) Bluhm, K.; Croot, P. L.; Huhn, O.; Rohardt, G.; Lochte, K.Distribution of iodide and iodate in the Atlantic sector of the southern ocean during austral summer. Deep Sea Res., Part II 2011, 58, 2733－2748.

KOPRI
극지연구소

## FIGURES

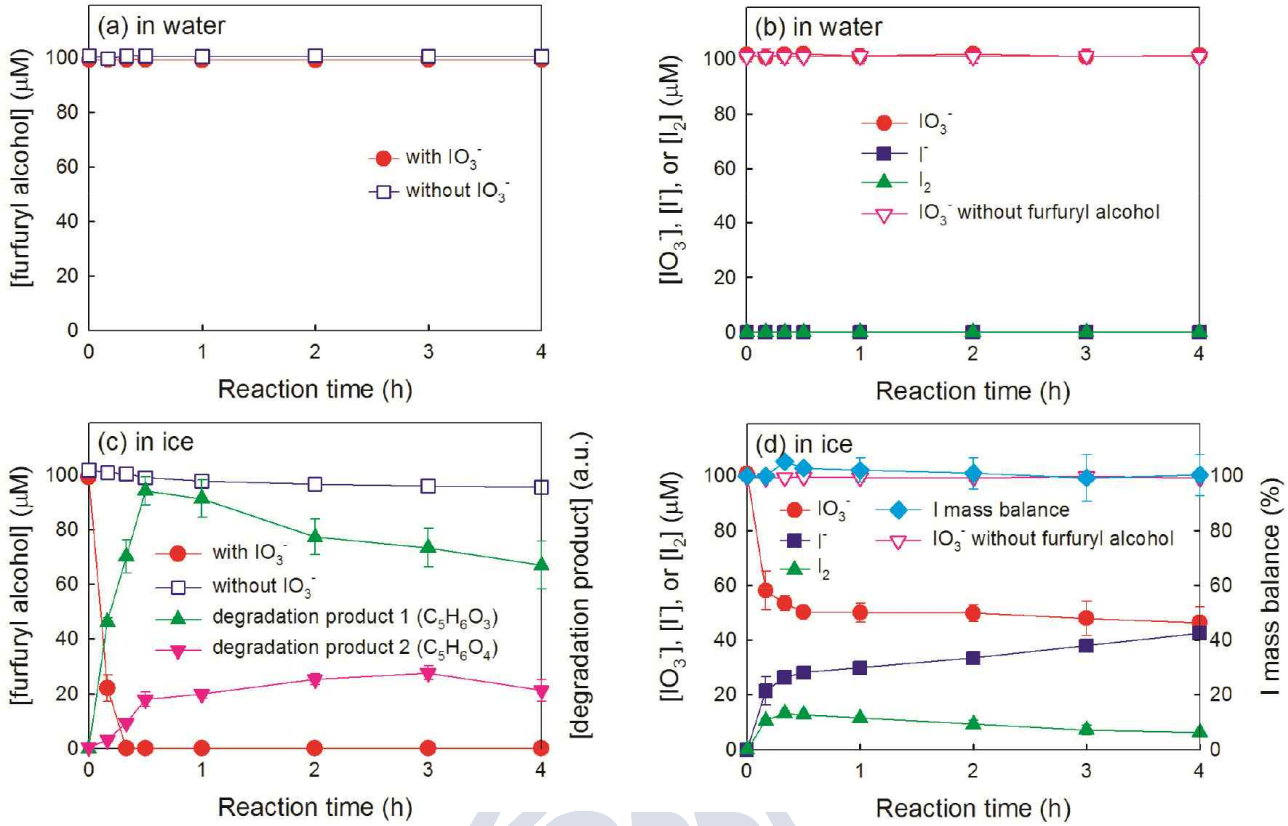



**Figure 1.** Time profiles of (a and c) furfuryl alcohol and degradation product concentrations, and (b and d) $IO_3^-$, $I^-$, and $I_2$ concentrations in the presence of $IO_3^-$ and furfuryl alcohol in (a and b) water at 25 °C and (c and d) ice at −20 °C. Experimental conditions: $[IO_3^-]$ = 100 μM, [furfuryl alcohol] = 100 μM, and pH 3.0.

KOPRI 극지연구소

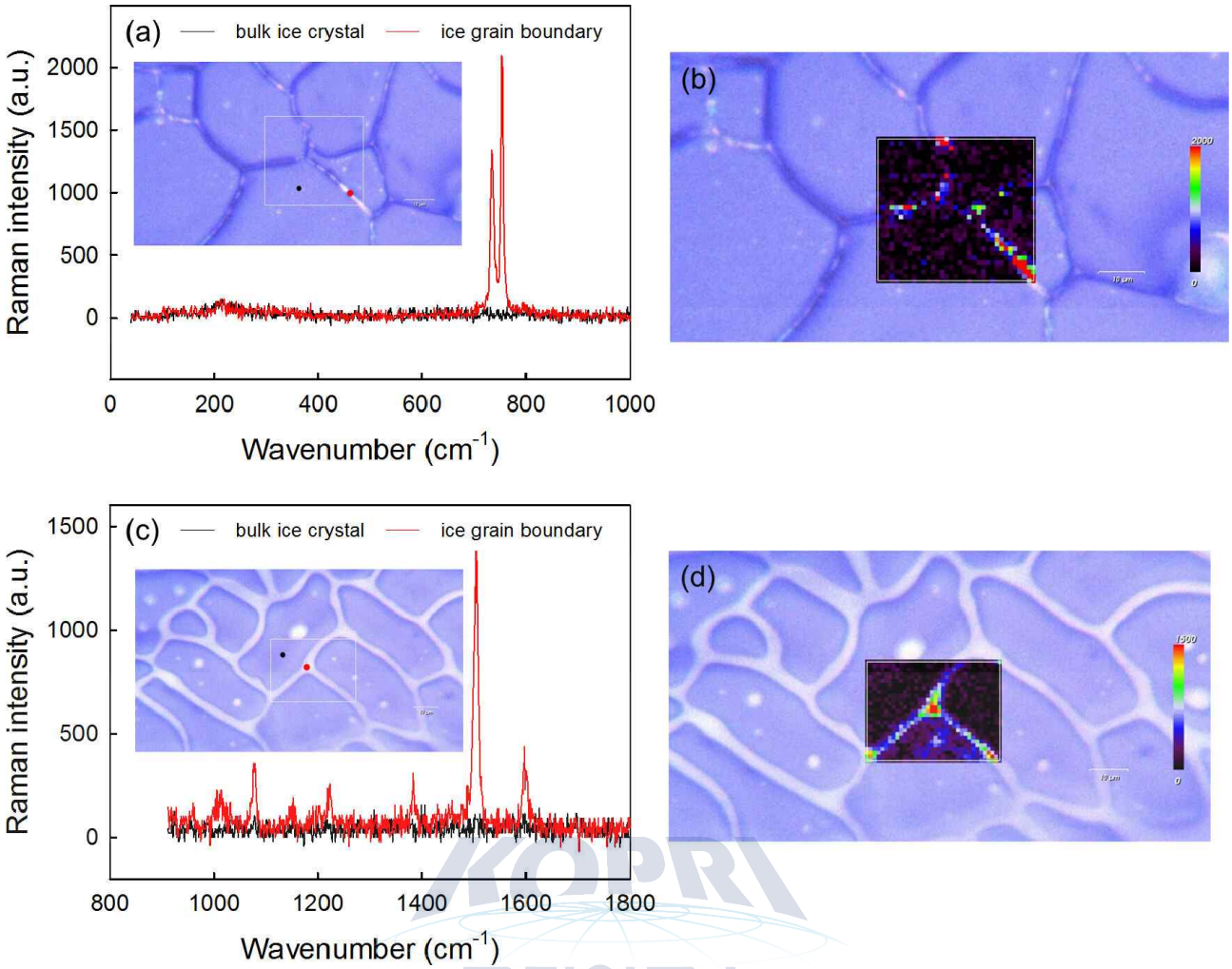



**Figure 2.** Raman spectra of (a) $IO_3^-$ and (c) furfuryl alcohol in the bulk ice crystal and ice grain boundary. Spatial distributions of (b) $IO_3^-$ and (d) furfuryl alcohol in ice. Experimental conditions: [$IO_3^-$] = 10 mM, [furfuryl alcohol] = 10 mM, and pH 3.0. Raman spectra were recorded in the sites marked with black (bulk ice crystal) and red circles (ice grain boundary) in parts (a) and (c).

KOPRI 극지연구소

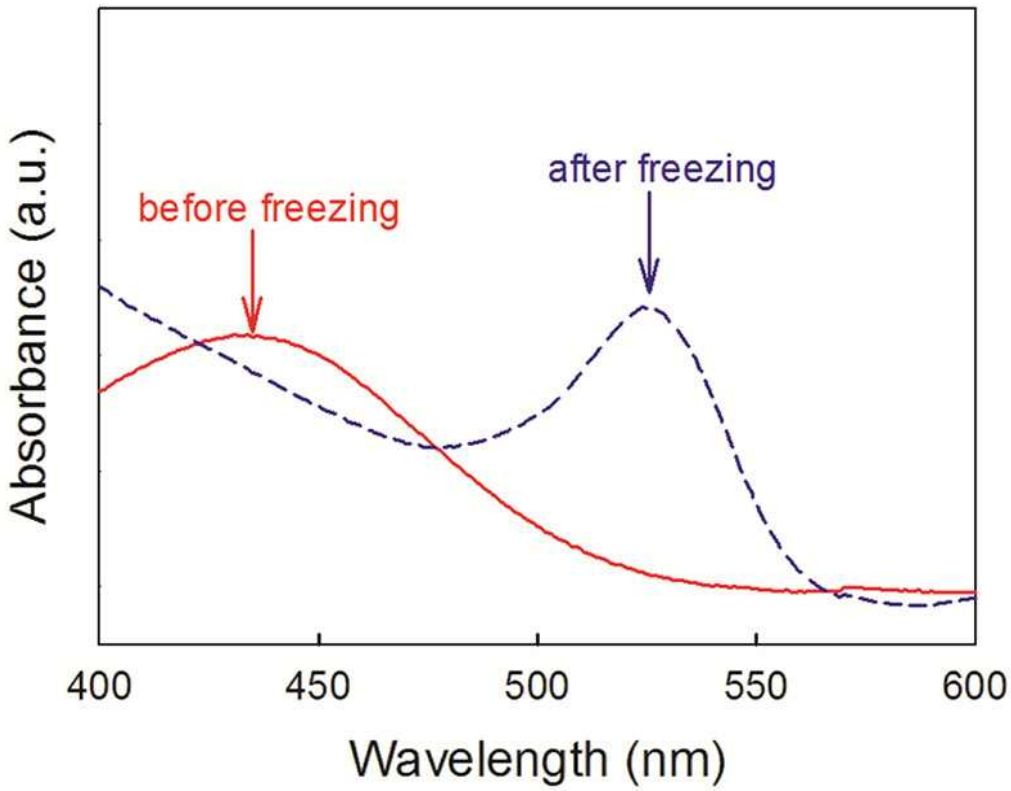



**Figure 3.** UV - visible absorption spectra of cresol red before and after freezing the solution of $IO_3^-$ and furfuryl alcohol. Experimental conditions: $[IO_3^-]$ = 100 μM, [furfuryl alcohol] = 100 μM, [cresol red] = 50 μM, and pH 3.0 before freezing.

KOPRI 극지연구소

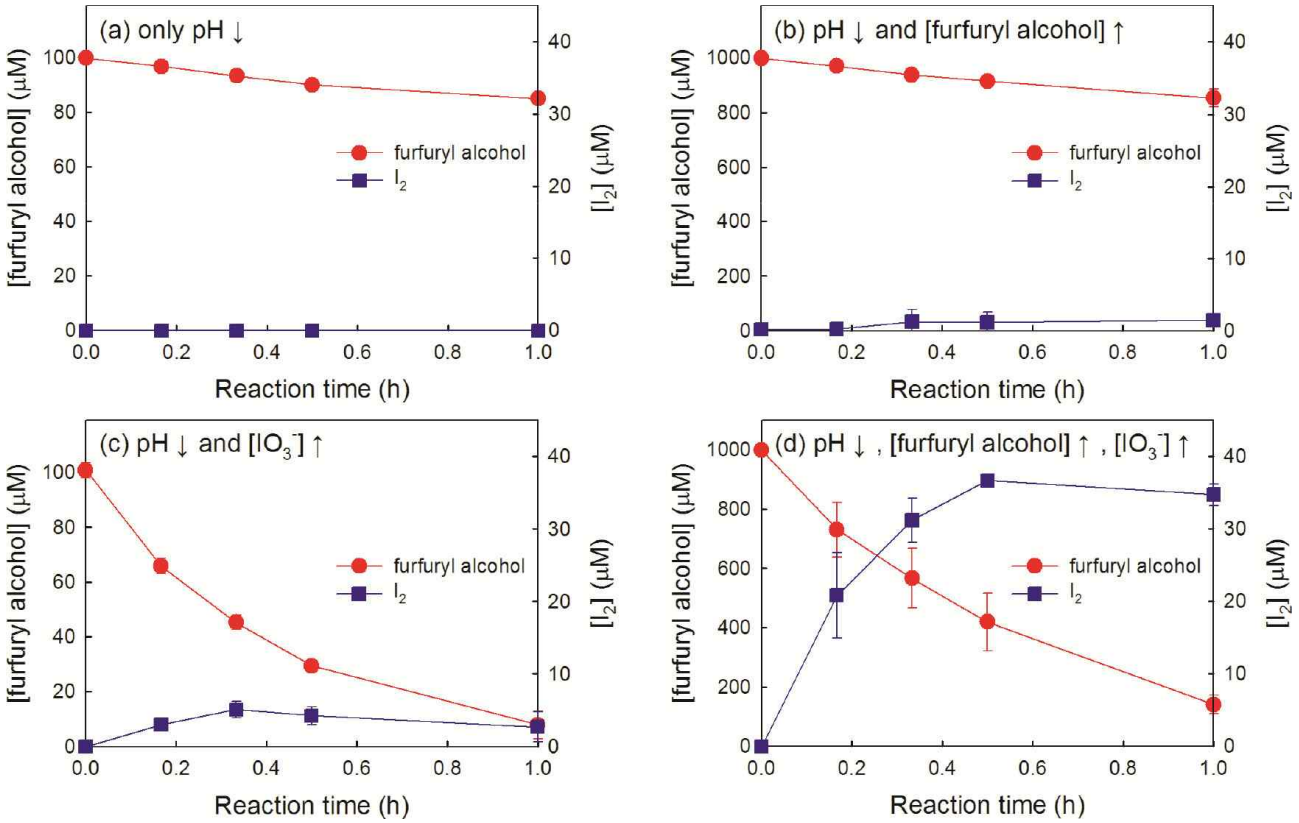



**Figure 4.** Production of $I_2$ accompanied by the degradation of furfuryl alcohol in water (25 °C) at pH 1.2. Experimental conditions: $[IO_3^-]$ = [furfuryl alcohol] = 100 μM for part (a), $[IO_3^-]$ = 100 μM and [furfuryl alcohol] = 1 mM for part (b), $[IO_3^-]$ = 1 mM and [furfuryl alcohol] = 100 μM for part (c), and $[IO_3^-]$ = [furfuryl alcohol] = 1 mM for part (d).

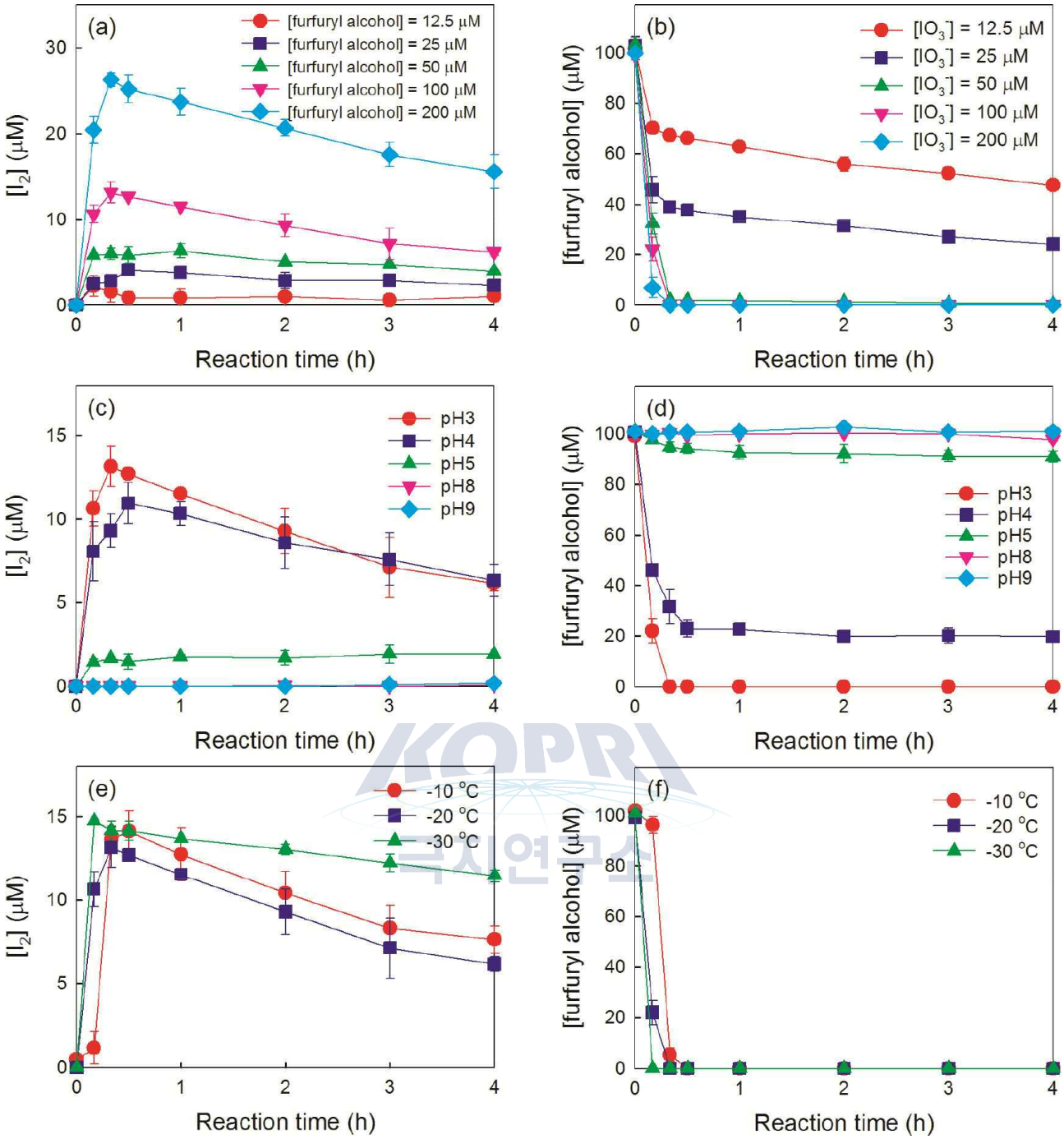



**Figure 5.** Effects of furfuryl alcohol concentration, $IO_3^-$ concentration, pH, and freezing temperature on the production of $I_2$ or the degradation of furfuryl alcohol in ice. Experimental conditions: [$IO_3^-$] = 100 μM except for part (b), [furfuryl alcohol] = 100 μM except for part (a), pH 3.0 except for parts (c) and (d), and temperature = −20 °C except for parts (e) and (f).

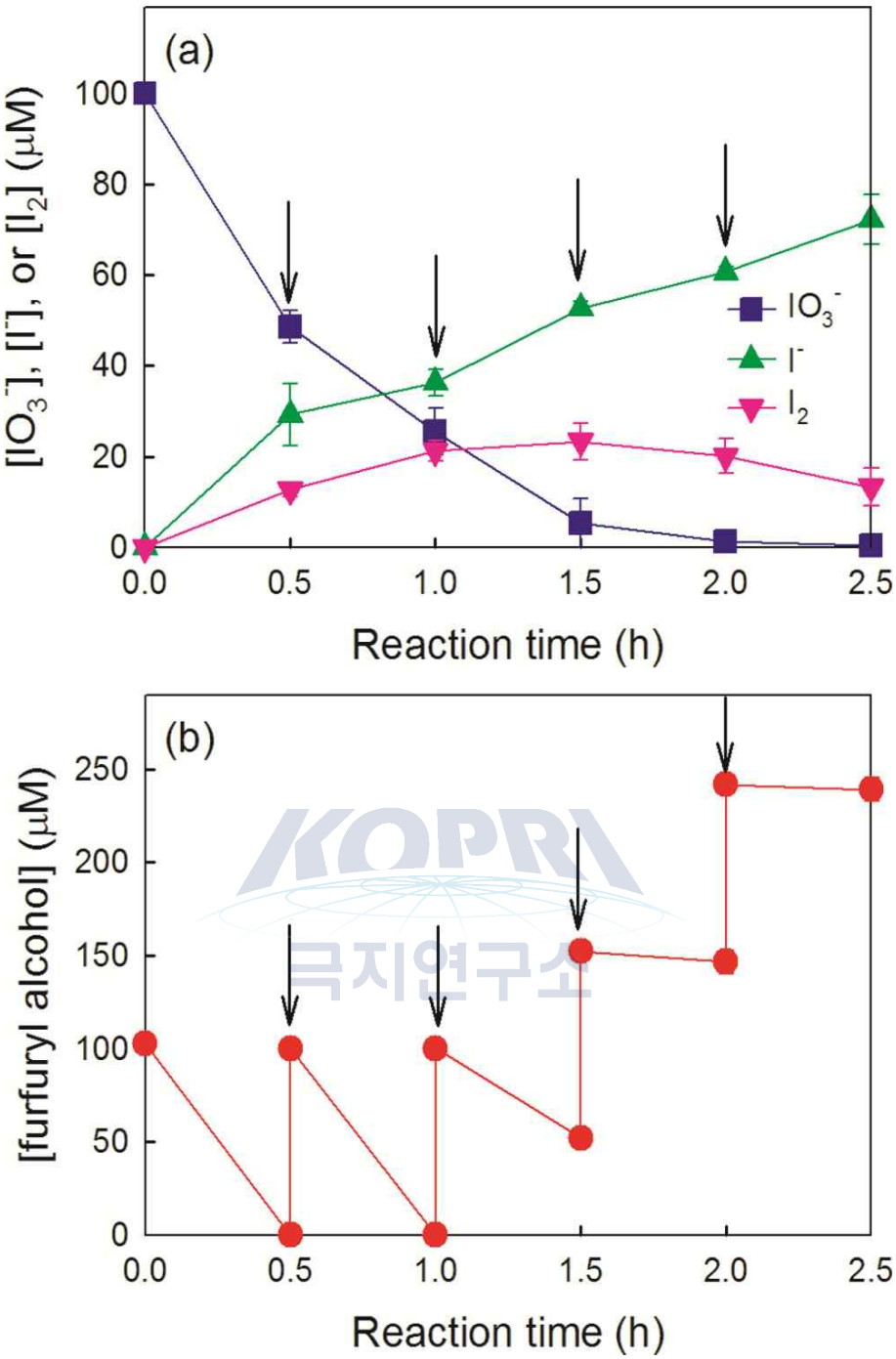



**Figure 6**. Effect of the additional injection of furfuryl alcohol during the freeze-thaw cycling processes on (a) $I_2$ production and (b) furfuryl alcohol degradation in ice at −20 °C. Experimental conditions: $[IO_3^-]$ = 100 μM, [furfuryl alcohol] = 100 μM, and pH 3.0. Furfuryl alcohol (100 μM) was periodically added to the reactor at times indicated by arrows.

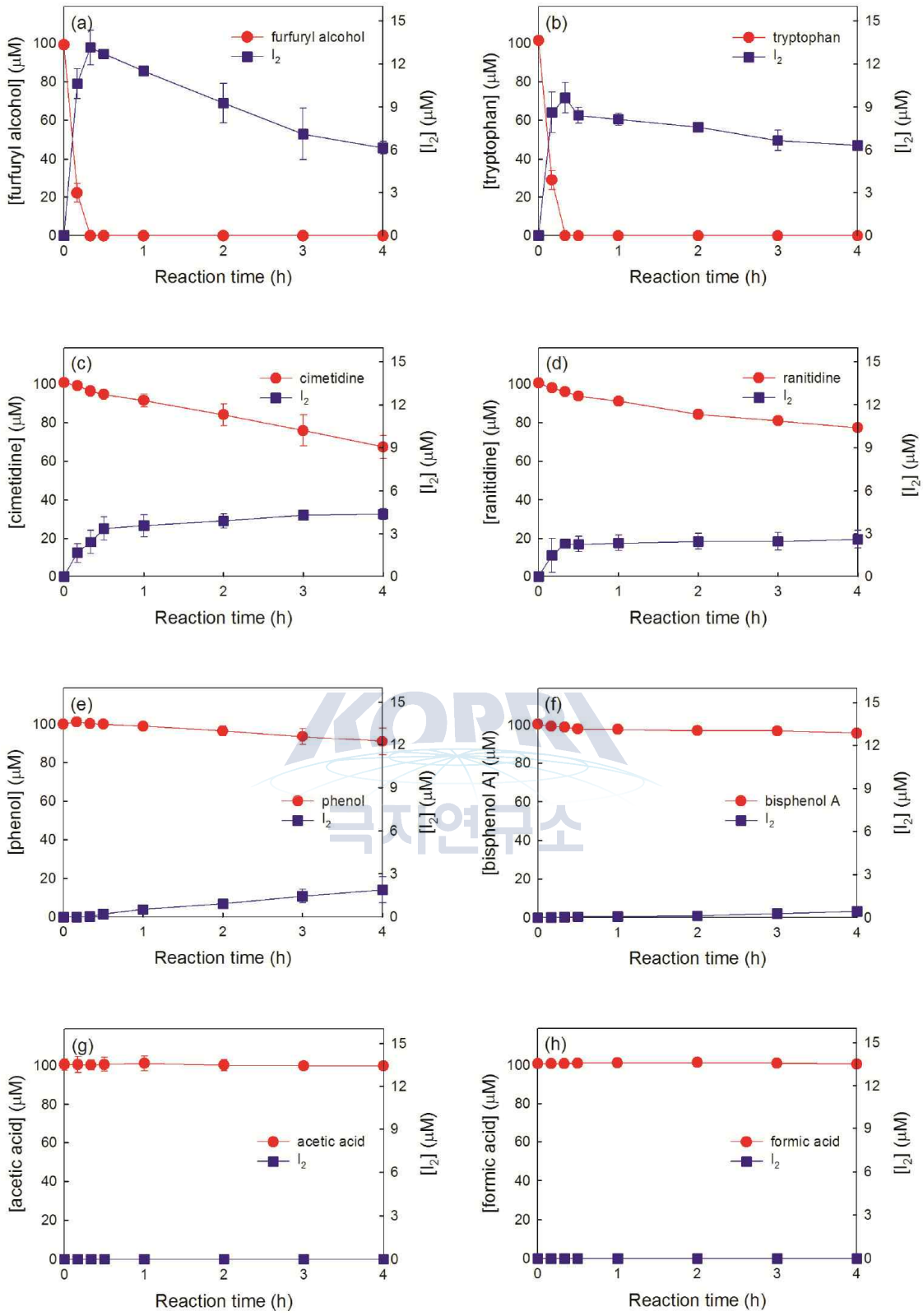



**Figure 7**. Production of $I_2$ from $IO_3^-$ and degradation of organic compounds in ice depending on the type of organic compound. Experimental conditions: [$IO_3^-$] = 100 μM, [organic compound] = 100 μM, and pH 3.0.

# 제 17 절. A novel simultaneous abatement of bromate and diphenyl phosphate using the freezing process⑰

Yong-Yoon Ahn and Kitae Kim

Korea Polar Research Institute

## Abstract

The purification of bromate ($BrO_3^-$)-contaminated water has become a challenge because of its persistence and adverse effects. Furthermore, there has been concern over the release of byproducts, such as diphenyl phosphate (DPHP), from flame retardants in wastewater treatment plant (WWTP). In this study, we designed the water treatment system for the oxidation of DPHP accompanied by bromate ($BrO_3^-$) reduction via freezing the solution. A sample containing 10 μM DPHP, 100 μM $Br^-$, and 50 μM $BrO_3^-$, with a pH of 3 was frozen at －20 ℃, approximately 25 μM $BrO_3^-$ was reduced, and DPHP was fully eliminated after a 0.5 h reaction time. Conversely, these reactions did not advance in water at 20 ℃. This increase in the rate of chemical reaction in ice is the consequence of the freeze concentration effect, which refers to the extraction of dissolved chemical species into the liquid-like regions of the polycrystalline ice micro-structure during the freezing of the solution. The redox reactions among DPHP, $Br^-$, and $BrO_3^-$ become thermodynamically favorable due to the distinctive environment in the liquid brine in ice. The efficiency of the DPHP oxidation significantly increased with an increase in $BrO_3^-$ concentration, and vice versa. The $Br^-/BrO_3^-$-induced HOBr production is proposed as a primary oxidant for DPHP degradation. The proton activity (pH) has a significant influence on the reaction efficiency. The low freezing temperature accelerated the reaction kinetics of DPHP degradation and $BrO_3^-$ reduction. The results of this study indicate the possibility of utilizing ice chemistry for the $BrO_3^-$ reduction that concomitantly removes DPHP for water treatment. This environmentally friendly water treatment method can be considered to implement in regions with a cold climate.

## 1. Introduction

Generally, polar regions are considered pristine areas free of anthropogenic pollution because they are located far from civilization. However, recent studies have demonstrated the exposure of these areas to a variety of anthropogenic pollutants, including

⑰ 본 연구는 본 과제(PE24120)로 수행되었으며, 결과는 *Chemosphere* 2024, 367, 143629에 출간되었다.

organophosphate esters (OPEs) (Wild et al., 2015; Choi et al., 2020; Xie et al., 2022; Balakrishna et al., 2023). OPEs are widely used in textiles, cosmetic products, plasticizers, pesticides, and flame retardants (Yao et al., 2021; Lim et al., 2023; Zhang et al., 2023). Because of their growing demand, they are frequently present in wastewater, necessitating an adequate treatment to mitigate adverse impacts on natural water (Zhang et al., 2023). However, conventional water treatment technologies are ineffective at controlling OPEs, leading to the exploration of advanced oxidation processes as alternative treatment technologies (Yuan et al., 2015; Zhang et al., 2023). In addition, the persistent characteristic and adverse effect on the human body of the disinfection byproduct $BrO_3^-$ during the wastewater treatment process has raised concerns, particularly for drinking water contamination (Huang et al., 2017; Cheng et al., 2018; Morrison et al., 2023).

Persistent organic pollutants are prevalent in polar regions, where they have never been used owing to long-range transport mechanisms such as air/water and air/soil gas exchange, bioaccumulation along food chains, ocean currents, and warm volatilization/cold deposition (Wang et al., 2019). Furthermore, a recent study found approximately 7 μg/L of triphenylphosphine oxide in the effluent from the permanent residency Ny-Alesund, Svalbard, in the Arctic (Choi et al., 2020). DPHP, a degradation product of OPEs, is formed from triphenyl phosphate (TPHP) and is part of a new class of OPEs, the di-OPEs. Notably, di-OPE emissions are significant owing to their comparable environmental impact to tri-OPEs, as they can be produced as byproducts and metabolites during tri-OPE transformation. According to Yao et al., environmental monitoring studies have reported DPHP concentrations of up to 1005 ng/L in wastewater influent, 554 ng/L in effluent, 1680 ng/g in sludge, 6646 ng/g in dust, and 35.4 ng/L in surface water, respectively. Furthermore, DPHP is toxic to organism reproduction and development (Yao et al., 2021). Given its prevalence, we selected DPHP as the target di-OPEs. Notably, wastewater treatment in polar regions is particularly limited owing to environmental factors like low microbial activity, making it crucial to develop technologies that can adapt to these unique characteristics.

In general, solutions are frozen to prevent chemical reactions during food or medicine preservation, but recent studies have demonstrated that pharmaceutical compounds in ice can be removed by $BrO_3^-$ during the freezing process (Sun et al., 2023a; Sun et al., 2023b; Sun et al., 2024). In addition, the distinct redox characteristics of $BrO_3^-$ with humic substances in ice have been demonstrated by our previous research (Min and Choi, 2017). Hypobromous acid (HOBr) and $Br^-$ were produced as a result of the reduction of $BrO_3^-$ in the presence of humic acid, which was utilized as an electron donor during the freezing process, but this reaction was negligible in the absence of humic acid or in the aqueous phase at room temperature. Therefore, we hypothesize that the organophosphate ester,

diphenyl phosphate (DPHP), might also oxidize in a freezing $BrO_3^-$ solution.

The unique chemical reaction in ice was ascribed to the freezing concentration effect: growing ice crystals expels the solutes, which are concentrated in the liquid brine between ice crystals (O'Concubhair and Sodeau, 2013). The freezing concentration effect accelerates chemical reactions, particularly those of high order, as the reaction rate depends on the concentration of reactants (Takenaka and Bandow, 2007). Besides, the acid-catalyzed chemical reactions can be significantly promoted by freezing due to an increase in proton activity (i.e., proton concentration) in ice. In this regard, the freezing reaction of $Br^-/BrO_3^-$ can be substantial, as described in the following equations (Bray and Liebhafsky, 1935; Côrtes and Faria, 2004; Schmitz, 2007).

$$BrO_3^- + 2Br^- + 3H^+ \rightarrow 3HOBr \quad (1)$$

$$d[BrO_3^-]/dt = -k_1[BrO_3^-][H^+]^2[Br^-] - k_2[BrO_3^-][H^+]^2[Br^-]^2 \quad (2)$$

At 25℃, the rate constants $k_1$ and $k_2$ were reported as 4.12 ± 0.05 $M^{-3}$ $s^{-1}$ and 0.810 ± 0.02 $M^{-4}$ $s^{-1}$, respectively (Cortes and Faria, 2004), and the half-life for $BrO_3^-$ is calculated to be approximately 40 years at the following conditions: $[BrO_3^-]_0$ = 50 μM, $[Br^-]_0$ = 100 μM, and $[HClO_4]_0$ = 1 mM (ca. pH 3). However, this reaction can be accelerated during the freezing process, eventually resulting in enhanced HOBr generation. Owing to the inherent oxidative reactivity of HOBr, we anticipate that the $Br^-/BrO_3^-$ reaction can remove several organic pollutants.

In the present study, we designed a water treatment system to simultaneously eliminate the carcinogenic $BrO_3^-$ and DPHP by freezing the solution. We investigated the $Br^-/BrO_3^-$ reaction in ice and monitored the DPHP degradation. We examined the effect of a variety of experimental parameters, such as reactant concentration, freezing temperature, initial pH, and type of halide species, on the $BrO_3^-$ reduction and DPHP degradation. Further, we measured the generation of HOBr in the frozen $Br^-/BrO_3^-$ solution and proposed that the DPHP degradation is caused by the HOBr generation. Finally, we monitored the DPHP and $BrO_3^-$ reduction in the natural arctic river water matrix from Bayelva, Svalbard (N 78° 55.725, E 11° 50.577) to evaluate the regional feasibility of the process. Our process can be considered an eco-friendly water treatment technology when it is implemented in polar areas, such as a high-latitude region or a mid-latitude region in winter, because the freezing phenomenon is spontaneous in these areas.

## 2. Materials & Methods

### 2.1. Chemical reagents

The chemical reagents used are listed below: diphenyl phosphate (DPHP, Sigma-Aldrich), sodium bromide (Sigma-Aldrich), sodium bromate (Sigma-Aldrich), sodium chloride (Sigma-Aldrich), sodium chlorate (Sigma-Aldrich), sodium hypochlorite (Sigma-Aldrich), sodium iodide (Sigma-Aldrich), sodium iodate (Sigma-Aldrich), perchloric acid (Sigma-Aldrich), sodium hydroxide (Sigma-Aldrich), 1,3,5-trimethoxybenzene (Sigma-Aldrich), 5-tert-butoxycarbonyl-5-methyl-1-pyrroline-N-oxide (BMPO, ENZO Life Science, Inc.), sodium bicarbonate (Sigma-Aldrich), sodium carbonate (Sigma-Aldrich), acetonitrile (MS grade, Supelco), methanol (MS grade, Supelco), and formic acid (MS grade, Sigma-Aldrich). Deionized water was prepared using a Barnstead water purification system and the resistivity was checked 18.2 MΩocm before use. The stock solutions of the chemical compounds were prepared by dissolving them in deionized water.

### 2.2. Experiment procedure

The freezing experiments were conducted in an ethanol bath operated at -20℃ to freeze the samples. The temperature effect was examined at -10℃ and -5℃. We prepared 10 mL of the DPHP and $NaBrO_3$ mixture at the desired concentration using stock solutions of each compound (0.1 mM and 100 mM, respectively). In order to prevent the formation of trace $Br^-$ in the stock solution, the $NaBrO_3$ stock solution was freshly prepared for each experiment. An aliquot of 10 mM NaBr stock solution was appropriately added to each DPHP/$NaBrO_3$ mixture as an additive substance. To adjust pH 3, we added 0.1 mL of 100 mM $HClO_4$ to the solution. The samples were placed into a 15-mL conical tube. The number of conical tubes was prepared according to the frequency of sampling during the reaction. The conical tubes were immersed in the pre-cooled ethanol bath. The samples were immersed within 3 min after preparation. The starting time of the reaction was designated as t = 0 when the conical tubes were immersed in the bath. The samples were kept in the bath during the reaction duration, and withdrawn at intervals after a certain reaction time, and thawed in a lukewarm water bath (30-40℃) to measure the products in liquid form. Each experiment was repeated twice to confirm its reproducibility.

To prepare standard hypobromite solution ($OBr^-$), 30 mM equivalent NaBr salt was dissolved in 20 mL of 28.7 mM NaOCl solution. This solution was stored at 4℃ in a refrigerator for one day. For each reaction, we prepared a blank and 0.5, 1, and 2 mM concentrations of standard solutions and adjusted the pH of all the standard solutions to 10.50. We determined the concentrations of $OCl^-$ and $OBr^-$ by using UV-vis spectroscopy

(Shimadzu, UV-2600) at the λmax of 292 and 329 nm with a molar absorptivity of 362 and 332 $M^{-1}$ $cm^{-1}$, respectively (Lei et al., 2004).

### 2.3. Chemical analysis

The concentration of DPHP in the sample was measured by UHPLC (Thermo Fisher Scientific, Vanquish) combined with a quadrupole-orbitrap mass spectrometer (Thermo Fisher Scientific, Q Exactive Focus). A Hypersil GOLD™ aQ column was used to confirm DPHP at specified retention time. The eluents were: formic acid solution (0.1% v/v; A) and acetonitrile/formic acid solution (0.1% v/v; B) at 5% B for 0-2 min, 5-100% B for 2-14 min, 100% B for 14-17 min, and 100-5% B for 17-21 min at a flow rate of 0.3 mL/min. The DPHP was ionized via a positive electrospray ionization (ESI) mode at a spray voltage of +3.80 kV, a capillary temperature of 320°C, a sheath gas flow rate of 40 a.u., an auxiliary gas flow rate of 10 a.u., an auxiliary gas heater temperature of 300°C, an S lens RF level of 50.0, a maximum injection time of 200 ms, and an automatic gain control (AGC) target of $1\times10^6$.

The halogen ion species concentrations were monitored by an ion chromatograph (Dionex ICS-1100) equipped with a suppressor (Dionex AERS 500), column (Dionex IonPac AS23), and conductivity detector. A mixture of sodium carbonate and bicarbonate solutions (0.477 and 0.067 g in 1 L, respectively) was used as the mobile phase at a flow rate of 1.00 mL/min, with a suppressor current of 32 mA.

The confocal Raman microscope (Renishaw, InVia Qontor) was used to identify the species in the frozen solution. Liquid sample (25 μL) on a silica sample holder (8 mm × 8 mm × 2 mm) was frozen by mounting on a temperature-controlled microscope stage (Linkam Scientific, THMS600). A monochromatic laser (λ = 532 nm DPSS) was used for Raman-Stoke scattering.

UV-vis spectroscopy (Shimadzu, UV-2600) was used to monitor the presence of $BrO^-$ in the solution. The absorbance of $BrO^-$ was determined at 329 nm using a 1-cm pathlength UV cuvette, and the concentration was calculated using the absorption coefficient of 332 $M^{-1}$ $cm^{-1}$ of $BrO^-$.

Electron paramagnetic resonance spectroscopy measurements were conducted by using EMXnano (Bruker). The experimental conditions were as follows: Microwave Frequency = 9.64 GHz, Microwave Power = 1 mW, Modulation Frequency = 100 kHz, Modulation Amplitude = 1 G, and Sweep Time = 240 s with continuous-wave-EPR (CW-EPR) mode. The temperature in the resonance chamber was controlled at 250 K using liquid nitrogen injection.

## 3. Result and Discussion

### 3.1. DPHP degradation by $BrO_3^-$ with the additive $Br^-$ in water and ice

The degradation of DPHP by $BrO_3^-$ at various concentrations of the additive $Br^-$ was demonstrated in Fig. 1. Under the experimental conditions of [$Br^-$] = 100 μM, [$BrO_3^-$] = 50 μM, [DPHP] = 10 μM, and pHi = 3 in aqueous solution (approximately 20℃), we found no degradation of DPHP (black line in Fig. 1a). However, DPHP degradation was significant when the solution was frozen at -20℃ (red lines in Fig. 1a). The initial $Br^-$ concentration (as an additive) affected the DPHP degradation in the frozen solution: approximately 2, 5, 7, 9, and 9.5 μM of DPHP were decreased in the presence of 0, 5, 10, 50, and 100 μM of $Br^-$, respectively, in a 50 μM $BrO_3^-$ solution during the 6 h reaction time (over 50 μM of $Br^-$ concentration sufficiently degraded 10 μM of DPHP within 60 min). We also found that $BrO_3^-$ is essential to degrade DPHP in the frozen system, as DPHP did not degrade in the absence of $BrO_3^-$ while significant DPHP was degraded when the $BrO_3^-$ dosage was more than 10 μM (note that 10 μM of $Br^-$ coexists in the solution, Fig. 1b). Therefore, we infer that $BrO_3^-$ in solution is reduced by DPHP, and the addition of $Br^-$ enhances the freezing-induced reaction. Concurrently, the $BrO_3^-$ reduction also gradually increased as $Br^-$ concentration increased, as shown in Fig. 1c. In the absence of $Br^-$, only 5 μM of $BrO_3^-$ was reduced by 10 μM of DPHP in the frozen solution (accompanied by only 2 μM of DPHP degradation, see Fig. 1a). Whereas, approximately 50% of initial $BrO_3^-$ was reduced at the 100 μM of $Br^-$ addition (accompanied by the complete elimination of DPHP). This $BrO_3^-$ reduction by 100 μM $Br^-$ (with 10 μM DPHP) did not progress during 6 h of reaction time when the solution was not frozen (black line in Fig. 1c). However, the $Br^-$-mediated $BrO_3^-$ reduction in the frozen solution was enhanced by the presence of DPHP, and during 6 h of reaction, ca. 20, 25, and 35 μM of $BrO_3^-$ were reduced by 0, 10, and 20 μM of DPHP addition, respectively (Fig. 1d). Importantly, the reduced pollutants were not restored, even after melting for 1 day. Hence, the DPHP and $BrO_3^-$ can be simultaneously abated in $Br^-$-containing solutions via freezing-induced acceleration of chemical reactions.

### 3.2. Effects of various temperatures, solution pH, and additive halide type on freezing induced DPHP degradation by $BrO_3^-$

The influence of freezing temperature on the degradation kinetics of DPHP and $BrO_3^-$ is shown in Fig. 2a and b, respectively. Neither DPHP nor $BrO_3^-$ were degraded at room temperature (black line). Notably, the degradation commenced when the solution started to freeze; the DPHP and $BrO_3^-$ concentrations were unchanged when the solution remained in the liquid phase irrespective of the freezing temperature (i.e., before freezing). Note that the solution at -5, -10, and -20℃ froze after ca. 90, 30, and 10 min, respectively (the freezing

process commences at a distinct time depending on the operating temperature). From this finding, it is evident that the chemical reaction was promoted by freezing the solution. Once frozen, the freezing-induced chemical reaction rapidly progressed and degraded DPHP within 1 hour. We emphasize that the 10 μM DPHP was completely eliminated regardless of the freezing temperature. Additionally, the $BrO_3^-$ concentration was reduced irrespective of the temperature. Only the degradation kinetics are dependent on the freezing temperature. Freezing temperature is related to the solution freezing rate, therefore, the reaction rate may be influenced by the freezing temperature (Kim et al., 2023). It is important to underscore that the amount of $BrO_3^-$ reduction is contingent upon the $Br^-$ and DPHP concentrations, as shown in Fig. 1c and 1d. Therefore, the terminal point of $BrO_3^-$ reduction in Fig. 2b (i.e., 25 μM $BrO_3^-$) is likely due to the initial $Br^-$ and DPHP concentrations (i.e., 100 μM $Br^-$ and 10 μM DPHP).

Fig. 3 demonstrates the influence of initial pH on the system for $BrO_3^-$ reduction and DPHP degradation. Under the experimental conditions of [$Br^-$] = 100 μM, [$BrO_3^-$] = 50 μM, [DPHP] = 10 μM, and 2 h of freezing time at −20 ℃, DPHP was degraded at ca. 9.5, 8, 2.5, and less than 1 μM at initial pH 3, 4, 5, and 8, respectively. Additionally, $BrO_3^-$ was concomitantly reduced to ca. 25, 15, 5, and less than 2 μM at pH 3, 4, 5, and 8, respectively. This result demonstrates the importance of $H^+$ ($H_3O^+$ in water) in the reaction. According to a previous study, the following chemical equation can be postulated for $Br^-$-mediated $BrO_3^-$ reduction (Min and Choi, 2017).

$$BrO_3^- + 6H^+ + 6e^- \rightarrow Br^- + 3H_2O;\ E_0 = 1.41\ V_{NHE} \quad (3)$$

As shown in Equation 3, $BrO_3^-$ reduction consumes six hydrogen ions and electrons, which indicates that a highly acidic condition favors the reaction. Furthermore, according to previous research, the acid-catalyzed reaction can be promoted by freezing, as the pH of the solution becomes more acidic during the freezing process (Ahn et al., 2021; Ahn et al., 2022; Ahn et al., 2023). Notably, the $BrO_3^-$ reduction did not progress at the basic pH level even in frozen conditions (Fig. 3).

The chemical reaction in ice can be influenced by dissolved oxygen (Ahn et al., 2023). To examine this, we monitored $BrO_3^-$ and DPHP degradation under both anoxic and oxic conditions and compared the results. The anoxic condition was created by bubbling Ar gas into the solution for 1 h. Only negligible difference was observed between the anoxic and oxic conditions, indicating that dissolved oxygen does not significantly affect $BrO_3^-$ and DPHP degradation.

The degradation of DPHP by $BrO_3^-$ is influenced by the additive halide type, as seen in Fig. 4. Not only $Br^-$ but also $Cl^-$ and $I^-$ explicitly enhanced DPHP and $BrO_3^-$ reduction

during the freezing process. Overall, the reduction efficiency increased with an increase in the concentration of halide species. However, the DPHP degradation efficiency in the presence of 200 μM $I^-$ was lower than that in the presence of 100 μM $I^-$; approximately 8 μM DPHP was removed at 100 μM $I^-$, and 6 μM DPHP was removed at 200 μM $I^-$ (yellow bar in Fig. 4a). We infer that the reduced DPHP degradation efficiency at high doses of $I^-$ was likely due to the excess amount of $I^-$ competing with DPHP degradation in the consumption of reactive species. It is important to note that DPHP degradation was negligible in the absence of $BrO_3^-$, regardless of the additive type and frozen condition (Fig. 4c). Therefore, we can conclude that the halide substances facilitate $BrO_3^-$ reduction to generate a responsible reactive species for DPHP degradation. According to previous research, the following equation depicts the reaction (Schmitz, 1999; Lente et al., 2009).

$$BrO_3^- + 6H^+ + 5X^- \rightarrow XBr + 2X_2 + 3H_2O;\ X = Cl, Br, I \quad (4)$$

$$X_2 + H_2O \leftrightarrow HOX + H^+ + X^- \quad (5)$$

$$X_2 + X^- \leftrightarrow X_3^- \quad (6)$$

Here, $BrO_3^-$ oxidizes $X^-$ and generates reactive halogen species, such as hypohalous acid and trihalide. Hence, we expect that $BrO_3^-$ reduction by halide could result in the evolution of HOCl, HOBr, and HOI as reactive species responsible for DPHP degradation. Intriguingly, we found that the ability to generate reactive halogen species by halide is a unique characteristic of $BrO_3^-$ because there was no DPHP degradation in the presence of $ClO_3^-$ and $IO_3^-$; as shown in Fig. 4d, $Cl^-/ClO_3^-$ and $I^-/IO_3^-$ system did not degrade DPHP in ice at all. We observed that the oxidation potential of $BrO_3^-$ is not likely to be influenced by the varying oxidative fate of oxyanions in ice: the standard oxidation potentials ($E_0$) of $ClO_3^-$, $BrO_3^-$, and $IO_3^-$ in the reaction $2XO_3^- + 12H^+ + 10e^- \rightarrow X_2 + 6H_2O$ (X = Cl, Br, I) are 1.45, 1.41, and 1.195 $V_{NHE}$, respectively (Min and Choi, 2017; Choi et al., 2018). Conversely, DPHP degradation depends on the chemical nature of each system. For instance, the halide species concentration of $Cl^-/ClO_3^-$–mediated system showed no chemical changes after reaction (Fig. 4d insert, green bars). This suggests that $Cl^-$–mediated $ClO_3^-$ reduction does not occur during the freezing procedure, so the DPHP was not degraded. The $IO_3^-$ can be reduced by $I^-$ in freezing procedures but it is likely that the potency of responsible reactive halogen species, such as $I_3^-$, is not sufficient to degrade DPHP.

### 3.3. The chemical reaction mechanism for the freezing induced DPHP degradation by $BrO_3^-$

Humic substances function as a reductant in frozen solutions and reduce $BrO_3^-$, which produces $Br^-$ and HOBr as reported in a previous study (Min and Choi, 2017). Besides,

$BrO_3^-$ reduction in the frozen solution can oxidize dissolved organic carbon due to the inherent oxidative property of HOBr (Hao et al., 2020). Hence, we investigated the HOBr generation in the frozen $Br^-/BrO_3^-$ system and the DPHP degradation by HOBr (Fig. 5a and 5b). As seen in Fig. 5a, the specific absorption peak at 329 nm appeared when the [$Br^-$] = 100 μM and [$BrO_3^-$] = 50 μM mixture was frozen at －20 ℃ and pHi = 3.0 (note that the sample pH was adjusted to 10.50 by adding NaOH before absorption measurement to deprotonate HOBr). The estimated $BrO^-$ (deprotonated HOBr) concentration at the 6 h reaction time was approximately 40 μM ($\varepsilon$ = 332 $M^{-1}$ $cm^{-1}$). As shown in the insert of Fig. 5a, the value determined by UV-Vis measurement matched well with the result using 1,3,5-trimethoxybenzene (TMB) as a HOBr derivatizing reagent. The bromination of 1,3,5-trimethoxybenzene leads to the formation of 1-bromo-2,4,6-trimethoxybenzene (Br-TMB), and this concentration was converted to HOBr. The concentration of HOBr determined by the TMB method was 36 μM. Figure 5b shows DPHP degradation by HOBr in the aqueous and frozen phases. Approximately 5 μM DPHP was degraded in 6 h by 20 μM HOBr (blue circles in Fig. 5b) in the aqueous phase. Whereas DPHP degradation by HOBr was accomplished in 1 h of reaction time when the solution was frozen (red circles in Fig. 5b). Hence, we concluded that the generation of HOBr in the $Br^-/BrO_3^-$ reaction is responsible for DPHP degradation.

Further, we used the Raman microscope to monitor the in-situ generation of HOBr in ice. Fig. 6 shows a Raman microscope image of the frozen $Br^-/BrO_3^-$/DPHP system. The red color indicates the high intensity of the signal at 805 $cm^{-1}$ of the Raman shift. The red color was clearly positioned at the center of the ice grain boundary. Owing to the low concentration of DPHP, the Raman signal for DPHP was not seen. The signals for $BrO_3^-$ and HOBr were detected at 805 and 932 $cm^{-1}$, respectively. The Raman microscope measurement was performed at the initial concentrations of 10 mM $Br^-$ and 2 mM $BrO_3^-$ to obtain a distinct Raman signal. However, the initial concentration of DPHP did not exceed 100 μM because of its limited water solubility. Note that the dissolved substances alter the phase transition characteristic of pure water, so the unsolidified metastable brine layer exists in the ice grain boundary region even below the eutectic point, which means that the liquid-like region can exist in the ice when the solution is frozen at a moderate temperature (Cho et al., 2002). During the freezing process, the solutes in the water accumulate in the ice grain boundary region because they are expelled from the ice crystals. Hence, the concentrations of solutes, including hydronium ion ($H_3O^+$), can be increased in ice. The freeze concentration effect is responsible for the accelerated generation of HOBr. Consequently, the DPHP in ice can be oxidized by HOBr that is produced during the freezing process.

According to previous research, hydroxyl radical (OH) could form in the frozen $BrO_3^-$

system (Sun et al., 2023b). We tested the EPR on the frozen $Br^-/BrO_3^-$/DPHP system using EPR with BMPO as an OH trapping agent but found no EPR signal. Additionally, adding a radical quenching reagent, methanol (1 mM), had no effect on the reaction. Therefore, OH generation in the frozen $Br^-/BrO_3^-$/DPHP system was negligible. However, UV illumination can potentially influence the reactive species in this system, as the current experiments were conducted in the dark.

### 3.4. The freezing induced DPHP degradation by $BrO_3^-$ in the natural arctic water matrix

The DPHP and $BrO_3^-$ reduction in the freezing process was monitored using the water matrix of Bayelva located at the Ny-Ålesund, Spitsbergen, Svalbard, Norway. The water was collected on June 2, 2023. The water that was collected was promptly filtered using a 0.7 μm pore size glass microfiber filter (Whatman GF/F) and stored in a polypropylene bottle at 4℃ without headspace. Before reaction, the water had the following characteristics: TOC = 6.002 ± 0.141 ppm, $Cl^-$ = 1065.392 ± 2.795 μM, $SO_4^{2-}$ = 114.259 ± 2.740 μM, $NO_3^-$ = 6.798 ± 0.379 μM, and pH 7.55. Because of the high $Cl^-$ contents of the water matrix, the additive $Br^-$ was not injected into the solution (refer to Fig. 4a and 4b). To demonstrate the freezing system, 10 μM DPHP and 50 μM $BrO_3^-$ were added to the Bayelva water matrix, and its pH was adjusted to 3.5 using $HClO_4$ (1 mM dose). We also compared freezing conditions using an ethanol bath and air-cooling, as we believe air-cooling better simulates natural conditions, mimicking the purification process that occurs in ice. We performed air-cooling using the custom-made Low Temperature Chamber which operated at -20℃ with marginal temperature variation from the programmed value. This allowed us to evaluate the freezing process under air-cooling in comparison with ethanol bath freezing.

As shown in Fig. 7, both DPHP degradation and $BrO_3^-$ reduction occurred in the frozen Bayelva water matrix, regardless of the freezing method. Nearly all the DPHP was eliminated, and approximately 40 μM $BrO_3^-$ (80%) was reduced after 6 h of freezing. We infer that dissolved organic compounds and other impurities in the natural water matrix slightly slowed the $BrO_3^-$ reduction compared to the purified water condition. In the air-cooling system, freezing began later than in the ethanol bath system, with the reactants remaining at their original concentrations for the first 60 min. Overall, the freezing method did not significantly affect DPHP or $BrO_3^-$ degradation, indicating that the system can operate effectively under air-cooling conditions.

### 3.5. Implications of the novel simultaneous abatement of $BrO_3^-$ and DPHP using the freezing process

We introduced a novel water treatment strategy that uses carcinogenic $BrO_3^-$ and DPHP as reactants to simultaneously mitigate both hazardous compounds. Previous research on water treatment has primarily focused on developing systems to reduce either $BrO_3^-$ or organophosphate pollutants, typically requiring the addition of external reactive substances like chemical activators or oxidants. However, these approaches can be typically inefficient to simultaneous degradation process, as the pollutants compete for the external source. In contrast, our method allows the pollutants themselves to act as reactive chemical reagents, reducing each other in the process. Although this reaction is insignificant at room temperature, it becomes effective when the solution is frozen. A key advantage of this ice-chemistry system is that freezing occurs naturally in cold regions, eliminating the need for external energy or resources to form ice. This makes it more sustainable compared to other energy-intensive methods, such as heat, ultrasound, or ultraviolet light, which require chemical activation. Additionally, the system's performance improves in the presence of $Cl^-$ and $I^-$ ions (see, Fig. 4). Typically, background species like $Cl^-$ are considered detrimental in water treatment systems, as they consume reactive species and reduce oxidation efficiency. However, in our system, these halogen ions enhance the reaction, providing an additional advantage. Overall, this dual-function freezing system offers a more economical and eco-friendly approach to water treatment.

KOPRI 극지연구소

## 4. Conclusion

In this research, we monitored DPHP and $BrO_3^-$ concentrations in the frozen DPHP/$Br^-$/$BrO_3^-$ solution. The DPHP degradation was concomitant with $BrO_3^-$ reduction in the freezing process. The DPHP degradation depends on the initial $Br^-$ and $BrO_3^-$ concentrations, reaction times, and initial pH. The reaction continued when $Br^-$ was replaced with $Cl^-$ and $I^-$ to activate $BrO_3^-$. The $Cl^-$/$ClO_3^-$ and $I^-$/$IO_3^-$ systems did not effectively degrade DPHP, but $BrO_3^-$ showed distinctive behavior in the freezing process. The generation of HOBr was found to be a major factor in DPHP degradation and $BrO_3^-$ reduction. Freezing facilitated the generation of HOBr from $BrO_3^-$ reduction through $Br^-$ oxidation, and the generated HOBr subsequently oxidized the DPHP. The Bayelva water, a natural water matrix in the polar region, was used to examine a simultaneous DPHP and $BrO_3^-$ removal scheme. The removal efficiency was comparable to that in the deionized water test.

There are numerous efforts to develop effective water treatment technology to diminish the emerging pollutant organophosphate flame retardant (OPFR). Based on this study, we

suggest an alternative degradation system for DPHP, which serves as a representative OPFR, using the freezing process that concomitantly reduces $BrO_3^-$. Our findings suggest that the process will be advantageous when employed in high latitude and polar regions.

KOPRI
극지연구소

# REFERENCES


Ahn, Y.-Y., J. Kim and K. Kim, 2021. Activation of peroxymonosulfate by bicarbonate and acceleration of the reaction by freezing. Science of The Total Environment 785, 147369.

Ahn, Y.-Y., J. Kim and K. Kim, 2022. Frozen Hydrogen Peroxide and Nitrite Solution: The Acceleration of Benzoic Acid Oxidation via the Decreased pH in Ice. Environmental Science & Technology 56, 2323-2333.

Ahn, Y.-Y., J. Kim and K. Kim, 2023. Catalytic behavior of nitrous acid for acetaminophen transformation during the freezing process. Journal of Hazardous Materials 456, 131652.

Balakrishna, K., Y. Praveenkumarreddy, D. S. Nishitha, C. M. Gopal, J. K. Shenoy, K. Bhat, N. Khare, K. Dhangar and M. Kumar, 2023. Occurrences of UV filters, endocrine disruptive chemicals, alkyl phenolic compounds, fragrances, and hormones in the wastewater and coastal waters of the Antarctica. Environmental Research 222, 115327.

Bray, W. C. and H. A. Liebhafsky, 1935. The Kinetic Salt Effect in the Fourth Order Reaction $BrO_3^-$ + $Br_-$ + $2H^+$ →. Ionization Quotients for $HSO_4^-$ at 25°. Journal of the American Chemical Society 57, 51-56.

Cheng, S., X. Zhang, X. Yang, C. Shang, W. Song, J. Fang and Y. Pan, 2018. The Multiple Role of Bromide Ion in PPCPs Degradation under UV/Chlorine Treatment. Environmental Science & Technology 52, 1806-1816.

Cho, H., P. B. Shepson, L. A. Barrie, J. P. Cowin and R. Zaveri, 2002. NMR Investigation of the Quasi-Brine Layer in Ice/Brine Mixtures. The Journal of Physical Chemistry B 106, 11226-11232.

Choi, Y., K. Kim, D. Kim, H.-b. Moon and J. Jeon, 2020. Ny-ñlesund-oriented organic pollutants in sewage effluent and receiving seawater in the Arctic region of Kongsfjorden. Environmental Pollution 258, 113792.

Choi, Y., H.-I. Yoon, C. Lee, L. u. Vetráková, D. Heger, K. Kim and J. Kim, 2018. Activation of Periodate by Freezing for the Degradation of Aqueous Organic Pollutants. Environ. Sci. Technol. 52, 5378-5385.

Côrtes, C. E. S. and R. B. Faria, 2004. Kinetics and Mechanism of Bromate-Bromide Reaction Catalyzed by Acetate. Inorganic Chemistry 43, 1395-1402.

Hao, Z., F. Shi, D. Cao, J. Liu and G. Jiang, 2020. Freezing-Induced Bromate Reduction by Dissolved Organic Matter and the Formation of Organobromine Compounds. Environmental Science & Technology 54, 1668-1676.

Huang, X., X. Zhou, J. Zhou, Z. Huang, S. Liu, G. Qian and N. Gao, 2017. Bromate inhibition by reduced graphene oxide in thermal/PMS process. Water Research 122, 701-707.

Kim, K., B. Kim, Y.-Y. Ahn, K. D. Tran, H. T. My Truong and J. Kim, 2023. Production of Molecular Iodine via a Redox Reaction between Iodate and Organic Compounds in Ice. The Journal of Physical Chemistry A 127, 2830-2838.

Lei, H., B. J. Mariñas and R. A. Minear, 2004. Bromamine Decomposition Kinetics in Aqueous Solutions. Environmental Science & Technology 38, 2111-2119.

Lente, G., J. Kalmár, Z. Baranyai, A. Kun, I. Kék, D. Bajusz, M. Takács, L. Veres and I. Fábián, 2009. One- Versus Two-Electron Oxidation with Peroxomonosulfate Ion: Reactions with Iron(II), Vanadium(IV), Halide Ions, and Photoreaction with Cerium(III). Inorganic Chemistry 48, 1763-1773.

Lim, J.-E., H. Kang, J. Lee, S. Kim, M. Bae, H.-B. Moon, K. Choi, C. Kim and K.-T. Kim, 2023. Urinary concentrations of organophosphate esters and associated health outcomes in Korean firefighters. Chemosphere 339, 139641.

Min, D. W. and W. Choi, 2017. Accelerated Reduction of Bromate in Frozen Solution. Environ. Sci. Technol. 51, 8368-8375.

Morrison, C. M., S. Hogard, R. Pearce, A. Mohan, A. N. Pisarenko, E. R. V. Dickenson, U. von Gunten and E. C. Wert, 2023. Critical Review on Bromate Formation during Ozonation and Control Options for Its Minimization. Environmental Science & Technology 57, 18393-18409.

O'Concubhair, R. and J. R. Sodeau, 2013. The Effect of Freezing on Reactions with Environmental Impact. Acc. Chem. Res. 46, 2716-2724.

Schmitz, G., 1999. Kinetics and mechanism of the iodate-iodide reaction and other related reactions. Physical Chemistry Chemical Physics 1, 1909-1914.

Schmitz, G., 2007. Kinetics of the bromate-bromide reaction at high bromide concentrations. International Journal of Chemical Kinetics 39, 17-21.

Sun, H., Z. Guo, L. Zhang, X. Hua and D. Dong, 2024. Degradation of carbamazepine in ice with bromate and nitrite: Role of reactive nitrogen species. Science of The Total Environment 923, 171376.

Sun, H., L. Zhang, D. Dong, W. Zhang and Z. Guo, 2023a. Freezing degradation of the anticonvulsant oxcarbazepine by bromate in water ice under sunlight irradiation. Science of The Total Environment 894, 165014.

Sun, H., L. Zhang, L. Wang, D. Dong, Y. Li and Z. Guo, 2023b. Enhanced freezing-induced carbamazepine degradation by bromate under solar irradiation via the formation of hypobromous acid and hydroxyl radical. Journal of Hazardous Materials 457, 131793.

Takenaka, N. and H. Bandow, 2007. Chemical Kinetics of Reactions in the Unfrozen Solution of Ice. The Journal of Physical Chemistry A 111, 8780-8786.

Wang, X., C. Wang, T. Zhu, P. Gong, J. Fu and Z. Cong, 2019. Persistent organic pollutants in the polar regions and the Tibetan Plateau: A review of current

KOPRI 극지연구소

knowledge and future prospects. Environmental Pollution 248, 191-208.

Wild, S., D. McLagan, M. Schlabach, R. Bossi, D. Hawker, R. Cropp, C. K. King, J. S. Stark, J. Mondon and S. B. Nash, 2015. An Antarctic Research Station as a Source of Brominated and Perfluorinated Persistent Organic Pollutants to the Local Environment. Environmental Science & Technology 49, 103-112.

Xie, Z., P. Zhang, Z. Wu, S. Zhang, L. Wei, L. Mi, A. Kuester, J. Gandrass, R. Ebinghaus, R. Yang, Z. Wang and W. Mi, 2022. Legacy and emerging organic contaminants in the polar regions. Science of The Total Environment 835, 155376.

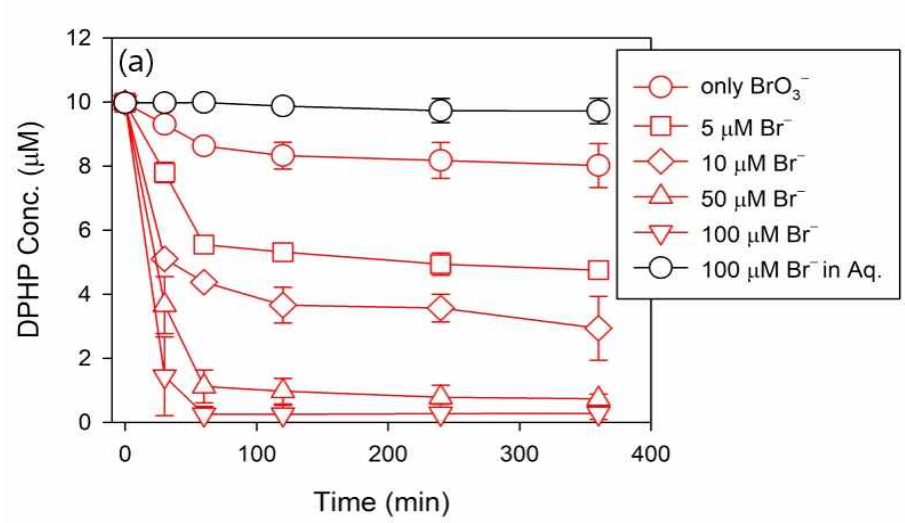
Yao, C., H. Yang and Y. Li, 2021. A review on organophosphate flame retardants in the environment: Occurrence, accumulation, metabolism and toxicity. Science of The Total Environment 795, 148837.

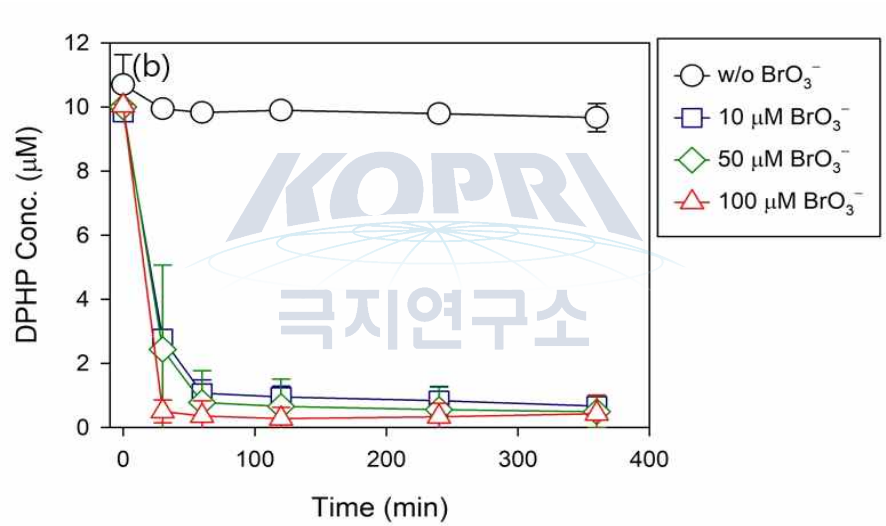
Yuan, X., S. Lacorte, J. Cristale, R. F. Dantas, C. Sans, S. Esplugas and Z. Qiang, 2015. Removal of organophosphate esters from municipal secondary effluent by ozone and UV/H2O2 treatments. Separation and Purification Technology 156, 1028-1034.

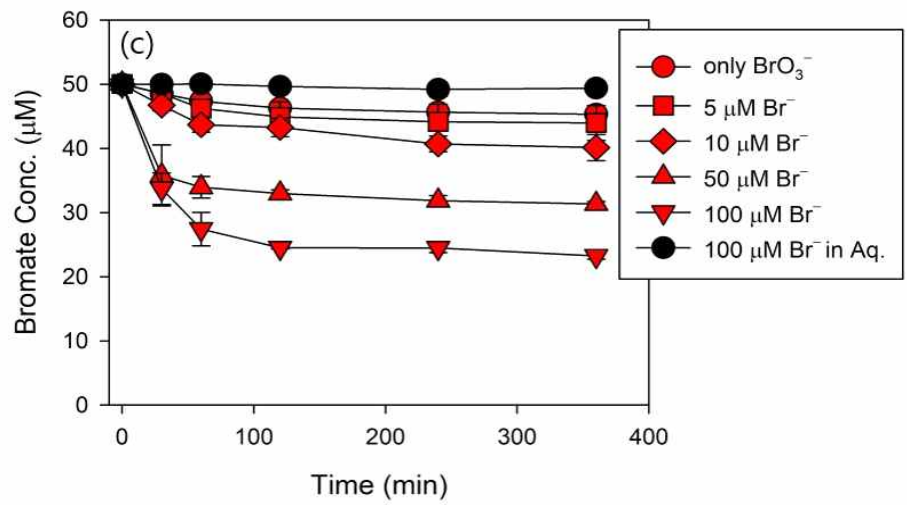
Zhang, Y., B. Zhou, H. Chen and R. Yuan, 2023. Heterogeneous photocatalytic oxidation for the removal of organophosphorus pollutants from aqueous solutions: A review. Science of The Total Environment 856, 159048.

KOPRI
극지연구소

FIGURES




KOPRI 극지연구소

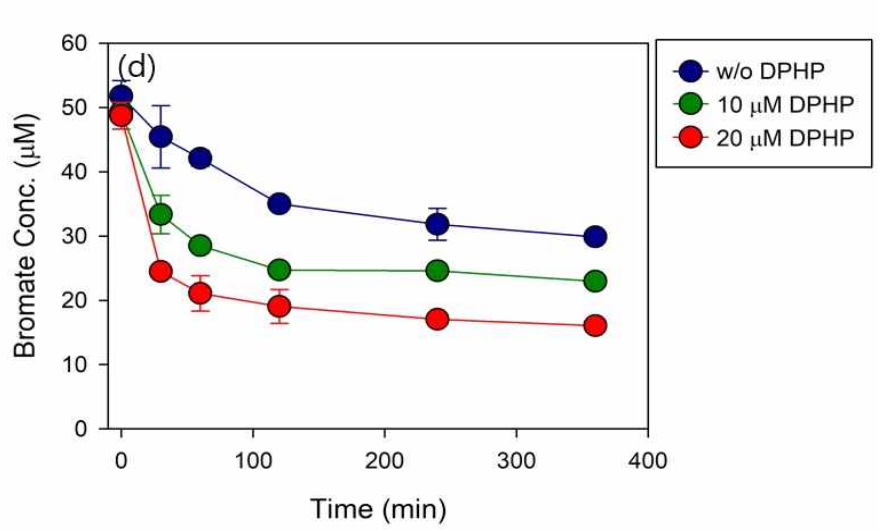



**Figure 1.** (a) DPHP degradation in bromide addition. Experimental condition: $[DPHP]_0$ = 10 μM; $[NaBrO_3]_0$ = 50 μM; pHi = 3 (adjusted by $HClO_4$); Temperature = -20 ℃ (Frozen), 20oC (Aqueous). (b) DPHP degradation in $BrO_3^-$ concentration. Experimental condition: $[NaBr]_0$ = 100 μM; [DPHP]0 = 10 μM; pHi = 3 (adjusted by $HClO_4$); Temperature = -20 ℃. (c) Bromate degradation in bromide concentration. Experimental condition: $[DPHP]_0$ = 10 μM; $[NaBrO_3]_0$ = 50 μM; pHi = 3 (adjusted by $HClO_4$); Temperature = -20 ℃ (Frozen), 20 ℃ (Aqueous). (d) Bromate degradation in DPHP concentration. Experimental condition: $[NaBr]_0$ = 100 μM; $[NaBrO_3]_0$ = 50 μM; pHi = 3 (adjusted by $HClO_4$); Temperature = -20 ℃.

KOPRI 극지연구소

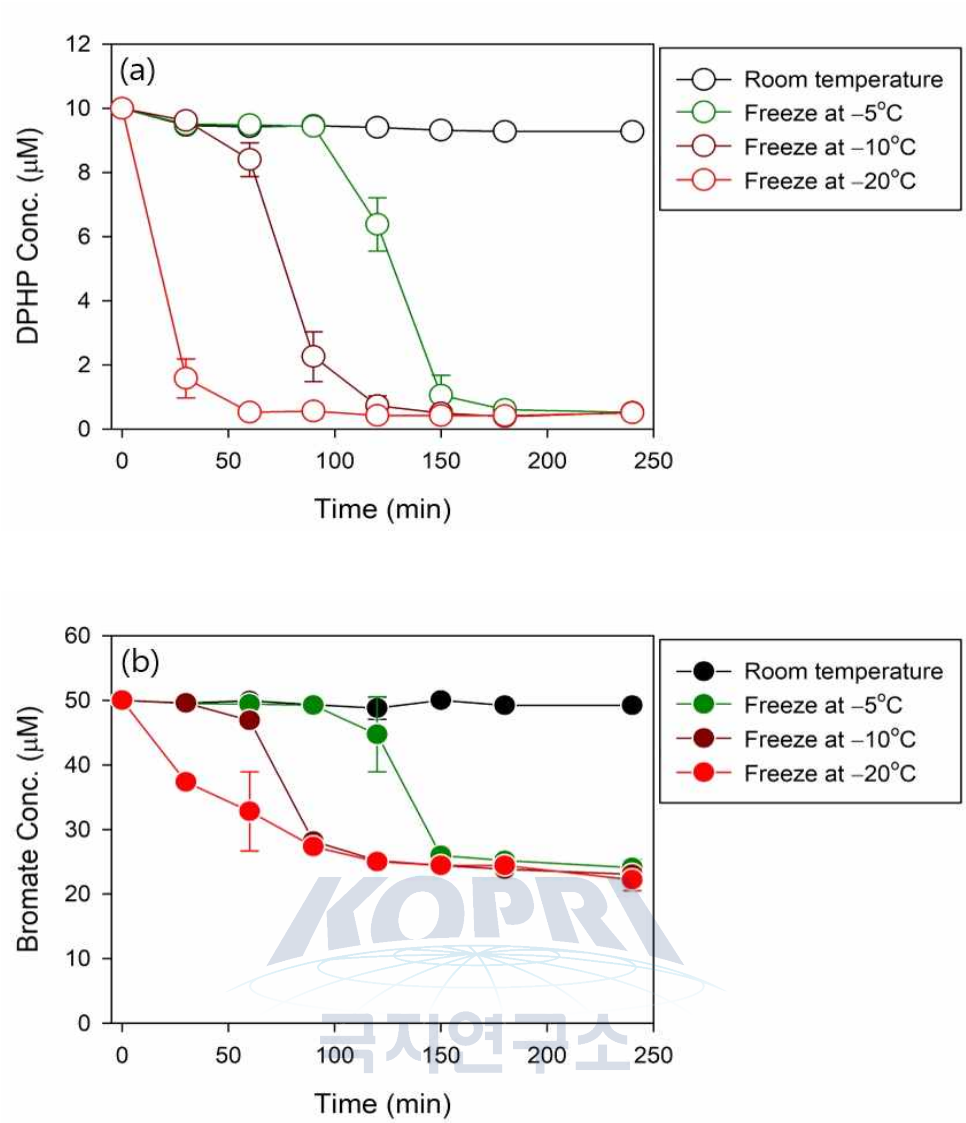



**Figure 2.** (a) DPHP degradation and (b) $BrO_3^-$ degradation in temperature. Experimental condition: $[DPHP]_0$ = 10 μM; $[NaBrO_3]_0$ = 50 μM; $[NaBr]_0$ = 100 μM; pHi = 3 (adjusted by $HClO_4$).

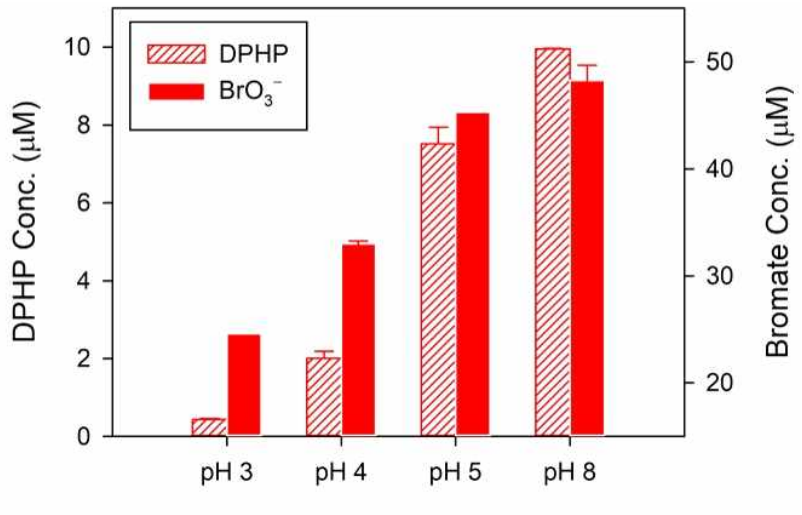
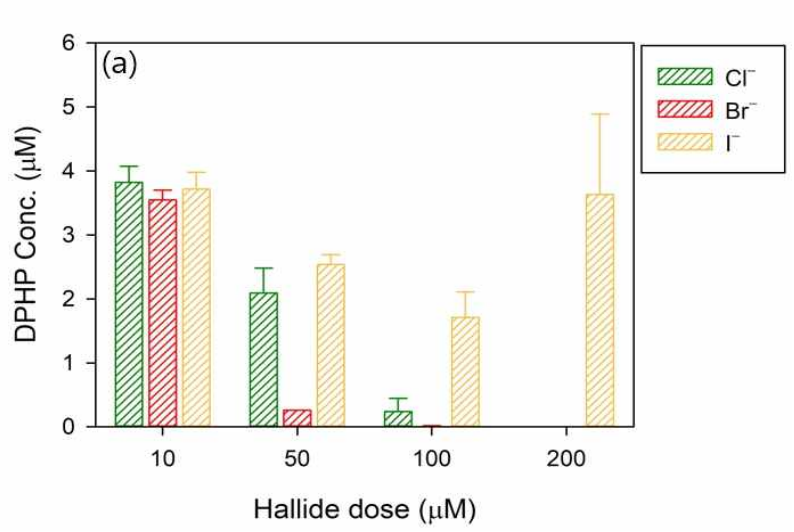
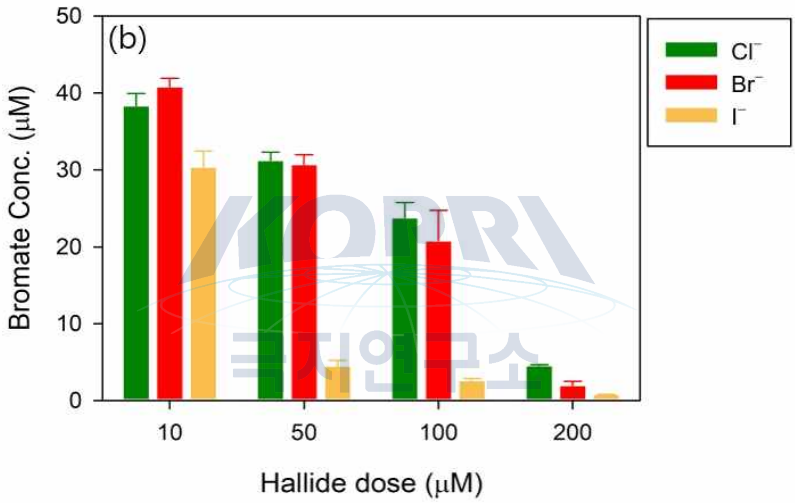
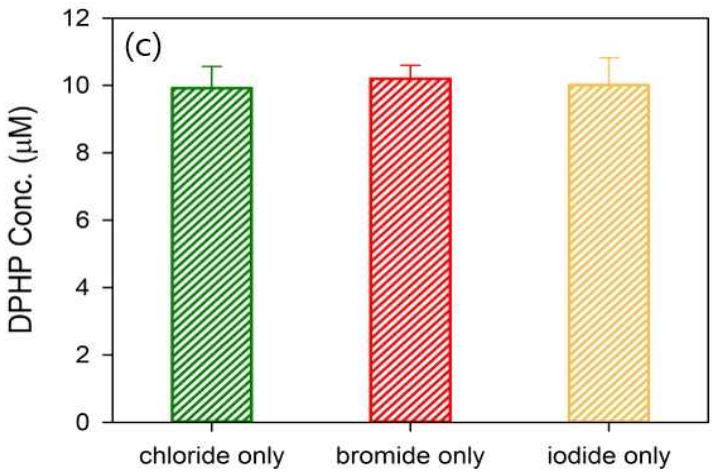



**Figure 3.** DPHP and $BrO_3^-$ degradation in pH of the solution. Experimental condition: $[DPHP]_0$ = 10 μM; $[NaBrO_3]_0$ = 50 μM; $[NaBr]_0$ = 100 μM; Reaction time = 2 h; Temperature = -20 ℃.

KOPRI
극지연구소


(a)
DPHP Conc. (μM)
Hallide dose (μM)
Cl⁻
Br⁻
I⁻
0
1
2
3
4
5
6
10
50
100
200


(b)
Bromate Conc. (μM)
Hallide dose (μM)
Cl⁻
Br⁻
I⁻
0
10
20
30
40
50
10
50
100
200


(c)
DPHP Conc. (μM)
0
2
4
6
8
10
12
chloride only
bromide only
iodide only

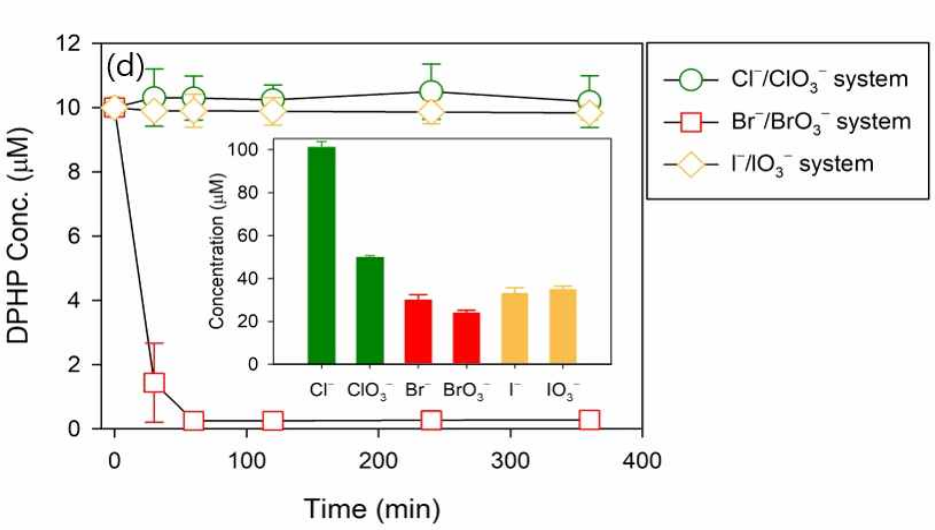



**Figure 4.** (a) DPHP and (b) $BrO_3^-$ degradation in the additive halide type. Experimental condition: $[DPHP]_0$ = 10 μM; $[NaBrO_3]_0$ = 50 μM; pHi = 3 ($HClO_4$); Reaction time = 6 h; Temperature = -20 ℃. (c) DPHP degradation without $BrO_3^-$ in the additive halide type. Experimental condition: $[DPHP]_0$ = 10 μM; [halide]0 = 100 μM; pHi = 3 ($HClO_4$); Reaction time = 6 h; Temperature = -20 ℃. (d) DPHP degradation in different halide/oxyhalide system. Insert: halide and oxyhalide concentration after completing the reaction. Experimental condition: $[DPHP]_0$ = 10 μM; $[halide]_0$ = 100 μM; $[oxyhalide]_0$ = 50 μM; pHi = 3 ($HClO_4$); Temperature = -20 ℃.

KOPRI 극지연구소

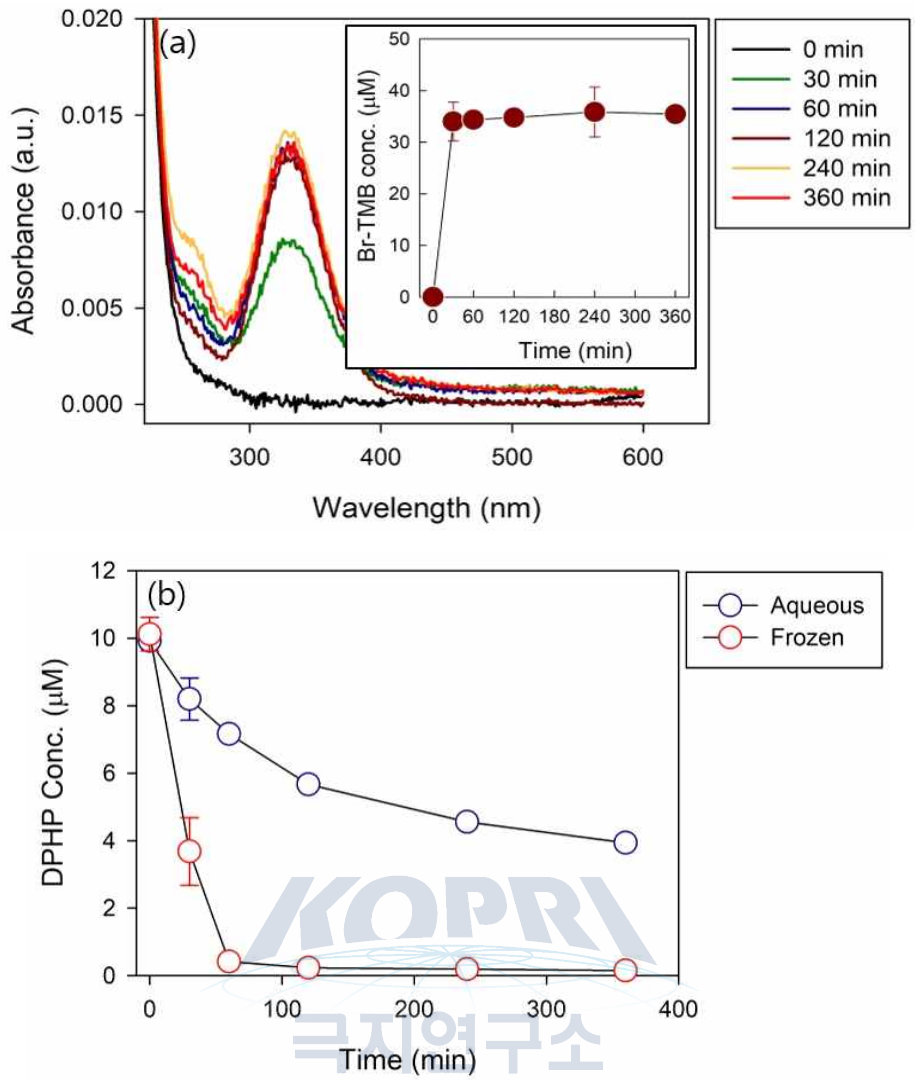



**Figure 5.** (a) UV-Vis spectra of $OBr^-$ in the solution. (b) The degradation of DPHP by HOBr. Experimental condition: $[DPHP]_0$ = 10 μM; $[BrO^-]_0$ = 20 μM; pHi = 3 (adjusted by $HClO_4$); Temperature = -20 ℃ (Frozen), 20 ℃ (Aqueous).

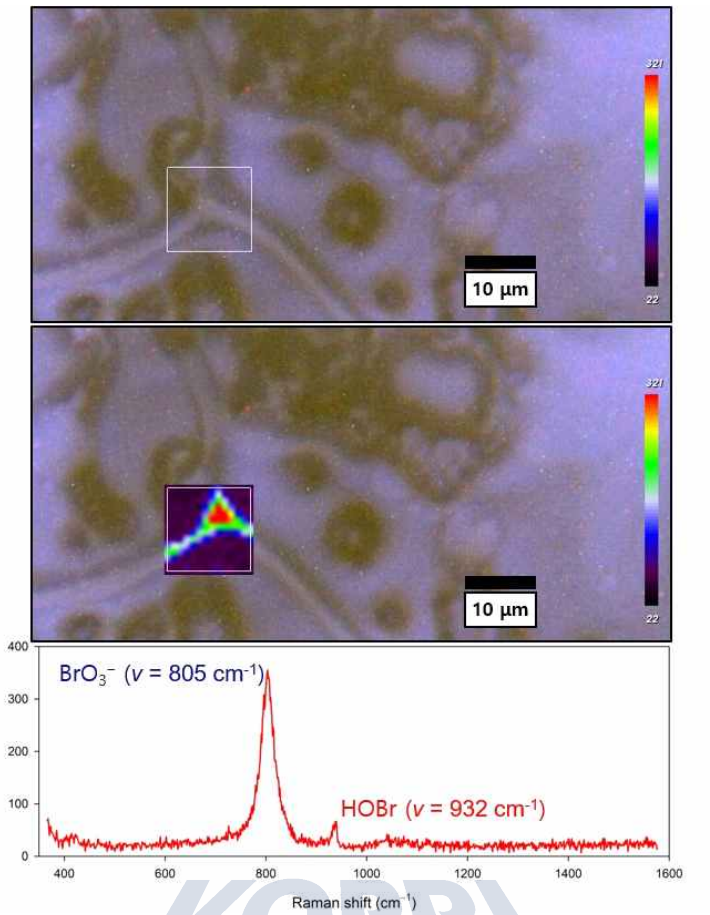



**Figure 6.** Raman microscope image of the frozen $Br^-/BrO_3^-$/DPHP system. Experimental condition: $[DPHP]_0$ = 100 µM; $[Br^-]_0$ = 10 mM; $[BrO3^-]_0$ = 2 mM; pHi = 3 (adjusted by $HClO_4$); Temperature = -20 ℃.

KOPRI 극지연구소

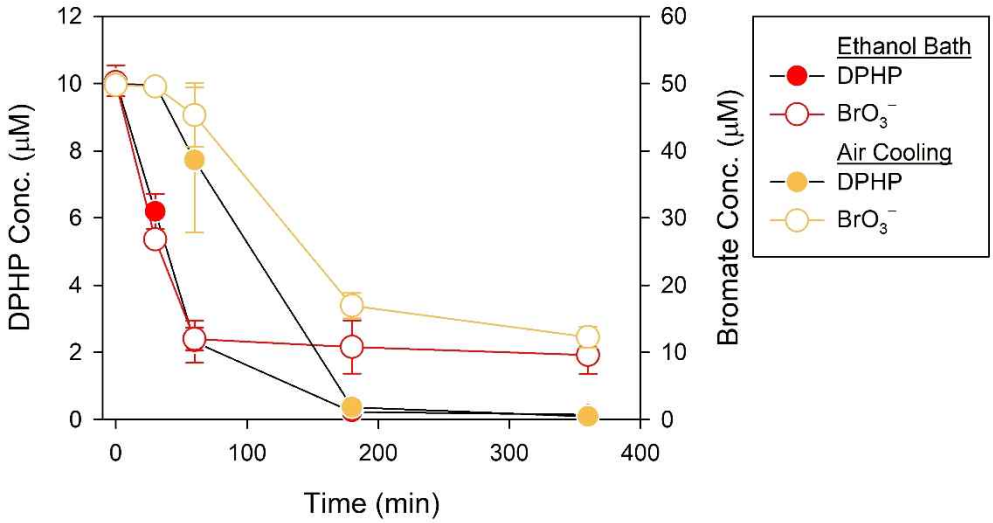



**Figure 7.** DPHP and $BrO_3^-$ reduction in the different freezing system (ethanol bath vs air-cooling). The water sample collected from Bayelva, Svalbard on June 2, 2023 (N 78° 55.725, E 11° 50.577). Experimental condition: $[DPHP]_0$ = 10 μM; $[BrO_3^-]_0$ = 50 μM; pHi = 3.5 (adjusted by $HClO_4$); Temperature = -20 ℃.

KOPRI
극지연구소

# 제 18 절. Cryoprotective Polyol-Induced Ice Microstructure Development and Enhanced Chromium(VI) Reduction in Polycrystalline Structures⑱

Bomi Kim[1,2], Kitae Kim[1,2,*]

[1]Korea Polar Research Institute (KOPRI), Incheon 21990, Republic of Korea
[2]Department of Polar Sciences, University of Science and Technology (UST), Incheon 21990, Republic of Korea

## Abstract

Cryoprotective polyols play a crucial role in inhibiting ice crystal growth, reducing the size of bulk ice crystals in polycrystalline structures, and increasing the volume of ice grain boundaries relative to the total solution volume. This study suggests these properties enable cryoprotective polyols to accelerate the reduction of hexavalent chromium (Cr(VI)) in ice despite the reducing agents being limited to aqueous environments. This reaction is mainly caused by the accumulation of cryoprotective polyols and Cr(VI) at the ice grain boundaries formed during freezing (i.e., the freeze concentration effect). Upon freezing a mixture of cryoprotective polyols and a 20 μM Cr(VI) solution, over 90% reduction in Cr(VI) concentration was achieved within 24 hr. Higher concentrations of cryoprotective polyols in Cr(VI) enhanced the reduction kinetics of Cr(VI) over the same reaction time, implying that the cryoprotective polyols function as reducing agents under freezing conditions. Confocal Raman spectroscopy confirmed cryoprotective polyols bind to ice crystal surfaces and concentrate Cr(VI) at the ice grain boundaries. Notably, the reductive capability of cryoprotective polyols towards Cr(VI) was observed under freezing conditions, using an electroplating wastewater sample contaminated with Cr(VI) as a model system, whereas negligible reduction was observed in the aqueous phase. Enhanced Cr(VI) reduction by cryoprotective polyols in frozen solutions presents a viable approach for treating contaminated wastewater and contributes to understanding the self-purification mechanism in natural environments where these polyols are present.

⑱ 본 연구는 본 과제(PE24120)로 수행되었으며, 결과는 *Cryst. Growth. Des.* 2024, 24, 21, 9030 - 9038에 출간되었다.

## 1. Introduction

Saccharides, naturally soluble carbohydrates, and several polyol molecules have been examined because they serve important roles as bioprotectants. These carbohydrates have been used as reducing agents because they naturally have an abundance of hydrogen and electron-donating properties. [1-4] Recent studies have demonstrated the reducing potential of polyol species towards transition metal ions in solution. [5, 6] Moreover, polyol species are being introduced as promising reducing agents that are inexpensive, eco-friendly, and compatible with biological systems. Polyol species produced during the metabolism of microorganisms in nature have been reported to have a significant impact on metal reduction in nature. [7] In addition to their properties as reducing agents, the cryobiological significance of polyols has been examined. [8-11] Cryoprotective polyols are polyol compounds such as ethylene glycol, [12, 13] glucose, [14, 15] and trehalose [16, 17] used to increase the osmotic pressure of the solvent around the cells and prevent cells from freezing damage in solution. Cryoprotective polyols impede the formation of ice nuclei and the growth of ice crystals on ice surfaces. [18, 19] Furthermore, cryoprotective polyols have both reducing and cryoprotective properties; therefore, the presence of cryoprotective polyols is expected to alter the reduction reaction between polyols and other solutes such as metal ions in ice, but no studies have yet reported this.

Chemical reactions that occur at temperatures below the freezing point (in frozen solutions) may differ from those occurring at temperatures above the freezing point (in aqueous solutions).[20] Traditionally, chemical reaction rates follow the Arrhenius equation, and because the temperature of ice is generally lower than that of an aqueous solution, the rate of chemical reaction in an ice crystal is lower than that of an aqueous solution. However, certain chemical reactions that occur in the liquid region of ice proceed more rapidly than those that occur in water, which has a relatively high temperature compared to ice. For example, the oxidation of nitrite to nitrate in water is markedly accelerated by freezing [21, 22], as is the dissolution of organic compounds or metal oxides such as iron oxide and manganese oxide by iodine in frozen aqueous solutions. [23, 24] More recently, it has also been reported that the reduction of chromate by organic compounds under acidic conditions is enhanced by freezing. [25, 26] These enhanced chemical reactions are primarily due to the freeze concentration effect, where the concentration of a solute is excluded from the ice crystal during the freezing process and accumulated at the ice crystal interface. The liquid regions between the ice crystals continuously decrease in volume as the ice crystals grow over time; however, at temperatures below the freezing point, they remain within solid ice crystals and on ice crystal surfaces. [27-29] In ice, these liquid regions are often referred to as quasi-liquid layers, liquid-like layers, brine channels, or micro-pockets. These ice microstructures provide a unique environment for

chemical reactions and different reaction pathways than those in the aqueous phase. [30, 31] The significantly increased concentration of solutes in the grain boundary regions of ice affects the kinetics of chemical transformations.[32] Previously, it was estimated that the local concentration of solutes in the ice grain boundary region increases by a factor of two to three in contrast to aqueous solutions;[33, 34] however, more recently, enrichments of even higher orders of magnitude have been reported. [35-37]

Hexavalent chromium (Cr(VI)) is a toxic element and environmental pollutant that contaminates the atmosphere and ground water from wastewater generated by the metal, leather, and textile industries, and leaches into the soil through unsecured landfills. It has been recently reported that the concentrations of Cr species in high-latitude areas and polar regions have increased due to long-range transport from mid-latitude areas. High concentration of metal ions including Cr(VI) released during mining process into the environment in mid-latitude areas. [38, 39] Exposure to Cr(VI) in the natural environment causes many biological toxicities. Cr(VI) is the thermodynamically stable oxidized state of chromium in oxidizing environments and exists primarily in its anionic forms ($HCrO_4^-$ and $CrO_4^{2-}$) with pH ranging from 3 - 10. [40, 41] The conversion of Cr(VI) to Cr(III) can occur in the presence of various reducing agents such as Fe(0), Fe(II), S(II), and organic compounds. [42-44]

In ice environments, cryoprotective polyols play a crucial role in inhibiting ice crystal growth, reducing the size of bulk ice crystals in the polycrystalline structure, and increasing the volume of the aqueous liquid phase relative to the total solution volume. This study explored how these properties enable cryoprotective polyols to accelerate the reduction of hexavalent chromium (Cr(VI)) in ice, even though the reducing agents are limited to water. We investigated reduction reactions in ice and water under various conditions, including different polyol species, polyol concentrations, and the initial pH of the solutions. Raman spectroscopy was used to visualize the freezing concentration effects of Cr(VI) and cryoprotective polyols at the ice grain boundaries. Significantly, electroplating wastewater containing Cr(VI) and other metals exhibited similar results to frozen Cr(VI) solutions in deionized water in the presence of cryoprotective polyols. This study aimed to validates the use of cryoprotective polyol compounds for freezing-induced Cr(VI) reduction in commercially available Cr(VI)-contaminated water systems and provide insights into the self-purification mechanisms in natural environments of polyols.

## 2. Materials and methods

### 2.1. Material and chemicals

Sodium dichromate dihydrate ($Na_2Cr_2O_7 \cdot 2H_2O$, as Cr(VI) source, ≥ 99.5 %), ethylene

glycol ($HOCH_2CH_2OH$, ≥99%), α-D-glucose ($C_6H_{12}O_6$, anhydrous, 96%), D-(+)-trehalose dehydrate ($C_{12}H_{22}O_{11}\cdot 2H_2O$, ≥99%), 1,5-diphenylcarbazide ($C_6H_5NHNHCONHNHC_6H_5$, DPC, ≥ 99.95 %), sulfuric acid ($H_2SO_4$, ≥ 96.0 %), perchloric acid ($HClO_4$, ACS reagent, 60%), *o*-*c*resolsulfonphthalein (CR, cresol red indicator, $C_{21}H_{18}O_5S$, indicator grade, dye content 95 %) were purchased from Sigma - Aldrich, Inc. (St. Louis, MO, USA) as analytical grades. Sodium hydroxide solution (NaOH, 1N) and acetone ($CH_3COCH_3$, ≥ 99.5%) were purchased from Samchun Chemicals (Seoul, South Korea). All aqueous solutions were prepared using ultrapure deionized water (R ≥ 18.0 MΩ · cm) prepared using a Barnstead purification system. Wastewater containing Cr(VI) was obtained from a local electroplating plant (South Korea).

### 2.2. Experimental procedure

Sample solutions were prepared by adding chemical stock solutions to deionized water in a beaker to establish the desired initial concentrations for the experiment, the experimental concentration of Cr(VI) was 20 μM and the concentrations of cryoprotective polyols (ethylene glycol, glucose and trehalose) were 100 μM each (denoted as [Cr(VI)] and [polyols]). The initial pH values of the solutions were adjusted using $HClO_4$ or NaOH (usually pH 3.0) without buffer ions. The sample solutions were transferred to conical tubes (total volume 5 mL) and immersed in a temperature-controlled bath to induce chemical reactions at the desired temperatures (20 °C for the aqueous solutions and −20 °C for the frozen solutions). The sample solutions were withdrawn from the bath at predetermined time intervals (0, 1, 2, 6, and 24 h) in lukewarm water (30−40 °C) for 1 min to thaw the frozen samples for further analysis. All experiments were performed in triplicate.

### 2.3. Analysis for the polycrystalline ice

The average thickness of the ice grain boundaries and the long-axis length of the ice crystals were measured from optical images obtained using a microscope with a cooling stage (Linkam Scientific THMS600) adjusted to -20 °C (cooling rate: -2.0 °C/min). For different concentrations ([polyol]=0, 50, 100, and 1000 uM) of frozen polyol solution, the size of 30 ice crystals and the thickness of the ice grain boundaries in corresponding regions were counted in optical images.

### 2.4. Chemical analysis

Quantitative analysis of [Cr(VI)] was measured by the colorimetric method using DPC with a UV−Vis spectrometer (Cary 4000, Agilent). The DPC reagent solution was prepared by dissolving the DPC powder (0.05 g) in a mixed solution of acetone (25 mL) and sulfuric

acid (0.25 mL). 0.1 mL of the DPC reagent solution was mixed with 0.5 mL of sample solution and 2.4 mL deionized water. The mixture was vigorously stirred using a vortex mixer and incubated in the dark for 1 h. After 1 h, the mixed solution was transferred to a 3 mL cuvette and the absorption spectrum was measured. Calibration curves for the DPC colorimetric method ($r^2$=0.998) were used to convert the measured absorbance of the mixed solution at 540 nm.

The UV-VIS absorption spectra of CR were measured to estimate the pH of the frozen samples. CR solutions, which exhibited different maximum absorption wavelengths depending on the pH of the samples, were used in both aqueous and frozen solutions without Cr(VI) to prevent interference in the absorption spectra. The sample solutions mixed with 20 μM of CR solution were added into a 3 mL cuvette and then frozen in an ethanol bath at -20 °C for 1 h. The absorption spectrum was immediately measured using a UV-Vis spectrometer without prior melting.

*In-situ* Raman measurements and chemical mapping of the frozen samples were performed to confirm the freeze concentration effect of Cr(VI) in the ice grain boundaries in the presence of cryoprotective polyols. The Raman signals from Cr-O bonding and the "finger print" signals from the polyols in the ice grain boundaries were investigated using confocal Raman spectroscopy (Renishaw inVia Qontor) combined with a cooling stage (Linkam Scientific THMS600). A 532-nm laser was used as the excitation source. A small droplet (~50 μL) of aqueous sample containing Cr(VI) (0.2 mM) and polyols (1 mM) was dropped onto the cooling stage, and the temperature was adjusted to -20 °C (cooling rate: -2.0 °C/min). The initial pH of the sample was adjusted to 5.0 to maintain Cr(VI) in the ice grain boundaries during the measurement.

## 3. Results

### 3.1. The ice microstructure changes against the concentration of cryoprotective polyols

Polyol molecules interact with water molecules in three key ways: 1) The hydroxyl groups on polyols form hydrogen bonds with water molecules, a process known as hydration. 2) The bulk structures of the polyol molecules exert steric effects that disrupt the tetrahedral arrangement and orientation of neighboring water molecules. 3) The hydrogen bonding network between water molecules is affected by polyols, which disturb the angles and lengths of the hydrogen bonds in the water structure. [45] Interactions between water and polyol molecules, including hydration, steric effects, and disruption of the hydrogen bonding network, can profoundly influence the ice crystal formation. Over the past few decades, numerous studies have demonstrated that polyols can interfere with ice

crystal development at various stages, such as ice nucleation, ice crystal growth, and recrystallization. [46]

We focused on determining how cryoprotective polyols alter ice microstructure and consequently affect chemical reactions in polycrystalline ice. Under such conditions, cryoprotective polyols expel water molecules and solutes associated with the ice-water interface. It is thought that this arrangement of water molecules disrupts the formation of the ice microstructure, including the unfrozen ice grain boundary regions at the ice-water interface, preventing the exchange of water molecules and consequently, ice crystal growth.

As the concentration of the cryoprotective polyols in the solution increased, the volume of the liquid brine increased, and the average size of the bulk ice crystals decreased. As the concentration of the cryoprotective polyols in the solution increased, the volume of the ice grain boundary regions increased, and the average size of the bulk ice crystals decreased (Table 1). Under distilled water conditions, the diameter of the liquid brine was less than 2 μm, which is not significantly different from previous studies. Compared to distilled water, solutions containing 50 μM of polyol, both ethylene glycol and glucose increased the thickness of the liquid brine and decreased the relative ice crystal size. In contrast, trehalose decreased the average size of ice crystals, even though the the thickness of the liquid brine did not change significantly. This effect is likely due to trehalose inhibiting crystal growth, resulting in more ice nuclei and smaller ice crystals.

At concentrations up 1 mM, there was a clear increase in the thickness of the liquid brine, regardless of the type of cryoprotective polyol used. This suggests that the concentration order of the solutes accumulated in the ice grain boundary regions in ice was reduced compared to conditions wherein no polyol was present. This allows freezing concentration-driven chemical reactions within the ice grain boundary regions to proceed at lower concentrations. However, the reducing nature of polyols competes with their decreasing concentration as the volume expands.

### 3.2. Effect of initial pH on the reduction of Cr(VI) by cryoprotective polyols in aqueous and ice phases

The reduction of Cr(VI) by cryoprotective polyols in ice (-20 °C) and aqueous solution (25 °C) was investigated, and the results were compared.(Fig. 1) The time profiles of the Cr(VI) concentration in the aqueous solution and ice show that in the aqueous phase, the reduction of Cr(VI) was negligible, regardless of the presence of cryoprotective polyols. However, in the ice phase, the reduction was significant, and the concentration of Cr(VI) was reduced, even in the absence of cryoprotective polyols. (Fig.1a DW(ice) and Fig.1b, Cr(VI)(ice)) This was due to the enhanced proton-mediated reduction reactions at the ice crystal boundaries during the freezing process (i.e., $4HCr(VI)O_4^- + 16H^+ \rightarrow 4Cr^{3+} + 3O_2 +$

$10H_2O$; $E_0$ = 0.15 $V_{NHE}$). [47] The reduction in the absence of cryoprotective polyols was much lower than that observed in the presence of cryoprotective polyols. After 24 h of reaction, Cr(VI) concentrations with cryoprotective polyols reached to 1–2 ❍M, compared to 13 ❍M when absent indicating that reduction by cryoprotective polyols was the main reduction pathway of Cr(VI) in ice.(Fig. 1b)

The cryoprotective polyols used in the experiments generally have the properties of "reducing sugars" that could act as reducing agents. The reduction potential of sugars has been extensively studied over the past few decades, and this observed enhancement of cryoprotective polyol-mediated Cr(VI) reduction observed on ice may also be attributed to the action of these reducing sugars[48–50]. Ethylene glycol has an oxidation potential of 1.65 V[51], and glucose has an oxidation potential of 0.6 V [52], both of which are higher than the reduction potential of Cr(VI). One implication of this chemical reaction is that, unlike other cryoprotective polyols (such as ethylene glycol or glucose), trehalose is a non-reducing sugar owing to its unique stabilizing properties arising from its symmetrical, low-energy structure, which consists of two 1,1-anomerically linked glucose moieties. The oxidation potential of trehalose in the liquid phase (25 °C) is known to be −0.36 V,[53] so Cr(VI) reduction by trehalose is not thermodynamically favored. Nevertheless, the results of this study show that trehalose had a similar level of Cr(VI) removal after 24 h of reaction with the other two cryoprotective polyols in ice. The disaccharide splits readily via hydrolysis to from two glucose molecules, which are strong reducing sugars. There is evidence in the literature that non-reducing sugars such as sucrose may be hydrolyzed during freezing under acidic conditions. The oxidation rate of trehalose in the freeze-dried model system was monitored at pH 2.5.[54] The initial pH used in this experiment was 3.0, which is not suitable for hydrolysis of trehalose in the aqueous phase. Therefore, the results suggested that Cr(VI) reduction by trehalose proceeded under experimental conditions lower than the initial pH (i.e., pH 3.0). To determine the decrease in pH that occurred during the freezing process, we used a colorimetric method with CR as a pH indicator (Fig. 2). The maximum absorption wavelength ($\lambda_{max}$) of CRs changes with the pH of the solution through protonation and deprotonation (i.e., the $\lambda_{max}$ of singly protonated CR (434 nm) is red-shifted by acidification and basification. As shown in Figure 2, in water at pH 3.0, the maximum absorption of CR was observed at 434 nm (singly protonated form of CR), which was equivalent to the initial pH value of the solution. In ice, two absorption bands were observed from 434 to 518 nm (the doubly-protonated form of CR). The decrease in the absorption band at 434 nm and the emergence of an absorption band at 518 nm after freezing indicated that the singly-protonated CR molecule was converted to a doubly-protonated CR molecule by decreasing the pH in ice. [55] Therefore, this result confirmed that the pH of the frozen solution was lowered by freezing to approximately

1.05. Although the extent of the pH decrease after freezing could be influenced by the solute concentration, initial pH of the aqueous solution, freezing temperature, and the freezing rate, it was clear that freezing reduced the pH under acidic conditions, thus leading to favorable conditions for cryoprotective polyol mediated Cr(VI) reduction.

Figures 3a and 3b show the effect of the initial pH on Cr(VI) reduction by cryoprotective polyols in the aqueous and ice phases. Cr(VI) reduction by cryoprotective polyols in ice (Fig. 3b) was higher than in water (Fig. 3a), even though frozen conditions have a much lower reaction temperature (25 °C in water vs. -20 °C in ice). The reduction of Cr(VI) in ice was pH-dependent and became insignificant above pH 5. These results indicate that the $pH_i$ of the system has a significant effect on Cr(VI) removal efficiency, which is further enhanced by low $pH_i$ values. This behavior was expected given that protons were required to reduce Cr(VI) to Cr(III) ($HCrO_4^- + 7H^+ + 3e^- \rightarrow Cr^{3+} + 4H_2O$). The enhanced reduction in Cr(VI) during freezing can be attributed to the lowering of the pH value at the ice crystal interface due to the freeze concentration effect. Under acidic conditions, the concentration of protons in ice is known to increase by a factor of 2 - 4 compared to water. [56] The removal of Cr(VI) from the ice phase was insufficient at pH 4 in the absence of cryoprotective polyols. However, in the presence of cryoprotective polyols, the Cr(VI) removal efficiency at pH 4 was lower than that at pH 3, but still achieved relatively low residual Cr(VI) concentrations of 5 ❍M. These results are significantly different from those obtained at pH 5. This behavior was similar to that consistently observed in previously reported results, including freezing experiments with Cr(VI) using organic acids as reducing agents. Notably, the Cr(VI) reduction rate in the presence of cryoprotective polyols was higher than in their absence, suggesting that the synergistic effect on Cr(VI) reduction by cryoprotective polyols in ice could be attributed to their accumulation at the ice crystal interface. Consequently, a larger reduction of Cr(VI) in ice by cryoprotective polyols could be achieved because of the freeze concentration effect under acidic solutions. This implies that pH in the cryosphere is exposed to real-world Cr(VI)-containing wastewater or natural systems through biometabolism, which is generally acidic[58, 59], making Cr(VI) reduction in ice suitable.

### 3.3. Ratio effect of cryoprotective polyols on Cr(VI) reduction

The effect of the concentration ratio of the cryoprotective polyols on Cr(VI) reduction was investigated under fixed time conditions (24 h)(Fig. 4). In aqueous solution at 25°C, no Cr(VI) reduction was observed for polyols up to 200 μM (i.e., [Cr(VI)] : [polyols] = 1:10). However, the reduction efficiency of Cr(VI) increased at −20 °C as polyols increased, suggesting that cryoprotective polyols act as primary reductants of Cr(VI) in frozen solutions. Trehalose exhibited slightly higher reduction efficiency than ethylene glycol and

glucose under all experimental conditions. This phenomenon can be attributed to the hydrolysis of trehalose, a non-reducing disaccharide that yields two equivalents of the reducing monosaccharide glucose under acidic conditions. However, the exact hydrolysis conditions and the results obtained under ice conditions require further investigation. In all three cryoprotective polyol species examined, a consistent observation was the diminished extent of the reduction reaction when the molar ratio of polyol to Cr(VI) reached tenfold. This phenomenon was attributed to the binding of cryoprotective polyols to the ice surface, which inhibited ice crystal growth and reduced the relative concentrations of Cr(VI) and polyols concentrated within the ice microstructure throughout the frozen solution. The size and volume of the ice microstructure are closely related to the concentration, and studies have shown that the presence of ice binding molecules on the ice crystal surface can affect the freeze concentration effect. [57] We observed that higher concentrations of cryoprotective polyols within the solution increased the volume of the ice crystal interface and decreased the average size of the ice crystals. This result indicates that the reduction of Cr(VI) by cryoprotective polyols is affected by both the molar ratio of the polyols acting as reducing agents and their ice binding properties.

### 3.4. Effect of cryoprotective polyols on ice crystal formation and freeze concentration effect

The accumulation of both Cr(VI) and cryoprotective polyols at ice grain boundaries during freezing increases the potential for collisions between Cr(VI) and polyols, which may result in a synergistic effect on redox reactions. To test the hypothesis that the freeze concentration effect accelerates the reduction of Cr(VI) by locally increasing the concentration of cryoprotective polyols and Cr(VI), confocal Raman spectroscopy was used to visualize the spatial distribution of the Raman peaks of Cr(VI) and polyols concentrated in the ice microstructure (Fig. 5). To simultaneously identify the Raman signals of the polyols and Cr(VI) gathered at the ice crystal boundaries, the experiment was conducted under conditions (pH 5) where the reduction reaction was slow in the ice phase. When the Cr(VI) aqueous solution and cryoprotective polyols mixed with Cr(VI) were frozen, the ice crystal and ice grain boundaries could be clearly distinguished in the optical images (Fig. 5a, 5c, 5f, 5i). The Raman signals detected on surface of the ice microstructure were visualized by identifying the peaks corresponding to Cr-O (Fig. 5b, 5d, 5g, 5j) and the peaks from polyols (Fig. 5e, 5h, 5k). In each mapping image, the relative Raman intensities (i.e., relative concentrations) are displayed on a rainbow scale, with red representing the highest concentration and black representing the lowest. Previous studies have demonstrated that in aqueous solutions, characteristic Raman bands arising from the Cr-O vibrational modes of Cr(VI) species are observed in the 800 - 1000 $cm^{-1}$ wavenumber

region, and the precise positions of these bands are dependent on the Cr(VI) concentration and solution pH.[47] No Raman peak of Cr-O was observed inside the ice crystal region, whereas a characteristic Raman Cr(VI) peak at 932 $cm^{-1}$ was clearly detected in the ice grain boundary region (Fig. 5b). The Cr(VI) distribution image of this frozen Cr(VI) solution suggests that Cr(VI) was excluded from the ice crystals during the freezing process, implying a large accumulation of Cr(VI) at the ice grain boundaries. Cryoprotective polyols inhibit ice crystal growth by binding to their surface.[40] Therefore, they were expected to have a spatial distribution at the ice crystal interface when the final polycrystalline ice surface formed. In freezing solutions mixed with Cr(VI), the Raman spectra of the cryoprotective polyols exhibited characteristic peaks that were distinct from those of Cr(VI), allowing Raman mapping to be performed with the fingerprint peaks of each polyol. Although no Raman signals from the three cryoprotective polyols were observed in the ice crystal region, a characteristic Raman peak was clearly detected in the ice grain boundary region, and its location corresponded exactly to the spatial distribution of Cr(VI). Based on the results shown in Figure 5, our findings indicated that cryoprotective polyols were preferentially excluded from the ice crystal lattice and spatially confined to the grain boundary regions by binding to the ice crystal surfaces. Consequently, the redox reaction between Cr(VI) and the cryoprotective polyols occurred predominantly in the ice grain boundary domains rather than within the ice crystals.

KOPRI 극지연구소

### 3.5. Reduction of Cr(VI) in Cr(VI)-contaminated wastewater by cryoprotective polyols

Cr(VI) is emitted as a result of human industrial activities and is widely distributed in various natural environments. Recently, it has been reported that Cr concentrations in high-latitude and polar regions have increased due to long-distance transport from mid-latitude regions. Therefore, the redox reactions between cryoprotective polyols and Cr(VI) present in the natural environment may contribute significantly to the natural purification of Cr(VI) in cold regions such as high-latitude and polar regions. Acid mine drainage contains a variety of metals, including high concentrations of Cr. [58, 59] From a practical point of view, the freezing process introduced by cryoprotective polyols could be applied to the remediation of Cr(VI)-contaminated wastewater. We selected a reaction condition with a high Cr(VI) reduction rate after 24 h of reaction on ice, and applied this condition to Cr(VI) contaminated wastewater (electroplating wastewater) that also contains various metals (Fig. 6). Figure 6a shows the time profile of the Cr(VI) concentration in water and ice, and Figure 6b shows the residual Cr(VI) concentration in the real Cr(VI)-contaminated wastewater after 24 h of reaction. In Cr(VI)-contaminated wastewater, the reduction of Cr(VI) by cryoprotective polyols was negligible in water but dramatically

increased in ice. Despite the presence of various metal ions, such as Fe, Ca, Cu, As, Al, and Mg, in the electroplating wastewater, the kinetics of Cr(VI) reduction in the electroplating wastewater at pH 3.0, was similar to that in the artificial Cr(VI) aqueous solution. These results suggest that the reduction of Cr(VI) in actual Cr(VI)-containing wastewater can be enhanced by freezing. As most Cr(VI)-contaminated wastewaters are highly acidic[60, 61] with low pH conditions in the natural environment, these results suggest that cryoprotective polyols could contribute to the self-purification mechanism of heavy metal reduction that occurs in nature.

## 4. Conclusions

This study investigated the enhanced reduction of Cr(VI) by cryoprotective polyols in ice compared with polyols in aqueous solutions. For this purpose, we selected ethylene glycol, glucose, and trehalose as cryoprotective polyols with different structures and simultaneously determined their ice surface binding properties. The efficiency of Cr(VI) redcution by cryoprotective polyols in ice was dramatically enhanced but was significantly less effective in water, indicating that cryoprotective polyols could act as the main electron donor for Cr(VI) reduction. In contrast to previous studies, trehalose, which is not classified as a reducing sugar, also showed reducing properties owing the strongly acidic conditions in ice. We found that the cryoprotective polyols used in our experiments were able to bind to the ice grain boundaries during ice growth and therefore showed strong Raman signals at the crystal interface rather than inside the ice crystal upon freezing. Owing to the action of these cryoprotective polyols, we were able to visualize via Raman spectroscopy that Cr(VI) was enriched with cryoprotective polyols at the ice crystal interface, resulting in an accelerated redox reaction. In Cr(VI)-contaminated wastewater, Cr(VI) reduction using cryoprotective polyols was accelerated in ice, and the results were similar to those for artificial Cr(VI) solutions. These findings suggest freezing with cryoprotective polyols is an effective and practical method for the reduction and removal of Cr(VI) from wastewater. In cold environments, such as winter permafrost, polar regions, and mid-latitudes, self-purification actions, such as toxicity reduction of heavy metals caused by cryoprotective polyols can be realized.

KOPRI 극지연구소

## REFERENCES


1. Chandna, N., et al., *Glucose promoted facile reduction of azides to amines under aqueous alkaline conditions.* Green Chemistry, 2017. **19**(18): p. 4268-4271.
2. Kumar, M., et al., *Catalyst-free water mediated reduction of nitroarenes using glucose as a hydrogen source.* RSC Advances, 2013. **3**(15): p. 4894-4898.
3. Kunz, T., et al., *Glucose - a Reducing Sugar? Reducing Properties of Sugars in Beverages and Food.* Brewing Science, 2011. **64,** p. 61-67.
4. Zhou, B., et al., *Using the hydrogen and oxygen in water directly for hydrogenation reactions and glucose oxidation by photocatalysis.* 2016. **7**(1): p. 463-468.
5. Holade, Y., et al., *Recent advances in carbon supported metal nanoparticles preparation for oxygen reduction reaction in low temperature fuel cells.* 2015. **5**(1): p. 310-348.
6. Luo, S., et al., *Investigating the mechanism of catalytic reduction of silver nitrate on the surface of barium titanate at room temperature: oxygen vacancies play a key role.* RSC Advances, 2015. **5**(5): p. 3377-3380.
7. Stoll, A. and J.R. Duncan, *Enhanced heavy metal removal from waste water by viable, glucose pretreated Saccharomyces cerevisiae cells.* Biotechnology Letters, 1996. **18**(10): p. 1209-1212.
8. Ali, J. and J.N. Shelton, *Successful vitrification of day-6 sheep embryos.* J Reprod Fertil, 1993. **99**(1): p. 65-70.
9. Hotamisligil, S., M. Toner, and R.D. Powers, *Changes in membrane integrity, cytoskeletal structure, and developmental potential of murine oocytes after vitrification in ethylene glycol.* Biol Reprod, 1996. **55**(1): p. 161-8.
10. Kasai, M., et al., *High survival of rabbit morulae after vitrification in an ethylene glycol-based solution by a simple method.* Biol Reprod, 1992. **46**(6): p. 1042-6.
11. Kasai, M., et al., *A simple method for mouse embryo cryopreservation in a low toxicity vitrification solution, without appreciable loss of viability.* J Reprod Fertil, 1990. **89**(1): p. 91-7.
12. Liu, X., et al., *Determination of Supercooling Degree, Nucleation and Growth Rates, and Particle Size for Ice Slurry Crystallization in Vacuum.* 2017. **7**(5): p. 128.
13. Utsumi, K., S. Hochi, and A. Iritani, *Cryoprotective effect of polyols on rat embryos during two-step freezing.* Cryobiology, 1992. **29**(3): p. 332-41.
14. Luyet, B.J. and J.F. Keane, Jr., *Comparative efficiency of ethylene glycol, glucose and sodium chloride in protecting tissues against freezing injury.* Biodynamica, 1952. **7**(137-140): p. 119-131.
15. Thanatuksorn, P., et al., *Freeze - thaw behaviour of aqueous glucose solutions - the crystallisation of cubic ice.* Physical Chemistry Chemical Physics, 2008. **10**(35): p.


KOPRI 극지연구소

5452-5458.

16. Chiu, P.-L., D. Kelly, and T. Walz, *The use of trehalose in the preparation of specimens for molecular electron microscopy.* Micron (Oxford, England : 1993), 2011. **42**: p. 762-72.
17. Whelan, A.P., et al., *Effect of trehalose on the glass transition and ice crystal growth in ice cream.* 2008. **43**(3): p. 510-516.
18. Storey, B.T., E.E. Noiles, and K.A. Thompson, *Comparison of glycerol, other polyols, trehalose, and raffinose to provide a defined cryoprotectant medium for mouse sperm cryopreservation.* Cryobiology, 1998. **37**(1): p. 46-58.
19. Weng, L., S. Ziaei, and G. Elliott, *Effects of Water on Structure and Dynamics of Trehalose Glasses at Low Water Contents and its Relationship to Preservation Outcomes.* Scientific reports, 2016. **6**: p. 28795.
20. O'Concubhair, R. and J.R. Sodeau, *The Effect of Freezing on Reactions with Environmental Impact.* Accounts of Chemical Research, 2013. **46**(11): p. 2716-2724.
21. Takenaka, N., et al., *Acceleration mechanism of chemical reaction by freezing: The reaction of nitrous acid with dissolved oxygen.* Journal of Physical Chemistry, 1996. **100**(32): p. 13874-13884.
22. Takenaka, N., A. Ueda, and Y. Maeda, *Acceleration of the rate of nitrite oxidation by freezing in aqueous solution.* Nature, 1992. **358**(6389): p. 736-738.
23. Du, J., et al., *MnO2-Induced Oxidation of Iodide in Frozen Solution.* Environmental Science & Technology, 2023. **57**(13): p. 5317-5326.
24. Kim, K., et al., *Simultaneous and Synergic Production of Bioavailable Iron and Reactive Iodine Species in Ice.* Environmental Science & Technology, 2019. **53**(13): p. 7355-7362.
25. Han, T.U., J. Kim, and K. Kim, *Accelerated chromate reduction by tea waste: Comparison of chromate reduction properties between water and ice systems.* Environmental Research, 2021. **197**: p. 111059.
26. Ju, J., et al., *Accelerated redox reaction between chromate and phenolic pollutants during freezing.* Journal of Hazardous Materials, 2017. **329**.
27. Bartels-Rausch, T., et al., *A review of air - ice chemical and physical interactions (AICI): liquids, quasi-liquids, and solids in snow.* Atmos. Chem. Phys., 2014. **14**(3): p. 1587-1633.
28. Boxe, C.S. and A. Saiz-Lopez, *Multiphase modeling of nitrate photochemistry in the quasi-liquid layer (QLL): implications for $NO_x$ release from the Arctic and coastal Antarctic snowpack.* Atmos. Chem. Phys., 2008. **8**(16): p. 4855-4864.
29. Park, S.-C., E.-S. Moon, and H. Kang, *Some fundamental properties and reactions of ice surfaces at low temperatures.* Physical Chemistry Chemical Physics, 2010. **12**(38):

p. 12000-12011.
30. Min, D.W., et al., *Abiotic Formation of Humic-Like Substances through Freezing-Accelerated Reaction of Phenolic Compounds and Nitrite.* Environmental Science & Technology, 2019. **53**(13): p. 7410-7418.
31. Cheng, J., et al., *Confocal Fluorescence Microscopy of the Morphology and Composition of Interstitial Fluids in Freezing Electrolyte Solutions.* The Journal of Physical Chemistry Letters, 2010. **1**(1): p. 374-378.
32. Takenaka, N. and H. Bandow, *Chemical Kinetics of Reactions in the Unfrozen Solution of Ice.* The Journal of Physical Chemistry A, 2007. **111**(36): p. 8780-8786.
33. Heger, D., J. Jirkovský, and P. Klán, *Aggregation of Methylene Blue in Frozen Aqueous Solutions Studied by Absorption Spectroscopy.* The Journal of Physical Chemistry A, 2005. **109**(30): p. 6702-6709.
34. Heger, D., J. Klánová, and P. Klán, *Enhanced Protonation of Cresol Red in Acidic Aqueous Solutions Caused by Freezing.* The Journal of Physical Chemistry B, 2006. **110**(3): p. 1277-1287.
35. Nguyen, Q.A., et al., *Detoxification of arsenite by iodide in frozen solution.* Chemosphere, 2023. **340**: p. 139903.
36. Kim, K., et al., *Production of Molecular Iodine via a Redox Reaction between Iodate and Organic Compounds in Ice.* The Journal of Physical Chemistry A, 2023. **127**(12): p. 2830-2838.
37. Ahn, Y.-Y., J. Kim, and K. Kim, *Catalytic behavior of nitrous acid for acetaminophen transformation during the freezing process.* Journal of Hazardous Materials, 2023. **456**: p. 131652.
38. Weinbruch, S., et al., *Chemical composition and sources of aerosol particles at Zeppelin Mountain (Ny Ålesund, Svalbard): An electron microscopy study.* Atmospheric Environment, 2012. **49**: p. 142-150.
39. Kozak, K., et al., *Arctic catchment as a sensitive indicator of the environmental changes: distribution and migration of metals (Svalbard).* International Journal of Environmental Science and Technology, 2016. **13**(12): p. 2779-2796.
40. Gaberell, M., et al., *Role of Dissolved Organic Matter Composition on the Photoreduction of Cr(VI) to Cr(III) in the Presence of Iron.* Environmental Science & Technology, 2003. **37**(19): p. 4403-4409.
41. Hug, S.J., H.-U. Laubscher, and B.R. James, *Iron(III) Catalyzed Photochemical Reduction of Chromium(VI) by Oxalate and Citrate in Aqueous Solutions.* Environmental Science & Technology, 1997. **31**(1): p. 160-170.
42. Kang, S., et al., *Highly efficient removal of hexavalent chromium in aqueous solutions via chemical reduction of plate-like micro/nanostructured zero valx'ent iron.* RSC

KOPRI 극지연구소

Advances, 2017. **7**(88): p. 55905-55911.

43. Nguyen, Q.A., et al., *Enhanced reduction of hexavalent chromium by hydrogen sulfide in frozen solution.* Separation and Purification Technology, 2020. **251**: p. 117377.
44. Qin, G., et al., *Hexavalent chromium removal by reduction with ferrous sulfate, coagulation, and filtration: a pilot-scale study.* Environ Sci Technol, 2005. **39**(16): p. 6321-7.
45. Politi, R., L. Sapir, and D. Harries, *The Impact of Polyols on Water Structure in Solution: A Computational Study.* The Journal of Physical Chemistry A, 2009. **113**(26): p. 7548-7555.
46. Deller, R.C., et al., *Ice recrystallisation inhibition by polyols: comparison of molecular and macromolecular inhibitors and role of hydrophobic units.* Biomaterials Science, 2013. **1**(5): p. 478-485.
47. Kim, K., et al., *Freezing-Induced Simultaneous Reduction of Chromate and Production of Molecular Iodine: Mechanism, Kinetics, and Practical Implications.* Environmental Science & Technology, 2020. **54**(24): p. 16204-16211.
48. Wang, K., et al., *Mechanisms of trehalose-mediated mitigation of Cd toxicity in rice seedlings.* Journal of Cleaner Production, 2020. **267**: p. 121982.
49. Samiee, L., et al., *Developing of Ethylene Glycol as a New Reducing Agent for Preparation of Pd-Ag/PSS Composite Membrane for Hydrogen Separation %J Journal of Petroleum Science and Technology.* 2012. **2**(2): p. 25-32.
50. Zhu, C., et al., *Reducing Sugar: New Functional Molecules for the Green Synthesis of Graphene Nanosheets.* ACS Nano, 2010. **4**(4): p. 2429-2437.
51. Sitta, E., R. Nagao, and H. Varela, *The Electro-Oxidation of Ethylene Glycol on Platinum over a Wide pH Range: Oscillations and Temperature Effects.* PLOS ONE, 2013. **8**(9): p. e75086.
52. Farrell, S. and C. Breslin, *Oxidation and photo-induced oxidation of glucose at a polyaniline film modified by copper particles.* Electrochimica Acta, 2004. **49**: p. 4497-4503.
53. Pothukuchy, A., et al., *A potentially insect-implantable trehalose electrooxidizing anode.* Biosens Bioelectron, 2006. **22**(5): p. 678-84.
54. O'BRIEN, J., *Stability of Trehalose, Sucrose and Glucose to Nonenzymatic Browning in Model Systems.* 1996. **61**(4): p. 679-682.
55. Rottman, C., et al., *Surfactant-induced modification of dopants reactivity in sol-gel matrixes.* Journal of the American Chemical Society, 1999. **121**(37): p. 8533-8543.
56. Kim, K. and W. Choi, *Enhanced Redox Conversion of Chromate and Arsenite in Ice.* Environmental science & technology, 2011. **45**: p. 2202-8.
57. Kim, B., et al., *Freezing-enhanced oxidation of iodide by hydrogen peroxide in the*

*presence of antifreeze proteins from the Arctic yeast Leucosporidium sp.AY30.* Environmental Research, 2022. **212**: p. 113233.

58. Luo, C., et al., *Distribution and mobilization of heavy metals at an acid mine drainage affected region in South China, a post-remediation study.* Science of The Total Environment, 2020. **724**: p. 138122.
59. RoyChowdhury, A., D. Sarkar, and R. Datta, *Removal of Acidity and Metals from Acid Mine Drainage-Impacted Water using Industrial Byproducts.* Environmental Management, 2019. **63**(1): p. 148-158.
60. Bankole, M.T., et al., *Selected Heavy Metals Removal From Electroplating Wastewater by Purified and Polyhydroxylbutyrate Functionalized Carbon Nanotubes Adsorbents.* Scientific Reports, 2019. **9**(1).
61. Bokare, A.D. and W. Choi, *Chromate-Induced Activation of Hydrogen Peroxide for Oxidative Degradation of Aqueous Organic Pollutants.* Environmental Science & Technology, 2010. **44**(19): p. 7232-7237.

KOPRI
극지연구소

FIGURES AND TABLES

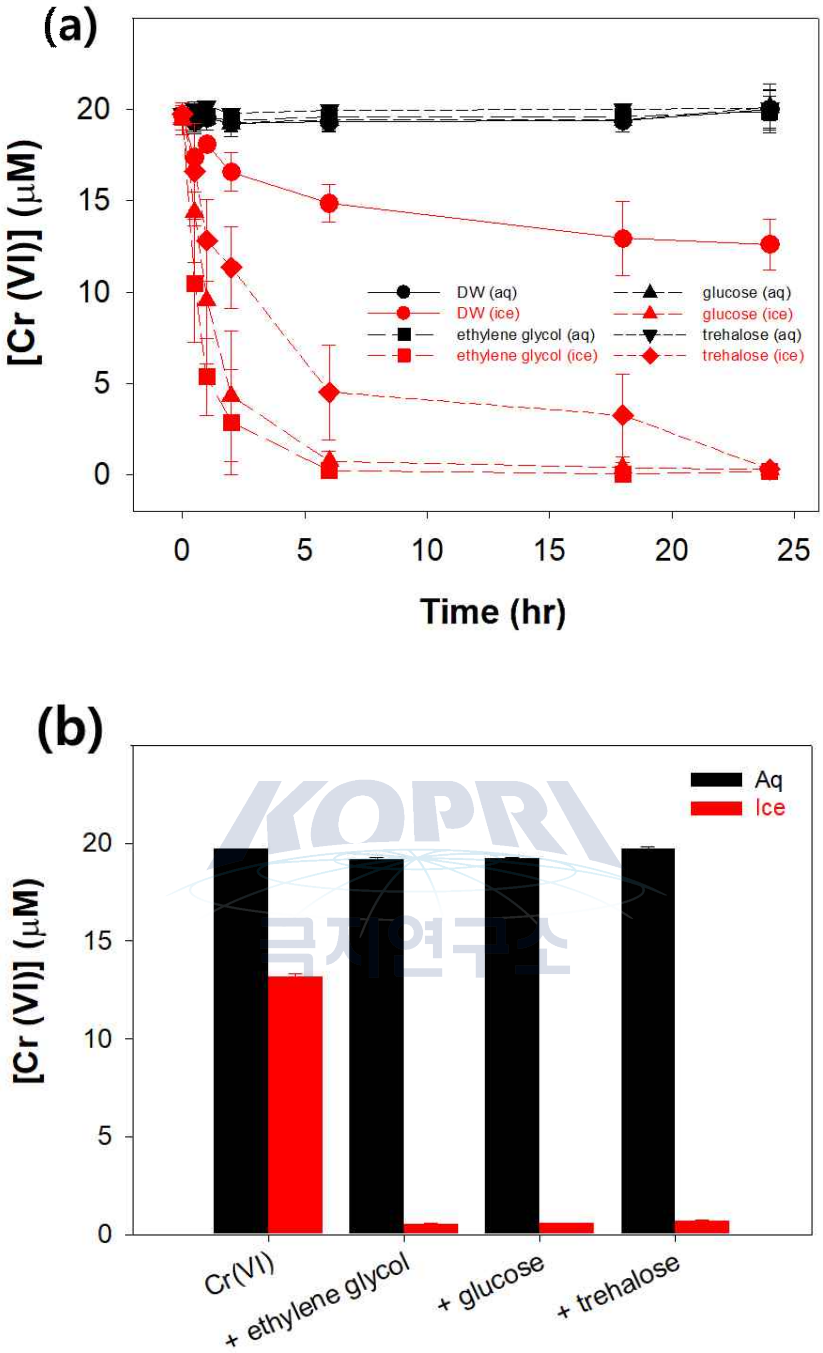



**Figure 1. [Cr (VI)] changes in aqueous and ice in the presence of cryoprotective polyols. (a)** Time profile of the [Cr(VI)] reduction in aqueous phase (at 25 °C) or in ice (at −20 °C), (b) reduction of [Cr(VI)] in aqueous phase or in ice after 24 hr reaction. Initial conditions: $[Cr(VI)]_i$ = 20 μM, [polyol] = 100 μM and $[pH]_i$ = 3.0.

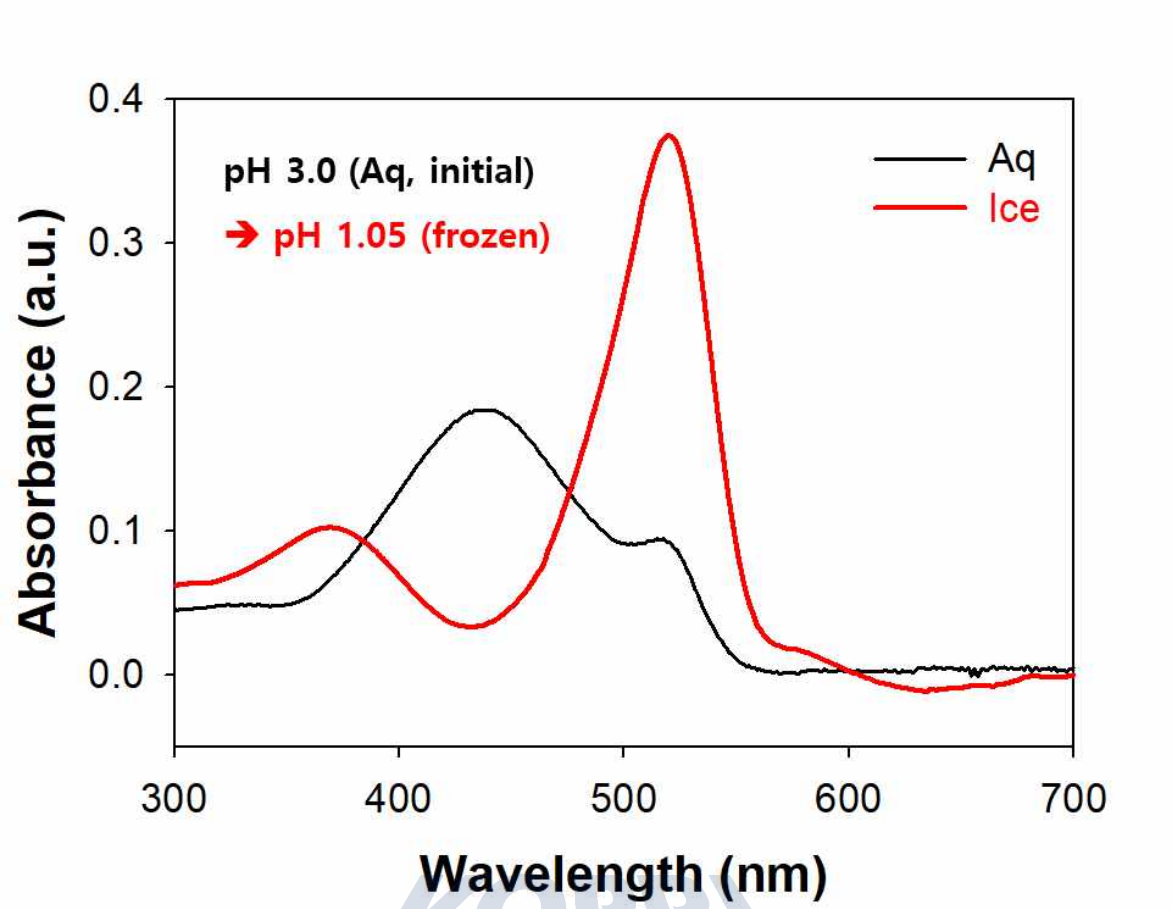



**Figure 2. The pH change in aqueous and in frozen solutions.** UV – visible absorption spectra change of cresol red solution before and after freezing. Experimental condition: freezing time = 1 hr, [CR] = 20 μM, $pH_i$ = 3.0.

KOPRI 극지연구소

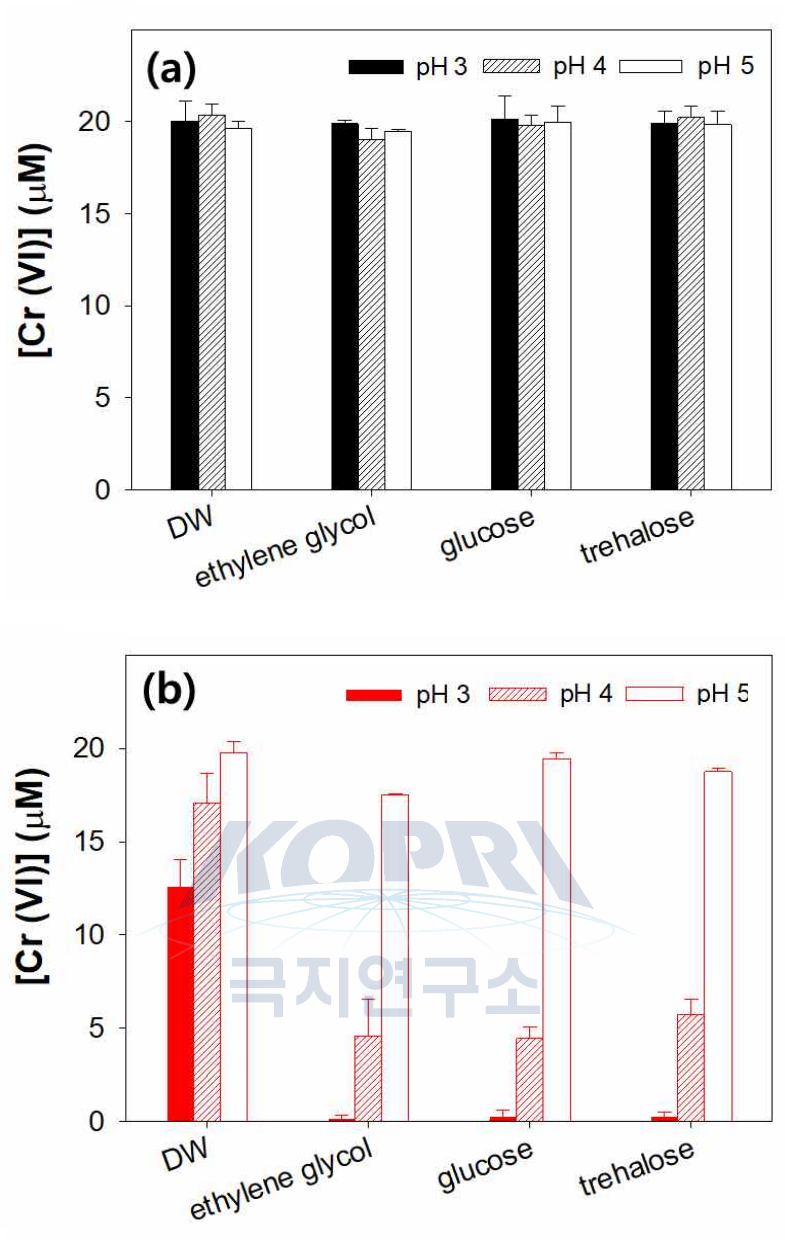



**Figure 3. Effects of initial pH on the Cr(VI) reduction in aqueous and frozen solutions by cryoprotective polyols.** (a) in aqueous solutions (at 25 °C) and (b) in frozen solutions (at −20 °C) after 24 hr reaction. Experimental condition: reaction time = 24 hr, $[Cr(VI)]_i$ = 20 μM, [polyol] = 100 μM, $[pH]_i$ = 3.0, 4.0, 5.0 each.

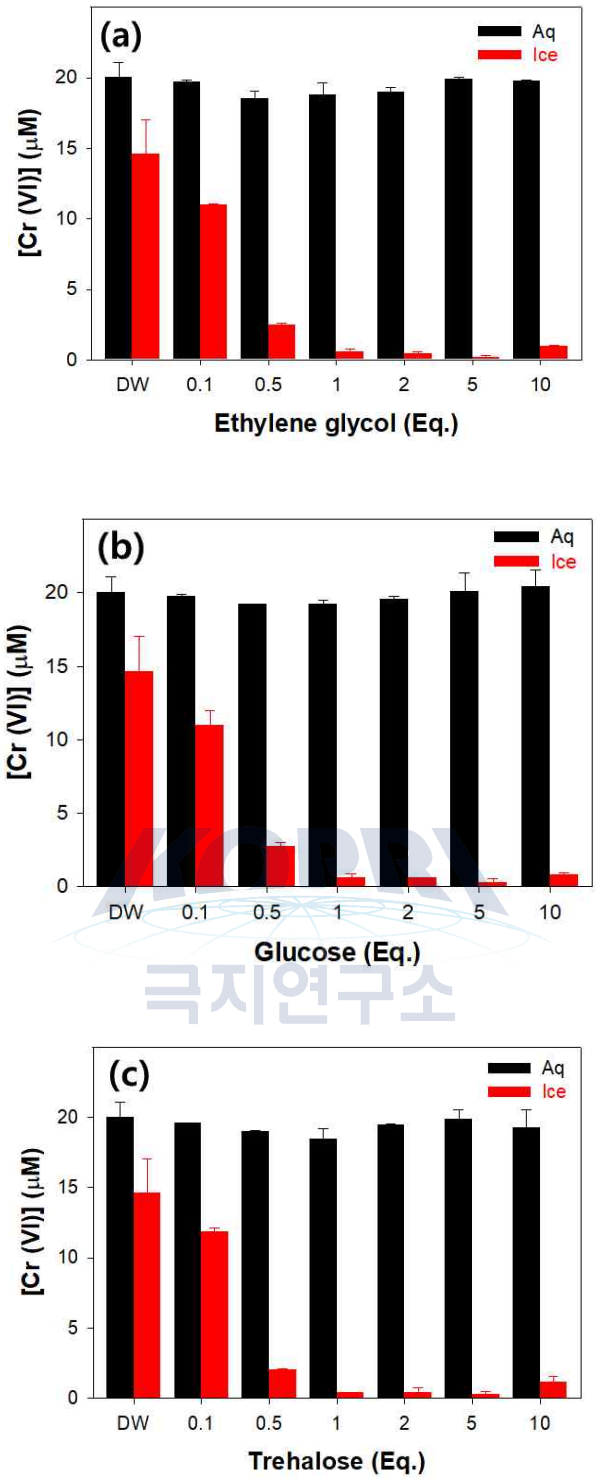



**Figure 4. Effect of cryoprotective polyols on Cr(VI) reduction against [Cr(VI)]:[polyol] ratio.** (a) ethylene glycol, (b) glucose and (c) trehalose in aqueous phase (at 25 °C, black bar) or in ice (at −20 °C, red bar). Experimental condition were as follow: reaction time = 24 hr, $[Cr(VI)]_i$ = 20 μM, and $[pH]_i$ = 3.0.

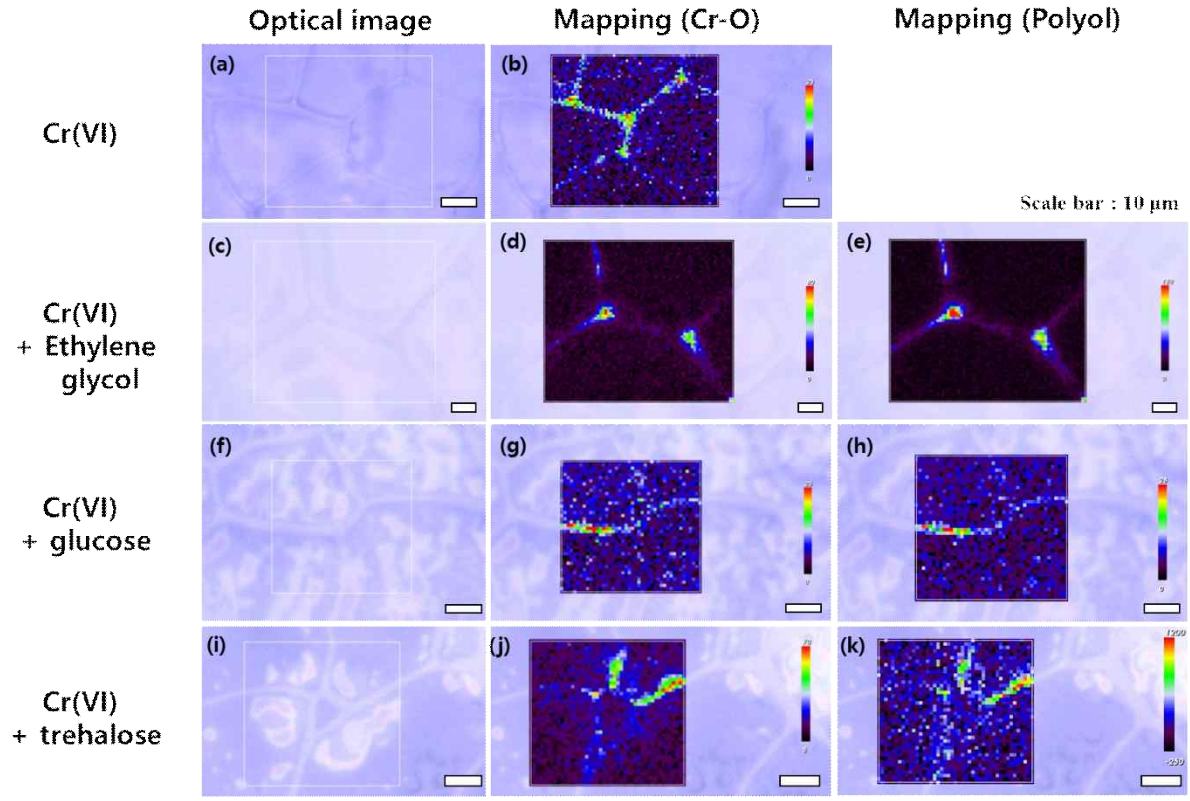



**Figure 5. *in-situ* chemical mapping images of Cr(VI) and cryoprotective polyols in the ice.** The optical images and Raman mapping images of the *in-situ* ice samples from (a,b) Cr(VI) solution, (c,d,e) Cr(VI) with ethylene glycol solution, (f,g,h) Cr(VI) with glucose solution and (i,j,k) Cr(VI)with trehalose solution. Initial condition: [Cr (VI)] = 0.2 mM, [polyol] = 1 mM, pH 5.0. Scale bar: 10 μm.

KOPRI 극지연구소

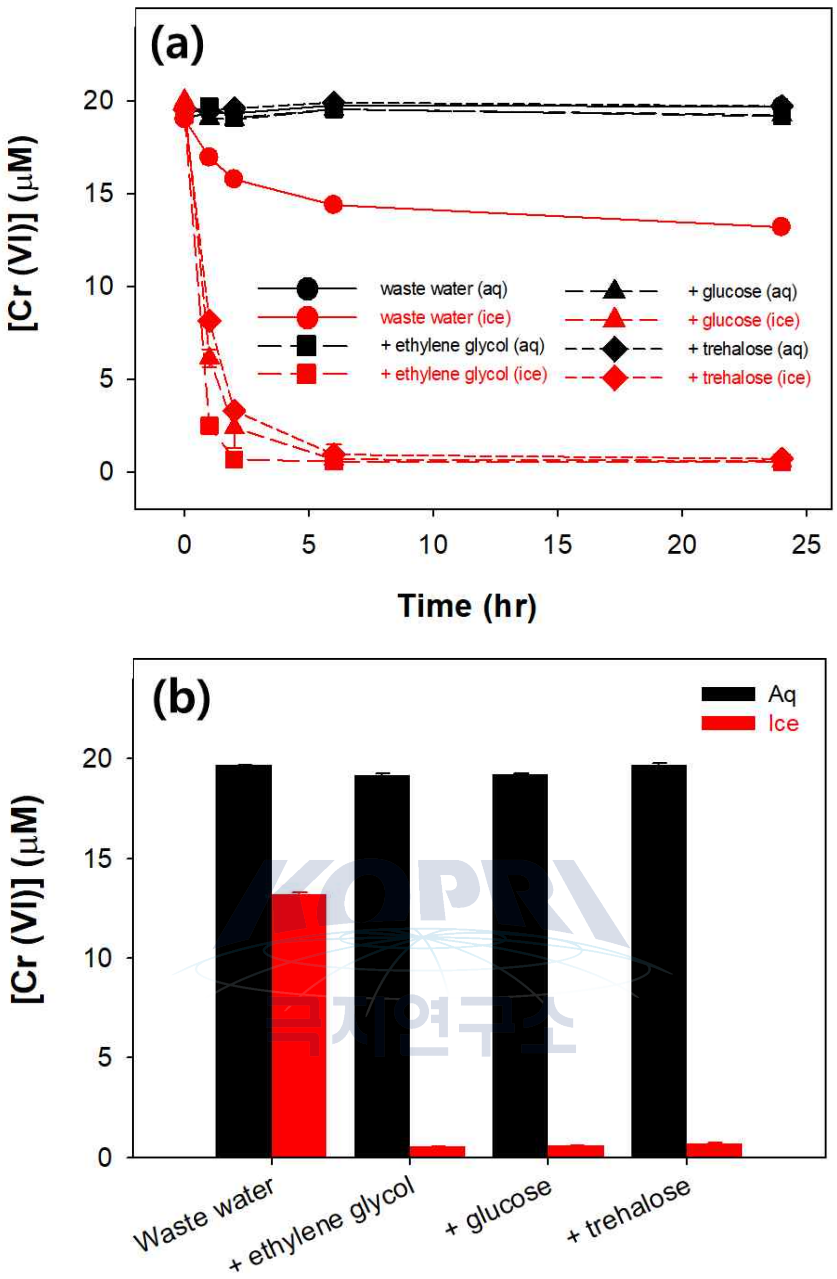



**Figure 6. [Cr (VI)] changes in aqueous and ice phase in the presence of cryoprotective polyols on Cr(VI)-contaminated wastewater .** (a) Time profile of the [Cr(VI)] reduction in aqueous phase (at 25 °C) or in ice (at −20 °C). (b) Reduction of [Cr(VI)] in aqueous phase or in ice after 24 hr reaction. Initial conditions: $[Cr(VI)]_i$ (in waste water) = 20 μM, [polyol] = 100 μM and $[pH]_i$ = 3.0.

| | | Thickness of the ice grain boundary regions | Ice crystal size |
|---|---|---|---|
| DW | | 1.87 (0.58) | 158.68 (59.81) |
| EG | 50 μM | 3.99 (2.33) | 145.08 (64.85) |
| | 100 μM | 5.88 (3.90) | 103.72 (45.24) |
| | 1 mM | 18.72 (15.24) | 80.02 (27.43) |
| Glucose | 50 μM | 2.31 (0.78) | 156.28 (58.17) |
| | 100 μM | 2.34 (0.69) | 139.82 (61.33) |
| | 1 mM | 3.17 (1.31) | 84.95 (51.07) |
| Trehalose | 50 μM | 1.25 (0.42) | 100.53 (81.40) |
| | 100 μM | 1.76 (0.60) | 78.45 (29.86) |
| | 1 mM | 3.38 (1.35) | 83.63 (24.36) |

N = 30, unit : μm, () : standard deviation

**Table 1.** Thickness of the ice grain boundary regions and average ice crystal size as a function of the concentration of cryoprotective polyols.

KOPRI
극지연구소

# 제 19 절. Freezing-enhanced degradation of azo dyes in the chloride-peroxymonosulfate system⑲

Yong-Yoon Ahn[1], Jungwon Kim[2], Junho Jeon[3], Kitae Kim[1,4]

[1]Korea Polar Research Institute (KOPRI)

[2]Department of Environmental Science and Biotechnology, Hallym University

[3]School of Civil, Environmental and Chemical Engineering, Changwon National University, Changwon, Gyeongsangnam-do, 51140, Republic of Korea

[4]Department of Polar Science, University of Science of Technology (UST)

## Abstract

In this study, we investigated the freezing-induced acceleration of dye bleaching by chloride-activated peroxymonosulfate (PMS). It has been observed that the oxidation of chloride by PMS generates a free chlorine species, such as hypochlorous acid (HOCl), under mild acidic and circumneutral pH condition. This process is the major reason for the enhanced oxidation capacity for electron-rich organic compounds (e.g., phenol) in the chloride-PMS system. However, we demonstrated that the chloride-PMS system clearly reduced the total organic carbon concentration (TOC), whereas the HOCl system did not lead to decrease in TOC. Overall, the chemical reaction is negligible in an aqueous condition if the concentrations of reagents are low, and freezing the solution accelerates the degradation of dye pollutants remarkably. Most notably, the pseudo-first order kinetic rate constant for acid orange 7 (AO7) degradation is approximately 0.252 $h^{-1}$ with 0.5 mM PMS, 1 mM NaCl, initial pH 3, and a freezing temperature of -20℃. AO7 degradation is not observed when the solution is not frozen. According to confocal Raman-microscope analysis and an experiment that used an extremely high dose of reactants, the freeze concentration effect is the main reason for the acceleration phenomenon. Because the freezing phenomenon is spontaneous at high latitudes and at mid-latitudes in winter, and the chloride is ubiquitous elsewhere, the frozen chloride-PMS system has potential as a method for energy-free and eco-friendly technology for the degradation of organic pollutants in cold environments.

## 1. Introduction

Synthetic organic dye compounds, such as azo dyes, are one of the most largely

⑲ 본 연구는 본 과제(PE24120)로 수행되었으며, 결과는 *Chemosphere* 2024, 359, 142261에 출간되었다.

produced industrial chemical products because of their wide use in textile, food, medicine, cosmetic, and pigment manufacturing.[1] According to the literature, those dye compounds are potentially hazardous to the environment and living things;[2] thus, dye-contaminated wastewater must be remediated before its release into natural water.[3, 4] However, dye pollutants are difficult to degrade using traditional biological and physicochemical wastewater treatment methods. Thus, many technical strategies, including advanced oxidation processes (AOPs), have been proposed to degrade organic dye compounds effectively.[5-8]

The effectiveness of AOPs relies on the generation of the hydroxyl radical (OH), which is a highly aggressive species owing to its high oxidation potential ($E_0(OH/H_2O)$ = 2.70 $V_{NHE}$).[9, 10] OH can be generated from the activation of hydrogen peroxide ($H_2O_2$) through a Fenton reaction[11] or 254 nm UV light illumination.[12] Meanwhile, persulfate-based AOPs have been demonstrated as an alternative to conventional $H_2O_2$-AOPs because of their stable precursor, powerful capability, and good working in broad operational conditions.[13, 14] Similar to $H_2O_2$, which is activated by catalyst and energy insertion, persulfate (that indicates peroxymonosulfate (PMS) and peroxidisulfate (PDS) collectively) can also be activated to generate various reactive species, such as OH, $SO_4^{\cdot-}$, $^1O_2$, and $O_2^{\cdot-}$. Notably, some nucleophiles can be oxidized by PMS and generate a selective oxidizing species, such as $ClO^-$ and $CO_3^{\cdot-}$ ($E_0(ClO^-/Cl^-)$ = 0.9 $V_{NHE}$[8] and $E_0(CO_3^{\cdot-}/CO_3^{2-})$ = 1.56 $V_{NHE}$[15]).[16, 17] Accordingly, the degradation of some electron-rich organic compounds in PMS-based AOP can be significantly improved by the presence of some anion species (e.g., $Cl^-$) because the selective secondary oxidant (e.g., $ClO^-$) can persist and intensely attack the target organic compound, while a non-selective oxidant could rapidly disappear due to its non-selective nature.[7, 18-20] It is remarkable that, the presence of background anions, such as $Cl^-$ or $HCO_3^-/CO_3^{2-}$, have been generally considered an efficiency-decreasing factor for the oxidative wastewater treatment system because the oxidation capability of the aforementioned selective reactive oxidizing species is less than that of the non-selective oxidants (e.g., $E_0(SO_4^{\cdot-}/SO_4^{2-})$ = 2.43 $V_{NHE}$ [15] and $E_0(OH/H_2O)$ = 2.70 $V_{NHE}$).[21-29]

Previously, the PMS activation by ozone ($O_3$) was studied.[30] The reaction mechanism is similar to the well-known peroxone reaction: the generation of OH from the reaction between $H_2O_2$ and $O_3$.[31] The noteworthy aspect of this research is that the oxidation efficiency derived from PMS can be improved not only by the presence of anion species but also by the coexistence of another oxidant, namely, $O_3$ in that study. In addition, the reaction between PMS and free chlorine (e.g., HOCl) in high-temperature conditions (above 50℃) has been demonstrated to generate OH.[17] Notably, many studies of PMS mediated systems have discussed that chloride can be oxidized by PMS to generate HOCl. However, HOCl has only been considered as a secondary generated oxidant from chloride oxidation

(not primary oxidant), and the influence of HOCl on the PMS system has not been considered.

Recently, it is recognized that the rate of redox reaction in solution is significantly enhanced by freezing process.[32, 33] Le et al. reported that the reactivity of PMS can be enhanced by freezing the solution through a non-radical oxidation mechanism (direct electron transfer from organic compounds to PMS).[34] Generally, the freezing process retards a chemical reaction by decreasing the temperature and hindering molecular mobility. However, the literature has suggested that the oxidation capability of PMS is significantly improved in the ice phase by the freezing concentration effect.[35] However, although the frozen PMS system effectively degraded furfuryl alcohol and pharmaceuticals in Le et al., the degradation of phenols such as phenol, bisphenol A, and methylphenol were not effectively degraded by PMS alone.[34] On the other hand, the addition of chloride significantly improved the efficacy of the frozen PMS system; the phenols were effectively degraded in the freezing/PMS/$Cl^-$ system because of the cascade generation of HOCl in ice. It is noteworthy that achieving comparable phenol degradation efficiency in the aqueous phase (~25℃) requires a much larger amount of chloride than in the frozen phase.[36] Similarly, Ahn et al. proposed that the frozen bicarbonate-cooperated PMS system needs smaller amounts of reactants (in here, sodium bicarbonate and PMS) than the liquid condition does to abate phenolic pollutants in water.[37] Because of (i) the low use of PMS and sodium chloride and (ii) the simplicity of the method, which requires no special equipment (spontaneous freezing) or follow-up process (natural reagents), the freezing-induced chloride-PMS system is a potential water treatment technology when operated in cold areas such as high latitude regions and at mild-latitudes in winter.

In this research, we demonstrated the efficacy of the freezing-induced chloride-PMS system on synthetic organic dye compound oxidation and considered the interactive NaCl/PMS mixture. We selected AO7 as a representative dye compound, monitored its degradation in the frozen condition, compared it with the aqueous condition, and conducted a detailed investigation of the oxidation system. The concentration changes of dye in the reaction time were monitored. The dependence on operation parameters, such as temperature, pH, reagent concentration, and background substances effect, were investigated. Next, the major oxidant was identified, and the oxidation mechanism was analyzed by measuring the total organic carbon (TOC) concentration and using the ultrahigh performance liquid chromatography electrospray ionization mass spectrometry (UHPLC-MS) equipment. Owing to the inherent reactivity of PMS, there are different oxidation mechanisms in the chloride-PMS system compared to the NaOCl system. Finally, we used ECOSAR prediction to consider and predict the toxic aspect of the AO7 degradation by-products.

## 2. Experimental Section

### 2.1. Chemical reagents

The chemical reagents used in this study included peroxymonosulfate compound (Sigma-Aldrich, OXONE), sodium chloride (Sigma-Aldrich), sodium hypochlorite (Sigma-Aldrich), orange II sodium salt (Sigma-Aldrich, Acid Orange 7), rhodamine B (Sigma-Aldrich), Methylene Blue (Sigma-Aldrich), triethyl phosphate (Sigma-Aldrich), tris(2-chloroethyl) phosphate (Sigma-Aldrich), diphenyl phosphate (Sigma-Aldrich), acetaminophen (Sigma-Aldrich), ibuprofen (Sigma-Aldrich), carbamazepine (Sigma-Aldrich), sulfuric acid (Sigma-Aldrich), phosphoric acid (Sigma-Aldrich), methanol (Supelco), acetonitrile (Supelco), formic acid (Sigma-Aldrich), sodium bicarbonate (Sigma-Aldrich), sodium carbonate (Sigma-Aldrich), sodium hydroxide (Sigma-Aldrich), water-$^{18}O$ (97 atom % $^{18}O$, Aldrich), and perchloric acid (Sigma-Aldrich). All chemicals were of reagent grade and used as received without any further purification. The chemical solutions used in this study were prepared with ultrapure deionized water (18.2 MΩ cm), which was produced using a Milli-Q Water Purification System (Millipore).

### 2.2. Experimental procedure

The test solution was prepared in a 15 mL conical tube. PMS and NaCl stock solutions (100 mM) were added to a conical tube to obtain the desired concentrations. The 100 mM of NaOH and $HClO_4$ solutions were used for adjusting pH condition. Total 10 mL of solution was poured into a conical tube and sealed with a cap. After, prepared conical tubes are immersed in an ethanol cooling bath that provide a cold environment for freezing. At the moment, we start the check for the elapsed time. The frozen solution was withdrawn from the cooling bath at a sampling time point and thawed in the lukewarm water bath 30℃ at for 10 min. The thawed liquid sample was analyzed immediately. The experiments were conducted at least twice to confirm the reproducibility.

### 2.3. Analysis

UV-vis spectroscopy (Shimadzu, UV-2600) was used to monitor the characteristics of dye compounds and concentration of PMS. TOC was measured using a TOC analyzer (TOC-LCPH, Shimadzu).

High-pressure liquid chromatography (HPLC) (Agilent, 1260 Infinity II) was used to analyze the 1,3,5-trimethoxybenzene, benzoic acid, and hydroxybenzoic acid in this study: they were identified by examining the retention time (Poroshell 120 EC-C18 column (4.6 mm × 150 mm) was used) and the light-absorbance with respect to them (using a variable wavelength detector (G7114 1260VWD)). In the analysis, 0.1% (v/v) phosphoric acid and acetonitrile were used as the eluents.

The anion species concentrations were measured using an ion chromatograph (Dionex ICS-1100) with a suppressor (Dionex AERS 500), column (Dionex IonPac AS23), and conductivity detector. Sodium carbonate and bicarbonate solutions (0.477 and 0.067 g in 1 L, respectively) were used for elution.

The various organic compounds and AO7 oxidation intermediates were detected by UHPLC (Thermo Fisher Scientific, Vanquish) combined with a quadrupole-Orbitrap mass spectrometer (Thermo Fisher Scientific, Q Exactive Focus). Separation was performed using a Hypersil GOLD$^{TM}$ aQ column. The mobile phase was a mixture of formic acid solution (0.1% v/v; A) and acetonitrile/formic acid solution (0.1% v/v; B) at a flow rate of 0.3 mL/min. Gradient elution was programmed as follows: 5% B for 0-2 min, 5-100% B for 2-14 min, 100% B for 14-17 min, and 100-5% B for 17-21 min. The ionization was carried out in negative electrospray ionization (ESI) mode, and the operating parameters were set as follows: a detection range of 65 to 650 m/z, with a resolution of 70,000, spray voltage of -2.50 kV, capillary temperature of 320 °C, sheath gas flow rate of 40 a.u., auxiliary gas flow rate of 10 a.u., auxiliary gas heater temperature of 300 °C, S lens RF level of 50.0, maximum injection time of 200 ms, and an automatic gain control (AGC) target of $1\times10^6$. The MS/MS fragmentation was conducted in the HCD collision cell that is filled with pure N2 gas. The collision energy is 10, 30, and 50 eV. To observe $OCl^-$ in sample using 18O-H2O, we manually injected sample into the mass spectrometer, and the ionization parameter was changed as follow: a detection range of 50 to 56 m/z, with a resolution of 12,500, spray voltage of ?2.50 kV, capillary temperature of 320 °C, sheath gas flow rate of 12 a.u., auxiliary gas flow rate of 1 a.u., auxiliary gas heater temperature of 300 °C, S lens RF level of 50.0, maximum injection time of 200 ms, and an automatic gain control (AGC) target of $2\times10^4$. The obtained results were analyzed using the Free Style 1.5 $^{TM}$ (Thermo Fisher Scientific) and Compound Discoverer 3.2$^{TM}$ (Thermo Fisher Scientific) software with Chemspider and mzCloud databases to identify and confirm the detected byproducts.

The in-silico toxicity prediction for the AO7 degradation byproduct is calculated by ECOSAR Application v2.2 (Unite States Environmental Protection Agency).

## 3. Result and discussion

### 3.1. The enhancing effect of freezing on the dye bleaching by chloride-PMS

The bleaching efficiencies of dye compound by the chloride-PMS system was compared in the freezing and aqueous conditions (Figure 1a). Here, we refer that the frozen condition indicates the solution was once frozen and thawed, and the aqueous condition means the solution stayed in 20℃. We used the AO7 as a representative dye compound. The initial

concentration of AO7 was set to 50 μM. During the reaction period of 4 h at $[PMS]_0$ = 0.5 mM, $[NaCl]_0$ = 1 mM, and pHi = 3, the prominent absorbance changes in AO7 were observed in the frozen condition (-20℃), and only slight changes were observed in the aqueous condition (20℃). According to the literature, the reaction of PMS and chloride produces hypochlorous acid (HOCl), an effective dye-bleaching reagent.[36] Thus, the increased dye bleaching in the freezing system can probably be attributed to the freezing-accelerated generation of HOCl, resulting from the reaction between chloride and PMS, owing to the freeze concentration effect.[36] Accordingly, AO7 showed that the absorbance value (note that the absorbance is $-\log10(I/I_0)$; $I_0$ = incident reference light intensity and I = transmitted light intensity) at 484 nm varied from ca. 1.23 to 1.17 in the aqueous condition and to ca. 0.21 in the frozen condition, respectively. The inserted picture in Figure 1a apparently show that the color in the frozen condition is lighter than that in the aqueous condition. Moreover, the degradation of another dye compound, rhodamine B, in the frozen system was also identified: the intensity at 552 nm for Rhodamine B changed from ca. 3.471 to 3.33 and 0.253 in the aqueous and frozen conditions, respectively. Therefore, dye bleaching can be effectively accomplished in the frozen chloride-PMS system. This dye bleaching induced by the frozen chloride-PMS system was not affected by adding $HClO_4$ to adjust the pH of the solution. As shown in Figure 1b, AO7 degradation occurred regardless of the type of utilized pH adjusting reagent (i.e., $HClO_4$ and $H_2SO_4$). In addition, there were no color changes when NaCl was absent in the solution regardless of freezing or aqueous condition (i.e., the w/o NaCl case in Figure 2a); thus, chloride is necessary to activate the PMS for dye bleaching.

### 3.2. AO7 degradation by the frozen chloride-PMS in various experimental condition

We further investigated the effect of reaction parameters, such as chloride concentration, PMS concentration, reaction temperature, and solution pH before freezing, on AO7 degradation. Figure 2a-d shows the chloride and PMS concentration dependence of AO7 degradation in the chloride-PMS. Marginal AO7 degradation was observed when NaCl or PMS were absent (i.e., w/o NaCl and w/o PMS). Especially, only PMS alone did not decompose AO7 effectively, despite PMS being a strong oxidizing reagent (w/o NaCl in Figure 2a). Thus, AO7 is inert to the inherent reactivity of PMS. In addition, as mentioned above, HOCl is generated from the oxidation of chloride by PMS; thus, chloride is essential to the PMS-mediated dye-bleaching system. Accordingly, AO7 degradation was increased by increasing the initial NaCl and PMS concentrations (Figure 2a and 2c). However, the AO7 degradation rate reached saturation when the NaCl and PMS concentration was increased over 1 mM. When the solution was not frozen, AO7 degradation was negligible regardless of the initial concentrations of NaCl and PMS (Figure 2b and 2d). This result

implies that the freezing significantly enhanced the activation of PMS by NaCl for AO7 degradation.

On the other hand, the influence of freezing temperature was not significant regarding the amount of AO7 degradation after 4 h of freezing but affected the AO7 degradation rate: decolorization was slightly faster at lower freezing temperatures (Figure 2e). According to the previous research, the growing speed of ice crystal is affected by freezing temperature: the lower the freezing temperature, the more rapidly the ice crystals grow, and the volume of liquid brine decreases.[33, 38, 39] Hence, the volume of the space among ice grains should be proportionally decreased as the freezing temperature decreases (the volume of the liquid-like portion in ice grain boundaries is eliminated at temperatures below the eutectic point). Consequently, the concentration of chemical compounds (e.g., PMS and chloride) in the ice grain-boundary increases as the freezing temperature decreases and probably increases the chemical reaction rate.

Figure 2f shows the influence of the initial pH on AO7 degradation. The freezing-induced AO7 degradation was clearly observed in all the examined pH ranges. The degradation efficiency marginally varied when the initial pH ranged from 3 to 8. Because the acid dissociation constant of PMS has been known as $pK_{a1}$ = 0.4 and $pK_{a2}$ = 9.31, the PMS molecular speciation is probably not altered in the acidic to neutral pH range. In contrast, the AO7 degradation rate increased when the initial pH was over 9. Furthermore, the degradation of AO7 in the aqueous condition also markedly occurred in the base pH condition. It is noted that the oxidation capability of PMS can be improved in the basic condition: the oxidation of hydroxide by PMS generates a hydroperoxyl anion, and subsequently, $^1O_2$, and $O_2^-$ are produced from the chemical transformation of the hydroperoxyl anion.[40] Thus, the addition of alkali species (NaOH) into the solution should be the reason for the increased AO7 degradation at the base conditions.

### 3.3. Reactive species identification

Figure 3 shows the degradation of various organic compounds in the chloride-PMS system. The freezing process accelerated markedly the degradation of most organic compounds; however, some substances, such as methylene blue, triethyl phosphate, tris(2-chloroethyl) phosphate, and ibuprofen, exhibited only slight enhancements via freezing. Hence, the major reactive species in the chloride-PMS system are selective to the specific organic compound being targeted.

To identify the involvement of free-chlorine species in the frozen chloride-PMS, we estimated the reactive chlorine species (RCS) concentration during the freezing process. We exploited 1,3,5-trimethoxybenzene to conduct a derivatization method to estimate the RCS

level in the frozen chloride-PMS system. Notably, chlorination of 1,3,5-trimethoxybenzene leads to the formation of 1-chloro-2,4,6-trimethoxybenzene.[41] Specifically, a sample volume of 0.8 mL was mixed with 0.2 mL of 10 mM 1,3,5-trimethoxybenzene to produce the product. The RCS level of the sample was determined from the calibration curve obtained using sodium hypochlorite (NaOCl) and the signal intensity of 1-chloro-2,4,6-trimethoxybenzene. With a linear correlation coefficient (R2) of 0.9989, the RCS level was accurately measured within the range of 1000 μM of RCS. As shown in Figure 4a, when the RCS level increased, the level of PMS and chloride concentration decreased, indicating that the PMS and chloride were consumed to generate the RCS during freezing. However, we did not observe the highly oxidized chlorine-oxyanion products, such as chlorate; thus, PMS likely did not further oxidize RCS (data not shown). Most notably, the chloride consumption, approximately 285 μM at 4 h, was comparable to that of the generation of RCS, approximately 300 μM at 4 h. Thus, we inferred that the decreased chloride ions, which is oxidized by PMS, were almost converted to RCS, such as HOCl.

The increased oxidation of chloride during the freezing of the chloride-PMS system was attributed to the accumulation of reactants into the ice grain-boundaries during the freezing process. The concentration of reactants in the ice grain-boundary increased as the ice crystals grew. This phenomenon was demonstrated by the confocal Raman microscope image of the frozen chloride-PMS system (Figure 4b). The red dots represent the 984 $cm^{-1}$ Raman signal intensity derived from the 532 nm excitation source, which indicates the symmetric S-O stretching vibration of sulfate molecular (unfortunately, we did not observe the peak at 721 $cm^{-1}$ for Cl-O vibration, but instead of it, we depicted the highly intense S-O vibration signal to demonstrate the freezing concentration phenomenon). Clearly, the red area was condensed in the junction of three boundary lines, and the black area manifested at the ice bulk. Further, to confirm the freeze concentration effect for accelerated chloride oxidation by PMS, we examined the RCS generation in the aqueous chloride-PMS solution (20℃) with a high dose of the reactants (Figure 4c). The RCS generation clearly increased as the concentration of reactants increased. When the 5 mM of PMS and 10 mM of NaCl solution stayed in the aqueous phase at 20℃, ca. 200 μM RCS was produced during 8 h of reaction time. However, when the 2.5 mM PMS and 5 mM NaCl solution remained in the same condition, only 60 μM of RCS was produced. There are no RCS was detected when the reactant concentrations were further reduced. According to these results, we inferred that the freeze concentration effect might be a reason for the accelerated reaction between PMS and chloride in ice. We also need to mention that the generation of RCS was much higher and faster in the frozen condition than in the aqueous condition: approximately 300 μM RCS was produced in the ice phase,

while only 200 μM RCS was produced at 10 times high reactant concentration during 8 h in the liquid phase.

To identify whether HOCl is the main RCS, we monitored the UV absorbance of the sample at 292 nm, which is characteristic of the $OCl^-$ anion. Before measuring the sample absorption, we adjusted the solution pH to 10.50 by adding NaOH to deprotonate the HOCl molecule. As shown in Figure 4d, the absorption of the frozen chloride-PMS system at 292 nm clearly increased as the reaction progressed. The measured concentration of $OCl^-$ agreed well with the result obtained from 1,3,5-trimethoxybenzene (Figure 4a), indicating that approximately 280 μM of $OCl^-$ was present in the frozen chloride-PMS at 240 min.

### 3.4. AO7 oxidation mechanism in the frozen chloride-PMS system

As aforementioned, HOCl is a main oxidant in the chloride-PMS system. Thus, we investigated AO7 oxidation by HOCl to confirm the role of HOCl in the frozen chloride-PMS system. We injected NaOCl in an equivalent amount to the PMS concentration (500 μM) into the 50 μM AO7 solution and adjusted the solution pH to 3 (note that the $OCl^-$ is monoprotonated when the solution pH is between 1 and 8). As shown in Figure 5a, the AO7 concentration was totally eliminated by HOCl during 4 h of reaction time, regardless of the freezing and aqueous conditions (yellow bars). It is noted that the initial concentration of the RCS in the NaOCl solution was much higher than that of the chloride-PMS system because the generation of RCS from the oxidation of chloride by PMS requires time to generate in the chloride-PMS system. Hence, the high bleaching efficiency of AO7 in the NaOCl solution was attributed to its high initial concentration. However, it is remarkable that the TOC removal tendency is significantly different between the chloride-PMS system and the NaOCl system (red bars): ca. 14% of TOC was removed from the frozen chloride-PMS system, whereas negligible TOC removal was observed for the NaOCl system. Although HOCl is an effective bleaching reagent, this result suggests that an oxidation mechanism different from that of HOCl would probably be suitable in the frozen chloride-PMS system.

According to the literature, the oxidation of chloride by PMS produces $Cl_2$ via the two-electron transfer process,[42] and $Cl_2$ is subsequently hydrolyzed to HOCl when the solution pH is neutral or weakly acidic ($pK_{a1}$ = 1.1 and $pK_{a2}$ = 7.5).[43] Therefore, the following chemical reactions can be suggested for the generation of HOCl from chloride oxidation by PMS:

$$HSO_5^- + 2Cl^- + H^+ \rightarrow SO_4^{2-} + Cl_2 + H_2O \quad (1)$$

$$Cl_2 + H_2O \rightarrow HOCl + Cl^- + H^+ \quad (2)$$

The use of $^{18}O$-labeled water supports the hydrolysis of $Cl_2$ in the chloride-PMS system: in a chloride-PMS solution with normal distilled water ($^{16}O$-$H_2O$), $^{35}Cl^{16}O$ and $^{37}Cl^{16}O$ were

prevalent; however, in an environment with $^{18}O$-$H_2O$, $^{35}Cl^{18}O$ and $^{37}Cl^{18}O$ were dominant (Figures 5b). Hence, the oxygen source of HOCl in the chloride-PMS solution is water. Further, $Cl_2$ can react with $Cl^-$ to produce strong oxidant $Cl_3^-$; however, it is questionable whether the $Cl_3^-$ could contribute to TOC removal, because the frozen NaOCl system also possibly involves this oxidant.

$$HOCl + Cl^- + H+ \rightarrow Cl_2 + H_2O \text{ (reverse reaction of eq. 2)} \quad (3)$$

$$Cl_2 + Cl^- \rightarrow Cl_3^- \quad (4)$$

Notably, eq. (3) can emerge at highly acidic condition, and freezing the pH 3 solution reduces the pH in ice to below 1;[36] however, the TOC was not reduced at all in the frozen NaOCl system (Figure 5a). The limited TOC reduction observed in the NaOCl system suggests that another oxidizing agent is involved in the TOC reduction besides HOCl in the frozen chloride-PMS system. Due to its inherent reactivity, PMS can play a key role in TOC reduction. While PMS has a limited ability to degrade the parent compound (AO7), it can serve as an oxidizing agent for degrading intermediates generated from the reaction of HOCl with AO7. Similar phenomena, where PMS exhibits limited reactivity towards the parent compound but high reactivity towards intermediates, have been observed in previous studies.[36, 44]

In the previous research for the chloride activated PMS, OH is generated in the heat-activated chloride-PMS system.[17] Hence, we examined whether the 4-hyrdoxybenzoic acid is generated from the oxidation of benzoic acid in the freezing-induced chloride-PMS system (Figure 5c). However, the oxidation of benzoic acid was not observed at all. Furthermore, as mentioned above, we did not observe the chlorate generation which can be a proxy for OH involved oxidation in the presence of $Cl^-$.[17] In addition, Cl and $Cl_2^-$ could participate in the reaction; however, we excluded this scenario, because the benzoic acid can be oxidized by Cl and $Cl_2^-$.[45] Thus, these radical species are probably not responsible for the TOC reduction in the frozen chloride-PMS system. Other experimental observations also support that OH is not involved in the TOC reduction in the frozen chloride-PMS system. Figure 5d shows the TOC level in varying initial AO7 concentrations in the 1 mM PMS and 2 mM $Cl^-$ solution with freezing. The TOC variation has a marginal correlation with the increase in AO7 concentration. Instead, the TOC reductions seem to be maintained at an almost same level in the initial AO7 concentration. According to those results, a likely explanation is that only a certain ratio (approximately 15%) in the initial AO7 contributed to the TOC decrease in the system, regardless of the intensity of the oxidation environment. Thus, we inferred that the decreased TOC in the frozen chloride-PMS system is resulted from the volatilization of the AO7 degradation intermediate, which is produced from the distinguishable oxidation pathway from the HOCl system. Notably, the TOC reduction is a principal advantage of the AOPs technique because the detoxification (note

that the toxicity is derived from the organic pollutant) can be accomplished by eliminating the TOC in the solution (for instance, its transformation into the non-toxic $CO_2$ via oxidation by OH). In this manner, the frozen chloride-PMS system apparently has benefits as against the direct chlorination process (that injects the free chlorine directly), owing to the TOC removal aspects.

### 3.5. The AO7 degradation pathway and the in-silico toxicity estimation for AO7 degradation intermediates in the frozen chloride-PMS system

The difference in the AO7 oxidation mechanism between the NaOCl system and frozen chloride-PMS system was also identified in the intermediate investigation by using the ultrahigh performance liquid chromatography electrospray ionization mass spectrometry (UHPLC-MS) equipment. Figure 6 presents the detected AO7 degradation intermediates and their signal intensities at 0.5, 1, 2, 3, 4, 6, and 10 h of reaction time. When the chloride-PMS system was in the aqueous condition, AO7 was not degraded; thus, no intermediates were detected at this case (dark-blue bars). Owing to that the HOCl is a common oxidant for the oxidation of AO7, chlorinated AO7 were identified in both of the NaOCl system and the frozen chloride-PMS system: Note that the chemical formula of m/z 361.0062 was assigned as the one-chlorine more and one-hydrogen less than the AO7 anion of m/z 327.0045. In addition, the intensity ratio between m/z 361.0062 (intensity for $^{35}Cl$) and 363.0029 (intensity for $^{37}Cl$) strongly supports that this compound contains a chloride atom (data not shown). Hence, we considered that the signal m/z 361.0062 corresponded to the chlorine-substituted anionic AO7 compound. As shown in the Figure 6, the intensity of m/z 361.0062 was highest at 0.5 h of reaction time and decreased as the reaction time elapsed. As a result, dichlorinated AO7 (m/z 394.9668) was detected, and its intensity was highest at 1 h of reaction time. However, the intensity of dichlorinated AO7 (m/z 394.9668) and trichlorinated AO7 (m/z 428.9729) in the NaOCl system was significantly abated while substantially high signal was detected in the frozen chloride-PMS system. This result is likely attributed to an azo linkage being readily dissociated in a high initial concentration of HOCl in the NaOCl system, whereas the AO7 molecule is sustained for a while in the chloride-PMS system because HOCl generation from the chloride oxidation requires time to generate. Further, as the reaction progresses, the AO7 molecule separated into two parts. Hence, the naphthalene-type intermediates (e.g., m/z 206.9850, and 189.0817) and benzene sulfonate-type intermediates (e.g., m/z 201.9810) were detected. The molecular structures were estimated based on the MS/MS analysis and references.[40, 46, 47] Interestingly, some species were markedly detected in the frozen chloride-PMS system exclusively (m/z 428.9729, 224.9334, 142.9897, 254.9137, 274.9079, and 269.9039). This finding implies that an alternative oxidation pathway, which does not

proceed via HOCl, occurred in the frozen chloride-PMS system. It is noted that PMS can oxidize various organic substances via the oxygen transfer process, without applying any activation method.[48] Thus, some intermediates produced from the oxidation by HOCl are plausibly vulnerable to the residual PMS in the chloride-PMS system. Subsequently, these intermediates can be oxidized by HOCl or PMS again, and those types of oxidation can be repeated. Hence, this synergetic progress presumably causes the TOC decrease in the frozen chloride-PMS system, which differs from that of the NaOCl system.

Figure 7 shows the chemical structure-based toxicity prediction for the detected AO7 degradation intermediates. The calculation was conducted using the ECOSAR program (Unite States Environmental Protection Agency provided). In the Figure 7, the half-lethal concentration for fish and daphnid (LC50) and the half-effective concentration for green algae (EC50) are presented on the right side: the height of the bar is a log scale of the exact value. Also, the intensities of the ion current at the Orbitrap (m/z analyzer) of the compounds are presented at the left side (note that the intensities are of 10 h reaction sample, which is the final reaction time). In fact, the intensity of AO7 (327.0445) is most intensive signal among the compounds because the c.a. 10% of the initial AO7 still remained in the frozen chloride-PMS solution. Notably, the intensities of the m/z 361.0062, 394.9668, 428.9729, 222.9800, 244.9334, 201.9810, and 269.9039 were exceeded the $10^7$ value at the frozen chloride-PMS system. However, according to the Figure 6, the varying tendencies of the m/z 361.0062, 394.9668, 428.9729, 222.9800, and 244.9334 decreased, while m/z 201.9810 and 269.9039 have increasing tendencies during the reaction time. Hence, we supposed that these two compounds were the major final product in the frozen chloride-PMS system. In addition, we need to mention that the m/z 201.9810 and 269.9039 have the largest LC50 value for fish and daphnid, and EC50 value for green algae. Thus, the frozen chloride-PMS system can be considered a toxicity-decreasing process. In contrast, the m/z 206.9850, 209.0007, and 189.0187 were the dominant intermediates in the frozen and aqueous NaOCl system. The LC50 and EC50 values of those compounds were less than those of the original AO7; hence, the toxic compound was produced during the chlorination process. It should be considered that, we could not provide the exact concentration of the final products in this research. Furthermore, the collected value from ECOSAR was only for the prediction of toxicity of by-products. Therefore, further biological testing is required to estimate the effect of the system on aquatic life.

## 4. Conclusion

In this study, we investigated the dye pollutant degradation in a frozen chloride-PMS system. The PMS oxidized chloride to produce the reactive chlorine species and the azo dye AO7 was decomposed by the reactive chlorine species. However, the degradation of

AO7 was marginally observed when the chloride/PMS mixture is remained in the aqueous phase. Apparently, the freezing process enhanced the chemical reaction and generated various AO7 degradation by-products. The chemical reaction boosting was attributed to the freezing concentration effect. Notably, AO7 degradation can also proceeded in the NaOCl system, but the TOC level in the system was not decreased. However, approximately a 15% TOC reduction was observed in the frozen chloride-PMS system. It is noted that the frozen chloride-PMS system apparently has benefits as against the direct chlorination process (that inject the free chlorine directly), owing to TOC removal. Taking into the account that the freezing phenomenon is spontaneous at high latitude regions and at mid-latitudes in winter, and chloride is ubiquitous elsewhere, the frozen chloride-PMS system is a potential method for energy-free, eco-friendly technology for the degradation of organic pollutants in cold environments.

## REFERENCES


[1] Bafana, A., S.S. Devi, T. Chakrabarti, Azo dyes: past, present and the future, Environmental Reviews 19 (2011) 350-371

[2] Tkaczyk, A., K. Mitrowska, A. Posyniak, Synthetic organic dyes as contaminants of the aquatic environment and their implications for ecosystems: A review, Science of The Total Environment 717 (2020) 137222

[3] Ahmad, A.A., B.H. Hameed, Fixed-bed adsorption of reactive azo dye onto granular activated carbon prepared from waste, Journal of Hazardous Materials 175 (2010) 298-303

[4] Osma, J.F., V. Saravia, J.L. Toca-Herrera, S.R. Couto, Sunflower seed shells: A novel and effective low-cost adsorbent for the removal of the diazo dye Reactive Black 5 from aqueous solutions, Journal of Hazardous Materials 147 (2007) 900-905

[5] Yang, S., P. Wang, X. Yang, L. Shan, W. Zhang, X. Shao, R. Niu, Degradation efficiencies of azo dye Acid Orange 7 by the interaction of heat, UV and anions with common oxidants: Persulfate, peroxymonosulfate and hydrogen peroxide, Journal of Hazardous Materials 179 (2010) 552-558

[6] Yuan, R., S.N. Ramjaun, Z. Wang, J. Liu, Effects of chloride ion on degradation of Acid Orange 7 by sulfate radical-based advanced oxidation process: Implications for formation of chlorinated aromatic compounds, Journal of Hazardous Materials 196 (2011) 173-179

[7] Wang, P., S. Yang, L. Shan, R. Niu, X. Shao, Involvements of chloride ion in decolorization of Acid Orange 7 by activated peroxydisulfate or peroxymonosulfate oxidation, Journal of Environmental Sciences 23 (2011) 1799-1807


KOPRI 극지연구소

[8] Kim, S., S.K. Choi, B.Y. Yoon, S.K. Lim, H. Park, Effects of electrolyte on the electrocatalytic activities of RuO2/Ti and Sb-SnO2/Ti anodes for water treatment, Applied Catalysis B: Environmental 97 (2010) 135-141

[9] Comninellis, C., A. Kapalka, S. Malato, S.A. Parsons, I. Poulios, D. Mantzavinos, Advanced oxidation processes for water treatment: advances and trends for R&D, Journal of Chemical Technology & Biotechnology 83 (2008) 769-776

[10] Fernández-Castro, P., M. Vallejo, M.F. San Román, I. Ortiz, Insight on the fundamentals of advanced oxidation processes. Role and review of the determination methods of reactive oxygen species, Journal of Chemical Technology & Biotechnology 90 (2015) 796-820

[11] Bokare, A.D., W. Choi, Review of iron-free Fenton-like systems for activating $H_2O_2$ in advanced oxidation processes, Journal of Hazardous Materials 275 (2014) 121-135

[12] Baxendale, J.H., J.A. Wilson, The photolysis of hydrogen peroxide at high light intensities, Transactions of the Faraday Society 53 (1957) 344-356

[13] Ahn, Y.-Y., E. Yun, Heterogeneous metals and metal-free carbon materials for oxidative degradation through persulfate activation: A review of heterogeneous catalytic activation of persulfate related to oxidation mechanism, Korean Journal of Chemical Engineering 36 (2019) 1767-1779

[14] Lee, J., U. von Gunten, J.-H. Kim, Persulfate-Based Advanced Oxidation: Critical Assessment of Opportunities and Roadblocks, Environmental Science & Technology 54 (2020) 3064-3081

[15] Huie, R.E., C.L. Clifton, P. Neta, Electron transfer reaction rates and equilibria of the carbonate and sulfate radical anions, International Journal of Radiation Applications and Instrumentation. Part C. Radiation Physics and Chemistry 38 (1991) 477-481

[16] Sun, Y., H. Xie, C. Zhou, Y. Wu, M. Pu, J. Niu, The role of carbonate in sulfamethoxazole degradation by peroxymonosulfate without catalyst and the generation of carbonate racial, Journal of Hazardous Materials 398 (2020) 122827

[17] Ahn, Y.-Y., J. Choi, M. Kim, M.S. Kim, D. Lee, W.H. Bang, E.-T. Yun, H. Lee, J.-H. Lee, C. Lee, S.K. Maeng, S. Hong, J. Lee, Chloride-Mediated Enhancement in Heat-Induced Activation of Peroxymonosulfate: New Reaction Pathways for Oxidizing Radical Production, Environmental Science & Technology 55 (2021) 5382-5392

[18] Rivas, F.J., R.R. Sol?s, Chloride promoted oxidation of tritosulfuron by peroxymonosulfate, Chemical Engineering Journal 349 (2018) 728-736

[19] Wang, Z., M. Feng, C. Fang, Y. Huang, L. Ai, F. Yang, Y. Xue, W. Liu, J. Liu, Both degradation and AOX accumulation are significantly enhanced in UV/peroxymonosulfate/4-chlorophenol/Cl? system: two sides of the same coin?, RSC Advances 7 (2017) 12318-12321

KOPRI 극지연구소

[20] Bennedsen, L.R., J. Muff, E.G. Søgaard, Influence of chloride and carbonates on the reactivity of activated persulfate, Chemosphere 86 (2012) 1092-1097

[21] Yang, J.-F., L.-M. Yang, S.-B. Zhang, L.-H. Ou, C.-B. Liu, L.-Y. Zheng, Y.-F. Yang, G.-G. Ying, S.-L. Luo, Degradation of azole fungicide fluconazole in aqueous solution by thermally activated persulfate, Chemical Engineering Journal 321 (2017) 113-122

[22] Mora, V.C., J.A. Rosso, G. Carrillo Le Roux, D.O. M?rtire, M.C. Gonzalez, Thermally activated peroxydisulfate in the presence of additives: A clean method for the degradation of pollutants, Chemosphere 75 (2009) 1405-1409

[23] Qian, Y., X. Guo, Y. Zhang, Y. Peng, P. Sun, C.-H. Huang, J. Niu, X. Zhou, J.C. Crittenden, Perfluorooctanoic Acid Degradation Using UV-Persulfate Process: Modeling of the Degradation and Chlorate Formation, Environmental Science & Technology 50 (2016) 772-781

[24] Lee, M.-Y., W.-L. Wang, Q.-Y. Wu, N. Huang, Z.-B. Xu, H.-Y. Hu, Degradation of dodecyl dimethyl benzyl ammonium chloride (DDBAC) as a non-oxidizing biocide in reverse osmosis system using UV/persulfate: Kinetics, degradation pathways, and toxicity evaluation, Chemical Engineering Journal 352 (2018) 283-292

[25] Ma, J., Y. Yang, X. Jiang, Z. Xie, X. Li, C. Chen, H. Chen, Impacts of inorganic anions and natural organic matter on thermally activated persulfate oxidation of BTEX in water, Chemosphere 190 (2018) 296-306

[26] Luo, C., J. Jiang, J. Ma, S. Pang, Y. Liu, Y. Song, C. Guan, J. Li, Y. Jin, D. Wu, Oxidation of the odorous compound 2,4,6-trichloroanisole by UV activated persulfate: Kinetics, products, and pathways, Water Research 96 (2016) 12-21

[27] Chen, L., T. Cai, C. Cheng, Z. Xiong, D. Ding, Degradation of acetamiprid in UV/$H_2O_2$ and UV/persulfate systems: A comparative study, Chemical Engineering Journal 351 (2018) 1137-1146

[28] Guan, Y.-H., J. Ma, D.-K. Liu, Z.-f. Ou, W. Zhang, X.-L. Gong, Q. Fu, J.C. Crittenden, Insight into chloride effect on the UV/peroxymonosulfate process, Chemical Engineering Journal 352 (2018) 477-489

[29] Yang, Y., J.J. Pignatello, J. Ma, W.A. Mitch, Comparison of Halide Impacts on the Efficiency of Contaminant Degradation by Sulfate and Hydroxyl Radical-Based Advanced Oxidation Processes (AOPs), Environmental Science & Technology 48 (2014) 2344-2351

[30] Yang, Y., J. Jiang, X. Lu, J. Ma, Y. Liu, Production of Sulfate Radical and Hydroxyl Radical by Reaction of Ozone with Peroxymonosulfate: A Novel Advanced Oxidation Process, Environmental Science & Technology 49 (2015) 7330-7339

[31] Lee, Y., D. Gerrity, M. Lee, S. Gamage, A. Pisarenko, R.A. Trenholm, S. Canonica, S.A. Snyder, U. von Gunten, Organic Contaminant Abatement in Reclaimed Water by

$UV/H_2O_2$ and a Combined Process Consisting of $O_3/H_2O_2$ Followed by $UV/H_2O_2$: Prediction of Abatement Efficiency, Energy Consumption, and Byproduct Formation, Environmental Science & Technology 50 (2016) 3809-3819

[32] Takenaka, N., A. Ueda, T. Daimon, H. Bandow, T. Dohmaru, Y. Maeda, Acceleration Mechanism of Chemical Reaction by Freezing: The Reaction of Nitrous Acid with Dissolved Oxygen, The Journal of Physical Chemistry 100 (1996) 13874-13884

[33] Kim, K., W. Choi, Enhanced Redox Conversion of Chromate and Arsenite in Ice, Environmental Science & Technology 45 (2011) 2202-2208

[34] Le, N.T.H., J. Ju, B. Kim, M.S. Kim, C. Lee, S. Kim, W. Choi, K. Kim, J. Kim, Freezing-enhanced non-radical oxidation of organic pollutants by peroxymonosulfate, Chemical Engineering Journal 388 (2020) 124226

[35] O'Concubhair, R., J.R. Sodeau, The Effect of Freezing on Reactions with Environmental Impact, Accounts of Chemical Research 46 (2013) 2716-2724

[36] Kim, K., N.T.H. Le, A.Q.K. Nguyen, Y.-Y. Ahn, B. Kim, G. Shin, W. Choi, J. Kim, Freezing-induced activation of the binary chloride-Oxone system to free chlorine and its application in water treatment, Chemical Engineering Journal 428 (2022) 131134

[37] Ahn, Y.-Y., J. Kim, K. Kim, Activation of peroxymonosulfate by bicarbonate and acceleration of the reaction by freezing, Science of The Total Environment 785 (2021) 147369

[38] Kim, K., J. Kim, A.D. Bokare, W. Choi, H.-I. Yoon, J. Kim, Enhanced Removal of Hexavalent Chromium in the Presence of $H_2O_2$ in Frozen Aqueous Solutions, Environmental Science & Technology 49 (2015) 10937-10944

[39] Ju, J., J. Kim, K. Vetráková, J. Seo, D. Heger, C. Lee, H.-I. Yoon, K. Kim, J. Kim, Accelerated redox reaction between chromate and phenolic pollutants during freezing, Journal of Hazardous Materials 329 (2017) 330-338

[40] Qi, C., X. Liu, J. Ma, C. Lin, X. Li, H. Zhang, Activation of peroxymonosulfate by base: Implications for the degradation of organic pollutants, Chemosphere 151 (2016) 280-288

[41] Lau, S.S., R.P. Dias, K.R. Martin-Culet, N.A. Race, M.H. Schammel, K.P. Reber, A.L. Roberts, J.D. Sivey, 1,3,5-Trimethoxybenzene (TMB) as a new quencher for preserving redox-labile disinfection byproducts and for quantifying free chlorine and free bromine, Environmental Science: Water Research & Technology 4 (2018) 926-941

[42] Lente, G., J. Kalmár, Z. Baranyai, A. Kun, I. Kék, D. Bajusz, M. Takács, L. Veres, I. Fábián, One- Versus Two-Electron Oxidation with Peroxomonosulfate Ion: Reactions with Iron(II), Vanadium(IV), Halide Ions, and Photoreaction with Cerium(III), Inorganic Chemistry 48 (2009) 1763-1773

[43] Deborde, M., U. von Gunten, Reactions of chlorine with inorganic and organic

KOPRI 극지연구소

compounds during water treatment-Kinetics and mechanisms: A critical review, Water Research 42 (2008) 13-51

[44] T. Chen, R. Wang, A. Zhang, T. Xu, R. Xiao, W. Chu, D. Yin, Peroxymonosulfate/chloride disinfection versus sodium hypochlorite disinfection in terms of the formation and estimated cytotoxicity of $CX_3R$-type disinfection by-products under the same dose of free chlorine, Chem. Eng. J. 391 (2020), 123557.

[45] Park, H., C.D. Vecitis, M.R. Hoffmann, Electrochemical Water Splitting Coupled with Organic Compound Oxidation: The Role of Active Chlorine Species, The Journal of Physical Chemistry C 113 (2009) 7935-7945

[46] Duan, L., Y. Chen, K. Zhang, H. Luo, J. Huang, A. Xu, Catalytic degradation of Acid Orange 7 with hydrogen peroxide using CoxOy-N/GAC catalysts in a bicarbonate aqueous solution, RSC Advances 5 (2015) 84303-84310

[47] Zheng, J., Z. Gao, H. He, S. Yang, C. Sun, Efficient degradation of Acid Orange 7 in aqueous solution by iron ore tailing Fenton-like process, Chemosphere 150 (2016) 40-48

[48] Yang, Y., G. Banerjee, G.W. Brudvig, J.-H. Kim, J.J. Pignatello, Oxidation of Organic Compounds in Water by Unactivated Peroxymonosulfate, Environmental Science & Technology 52 (2018) 5911-5919

KOPRI
극지연구소

## FIGURES

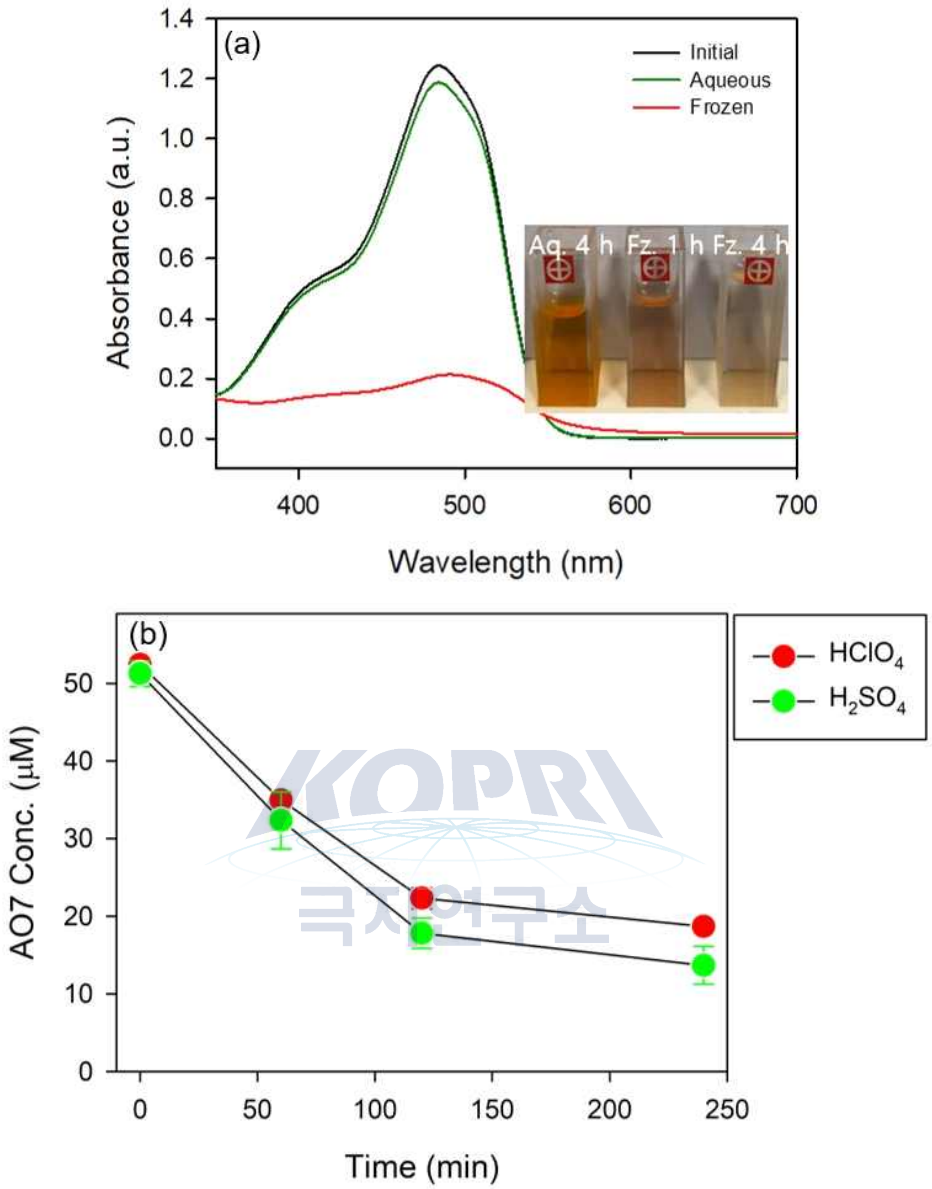



**Figure 1.** (a) The absorbance spectrum of AO7 in the chloride-PMS system. Experiment condition: $[PMS]_0$ = 0.5 mM; $[NaCl]_0$ = 1 mM; $[AO7]_0$ = 50 μM; pHi = 3 ($HClO_4$ adjusted); Temperature = 20℃ (Aq.) / -20℃ (Fz.); Reaction time = 4 h. (b) AO7 degradation in the chloride-PMS system using $HClO_4$ and $H_2SO_4$ as pH adjusting reagent. Experiment condition: $[PMS]_0$ = 0.5 mM; $[NaCl]_0$ = 1 mM; $[AO7]_0$ = 50 μM; pHi = 3 using $HClO_4$ and $H_2SO_4$; Temperature = -20℃

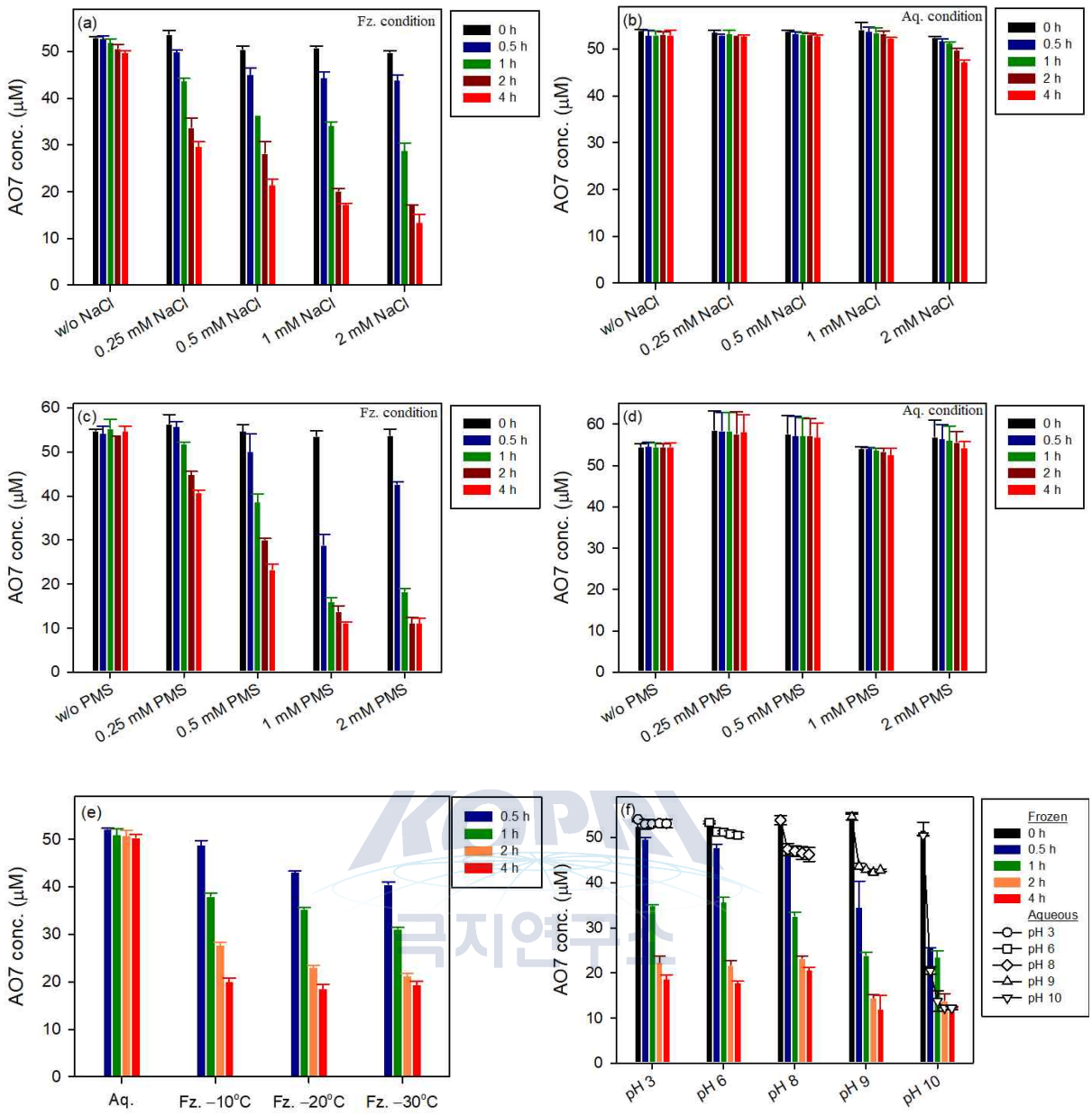



**Figure 2.** The degradation of AO7 in various experimental condition. (a) AO7 degradation in initial NaCl concentration change in ice. (b) AO7 degradation in initial NaCl concentration change in water. Experiment condition: $[PMS]_0$ = 0.5 mM; $[AO7]_0$ = 50 μM; pHi = 3 ($HClO_4$ adjusted); Temperature = 20℃ (Aq.) / -20℃ (Fz.). (c) AO7 degradation in initial PMS concentration change in ice. (d) AO7 degradation in initial PMS concentration change in water. Experiment condition: $[NaCl]_0$ = 1 mM; $[AO7]_0$ = 50 μM; pHi = 3 ($HClO_4$ adjusted); Temperature = 20℃ (Aq.) / -20℃ (Fz.). (e) The freezing temperature effect on AO7 degradation. Experiment condition: $[PMS]_0$ = 0.5 mM; $[NaCl]_0$ = 1 mM; $[AO7]_0$ = 50 μM; pHi = 3 ($HClO_4$ adjusted). (f) The initial pH effect on AO7 degradation. Experiment condition: $[PMS]_0$ = 0.5 mM; $[NaCl]_0$ = 1 mM; $[AO7]_0$ = 50 μM; Temperature = 20℃ (Aq.) / -20℃ (Fz.).

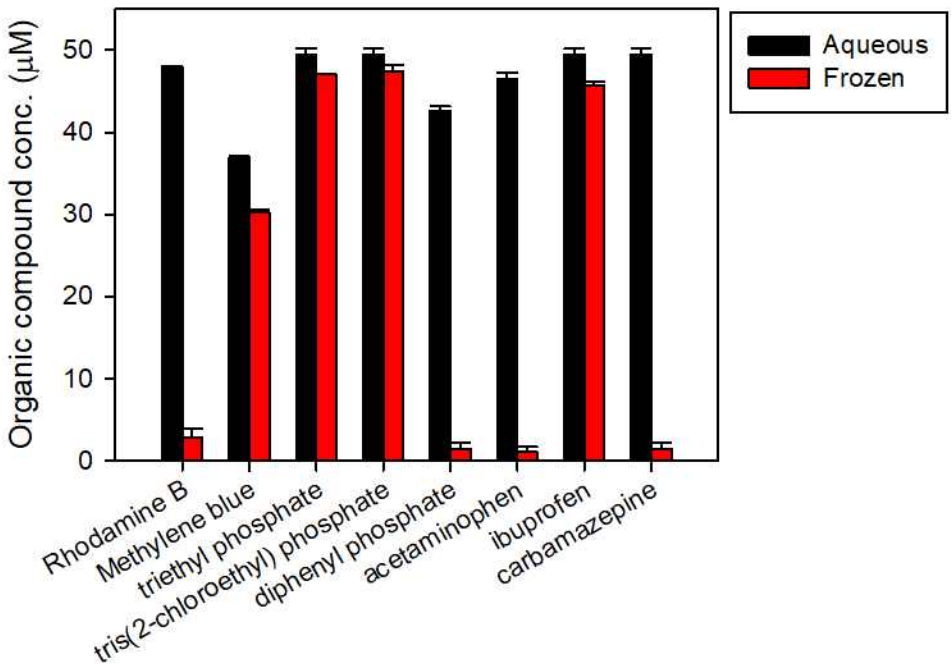
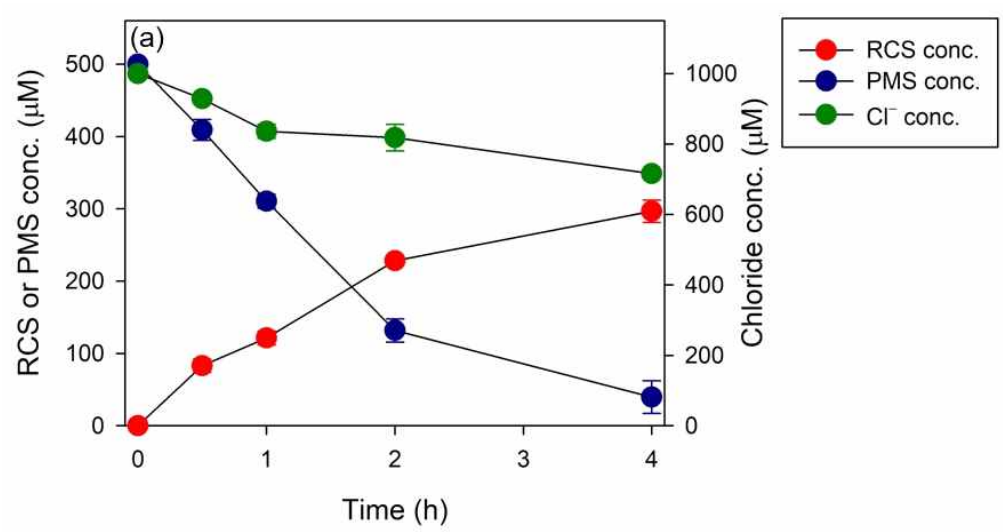
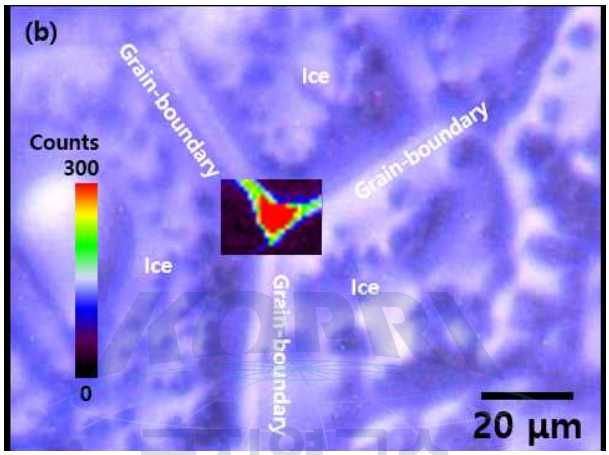
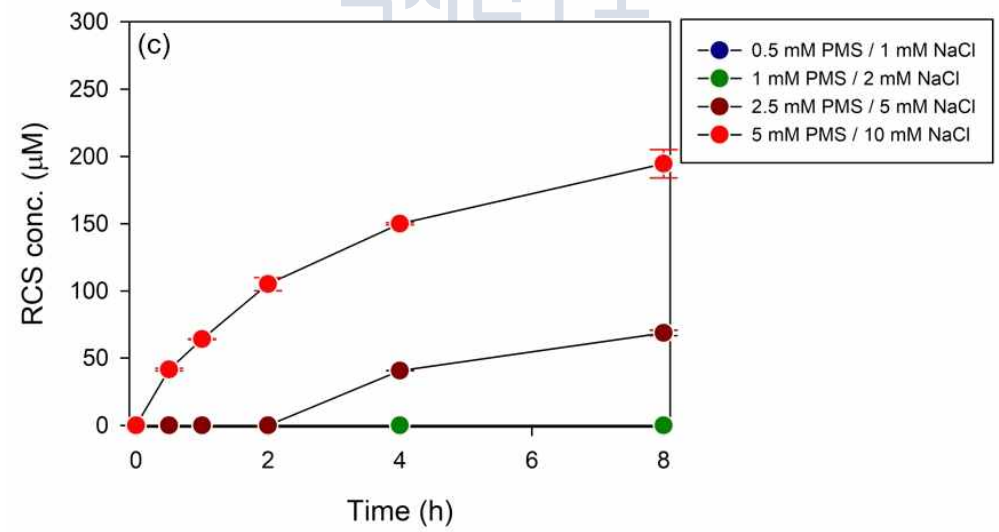



**Figure 3.** Degradation of various organic compounds in the chloride-PMS system. Experiment condition: $[PMS]_0$ = 0.5 mM; $[NaCl]_0$ = 1 mM; $[organic\ compound]_0$ = 50 μM; pHi = 3 (HClO4 adjusted); Temperature = 20℃ (Aq.) / -20℃ (Fz.); Reaction time = 4 h.

KOPRI
극지연구소


(a)
RCS conc.
PMS conc.
Cl⁻ conc.
RCS or PMS conc. (μM)
Chloride conc. (μM)
Time (h)
0
100
200
300
400
500
0
200
400
600
800
1000
0
1
2
3
4


(b)
Grain-boundary
Ice
Grain-boundary
Counts
300
0
Ice
Ice
Grain-boundary
20 μm


(c)
0.5 mM PMS / 1 mM NaCl
1 mM PMS / 2 mM NaCl
2.5 mM PMS / 5 mM NaCl
5 mM PMS / 10 mM NaCl
RCS conc. (μM)
Time (h)
0
50
100
150
200
250
300
0
2
4
6
8

KOPRI 극지연구소

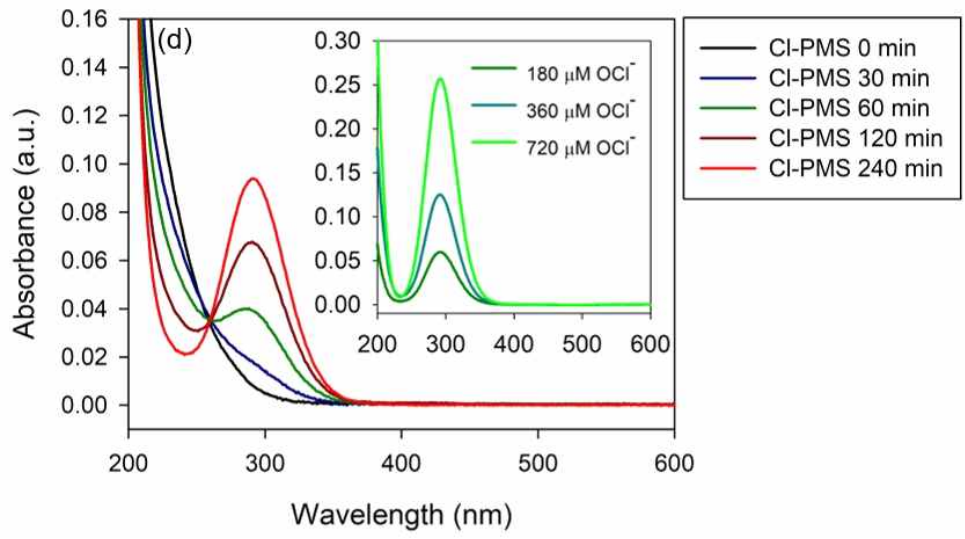
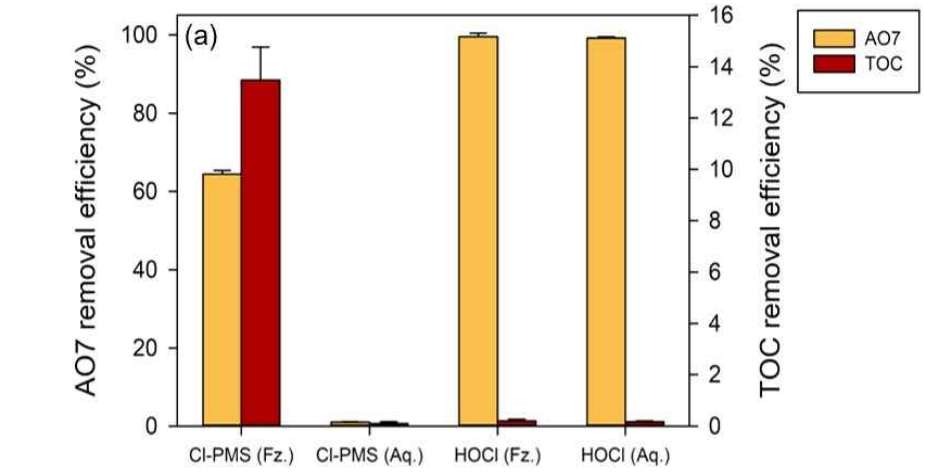
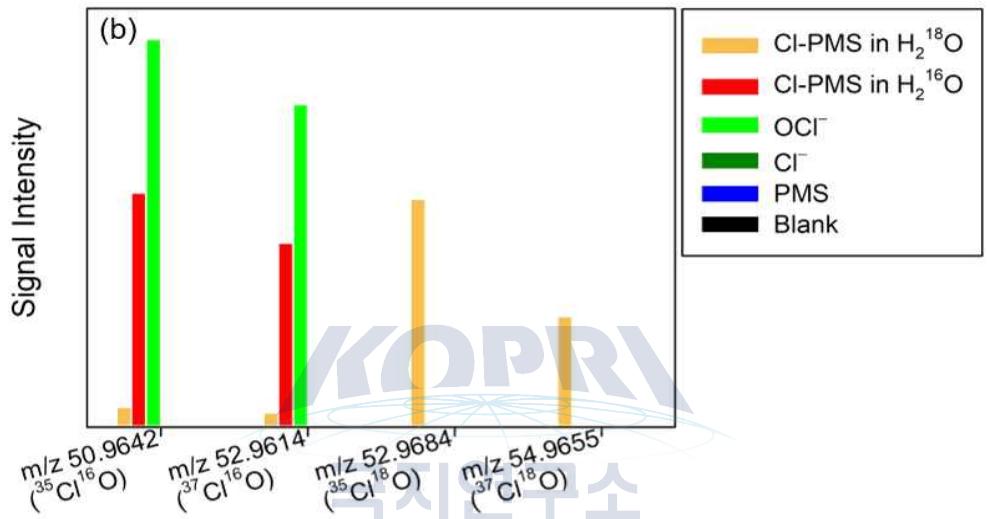
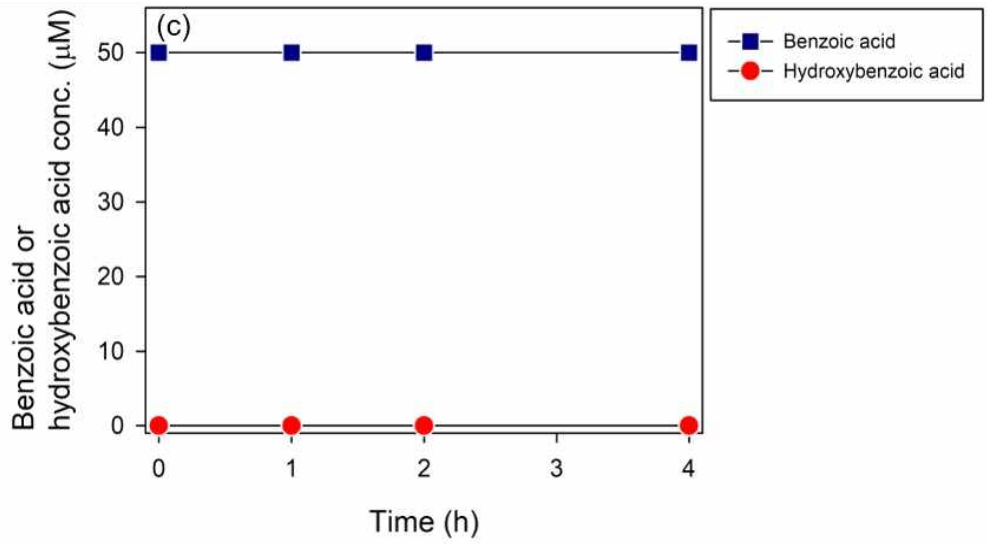



**Figure 4.** (a) Production of RCS and consumption of PMS and chloride in the freezing induced chloride-PMS system. Experiment condition: $[PMS]_0$ = 0.5 mM; $[NaCl]_0$ = 1 mM; pHi = 3 ($HClO_4$ adjusted); Temperature = -20℃. (b) Confocal Raman microscope image of ice grain boundary and the sulfate distribution. (c) Production of RCS in various PMS/NaCl ratio in the chloride-PMS system in aqueous solution. Experiment condition: pHi = 3 (HClO4 adjusted); Temperature = 20℃ (aqueous). (d) UV absorption spectrum of the frozen chloride-PMS solution with freezing time. Before measurement, the sample pH was adjusted to 10.50 by NaOH addition. Experiment condition: $[PMS]_0$ = 0.5 mM; $[NaCl]_0$ = 1 mM; pHi = 3 ($HClO_4$ adjusted); Temperature = -20℃ (Fz.).

KOPRI 극지연구소


(a)
AO7 removal efficiency (%)
TOC removal efficiency (%)
AO7
TOC
Cl-PMS (Fz.)
Cl-PMS (Aq.)
HOCl (Fz.)
HOCl (Aq.)


(b)
Signal Intensity
Cl-PMS in $H_2{}^{18}O$
Cl-PMS in $H_2{}^{16}O$
$OCl^-$
$Cl^-$
PMS
Blank
m/z 50.9642' ($^{35}Cl^{16}O$)
m/z 52.9614' ($^{37}Cl^{16}O$)
m/z 52.9684' ($^{35}Cl^{18}O$)
m/z 54.9655' ($^{37}Cl^{18}O$)


(c)
Benzoic acid or hydroxybenzoic acid conc. (μM)
Benzoic acid
Hydroxybenzoic acid
Time (h)

KOPRI 극지연구소

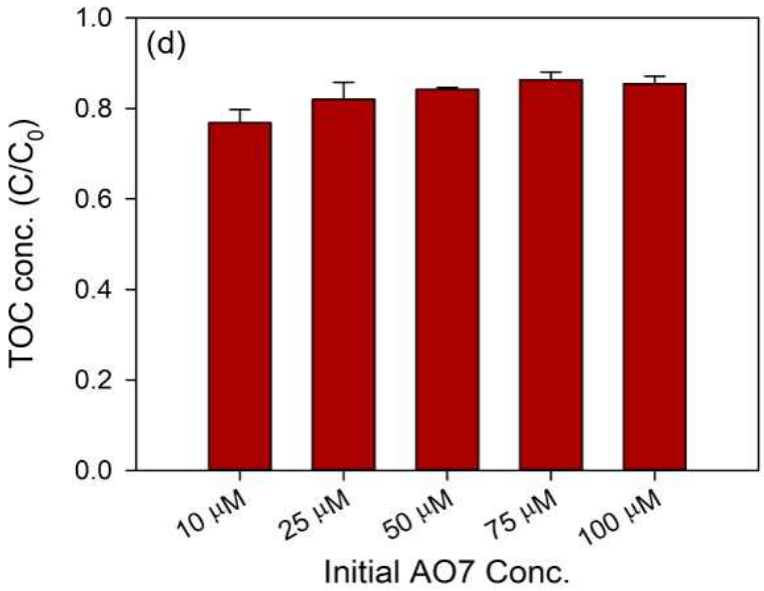



**Figure 5.** (a) AO7 degradation and TOC reduction in the chloride-PMS and NaOCl system. Experiment condition: $[PMS]_0$ = 0.5 mM; $[NaCl]_0$ = 1 mM; $[NaOCl]_0$ = 0.5 mM; $[AO7]_0$ = 50 μM; pHi = 3 ($HClO_4$ adjusted); Temperature = 20℃ (Aq.) / -20℃ (Fz.); Reaction time = 4 h. (b) Mass spectrum of $OCl^-$ in the chloride-PMS system in 18O-labeled water, in normal water, NaOCl solution, NaCl solution, PMS solution, and blank solution. Experiment condition: $[NaOCl]_0$ = 0.35 mM; $[PMS]_0$ = 1 mM; $[NaCl]_0$ = 1 mM; Temperature = -20℃; Reaction time = 4 h. Note that the mass defect of each species is -2.276 ppm ($^{35}Cl^{16}O$), 0.642 ppm ($^{37}Cl^{16}O$), -3.039 ppm ($^{35}Cl^{18}O$), and -2.019 ppm ($^{37}Cl^{18}O$), respectively. (c) The hydroxybenzoic acid generation from the oxidation of benzoic acid. Experiment condition: $[PMS]_0$ = 0.5 mM; $[NaCl]_0$ = 1 mM; [Benzoic acid]$_0$ = 50 μM; pHi = 3 ($HClO_4$ adjusted); Temperature = -20℃. (d) TOC reduction in the frozen chloride-PMS system in various initial AO7 concentrations. Experiment condition: $[PMS]_0$ = 1 mM; $[NaCl]_0$ = 2 mM; $pH_i$ = 3 ($HClO_4$ adjusted); Temperature = -20℃; Reaction time = 4 h.

KOPRI 극지연구소

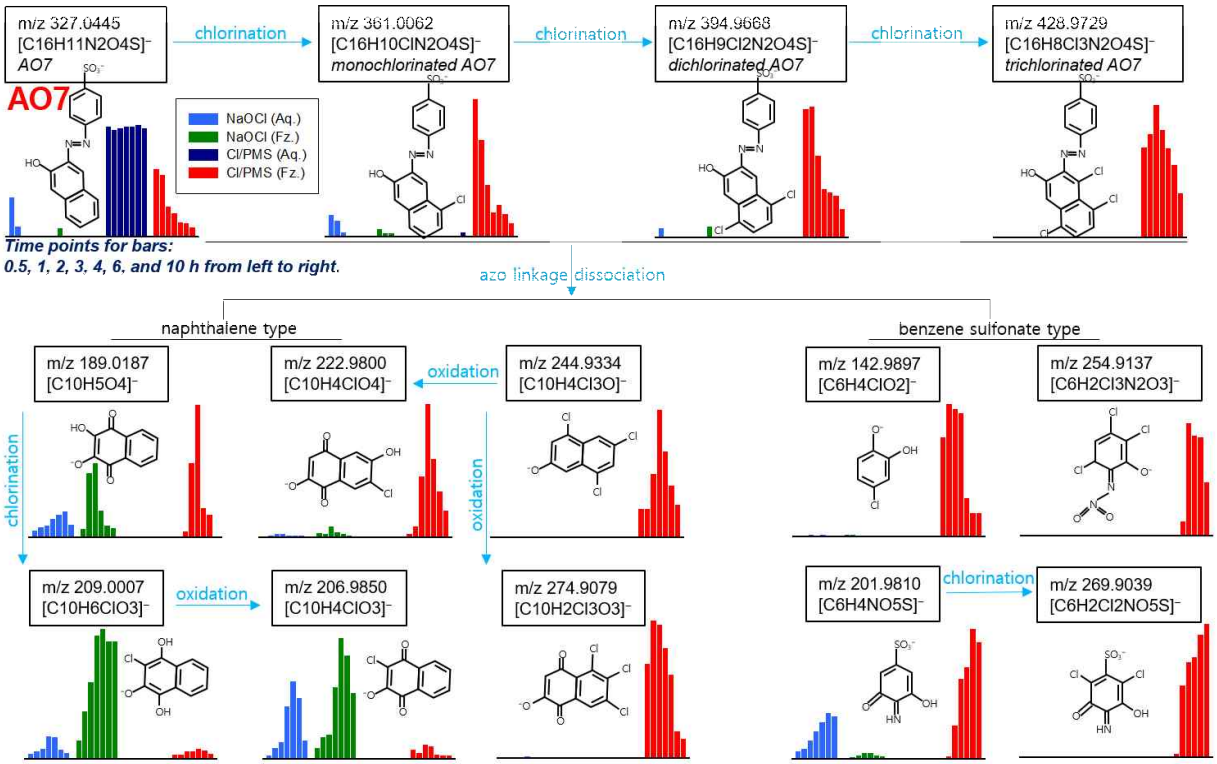



**Figure 6.** Detected degradation by-products from LC-MS analysis. Experiment condition: $[PMS]_0$ = 0.5 mM; $[NaCl]_0$ = 1 mM; $[NaOCl]_0$ = 0.5 mM; $[AO7]_0$ = 50 μM; pHi = 3 ($HClO_4$ adjusted); Temperature = 20℃ (Aq.) / -20℃ (Fz.).

KOPRI 극지연구소

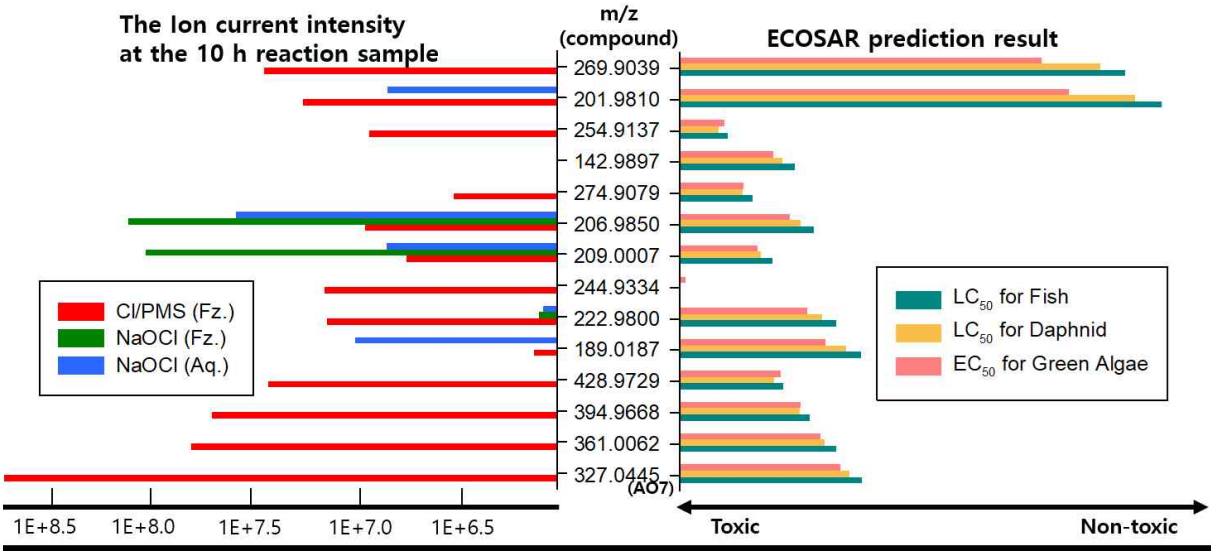



**Figure 7.** The detection intensity at the final reaction time (10 h; left part) and ecotoxicity (right part) of degradation by-products of AO7.

KOPRI
극지연구소

# 제 20 절. Crystallization Mechanisms of Porous and Compact Amorphous Solid Water Films⑳

Du Hyeong Lee and Kitae Kim

Korea Polar Research Institute

## Abstract

Amorphous solid water (ASW), formed by vapor deposition on cryogenic substrates (<130 K), transforms into crystalline ice at high temperatures. However, some aspects of the crystallization mechanism, such as the nucleation process, remain unclear. In this study, the crystallization kinetics of porous ASW (pASW) and compact ASW (cASW) were evaluated to identify their nucleation sites. ASW films were grown under ultrahigh vacuum conditions by background and tube-doser deposition, and their porosities were controlled by adjusting the deposition temperature and angle. In addition, the crystallized fractions were measured using desorption spectrometry. The results reveal that the pASW crystallization is triggered within the film interior, whereas the nucleation of cASW films occurs on their surfaces. Owing to the presence of pores, the pASW films crystallize faster than the cASW ones, and the crystallization activation energy of the former (68.9 kJ $mol^{-1}$) is lower than that of the latter (79.8 kJ $mol^{-1}$). These findings highlight the role of porosity in the crystallization of ASW, providing insights into the behavior of water molecules in cryogenic environments including polar atmospheres and the surfaces of planets and satellites.

## 1. Introduction

Water is well-known for its numerous solid phases, including more than 19 crystalline phases[1] and amorphous phases such as low-density amorphous (LDA), high-density amorphous (HDA), and the recently proposed medium-density amorphous (MDA) phases[2]. Among these ice phases, amorphous solid water (ASW) has garnered considerable attention owing to its potential presence in the polar atmosphere[3, 4] and outer space[5, 6]. ASW can be produced by depositing water vapor onto cryogenic substrates at temperatures below ~130 K. The characteristics of ASW, including its structures, phase transitions, and radiolysis, have been studied in detail.[7-14]

Metastable amorphous ice transforms into crystalline ice (CI) at high temperatures (>135

⑳ 본 연구는 본 과제(PE25120)로 수행되었으며, 결과는 *Cryst. Growth Des.* 2025, 25, 978 - 985에 출간되었다.

K on the laboratory scale), and the mechanisms and kinetics of this crystallization phenomenon have been investigated using various methods, including diffraction,[6, 15-17] vapor desorption,[18-28] infrared absorption spectroscopy,[27-33] and electron microscopy.[34, 35] In many studies, the crystallization process is divided into two steps: nucleation and growth. However, the origin of the nucleation remains unclear. In ASW films, crystalline nuclei may form either on the surfaces or in the interior. To identify the nucleation sites, two types of methods, viz. analysis of ASW films with various thicknesses[23-27] and incorporation of probe molecules on or within ASW films[28, 31-33, 36, 37], have been primarily employed. However, the results obtained using these approaches remain inconclusive, with some studies suggesting random bulk nucleation[23-27, 29] and others indicating surface-induced nucleation[28, 31-33, 36, 37].

An important characteristic of ASW films is their porosity, which depends on various deposition conditions such as the deposition rate and the presence of residual gases;[10] However, the primary factors influencing the porosity are deposition temperature and the deposition angle at which vapors are incident on the substrate. High temperatures or small angles produce compact ASW (cASW), whereas low temperatures and large angles result in porous ASW (pASW).[13, 38-41] Heating pASW films can reduce their porosity; however, this process may not completely convert them into cASW films.[39, 41-43]

According to recent studies, the porosity of ASW affects its crystallization process. Maté et al.[44] demonstrated that the preparation temperatures of ASW and hyperquenched glassy water affect their crystallization kinetics, specifically the Avrami time exponent[45, 46]. Mitchell et al.[41] reported that the internal pore surfaces of pASW play a dominant role in the nucleation process, responsible for ~90% of the crystallization of the entire film. According to Vishwakarma et al.[47], acetonitrile can induce porosity in ASW via diffusion-desorption and facilitate ASW crystallization at relatively low temperatures (128 - 134 K). These studies suggest that porous structures tend to induce nucleation in the interior of ASW films.

In the present study, cASW and pASW films were compared in terms of their crystallization mechanisms and properties. ASW films were grown using background and angle-controlled tube-doser deposition techniques, and their porosity was controlled by modulating the deposition temperature and angles. The crystallization of the films was assessed by monitoring the decrease in the vapor desorption rate using a quadrupole mass spectrometer (QMS). The results revealed that cASW crystallization initiated on the film surfaces, whereas pASW nucleation occurred in the film interior. In addition, the pores increase the crystallization rate by lowering the activation energy.

## 2. Experimental Section

To study the effect of porosity on ASW crystallization, the experiments were conducted in an ultrahigh vacuum (UHV) chamber with a base pressure of $10^{-8}$ Pa. The chamber was equipped with a Pt(111) substrate and a QMS for performing temperature-programmed desorption (TPD) and isothermal desorption measurements. Further details are provided in Section S1 of the Supporting Information.

A Pt(111) single crystal was used as the substrate for the ASW film deposition. The sample temperature was measured using a spot-welded Type N thermocouple. The substrate could be cooled to ~92 K using liquid nitrogen and heated to ~1300 K through resistive heating. Its surface was cleaned daily by $Ar^+$ ion beam sputtering and heating to 1250 K before each experiment.

ASW films were grown on the Pt(111) substrate using two methods: background deposition and tube-doser deposition. For both methods, triply freeze - pump-thawed deionized water was used as the source of $H_2O$ vapor. In the background deposition process, the UHV chamber was filled with vapor at a partial pressure of $1 - 2 \times 10^{-7}$ Torr ($1.33 - 2.67 \times 10^{-5}$ Pa). In the tube-doser deposition process, the deposition angle was controlled using a 1/8-inch (3.175 mm) stainless-steel tube connected to a leak valve, which emitted vapor flux, and the tube end was positioned ~5 cm from the substrate. The deposition angle $\Theta$ of vapor incidence on the Pt(111) substrate was controlled by rotating the Pt(111) crystal (Figure S1 in the Supporting Information). The thicknesses of the ASW films were calibrated through TPD experiments. First, the desorption peak area of a water monolayer on Pt(111) ($1.23 \times 10^{19}$ molecules $m^{-2}$)[12] was measured. Subsequently, the desorption peak area of thick ASW films was divided by the monolayer peak area, and the surface density difference was adjusted using the value of 1 ML = $1.14 \times 10^{19}$ molecules • $m^{-2}$ for CI.

Preliminary TPD experiments were also performed to estimate the crystallization temperature of the various ASW films. For a quantitative analysis, the crystallized fractions were determined through isothermal desorption experiments. Because the desorption rate decreased after crystallization, isothermal desorption spectra were collected to track the crystallized fractions over time. The thickness variation method was employed to identify nucleation sites. As reported by Safarik et al.,[23-26] thicker films crystallized faster when random bulk nucleation occurred, as each nucleus could crystallize a larger volume. Conversely, if nucleation only occurs on the surfaces, more time is required to complete the crystal growth in thicker films. Because the vapor desorption method used in this study measured only the surface crystallized fractions, the observed crystallization time

for the film surfaces remained constant regardless of film thickness.

## 3. Results

### 3.1. Crystallization Kinetics with Porosity Controlled via Deposition Temperature

The primary objective of this study was to investigate the effect of porosity on the crystallization kinetics of ASW. One way to control the porosity of the ASW films is to change the deposition temperatures. For a preliminary study, ASW films with different porosities were grown on a Pt(111) surface via background deposition at various temperatures, and TPD experiments were conducted to compare the crystallization temperature of the films. The lowest temperature that could be attained in the UHV chamber employed in the study was 92 K, whereas 125 K was the highest limit for ASW formation (see Section S2 in the Supporting Information). Because low temperatures increase the porosity of ASW films,[39, 42, 44] in this paper, the films deposited at 92 K and 125 K are referred to as pASW and cASW, respectively.

To locate the nucleation sites, the thicknesses of the ASW films were varied with the minimum thickness being 80 ML. A thickness of at least 50 ML is required to avoid the roughening transition of CI on Pt(111),[12, 48-51] which may affect the crystallization process. Additionally, a thickness of ~10 ML of the ASW films was desorbed during the heating of the films to crystallization temperatures. Considering these factors, a thickness of 80 ML is sufficient to prevent the roughening transition.

Figure 1a shows the TPD spectra of the pASW films deposited at 92 K. The bumps near 160 K indicate the occurrence of crystallization; an enlarged view of these crystallization features is shown the inset of Figure 1a. As the film thickness increased, the bump shifted to lower temperatures, indicating faster crystallization. This thickness dependence indicates random bulk nucleation within the film, as mentioned in the previous section. By contrast, the cASW films deposited at 125 K crystallized at similar temperatures regardless of the film thickness (Figure 1b). As shown in the inset in Figure 1b, the change in the cASW crystallization bump is less noticeable than that in the pASW crystallization bump. This similar crystallization temperature suggests that crystallization of cASW mainly initiates on the film surfaces.

Isothermal desorption experiments were performed at a fixed temperature to measure the ASW crystallization rates. The details of the isothermal experimental procedures are presented in Section S3 of the Supporting Information. Because ASW films desorb faster than CI films, a sigmoidal decrease in the desorption rates is observed.[18, 22, 24] As shown in Figure 2a, the crystallization of pASW films became faster as the film thickness increased. In contrast, cASW films of different thicknesses exhibited similar crystallization rates

KOPRI 극지연구소

(Figure 2b). These differing thickness dependences on the crystallization kinetics suggest the presence of distinct crystallite nucleation sites—the crystallization commences in the interior of pASW and on the surface of cASW.

To quantitatively interpret the crystallization kinetics, the Avrami equation[45, 46] was used to analyze the crystallized fractions as a function of time (eq 1).

$$f(t) = 1 - e^{-kt^n} \quad \text{(eq 1)}$$

where $k$ is the crystallization rate coefficient, and $n$ is the time exponent. The crystallization rate, $k$, can be expressed in terms of two parameters: the nucleation rate ($R$) and growth rate ($u$). For instance, when the crystallization begins at random bulk nucleation sites and expands isotropically in three dimensions, $n$ becomes 4, and $k$ is given by $\pi Ru^3/3$. For thin films, one growth direction is constrained, making $k$ proportional to $Ru^2$, and $n \approx 3$.[52, 53]

Using the Avrami equation to the measured crystallized fractions, the solid lines in Figure 2a,b demonstrate that the desorption results align well with the model. For the pASW films deposited at 92 K, the crystallization half-time ($t_{1/2}$) decreased as the film thickness increased (black squares in Figure 2c); specifically, the $t_{1/2}$ of the 80 ML pASW film was 621 s, whereas that of the 480 ML film decreased to 298 s. Contrarily, the cASW films exhibited consistent $t_{1/2}$ values, ranging from 465 s to 561 s, irrespective of the film thickness, as indicated by the red squares in Figure 2c. The slight variations might be attributed to experimental errors, such as temperature fluctuation during the measurements.

The crystallized fractions were determined from the water desorption intensities of the ice films. However, this method has two major limitations. First, it only measures the crystallized fractions on the surfaces; this issue can be addressed by carefully interpreting the results, as described in Section 2. Second, the morphological changes on the film surfaces during crystallization may affect desorption intensity[21, 24] as well as crystallized fractions. Despite these challenges, as shown in Figure 2a (and the original data in Figure S4 of the Supporting Information), the results fit well with the Avrami model, with distinct thickness dependence.

For thin films, the Avrami time exponent $n$ is typically 3, with contributions of 1 from nucleation and 2 from two-dimensional growth.[52, 53] Assuming that $n$ is 3, the crystallization rate coefficients $k$ of the different samples were estimated for comparison (Figure 2d). The $k$ values of pASW films are linearly proportional to the film thickness. Because a constant growth rate is expected after crystallite formation, this linearity suggests that the nucleation rate is proportional to the film thickness, and consequently to the bulk volume of the films. Therefore, the pASW nucleation originated within the film rather than at vacuum/ASW or ASW/Pt interfaces. By contrast, cASW films exhibited similar $k$ values across different thicknesses, indicating that nucleation likely occurred at

the interfaces. Previous studies with probe molecules[28, 31] also confirmed that cASW crystallization began at ASW surfaces with a "top-down" propagation.

### 3.2. Effect of ASW Deposition Angle on the Crystallization

In this section, the porosity of ASW films was controlled by deposition angle, and the crystallization behaviors of the films were investigated. The deposition angle $\Theta$ is defined as the angle between the direction of the incident water vapor flux and the surface normal of the substrate (Figure S1 in the Supporting Information). As the deposition angle increases, the porosity of ASW increases as well.[39-42, 54, 55] For $\Theta$ = 0°, ASW films with little porosity were formed; therefore, 0° was selected to deposit cASW. In addition, pASW films were grown at $\Theta$ = 60°. Both types of films were deposited at a deposition temperature of 92 K.

The crystallization of cASW films was evidently not affected by the film thickness, as the cASW films of various thicknesses exhibited identical crystallization trends (Figure 3a). However, for pASW films, thicker films crystallized faster (Figure 3b). These contrasting results confirm that the crystallization of pASW and cASW was initiated within the interior and on the surface, respectively.

Figure 3c presents the correlation between $t_{1/2}$ values and film thickness to compare the crystallization kinetics of cASW and pASW. The $t_{1/2}$ values of the cASW films were consistent across different thicknesses. However, unlike cASW or background-deposited pASW films, the $t_{1/2}$ value of 60°-deposited pASW films decreased up to a thickness of 160 ML and remained constant in thicker films. This saturation behavior implies the existence of limiting factors, which may be attributed to the film morphology. Unlike background-deposited pASW films, pASW films with high deposition angles have large pores and column-like structures.[39, 40, 56, 57] These structural characteristics may restrict the three-dimensional growth of microcrystallites and limit the size of each crystal.

### 3.3. Temperature Dependencies

The crystallization activation energies ($E_a$) of the ASW films were estimated using Arrhenius plots. 320 ML cASW and pASW films were prepared at 92 K using a directed tube doser (deposition angle: 0°) and background deposition, respectively. Subsequently, the crystallized fractions at different times were measured within a temperature range of 146 - 151 K. Figure 4a,b presents the measured crystallized fractions, indicating that both sample types exhibit typical temperature-dependent crystallization kinetics, with faster crystallization at higher temperatures. At the same temperatures, the crystallization half-times of the cASW films were approximately twice those of the pASW films.

The Arrhenius plot of the crystallization half-time is shown in Figure 4c. The $E_a$ values

for the crystallization of cASW and pASW were 79.8 ± 3.8 and 68.9 ± 2.7 kJ • mol$^{-1}$, respectively, within the range of previously reported crystallization activation energies (60 - 84 kJ • mol$^{-1}$).[18, 22, 26, 29, 32, 58, 59] Evidently, $E_a$ of pASW was approximately 11 kJ • mol$^{-1}$ lower than that of cASW suggesting that the porous structures in pASW facilitated crystallization. However, unlike proton-induced crystallization,[60] the high porosity did not reduce $E_a$ to that for the crystal-growth step (40 - 56 kJ • mol$^{-1}$),[21, 26, 33] indicating that the nucleation step remained the bottleneck of this crystallization phenomenon.

To examine the effect of the ASW deposition temperature without the influence of porosity, the crystallization rates of the cASW films deposited at different temperatures were measured. For this analysis, 320 ML cASW films were grown at a 0° deposition angle and a temperature range of 93 - 120 K. As shown in Figure 5, all cASW samples prepared at different temperatures exhibited similar crystallized fraction curves and $t_{1/2}$ values. This result indicates that the crystallization kinetics of the cASW films remained independent of their deposition temperatures. This also implies that the temperature-dependent crystallization behavior of the pASW films (described in Section 3.1) can be primarily attributed to their porosity.

## 4. Discussion

To examine the crystallization behaviors of cASW and pASW films, their porosities were controlled by varying their growth temperature and deposition angle, and their crystallization process was observed via desorption spectrometry. The results indicate that the apparent nucleation sites of pASW crystallization exist within the interior of the films, whereas cASW crystallization is initiated on the film surfaces. Moreover, pASW crystallizes faster than cASW, and the corresponding activation energy is ~11 kJ • mol$^{-1}$ lower than that of cASW. Interestingly, the deposition method of pASW films also has an impact on the crystallization rate. The crystallization rate of the background-deposited pASW films increases upon increasing the film thickness. By contrast, the thick pASW films (thickness > 160 ML), which are deposited via tilted directional impingement and may contain large pores and columnar structures,[39, 40] are characterized by a crystallization half-time.

The observed initiation of cASW crystallization on the film surface confirms that the water molecules on the surface function as nucleation sites. By contrast, the bulk nucleation of pASW likely originates from the molecules near the pores because the interfacial molecules with fewer hydrogen bonds can provide a more favorable environment for nucleation. According to the classical nucleation theory,[52, 53] nucleation kinetics are affected by the nucleation energy barrier and molecular transport rate. It is well known

that heterogeneous crystalline nuclei have smaller surface areas than homogeneous spherical nuclei completely surrounded by an amorphous phase. Furthermore, surface water molecules are less hydrogen-bonded than interior molecules,[42, 43] facilitate their migration.

As mentioned in the Introduction, previous studies reported different results on ASW nucleation sites. Certain researchers[23-26, 29] proposed homogeneous nucleation within the bulk of the films, whereas others[28, 30-33] proposed heterogeneous nucleation on the surfaces. These differences arise from the variations in the ASW formation conditions, including deposition angles and temperatures. For example, Kondo et al.,[29] who observed bulk nucleation, used the background deposition, which resulted in the formation of pASW films. Similarly, Safarik et al.[23-26] deposited ASW films at 77 K, which was sufficiently low for creating slightly porous ASW samples even at normal incidence, as reported by Mitchell et al.[41] Different crystallization measurement methods, which may also lead to inconsistencies, are broadly categorized into two types: comparison of the crystallization rates using variable-thickness ASW films[23-26] and utilization of probe molecules to measure crystallization rates at various positions in films of similar thicknesses.[28, 30-33] These approaches yield different results. If both homogeneous and heterogeneous nucleation occurs at comparable rates in ASW, then the former would result in fast crystallization for thick films, whereas the latter would lead to early crystallization on film surfaces. Consequently, the method selected for the crystallization rate measurement can significantly affect the observed nucleation behavior and lead to discrepancies in the studies.

In this study, the nucleation sites of ASW crystallization were investigated using the approach of Safarik et al.[23, 24, 26] However, the crystallized fractions were measured via water desorption from the surfaces of the films. As mentioned before, this experimental method has several limitations. First, the measured crystallized fraction only represents the status of the surface layer of the ASW film samples; however, this limitation does not affect the determination of the nucleation sites. Second, the desorption intensities are affected by the crystallized fractions as well as changes in the surface area during crystallization,[24, 61] which may introduce some errors in determining the Avrami fitting parameters and crystallization half-time. Despite these limitations, the similar desorption intensities ($I_{ASW}$ and $I_{CI}$) from films of different thicknesses, the excellent fit to the Avrami model and the porosity effects observed in the raw data (Figures S4 - 7 and Tables S1 - 4 in Section S4 of the Supporting Information) confirm that pASW and cASW crystallization were initiated in the interior and at the surface, respectively.

To gain a more detailed understanding of the crystallization behavior of ASW films with varying porosities, future studies should measure crystallized fractions at different locations within the film interior using probe molecules. Additionally, exploring films grown at temperatures below the boiling point of nitrogen and those fabricated via vapor deposition

from different directions will provide further insights into water molecules in astrophysical environments, including cosmic dust, comets, and icy satellites.

## 5. Conclusion

In this study, the effect of porosity on the crystallization characteristics of ASW was investigated, with a focus on comparing the crystallization kinetics of cASW and pASW films. Porosity was controlled by adjusting the deposition temperature and vapor incidence angle using two deposition methods: background deposition and tube-doser deposition. The crystallized fractions were measured through TPD and isothermal desorption experiments.

The results demonstrate that the porosity of the ASW films significantly affects their crystallization rates and the location of nucleation sites. The crystallization of cASW films was initiated on the surfaces, whereas the pASW films appeared to crystallize within the film interior. For the background-deposited pASW films, the crystallization rate constant was proportional to the film thickness, indicating bulk nucleation. Temperature-dependent crystallization kinetics revealed that the pores in ASW facilitated nucleation by lowering the crystallization activation energy from 79.8 ± 3.8 kJ • $mol^{-1}$ for cASW to 68.9 ± 2.7 kJ • $mol^{-1}$ for pASW. These results suggest that the heterogeneous nucleation primarily occurs on the film surfaces of cASW and at the pore surfaces of pASW.

These findings emphasize the role of porosity in ASW crystallization and can untangle the discrepancies related to nucleation sites reported in previous studies. Understanding the crystallization mechanism can provide valuable insights into the behavior of water molecules in cryogenic environments, such as the outer solar system and interstellar medium.

The ASW films used in this study were grown under limited conditions, particularly a limited deposition temperature range, and only the crystallized fractions of the film surfaces were measured. Further investigations are required to explore a broader range of deposition conditions, and the crystallized fractions in various regions of ASW films should be measured.

## REFERENCES

(1) Yamane, R.; Komatsu, K.; Gouchi, J.; Uwatoko, Y.; Machida, S.; Hattori, T.; Ito, H.; Kagi, H., Experimental evidence for the existence of a second partially-ordered phase of ice VI. *Nat. Commun.* **2021,** 12, 1129.

(2) Rosu-Finsen, A.; Davies, M. B.; Amon, A.; Wu, H.; Sella, A.; Michaelides, A.; Salzmann, C. G., Medium-density amorphous ice. *Science* **2023,** 379, 474-478.

(3) Fritts, D. C.; Williams, B. P.; She, C. Y.; Vance, J. D.; Rapp, M.; Lübken, F. J.;

Müllemann, A.; Schmidlin, F. J.; Goldberg, R. A., Observations of extreme temperature and wind gradients near the summer mesopause during the MaCWAVE/MIDAS rocket campaign. *Geophys. Res. Lett.* **2004,** 31, L24S06.

(4) Zasetsky, A. Y.; Petelina, S. V.; Svishchev, I. M., Thermodynamics of homogeneous nucleation of ice particles in the polar summer mesosphere. *Atmos. Chem. Phys.* **2009,** 9, 965-971.

(5) Leger, A.; Klein, J.; de Cheveigné, S.; Guinet, C.; Defourneau, D.; Belin, M., The 3.1 micron absorption in molecular clouds is probably due to amorphous $H_2O$ ice. *Astron. Astrophys.* **1979,** 79, 256-259.

(6) Jenniskens, P.; Blake, D., Structural transitions in amorphous water ice and astrophysical implications. *Science* **1994,** 265, 753-756.

(7) Petrenko, V. F.; Whitworth, R. W., *Physics of ice*; Oxford University Press: Oxford; New York, 1999.

(8) Fraxedas, J., *Water at Interfaces: A Molecular Approach*; CRC Press: Boca Raton, 2014.

(9) Smith, R. S.; Dohnálek, Z.; Kimmel, G. A.; Teeter, G.; Ayotte, P.; Daschbach, J. L.; Kay, B. D., Molecular Beam Studies of Nanoscale Films of Amorphous Solid Water. In *Water in Confining Geometries*, Buch, V.; Devlin, J. P., Eds. Springer Berlin Heidelberg: Berlin, Heidelberg, 2003; pp 337-357.

(10) Baragiola, R. A., Microporous Amorphous Water Ice Thin Films: Properties and Their Astronomical Implications. In *Water in Confining Geometries*, Buch, V.; Devlin, J. P., Eds. Springer Berlin Heidelberg: Berlin, Heidelberg, 2003; pp 359-395.

(11) Angell, C. A., AMORPHOUS WATER. *Annu. Rev. Phys. Chem.* **2004,** 55, 559-583.

(12) Hodgson, A.; Haq, S., Water Adsorption and the Wetting of Metal Surfaces. *Surf. Sci. Rep.* **2009,** 64, 381-451.

(13) Smith, R. S.; Petrik, N. G.; Kimmel, G. A.; Kay, B. D., Thermal and Nonthermal Physiochemical Processes in Nanoscale Films of Amorphous Solid Water. *Acc. Chem. Res.* **2012,** 45, 33-42.

(14) Tonauer, C. M.; Fidler, L.-R.; Giebelmann, J.; Yamashita, K.; Loerting, T., Nucleation and growth of crystalline ices from amorphous ices. *J. Chem. Phys.* **2023,** 158, 141001.

(15) Jenniskens, P.; Blake, D. F., Crystallization of amorphous water ice in the solar system. *Astrophys J.* **1996,** 473, 1104-13.

(16) Huang, J.; Bartell, L. S., Kinetics of Homogeneous Nucleation in the Freezing of Large Water Clusters. *J. Phys. Chem.* **1995,** 99, 3924-3931.

(17) Souda, R.; Aizawa, T., Crystallization kinetics of thin water films on Pt(111): effects of oxygen and carbon-monoxide adspecies. *Phys. Chem. Chem. Phys.* **2019,** 21, 1123-1130.

(18) Smith, R. S.; Huang, C.; Wong, E. K. L.; Kay, B. D., Desorption and crystallization kinetics in nanoscale thin films of amorphous water ice. *Surf. Sci.* **1996,** 367, L13-L18.

(19) Smith, R. S.; Huang, C.; Kay, B. D., Evidence for molecular translational diffusion during the crystallization of amorphous solid water. *J. Phys. Chem. B* **1997,** 101, 6123-6126.

(20) Dohnalek, Z.; Ciolli, R. L.; Kimmel, G. A.; Stevenson, K. P.; Smith, R. S.; Kay, B. D., Substrate induced crystallization of amorphous solid water at low temperatures. *J. Chem. Phys.* **1999,** 110, 5489-5492.

(21) Dohnálek, Z.; Kimmel, G. A.; Ciolli, R. L.; Stevenson, K. P.; Smith, R. S.; Kay, B. D., The effect of the underlying substrate on the crystallization kinetics of dense amorphous solid water films. *J. Chem. Phys.* **2000,** 112, 5932-5941.

(22) Löfgren, P.; Ahlström, P.; Lausma, J.; Kasemo, B.; Chakarov, D., Crystallization Kinetics of Thin Amorphous Water Films on Surfaces. *Langmuir* **2003,** 19, 265-274.

(23) Safarik, D. J.; Mullins, C. B., Surface phase transformation kinetics: A geometrical model for thin films of nonvolatile and volatile solids. *J. Chem. Phys.* **2002,** 117, 8110-8123.

(24) Safarik, D. J.; Meyer, R. J.; Mullins, C. B., Thickness dependent crystallization kinetics of sub-micron amorphous solid water films. *J. Chem. Phys.* **2003,** 118, 4660-4671.

(25) Safarik, D. J.; Mullins, C. B., A new methodology and model for characterization of nucleation and growth kinetics in solids. *J. Chem. Phys.* **2003,** 119, 12510-12524.

(26) Safarik, D. J.; Mullins, C. B., The nucleation rate of crystalline ice in amorphous solid water. *J. Chem. Phys.* **2004,** 121, 6003-6010.

(27) Harada, K.; Sugimoto, T.; Kato, F.; Watanabe, K.; Matsumoto, Y., Thickness dependent homogeneous crystallization of ultrathin amorphous solid water films. *Phys. Chem. Chem. Phys.* **2020,** 22, 1963-1973.

(28) Backus, E. H. G.; Grecea, M. L.; Kleyn, A. W.; Bonn, M., Surface crystallization of amorphous solid water. *Phys. Rev. Lett.* **2004,** 92, 236101.

(29) Kondo, T.; Kato, H. S.; Bonn, M.; Kawai, M., Deposition and crystallization studies of thin amorphous solid water films on Ru(0001) and on CO-precovered Ru(0001). *J. Chem. Phys.* **2007,** 127, 094703.

(30) Xu, Y.; Petrik, N. G.; Smith, R. S.; Kay, B. D.; Kimmel, G. A., Growth rate of crystalline ice and the diffusivity of supercooled water from 126 to 262 K. *Proc. Natl. Acad. Sci. U.S.A.* **2016,** 113, 14921-14925.

(31) Yuan, C.; Smith, R. S.; Kay, B. D., Surface and bulk crystallization of amorphous solid water films: Confirmation of “top-down” crystallization. *Surf. Sci.* **2016,** 652, 350-354.

(32) Yuan, C.; Smith, R. S.; Kay, B. D., Communication: Distinguishing between bulk and interface-enhanced crystallization in nanoscale films of amorphous solid water. *J.*

KOPRI 극지연구소

*Chem. Phys.* **2017,** 146, 031102.

(33) Smith, R. S.; Yuan, C.; Petrik, N. G.; Kimmel, G. A.; Kay, B. D., Crystallization growth rates and front propagation in amorphous solid water films. *J. Chem. Phys.* **2019,** 150, 214703.

(34) Kouchi, A.; Tsuge, M.; Hama, T.; Oba, Y.; Okuzumi, S.; Sirono, S.-i.; Momose, M.; Nakatani, N.; Furuya, K.; Shimonishi, T.; Yamazaki, T.; Hidaka, H.; Kimura, Y.; Murata, K.-i.; Fujita, K.; Nakatsubo, S.; Tachibana, S.; Watanabe, N., Transmission Electron Microscopy Study of the Morphology of Ices Composed of $H_2O$, $CO_2$, and CO on Refractory Grains. *The Astrophysical Journal* **2021,** 918, 45.

(35) Lee, M.; Lee, S. Y.; Kang, M.-H.; Won, T. K.; Kang, S.; Kim, J.; Park, J.; Ahn, D. J., Observing growth and interfacial dynamics of nanocrystalline ice in thin amorphous ice films. *Nat. Commun.* **2024,** 15, 908.

(36) Backus, E. H. G.; Bonn, M., Theory of bulk, surface and interface phase transition kinetics in thin films. *J. Chem. Phys.* **2004,** 121, 1038-1049.

(37) Bonn, M.; Backus, E. H. G., Geometrical vs. statistical models for describing phase transition kinetics in thin films. *Phys. Chem. Chem. Phys.* **2004,** 6, 5516-5522.

(38) Stevenson, K. P.; Kimmel, G. A.; Dohnalek, Z.; Smith, R. S.; Kay, B. D., Controlling the morphology of amorphous solid water. *Science* **1999,** 283, 1505-1507.

(39) Kimmel, G. A.; Stevenson, K. P.; Dohnalek, Z.; Smith, R. S.; Kay, B. D., Control of amorphous solid water morphology using molecular beams. I. Experimental results. *J. Chem. Phys.* **2001,** 114, 5284.

(40) Kimmel, G. A.; Dohnálek, Z.; Stevenson, K. P.; Smith, R. S.; Kay, B. D., Control of amorphous solid water morphology using molecular beams. II. Ballistic deposition simulations. *J. Chem. Phys.* **2001,** 114, 5295-5303.

(41) Mitchell, E. H.; Raut, U.; Teolis, B. D.; Baragiola, R. A., Porosity effects on crystallization kinetics of amorphous solid water: Implications for cold icy objects in the outer solar system. *Icarus* **2017,** 285, 291-299.

(42) Bu, C.; Shi, J.; Raut, U.; Mitchell, E. H.; Baragiola, R. A., Effect of microstructure on spontaneous polarization in amorphous solid water films. *J. Chem. Phys.* **2015,** 142, 134702.

(43) Sagi, R.; Akerman, M.; Ramakrishnan, S.; Asscher, M., The role of thermal history on spontaneous polarization and phase transitions of amorphous solid water films studied by contact potential difference measurements. *J. Chem. Phys.* **2020,** 153, 144702

(44) Maté, B.; Rodríguez-Lazcano, Y.; Herrero, V. J., Morphology and crystallization kinetics of compact (HGW) and porous (ASW) amorphous water ice. *Phys. Chem. Chem. Phys.* **2012,** 14, 10595-10602.

(45) Avrami, M., Kinetics of Phase Change. I General Theory. *J. Chem. Phys.* **1939,** 7,

1103-1112.

(46) Avrami, M., Kinetics of Phase Change. II Transformation Time Relations for Random Distribution of Nuclei. *J. Chem. Phys.* **1940,** 8, 212-224.

(47) Vishwakarma, G.; Malla, B. K.; Methikkalam, R. R. J.; Pradeep, T., Rapid crystallization of amorphous solid water by porosity induction. *Phys. Chem. Chem. Phys.* **2022,** 24, 26200-26210.

(48) Haq, S.; Harnett, J.; Hodgson, A., Growth of Thin Crystalline Ice Films on Pt(111). *Surf. Sci.* **2002,** 505, 171-182.

(49) Zimbitas, G.; Haq, S.; Hodgson, A., The structure and crystallization of thin water films on Pt(111). *J. Chem. Phys.* **2005,** 123, 174701.

(50) Thurmer, K.; Bartelt, N. C., Nucleation-limited dewetting of ice films on Pt(111). *Phys. Rev. Lett.* **2008,** 100, 186101.

(51) Thurmer, K.; Bartelt, N. C., Growth of multilayer ice films and the formation of cubic ice imaged with STM. *Phys. Rev. B* **2008,** 77, 195425.

(52) Jena, A. K.; Chaturvedi, M. C., *Phase transformation in materials*; Prentice Hall: Englewood Cliffs, NJ, 1992.

(53) Rao, C. N. R.; Rao, K. J., Various Kinds of Phase Transitions. In *Phase Transitions in Solids: An Approach to the Study of the Chemistry and Physics of Solids*, McGraw-Hill: New York, 1978; pp 81-173.

(54) Berland, B. S.; Brown, D. E.; Tolbert, M. A.; George, S. M., Refractive index and density of vapor-deposited ice. *Geophys. Res. Lett.* **1995,** 22, 3493-3496.

(55) Dohnálek, Z.; Kimmel, G. A.; Ayotte, P.; Smith, R. S.; Kay, B. D., The deposition angle-dependent density of amorphous solid water films. *J. Chem. Phys.* **2003,** 118, 364-372.

(56) Clements, A. R.; Berk, B.; Cooke, I. R.; Garrod, R. T., Kinetic Monte Carlo simulations of water ice porosity: extrapolations of deposition parameters from the laboratory to interstellar space. *Phys. Chem. Chem. Phys.* **2018,** 20, 5553-5568.

(57) Tomaru, T.; Hidaka, H.; Kouchi, A.; Watanabe, N., Atomic force microscopy observation of surface morphologies and measurements of local contact potential differences of amorphous solid water samples deposited at 15 and 100 K. *Phys. Chem. Chem. Phys.* **2024,** 26, 15232-15239.

(58) Ahlstrom, P.; Lofgren, P.; Lausma, J.; Kasemo, B.; Chakarov, D., Crystallization kinetics of thin amorphous water films on surfaces: Theory and computer modeling. *Phys. Chem. Chem. Phys.* **2004,** 6, 1890-1898.

(59) Smith, R. S.; Matthiesen, J.; Knox, J.; Kay, B. D., Crystallization Kinetics and Excess Free Energy of $H_2O$ and $D_2O$ Nanoscale Films of Amorphous Solid Water. *J. Phys. Chem. A* **2011,** 115, 5908-5917.

KOPRI 극지연구소

(60) Lee, D. H.; Kang, H., Acid-Promoted Crystallization of Amorphous Solid Water. *J. Phys. Chem. C* **2018,** 122, 24164-24170.

(61) McClure, S. M.; Barlow, E. T.; Akin, M. C.; Tanaka, P. L.; Safarik, D. J.; Truskett, T. M.; Mullins, C. B., Effect of Dilute Nitric Acid on Crystallization and Fracture of Amorphous Solid Water Films. *J. Phys. Chem. C* **2007,** 111, 10438-10447.

KOPRI
극지연구소

## FIGURES

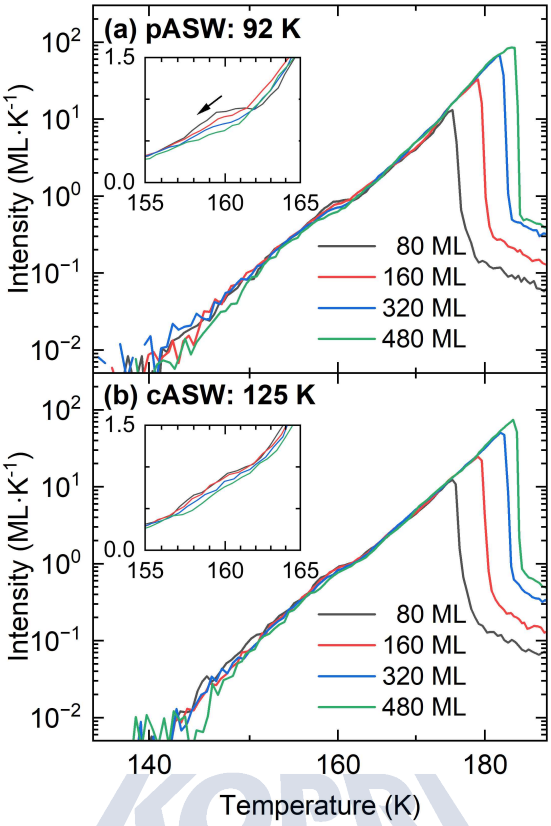



**Figure 1.** Water TPD spectra of background-deposited films: (a) pASW at 92 K and (b) cASW at 125 K. The temperature ramp rate was 0.5 K • s$^{-1}$. The insets display enlarged spectra near the crystallization bumps on a linear scale. An arrow in the inset of (a) indicates the change in the crystallization bumps.

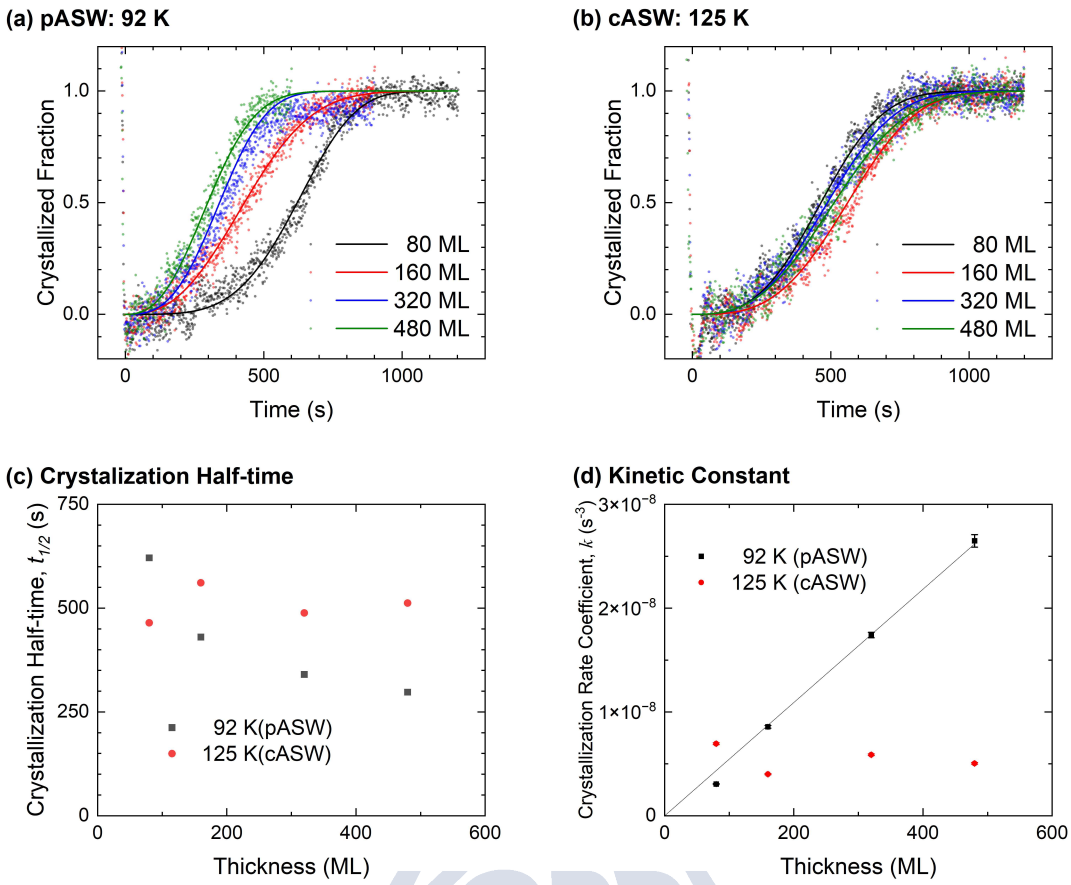



**Figure 2.** Crystallized fractions obtained from the isothermal experiments (points) and their Avrami fitting (lines) for the ASW films as a function of time at 148 K. (a) pASW films and (b) cASW films were grown by background deposition at 92 K and 125 K, respectively. Solid lines represent the Avrami-fitted results to the data points. (c) Crystallization half-time ($t_{1/2}$) versus ASW film thickness. (d) Crystallization rate coefficient ($k$) versus ASW film thickness, assuming an Avrami time exponent $n$ of 3. The black line is a linear fit for pASW data with a $y$-intercept of 0.

KOPRI 극지연구소

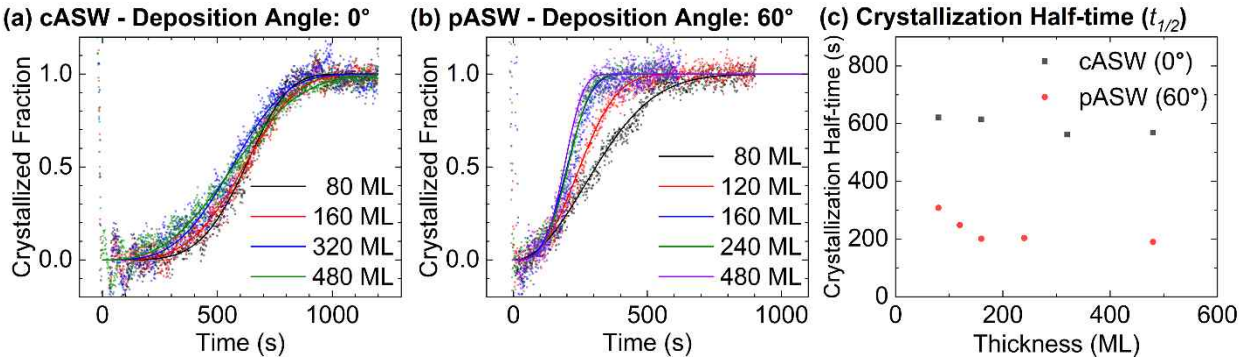



**Figure 3.** Crystallized fractions measured from isothermal desorption of the ASW films at 148 K. The ASW films were prepared by tube-doser deposition at 92 K with deposition angles of (a) 0° and (b) 60°. Solid lines are the Avrami-fitted results. (c) Crystallization half-time ($t_{1/2}$) versus ASW film thickness.

KOPRI
극지연구소

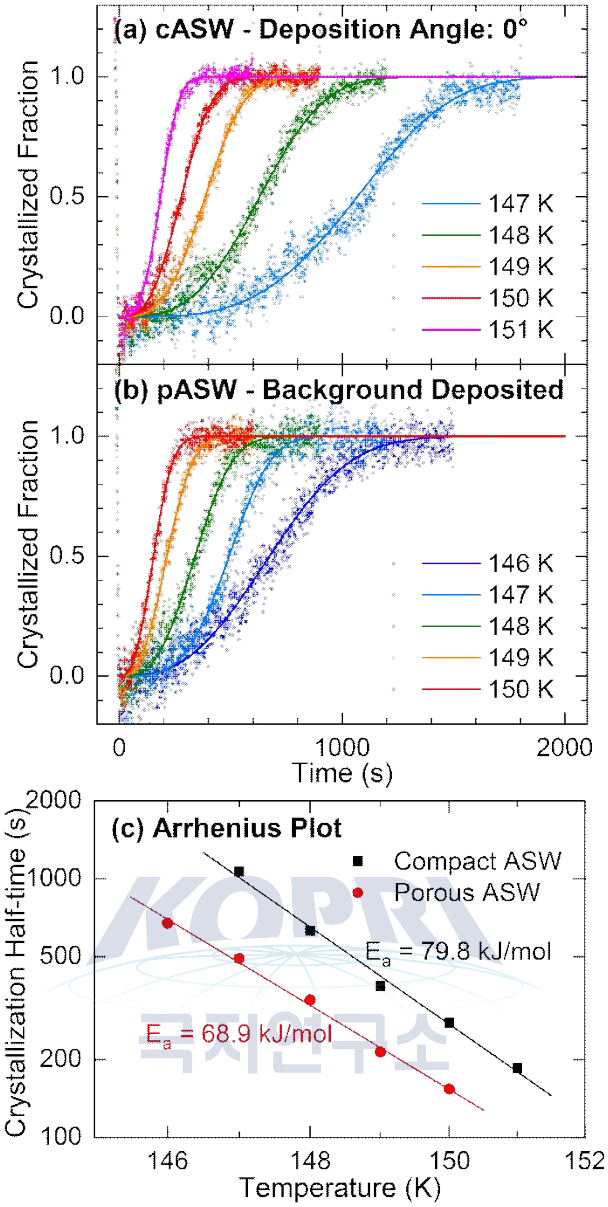



**Figure 4.** Temperature dependence of crystallization kinetics. 320 ML ASW films of (a) 0°-deposited cASW and (b) background-deposited pASW were prepared at 92 K, and their crystallized fractions as a function of time were measured at different temperatures. Solid lines are the Avrami-fitted results. (c) Arrhenius plot of crystallization half-time ($t_{1/2}$) versus temperature.

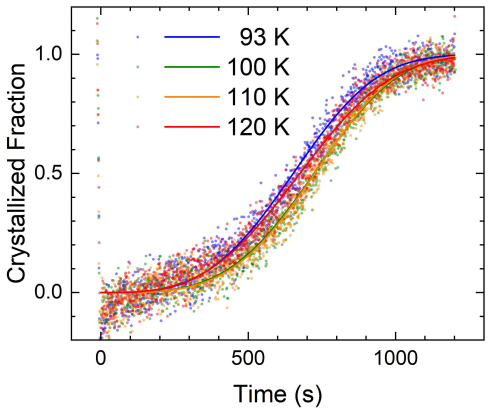



**Figure 5.** Crystallized fractions measured from the isothermal desorption of the cASW films at 148 K. The 320 ML cASW films were grown at various deposition temperatures using a tube doser at a deposition angle of 0°. Solid lines are the Avarmi-fitted results.

KOPRI
극지연구소

# 제 21 절. Bromide oxidation by bromate in a frozen solution and reactive bromine species production①

Yong-Yoon Ahn[1], Quoc Anh Nguyen[1,2], Andrea Spolaor[3,4], Stefano Frassati[3,4], Elena Barbaro[3,4], Giulio Cozzi[4], Clara Turetta[4], Hoon Oh[5], Jaesang Lee[5], Kitae Kim[1,2]

[1]Korea Polar Research Institute (KOPRI)

[2]Department of Polar Science, University of Science of Technology (UST)

[3]Ca′ Foscari University of Venice, Department of Environmental Sciences, Informatics and Statistics, Venice Mestre, Italy.

[4]Institute of Polar Sciences-National Research Council (CNR-ISP), Venice Mestre, Italy

[5]Civil, Environmental, and Architectural Engineering, Korea University, Seoul 02841, Republic of Korea

## Abstract

A sudden increase in tropospheric reactive bromine species (such as BrO radical) concentration has been observed in the Arctic springtime (bromine explosion). The reactive bromine radicals originate from the $Br_2$ oxidation; however, the role of ice chemistry in bromine activation, especially freezing-induced $Br^-$ oxidation for $Br_2$ production, is not significantly considered yet. Notably, the freezing phenomenon is prevalent in polar region. In this study, we demonstrate that the $Br^-$ containing water freezing can provide a potential $Br^-$ oxidation pathway. The oxidation of $Br^-$ by $BrO_3^-$ was negligible under aqueous conditions, while it was highly accelerated (time scale of several years to minute) by freezing the solution. We proposed that the accelerated chemical reaction was due to the freezing concentration effect. The chemical transformation mechanism was suggested. The chemical transformation of $Br^-$ was considered using the UV-visible absorbance spectrometer and the high-resolution mass spectroscopy (HRMS) measurement. The total Br content was measured using inductive coupled plasma mass spectroscopy (ICP-MS) and the dissolved Br species was monitored using ion chromatography. The spatial distribution of in-situ generated hypobromous acid in ice was analyzed using the Raman microscopy. The $Br^-$ oxidation is increased as the decrease of initial pH and increase of reactant dose, but the influence of freezing temperature was not significant. This study provides experimental evidence for the freezing-induced bromide activation in the ice.

① 본 연구는 본 과제(PE25120)로 수행되었으며, 결과는 *Water Research* 2025, 285, 124127에 출간되었다.

## 1. Introduction

Highly soluble $Br^-$ is a minor constituent in natural waters and has traditionally been considered a conservative element due to its chemical stability. As a result, it has received relatively little attention in aquatic systems for many years (notably, $Br^-$ has been used as a hydrological tracer) [1]. Historically, concerns regarding the impact of $Br^-$ in water environments have primarily focused on its role in anthropogenic emissions, particularly in the formation of toxic brominated disinfection byproducts, including $BrO_3^-$ [2]. However, interest in natural $Br^-$ has grown in recent years, especially in studies of marine sediments, soils, and oceanic aerosols. This growing attention is attributed to the newly recognized redox activity of $Br^-$ and its involvement in the formation of organo-bromine species. It is worth noting that approximately 6.2 Tg of Br is released annually into the atmosphere from the sea [3]. In atmospheric chemistry, the fate of $Br^-$ is comprehensively explored owing to its important role in the troposphere ozone stability.

Historically, the important role of halogens in the troposphere was firstly identified in the polar regions [4]. The presence of reactive bromine species in the Arctic atmosphere can be rapidly increased via the bromine explosion event during the sunlit season [5]. It is noted that the local ozone can be completely eliminated in a few days by the BrO at a mixing ratio of tens of parts per trillion [5]. The source of atmosphere $Br^-$ in the polar region is seawater, and $Br^-$ in seawater originates from the oceanic lithosphere [6]. In polar region, $Br^-$ contained brine is separated from the frozen water matrix during seawater freezing [7]. Therefore, high salinity is found on young (first-year) sea ice surface. Possibly, the newly formed sea ice surfaces supply $Br^-$ from seawater to the air by lifting through blowing [8]. In addition, the protonation of $Br^-$ to HBr by the atmospheric acid deposition, such as $SO_2$ and $HNO_3$, can contribute bromine mass transport between sea and air. Under the oxidative environment, $Br^-$ is oxidized to generate various reactive bromine species [4]. The ice surface catalyzed photochemical process was considered the major oxidation factor [9, 10], but some literature inferred the possibility of dark reaction for bromide activation in the region of high ionic strength in snow and ice [11]. Notably, several studies have detected the freezing-facilitated generation of volatile halogen gases including interhalogen species [12-16]. However, there are no consideration on the $BrO_3^-$ mediated $Br^-$ oxidation at all up to now because two species are chemically stable in general [17]. It is noted that $BrO_3^-$ production from $Br^-$ oxidation by $O_3$ need to be considered: though the $O_3$ possibly reduces HOBr, the trace amount of $BrO_3^-$ also can be produced by $O_3$ induced $Br^-$ oxidation [18]. Here, we first report the ice chemistry between two stable bromine species for $Br_2$ production.

Previously, it is known that the chemical reaction between $Br^-$ and $BrO_3^-$ can be take place but in the extremely acidic condition and high reactants concentration [19-22].

KOPRI 극지연구소

$$-d[BrO_3^-]/dt = k_1[BrO_3^-][H^+]^2[Br^-] + k_2[BrO_3^-][H^+]^2[Br^-]^2 \quad (1)$$

The kinetic reaction constant k1 and k2 at 25 ℃ were estimated to be 4.12 ± 0.05 $M^{-3}$ s-1 and 0.810 ± 0.02 $M^{-4}$ $s^{-1}$, respectively [20]. Therefore, at $[BrO_3^-]_0$ = 20 μM, $[Br^-]_0$ = 150 μM, and $[HClO_4]_0$ = 1 mM (ca. pH 3), the half-life for $BrO_3^-$ (the period to reach $[BrO_3^-]$ = 10 μM) was calculated to be approximately 25 years, which can be considered as a negligible progression at this diluted solution under room temperature and 1 atmosphere (~101.3 kPa). We again emphasize that the previous study for the $Br^-/BrO_3^-$ system was investigated at a significantly higher concentration of reactants (in an extremely acidic solution) than the above-calculated condition: the ionic strength was adjusted to 3 M which is approximately 5000 times higher than the above. However, as we demonstrate in the present study, the $Br^-/BrO_3^-$ reaction at diluted conditions, as mentioned above, can be notably accelerated within 30 min via freezing of the solution. This freezing-induced chemical reaction is poorly understood and has been overlooked until the present: although several studies have reported the intriguing $BrO_3^-$ derived chemical reaction in ice, the unique behavior of $BrO_3^-$ for $Br^-$ oxidation in ice has not been reported yet [23-28]. To the best of our knowledge, this is the first study to report on $BrO_3^-$ induced $Br^-$ oxidation in ice.

Freezing process is considered as a chemical reaction freezing procedure because the chemical reaction rate is normally inhibited by temperature decrease. Therefore, many violent chemical experiments were conducted under low temperatures for safety. The temperature dependence of the chemical reaction can be expressed by the decline in molecular energy in cold conditions. However, several studies have been reported that are associated with the accelerated chemical reaction during the freezing process [29]. These indicate that there are some factors that overcome the empirical Arrhenius relationship when freezing a solution [30]. Notably, water impurity results in a decrease in the ice melting point (eutectic point); therefore, a liquid phase in the ice grain boundary region can possibly be established if the water is frozen at moderate temperatures [31]. Because the increasing ice crystal repels the impurities, these impurities accumulate in the ice grain boundary region. Ultimately, the concentration of impurities in this region considerably increases, and this effect probably enhances the chemical reaction between reactants [32]. This phenomenon is called the freeze concentration effect. In addition, not only the freeze concentration effect but also the freeze potential effect is suggested to interpret the increasing chemical reaction; however, sufficient studies are still needed to confirm the influence of the phenomenon [33-36]. The scheme for freeze potential affirmed that the reaction can be enhanced by the electrochemical effect that is created by disproportionate ion distribution between ice crystals and liquid-like regions. In addition, the liquid water contents in ice grain boundary region is reduced during the freezing process, and the

acid-base equilibrium possibly affects the chemical equilibrium in the brine in the region [37].

This study compared the transformation of $Br^-$ and $BrO_3^-$ in water and ice and attempted to reveal the chemical transformation mechanism using the ion chromatography (IC), UV-vis spectrometer, high-resolution mass spectrometry (HRMS), and inductively coupled plasma mass spectroscopy (ICP-MS). Then, we confirmed the freeze concentration phenomenon in the ice using the Raman spectroscopy. We tested the $Br^-/BrO_3^-$ reaction in various experimental conditions, such as freezing temperature, initial pH, and initial dosage. Finally, we discussed the natural relevance of the frozen $Br^-/BrO_3^-$ system through investigation of $O_3$ induced $Br^-$ oxidation and the experiment in extremely low reactant concentration conditions. This study demonstrated that the $Br^-/BrO_3^-$ reaction can be accelerated by freezing the solution. Because bromine behavior in polar regions is important, and insufficient attention has focused on the freezing-induced chemical reaction on the bromine explosion phenomenon, our study provides experimental evidence of a novel alternative $Br_2$ generation scenario in the Arctic.

## 2. Materials and Methods

### 2.1. Materials

The following chemicals were used in this study: sodium bromate (Sigma Aldrich, ≥ 99%), sodium bromide (Sigma Aldrich, ≥99%), sodium iodide (Sigma Aldrich, ≥99%), 2,2-azino-bis(3-ethylbenzothiazoline)-6-sulfonic acid-diammonium salt (ABTS, Sigma Aldrich, ≥98%), hydrochloric acid (Sigma Aldrich, 35%), perchloric acid (Sigma Aldrich, 60%), nitric acid (Sigma Aldrich, 70%), sodium hydroxide (Sigma Aldrich, 1N), cresol red (CR, Aldrich, 95%), 18O-labeled $H_2O$ (Sigma Aldrich, 97%), sodium carbonate (Sigma Aldrich, ≥ 99.5%), and sodium bicarbonate (Sigma Aldrich, ≥ 99.7%). All solutions in this study were prepared using deionized water (18.2 MΩ cm), which was purified using a Barnstead water purification system (Mili-Q Direct 16).

### 2.2. Experiment procedure

The working solution samples of $BrO_3^-$ and $Br^-$ (typically $[BrO_3^-]$ = 20 μM, and $[Br^-]$ = 150 μM) were prepared by adding aliquots of chemical stock solutions (typically 0.8 mL of 10 mM $BrO_3^-$ and 6 mL of 10 mM $Br^-$) to 393.2 mL of deionized water in a glass beaker. The initial pH of solution samples was controlled by 60% $HClO_4$ or 1N NaOH using a Thermo Scientific Orion 2-Star Benchtop pH meter (typically pH 3). Aqueous samples (10 mL) were placed in 15 mL VWR centrifuge tubes. These tubes were introduced in the temperature-controlled system using ethanol as a coolant, which was pre-maintained at -

20 ℃. In this study, experiments were conducted at -20 ℃ for reactions in the ice phase and 25° C for reactions in the aqueous phase. The time zero was defined as the moment the tubes were placed in the ethanol bath with the reaction temperature maintained constant at -20 ℃. At pre-determined time points, the frozen centrifuge tubes were withdrawn from the ethanol bath, and a beaker containing lukewarm water at 30 ℃ was immediately introduced for 2 min to thaw completely frozen samples before analysis.

### 2.3. Analytical methods

The concentrations of $BrO_3^-$ and $Br^-$ were quantitatively measured using an ion chromatography system (Thermo Fisher Scientific, Dionex Aquion) equipped with a suppressor (AERS 500), a 4-mm column (AS 23), and guard column (AG 23). The eluent solution was a mixture of 0.8 mM sodium bicarbonate ($NaHCO_3$) and 4.5 mM sodium bicarbonate ($Na_2CO_3$) with a flow rate of 1 mL min-1. To convert the heights of $BrO_3^-$ and $Br^-$ peaks to their respective concentrations, calibration curves were constructed using six known standard solutions of $BrO_3^-$ and $Br^-$ (200, 100, 50, 25, 12.5, and 6.25 μM).

High resolution mass spectroscopy (Thermo Fisher Scientific, Q Exactive Focus) with an 18O-water experiment was conducted to confirm the oxygen source. We manually injected the samples into the mass spectrometer using the Hamilton syringe with 5 μL $min^{-1}$ of injection speed. The ionization parameters were changed as follows: a detection range of m/z 94 to 99 for $OBr^-$, m/z 125 to 135 for $BrO_3^-$, m/z 232 to 247 for $Br_3^-$, m/z 180 to 190 for $IBr_2^-$ a resolution 12500, spray voltage of -2.50 kV, a capillary temperature of 320 ℃, sheath gas flow rate of 12 a.u., auxiliary gas flow rate of 1 a.u., auxiliary gas heater temperature of 300 ℃, S lens RF level of 50.0, maximum injection time of 100 ms, and an automatic gain control (AGC) target of $1\times10^5$. The results were analyzed using FreeStyle 1.5 ™ (Thermo Fisher Scientific) software.

The spatial distribution of $BrO_3^-$ during freezing was visualized using a confocal Raman spectroscope (Renishaw, inVia Qontor) equipped with a microscope stage [38]. An aqueous sample containing 2 mM of $BrO_3^-$, 2 mM of $Br^-$, and pH 3 was frozen at -20 ℃ (liquid nitrogen was used as a coolant) by mounting on a temperature-controlled microscope stage (Linkam Scientific, THMS600) at a rate of -2 ℃ min-1. $BrO_3^-$ and HOBr distributions were in-situ scanned by measuring the intensities at 805 and 932 $cm^{-1}$, respectively. The excitation source was a monochromatic 532 nm laser.

UV-vis spectroscopy (Shimadzu, UV-2600) was used to monitor the presence of hypobromite ($BrO^-$) in the solution. The absorbance of $BrO^-$ was determined at 329 nm using a 1-cm pathlength UV cuvette, and the concentration was calculated using Beer-Lambert's law: Abs. = εlc, where l = 1 cm and ε = 332 $M^{-1}$ $cm^{-1}$ [39]. The concentration $BrO^-$ was also double-checked using the ABTS method [40]. Samples (2.5

mL) were placed in 15 mL centrifuge tubes filled with 2 mL of deionized water, 0.25 mL of 1g $L^{-1}$ ABTS, and 0.25 mL of 0.05 M $H_2SO_4$. The mixed samples were maintained in the dark for 2 h before analysis. The absorbance values of the samples at 405 nm were measured using a UV-Vis spectrophotometer. The concentration of ABTS+, generated via the reaction between ABTS and $BrO^-$, was calculated using absorption coefficient of 31,600 $M^{-1}$ $cm^{-1}$ of ABTS+. The concentration of $BrO^-$ was estimated by the responsible ABTS+ intensity.

The change in pH during freezing was examined using the UV-Vis absorption spectra of cresol red (CR), an acid-base indicator [41, 42]. A 3 mL sample containing 20 μM of $BrO_3^-$, 150 μM of $Br^-$, 66.7 μM of CR, and pH 3 was placed in a 4 mL plastic rectangular cuvette. The cuvette was placed in the ethanol bath, pre-maintained at -20 ℃ for 1 h. The frozen cuvette was removed from the ethanol bath, and then UV-Vis absorption spectra were performed immediately without thawing, using a UV-Vis spectrophotometer. A frozen deionized water was compared as a reference.

The total Br contents analysis were performed using inductively coupled plasma mass spectroscopy (Thermo Fisher Scientific, iCAP TQe). The Br measurement was performed at single quadrupole and KED mode: cool gas (Ar) flow 14 L/min, auxilliary flow 0.8 L/min, nebulizer flow 1.08 L/min, cr gas (He) flow 4.73 L/min for KED mode.

The bromide speciation analysis was performed using an ion chromatography system (Thermo Scientific, Dionex-2100,) coupled to an inductively coupled plasma sector-field mass spectrometer (ICP-SFMS, Thermo Scientific, Element XR). The chromatographic separation was performed using a Dionex Ion AS19 anion exchange column (2 × 250 mm) coupled to a Dionex IonPac AG19 guard column (2 × 50 mm). The column temperature was maintained at 30 ℃ using a thermostatically controlled oven. The sodium hydroxide (NaOH) gradient, generated by an eluent generator at a flow rate of 0.25 mL $min^{-1}$, used the following protocol: isocratic elution at 0.5 mM from 0 to 6 min, gradient increase from 15 to 45 mM from 6 to 15 min, column clean-out at 45 mM from 15 to 18 min, and equilibration at 15 mM from 18.1 to 25 min. A suppressor (Thermo Scientific, ASRS 600, 2 mm) was used to remove NaOH before the solution entered the ICP-SFMS. Samples (1 mL) were injected manually using a Peak Rheodyne valve with 5 mL plastic syringes. LODs were determined to be 4 pg $g^{-1}$ for $Br^-$ and 2 pg g-1 for $BrO_3^-$.

Concentrated $O_3$ stock solution (~ 1.3 mM) was prepared by purging $O_3$ gas into deionized water cooled with ice bath while $O_3$ gas was produced by discharging pure oxygen gas using $O_3$ generator (Ozone Tech, LAB-1). Concentration of $O_3$ stock solution was spectrophotometrically determined with a molar absorption coefficient of 3200 $M^{-1}cm^{-1}$ at 260 nm wavelength.

## 3. Result and Discussion

### 3.1. Freezing-induced oxidation of $Br^-$ by $BrO_3^-$

Figure 1a and 1b shows the $Br^-$ and $BrO_3^-$ concentration change in solution that was frozen or stayed in aqueous condition during 6 h. Under the aqueous condition, there was no concentration change of $Br^-$. Accordingly, negligible $BrO_3^-$ reduction was also observed in the aqueous condition (data not shown). However, when the solution was frozen, the rapid chemical transformation of $Br^-$ and $BrO_3^-$ were found: $Br^-$ removal were 50, 65, 57, 52, and 47%, and $BrO_3^-$ removal were 20, 47, 80, 90, and 100% at 20, 50, 100, 150, and 200 μM of initial $Br^-$ concentration, respectively (note that the initial $BrO_3^-$ concentration was set to 20 μM constantly). The $Br^-$ concentration did not decrease in the absence of $BrO_3^-$, and vice versa. These results indicate that the reaction between $Br^-$ and $BrO_3^-$ is considerably promoted in ice than that in water, and the both reactants are reciprocally responsible in the freezing-induced chemical reaction. According to a previous study, the reaction between $Br^-$ and $BrO_3^-$ is proposed to proceed via the formation of HOBr as follow:

$$BrO_3^- + Br^- + 2H^+ \rightarrow HBrO_2 + HOBr \quad (2)$$

$$HBrO_2 + Br^- + H^+ \rightarrow 2HOBr \quad (3)$$

$$\text{Overall; } BrO_3^- + 2Br^- + 3H^+ \rightarrow 3HOBr \quad (4)$$

To evaluate the HOBr production, we adjusted the sample pH to 10.50 using NaOH to deprotonate HOBr (pKa = 8.8) [25], and monitored the 329 nm light absorbance (Figure 1c). Notably, there was negligible HOBr production at the aqueous condition, while the concentration of HOBr rapidly increased as the solution started to freeze and reached approximately 50 μM at the 150 μM initial $Br^-$ concentration. This trend is similar to the $Br^-$ and $BrO_3^-$ concentration change, as shown in Figure 1a and 1b. Note that the HOBr generation was also supported by the measurement using ABTS method and the result was not significantly different with the above. From the stoichiometry in reaction (4), we can balance the $Br^-$ and $BrO_3^-$ ratio: one molecule of $BrO_3^-$ consumes two $Br^-$ molecules and generates three molecules of HOBr. However, we emphasize here that the 85 μM $Br^-$ was consumed by the reduction of 18 μM $BrO_{3-}$ in 50 μM HOBr generation: i.e., $Br^-/BrO_3^-$ ratio is 4.72/1 and $HOBr/BrO_3^-$ ratio is 2.77/1. Considering that the HOBr can be hydrolyzed by $H_2O$ to produce $Br_2$, as shown in reaction (5) [43].

$$Br_2 + H_2O \rightarrow HOBr + Br^- + H^+ \quad (5)$$

Note that the equilibrium constant $K_{eq}$ for reaction (5) is $7.2 \times 10^{-9}$ $M^2$ ($[HOBr][H^+][Br^-]/[Br_2]$), which empirically means that the rate constant for forward reaction is lower than the backward reaction (prefer to go left-hand side in reaction (5)). Therefore, the equation (4) and (5) can be combined to induce the equation (6).

$$BrO_3^- + 5Br^- + 6H^+ \rightarrow 3Br_2 + 3H_2O \quad (6)$$

From the stoichiometry of equation (6), we can balance the $Br^-$ and $BrO_3^-$ ratio as 5/1, which is approximately agreed to the above experimentally determined value (4.72/1). We infer that the error is ascribed to that the intermediate species HOBr is remained in the solution (note that the HOBr concentration in the solution is ca. 50 μM).

### 3.2. Chemical transformation of $Br^-$ and $BrO_3^-$ to $Br_2$ generation

The equation (5) describes that the $Br_2$ can be generated from $Br^-$ oxidation by HOBr (backward direction). However, the hydrolysis of (dissolved) $Br_2$ also can generate HOBr in solution (forward direction), therefore there are two pathways for the HOBr in solution: the reduction of $BrO_3^-$ and the hydrolysis of $Br_2$. To identify the oxygen source of HOBr, we conducted high-resolution mass spectroscopy (HRMS) using 18O-water. Here, we want to proof $Br_2$ generation in the frozen $Br^-/BrO_3^-$ system, hence presence of 18O-HOBr can be one of the evidences for $Br_2$ generation (note that if the HOBr comes from $BrO_3^-$, 16O-HOBr is generated). In HRMS measurement, we used HCl as a pH-adjusting reagent because the high abundance of $HClO_4$ ($ClO_4^-$, m/z 98.9490) interferes with the $BrO^-$ (deprotonated HOBr) detection (m/z range of 94-100 in SIM mode). In addition, the pH of the thawed sample, namely, after reaction, was adjusted to 10.5 to deprotonate HOBr (to make $BrO^-$). As shown in Figure 2a, the HOBr originated from the reduction of $BrO_3^-$ as well as from the hydrolysis of $Br_2$: the detection of 79Br18O and 81Br18O evidently suggests the occurrence of $Br_2$ hydrolysis. In our previous study, we proved that when the $OCl^-$ results from the sole hydrolysis of $Cl_2$, it produces only Cl18O but not Cl16O species [44]. Additionally, oxygen exchange between Br16O3$^-$ and H218O may plausibly contribute to the detection of H18OBr; however, we note that the hydrolysis of $Br_2$ also plays a significant role and cannot be disregarded as a source of H18OBr. Therefore, we confirmed that some portion of $BrO^-$ was resulted from the $BrO_3^-$ reduction but another portion was resulted from the reaction of $Br_2$ with $H_2O$ (Figure 2a).

Second, we expect that if the dissolved $Br_2$ presents in the solution, we can observe $Br_3^-$ in the solution because $Br_3^-$ can be generated from the equilibrium with $Br_2$ and $Br^-$.

$$Br_2 + Br^- \leftrightarrow Br_3^- \quad (7)$$

The equilibrium constant for equation (7) is 19 $M^{-1}$ at 20 ℃, which indicates that the [$Br_3^-$] value is greater than the multiplication of [$Br^-$] and [$Br_2$] [43]. As shown in Figure 2b, we found m/z 236.7555 for 79Br3, 238.7535 for 79Br281Br, 240.7514 for 79Br81Br2, and 242.7494 for 81Br3. Furthermore, the m/z signal pattern is comparable with the simulated result. Hence, the HRMS result confirmed the occurrence of $Br_3^-$ in the system.

Third, we tried to trap dissolved $Br_2$ via chemical ionization method with 1 mM of $I^-$ addition [45]. Here, $IBr_2^-$ can be produced which is an indicator for $Br_2$ in the solution. In Figure 2c, the signal for $IBr_2^-$ is clearly detected in HRMS measurement. Notably, the $IBr_2^-$

signal does not appear when the solution was stayed in the aqueous condition. This is well corresponded to the HOBr generation aspect: HOBr is generated at the frozen condition but not in the aqueous condition. Therefore, we can confirm the production of $Br_2$ in the frozen $Br^-/BrO_3^-$ system by HRMS measurement.

To demonstrate the volatilization of $Br_2$ in the solution, we monitored the total Br contents in the solution using the inductively coupled plasma mass spectroscopy (ICP-MS). As demonstrated in the Figure 2d, the 170 μM of initial Br contents decreased to 120 μM at the frozen condition, while the value does not decrease and remained at 170 μM when the solution was not frozen. The calculation for $Br_{tot}$ ($Br_{tot}$ = $[BrO_3^-]$ + $[Br^-]$ + $[BrO^-]$) also well agreed with the ICP-MS measurement (insert in Figure 2d). The Brtot at the initial stage was 170 μM (150 μM $Br^-$ and 20 μM $BrO_3^-$), but approximately 50 μM $Br_{tot}$ disappeared during the freezing process. Therefore, we confirm the volatilization of $Br_2$ from the ice: but some portion of $Br_2$ contribute the HOBr in solution, as discussed in the above section.

### 3.3. Freeze concentration effect

To confirm the increase in freeze concentration during the freezing process, we conducted in situ measurements of the ice using the Raman microscope technique (Figure 3a). We used a high concentration of reagents (10 mM $Br^-$ and 2 mM $BrO_3^-$) to acquire the intense Raman signal of the substances. In the map scan view, the red-color scale represented the 805 $cm^{-1}$ signal intensity for the Br-O vibration of $BrO_3^-$, and the green-color scale represented the 932 $cm^{-1}$ signal intensity for the Br-O vibration of HOBr (see the raman spectrum at the bottom). Thus, the spatial distribution of substances in ice can be visualized (note that the $Br^-$ (single atom) and $Br_2$ (low polarizability) signal cannot be presented in the Raman spectroscopy due to the nature of the measurement mechanism). Overall, the intense color expression appeared at the center of the crystal junction, whereas the black color was at the crystal bulk. In addition, the $BrO_3^-$ signal intensity was evidently decreased when the $Br^-$ and $BrO_3^-$ were frozen together whereas $BrO_3^-$ signal was not decreased at the absence of $Br^-$ and there are no HOBr responsible peak appeared. Therefore, we confirmed that the $Br^-$ mediated $BrO_3^-$ reduction is the in-situ reaction in the ice. The estimated thickness of the ice grain boundary region and ice crystal was less than 5 and 50 μm, respectively. This indicated that the dissolved $BrO_3^-$ in a few-tenth length accumulated in only a few μm sized regions during the freezing of the solution. Therefore, we assumed that the substrates could be approximately 1000 times (10 × 10 × 10) more concentrated in the ice than water.

Further, the $Br^-$ oxidation in water was monitored at a high $Br^-$ and $BrO_3^-$ dose (1000 times higher than the regular experimental condition) to confirm the freezing-induced

accumulation hypothesis (Figure 3b). In aqueous condition, the chemical reaction at pH 3 was negligible even the elevation of reactant concentration, but the rapid chemical reaction was found when the pH was adjusted to 2: approximately 90 of 150 mM $Br^-$ and 14 of 20 mM $BrO_3^-$ were decreased within 10 min. The $Br^-/BrO_3^-$ reaction at a high reagent dose and strong acidic condition is consistent with previously investigated kinetic studies [20, 22]. Accordingly, the significance of pH was also confirmed. When only pH decreased from 3 to 1 at 0.15 mM $Br^-$, only the marginal $BrO_3^-$ reduction was found. The $BrO_3^-$ reduction was also negligible at 1.5 mM $Br^-$ at pH 3; however, 15 mM $Br^-$ explicitly resulted in half of $BrO_3^-$ removal within 6 h reaction time in water. In addition, the $BrO_3^-$ reduction efficiency was enhanced with decreasing pH, and the $BrO_3^-$ completely diminished by 15 mM $Br^-$ at pH 1 condition in water.

Also, the proton accumulation in ice was confirmed in situ using the cresol red (CR) as an acid-base indicator (Figure 3c). A peak of 434 nm was found in the aqueous CR solution, which indicates the mono-protonated CR ($HA^-$). The first acid dissociation constant ($pK_{a1}$) of CR is 1.1 [46]. However, the principal peak of CR moved to approximately 518 nm, which was the corresponding signal of the di-protonated CR ($H_2A$) when the solution was frozen for 1 h. Owing to the oxidative property of $BrO_3^-$, the CR in ice could be oxidized; thus, we did not estimate the pH value in the ice grain boundary using the Henderson-Hasselbalch equation. However, the color change of CR evidently indicated that the pH in ice was approximately 1.1 because of the $pK_{a1}$ of CR. We believe that the peak that slightly appeared at 580 nm of CR in ice is probably responsible for the brominated CR. This result implies that the accelerated reaction of $Br^-/BrO_3^-$ in ice results from the freeze concentration effect. During the freezing of the circumneutral solution, the growing ice crystal repels the dissolved species and proton. These are accumulated in the ice grain boundary region, and consequently, the area becomes highly concentrated and acidic, which promotes the $Br^-/BrO_3^-$ reaction. This freeze concentration effect should be seriously considered in the environmental chemistry of polar areas and stratosphere.

### 3.4. Investigation of the $Br^-/BrO_3^-$ reaction at various conditions

Figure 4 shows the temperature effect on the $Br^-/BrO_3^-$ system. The $BrO_3^-$ reduction did not progress when the solution was not frozen (25 and 0 ℃): the solution at 0 ℃ was not frozen during the entire reaction time, although water freezes at 0 ℃ at 101.3 kPa. A significant $BrO_3^-$ decrease was achieved when the solution started to freeze; however, the freezing temperature marginally differed.

The pH effect on the frozen $Br^-/BrO_3^-$ system is shown in Figure 5. The reaction was evidently hindered as the initial pH increased. This is because the reaction consumes protons (refer to reaction (6)). In addition, based on previous studies, the concentration of

protons in the ice grain boundary region is 2-3 orders of magnitude increase compared to that in the water; therefore, the acid-catalyzed chemical reaction is promoted in the ice grain boundary region, as discussed in the above section [47].

We investigated the effect of the initially injected $BrO_3^-$ concentration on the frozen $Br^-/BrO_3^-$ system (Figure 6). The reduction efficiency of $BrO_3^-$ decreased with increasing $BrO_3^-$ concentration at 150 μM $Br^-$ (Figure 6a). During the reaction, $Br^-$ was used for $BrO_3^-$ reduction, therefore intense $Br^-$ concentration with respect to $BrO_3^-$ concentration was preferred for BrO3? reduction: the $Br^-/BrO_3^-$ concentration ratio was 15, 7.5, 5, 3.75, and 3 at 10, 20, 30, 40, and 50 μM of the initial $BrO_3^-$ concentration, respectively. Apparently, $Br^-$ consumption ($[Br^-]_0$ - $[Br^-]$) increased with increasing $BrO_3^-$ concentration.

Further, we monitored the HOBr generation by varying the initial $BrO_3^-$ concentrations (Figure 6b). The HOBr generation was enhanced by increasing the initial dose of reactants. However, the HOBr generation was asymptotically saturated as the initial concentrations of $BrO_3^-$ reached 150 μM, respectively. The estimated conversion ratio from the total Br to HOBr was calculated and presented in Table 1. The HOBr generation was likely maximized at approximately 5 of the $Br^-/BrO_3^-$ ratio that is responsible for the stoichiometry of reaction (6).

### 3.5. The natural relevance of the feezing-induced $Br^-$ and $BrO_3^-$ reaction

According to previous studies, the $Br^-$ concentration in Arctic and Antarctica surface snow samples was approximately 10 ppb range (< 125 nM) [7, 48, 49]. Although information on the concentration of $BrO_3^-$ in the ocean and snow is limited, we note that HOBr can be efficiently produced via the oxidation of $Br^-$ by $O_3$ and OH. Subsequently, trace amounts of $BrO_3^-$ can be formed [50]. It is also worth mentioning that $BrO_3^-$ has been detected as a minor constituent in Arctic aerosol particles [51]. To investigate the $BrO_3^-$ generation trend from $Br^-$ oxidation in our regular experimental condition ($[Br^-]_0$ = 170 μM), we monitored the $BrO_3^-$ generation in the $O_3$ induced $Br^-$ oxidation (Figure 7a). The $Br^-$ concentration was decreased approximately 20, 50, 80, and 100 μM at 20, 50, 100, and 200 μM $O_3$ dosage, respectively, at 1 h of reaction time. Accordingly, the $BrO_3^-$ production was approximately 2, 4, 20, and 30 μM, respectively. From this, we know that the 100 μM $O_3$ can produce 20 μM $BrO_3^-$ from 170 μM $Br^-$ (but final concentrations are 90 μM $Br^-$ and 20 μM $BrO_3^-$ at 1 h). According to the research, the tropospheric $O_3$ concentration in Arctic region is approximately 36 ppbv in average [52], which can be converted to 1.6 nM using the value 22.414 L/mol at 0 ℃ 101.3 kPa. Hence, we believe that the $BrO_3^-$ generation from $Br^-$ oxidation by $O_3$ cannot be ignored.

We conducted the $Br^-/BrO_3^-$ reaction at extremely low concentration conditions to reveal the environmental relevance of the reaction (Figure 7b). Here, the diluted concentrations of

$Br^-/BrO_3^-$ (1 nM each) were investigated to confirm the progression of the freezing-induced chemical reaction. In the chromatography, we observed the presence of 79Br of $Br^-$ and 79Br of $BrO_3^-$ in the solution at the retention time of 590 and 730 s, respectively. The signals were well calibrated from 30 to 150 ppt using a $Br^-/BrO_3^-$ solution mixture. The measurement was conducted with a thorough pre-rinse process at every measurement, and the baseline was rigorously monitored to exclude the memory effect on signal acquisition. As shown in Figure 7b, the $BrO_3^-$ was apparently reduced by freezing: 0.412 and 0.999 nM $BrO_3^-$ were found in the frozen and aqueous solutions, respectively. However, the $Br^-$ concentrations were not notably different in the aqueous and frozen systems. Notably, the $Br^-$ concentration decreased under high $Br^-/BrO_3^-$ conditions; however, the difference between the concentrations in water and ice became less pronounced as the solution was diluted. We infer that the comparable $Br^-$ concentrations at lower levels are due to: (1) the generation of $Br^-$ via $BrO_3^-$ reduction, which compensates for the initial $Br^-$ loss in the frozen solution, and (2) the reduction of HOBr in ice by trace dissolved species, such as dissolved $O_2$. It is worth noting that dissolved $O_2$ has been suggested to play a key role in ice-phase chemistry [14, 53-55]. Consequently, we believe that the HOBr, the source of $Br_2$, is generated from the reduction of $BrO_3^-$.

As the freezing $Br^-/BrO_3^-$ system significantly influenced by pH, the environmental acidity can affect the ice chemistry of $Br^-$ oxidation. Hence, the acidic ice and snow should be of interest at the present study. Since we found through literature survey that the pH of snow and ice in polar region can be slightly acidic [12, 56, 57], the freezing induced $Br^-$ oxidation by $BrO_3^-$ can be naturally relevant. The importance of the role of reactive bromine species has been suggested during the Arctic ozone depletion event. Field campaigns and satellite observations have highlighted high levels of reactive bromine species (such as BrO) in snowpacks and sea ice regions [5, 9, 45, 58]. The reactive bromine species in the atmosphere are generated from the oxidation of $Br_2$ by oxidants, such as nitrous acid and the hydroperoxyl radical, and photochemical processes. However, the source of $Br_2$ has not been clearly elucidated.

## 4. Conclusion

In this study, we demonstrated the ice chemistry for $Br_2$ generation by the reaction of $Br^-/BrO_3^-$. The experimental studies for HOBr (hydrated $Br_2$) generation from the $Br^-/BrO_3^-$ reaction were conducted with varying reaction conditions, such as freezing temperature, pH, and reactant concentrations. The in-situ measurement of ice chemistry apparently showed the generation of HOBr from the reaction of $Br^-/BrO_3^-$. We proposed the possible transformation of Br species from the experimental result using HRMS and ICP-MS. The

freezing-induced $Br^-/BrO_3^-$ reaction has significant environmental relevance because this reaction was observed to occur even in the naturally relevant low concentration condition. Thus, the freezing-induced chemical reactions involving bromine compounds significantly impact polar environments. We provided experimental evidence for the significance of $Br_2$ generation in ice and believe that our experimental results support the novel $Br_2$ generation pathway in the Arctic.

## REFERENCES


[1] Magazinovic, R.S., B.C. Nicholson, D.E. Mulcahy, D.E. Davey, Bromide levels in natural waters: its relationship to levels of both chloride and total dissolved solids and the implications for water treatment, Chemosphere 57 (2004) 329-335

[2] Leri, A.C., O. Hettithanthri, S. Bolan, T. Zhang, J. Unrine, S. Myneni, D.R. Nachman, H.T. Tran, A.J. Phillips, D. Hou, Y. Wang, M. Vithanage, L.P. Padhye, T. Jasemi Zad, A. Heitz, K.H.M. Siddique, H. Wang, J. Rinklebe, M.B. Kirkham, N. Bolan, Bromine contamination and risk management in terrestrial and aquatic ecosystems, Journal of Hazardous Materials 469 (2024) 133881

[3] Sander, R., W.C. Keene, A.A.P. Pszenny, R. Arimoto, G.P. Ayers, E. Baboukas, J.M. Cainey, P.J. Crutzen, R.A. Duce, G. Hönninger, B.J. Huebert, W. Maenhaut, N. Mihalopoulos, V.C. Turekian, R. Van Dingenen, Inorganic bromine in the marine boundary layer: a critical review, Atmos. Chem. Phys. 3 (2003) 1301-1336

[4] Simpson, W.R., S.S. Brown, A. Saiz-Lopez, J.A. Thornton, R. von Glasow, Tropospheric Halogen Chemistry: Sources, Cycling, and Impacts, Chemical Reviews 115 (2015) 4035-4062

[5] Wennberg, P., Bromine explosion, Nature 397 (1999) 299-301

[6] Kendrick, M.A., Halogens in Seawater, Marine Sediments and the Altered Oceanic Lithosphere, in The Role of Halogens in Terrestrial and Extraterrestrial Geochemical Processes: Surface, Crust, and Mantle, D.E. Harlov and L. Aranovich, Editors. 2018, Springer International Publishing: Cham. p. 591-648.

[7] Maffezzoli, N., A. Spolaor, C. Barbante, M. Bertò, M. Frezzotti, P. Vallelonga, Bromine, iodine and sodium in surface snow along the 2013 Talos Dome-GV7 traverse (northern Victoria Land, East Antarctica), The Cryosphere 11 (2017) 693-705

[8] Yang, X., J.A. Pyle, R.A. Cox, Sea salt aerosol production and bromine release: Role of snow on sea ice, 35 (2008)

[9] Pratt, K.A., K.D. Custard, P.B. Shepson, T.A. Douglas, D. Pöhler, S. General, J. Zielcke, W.R. Simpson, U. Platt, D.J. Tanner, L. Gregory Huey, M. Carlsen, B.H. Stirm, Photochemical production of molecular bromine in Arctic surface snowpacks,

Nature Geoscience 6 (2013) 351-356

[10] Tolbert, M.A., M.J. Rossi, D.M. Golden, Antarctic Ozone Depletion Chemistry: Reactions of $N_2O_5$ with $H_2O$ and HCl on Ice Surfaces, 240 (1988) 1018-1021

[11] Cho, H., P.B. Shepson, L.A. Barrie, J.P. Cowin, R. Zaveri, NMR Investigation of the Quasi-Brine Layer in Ice/Brine Mixtures, The Journal of Physical Chemistry B 106 (2002) 11226-11232

[12] O'Sullivan, D., J.R. Sodeau, Freeze-Induced Reactions: Formation of Iodine-Bromine Interhalogen Species from Aqueous Halide Ion Solutions, The Journal of Physical Chemistry A 114 (2010) 12208-12215

[13] O'Driscoll, P., K. Lang, N. Minogue, J. Sodeau, Freezing Halide Ion Solutions and the Release of Interhalogens to the Atmosphere, The Journal of Physical Chemistry A 110 (2006) 4615-4618

[14] Kim, K., A. Yabushita, M. Okumura, A. Saiz-Lopez, C.A. Cuevas, C.S. Blaszczak-Boxe, D.W. Min, H.-I. Yoon, W. Choi, Production of Molecular Iodine and Tri-iodide in the Frozen Solution of Iodide: Implication for Polar Atmosphere, Environmental Science & Technology 50 (2016) 1280-1287

[15] Kim, K., B. Kim, Y.-Y. Ahn, K.D. Tran, H.T. My Truong, J. Kim, Production of Molecular Iodine via a Redox Reaction between Iodate and Organic Compounds in Ice, The Journal of Physical Chemistry A 127 (2023) 2830-2838

[16] O'Driscoll, P., N. Minogue, N. Takenaka, J. Sodeau, Release of Nitric Oxide and Iodine to the Atmosphere from the Freezing of Sea-Salt Aerosol Components, The Journal of Physical Chemistry A 112 (2008) 1677-1682

[17] Grguric, G., J.H. Trefry, J.J. Keaffaber, Ozonation products of bromine and chlorine in seawater aquaria, Water Research 28 (1994) 1087-1094

[18] von Gunten, U., J. Hoigne, Bromate Formation during Ozonization of Bromide-Containing Waters: Interaction of Ozone and Hydroxyl Radical Reactions, Environmental Science & Technology 28 (1994) 1234-1242

[19] Bray, W.C., H.A. Liebhafsky, The Kinetic Salt Effect in the Fourth Order Reaction BrO3- + Br- + 2H+ →. Ionization Quotients for HSO4- at 25°, Journal of the American Chemical Society 57 (1935) 51-56

[20] Côrtes, C.E.S., R.B. Faria, Kinetics and Mechanism of Bromate-Bromide Reaction Catalyzed by Acetate, Inorganic Chemistry 43 (2004) 1395-1402

[21] Schmitz, G., Kinetics and mechanism of the iodate-iodide reaction and other related reactions, Physical Chemistry Chemical Physics 1 (1999) 1909-1914

[22] Schmitz, G., Kinetics of the bromate-bromide reaction at high bromide concentrations, International Journal of Chemical Kinetics 39 (2007) 17-21

[23] Hao, Z., F. Shi, D. Cao, J. Liu, G. Jiang, Freezing-Induced Bromate Reduction by

Dissolved Organic Matter and the Formation of Organobromine Compounds, Environmental Science & Technology 54 (2020) 1668-1676

[24] Min, D.W., K. Kim, B. Kim, G. Lee, W. Choi, Cr(VI) Formation via Oxyhalide-Induced Oxidative Dissolution of Chromium Oxide/Hydroxide in Aqueous and Frozen Solution, Environmental Science & Technology 54 (2020) 14413-14421

[25] Min, D.W., W. Choi, Accelerated Reduction of Bromate in Frozen Solution, Environ. Sci. Technol. 51 (2017) 8368-8375

[26] Sun, H., L. Zhang, D. Dong, W. Zhang, Z. Guo, Freezing degradation of the anticonvulsant oxcarbazepine by bromate in water ice under sunlight irradiation, Science of The Total Environment 894 (2023) 165014

[27] Sun, H., L. Zhang, L. Wang, D. Dong, Y. Li, Z. Guo, Enhanced freezing-induced carbamazepine degradation by bromate under solar irradiation via the formation of hypobromous acid and hydroxyl radical, Journal of Hazardous Materials 457 (2023) 131793

[28] Sun, H., Z. Guo, L. Zhang, X. Hua, D. Dong, Degradation of carbamazepine in ice with bromate and nitrite: Role of reactive nitrogen species, Science of The Total Environment 923 (2024) 171376

[29] O'Concubhair, R., J.R. Sodeau, The Effect of Freezing on Reactions with Environmental Impact, Acc. Chem. Res. 46 (2013) 2716-2724

[30] Takenaka, N., H. Bandow, Chemical Kinetics of Reactions in the Unfrozen Solution of Ice, The Journal of Physical Chemistry A 111 (2007) 8780-8786

[31] Fukazawa, H., K. Sugiyama, S. Mae, H. Narita, T. Hondoh, Acid ions at triple junction of Antarctic ice observed by Raman scattering, Geophysical Research Letters 25 (1998) 2845-2848

[32] Takenaka, N., A. Ueda, T. Daimon, H. Bandow, T. Dohmaru, Y. Maeda, Acceleration Mechanism of Chemical Reaction by Freezing:? The Reaction of Nitrous Acid with Dissolved Oxygen, J. Phys. Chem. 100 (1996) 13874-13884

[33] Workman, E.J., S.E. Reynolds, Electrical Phenomena Occurring during the Freezing of Dilute Aqueous Solutions and Their Possible Relationship to Thunderstorm Electricity, Physical Review 78 (1950) 254-259

[34] Bronshteyn, V.L., A.A. Chernov, Freezing potentials arising on solidification of dilute aqueous solutions of electrolytes, Journal of Crystal Growth 112 (1991) 129-145

[35] Wilson, P.W., A.D.J. Haymet, Workman-Reynolds Freezing Potential Measurements between Ice and Dilute Salt Solutions for Single Ice Crystal Faces, The Journal of Physical Chemistry B 112 (2008) 11750-11755

[36] Haymet, A.D.J., P.W. Wilson, The Workman-Reynolds "Freezing Potential": A new look at the inherent physical process, Journal of Molecular Liquids 228 (2017) 243-246

[37] Heger, D., R. Govindarajan, E. Lu, S. Ewing, A. Lay-Fortenbery, X. Yuan, L. Veselý, E. Munson, L. Gatlin, B. Hancock, R. Suryanarayanan, E. Shalaev, Beyond pH: Acid/Base Relationships in Frozen and Freeze-Dried Pharmaceuticals, in Principles and Practices of Lyophilization in Product Development and Manufacturing, F. Jameel, Editor. 2023, Springer International Publishing: Cham. p. 39-61.

[38] Alves, W.A., R.B. Faria, Vibrational investigation of the stretching region of bromate ion in solution, Spectrochimica Acta Part A: Molecular and Biomolecular Spectroscopy 58 (2002) 1395-1399

[39] Lei, H., B.J. Mariñas, R.A. Minear, Bromamine Decomposition Kinetics in Aqueous Solutions, Environmental Science & Technology 38 (2004) 2111-2119

[40] Pinkernell, U., B. Nowack, H. Gallard, U. von Gunten, Methods for the photometric determination of reactive bromine and chlorine species with ABTS, Water Research 34 (2000) 4343-4350

[41] Vetráková, L'., V. Vykoukal, D. Heger, Comparing the acidities of aqueous, frozen, and freeze-dried phosphate buffers: Is there a "pH memory" effect?, International Journal of Pharmaceutics 530 (2017) 316-325

[42] Krausková, L'., J. Procházková, M. Klašková, L. Filipová, R. Chaloupková, S. Malý, J. Damborsk?, D. Heger, Suppression of protein inactivation during freezing by minimizing pH changes using ionic cryoprotectants, International Journal of Pharmaceutics 509 (2016) 41-49

[43] Lente, G., J. Kalmár, Z. Baranyai, A. Kun, I. Kék, D. Bajusz, M. Takács, L. Veres, I. Fábián, One- Versus Two-Electron Oxidation with Peroxomonosulfate Ion: Reactions with Iron(II), Vanadium(IV), Halide Ions, and Photoreaction with Cerium(III), Inorganic Chemistry 48 (2009) 1763-1773

[44] Ahn, Y.-Y., J. Kim, J. Jeon, K. Kim, Freezing-enhanced degradation of azo dyes in the chloride-peroxymonosulfate system, Chemosphere 359 (2024) 142261

[45] Liao, J., L.G. Huey, D.J. Tanner, F.M. Flocke, J.J. Orlando, J.A. Neuman, J.B. Nowak, A.J. Weinheimer, S.R. Hall, J.N. Smith, A. Fried, R.M. Staebler, Y. Wang, J.-H. Koo, C.A. Cantrell, P. Weibring, J. Walega, D.J. Knapp, P.B. Shepson, C.R. Stephens, Observations of inorganic bromine (HOBr, BrO, and Br2) speciation at Barrow, Alaska, in spring 2009, 117 (2012)

[46] Heger, D., J. Klánová, P. Klán, Enhanced Protonation of Cresol Red in Acidic Aqueous Solutions Caused by Freezing, The Journal of Physical Chemistry B 110 (2006) 1277-1287

[47] Ahn, Y.-Y., J. Kim, K. Kim, Frozen Hydrogen Peroxide and Nitrite Solution: The Acceleration of Benzoic Acid Oxidation via the Decreased pH in Ice, Environmental Science & Technology 56 (2022) 2323-2333

KOPRI 극지연구소

[48] Spolaor, A., C. Varin, X. Pedeli, J.M. Christille, T. Kirchgeorg, F. Giardi, D. Cappelletti, C. Turetta, W.R.L. Cairns, A. Gambaro, A. Bernagozzi, J.C. Gallet, M.P. Björkman, E. Barbaro, Source, timing and dynamics of ionic species mobility in the Svalbard annual snowpack, Science of The Total Environment 751 (2021) 141640

[49] Spolaor, A., E. Barbaro, D. Cappelletti, C. Turetta, M. Mazzola, F. Giardi, M.P. Björkman, F. Lucchetta, F. Dallo, K.A. Pfaffhuber, H. Angot, A. Dommergue, M. Maturilli, A. Saiz-Lopez, C. Barbante, W.R.L. Cairns, Diurnal cycle of iodine, bromine, and mercury concentrations in Svalbard surface snow, Atmos. Chem. Phys. 19 (2019) 13325-13339

[50] Morrison, C.M., S. Hogard, R. Pearce, A. Mohan, A.N. Pisarenko, E.R.V. Dickenson, U. von Gunten, E.C. Wert, Critical Review on Bromate Formation during Ozonation and Control Options for Its Minimization, Environmental Science & Technology 57 (2023) 18393-18409

[51] Hara, K., K. Osada, K. Matsunaga, Y. Iwasaka, T. Shibata, K. Furuya, Atmospheric inorganic chlorine and bromine species in Arctic boundary layer of the winter/spring, 107 (2002) AAC 4-1-AAC 4-15

[52] Law, K.S., J.L. Hjorth, J.B. Pernov, C.H. Whaley, H. Skov, M. Collaud Coen, J. Langner, S.R. Arnold, D. Tarasick, J. Christensen, M. Deushi, P. Effertz, G. Faluvegi, M. Gauss, U. Im, N. Oshima, I. Petropavlovskikh, D. Plummer, K. Tsigaridis, S. Tsyro, S. Solberg, S.T. Turnock, Arctic Tropospheric Ozone Trends, Geophysical Research Letters 50 (2023) e2023GL103096

[53] Takenaka, N., A. Ueda, T. Daimon, H. Bandow, T. Dohmaru, Y. Maeda, Acceleration Mechanism of Chemical Reaction by Freezing: The Reaction of Nitrous Acid with Dissolved Oxygen, The Journal of Physical Chemistry 100 (1996) 13874-13884

[54] Baek, Y.S., K. Kim, A. Saiz-Lopez, D.W. Min, B. Kim, W. Choi, C.H. Choi, Entangled iodine and hydrogen peroxide formation in ice, Physical Chemistry Chemical Physics 22 (2020) 16532-16535

[55] Ahn, Y.-Y., J. Kim, K. Kim, Catalytic behavior of nitrous acid for acetaminophen transformation during the freezing process, Journal of Hazardous Materials 456 (2023) 131652

[56] de Caritat, P., G. Hall, S. Gìslason, W. Belsey, M. Braun, N.I. Goloubeva, H.K. Olsen, J.O. Scheie, J.E. Vaive, Chemical composition of arctic snow: concentration levels and regional distribution of major elements, Science of The Total Environment 336 (2005) 183-199

[57] Nawrot, A.P., K. Migała, B. Luks, P. Pakszys, P. Głowacki, Chemistry of snow cover and acidic snowfall during a season with a high level of air pollution on the Hans Glacier, Spitsbergen, Polar Science 10 (2016) 249-261

KOPRI 극지연구소

[58] Foster, K.L., R.A. Plastridge, J.W. Bottenheim, P.B. Shepson, B.J. Finlayson-Pitts, C.W. Spicer, The Role of Br2 and BrCl in Surface Ozone Destruction at Polar Sunrise, 291 (2001) 471-474

KOPRI
극지연구소

## TABLE

**Table 1.** The values for the $Br^-/BrO_3^-$ system in HOBr generation.

| Condition for initial concentration | | $Br^-/BrO_3^-$ ratio | HOBr generation (μM) | HOBr/total Br ratio |
|---|---|---|---|---|
| $Br^-$ (μM) | $BrO_3^-$ (μM) | | | |
| 150 | 10 | 15 | 28.038 | 0.17 |
| 150 | 20 | 7.5 | 55.791 | 0.33 |
| 150 | 30 | 5 | 71.329 | 0.39 |
| 150 | 40 | 3.75 | 79.050 | 0.41 |
| 150 | 50 | 3 | 78.591 | 0.39 |
| 20 | 20 | 1 | 10.316 | 0.26 |
| 50 | 20 | 2.5 | 24.841 | 0.35 |
| 100 | 20 | 5 | 43.924 | 0.36 |
| 150 | 20 | 7.5 | 55.791 | 0.32 |
| 200 | 20 | 10 | 57.215 | 0.26 |

KOPRI
극지연구소

## FIGURES

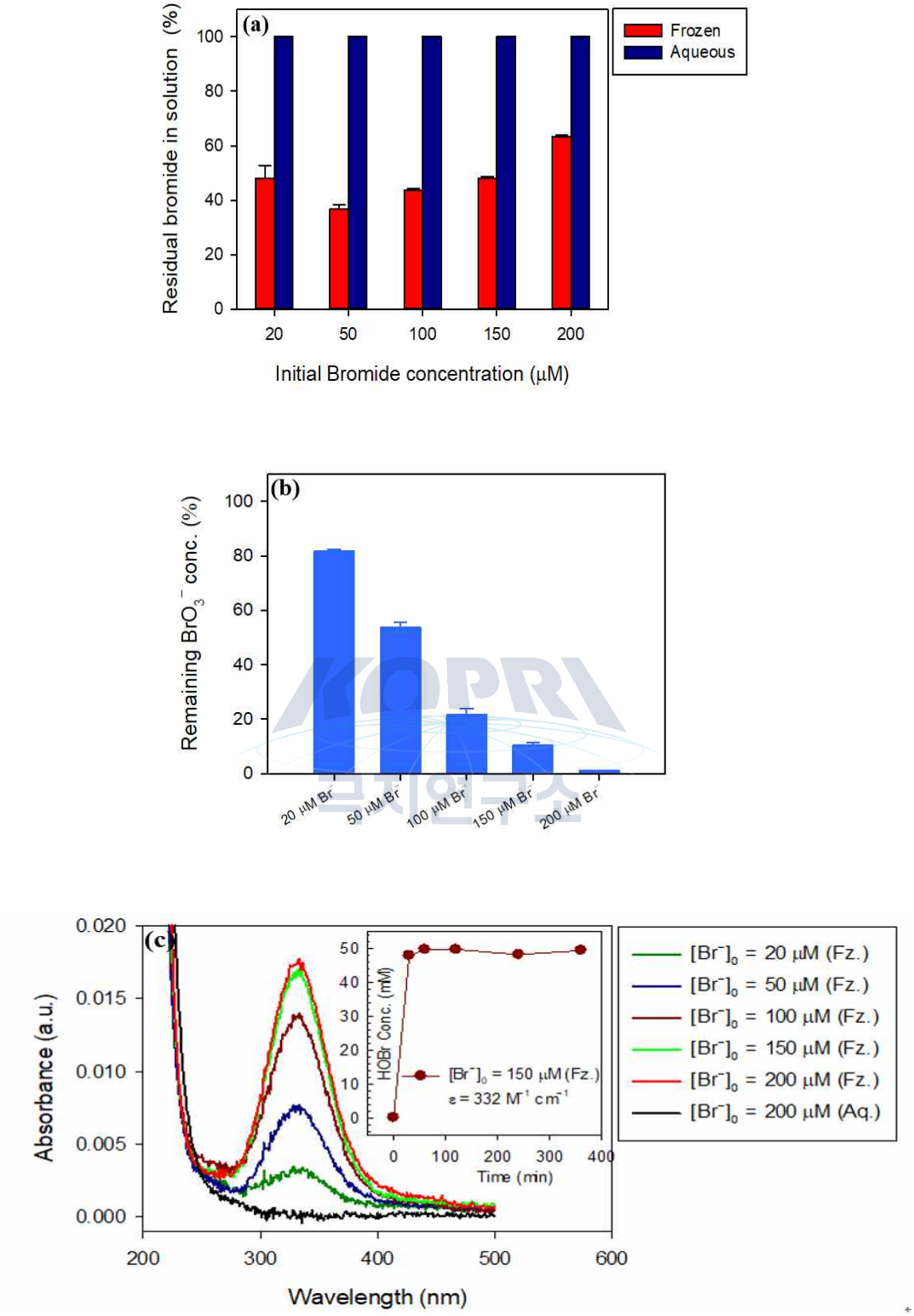
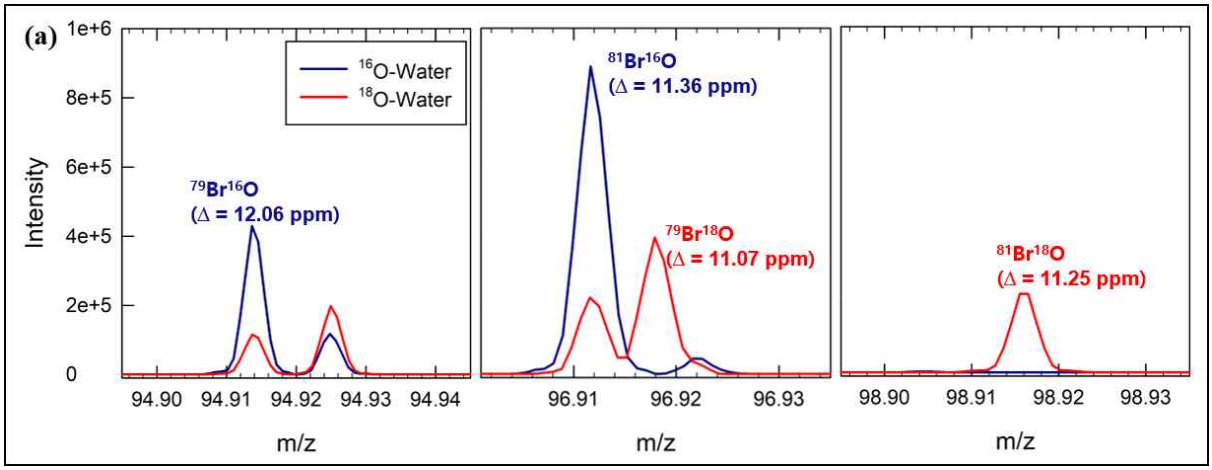
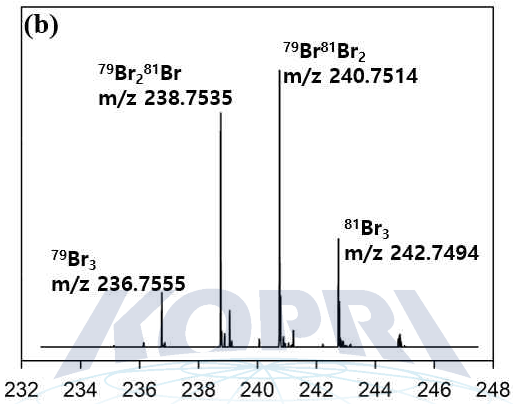
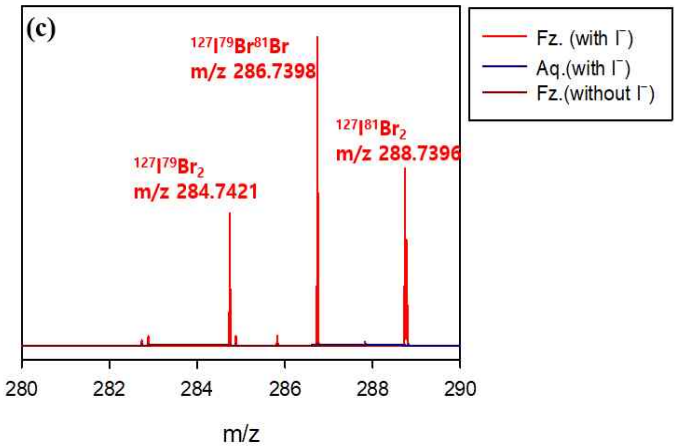



**Figure 1.** (a) Bromide removal in the $Br^-/BrO_3^-$ system. (b) Bromate removal in the frozen $Br^-/BrO_3^-$ system. (c) Hypobromous acid production in the $Br^-/BrO_3^-$ system (insert: HOBr concentration profile at $[Br^-]_0$ = 150 μM during 6 h freezing). The initial $Br^-$ concentration was controlled from 20 to 200 μM. Experimental condition: $[BrO_3^-]_0$ = 20 μM; pHi = 3.0 ($HClO_4$ adjusted); Temperature = 25 ℃ (Aqueous)/ -20 ℃ (Frozen); Reaction time = 6 h.


(a)
Intensity
1e+6
8e+5
6e+5
4e+5
2e+5
0
16O-Water
18O-Water
79Br16O
(Δ = 12.06 ppm)
81Br16O
(Δ = 11.36 ppm)
79Br18O
(Δ = 11.07 ppm)
81Br18O
(Δ = 11.25 ppm)
94.90 94.91 94.92 94.93 94.94
96.91 96.92 96.93
98.90 98.91 98.92 98.93
m/z
m/z
m/z


(b)
79Br2 81Br
m/z 238.7535
79Br81Br2
m/z 240.7514
81Br3
m/z 242.7494
79Br3
m/z 236.7555
232 234 236 238 240 242 244 246 248
m/z

KOPRI
극지연구소


(c)
127I79Br81Br
m/z 286.7398
127I81Br2
m/z 288.7396
127I79Br2
m/z 284.7421
Fz. (with I-)
Aq.(with I-)
Fz.(without I-)
280 282 284 286 288 290
m/z

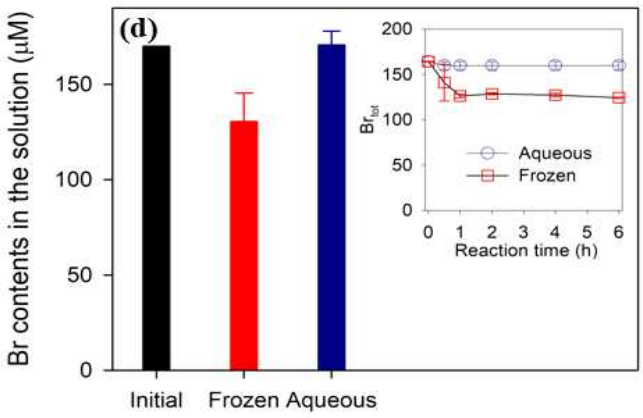



**Figure 2.** The high-resolution mass spectrometer (HRMS) of (a) $OBr^-$, (b) $Br_3^-$, and (c) $IBr_2^-$ in the frozen $Br^-/BrO_3^-$ solution. The solution pH was initially adjusted to 3.0 using HCl and finally adjusted to 10.50 by NaOH addition after thawing. (d) ICP-MS result in the total Br contents (insert: time profile in the calculation for $Br_{tot}$ ($[BrO_3^-]$ + $[Br^-]$ + $[BrO^-]$) in the solution).

KOPRI
극지연구소

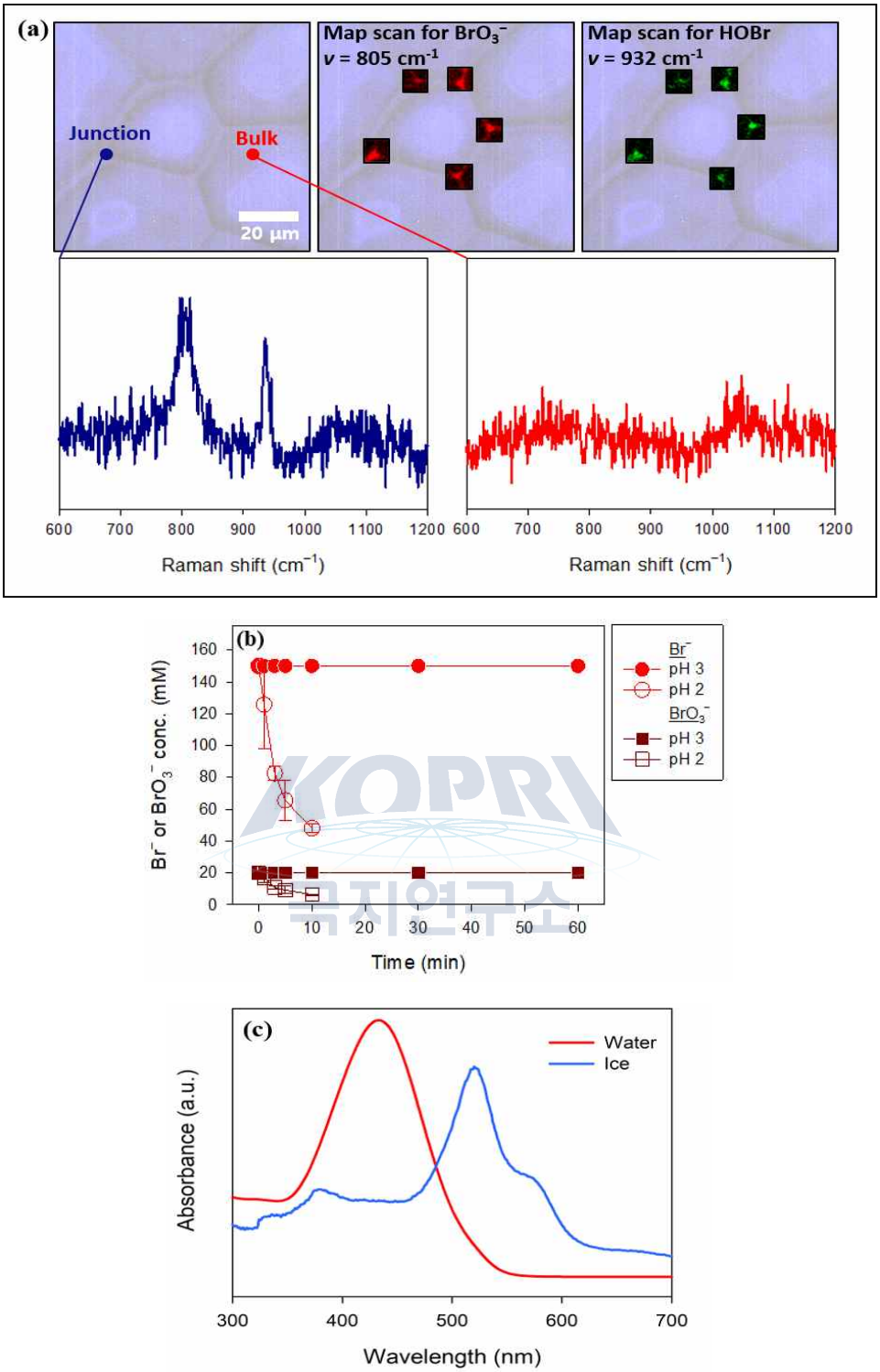



**Figure 3.** (a) The Raman microscope image of the frozen $Br^-/BrO_3^-$ solution. Experimental condition: $[BrO_3^-]_0$ = 2 mM; $[Br^-]_0$ = 10 mM; pHi = 3.0 ($HClO_4$ adjusted); Temperature = -20 ℃. (b) Time profile of high reactant concentration (1000 times higher than the regular condition) for the aqueous $Br^-/BrO_3^-$ solution. Experimental condition: $[BrO_3^-]_0$ = 20 mM; $[Br^-]0$ = 150 mM; Temperature = 25 ℃. (c) UV-vis absorption spectra of CR in water and ice. Experimental condition: $[BrO_3^-]_0$ = 20 μM; $[Br^-]_0$ = 150 μM; $[CR]_0$ = 66.7 μM; pHi = 3.0 ($HClO_4$ adjusted); Temperature = 25 ℃ (water)/ -20 ℃ (ice); freezing time = 1 h.

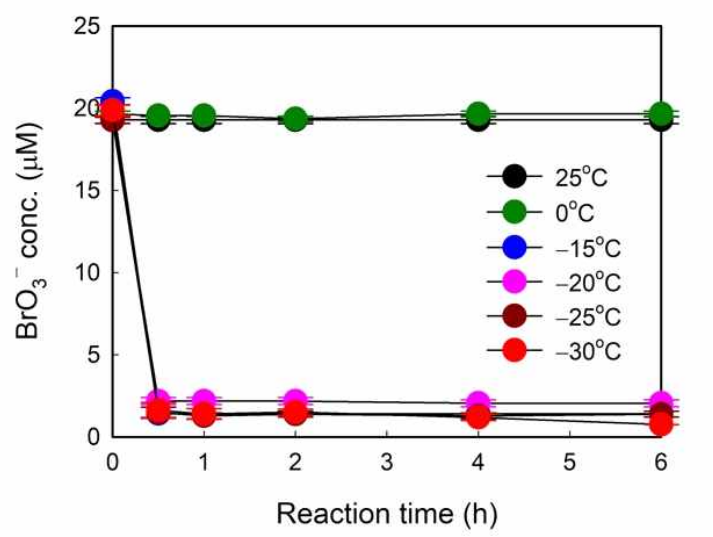



**Figure 4.** The effect of temperature on the $Br^-/BrO_3^-$ reaction. Experimental condition: $[BrO_3^-]_0$ = 20 μM; $[Br^-]_0$ = 150 μM; pHi = 3.0 ($HClO_4$ adjusted).

KOPRI
극지연구소

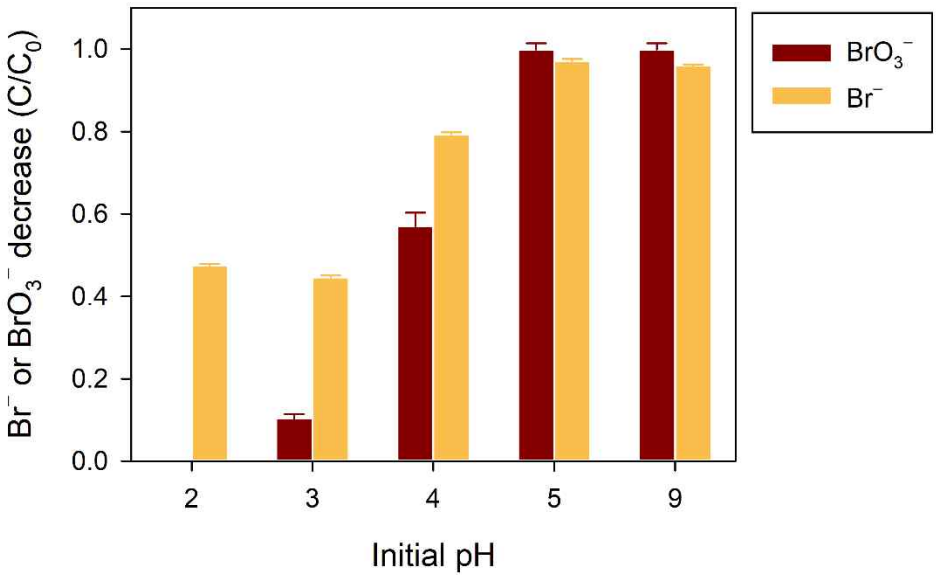



**Figure 5.** The initial pH effect on the frozen $Br^-/BrO_3^-$ system. Experimental condition: $[BrO_3^-]_0$ = 20 μM; $[Br^-]_0$ = 150 μM; Temperature = -20 ℃; reaction time = 6 h.

KOPRI
극지연구소

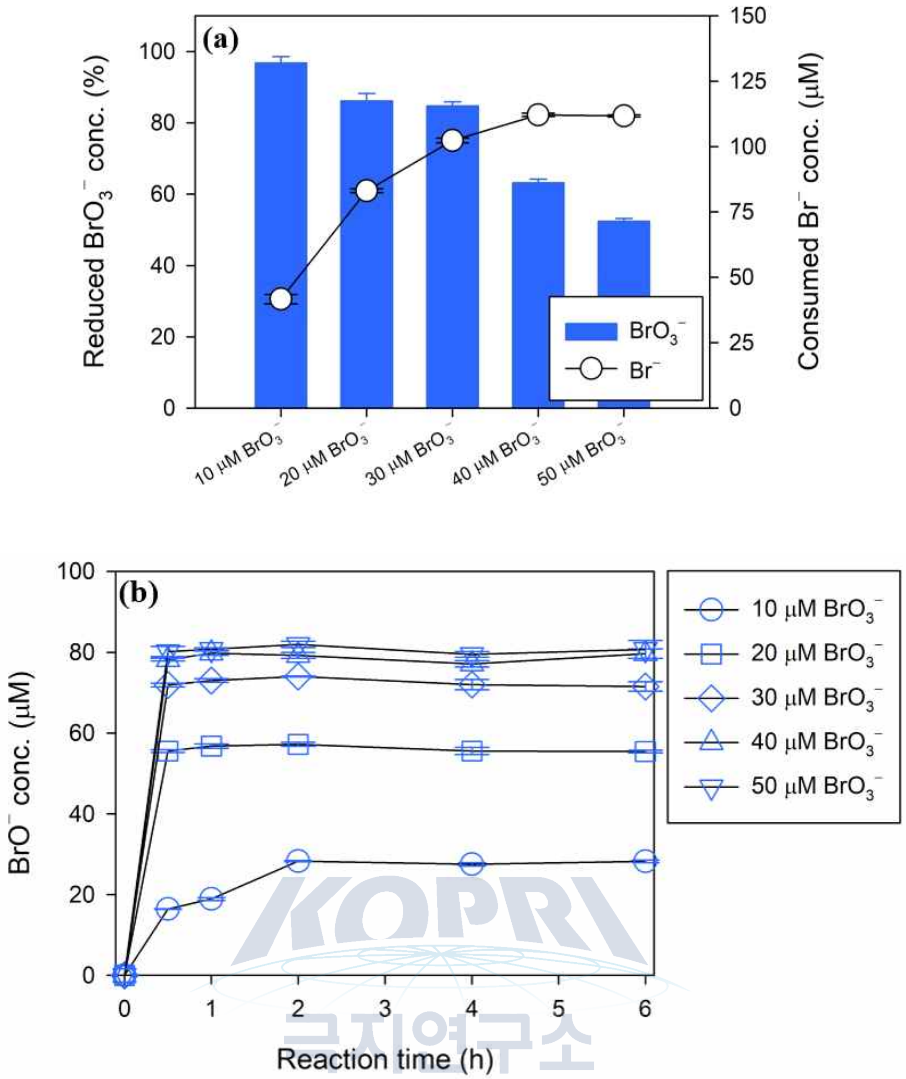



**Figure 6.** (a) The $BrO_3^-$ concentration effect on the frozen $Br^-/BrO_3^-$ system. Experimental condition: $[Br^-]_0$ = 150 μM; pHi = 3.0 ($HClO_4$ adjusted); Temperature = -20 ℃; reaction time = 6 h. (b) The HOBr generation in varying $BrO_3^-$ concentration

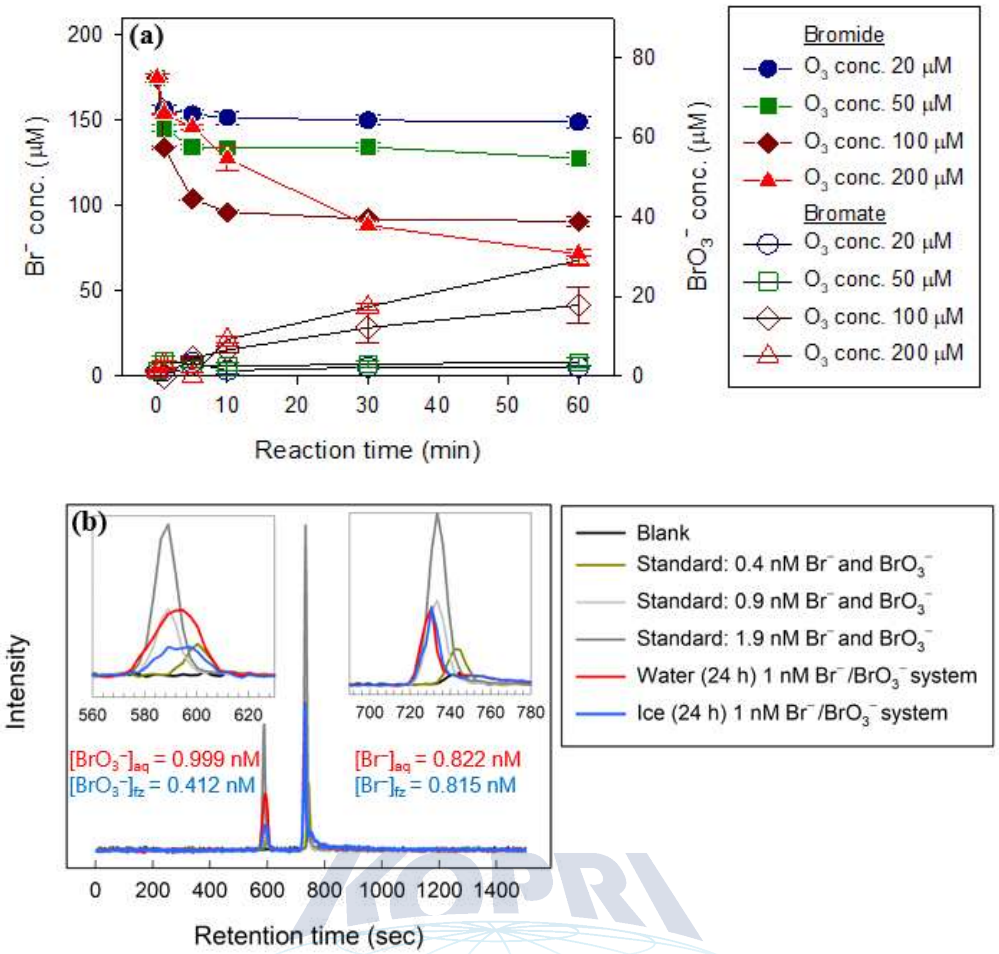



**Figure 7.** (a) Oxidative conversion of bromide to bromate under varying ozone dosage. Experimental condition: $[Br^-]_0$ = 170 μM; pHi = 3.0 ($HClO_4$ adjusted); Temperature = 20 ℃. (b) The IC-ICP MS chromatogram of the 1 nM $Br^-/BrO_3^-$ in water and ice after 24 h. Experimental condition: $[BrO_3^-]_0$ = 1 nM; $[Br^-]_0$ = 1 nM; pHi = 3.0 ($HClO_4$ adjusted); Temperature = 25 ℃ (water)/ -20 ℃ (ice); reaction time = 24 h.

KOPRI 극지연구소

# 제 4 장

# 연구개발목표 달성도 및 대외기여도

## 제 1 절. 연구개발목표 달성도

| 구분 | 년도 | 성과목표 | 지표 | 세계최고 수준주) (보유국/ 보유기관) | 목표치 | 가중치 (%) | 평가기준 | 설정근거 | 달성치 |
|---|---|---|---|---|---|---|---|---|---|
| 1단계 성과목표 | 2020~ 2022 | 논문게재 | SCI(E) 논문 mrnIF 40이상~80미만 | - | 3 건 | 20 | ○SCI(E) 게재논문중 mrnIF 40 이상 논문건수 | 우수논문 발표 | 100 |
| | | | SCI(E) 논문 mrnIF 80이상 | - | 7 건 | 20 | ○SCI(E) 게재논문중 mrnIF 80 이상 논문건수 (※mrnIF 90이상 논문은 1.5편으로 계산) | 우수논문 발표 | 100 |
| | | 얼음 미세구조 특성연구 | 얼음화학 실험시스템개발 | 체코/마사릭 대 | 실험 시스템 2건 | 5 | ○얼음화학 실험을 위한 시스템 개발여부 | 얼음화학 연구를 위한 독창적 실험 시스템 개발 | 100 |
| | | | 얼음 미세구조 내 화학물질 농축특성 연구 | 일본/도쿄공 업대학 | 동결 라만 이미지 3 건 | 5 | ○얼음 내 농축된 화학물질 분포에 대한 라만 이미지 제시 여부 | 얼음미세 구조에 농축되는 화학물질의 농축 특성 검증 | 100 |
| | | | 재조합 결빙방지단백질 제작 | 캐나다/퀸즈 대 | 1 건 | 2 | ○합성한 재조합단백질 제시 여부 | 자연유래 결빙방지 단백질을 바탕으로 성능 및 특성이 향상된 결빙방지단백질 제작 | 100 |
| | | | 결빙방지단백질에 의한 얼음미세구조 및 활성 측정 | 캐나다/퀸즈 대 | 1 건 | 2 | ○얼음결정 성장억제 활성도 측정 결과 제시 여부 | 결빙방지 단백질이 얼음미세 구조에 미치는 영향 | 100 |

KOPRI 극지연구소

| | | | | | | | | | |
|---|---|---|---|---|---|---|---|---|---|
| | | | | | | | | 연구 | |
| | | | 극지생물 유래 결빙방지 물질제시 | 캐나다/퀸즈대 | 4 건 | 3 | ○결빙방지물질제시 여부 | 극지생물 유래 결빙방지 물질의 얼음 결정 조절 특성 평가 | 100 |
| | | | 결빙방지물질에의한 얼음결정변화 실험자료제시 | 캐나다/퀸즈대 | 4 건 | 3 | ○얼음결정형성이미지 제시여부 | 결빙방지 특성을 지닌 물질의 얼음 결정 변화 활성 평가 | 100 |
| | | 얼음 미세구조에서 일어나는 환경화학반응 이해 | 얼음 내 오염물질 독성변화 실험 및 분석자료 | 싱가포르/난양공대 | 3 세트 | 10 | ○실험 및 분석결과 제시 여부 | 동결수처리공정 기술개발을 위한 원천기술 확보 | 100 |
| | | | 극지환경화학반응 실험 및 분석자료 | 미국/칼텍 | 2 세트 | 10 | ○실험 및 분석결과 제시 여부<br>○KPDC 등록 | 극지방 환경화학반응에 있어서 얼음의 역할 규명 | 100 |
| | | | 얼음화학반응 생성물의 생물독성 평가 | 싱가포르/난양공대 | 3 건 | 10 | ○독성평가 결과 제시 여부 | 얼음화학반응으로 변환된 오염물질의 생태영향 규명 | 100 |
| | | 저온응용기술 기초연구 | 얼음화학 응용기술 지적재산권 확보건수 | - | 특허 출원 2건 | 3 | ○특허 출원 여부 | 극지연구 신성장 동력 및 실용화 성과 창출과 연계 | 100 |
| | | | | - | 특허 등록 1건 | 2 | ○특허 등록 여부 | | 100 |
| | | | 얼음 특성을 활용한 환경/에너지 신소재 개발 기초연구 | - | 신소재 2 건 | 5 | ○환경정화 또는 에너지 분야에 활용 가능한 신소재 합성법 또는 합성물 제시 여부 | 얼음미세구조 특성 기반의 실용화 기술 개발 | 100 |

KOPRI 극지연구소

| | | | | | | | | | |
|---|---|---|---|---|---|---|---|---|---|
| 1차년도 | 2020 | 논문게재 | SCI(E) 논문 mrnIF 40이상~80미만 | - | 1 건 | 15 | ○SCI(E) 게재논문중 mrnIF 40 이상 논문건수 | 우수논문 발표 | 100 |
| | | | SCI(E) 논문 mrnIF 80이상 | - | 2 건 | 15 | ○SCI(E) 게재논문중 mrnIF 80 이상 논문건수 (※mrnIF 90이상 논문은 1.5편으로 계산) | 우수논문 발표 | 100 |
| | | 얼음 미세구조 특성연구 | 얼음화학 실험시스템개발 | 체코/마사릭대 | 실험 시스템 1건 | 10 | ○얼음화학 실험을 위한 시스템 개발여부 | 얼음화학 연구를 위한 독창적 실험 시스템 개발 | 100 |
| | | | 얼음 미세구조 내 화학물질 농축특성 연구 | 일본/도쿄공업대학 | 동결 라만 이미지 1 건 | 5 | ○라만 화학 mapping 자료 제시 여부 | 얼음 미세구조에 농축되는 화학물질의 농축 특성 검증 | 100 |
| | | | 재조합 결빙방지단백질 제작 | 캐나다/퀸즈대 | 1 건 | 5 | ○합성한 재조합단백질 제시 여부 | 자연유래 결빙방지단백질을 바탕으로 성능 및 특성이 향상된 결빙방지단백질 제작 | 100 |
| | | | 결빙방지단백질에 의한 얼음미세구조 및 활성 측정 | 캐나다/퀸즈대 | 1 건 | 10 | ○얼음결정 성장억제 활성도 측정 결과 제시 여부 | 결빙방지단백질이 얼음미세구조에 미치는 영향 연구 | 100 |
| | | 얼음 미세구조에서 일어나는 환경화학반응 이해 | 얼음 내 오염물질 독성변화 실험 및 분석자료 | 싱가포르/난양공대 | 1 세트 | 10 | ○실험 및 분석결과 제시 여부 | 동결수처리공정 기술개발을 위한 원천기술 확보 | 100 |
| | | | 극지환경화학반응 실험 및 분석자료 | 미국/칼텍 | 1 세트 | 10 | ○실험 및 분석결과 제시 여부<br>○KPDC 등록 | 극지방 환경화학반응에 있어서 얼음의 역할 규명 | 100 |
| | | | 얼음화학반응 생성물의 생물독성 평가 | - | 1 건 | 10 | ○독성평가 결과 제시 여부 | 얼음화학반응으로 변환된 오염물질의 생태영향 규명 | 100 |
| | | 저온응용기술 기초연구 | 얼음화학 응용기술 지적재산권 확보건수 | - | 특허 출원 1건 | 10 | ○특허 출원 여부 | 극지연구 신성장 동력 및 실용화 성과 창출과 연계 | 100 |

KOPRI 극지연구소

| | | | | | | | | | |
|---|---|---|---|---|---|---|---|---|---|
| 2차년도 | 2021 | 논문게재 | SCI(E) 논문 mrnIF 40이상~80미만 | - | 1 건 | 20 | ○SCI(E) 게재논문중 mrnIF 40 이상 논문건수 | 우수논문 발표 | 100 |
| | | | SCI(E) 논문 mrnIF 80이상 | - | 2 건 | 20 | ○SCI(E) 게재논문중 mrnIF 80 이상 논문건수 (※mrnIF 90이상 논문은 1.5편으로 계산) | 우수논문 발표 | 100 |
| | | 얼음 미세구조 특성연구 | 얼음화학 실험시스템개발 | 체코/마사릭대 | 실험 시스템 1건 | 5 | ○얼음화학 실험을 위한 시스템 개발여부 | 얼음화학 연구를 위한 독창적 실험 시스템 개발 | 100 |
| | | | 얼음 미세구조 내 화학물질 농축특성 연구 | 일본/도쿄공업대학 | 동결 라만 이미지 1 건 | 5 | ○얼음 내 농축된 화학물질 분포에 대한 라만 이미지 제시 여부 | 얼음 미세구조에 농축되는 화학물질의 농축 특성 검증 | 100 |
| | | | 극지생물 유래 결빙방지 물질제시 | 캐나다/퀸즈대 | 2 건 | 5 | ○결빙방지물질제시 여부 | 자연유래 결빙방지 단백질을 바탕으로 성능 및 특성이 향상된 결빙방지 단백질 제작 | 100 |
| | | | 결빙방지물질에 의한 얼음결정 변화 실험자료제시 | 캐나다/퀸즈대 | 2 건 | 5 | ○얼음결정형성이미지 제시여부 | 결빙방지 단백질이 얼음 미세구조에 미치는 영향 연구 | 100 |
| | | 얼음 미세구조에서 일어나는 환경화학반응 이해 | 얼음 내 오염물질 독성변화 실험 및 분석자료 | 싱가포르/난양공대 | 1 세트 | 10 | ○실험 및 분석결과 제시 여부 | 동결수처리공정 기술개발을 위한 원천기술 확보 | 100 |
| | | | 극지환경화학반응 실험 및 분석자료 | 미국/칼텍 | 1 세트 | 10 | ○실험 및 분석결과 제시 여부<br>○KPDC 등록 | 극지방 환경화학반응에 있어서 얼음의 역할 규명 | 100 |
| | | | 얼음화학반응 생성물의 생물독성 평가 | 싱가포르/난양공대 | 1 건 | 10 | ○독성평가 결과 제시 여부 | 얼음화학반응으로 변환된 오염물질의 생태영향 규명 | 100 |
| | | 저온응용기술 기초연구 | 얼음화학 응용기술 지적재산권 확보건수 | - | 특허 출원 1건 | 5 | ○특허 출원 여부 | 극지연구 신성장 동력 및 실용화 성과 창출과 연계 | 100 |
| | | | 얼음 특성을 활용한 환경/에너지 신소재 개발 기초연구 | - | 신소재 1 건 | 5 | ○환경정화 또는 에너지 분야에 활용 가능한 신소재 합성법 또는 합성물 제시 여부 | 얼음 미세구조 특성 기반의 실용화 기술 개발 | 100 |

KOPRI 극지연구소

| | | | | | | | | | |
|---|---|---|---|---|---|---|---|---|---|
| 3차년도 | 2022 | 논문게재 | SCI(E) 논문 mrnIF 40이상~80미만 | - | 1 건 | 25 | ○SCI(E) 게재논문중 mrnIF 40 이상 논문건수 | 우수논문 발표 | 100 |
| | | | SCI(E) 논문 mrnIF 80이상 | - | 3 건 | 25 | ○SCI(E) 게재논문중 mrnIF 80 이상 논문건수 (※mrnIF 90이상 논문은 1.5편으로 계산) | 우수논문 발표 | 100 |
| | | 얼음 미세구조 특성연구 | 얼음 미세구조 내 화학물질 농축특성 연구 | 일본/도쿄공업대학 | 동결 라만 이미지 1 건 | 10 | ○얼음 내 농축된 화학물질 분포에 대한 라만 이미지 제시 여부 | 얼음미세구조에 농축되는 화학물질의 농축 특성 검증 | 100 |
| | | | 극지생물 유래 결빙방지 물질제시 | 캐나다/퀸즈대 | 2 건 | 5 | ○결빙방지물질제시 여부 | 자연유래 결빙방지 단백질을 바탕으로 성능 및 특성이 향상된 결빙방지단백질 제작 | 100 |
| | | | 결빙방지물질에 의한 얼음결정 변화 실험자료제시 | 캐나다/퀸즈대 | 2 건 | 5 | ○얼음결정형성이미지 제시여부 | 결빙방지 단백질이 얼음미세구조에 미치는 영향 연구 | 100 |
| | | 얼음 미세구조에서 일어나는 환경화학반응 이해 | 얼음 내 오염물질 독성변화 실험 및 분석자료 | - | 1 세트 | 10 | ○실험 및 분석결과 제시 여부 | 동결수처리공정 기술개발을 위한 원천기술 확보 | 100 |
| | | | 얼음화학반응 생성물의 생물독성 평가 | 싱가포르/난양공대 | 1 건 | 10 | ○독성평가 결과 제시 여부 | 얼음화학반응으로 변환된 오염물질의 생태영향 규명 | 100 |
| | | 저온응용기술 기초연구 | 얼음화학 응용기술 지적재산권 확보건수 | - | 특허 등록 1건 | 5 | ○특허 등록여부 | 극지연구 신성장 동력 및 실용화 성과 창출과 연계 | 100 |
| | | | 얼음 특성을 활용한 환경/에너지 신소재 개발 기초연구 | - | 신소재 1 건 | 5 | ○환경정화 또는 에너지 분야에 활용 가능한 신소재 합성법 또는 합성물 제시 여부 | 얼음미세구조 특성 기반의 실용화 기술 개발 | 100 |

KOPRI 극지연구소

| 구분 | 년도 | 성과목표 | 지표 | 세계최고수준주)(보유국/보유기관) | 목표치 | 가중치(%) | 평가기준 | 설정근거 | 달성치 |
|---|---|---|---|---|---|---|---|---|---|
| 2단계 성과목표 | 2023~2025 | 논문게재 | SCI(E) 논문 mrnIF 40 이상~80미만 | - | 3 건 | 10 | ○SCI(E) 게재논문중 mrnIF 40 이상 논문건수 | 우수논문발표 | 100 |
| | | | SCI(E) 논문 mrnIF 80 이상 | - | 5 건 | 20 | ○SCI(E) 게재논문중 mrnIF 80 이상 논문건수 | 우수논문발표 | 100 |
| | | | SCI(E) 논문 mrnIF 90 이상 | - | 3 건 | 10 | ○SCI(E) 게재논문중 mrnIF 90 이상 논문건수 | 우수논문발표 | 100 |
| | | 얼음 미세구조 특성 및 제어기작 연구 | 물리·화학적 요인에 따른 얼음 미세구조변화 연구 | 스위스/PSI | 2 건 | 5 | ○얼음 미세구조 변화 이미지 제시 | 얼음 미세구조의 변화 및 성장 특성 검증 | 100 |
| | | | 얼음재결정화에 따른 동결농축 및 미세구조변화 연구 | 일본/도쿄공업대학 | 3 건 | 5 | ○얼음 미세구조 변화 이미지 제시 | 얼음재결정화 공정 후 얼음 미세구조로의 화학 물질 농축 특성 검증 | 100 |
| | | | 얼음 미세구조 제어방법 연구 | 미국/다트머스대 | 2 건 | 5 | ○얼음 미세구조 변화 이미지 제시 | 다양한 유무기물질 존재 하에서의 얼음 미세구조 제어 및 변화 특성 확인 | 100 |
| | | | 얼음 미세구조 조절에 따른 얼음화학반응 변화 연구 | 체코/마사릭 대 | 2 건 | 5 | ○실험 및 분석결과 제시 여부 | 얼음 미세구조 조절이 얼음화학반응에 미치는 영향연구 | 100 |
| | | 얼음 내 생지화학 현상 특성연구 | 극지방에 존재하는 오염물질 탐색 | 미국/칼텍 | 10 종 이상 | 5 | ○극지방에서 검출된 오염물질 목록 제시 | 극지방 환경화학반응에 영향을 미치는 오염물질 탐색 | 100 |
| | | | 얼음 내 오염물질 독성변화 실험 및 분석자료 | 싱가포르/난양공대 | 3 세트 | 5 | ○실험 및 분석결과 제시 여부 | 자연계 오염물질의 독성변화 메커니즘 규명을 위한 배경지식 확보 | 100 |
| | | | 결빙방지활성물질 탐색 | 캐나다/퀸즈대 | 4 건 | 5 | ○결빙방지활성물질제시 여부 | 결빙방지활성물질이 얼음 미세구조에 미치는 영향 연구 | 100 |
| | | | 극지방에서 일어나는 독특한 지구화학반응특성 연구 | 미국/칼텍 | 3 세트 | 5 | ○실험 및 분석결과 제시 여부 | 극지방 환경화학반응에 있어서 얼음의 역할 규명 | 100 |
| | | | 얼음화학반응 산물의 생물독성 평가 | - | 1 건 | 5 | ○독성평가 결과 제시 여부 | 얼음화학반응으로 인해 변환된 오염물질의 생태영향 규명 | 100 |
| | | 저온 정화기술 및 환경/에너지 신소재 개발 | 동결수처리공정 및 응용기술 관련 지식재산권 확보 | - | 3 건 | 5 | ○특허 출원 및 등록 여부 | 동결 공정을 통한 실용화 기술 개발 | 100 |
| | | | 동결정화기술 실용화를 위한 파일럿 스케일 테스트 | - | 20 리터 규모 | 5 | ○파일럿 플랜트 구축 여부 | 동결을 통한 오염물질 정화 기술의 산업적 응용 가능성 탐색 | 100 |
| | | | 얼음 특성을 활용한 환경/에너지 신소재 개발 | - | 3 건 | 5 | ○합성법 및 신소재 제시* 여부<br>*신소재에 대한 환경 또는 에너지 지표 달성여부(1,2,3 중 1항목 이상)<br>① 오염물 2종에 대한 제 | 얼음 미세구조 특성기반의 실용화 기술 개발 | 100 |

KOPRI 극지연구소

| | | | | | | | | | |
|---|---|---|---|---|---|---|---|---|---|
| | | | | | | | 거효율 90% 이상 달성<br>② 전극소재로 이용 시 전기전도도 1 S/cm 이상 달성<br>③ 수소생성 효율 AM 1.5 조건에서 STH (solar - to - hydrogen) 1% 이상 (1.23V) | | |
| 1차년도 | 2023 | 논문게재 | SCI(E) 논문 mrnIF 40 이상~80미만 | - | 1 건 | 10 | ○SCI(E) 게재논문중 mrnIF 40 이상 논문건수 | 우수논문발표 | 100 |
| | | | SCI(E) 논문 mrnIF 80 이상 | - | 3 건 | 30 | ○SCI(E) 게재논문중 mrnIF 80 이상 논문건수 | 우수논문발표 | 100 |
| | | 얼음 미세구조 특성 및 제어기작 연구 | 물리·화학적 요인에 따른 얼음 미세구조변화 연구 | 스위스/PSI | 2 건 | 10 | ○물리화학적 변수에 따른 얼음 미세구조 변화 이미지 제시 | 얼음 미세구조의 변화 및 성장 특성 검증 | 100 |
| | | | 얼음재결정화에 따른 동결농축 및 미세구조변화 연구 | 일본/도쿄공업대학 | 1 건 | 10 | ○동결농축 및 미세구조 변화 이미지 제시 | 얼음재결정화 공정 후 얼음 미세구조로의 화학 물질 농축 특성 검증 | 100 |
| | | 얼음 내 생지화학 현상 특성연구 | 극지방에 존재하는 오염물질 탐색 | 미국/칼텍 | 10 종 이상 | 5 | ○극지방에서 검출된 오염물질 목록 제시 | 극지방 환경화학반응에 영향을 미치는 오염물질 탐색 | 100 |
| | | | 인간유래 오염물질의 얼음 내 변화기작 기초연구 | - | 1 세트 | 5 | ○실험 및 분석결과 제시 여부 | 얼음화학반응으로 인해 변환된 오염물질의 생태영향 규명 | 100 |
| | | | 결빙방지활성물질 탐색 | 캐나다/퀸즈대 | 2 건 | 5 | ○결빙방지활성물질제시 여부 | 결빙방지활성물질이 얼음 미세구조에 미치는 영향 연구 | 100 |
| | | | 극지방에서 일어나는 독특한 지구화학반응특성 연구 | 미국/칼텍 | 1 세트 | 5 | ○실험 및 분석결과 제시 여부 | 극지방 환경화학반응에 있어서 얼음의 역할 규명 | 100 |
| | | 저온 정화기술 및 환경/에너지 신소재 개발 | 동결수처리공정 및 응용기술 관련 지식재산권 확보 | - | 1 건 | 10 | ○특허 출원 및 등록 여부 | 동결 공정을 통한 실용화 기술 개발 | 100 |
| | | | 얼음표면특성 제어를 통한 나노구조체 개발 | - | 1 건 | 10 | ○합성법 및 신소재 물성 분석자료 제시<br>*신소재에 대한 환경 또는 에너지 지표 달성여부(1,2,3 중 1항목 이상)<br>① 오염물 2종에 대한 제거효율 90% 이상 달성<br>② 전극소재로 이용 시 전기전도도 1 S/cm 이상 달성<br>③ 수소생성 효율 AM 1.5 조건에서 STH (solar - to - hydrogen) 1% 이상 (1.23V) | 얼음 미세구조 특성기반의 실용화 기술 개발 | 100 |

KOPRI 극지연구소

| | | | | | | | | | |
|---|---|---|---|---|---|---|---|---|---|
| 2차년도 | 2024 | 논문게재 | SCI(E) 논문 mrnIF 40 이상~80미만 | - | 1 건 | 10 | ○SCI(E) 게재논문중 mrnIF 40 이상 논문건수 | 우수논문발표 | 100 |
| | | | SCI(E) 논문 mrnIF 80 이상 | - | 1 건 | 30 | ○SCI(E) 게재논문중 mrnIF 80 이상 논문건수) | 우수논문발표 | 100 |
| | | 얼음 미세구조 특성 및 제어기작 연구 | 얼음재결정화에 따른 동결농축 및 미세구조변화 연구 | 일본/도쿄공업대학 | 2 건 | 10 | ○동결농축 및 미세구조 변화 이미지 제시 | 얼음재결정화 공정 후 얼음 미세구조로의 화학 물질 농축 특성 검증 | 100 |
| | | | 얼음 미세구조 제어방법 연구 | 미국/다트머스대 | 2 건 | 10 | ○물리화학적 변수에 따른 얼음 미세구조 변화 이미지 제시 | 다양한 유무기물질 존재 하에서의 얼음 미세구조 제어 및 변화 특성 확인 | 100 |
| | | 얼음 내 생지화학 현상 특성연구 | 얼음 내 오염물질 독성변화 실험 및 분석자료 | 싱가포르/난양공대 | 1 세트 | 5 | ○실험 및 분석결과 제시 여부 | 자연계 오염물질의 독성변화 메커니즘 규명을 위한 배경지식 확보 | 100 |
| | | | 결빙방지활성물질 탐색 | 캐나다/퀸즈대 | 1 건 | 5 | ○결빙방지활성물질제시 여부 | 결빙방지활성물질이 얼음 미세구조에 미치는 영향 연구 | 100 |
| | | | 극지방에서 일어나는 독특한 지구화학반응특성 연구 | 미국/칼텍 | 1 세트 | 5 | ○실험 및 분석결과 제시 여부 | 극지방 환경화학반응에 있어서 얼음의 역할 규명 | 100 |
| | | | 얼음화학반응 산물의 생물독성 평가 | - | 1 건 | 5 | ○독성평가 결과 제시 여부 | 얼음화학반응으로 인해 변환된 오염물질의 생태영향 규명 | 100 |
| | | 저온 정화기술 및 환경/에너지 신소재 개발 | 동결수처리공정 및 응용기술 관련 지식재산권 확보 | - | 1 건 | 10 | ○특허 출원 및 등록 여부 | 동결 공정을 통한 실용화 기술 개발 | 100 |
| | | | 얼음표면특성 제어를 통한 나노구조체 개발 | - | 1 건 | 10 | ○합성법 및 신소재 물성 분석자료 제시<br>*신소재에 대한 환경 또는 에너지 지표 달성여부(1,2,3 중 1항목 이상)<br>① 오염물 2종에 대한 제거효율 90% 이상 달성<br>② 전극소재로 이용 시 전기전도도 1 S/cm 이상 달성<br>③ 수소생성 효율 AM 1.5 조건에서 STH (solar - to - hydrogen) 1% 이상 (1.23V) | 얼음 미세구조 특성기반의 실용화 기술 개발 | 100 |

KOPRI 극지연구소

| | | | | | | | | | |
|---|---|---|---|---|---|---|---|---|---|
| 3차년도 | 2025 | 논문게재 | SCI(E) 논문 mrnIF 40 이상~80미만 | - | 1 건 | 10 | ○SCI(E) 게재논문중 mrnIF 40 이상 논문건수 | 우수논문발표 | 100 |
| | | | SCI(E) 논문 mrnIF 80 이상 | - | 1 건 | 30 | ○SCI(E) 게재논문중 mrnIF 80 이상 논문건수) | 우수논문발표 | 100 |
| | | 얼음 미세구조 특성 및 제어기작 연구 | 얼음 미세구조 조절에 따른 얼음화학반응 변화 연구 | 체코/마사릭 대 | 2 건 | 10 | ○실험 및 분석결과 제시 여부 | 얼음 미세구조 변화 제어 및 얼음 미세구조로의 화학 물질 농축 특성 검증 | 100 |
| | | 얼음 내 생지화학 현상 특성연구 | 얼음 내 오염물질 독성변화 실험 및 분석자료 | 싱가포르/난양공대 | 1 세트 | 5 | ○실험 및 분석결과 제시 여부 | 얼음화학반응으로 인해 변환된 오염물질의 생태영향 규명 | 100 |
| | | | 결빙방지활성물질 탐색 | 캐나다/퀸즈대 | 1 건 | 5 | ○결빙방지활성물질제시 여부 | 결빙방지활성물질이 얼음 미세구조에 미치는 영향 연구 | 100 |
| | | | 극지방에서 일어나는 독특한 지구화학반응특성 연구 | 미국/칼텍 | 1 세트 | 5 | ○실험 및 분석결과 제시 여부 | 극지방 환경화학반응에 있어서 얼음의 역할 규명 | 100 |
| | | | 얼음화학반응 산물의 생물독성 평가 | - | 1 건 | 5 | ○독성평가 결과 제시 여부 | 자연계 오염물질의 독성변화 메커니즘 규명 | 100 |
| | | 저온 정화기술 및 환경/에너지 신소재 개발 | 동결수처리공정 및 응용기술 관련 지식재산권 확보 | - | 1 건 | 10 | ○특허 출원 및 등록 여부 | 동결 공정을 통한 실용화 기술 개발 | 100 |
| | | | 동결정화기술 실용화를 위한 파일럿 스케일 테스트 | - | 20 리터 규모 | 10 | ○파일럿 플랜트 구축 여부 | 동결을 통한 오염물질 정화 기술의 산업적 응용 가능성 탐색 | 100 |
| | | | 저온합성 나노구조체 및 복합체 시제품 제작 | - | 1 건 | 10 | ○신소재 시제품 제시 여부<br>*신소재에 대한 환경 또는 에너지 지표 달성여부(1,2,3 중 1항목 이상)<br>① 오염물 2종에 대한 제거효율 90% 이상 달성<br>② 전극소재로 이용 시 전기전도도 1 S/cm 이상 달성<br>③ 수소생성 효율 AM 1.5 조건에서 STH (solar - to - hydrogen) 1% 이상 (1.23V) | 얼음 미세구조 특성기반의 실용화 기술 개발 | 100 |

KOPRI 극지연구소

# 제 2 절. 대외 기여도

“얼음의 미세구조 특성연구를 통한 저온 정화기술 및 환경·에너지 신소재 개발” 과제는 얼음의 미시적 특성과 화학 반응을 체계적으로 규명함으로써, 극지 자연현상 이해를 넘어 환경과학, 재료과학, 에너지 분야 등 다양한 학문 영역의 발전에 기여하였다. 2020~2022년 수행된 1단계 연구에서는 얼음화학 연구의 초석을 다지는 시기로 원활한 수행을 위해 다양한 저온 화학실험 및 분석 인프라를 구축하였다. 2023~2025년의 2단계 연구에서는 이전에 구축한 연구 인프라와 성과를 바탕으로, 얼음 미세구조 제어 기술 고도화와 동결 기반 응용 기술의 실증 가능성을 제시하며 연구 성과의 활용도를 크게 향상하였다.

본 연구에서는 얼음 미세구조 및 얼음 화학 반응을 정밀하게 분석할 수 있는 저온 실험·분석 플랫폼을 안정적으로 운영하고, 파일럿 스케일의 동결농축·정화 장비를 개발함으로써, 기존 저온과학 연구기관과 차별화된 실험 인프라를 확립하였다. 이는 향후 저온 환경에서의 화학 반응, 극지 환경 변화, 저에너지 수처리 및 소재 공정 연구를 선도할 수 있는 기반으로서, 극지연구소의 연구 경쟁력과 위상을 강화하는 데 기여하였다.

또한 국내외 연구기관과의 지속적인 교류와 공동연구를 통해 극지 환경화학, 얼음 미세구조 제어, 저온 응용기술 등 다양한 연구를 수행하였으며, 해당 성과는 향후 대형 국제공동연구 및 융합연구 과제 기획을 위한 핵심 기초자료로 활용될 수 있을 것으로 기대된다.

연구 성과 측면에서는 2단계 기간 동안 얼음 미세구조, 동결농축 기반 정화 기술, 얼음 기반 소재 합성 관련 다수의 연구 결과를 국제 학술지에 발표하였으며, 일부 연구는 학문적 중요성과 독창성을 인정받아 주목받는 논문 및 학술지 표지논문으로 소개되었다. 또한 동결을 이용한 오염물질 분리·정화 기술과 관련하여 지적재산권을 확보함으로써, 얼음 화학 연구가 학문적 성과를 넘어 기술적·산업적 가치로 확장될 수 있음을 입증하였다.

국제공동연구를 통해서는 극지방 대기 및 해빙 환경에서의 할로겐·금속 물질 거동, 얼음 미세구조 변화와 자연현상 간의 상관관계 등 지구환경 이해에 중요한 학술 성과를 도출하였다. 이러한 연구는 극지 환경 변화와 기후 시스템을 이해하는 데 필요한 핵심 자료를 제공하며, 국제 극지 연구 커뮤니티 내에서 국내 연구진의 학문적 기여도를 높이는 데 이바지하였다.

아울러 학연 협력 연구를 통해 얼음 화학, 극지 환경화학, 저온 응용기술 분야의 전문 인력을 양성하였다. 학생연구원과 신진 연구자를 중심으로 실험·분석·현장 연구 경험을 제공함으로써, 향후 극지 연구 및 환경·에너지 분야 연구개발을 주도할 수 있는 연구 인력을 체계적으로 육성하였다. 이는 장기적으로 국내 극지과학 및 저온 응용기술 분야의 연구 저변 확대와 지속가능한 연구 생태계 구축에 기여할 것으로 기대된다.

KOPRI 극지연구소

# 제 5 장

# 연구개발결과의 활용계획

“얼음의 미세구조 특성연구를 통한 저온 정화기술 및 환경·에너지 신소재 개발” 과제는 2020~2022년의 1단계 연구를 통해 얼음 화학 및 미세구조 연구를 수행하기 위한 인적·물적 연구 기반을 구축하였으며, 2023~2025년의 2단계 연구에서는 이를 토대로 얼음 미세구조 제어 기술과 동결 기반 응용 기술의 실증 가능성을 제시하였다. 본 연구단계에서 도출된 성과는 학문적 확장, 정책 지원, 기술 실용화 등 다양한 측면에서 활용될 수 있을 것으로 기대된다.

첫째, 얼음 미세구조 및 얼음 화학 반응에 관한 연구 성과는 교육·인력 양성 자료로 적극 활용될 수 있다. 얼음 표면과 준액체층을 포함한 미세구조의 형성과 반응 특성을 체계적으로 정리한 연구 결과는 대학, 대학원 및 연구자 교육과 대중 과학 홍보자료로 활용할 수 있다. 이를 통해 얼음 과학 및 저온 응용기술 분야의 전문 인력을 지속적으로 양성하고, 신진 연구자의 연구 진입 장벽을 낮추는 데 기여할 수 있다.

둘째, 본 과제는 얼음 화학 및 미세구조 연구라는 학문적 미개척 분야를 국내에서 선도하고, 관련 연구 영역을 환경과학, 재료과학, 에너지공학 등 자연과학 및 공학 전반으로 확장하는 데 이바지한다. 얼음 내 할로겐·금속 물질 순환, 생지화학 반응, 얼음 미세구조 제어에 관한 성과는 향후 심화 연구 및 대형 융합 연구 과제의 기초자료로 활용될 수 있으며, 얼음 과학 분야의 장기적 학문 성장을 견인할 것으로 기대된다.

셋째, 얼음에서 일어나는 화학반응과 미세구조 변화에 대한 이해는 극지방 자연환경과 기후변화 해석에 중요한 과학적 근거를 제공한다. 본 연구에서 축적된 실험 및 현장 연구 결과는 해빙에 따른 환경변화, 극지 대기·해양 화학 반응, 기후 변화 예측 모델의 정확도 향상에 기여할 수 있다. 또한 연구 성과를 국제 학술대회 및 관련 국제기구와 공유함으로써, 환경 정책 수립과 국제 협력 연구에 필요한 과학적 근거 자료로 활용될 수 있을 것이다.

넷째, 본 연구단계에서 개발된 얼음 미세구조 제어 기술과 동결농축 기반 정화 및 소재 기술은 실용화 가능성이 높은 응용 성과로써 활용될 수 있다. 동결농축효과를 이용한 저온 수처리·정화 기술은 기존 고에너지 공정을 대체하거나 보완할 수 있는 친환경 기술로 확장 가능하며, 얼음의 특이한 반응 환경을 활용한 전도성 고분자 및 3차원 나노구조 환경·에너지 소재는 시제품 제작 및 성능 평가를 통해 산업 적용 가능성을 검증하였다. 향후 이러한 기술은 환경 정화, 에너지 소재, 고부가가치 소재 분야의 기업과 연계하여 기술이전 및 공동 개발 형태로 실용화가 가능할 것으로 기대된다.

마지막으로, 본 과제를 통해 구축된 저온 실험 인프라와 분석 플랫폼은 얼음 화학 연구뿐만 아니라 저온 환경 과학, 재료 공정, 에너지 응용 연구 등 다양한 분야에서 공동 활용이 가능하다. 이는 극지연구소 내·외부 연구자 간 협력 연구를 촉진하고, 국가 차원의 저온 과학·기술 연구 역량을 강화하는 공용 연구 자산으로 기능할 것이다. 본 연구에서 축적된 기술과 경험은 향

KOPRI 극지연구소

후 후속 연구 및 산업 연계 과제의 출발점으로 활용되어, 지속 가능한 연구·기술 확산 구조를 형성할 것으로 기대된다.

KOPRI
극지연구소

# 제 6 장

# 연구개발과정에서 수집한 해외과학기술정보

이 장에서는 연구개발과정에서 방문한 얼음 관련 연구 기관 및 참가한 얼음 관련 학회에 관한 정보를 기술하였다.

## 제 1 절. 일본 홋카이도 대학교 저온과학연구소(Institute of Low Temperature Science, Hokkaido University)

일본 홋카이도 대학교 부속 저온 과학 연구소(ILTS, Institute of Low Temperature Science)는 빙권에서 발생하는 다양한 자연 현상에 대한 학제 간 연구를 위해 1941년 설립됨. 2022년에는 물·물질 순환 부문, 설빙 신영역 부문, 생물 환경 부문에서의 연구를 진행하며 환-오호츠크 관측 연구 센터와 공동연구 추진부를 운영 중임.

KOPRI 극지연구소

### 1. 저온과학연구소 조직 구성

○ 공동연구부(Joint Research Division)
- 남극해양-빙상-해빙결합시스템(Antarctic Coupled Ocean-Ice System)
- 그린란드 환경변화 (Environmental changes in Greenland)
- 메조스코픽 설빙계면과학 (Mesoscopic interface science of snow and ice)
- 한랭권 수목광 적응(Adaptation of evergreen trees to light environments in boreal regions)
- 환오호츠크 육해결합시스템 (Pan-Okhotsk land-ocean linkage)
- 우주저온물질진화 (Evolution of extraterrestrial materials at low temperatures)
- 국제 남극 연구소 프로그램(International Antarctic Institute Program)

○ 물·물질 순환 연구부(Water and Material Cycles Division)
- 해수, 해빙, 눈/얼음, 구름, 가스에 초점을 맞춘 대기 화학, 빙하학, 수문학, 물리 해양학, 해양 화학 및 지구 화학 등의 연구 수행

○ 설빙 신영역 연구부(Frontier Ice and Snow Science Division)
- 얼음 및 눈 과학을 바탕으로 행성 및 지면 현상에 대한 포괄적인 연구 수행

○ 생물 환경 연구부(Environmental Biology Division)
- 극한지 생물 다양성 분석과 생물체 적응 메커니즘 규명 등 극한 환경과 생물간의 상호 작용 연구

○ 환-오호츠크 관측 연구 센터 (Pan-Okhotsk Research Center)

- 환-오호츠크 지역(유라시아 대륙, 북태평양, 북극 지역 및 아열대 지역으로 둘러싸인 지역)과 전지구적 기후변화의 상호작용 평가

○ 기술부(Technical Division), 행정부(Administratie Office)

## 2. 저온과학연구소 주요 연구 현황

○ 물·물질 순환 연구부, 빙설 신영역 연구부, 생물 환경 연구부

○ 메조스코픽 설빙계면과학 (Mesoscopic interface science of snow and ice) 연구 부문 (Gen Sazaki 교수; 상전이 역학, Murata Ken-ichiro: 응축계 물리학)

○ 현재 저온과학연구소 내에 정규직 기준, 연구원은 40명/기술원 5명/행정인력 15명 정도, 계약직과 학생을 포함하여 100명 이상의 얼음 전문가를 보유. 규정상 박사과정생은 받을 수 없고 몇몇 교수들만 석사과정의 학생을 받을 수 있어 전체적인 연구 인력이 많지 않으나 연구분야의 선택과 집중으로 세계적인 연구성과를 창출하고 있음.

○ Gen Sazaki 연구팀에서 현재 진행중인 AFM(Atomic Force Microscope)을 사용한 얼음을 분자수준에서 관측하려는 시도는 얼음기초연구 및 저온장비 분야에 있어서 세계적인 수준을 달성함.

○ 저온과학연구소는 이미 PRIC(중), AWI(독) 등 여러 국외 기관과 협력을 하고 있으며, 몇십 년간 축적된 얼음의 기초연구 부분 및 저온연구를 위한 장비설계의 방대한 노하우를 보유함. 향후 연구자 교환프로그램을 통하여 협력분야 발굴 및 공동 연구 수행에 대한 필요성이 요구됨.

KOPRI 극지연구소

## 3. 저온과학연구소 연구실

○ 상전이역학 연구실

- 고해상도 광학현미경(자체개발)을 이용한 얼음 결정 표면의 분자 수준 관찰
- 얼음 결정의 바닥에서 생성되는 2종의 표면 액체상 발견
- 얼음 결정 형태의 비정형(불안정)에 대한 우주 실험 수행
- 자체적으로 개발한 온도조절 얼음결정 관찰 체임버 및 현미경 시스템을 통한 얼음 결정 성장 이미지 확인 가능. 얼음 결정 성장에 관한 물리적, 결정학적 실험 수행 (그림 1, 2)
- 극저온 (액체질소) 온도까지의 온도 조절이 가능한 얼음결정 성장 관측을 위한 체임버 셋업을 통한 얼음 결정의 초미세 구조 (원자 수준) 분석 (그림 3)
- 세계 최초로 얼음에서 동작하는 AFM(Atomic Force Microscope)을 개발하여 얼음 결정의 화학적 조건에 따른 물리 미세구조 분석 기법 보유



**그림 1.** 맞춤 제작된 온도조절 얼음결정 관찰 체임버 및 현미경 시스템

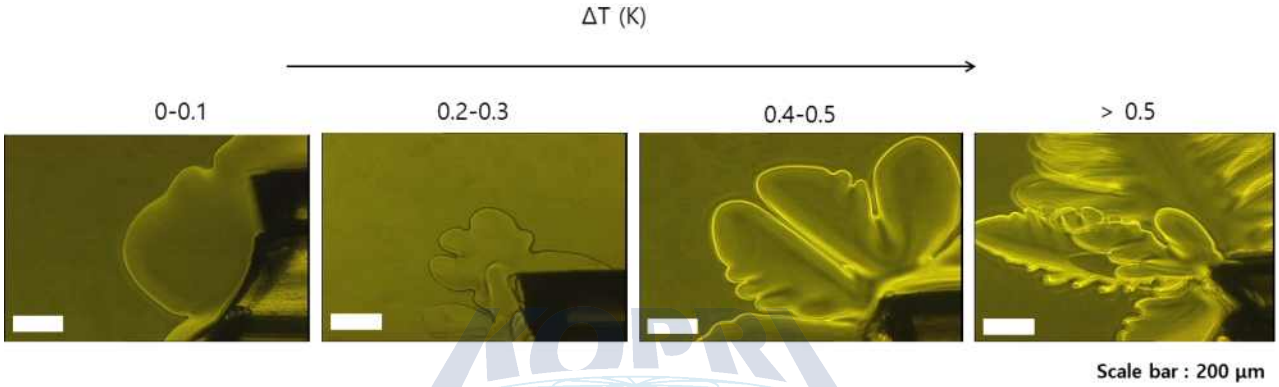



**그림 2.** 저온연구소 상전이역학 연구실 내 보유 현미경 및 얼음 성장 체임버를 이용한 얼음 결정 성장 확인

KBSI 극지연구소



**그림 3.** (좌) 온도 조절 및 극저온 온도에서 얼음결정 성장 관측을 위한 챔버 셋업, (우) Gen Sazaki 교수

# 제 2 절. 이탈리아 CNR-ISP (Consiglio Nazionale delle Ricerche - Istituto di Scienze Polari)

이탈리아 극지연구소(CNR-ISP)를 방문하여 연구 교류 및 IC-ICP-SFMS, ICP-MS 등의 기기를 활용하여 자연환경을 모사한 저농도 실험 및 분석을 수행하였음.

## 1. 이탈리아 CNR-ISP 연구소 소개

○ 이탈리아 국립연구기관(CNR)의 산하기관인 이탈리아 극지연구소(ISP)는 대기과학, 생명과학, 빙권 연구, 해양 연구 분야에서 극지 과학 연구를 수행하고 있음. 특히 빙권 분야에서는 빙하 연구를 통한 고기후 연구와 기후변화를 연구하고 있음. 눈과 얼음의 화학 성분 및 물리적 인자, 영구 동토층의 변화와 이들이 기후변화로 녹게 되었을 때의 대기, 생물, 수계에 대한 영향을 연구하고 있음.

## 2. 연구 교류 내용

○ 현재 극지연구소에서는 철과 할로겐 물질의 동결 산화환원반응과 관련하여 연구를 수행하고 있으며, UV/Vis spectrophotomter, ICP-OES, Ion chromatography, HPLC 등의 기기를 이용하여 철과 할로겐 물질을 분석하고 있지만 자연환경에 존재하는 정도의 극미량의 철 및 할로겐물질을 분석할 만큼 검출한계가 낮지 않음. 따라서 극지연구소에서는 현재 상대적으로 높은 농도의 철 및 할로겐 물질, 낮은 pH의 실험실 조건에서의 실험만 가능한 상황이며, 이는 자연환경을 반영한다고 말하기 어려움. 이탈리아 CNR-ISP 연구팀의 IC-ICP-SFMS와 ICP-MS를 공동 활용하여 더욱 자연환경에 가까운 실험 조건(낮은 농도의 철 및 할로겐 물질, 상대적으로 높은 pH)에서 실험을 수행하고 분석하고자 하였음. CNR-ISP의 Dr. Andrea Spolaor은 기존 공동 연구를 통해 극지방 할로겐 원소 관련하여 Nature communications에 함께 논문을 출간한 바 있음. 이번 공동 연구에서는 할로겐 종의 동결 산화환원반응 및 철 용출 반응을 수행, 분석 후 실험 분석 결과를 함께 논의하였으며, 기타 할로겐 물질 및 금속의 극지방 거동에 관해서도 논의함. 추후 연구할 오염물질의 동결 광화학 실험 및 극지방 수은 거동 실험에 대하여도 논의하였음.



**그림 1.** 베네치아 Ca' Foscari 대학 내 CNR-ISP 연구소 외부 전경

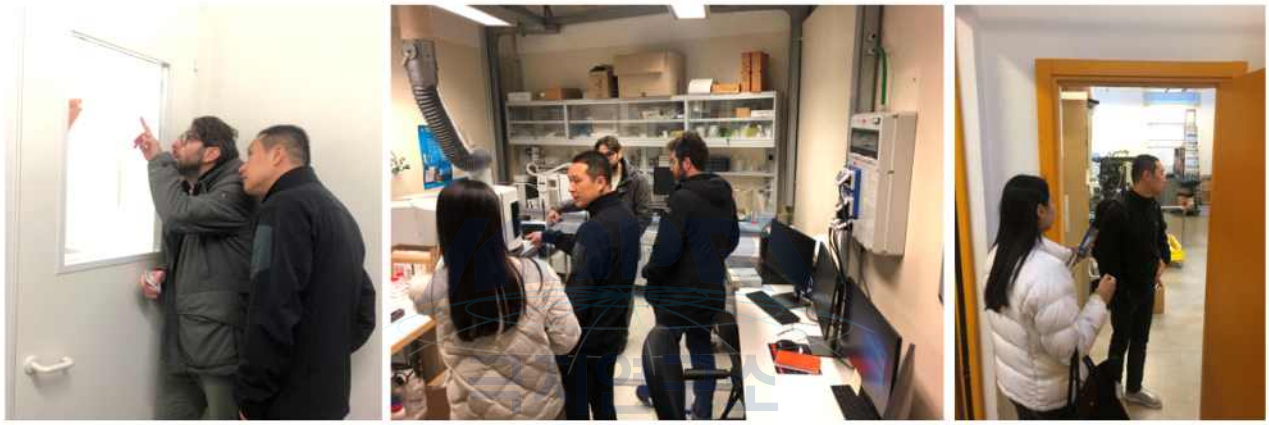


**그림 2.** CNR-ISP 연구소 내부 소개

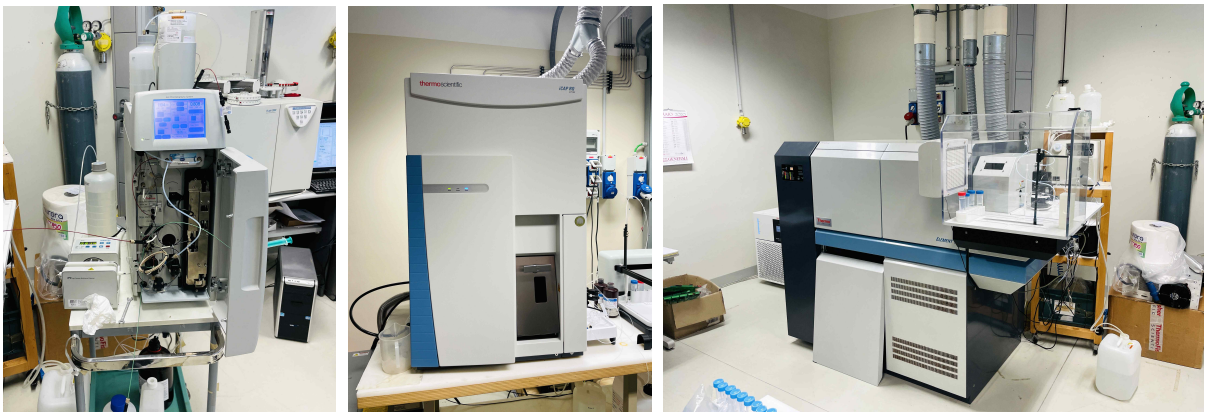


**그림 3.** 공동 연구에 활용된 IC, ICP-MS, ICP-SFMS 장비



**그림 4.** 연구 교류 세미나



**그림 5.** ICP-SFMS와 IC를 연결하여 저농도의 할로겐 화학종 분석

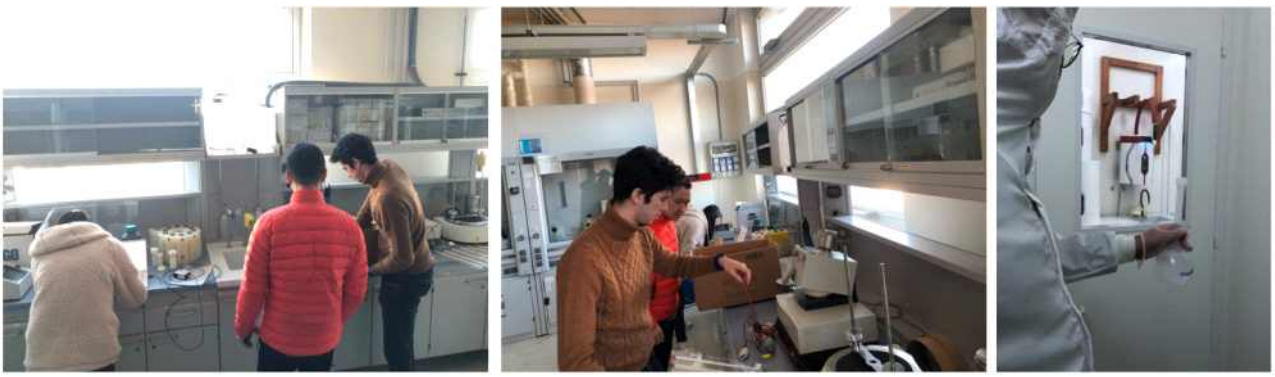


**그림 6.** 동결 광화학 실험 테스트

## 주 의

1. 이 보고서는 극지연구소에서 수행한 기본연구사업의 연구결과보고서입니다.

2. 이 보고서 내용을 발표할 때에는 반드시 극지연구소에서 수행한 기본연구사업의 연구결과임을 밝혀야 합니다.

3. 국가과학기술 기밀유지에 필요한 내용은 대외적으로 발표 또는 공개하여서는 안 됩니다.

KOPRI
극지연구소